Observations en infrarouge de disqus circumstallaires et d'exoplanètes

Eric Pantin

▶ **To cite this version:**

Eric Pantin. Observations en infrarouge de disqus circumstallaires et d'exoplanètes. Astrophysique [astro-ph]. Université Paris-Diderot - Paris VII, 2010. tel-00553645

HAL Id: tel-00553645
https://theses.hal.science/tel-00553645

Submitted on 7 Jan 2011

HAL is a multi-disciplinary open access archive for the deposit and dissemination of scientific research documents, whether they are published or not. The documents may come from teaching and research institutions in France or abroad, or from public or private research centers.

L'archive ouverte pluridisciplinaire **HAL**, est destinée au dépôt et à la diffusion de documents scientifiques de niveau recherche, publiés ou non, émanant des établissements d'enseignement et de recherche français ou étrangers, des laboratoires publics ou privés.

HABILITATION A DIRIGER DES RECHERCHES

Présentée par

Eric Pantin

Observations en infrarouge de disques circumstellaires et d'exoplanètes

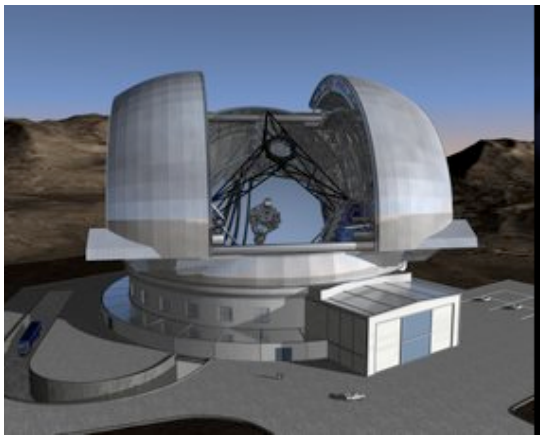

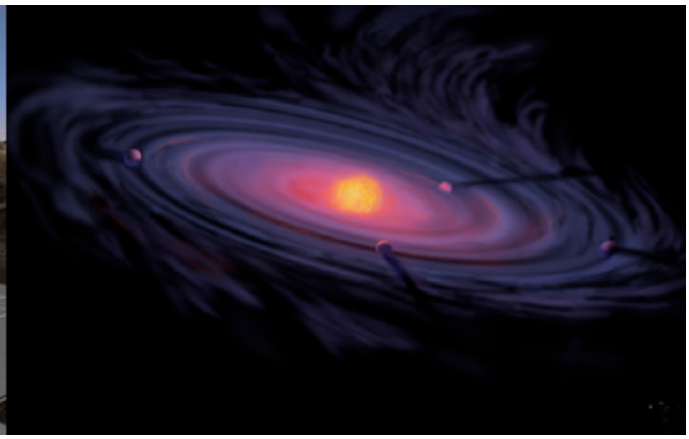

Soumise aux rapporteurs le 28 août 2009
Soutenue le 12 Novembre 2010 devant le jury composé de :

Marcello Fulchignoni	Président et rapporteur interne
Bradford Smith	Rapporteur
Charles Telesco	Rapporteur
Cécile Ferrari	Examinateur
André Brahic	Examinateur
Pierre-Olivier Lagage	Examinateur
François Ménard	Examinateur

Commissariat à l'énergie atomique – Centre de Saclay
Institut de recherche sur les lois fondamentales de l'Univers
Service d'astrophysique

Acknowledgements

The process that leads to the defense of an "Habilitation à diriger des recherches" is long and requires the gathering of several favorable conditions.
This cannot be achieved without a strong support from different parties. First, I would like to warmly thank Marcello, Bradford and Charlie for having accepted to referee this work. I am particularly grateful to Bradford and Charlie who have accepted to travel overseas for the defense. I consider Bradford and Charlie as spiritual fathers; indeed both of them have been pioneers in the fields I am currently working in. Bradford has imaged for the first time ever a debris disk (β Pictoris); Charlie has both worked on imaging in of circumstellar disks in the mid-infrared range and developing the mid-infrared instrumentation from the ground. I am also deeply indebted to all the members of the jury for having accepted to be examinators of this HDR and participate to the defense: Cécile Ferrari, François Ménard, Pierre-Olivier Lagage, and André Brahic. I thank the Service and d'Astrophysique and Pierre-Olivier Lagage its head, for having promoted and supported this research work and field over almost 20 years. Pierre-Oliviers's critical eye was always of great help to push ahead and make progress. Finally, all this work could not have been achieved without a constant and steadfast support from my wife and my children.

Contents

List of Tables

List of Figures

Originalty of the work: a transversal approach of infrared astronomy in the context of planetary formation and evolution

The availability of bi-dimensional infrared detectors (5-20 μm) at the beginning of the 90's has offered the possibility to achieve high angular resolution mid-infrared astronomy from the ground on large telescopes. It was a totally new "toolbox" for the astronomers which is particularly well adapted to study circumstellar material and moderately embedded object at a sub-arcsec scale. It is thus a precious source of informations in the context of exoplanetary systems formation and evolution.

My work in astronomy is closely linked to the mid-infrared imaging instrumentation and its application in the context of planetary formation and evolution. I have started this work during my Ph.D thesis by observing the inner parts (10-200 AU) of the β Pictoris debris disk. The debris disks are believed to be second generation, re-generated dusty disks, that result from giant collisions of planetesimals. For this study I have developed a new radiative transfer model in which the chemical composition (mixture of silicates, ice mantle), the particles sizes, and shapes (porous particles) were constrained ([Pantin et al., 1997]). In parallel, the need of the best angular resolution (limited by the diffraction on 4m class telescopes), and the relatively low signal-to-noise achieved in mid-infrared range data (limited by the background thermal noise) have entailed the development of a new algorithm of image deconvolution adapted to the specificities of mid-infrared data and based on a multiresolution approach to efficiently reject the noise ([Pantin and Starck, 1996]). On top of that given the fact that the β Pictoris disk is observed edge-on, I also developed a deprojection method. This method was necessary to reconstruct the radial density structure of the disk and then highlight the presence of an inner void of matter also as some rings of higher density probably linked to massive exoplanetary companions ([Lagage and Pantin, 1994]).

In the following years, I have extended this approach in a transversal work between mid-infrared observations in a context of planet formation, the development of new tools to extract the information from these data, and some physical models to interpret the observations. These observations were based on data mainly collected with CAMIRAS on the CFHT and VISIR, the VLT Imager and spectrometer. The observations have focused on younger systems i.e. protoplanetary disks around intermediate mass (3-6 $M_\odot$) Herbig Ae stars. The main scientific results are the following:

- A ring of emission at 20 μm discovered at a distance of ∼250 AU from AB Auriga and interpreted as a "wall-like" structure in the disk in direct wiev of the star and potentially created by an unseen

yet massive companion. By making a geometric analysis of this peculiar emission and for the first time, the thickness of an Herbig Ae protoplanetary disk could be evaluated ([Pantin et al., 2005]).

- 3 resolved disks at 20 μm(HD135344, HD163296 and CQ Tau); these observations provided to us tight constraints on the extent (outer radii) of these disks ([Doucet et al., 2006b]).

- A spatially well resolved disk around HD97048. The analysis of the image allowed to well constrain the disk geometry (flared surface) and for the first time to precisely estimate the flaring index ([Lagage et al., 2006]). A direct consequence is also the presence of large amounts of gas in a disk aged of about 3 Myr.

- An intermediate-stage (transition) disk observed around HD95881 having a flat dusty part and a flared gasesous part. This disk could be at a transition stage the geometrically/optically very thick less evolved disks and the debris disks ([Verhoeff et al., 2009]).

On top of that I have also strongly strengthened my experience in mid-infrared instrumentation. First as the VISIR instrument scientist I have followed the building of the instrument and was in charge of the commissioning phase in Europe and then on the VLT in Chile. During this phase, I have evaluated the performances of the VISIR instrument (sensitivity, angular resolution, stability), studied its characteristics, proposed some methods to some spurious features that would otherwise degrade the performances (e.g. the detector striping), and was one of the promotors of the new fast imaging observing mode (the "burst mode").

One of the main challenges for the astronomy of the next decade will be the detection and the characterization of exoplanets. As a co-investigator on the E-ELT/METIS project I work now on the development of high angular resolution new mid-infrared observing modes that will allow to tackle this challenge. These two modes are the phase mask coronography and the differential imaging. They have been identified as the best suited modes to detect and characterize exoplanets in the mid-infrared range on next generation Extremely Large Telescopes such as the ESO E-ELT. These modes are not only extremely absolutely mandatory to avoid any desastrous detector responses to bright stars but is also very promising to observe the direct proper emission from self-luminous giant exoplanets placed on intermediate orbits (10-50 AU). This mode will also provide to METIS instrument an interesting niche: the direct imaging observation of irradiated giant exoplanets placed on relatively close orbits in the range 0.1-1 AU. My work is currently and will be in the coming years focused on:

1. the optimization of these modes by performing state-of-art numerical simulations of observations,

2. the development of the associated devices (phase mask coronograph, dual band detectors) that will allow their implementation into the forthcoming mid-infrared instruments such as METIS.

Students supervision

Along this tranversal work at the interface between the mid-infrared instrumentation, the associated observations, the high-level data improvement, and the physical modeling, I has also supervised the work of several students in these fields :

2003-2007	Ph.D	Coralie Doucet (3 refereed papers published and several communications) Protoplanetary disks around intermedaite-mass stars: the assets of mid-infrared imaging
03/04-07/04	Master	Médéric Boquiem Dynamic and photometric of a post-planetary disk
03/06-08/06	Master	Pierrick François Blind deconvolution applied to mid-infrared images
03/07-07/07	Master	Damien Borel Search for disks in mid-infrared imaging data
05/07-08/07	Master	Julien Wengler Radiative transfert applied to circumstellar disks
05/09-07/09	Master	Justine Ibanez Exploitation of burst mode VISIR data obtained on circumstellar disks
06/09-07/09	Master	François Lamare Simulations of performances of the ELT/METIS instrument in the field of exoplanets

Outreach

In addition I consider that, as a researcher, the task of making outreach for the non experts is also an important aspect of our work. I have thus proposed and made several "general public" conferences in the field of planetary formation in the last 3 years in the framework of various amators astronomical conferences.

2006-2007	Conferences at the "Festival d'astronomie de Fleurance" on comets, circumstellar disks and planetary formation
2006	Conferences at the "Festival de Haute Maurienne" on circumstellar disks and planetary formation
2008	Conferences at the "Festival d'astronomie Astro-Gard" on circumstellar disks and planetary formation

Curriculum Vitae

Eric PANTIN **Curriculum Vitae**

Astronomer Ph.D in astrophysics
B.A. in Pedagogy/Educational Sciences

Current Employment

July 1998- Permanent position, Service d'Astrophysique CE Saclay, France

Mid-infrared astronomer:

– dynamics and emission of circumstellar discs around main-sequence and pre-main-sequence stars;
– signal processing and inverse problems in physics, filtering and deconvolution of images

Mid-infrared instrumentation astronomer:

– French Co-investigator for the ELT project METIS
– Instrument scientist for the VLT/VISIR project

Diploma

2009	Under completion : **Habilitation de l'université (Paris VII)**, speciality Astrophysics. Will be defended fall 2009. Subject : *Mid-infrared observations of circumstellar disks and exoplanets.*
1996	**Doctorat de l'Université en Sciences Physique (Ph.D.**, speciality Astrophysics. Thesis defended on May 20, 1996 at the University of Paris XI (highest distinction, equ. Summa cum laude). Subject : *Study of the β Pictoris dust disk : Deconvolution of 10 μm images and modeling of the disk emission.*, conducted at the Service d'Astrophysique of CE Saclay, Gif-sur-Yvette, FRANCE.
1992	**Master of Science in Solid State Physics** at the University of Paris VI.
1991	**Master in Signal Processing, Master in Astrophysics** at the University of Paris XI (distinction : good).
1990	**Agrégation de physique** (equ. to B.A. in Pedagogy/Educational Sciences), in applied physics. Rank : 2$^{\text{nd}}$.
1987-91	Schooling at the "Ecole Normale supérieure de Cachan", superior school for the training of professors and researchers, in parallel with physics studies at the university.

Professional experience

Responsabilities

2008-	Co-Investigator for the European ELT/METIS project in charge of the coronography, calibration and detector packages
2004-2005	Commissionning scientist for the VLT/VISIR instrument at ESO Chile
2003-	Instrument scientist of the VLT/VISIR instrument Calibration, data reduction, scientific return

Teaching

1990-96	Oral interrogations in physics in "classes mathematiques superieures" (preparation for entering engineering schools)
1991-92	Lectures in mathematics at technician school level
1992-93	Practical work classes in plasma physics at Paris XI University
1993-95	Lectures in electromagnetism at University of Paris XI
1995-96	A.T.E.R. (1 year contract as teacher and researcher) at University of Paris VI : lectures and practical work classes in electronics, electrotechnics, physics, and automatics.
2001-03	Oral examinations for entering the Ecole Polytechnique
2000-02	Lectures in signal and images processing at the Master in Astrophysics, University of Paris VII
2003-05	Lectures in signal and images processing at the Ecole Supérieure d'Informatique, Electronique, Automatique (Paris)
2005-08	Lectures in signal and images processing at the Master of photodetection, University of Paris VII
2005-08	Lectures on detectors for the mid-infrared range at the Master of photodetection, University of Paris VII

Others

- Referee for *Astronomy and Astrophysics*
- Referee for *Astrophysical Journal*
- Referee for *Icarus*
- Coordinator of the imaging observing program of protoplanetary disks for the JWST/MIRI instrument
- PI of approved observing programs on the La Silla, CFHT, VLT telescopes

Research Experience

July 1988	Training period (2 months) : use of the LEDA database to study the Malmquist bias in the case of galaxies distances Lyon observatory (France), under supervision of G.Paturel
August 1989	Training period (3 months) : use of the LEDA database to compute the correlation of different magnitudes standards Lyon observatory (France), under supervision of G.Paturel
May-July 1991	Training period (3 months) : study of various reading modes for the CCD on board the XMM satellite, Service d'Astrophysique, CE Saclay
1992-93	Military service in a military research institute (E.T.C.A., France) work on the Modeling of the blooming of a CCD due to a moderately powerful laser
1992-96	**Ph.D in astrophysics** on the subject : *Study of the β Pictoris dust disk : Deconvolution of 10 μm images and modeling of the disk emission*, Service d'Astrophysique, CE Saclay, Gif-sur-Yvette, FRANCE
1996-97	**Post-Doctorate** : fellowship at the European Southern Observatory (Chile) in charge of the mid-infrared instrument TIMMI (Instrument Scientist); support astronomer for the adaptive optics system ADONIS
1997-98	**Post-Doctorate** : fellowship the Catholic University of Leuven (Belgium) : Processing and interpretation of spectrometric data obtained with the ISO (Infrared Space Observatory) satellite
1998-	**Permanent astronomer** position at the Service d'Astrophysique of CE Saclay, assigned to the VISIR (Vlt Infrared and Spectrometer for the InfraRed) project
1993-	Several observing runs on telescopes : 3.6m, NTT La Silla (Chile, ESO), NOT (Canarias, Spain), CFHT telescope (Hawaii)

Outreach

2006-2007	Conferences at the "Festival d'astronomie de Fleurance" on comets, circumstellar disks
2006	Conferences at the "Festival de Haute Maurienne" on circumstellar disks
2008	Conferences at the "Festival d'astronomie Astro-Gard" on circumstellar disks

Students supervised

2003-2007	Ph.D	Coralie Doucet (3 refereed papers published and several communications) Protoplanetary disks around intermedaite-mass stars: the assets of mid-infrared imaging
03/04-07/04	Master	Médéric Boquiem Dynamic and photometric of a post-planetary disk
03/06-08/06	Master	Pierrick Franois Blind deconvolution applied to mid-infrared images
03/07-07/07	Master	Damien Borel Search for disks in mid-infrared imaging data
05/07-08/07	Master	Julien Wengler Radiative transfert applied to circumstellar disks
05/09-07/09	Master	Justine Ibanez Exploitation of burst mode VISIR data obtained on circumstellar disks
06/09-07/09	Master	Francois Lamare Simulations of performances of the ELT/METIS instrument in the field of exoplanets

Publications

see separate annex "Bibliography"

Other informations

Computer Languages : Fortran 77 and 90
C et C++
IDL (Interactive Data Language)
MATLAB (Matrix Laboratory)

Foreign Languages: English (written and spoken),
Spanish (written and spoken, fluent)

Leisure: Sports : Tennis (competition, regional ranked), nanbudo (1^{st} dan),
rock climbing, running, scubadiving (dive master).
Music : classical, jazz : piano and saxophone

Introduction

Ce manuscrit d'habilitation à diriger des recherches décrit mes travaux scientifiques sur 10 ans dans les domaines de l'instrumentation en infrarouge moyen (8-20 μm) depuis le sol et des observations associées. Ces longueurs d'ondes apportent de précieuses informations, souvent impossibles à obtenir à d'autres longueurs d'ondes, sur la nature de certains objects astrophysiques. La possibilité qui nous est offerte, depuis les années 90 et l'apparition de détecteurs bi-dimensionnels, d'observer à ces longueurs d'ondes sur les grands telescopes avec des résolutions de l'ordre de 0.5 arcsec, est un atout majeur pour étudier la structure nature d'objets relativement compacts tels que les disques circumstellaires. Ce manuscrit illustre ce point grâce à de nombreux exemples d'observations d'objets entourés de, ou enfouis dans, les poussières.
Dans le chapitre 1 je décris les difficultés et la technicité de l'observation en infrarouge moyen depuis le sol. Dans le chapitre 2 je décris en détails l'instrument infrarouge moyen VISIR que le CEA/DAPNIA a construit pour le VLT. J'y détaille ma contribution au projet ainsi que les différents problèmes rencontrés. Dans le chapitre 3 je fais le bilan du projet VISIR et des observations associées grâce à une expérience acquise sur 4 ans. Je montre que les performances de l'instrument ne sont pas tout à fait celles attendues et propose une série d'analyses pour en comprendre l'origine. Dans le chapitre 4 je décris les résultats des principaux programmes scientifiques que nous avons menés avec les instruments CAMIRAS et VISIR dans le domaine des disques protoplanétaires et de la formation planétaire. Ce chapitre est suivi d'un chapitre 5 qui décrit des résultats scientifiques que j'ai obtenus sur des companions de faible masse en lien avec la formation planétaire. Finalement, je montre dans le chapitre 6 les potentialités des observations en infrarouge moyen depuis le sol sur la prochaine génération de télescopes géants (ELTs) de la gamme 30-42 m. Lors de la prochaine décade, l'astronomie fera très probablement un bond spectaculaire dans le domaine de l'étude des planètes extra-solaires. Les observations en infrarouge moyen apporteront des informations précieuses concernant leur caractérisation. Tout d'abord une information directe par l'imagerie de ces planètes à des longueurs d'ondes auxquelles elles émettent leur maximum de flux propre. Deuxièmement, une information sur leur environnement et plus précisément la présence de disques exo-zodicaux. Je montre que l'instrument E-ELT/METIS apportera des informations cruciales pour la sélection des étoiles cibles pour les expériences DARWIN ou TPF-I.

This manuscript describes my scientific work over the last 10 years in the domain of instrumentation in the mid-infrared range from the ground and associated observations. These wavelength provide some valuable and unique informations on the nature of certain categories of astrophysical objects. Since the 1990's and the avent of bi-dimentional detector we have the possibility of collecting data at high angular, sub-arcsec, resolution on large telescopes. This is of major interested to study the structure of relatively compact objects such as e.g. circumstellar disks. In this manuscript I illustrate this by numerous examples of observations of objects composed of or embedded in dust.
In chapter 1 I show the complexity of the observations in the mid-infrared range from the ground. In chapter 2 I describe in details the mid-infrared instrument VISIR that the CEA/DAPNIA has built for the ESO/VLT telescope. I list my contribution to the project also as the various problem encountered. In chapter 3 I try to draw the essence of the VISIR project and the associated observations we have performed over 4 years. I show that the performances of the instrument differ from those expected and I propose a set of analysis to understand this. In chapter 4 I describe the results of the main scientific programs that we have conducted using the CAMIRAS and the VISIR mid-infrared instruments in the fields of protoplanetary disks and planetary formation. This chapter is followed by by the chapter 5 in which the results I have obtained in the domain of low-mass companions in the framework of planetary formation are displayed. Finally I show in chapter 6 the potentialities brought by mid-infrared observations from the ground on giant (30-42m) next generation telescopes (ELTs). The next decade will probably rich in discoveries and major steps in the field of extra-solar planets. Mid-infrared observations of these exo-planets will bring valuable informations concerning their characterization. First, we will collect direct informations by direct imaging in a wavelength range where the maximum of their thermal emission is produced. Second we will obtain some informations concerning their planetary environment and more precisely the presence of exo-zodical disks will be assessed with a good accuracy. In the context of the DARWIN and TPF-I projects that will search for bio-markers, the capabilities of E-ELT/METIS instrument will be crucial for target selection.

Part I

Mid-infrared instrumentation

Chapter 1

Observing from the ground in the mid-infrared range

Résumé

Les observations en infrarouge moyen aux longueurs d'ondes les plus grandes possibles sur un télescope optique au sol, bénéficient des tailles de plus en plus importantes des télescopes géants pour offrir à leurs utilisateurs des performances de plus en plus bonnes en termes de résolution angulaire. Cependant, les observations en infrarouge moyen depuis le sol sont 1) limitées en couverture de longueurs d'onde par les fentres atmosphériques 2) relativement limitées en sensibilité par comparaison avec celles obtenues depuis l'espace. J'explique dans un premier temps les raisons pour lesquelles les observations depuis le sol sont limités en sensibilité. Je décris ensuite les techniques d'observations employées pour annuler le fond important inhérent aux observations depuis le sol. Je montre finalement que les observations depuis le sol et celles obtenues par les observatoires spatiaux sont complémentaires.

Abstract

The observations in the mid-infrared range, the longest wavelength at which we observe with optical telescopes from the ground, beneficiate largely from the growing size of the giant telescopes to provide the users with data at high angular resolution. However the observations in the mid-infrared range from the ground are 1) limited in wavelength by the atmospheric windows 2) relatively limited in sensitivity when compared to space-born ones. I first explain the physical reasons why these observations are limited in sensitivity. I describe then the observational techniques used to cancel the huge background the observations from the ground deal with. I finally show that the mid-infrared observations from the ground and those obtained by the spatial satellites are complementary.

Contents

The average temperature of the Earth's atmosphere is about 260 K. The atmosphere emits thus a maximum of thermal emission in the range 10-20 μm precisely in the range of wavelength we deal with. The thermal infrared background, is a Planck function (blackbody) modulated by the atmosphere characteristics of absorption/emission depending on the wavelength. This transmission is mainly defined by the principal components such as oxygen, carbon dioxide, water vapor or ozone. The suite of lines of these molecules creates a pseudo-continuum at low spectral resolution (see Fig. 1.1). However, some "holes" in this continuum are found and define the astronomical atmospheric observing windows (or bands) named L(2.8-4.2 μm), M(4.4-5.8 μm), N(8-13.5 μm), Q (16.5-28 μm). In the following, we will focus on the N and Q bands exclusively because they are accessible to VISIR. The Q band is actually a set of narrow windows which peak transmission decreases with the wavelength. Thus the Q band filters need to be matched to the shape of these sub-bands. In a moderately good observing site (precipitable water vapor (PWV) in the range [1-5] mm), Q band observations can hardly be performed beyond the 24.5 μm sub-band. In a very dry site (at higher altitudes, e.g. Mauna Kea (Hawaii, U.S.A.), Cerro Macon (Argentina) or Chajnantor (Chile), the peak transmissions are higher which in principle allows to go up to 30 μm(Fig.1.2). Within the atmospheric windows, the atmospheric transmission can be as high as 99% around 11 μm, but reaches very low levels (10^{-5}) at 15 μm. At a level of transmission of 99%, the amount of atmospheric background flux becomes negligible against telescope proper emission which behaves as a grey body at a temperature of 280 K with an emissivity in the range 5-10%.

The third component of the external background is the entrance window which is generally designed to produce an emission negligible against the atmosphere and telescope ones. In the particular case of VISIR, the choice of a unique entrance window (by opposition to exchangeable one) leads to a trade-off in which its emission in Q band is larger than that of the telescope although lower than the atmospheric one. The instrument itself produces it own (internal) infrared background. This proper emission is lowered to negligible levels thanks to the use of cryogenically cooled optics and baffling. The detector itself needs to be cooled down toabout 6 K to maintain the dark current at acceptable levels. When the detector delivers data which noise is dominated by the background(s) shot-noise, one reaches BLIP performances (Background LImited Performances) which any observing instrument should aim at.

Fig.1.3 shows the emission spectra of the different components cited above. It should be also noted that the sky and telescope background should produce flat structures in the focal plane, while the entrance window can produce structures at low spatial frequencies (see Sec.3.3).

Any mid-infrared astronomer needs to have a reasonably good model of the different background emissions in his toolbox. If the emission of the telescope and the entrance window are relatively simple to model (although one needs a quite precise table of transmission of the substrate the entrance window is made of), the modeling of the atmospheric transmission requires the use of advanced radiative transfer codes which take into account not only the relative content of species (e.g. such as water) but also the altitude, the pressure and the temperature profiles of the zenithal angle (or airmass). Several numerical codes exist on the market among which the ATRAN commercial model (and the associated HITRAN database of species) is widely used and serves as "reference" [Lord, 1992, Rothman et al., 1992]. I have chosen the freeware RFM code [Dudhia, A., 2005] which is slightly less flexible than ATRAN but uses the same HITRAN database. One of the limitations is the relatively narrow wavelength range the code is able to handle but this limitation can be overcome by using a macro (e.g. written in the IDL high level langage) which divides a large wavelength interval into a set of small ones that RFM can handle. Modern multiple CPUs workstation allow then to perform parallel computations and produce results in

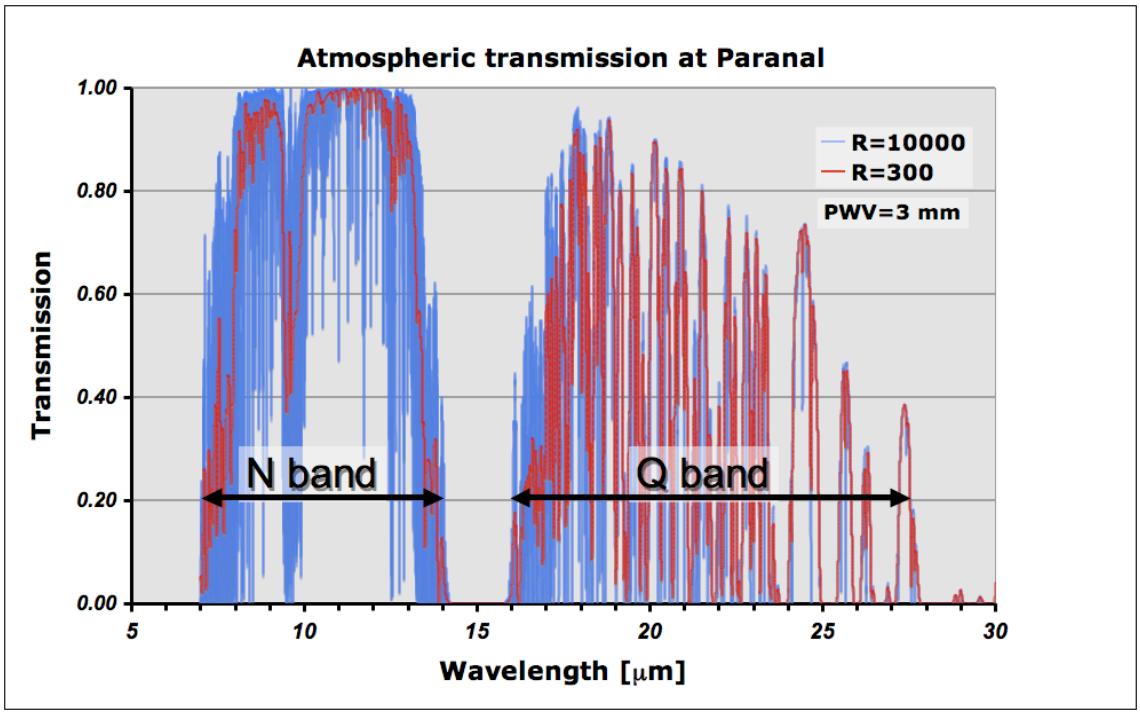

Figure 1.1: Plot of the mid-infrared atmospheric transmission at low and high spectral resolutions. At low spectral resolution the pseudo-continuum defines the N and Q windows. The amount of precipitable water content (PWV) has been set to 3 mm which is typical of a moderately dry site such as Paranal.

a reasonable amount of CPU time. In the RFM model, the water vapor content, the zenithal distance, the altitude, and the temperature profile are input parameters. This allows for instance to study the influence of each of the parameters on the output transmission. Concerning the site of Paranal where VISIR is installed, I assumed a U.S. standard model of sub-tropical atmosphere.

1.1 Why observing with large telescopes ?

1.1.1 Sensitivity

The number of photons produced by the atmospheric infrared background is around 1500 Jy/arcsec^2 in the N band, and 5000 Jy/arcsec^2 in the Q band (see Fig.1.3). It increases proportionally to square of telescope diameter D^2. The number of photons emitted by an astrophysical source and collected by a telescope growths also as D^2. One would then naively deduce that there is no point to observe in the mid-infrared range with large telescopes. However, the achieved spatial resolution makes a crucial difference. In the mid-infrared range and for telescope sizes up to ∼8m (in the best observing sites), the angular resolution is determined by the diffraction limit (whereas fixed by the atmospheric turbulence ("seeing") in the visible/near-infrared). Since the diffraction limited angular resolution depends inversely to the telescope diameter, an instrument which complies with Nyquist principle of sampling (i.e. the pixel size is adapted to the angular resolution) must have a pixel field of view which is inversely proportional to the square of the telescope diameter (pfov$\propto \lambda/(D^2)$, λ: wavelength of observation, D: telescope diameter), at the risk of losing spatial information otherwise. Since the telescope background (in W/Hz/arcsec^2)

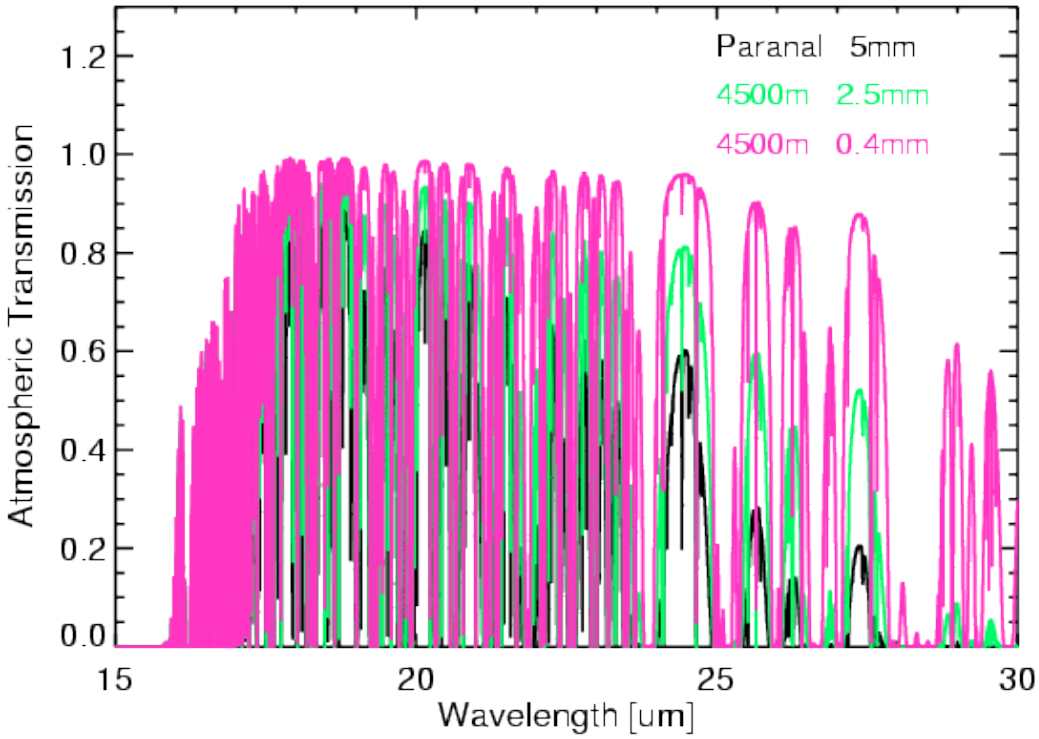

Figure 1.2: Dependence of atmospheric transmission in Q band as a function of the PWV content. The peak transmission of the sub-bands beyond 20 µm directly depends on the PWV value. At a very dry site (PWV = 0.4 mm) it is possible to observe up to wavelength of ∼30 µm

scales with the telescope diameter, an instrument Nyquist sampled (adapted) collects a constant number of photons per pixel whatever the telescope size is. On the other hand, an imaged point source always covers the same number of pixels on an adapted sampling detector, for a number of collected photons which scales with D^2. As a result, the point source sensitivity also scales with D^2. At the other edge for a pure flat extended source (e.g. an homogeneous galactic cirrus, extended background emission of galaxies), this property does not apply. The number of pixels covered increases as D^2 and the resulting signal-to-noise ratio stays constant no matter how large is the telescope. This domains stays the reserved property of cooled space born telescopes. Extended astronomical sources a often actually a mixture of relatively flat underlying emission and some structuring at higher (intermediate) spatial frequencies on top which reflect the auto-similarity of physical processes at work (e.g. turbulence). In this case, the instrument sensitivity will improve of larger telescopes, but not as much as in the case of point sources.

1.1.2 Angular resolution

Visible and near-infrared instruments are seeing-limited which means that their angular resolution is not determined by the size of the telescope but by the turbulence of the atmosphere (seeing). Mid-infrared observations on telescopes smaller than ∼8 m are not only diffraction-limited because the diffraction dominates the seeing, but also because the seeing decreases at longer wavelength. At visible wavelength, the Fried parameter r_o which represents the length-scale over which the turbulence becomes supersedes

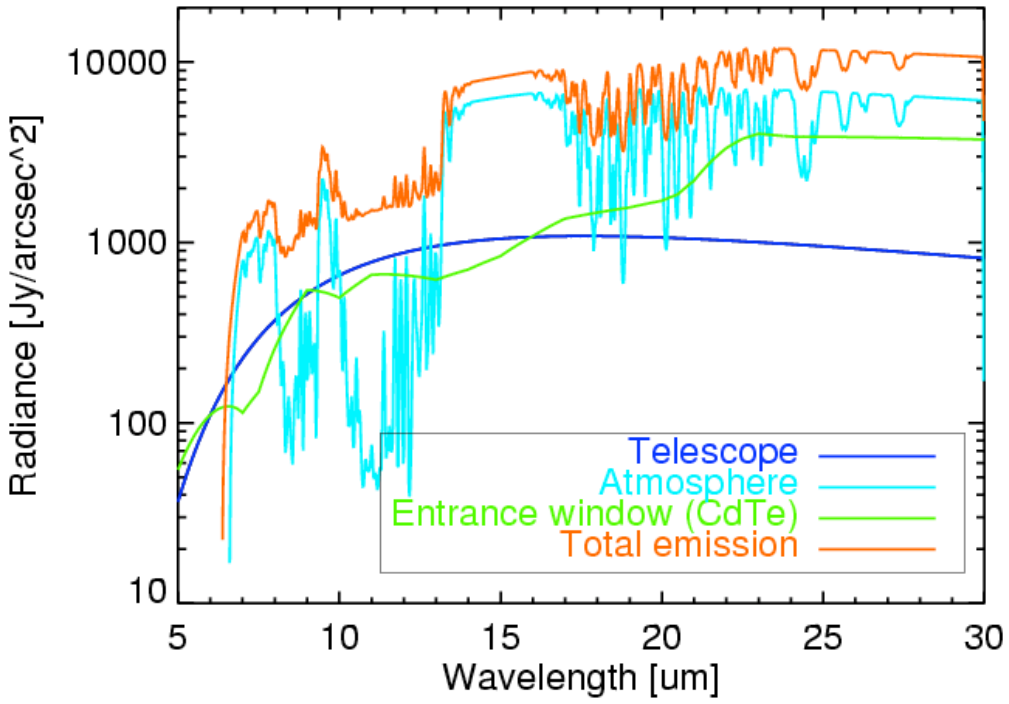

Figure 1.3: Plot of the different contributions to the mid-infrared background when observing from on ground-based facilities.

the diffraction. It is in the range [10-20] cm depending on the level of turbulence above the observing site. In the classical Kolmogorov cascade model the Fried parameter scales with the wavelength as $r_o \propto \lambda^{6/5}$. Consequently the angular resolution of seeing-limited observations $\alpha = \lambda/r_o$ scales with the wavelength as $\lambda^{-1/5}$.

Figures 1.4 compares the angular resolutions in the mid-infrared range that we currently, or we will in the next 5 years, achieve. Once the JWST will be launched and operational the current mid-infrared facilities on ground-based 8 m class telescopes will probably be hardly competitive any longer. Hence the need for larger telescopes such as ELTs that will achieve angular resolutions 5 times better.

1.2 Constraints on the design of mid-infrared means of observation

Mid-infrared observations from the ground are technically difficult because of the high level of background one deals with (see above). It is however possible to partially reduce the thermal infrared background by making a careful design of the instrument. First, the close environment of the detector shall be cooled to sufficiently low temperatures so that the optical elements also as the opto-mechanical elements that the detector "sees" produce a flux which is negligible against the background flux coming from the atmosphere and the telescope. A mid-infrared instrument must be cryogenically cooled to temperatures in the range 30-50 K, depending on the type of observation that must be made (imaging, spectroscopy)

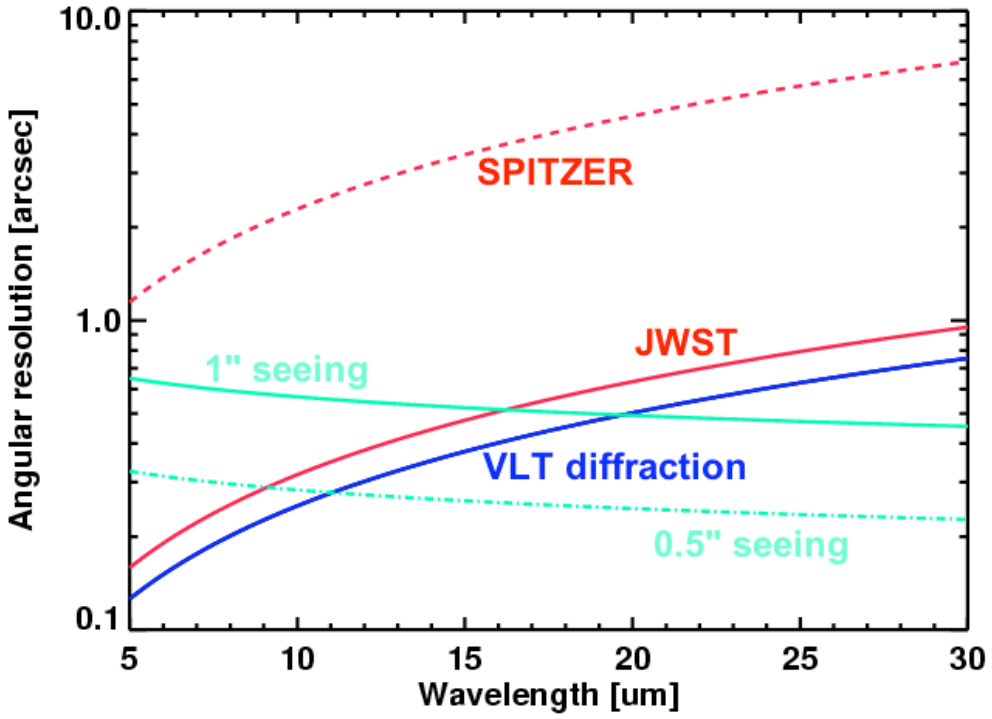

Figure 1.4: Compared angular resolutions from space and ground. For a 0.5″ optical seeing, VISIR angular resolution is seeing-limited for wavelength $\lesssim$11 µm. For a 1.0″ seeing, VISIR is seeing limited up to a wavelength of $\sim$ 18 µm.

and the type of elements (filters, diaphragms, gratings) on the lightpath. As a consequence, the design and building are complex because one has to take care of new constraints such as differential dilatations, heat conduction, insulation, ... Cool-down and warm-up procedures must be also carefully controlled.

Second, one has to block the light coming from any warm and emissive elements on or surrounding the light beam. The first one is controlled by implementing a mask (the cold stop) in the pupil plane usually (in the case of the VLT/VISIR, only the M1 surroundings emission are baffled). The second one requires an internal baffling to avoid any possible unwanted straylight coming from a warm component of the surroundings (e.g. the telescope dome) and the detector. Third, the number of warm optical elements (mirrors, lenses, windows, etc...) shall be reduced. Indeed, even a relatively low emissivity component (e.g. 10%) at room temperature produces a spurious emission at the level of the detector which is comparable to the telescope background emission. The preferred focus for a mid-IR instrument is Cassegrain focus rather than at Nasmyth focus. Infrared optimized telescopes (like Gemini or UKIRT telescopes) are designed to reduce the number of black parts, tend to reduce the size of the M2 mirror (to reduce its emissive component, offer chopping, and narrow the beam which allows to have smaller entrance windows). They also can be coated with silver (e.g. the Gemini telescopes) instead of aluminum which allows to decrease also the M1-M2 emissivity.

1.3 Specific observing techniques for ground-based mid-infrared observations.

Although much efforts are devoted to minimize the thermal infrared background it remains dominant over most of the astrophysical sources emission by a large factor (radiance $\approx$ 1000 Jy/arcsec^2 in the N band and $\approx$ 4000 Jy/arcsec^2 in the Q band). Since its emission is a stochastic process following a poissonian law, the emission is not strictly constant with time but is fluctuating. The resulting shot noise implies the the ultimate sensitivity is physically limited and can be only improved by going to higher altitude or/and dryer/cooler sites (e.g. Antartica). But before reaching this shot-noise limit (background limited performances; BLIP), one has first to overcome another set of constraints.

The faintest astrophysical sources observable are typically producing in a given pixel of a detector 10^4 to 10^5 less photo-electrons than the background. On the other hand, the gains of the current burried Impurity band (BIB) detectors are known at a precision level around 1% only. The mid-infrared background produced by the atmosphere is varying in time. In order to subtract it properly, one must then measure the sky background *on the same pixel that just observed a source hidden in the background* at a sufficiently short interval to freeze any detector gain and sky emission level variation. If the mid-infrared the atmospheric turbulence has a typical timescale of 200-300 ms, a study made using the TIMMI2 instrument in low-resolution spectroscopy mode (M.Sterzik, priv.comm., see Fig.1.5) also as other various experiments or modeling [Kaeufl et al., 1991, Papoular, 1983] show that the sky background must be measured at a frequency of at least 1 Hz (the minimum value varies depending on the wavelength). It is practically impossible to move (nod) the telescope at such a high rate. Hence only the secondary mirror (the chopper) usually moves by few arcsec; this process is called *chopping*. A too low chopping frequency leads to degraded performances of sensitivity, especially on faint extended sources (see Sec.3.3). The chopping offset cannot be too large because first the spatial coherence of the atmosphere background would not be preserved which would create an extra noise ([Papoular, 1983]), but also a large amplitude of chopping would degrade the angular resolution (overshoot, telescope coma and other optical aberrations etc ...). When subtracting the on-source B (sky) chopping frame to the A (source) one, one gets a residual pattern which is due to the fact that optical paths are not strictly the same (different emissivities, temperatures) between the two positions of the chopper. These residuals are slowly varying in time (typically at the speed of the pupil rotation or at timescales defined by temperature variations of the telescope and entrance window). They can be calibrated out by the process of *nodding* which consists in offsetting the telescope every 30s-60 s and measure them by replaying the chopping process on empty sky. The full process of chopping-nodding background correction is illustrated in Fig.1.6. When a detector is large enough to cover about 4 times the field needed to observe an astrophysical target, it is then possible to maintain the different beams on the detector and preserve a reasonably high instrument efficiency. The nodding period is a parameter which depends on the telescope mount and eventually on the zenithal distance (e.g. for a Ritchey-Chretien design). It must be also noticed that some information is lost in the process of chopping-nodding. Indeed, when computing the corresponding transfer function, the spatial frequencies corresponding to the chopping offset are irremediably lost at spatial frequencies corresponding to the chopping amplitude. Advanced signal reconstruction methods must be then used to recover the spatial frequencies lost in the process (see e.g. [Bertero et al., 2003]). It is also interesting in the context of future ELTs to compare the performances of the chopping-nodding scheme to the chopping-only scheme that do not require any movement of the telescope if an internal chopping mirror is used. Figure 1.7 shows a temporal set of VISIR frames in which chopping-nodding and chopping-only background corrections are applied. After only $\sim$1 mn of integration time, the chopping-only data are not BLIP any longer and their background residuals have a non-gaussian/non-white distribution. After 5 minutes of integration time the sensitivity in the chopped-only frame is degraded by a factor of 5 with respect to the chopping-nodding corrected frame.

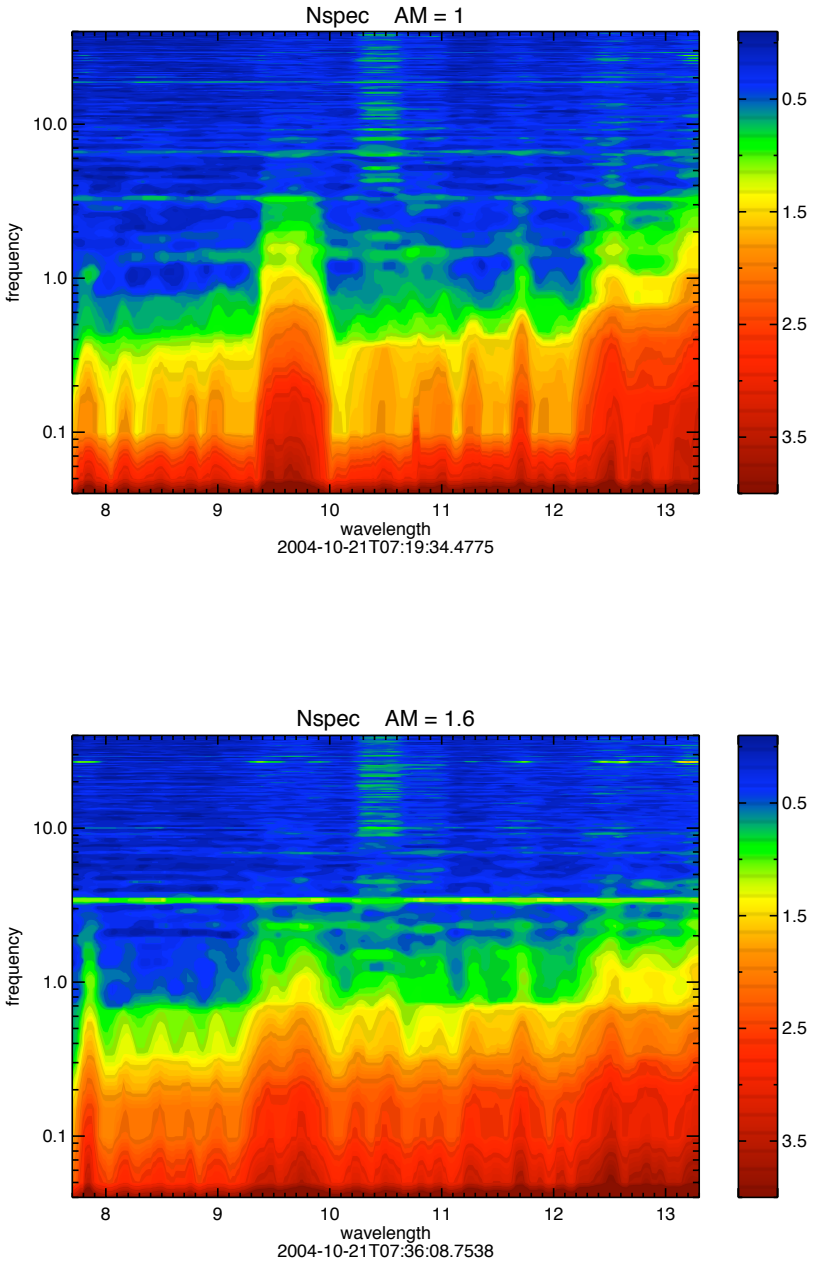

Figure 1.5: Relative power spectrum of sky noise in the mid-infrared (courtesy of M.Sterzik). The upper panel shows the measurement at zenith; the lower panel, at an airmass of 1.6. The peak of noise observed at ∼3.2 Hz is probably of instrumental origin. Note the relative strength of the ozone band (9.4-9.9 μm) depending on the airmass.

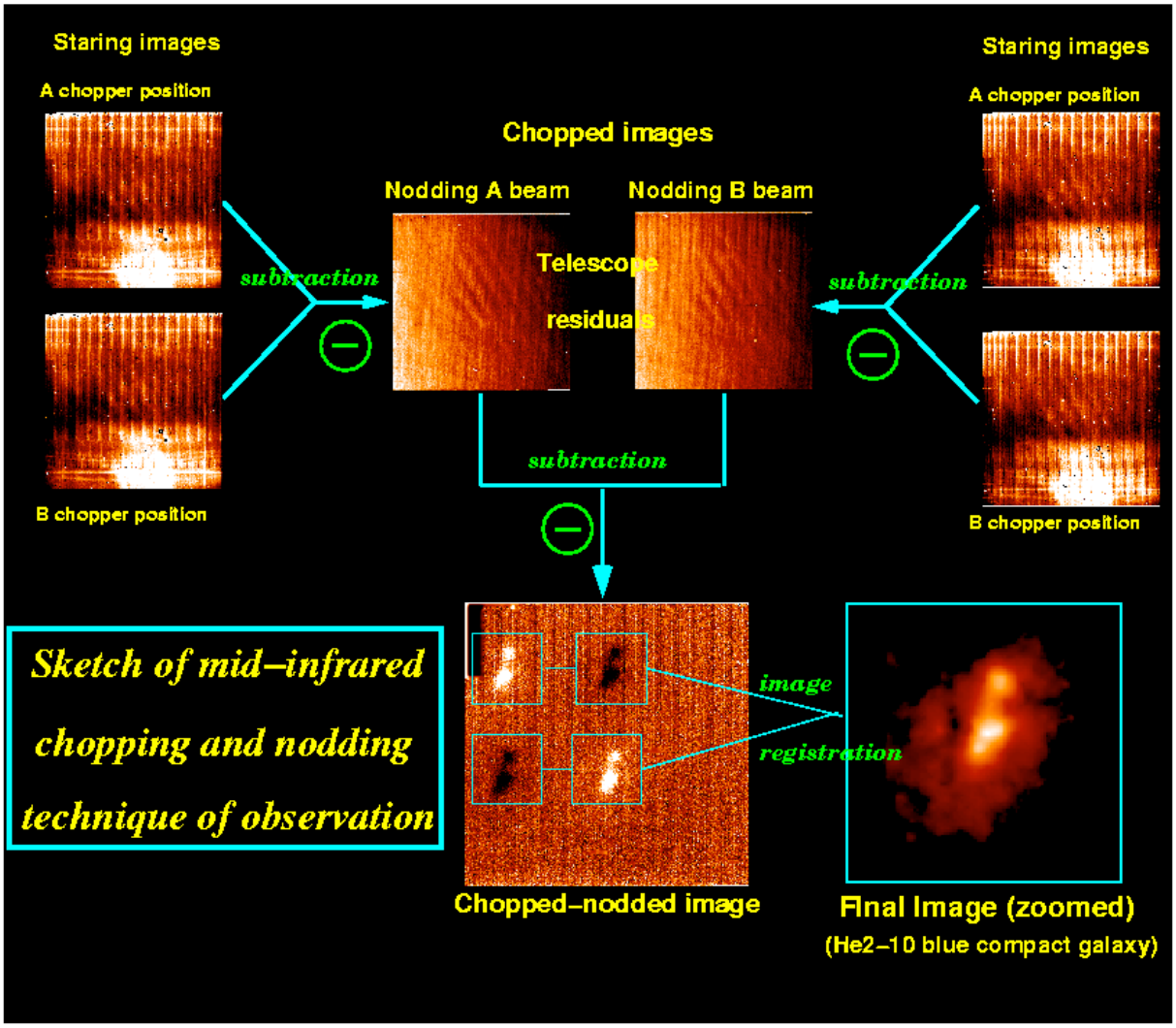

Figure 1.6: Sketch of the chopping/nodding correction. The upper left and right raw frames are first combined by subtraction to form the chopped A and B frames (upper middle panel). These two images are still domined by the chopping residuals that are canceled out by subtracting the two chopped frames (right middle panel). The resulting image contains usually 3 or 4 (this case) beams. The beams can be combined by sub-frame extraction and registering to form the final image (lower right panel).

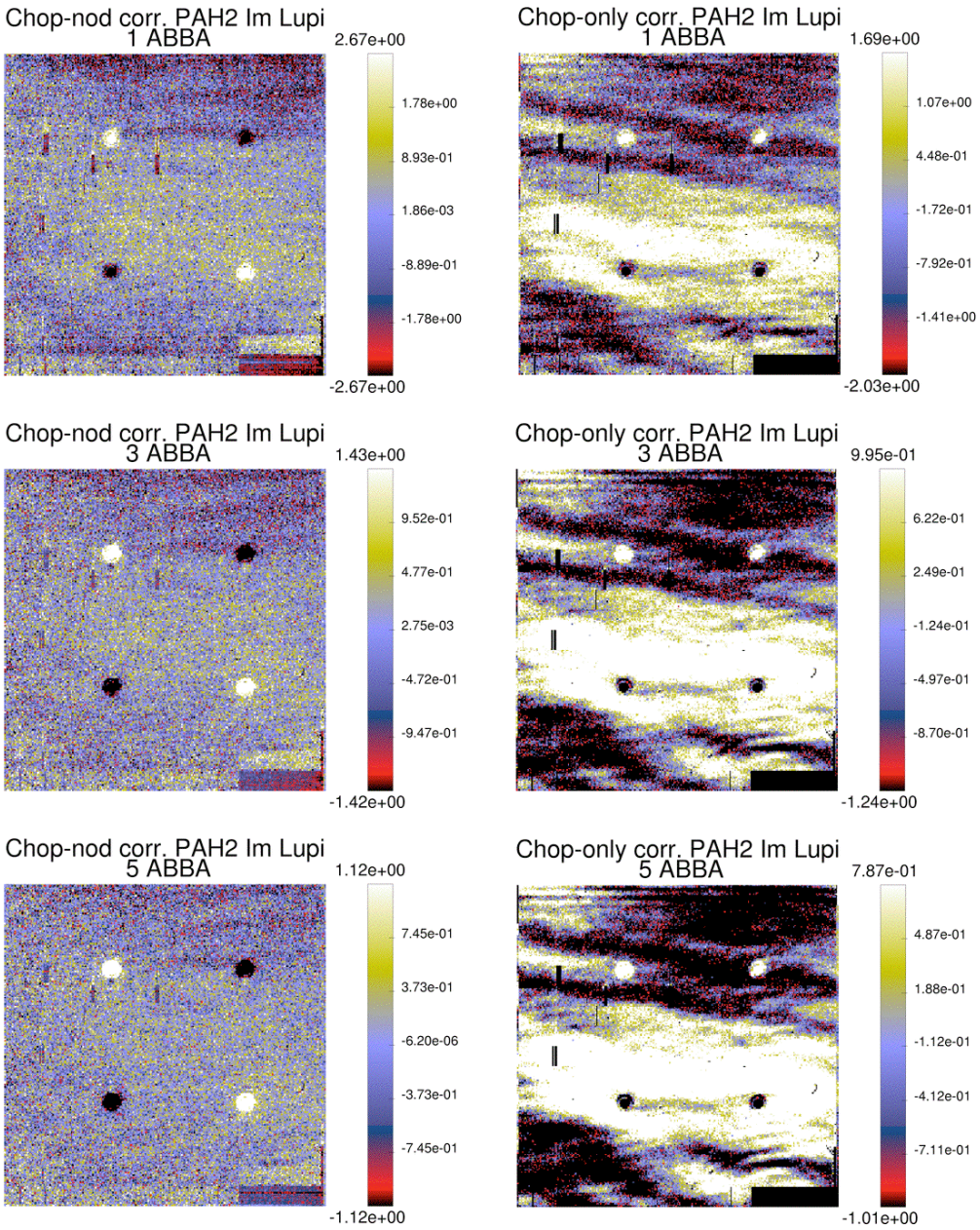

Figure 1.7: The Im Lupi source (unresolved T-Tauri disk) observed with VISIR in the PAH2 filter (11.2 μm) using the chopping-nodding scheme (left column) and chopping-only scheme (right column). The chopping-only scheme is simulated by summing the chopped frames in the two nodding positions instead of subtracting them. Three different integration times are considered : ∼1 mn (1 ABBA), ∼3 mn (3 ABBA), ∼5 mn (5 ABBA) In the case of chop-nod background removal, the background noise is spatially uniform and has the typical whiteness and Gaussian distribution as expected from a background shot noise. In the chop-only frames, a gradient estimated by a 2D polynomial fit has been subtracted out. The background is dominated by residuals originating from the change of optical path between the two positions of the chopper. As the integration time increases, the gaussian background shot-noise (left column, chopping-nodding scheme) averages out. In the right column, the chopping residuals stay at a very high level. The chopping-only scheme has sensitivity performances comparable (in terms of standard deviation of the background noise) only for integration times smaller than ∼1 mn.

1.4 Complementarity between space and ground-based observations

Space-born infrared observatories are not affected by the thermal emission of the atmosphere. On top of that, their telescopes are usually cooled-down. As a result, their sensitivity is much better than ground-based ones. On the other hand, space-born observatories cannot have very large primary mirrors. The ISO telescope was 60 cm wide; SPIZER one has a diameter of 90 cm. Their angular resolution, limited by the diffraction (2.2 arcsec at 8 µm in the case of SPITZER), is thus relatively modest when compared to much bigger ground-based ones (3.6m ESO : 0.7 arcsec at 10 µm, 8.2m VLT : 0.25 arcsec at 8.6 µm). The performances of mid-infrared observations of the future space telescope JWST will outmatch by a large factor (100 and more) current possibilities either from the the ground (in sensitivity for a comparable angular resolution) or from space (in sensitivity and angular resolution). However, a certain number of observing modes as for instance high-resolution spectroscopy will remain the exclusivity of ground-based instruments mainly because of a considerations such as limited space available. Once the European extremely large ground-based telescope E-ELT (42 m) will be ready, ground-based mid-infrared observations should be once again more performant in terms of angular resolution over space-born facilities. In particular, a mid-infrared instrument mounted on the E-ELT will open widely a new field of direct exoplanet detection and characterization (Sec.6.3). However, recalling that ground-based have a very poor sensitivity to extended (more than $\sim$5 λ/D) sources (see Sec.1.1), their detection will remain the reserved domain of space observatories. Fig.1.8 summarizes the evolution of performances of ground-based European mid-infrared instrumentation over the last 15 years. In Fig.1.9 is displayed a comparison between ground-based and space-born mid-infrared current and future instruments in terms of spatial resolution performances.

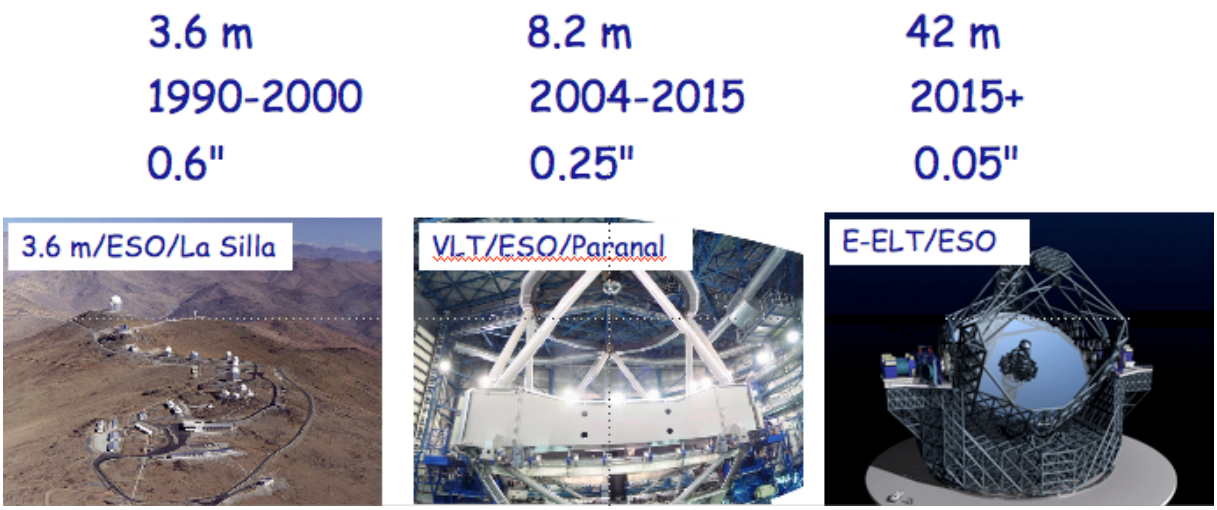

Figure 1.8: Evolution of the European mid-IR facilities

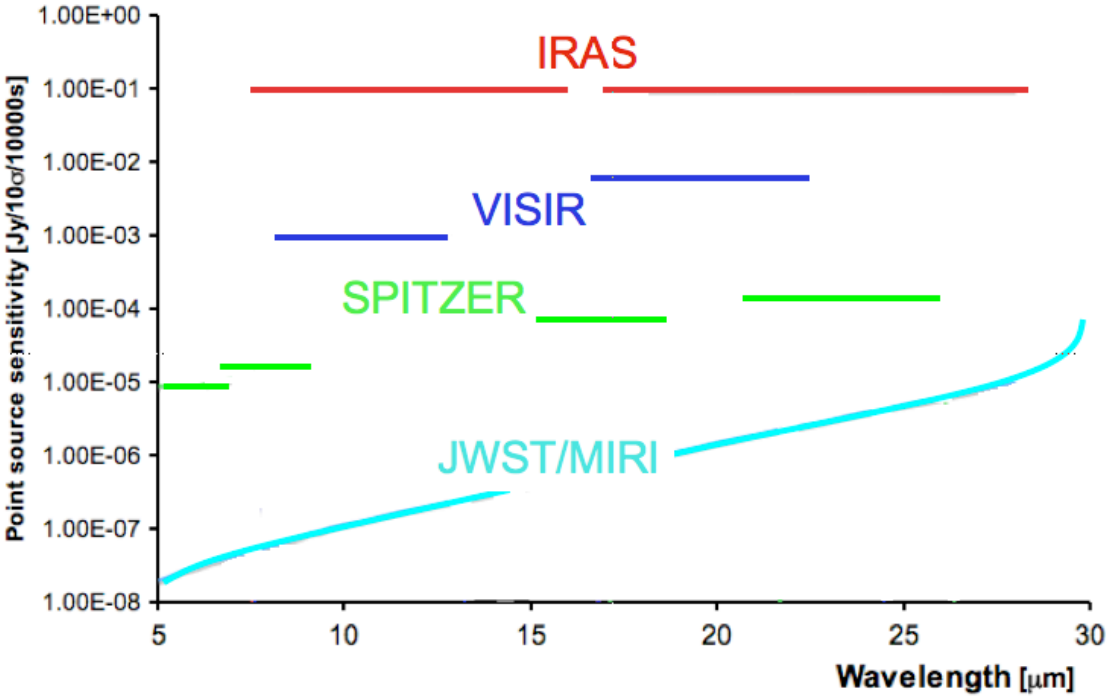

Figure 1.9: Compared point-source sensitivities of various instruments, either from the ground (VISIR) or from space (IRAS, SPITZER, JWST/MIRI)

Chapter 2

VISIR at commissioning

Résumé

The projet VISIR débutait en 1994 par une proposition pour sa construction faite l'ESO dans la cadre du plan d'instruments de première génération pour le VLT. Je décris tout d'abord dans ce chapitre la conception de l'instrument et plus particulièrement celle de l'unité de calibration qui permet de calibrer l'instrument sans avoir besoin de "consommer" de temps de télescope. Je décris ensuite les tests préliminaires en laboratoire qui furent au coeur de la phase de PAE (Preliminary Acceptance in Europe) qui précédait l'envoi au Chili de l'instrument. Une fois monté sur le VLT, VISIR a passé les phases de commissionning et de vérifiation de performances scientifiques. Durant ces phases, les performances de VISIR ont été minutieusement estimées. Enfin, je décris en détails la réduction des données produites par VISIR pour laquelle j'ai développé un software dédié; le "pipeline VISIR". Les données produites par VISIR sont relativement particulières en comparaison de celles produites par d'autres instruments. J'ai dû donc développer de nouvelles méthodes originales de traitement de données. En particulier, le mode "burst" qui permet d'obtenir une résolution temporelle de quelques dizaines de millisecondes et ainsi de pallier certaines erreurs (déformations de PSF, tip-tilt) a nécessité le développement d'un software complet de haut niveau. Ce software est essentiellement axé sur la détection de sources faibles, un tri d'images efficace (connu sous le nom de "lucky imaging"), et un algorithme précis de recentrage d'images.

Abstract

The VISIR project started in 1994 with a proposal sent to ESO in the context of the first generation instrumentation plan for the VLT. I first describe in this chapter the building phase of the instrument. In particular, I focus on the conception and the internal calibration devices that provide an easy way of self-calibrating the instrument. I describe then the tests in laboratory which were the core of the PAE (Preliminary Acceptance in Europe) phase. Once shipped to Chile, VISIR passed the commisionning and science verification phases during which the on-sky calibration and performance estimates were assessed. Finally, I describe in details the VISIR data reduction for which I developed a dedicated pipeline. Given the specificities of VISIR data, I have developed new and original data processing methods which are described here. In particular, the burst mode which allows to achieve a time resolution of ∼20 ms has prompted the development of a complete package for "rapid imaging" data reduction. This package is based on faint source detection, efficient image sorting (the so-called "lucky imaging") and accurate shift-and-add algorithms.

Contents

2.1 The VISIR project

Following the fruitful harvest obtained by the space infrared observatory ISO and more particularly using the ISOCAM camera, the Service d'Astrophysique of the CEA has developed mid-infrared instruments for observations at high angular resolution from the ground. The triggering opportunity was the availability of detectors developed by the CEA/LETI-LIR in the context of the space-born ISOCAM instrument. The original detectors technology was adapted for ground-based conditions (high flux, high read-out speed). In parallel, the CAMIRAS instrument was a proprietary instrument of the SAp that was mounted on various large telescopes around the world (ESO 3.6m, Chile; CFHT, Hawaii; NOT, Canarias Islands) between 1990 and 2002. This experience for building mid-infrared instruments led to propose a mid-infrared instrument for the VLT when the call was open in 1992 in the framework of the first generation

VLT instrumentation plan. In 1994, a proposal was sent to ESO to build a mid-infrared instrument, with imaging and spectrometry at high angular and spectral resolutions capabilities between 8 and 24 μm. The imager and the spectrometer are actually two independent sub-systems. One of its originality lies in the very high spectral resolution mode which offers resolutions in the range 15000-30000 (accuracy of 10 km/s in velocity). This mode is unique in the southern hemisphere. The instrument named VISIR (which stands for VLT Imager and Spectrograph for the mid-InfraRed) was built between 1996 and 2004 by a consortium consisting in the DAPNIA (Département d'Astrophysique, physique de Particules, physique Nucléaire et Instrumentation Associée) at CEA, the "Netherlands Foundation for Research in Astronomy (NFRA, Hollande)", SRON (Netherlands Foundation for Space Research), the project being supervised by the Service d'Astrophysique du CE Saclay (SAp, PI P.O. Lagage). The DAPNIA has contributed about 65% of the work involved in this project. One year later (1997), VISIR passed the Preliminary Design Review at which the proposed design has been validated by ESO. The final design review (FDR) was passed april 1999 and the "true building phase" could start. The Preliminary Acceptance in Europe (PAE) took place from September 2003 to April 2004. During this critical phase, the basic functionalities and also some off-telescope performances were assessed before final shipping to the VLT in Chile (April 2004). For this PAE phase, a large number of qualification devices (mechanical and optical telescope simulators, simulated sources, gas cell, etc) were developed to assess these performances. The commissioning phase which aimed at precisely check the on-telescope performances took place between April and September 2004.

2.2 Instrument description

The VISIR instrument is actually composed of two sub-systems: an imager and a spectrometer. The imager provides images at high angular resolution (in principle limited by the diffraction of the telescope except in cases of strong atmospheric turbulence, see [Doucet et al., 2006a]). It includes a filter wheel with a set of filters to observe between 8.6 and 19.8 μm with spectral resolutions ranging from 5 to around 70. The optics are based on a pure reflective mirrors design. In the focal plane of the telescope are placed a set of diaphragms mounted on a wheel. The collimator (M1 mirror, see Fig.2.1) produces a pupil plane in which filters and the cold-stop are placed. A second wheel in the imager (filter wheel) allows to use any combination of magnifications (0.075, 0.127 and by 0.2 arcsec per pixel) and filter. The detector used is a DRS-Boeing BIB 256x25; the corresponding field sizes on the sky are 19.2x19.2, 32.5x32.5 and 51.2x51.2 arcsec respectively.

The spectrometer is almost an independent instrument. It only shares the entrance window and the cryostat with the imager. It has its own optical system and its own sensor (see Fig.2.2). The spectrometer provides long-slit spectra in the N and Q bands at low (R = 200-350 in N band), medium (R = 2500 in N band), and high spectral resolutions (R = 30000 in N band) with a spatial information along the slit at an angular resolution limited by the diffraction. It should be mentioned here that the high-resolution mode is unique in the southern hemisphere, and that are only 2 other instruments in the world which offer such a mode (Michelle on GEMINI North telescope, Texes [Lacy et al., 2006] on GEMINI).

2.3 Tests in laboratory and Preliminary acceptance in Europe

VISIR had to undergo a full set of test in Europe before being shipped to Chile. These tests were meant to check as much as possible prior to VISIR being mounted on the VLT telescope whether VISIR complies with the specifications. For that purpose, VISIR was equipped with two simulated sources:

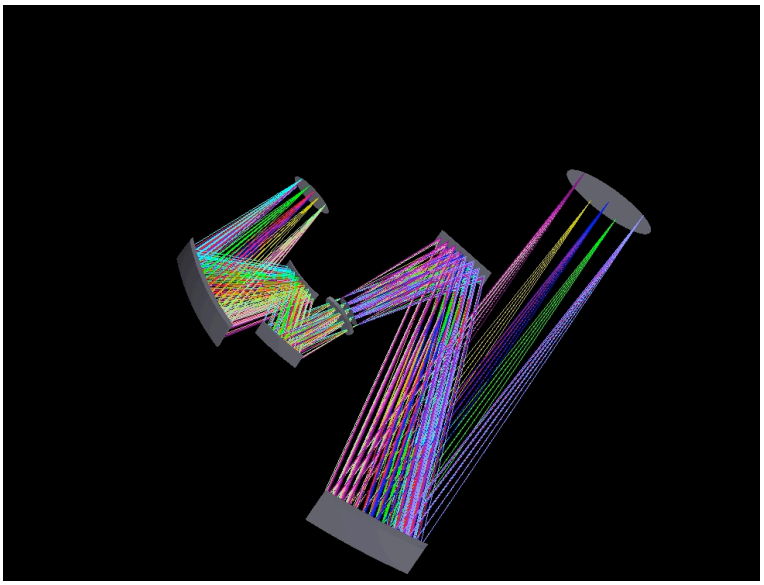

Figure 2.1: Optical design of the VISIR imager.

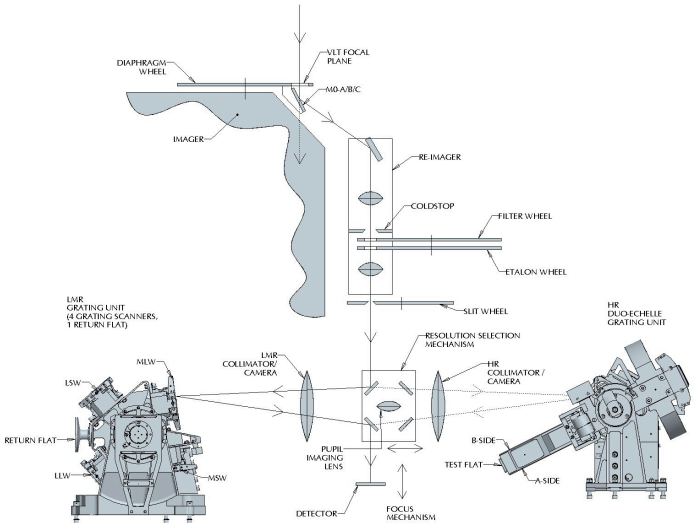

Figure 2.2: Optical layout of the VISIR spectrometer.

- Monochromatic point source with adjustable flux
- Extended source with adjustable temperature (Peltier plate) between -20 and 50 degrees Celsius

and some optical calibration devices:

- Imager
  - distortion grid (pinholes mask) for image quality assessment
  - pupil imaging to check optical alignment
- Spectrometer
  - Hartmann masks for focus check
  - pinhole mask for image quality checks
  - pupil imaging
  - plastic foils used as absorption etalons for coarse wavelength calibration
  - Fabry-Perot etalons for fine wavelength calibration (medium and high resolutions)
  - gas cell (NH_3) for spectral resolution checks (high resolution) and wavelength calibration cross-check

On top of that, a "stiff source" whose mounting has been designed to be stiff enough to be used as reference for measuring possible flexures in the optical elements was added to the bench.
Starting from the specifications documents 'VISIR statement of work', a tests matrix was defined. All the tests and their analysis are described in the document 'VISIR Commissioning Plan for tests in Europe' that I wrote.

2.3.1 Commissioning phase at Paranal

The commissioning i.e. the testing phase of on-telescope and on-sky assessment of the instrument performances took place between April and September 2004. I wrote for this phase the 'Commissioning Plan' document which is the master document describing all the tests to be performed also as the corresponding analysis. These measurements and tests are reported in the "VISIR comissionning report" document in which the compliance of VISIR with the specifications is also reported.

Photometric calibration

Infrared photometric calibration is a delicate operation because of the major impact of the Earth's atmosphere on the recorded flux of an astrophysical source (absorption). In addition, observing in the mid-infrared from the ground is a relatively recent technique compared to other wavelength which partly explains the difficulty to define accurate calibration sources. Until very recently the models of infrared emission from the stars were poorly constrained and their intrinsic accuracy was limited. Using the recent infrared space missions equipped with spectrographs (ISO/SWS or SPITZER/IRS) it has been possible to obtain both observations and models of stars infrared emission having an accuracy similar to that achieved in the visible range ([Decin et al., 2000]). Concerning VISIR, we have selected the all-sky survey catalog of [Cohen et al., 1999]. It covers both the northern and the southern hemisphere with a fairly good spatial coverage (422 stars regularly spaced) and photometric precision. Cohen's calibration is based on two

primary standards: Alpha Lyr (A0 V) and Alpha CMa (A1 V). Alpha Lyr is defined to be 0 mag between 1 and 20 microns but at longer wavelengths allowance must be made for emission from dust. For this reason Cohen favors Alpha CMa as the primary standard over all wavelengths. Kurucz model-atmospheres fitted to observational data of these two stars define the absolute flux calibration ([Cohen et al., 1992a]). Cohen extends his system to ten bright secondary standards which are tied to the primaries via well-documented ratio spectra derived from several ground-based, airborne, and space-based platforms (Papers II, IV, VI, and VII, [Cohen et al., 1992b, Cohen et al., 1995, Cohen et al., 1996a, Cohen et al., 1996b]). The secondary standards are K and M giants which exhibit broad CO and SiO absorption features in the M band and near 8 microns, so approximating their spectra with blackbodies would introduce calibration errors of 10-20%. Using Cohen's absolute spectra, errors should be under a few percent on the reference stars. In the latest paper in the serie ([Cohen et al., 1999]), spectral templates for 422 stars are presented, defining a dense all-sky calibration network. However, many of these templates have not been fully verified observationally, so these spectra must be used with some precautions. It can be noted here that a very careful photometric calibration using bright and well calibrated standard stars allows to achieve typical absolute photometric error of 5-6% in the N band and 7-8% in the Q band on bright (several tens of Janskys) asteroids .

I have developed a tool which, given a source in the sky, finds in Cohen's database the "best" calibrator based on combined criteria of distance on the sky, airmass or magnitude. An example of the output of the software is shown in Fig.2.3. This tool has been used by myself and my collaborators during the VISIR guaranteed time observations; a derived tool has also been implemented at ESO Paranal on UT3. Since the filters we use with VISIR are relatively narrow, a color correction is not necessary except for very "red" objects.

```
--          14 sources selected on flux criterium and airmass
  1  Flux for HD187642 is  9.37 Jy, airmass=1.127  , distance to object =   112.9 deg
  2  Flux for   HD1522 is  5.61 Jy, airmass=1.266  , distance to object =    81.4 deg
  3  Flux for HD169916 is  8.91 Jy, airmass=1.485  , distance to object =    70.1 deg
  4  Flux for HD175775 is  5.63 Jy, airmass=1.341  , distance to object =   138.4 deg
  5  Flux for HD177716 is  7.66 Jy, airmass=1.282  , distance to object =   115.4 deg
  6  Flux for HD186791 is 22.75 Jy, airmass=1.491  , distance to object =   105.3 deg
  7  Flux for HD196171 is  5.82 Jy, airmass=1.127  , distance to object =   124.5 deg
  8  Flux for HD198542 is 11.53 Jy, airmass=1.037  , distance to object =   146.7 deg
  9  Flux for HD200914 is  8.51 Jy, airmass=1.022  , distance to object =   137.2 deg
 10  Flux for HD211416 is 16.44 Jy, airmass=1.225  , distance to object =   118.2 deg
 11  Flux for HD216032 is 11.35 Jy, airmass=1.046  , distance to object =    59.5 deg
 12  Flux for   HD2261 is 14.86 Jy, airmass=1.218  , distance to object =   116.2 deg
 13  Flux for   HD4128 is 15.23 Jy, airmass=1.293  , distance to object =    88.6 deg
 14  Flux for   HD6805 is  5.85 Jy, airmass=1.475  , distance to object =   117.1 deg
Select a source1
```

Figure 2.3: Tool for the selection of standard stars based on airmass, flux, and proximity to the main target.

The spectro-photometric calibration of VISIR data actually consists of two sub-operations: correction of the atmospheric and instrumental absorptions (called "telluric correction", which varies with wavelength) and the actual photometry. These two operations are simultaneously worked out by division of raw data by that of a calibrator observed with exactly the same instrument configuration and observing (e.g. weather, airmass, etc ..) conditions and multiplication by the standard star model. Two or more observations of calibrators can be combined to increase the accuracy of the result (see Sec.3.7). In the visible and near-infrared range, the two operations are usually split. One standard star observation using the same slit width is used to correct for the atmospheric and instrumental absorptions (telluric calibra-

tor) while a second one (photometric calibrator) using a much wider slit (3-4 λ/D, thus at a degraded spectral resolution) allows to perform the absolute spectro-photometric calibration. In the case of VISIR, the PSF stability and "diffraction-limited" characters allow to combine the two operations into a single one. However, in the particular case of extended objects one has to correct for the fraction of the calibrator flux lost because of using a narrow slit.

Concerning the spectroscopy at low and medium resolutions, spectro-photometric calibrators are also chosen from Cohen's database. The limited intrinsic spectral resolution of the database should restrict its applicability to spectroscopic data with resolutions lower than ∼1000. However, we are also using this database for medium-resolution data[1] because the alternative databases (e.g. ISO/SWS standard stars) are still rather incomplete and inhomogeneous. SPITZER/IRS (SH/LH modes) will probably produce a more complete and accurate spectral database in the forthcoming years. This database will be however limited in resolution to about R=600.

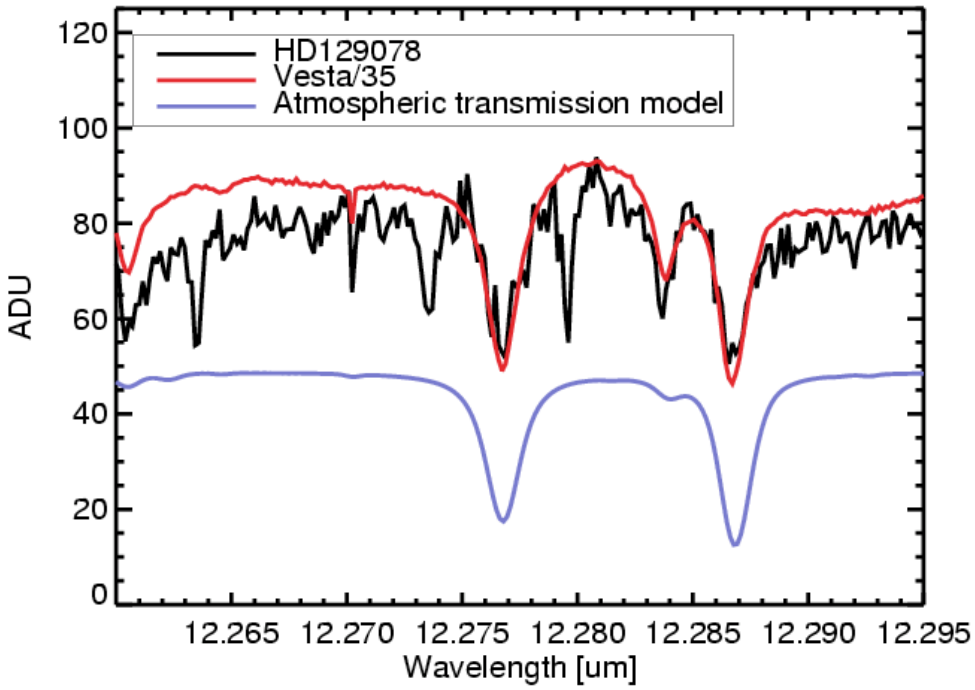

Figure 2.4: Raw spectra obtained in high-resolution spectroscopy mode (R≈25000). The black line plots the HD129078 standard star (K3III spectral type). The red line is the spectrum of the Vesta asteroid (divided by 35). In blue the atmospheric transmission deduced from a radiative transfer model (ATRAN/HITRAN). The raw spectrum of Vesta reveals with a good signal-to-noise the presence of atmospheric absorptions at 12.2768 et 12.2838 et 12.2868 µm. These absorptions are poorly reproduced by the atmospheric transmission model that we currently use for wavelength calibration because of an assumed precipitable water vapor content of 3 mm lower than the true one.

The spectro-photometric calibration of the high-resolution spectrometer mode is more delicate, not only because the existing data of standard stars at such high a resolution are sparse, but also because of the relatively low sensitivity in this mode, hence the need for bright standards. Cohen's database remains

[1] R=1500-3000

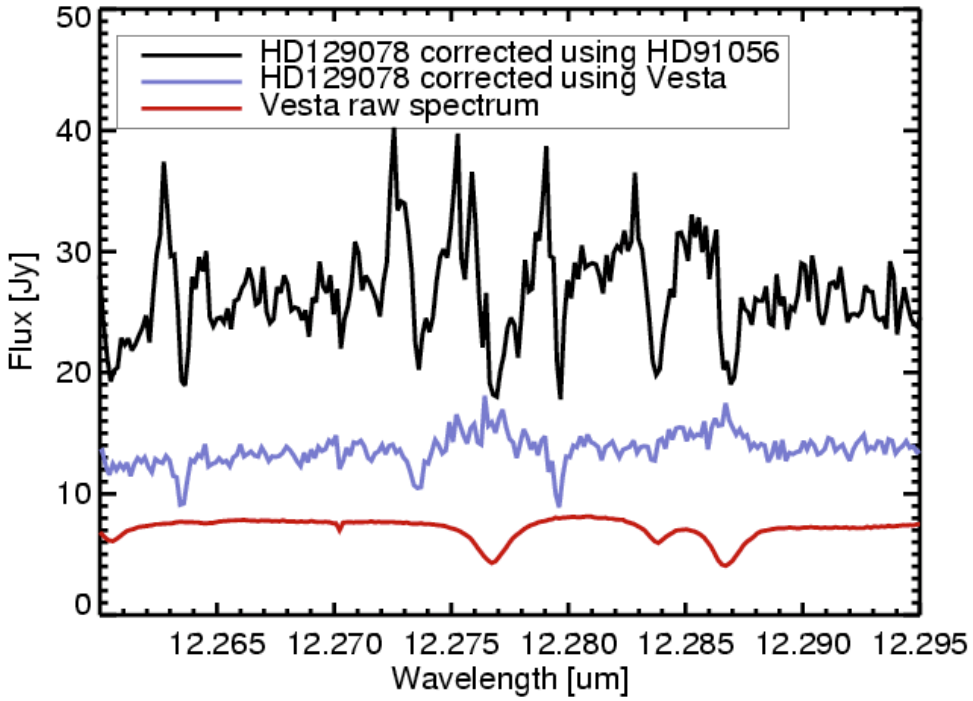

Figure 2.5: Spectra of the HD129078 standard star calibrated using another standard star (HD91056, black line) or Vesta (blue line, offset by -10 Jy for clarity). The relatively poor signal-to-noise ratio and lack of accuracy on the HD91056 true spectrum at high spectral resolution produces the relatively large errors The spectrum of a K3III star is expected to be virtually featureless in this wavelength range according to NextGen models ([Hauschildt et al., 1999]). When using Vesta (which spectrum is almost a pure continuum) as a telluric calibrator the errors are dramatically reduced (blue line) but the absolute photometric calibration is uncertain because asteroids have a varying flux level in the mid-infrared range (distance to the Sun, distance to Earth, asteroid rotation). One can notice 3 absorption features in the corrected spectrum (blue), these are identified as OH absorption lines.

useful even at high resolution for the absolute photometric calibration which can be performed on the continuum part of the spectra. However, the limited sensitivity of this mode obliges to restrict oneself to bright standards (F_ν larger than 10 Jy). The telluric correction using these stars remains very difficult (typical errors larger than ∼20%, see Fig.2.4 and Fig.2.5) even with the brightest reference stars (10-50 Jy) found in Cohen's database.

An accurate telluric correction can be obtained by performing observations of bright asteroids. Fairly accurate models of their infrared emission, which is devoid of any lines (pure continua) are now available in the literature ([Mueller and Lagerros, 1998]). The other advantage is the fairly high brightness of large asteroids (100-300 Jy) which saves some observing time and produce high signal-to-noise ratio data. We have measured the performances when using this type of calibrator on several different asteroids such as Ceres, Pallas, Diotima, or Juno. The telluric correction on the high-resolution spectra (tested on standard stars) is of much higher quality than when using standard stars. A typical reduction of calibration errors from ∼30% to 5-10% (depending on the wavelength, the asteroid brightness, the atmosphere stability etc) is achieved (see Fig.2.5). However because the flux of an asteroid varies on a day timescale basis, the precision on the absolute photometry is limited. A cross-calibration (to obtain an accurate absolute calibration) using a standard star is then compulsory.
Another option is to use only A0 type standard stars whose IR spectrum is almost free of lines and a accurate template spectrum (Vega) is available. We have selected a set of 44 A0 stars observable from Paranal from the Hipparcos catalog. However their relatively low flux in the infrared domain (only 3 of them have fluxes larger than 10 Jy in the N band) is quite penalizing in terms of achieved signal-to-noise ratio.

Wavelength calibration

Although a precise optical model for wavelength calibration is implemented in the pipeline reduction software, a slight random offset in wavelength is usually observed in the data because the scanner that holds the grating has its intrinsic positioning error, because of flexures in the mechanical structure of the instrument and so forth. A very precise wavelength calibration can be obtained by using the staring frames (sky emission) interlaced with chopped data. The sky emission contains a sufficient number of bright sky lines that once compared with a model of sky emission, lead to a precise wavelength recalibration. This recalibration is implemented as follows: the pipeline first assumes a wavelength range on the detector deduced from the optical model; then a sky emission model is computed over this range. The refined wavelength offset is computed using the cross-correlation function between sky observations and sky emission model. Fig.2.6 shows how the sky spectrum is compared to the observed spectrum and the wavelength calibration is achieved.

2.3.2 The "Paranalisation" phase

I spent 6 months in Chile to ensure a proper transfer of knowledge between the consortium which has built the VISIR instrument and ESO. During this stay, I participated in the "Paranalization phase" which consists in standardizing VISIR to ESO operations in Paranal. This process at the interface between the purely technical side of the VLT operations and the scientific community allowed VISIR to fit into Paranal operational organization which renders almost transparent for the ESO staff the tasks of VISIR maintenance and upgrades. In the Paranalization phase, one of the most important tasks in the definition of *observing templates* i.e. pre-programmed observations which are defined by and for the wished type of data. Four types of templates are defined. The *science* templates are the ones used on the scientific targets. A standard imaging observation (chopping and nodding scheme) is for instance defined by the `VISIR_img_obs_AutoChopNod` template. Each template contains several

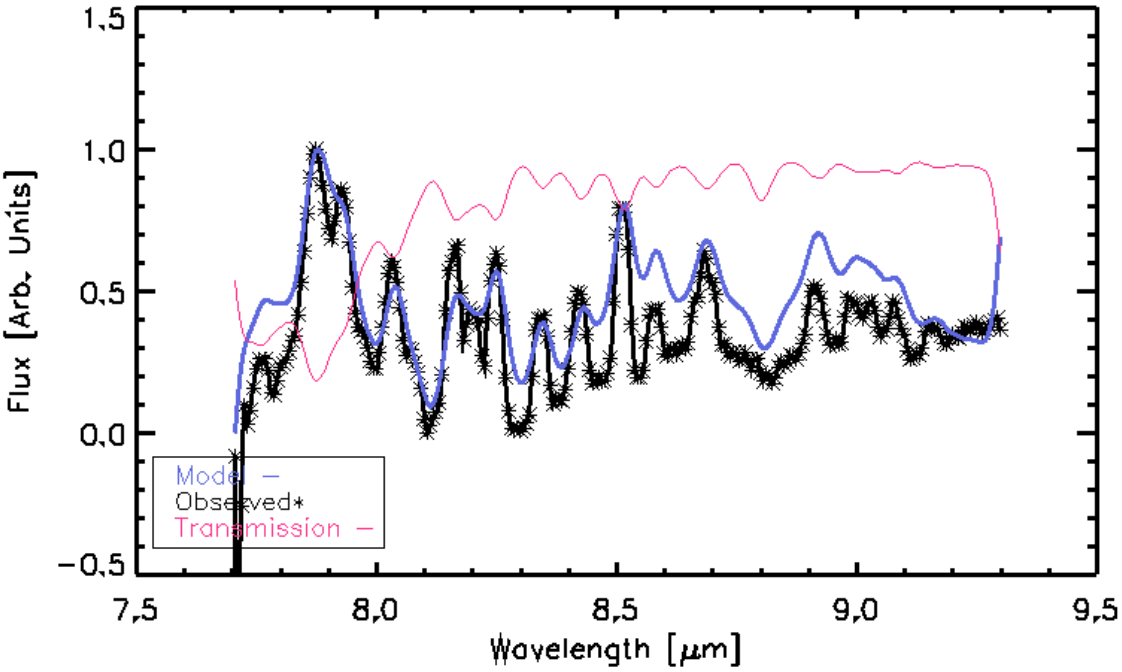

Figure 2.6: Wavelength calibration of low resolution spectroscopic data. The observed sky spectrum (black line with stars) is compared to a sky emission model (blue plain line) and its wavelength scale is recalibrated. The atmospheric transmission is also plotted (pink plain curve) for comparison.

adjustable parameters such as filter, magnification or observing time. Each observing science template is preceded by an *acquisition* observation based on an acquisition template. This template presets the telescope to the source coordinates, performs a short exposure of the source in a sensitive filter in order to check the position of the source, and eventually recenters the source into the VISIR field of view. Some of the *calibration* templates are almost identical to the *science* templates except that they apply to the observations of standard sources. The calibration of a *science* observation is obtained by launching a *calibration* template on a standard source, using exactly the same instrument settings/parameters as used in the *science* template. In addition, several *calibration* templates are defined to perform specific calibrations e.g. flat-field recordings. Finally, some *technical* templates are defined to perform instrument tests and checks (eventually during the day). A set of *science* templates and an *acquisition* template define an *observing block* which is the base unit for *service mode* observing. These observing blocks are programmed using the P2PP tool [2]

It must be stressed that in the case of mid-infrared observations from the ground the elementary detector integration time (DIT) is a parameter which is not defined by the observer (e.g. based on source brightness) but tuned to the background level (depending on the filter, the magnification, the weather, etc). One the most important task of the Paranalization phase is the tuning of this DIT parameter. For each instrument setting (filter or wavelength setting/magnification), four DIT values are defined and chosen according to the SEQ.WEATHER keyword. These four values correspond to four levels of atmospheric quality. At the beginning of the night, the optimal value is iteratively assessed and usually stays fixed for the night. Once the DIT value fixed, the instrument control software computes the number of frames per chopping position (NDIT) and the number of chopping/nodding cycles to obtain the total observing time asked for.

The knowledge that we gained during the building phase in Europe and the Paranalization phase in Chile is summarized in the VISIR Users Manual which is the reference document for VISIR observers. I wrote the first versions of this manual. The ESO Paranal staff has taken over since then. This document can be found at:
http://www.eso.org/sci/facilities/paranal/instruments/visir/doc/index.html

2.4 Burst mode

The burst mode is an infrared version of the fast imaging mode used in the visible range. Given the high background in the mid-infrared, the elementary exposure time is in any case of the order of 10-50 ms. Standard data are a compacted version of all these elementary images. A “frame cruncher” averages in real time the elementary frames (DIT) corresponding to one chopper position into a single frame which is stored. At frame rates in the range 20-100 Hz, the read-outs every DIT cannot be stored on the hard disk because of bandwidth limitations. A set of about 1000-1500 (this value has been very recently increased to 3000) frames are stored in real time into random access memory and then dumped on the hard disk when the OB is finished or during a slack period in the observation. The access to these elementary frames is important to:

- measure and understand the observing parameters that vary on short timescales like the seeing, the response of the active optics, the detector behavior, etc ...
- be able to select the best frames in order to improve the quality of the final products
- freeze any instability which has a timescale larger than the DIT.

[2] P2PP is the ESO software to program service mode observations; it is also used in visitor observing mode locally at the telescope

The burst mode has been historically used since the 90's in the framework of lunar occulations observations in the mid-infrared ([Stecklum et al., 1999]). It has been recently added as an observing mode offered in visitor mode on VISIR. It allows to reach better point source sensitivities (see Fig.2.7). Using a lucky imaging algorithm in which the individual frames are selected (some "bad" frames are rejected according to some pre-defined criteria), a typically an enhancement of the sensitivity by a factor of 1.5-2 can be achieved (see Tab.2.1). This mode is particularly well adapted to get the best return from VISIR programs which need either a good time resolution (e.g. speckle observations ([Poncelet et al., 2007]), or an efficient frame selection enabling to correct the data degraded by high seeing or PSF distortions. However, this mode is restricted to bright and compact sources that can be detected in one DIT by nodding corrections only (see Sec.2.7); it is otherwise virtually impossible to determine the phase of the chopper because the chopper is not synchronized with the "start exposure" signal. In practice, this means that a point source fainter than 2-3 Jy in PAH2 filter (11.2 µm) is very difficult to observe depending on the weather conditions.

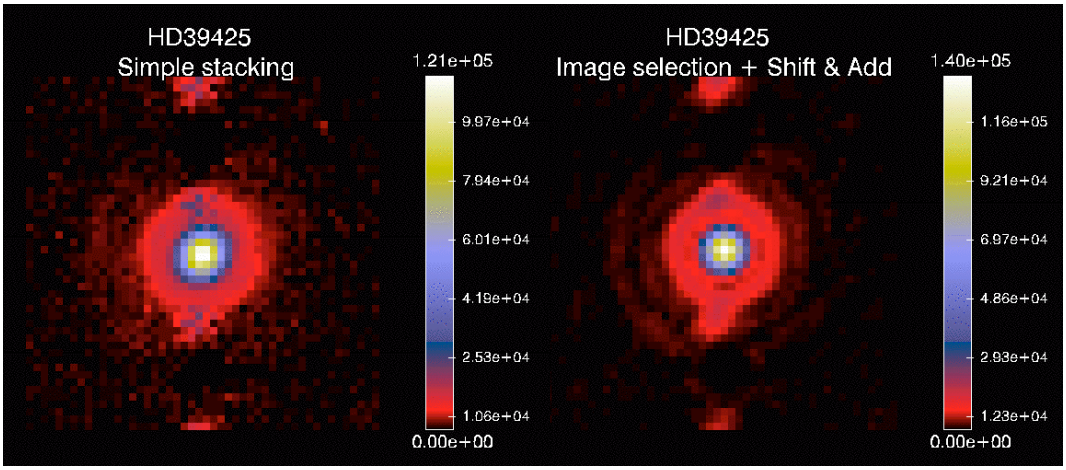

Figure 2.7: Left panel: simulated (using burst mode data) standard observation of a standard star (HD39425, 18.27 Jy in PAH2_2 filter). In the right panel, the same dataset has been registered (for eventual tip-tilt residual) and frame selection has been applied (criteria of peak of the source, correlation with a reference frame, and source roundness). In this particular example, the spatial resolution is improved by 20% and the sensitivity a factor of 2.74 (taking into account the frames loss due to the selection process).

2.5 ETC

ESO proposes to its users a complete set of software tools to prepare observing proposals and observations. One of them is the Exposure Time Calculator (*ETC*) which computes either the signal-to-noise ratio achieved on a given source in a given time, or alternatively the time needed to reach a given sensitivity level. All VLT instruments offer this type of tool, as does VISIR. An ETC is actually a model of the instrument and atmosphere throughputs based on our knowledge about the different sub-systems (telescope, optics, filters, detector, gratings, etc ...). I was in charge of building the prototype of the *VISIR ETC*. The (*ETC* includes the transmission/emission factors of the atmosphere, that of the entrance window, the optics, and a detection/noise model of the detector. Tables 2.8 and 2.9 display the predicted sensitivities of VISIR in imaging mode assuming telescope emissivities in the range 6 to 14% as measured during the commissioning phase. Fig.2.10 shows the predicted sensitivity for the spectrometer low-resolution mode.

Computed Sensitivities using a model Tue Aug 12 16:49:31 2008

Parameters used:

Telescope emissivity= 0.0600000
Temperature telescope= 290.000
Temperature atmosphere= 253.000
Temperature window= 290.000

Filter	Centr.wav.	FWHM	transm. (%)	Sensitivity(mJy/10sigmas/1h) integrated	mean per pixel	# beams
N-Band	10.55	5.37	70.00	0.50	4.3268	4
SIC	11.85	2.34	75.35	0.84	8.9673	4
PAH1_1	8.19	0.15	75.00	1.36	32.0034	4
PAH1	8.58	0.42	77.50	1.03	15.3670	4
ARIII	8.99	0.14	72.07	2.27	57.1596	4
SIV_1	10.03	0.18	72.00	2.29	55.4247	4
SIV	10.48	0.16	74.45	2.52	60.6409	4
PAH2_1	10.75	0.69	76.50	1.29	17.2848	4
SIV_2	11.09	0.19	70.00	2.70	62.3386	4
PAH2	11.26	0.59	75.52	1.55	22.8387	4
PAH2_2	12.13	0.37	58.00	2.55	54.4851	4
NEII_1	12.51	0.18	51.00	3.81	115.9325	4
NEII	12.80	0.21	64.24	3.52	99.5345	4
NEII_2	13.03	0.22	68.42	3.54	100.5938	4
J7.9	7.81	0.71	85.00	1.56	14.0731	4
J8.9	8.74	0.88	90.00	0.71	7.4937	4
J9.8	9.65	0.93	70.00	1.25	13.7772	4
J12.1	12.08	0.53	63.00	2.00	35.1732	4
B9.7	9.83	0.42	85.00	1.67	22.4386	4
B10.7	10.65	1.37	85.00	0.86	9.2212	4
B11.7	11.52	0.85	80.00	1.29	16.8502	4
B12.4	12.47	0.99	90.00	1.29	17.1214	4
Q0	16.55	0.40	57.93	26.74	511.7983	4
QH2	17.11	0.40	48.73	17.81	396.6446	4
Q1	17.65	0.83	59.57	9.28	172.9999	4
Q2	18.72	0.88	49.77	11.36	239.0963	4
Q3	19.51	0.40	50.00	34.46	896.8105	4
Q4	20.49	1.00	40.00	17.70	412.4832	4
Q7	23.10	0.80	40.00	93.35	2430.2140	4
Q8	24.50	0.80	40.00	66.88	2054.9863	4

Figure 2.8: Predicted sensitivities using an emissivity of 6% for the telescope (optimistic case). The integrated values of the sensitivity are computed over the full PSF spatial support.

Computed Sensitivities using a model Tue Aug 12 16:48:30 2008

Parameters used:

Telescope emissivity= 0.140000
Temperature telescope= 290.000
Temperature atmosphere= 253.000
Temperature window= 290.000

Filter	Centr.wav.	FWHM	transm. (%)	Sensitivity(mJy/10sigmas/1h) integrated	mean per pixel	# beams
N-Band	10.55	5.37	70.00	0.62	5.1396	4
SIC	11.85	2.34	75.35	1.06	10.4994	4
PAH1_1	8.19	0.15	75.00	1.72	32.5810	4
PAH1	8.58	0.42	77.50	1.27	16.0472	4
ARIII	8.99	0.14	72.07	2.77	58.0687	4
SIV_1	10.03	0.18	72.00	2.88	56.8377	4
SIV	10.48	0.16	74.45	3.16	62.3124	4
PAH2_1	10.75	0.69	76.50	1.61	18.8183	4
SIV_2	11.09	0.19	70.00	3.37	64.3618	4
PAH2	11.26	0.59	75.52	1.94	24.6965	4
PAH2_2	12.13	0.37	58.00	3.22	57.1321	4
NEII_1	12.51	0.18	51.00	4.85	119.0109	4
NEII	12.80	0.21	64.24	4.49	102.7758	4
NEII_2	13.03	0.22	68.42	4.53	104.0101	4
J7.9	7.81	0.71	85.00	1.75	14.7643	4
J8.9	8.74	0.88	90.00	0.87	8.1355	4
J9.8	9.65	0.93	70.00	1.49	14.8548	4
J12.1	12.08	0.53	63.00	2.53	37.6222	4
B9.7	9.83	0.42	85.00	1.99	23.7195	4
B10.7	10.65	1.37	85.00	1.08	10.4658	4
B11.7	11.52	0.85	80.00	1.62	18.6877	4
B12.4	12.47	0.99	90.00	1.64	19.3643	4
Q0	16.55	0.40	57.93	28.56	525.5300	4
QH2	17.11	0.40	48.73	19.29	407.0223	4
Q1	17.65	0.83	59.57	10.19	180.9431	4
Q2	18.72	0.88	49.77	12.42	248.4894	4
Q3	19.51	0.40	50.00	36.73	914.3647	4
Q4	20.49	1.00	40.00	19.04	425.2271	4
Q7	23.10	0.80	40.00	97.02	2469.5840	4
Q8	24.50	0.80	40.00	69.74	2084.2600	4

Figure 2.9: Predicted sensitivities using an emissivity of 14% for the telescope (pessimistic case).

	HD97576, PAH2 filter (11.25 µm) 8.02 Jy						
	# of fram.	Peak val. [ADU]	$FWHM_1$ ["] ["]	$FWHM_2$ ["] ["]	Elliptic. [%] [%]	Str.rat. [%] [%]	Sens. [mJy/10σ/1h]
Diffraction limit			0.225	0.225	0.0	100	
Stack	12042	8.6e4	0.296	0.262	11	47	5.5
Register+stack	12010	1.01e5	0.264	0.240	8.7	55	2.6
Fr.sel.+reg.+stack	7032	1.03e5	0.242	0.246	4	59	1.5/2.15
	HD97576, PAH1 filter (8.6 µm) 11.63 Jy						
Diffraction limit			0.170	0.170	0.0	100	
Stack	29131	1.04e6	0.276	0.336	18	26	5.4
Register+stack	29034	1.48e6	0.262	0.219	16	37	4.9
Fr.sel.+reg.+stack	13483	1.51e6	0.224	0.214	4	42	2.65/4.6

Table 2.1: Burst mode performances measured on a reference star (HD 97576) according to the filter/wavelength. The lucky imaging mode (Fr.sel.+reg.+stack) is compared for reference to the simpler methods of frame registering (Register+stack) and simple frames stacking (Stack) which corresponds to the standard observing mode. The diffraction limits which are the ultimate performances achievable are also indicated (Diffraction limit). The achieved sensitivities are computed using either the equivalent observing time after frame selection or based on the telescope time. In both observations, the seeing was in the range 0.6-0.7 arcsec. The frame selection was based on the maximum value combined with the correlation function and ellipticity (e<0.2) criteria.

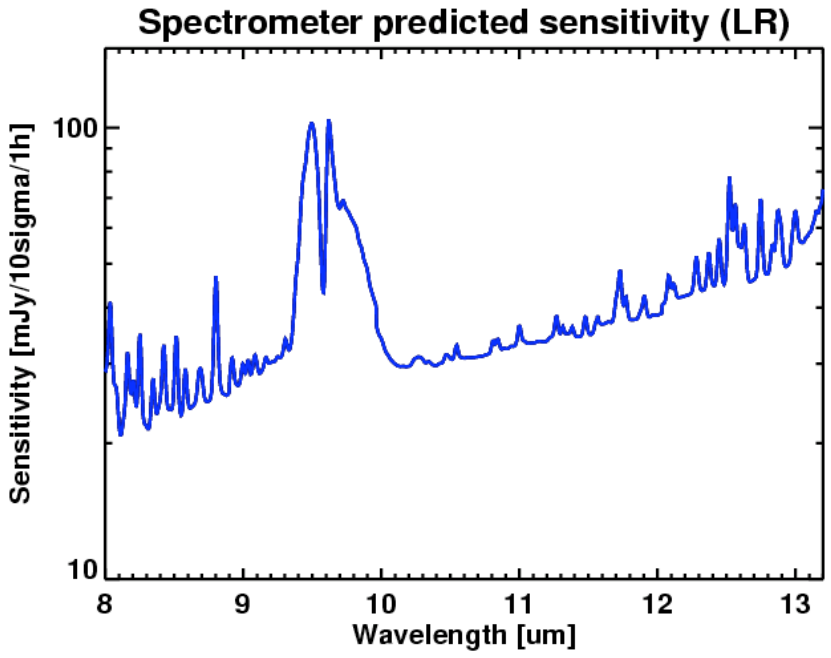

Figure 2.10: Spectrometer low-resolution predicted sensitivity. The values are computed using a model of the instrument and the background emission.

2.6 Science verification phase

Each new instrument installed at the VLT has its *Science Verification Phase*. This phase allows to assess the instrument performances using scientific targets. This is particularly important to assess the scientific potential of the instrument newly commissioned. The astronomers from the instrument consortium and from the contractor (ESO) can submit proposals for this phase in order to demonstrate the scientific capabilities of the instrument. I have selected a certain number of these observations to illustrate the scientific potential of VISIR and write an article in the ESO Messenger review (annex 2.8). Other examples of VISIR scientific applications are also shown in the conference paper in annex 3.10.

Sensitivities

While it is relatively easy to define a theoretical sensitivity, to measure the real sensitivity can be challenging in practice. A theoretical sensitivity can be for instance defined simply by comparing the signal of a standard source to the background noise. The source photon noise can be neglected in most of the cases in the mid-infrared range. A practical problem which arises immediately is the definition of the spatial support of the source given the fact that at modest (10-100) signal-to-noise ratios the wings of the PSF rapidly fall below the noise level. On top of that a finite aperture corresponds theoretically speaking to an infinite extent of the PSF in the focal plane. We have chosen to define the sensitivity using the signal-to-noise ratio of a reference point source integrated inside a circle of optimal radius centered on the centroid of the source. This optimal radius is defined where the signal-to-noise ratio reaches its maximum value. For the small pixel field of view (0.075 arcsec/pixel), this radius is 2-3 pixels for filters in the N-band and 5-6 pixels in the Q-band (see Fig.2.11).

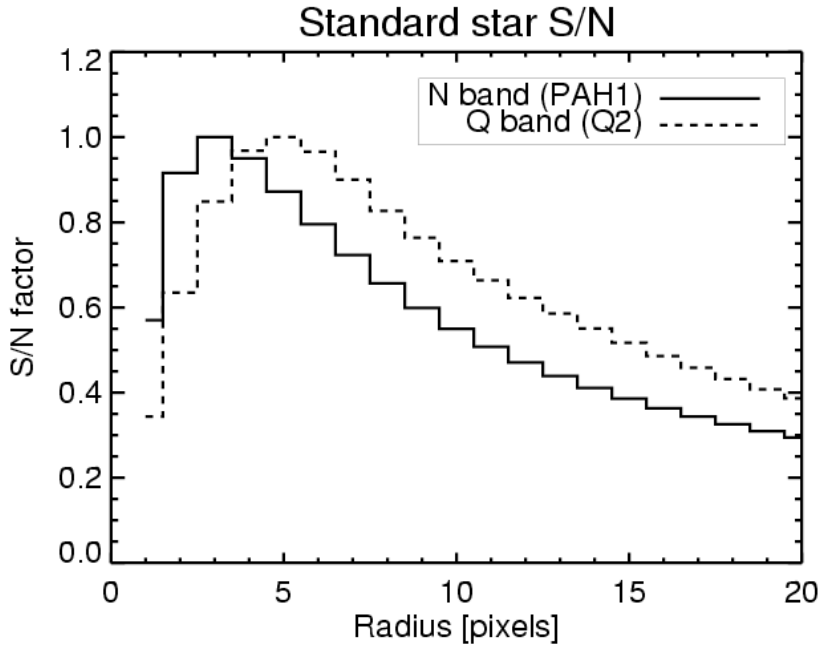

Figure 2.11: Signal to noise of a point source as a function of the aperture radius

The measured imager sensitivities over a period of 4 years of VISIR operations are displayed in Fig.2.12.

The measured imager sensitivities are 1.5-2 times worse than the theoretically predicted ones. Possible errors in the models, combined with the sometimes uncertainties on some parameters (transmission, entrance window emissivity, telescope emissivity, etc. ...), may lead to an overestimated sensitivity. It is also possible that some degradation factors in the transmission have been forgotten or neglected (mirrors efficiency, hot spots in the structure of the telescope, grating efficiency, ...). Moreover, some trade-offs have been made to limit some unexpected effects (such as detector striping), which has also has degraded the achievable sensitivity. Surprisingly, the sensitivities in the intermediate pixel scale (127 mas/pixel) are systematically worse than the ones measured using the finest grid (75 mas/pixel). This is probably linked to the sampling of the PSF and the optimal radius at which the sensitivity is evaluated. Indeed, our sensitivity criterium is based on a signal-to-noise ratio in an optimum radius which is of the order of 2-3 pixels when using the finest pixel scale. This radius is an integer value; its value is 1-2 pixels in the intermediate pixel scale. But such a crude rounding definitively degrades the derived sensitivity; the finest pixel scale allows only to define more precisely a criterium which is optimized on a finer grid. The fact that the discrepancy between the sensitivities vanished as the wavelength increases sustains this hypothesis.

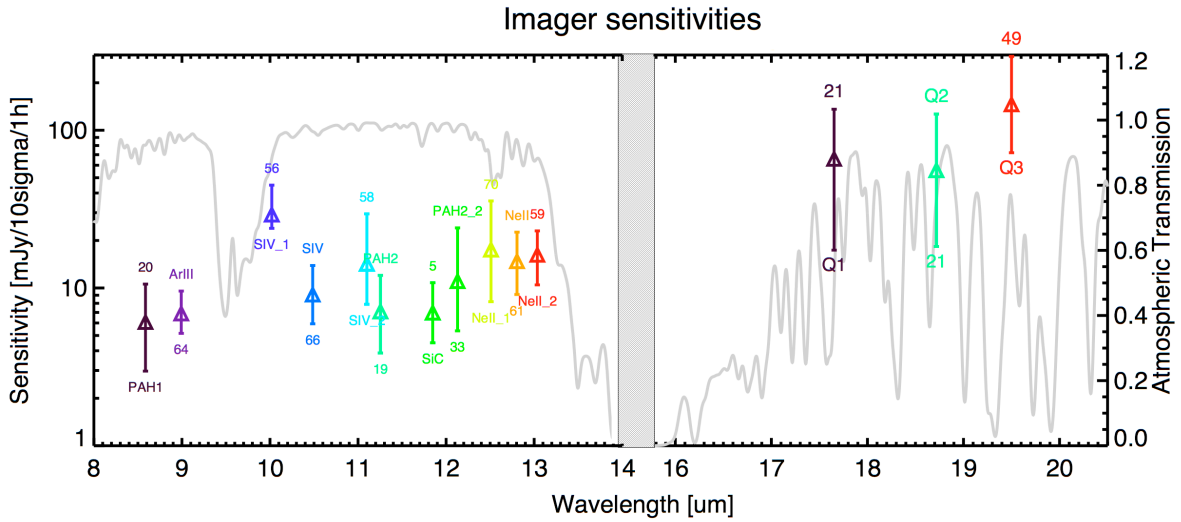

Figure 2.12: Measured sensitivities of the VISIR imager as a function of the filter. The triangles give the median values while the vertical bars show the range of sensitivities (1^{st}-4^{th} quartiles).

The conversion factors

The conversion factor measures the ratio between ADUs and spectral irradiance in Jy in a given filter and magnification. They are linked to the sensitivity but not at a 1:1 correlation level. These numbers are monitored every VISIR observing night using standard stars from Cohen's catalog ([Cohen et al., 1999]). The conversion factors for two filters in the N-band are displayed in Fig.2.13 and 2.14. The conversion factor for the PAH2 filter is remarkably stable over several years, with a total dispersion (apart from an instrument upgrade on day #1175) smaller than 10%. This noteworthy stability is awaited since the atmosphere is quasi-transparent in the PAH2 filter (transmission larger than 90% in average). In the NeII filter (Fig.2.14), the conversion factor is less stable with a standard deviation of the order of about 15%. The lower and less stable atmospheric transmission in this filter is the probable cause of

the larger variations of the conversion factor. This also explains why this filter is much more sensitive to weather conditions. In any case, the stability of the conversion factors in N-band allows to obtain a relatively precise (10-20 % error depending on the filter) photometric calibration in absence of a dedicated photometric calibration observation, by using the median value of the conversion factors recorded in the past.

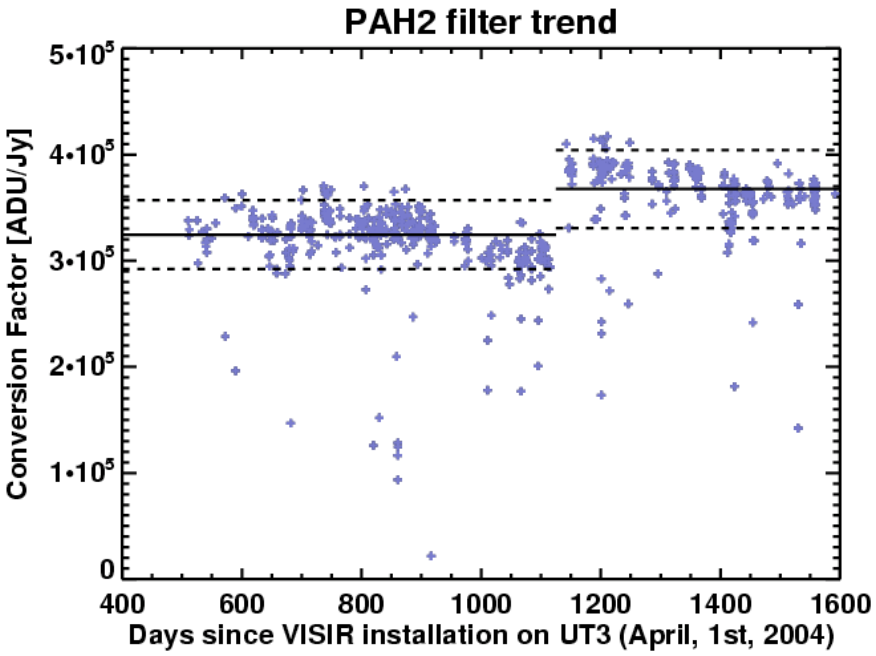

Figure 2.13: Conversion factors for the PAH2 filter (11.2 μm) in small-field pixel scale. The dashed lines plot the limits of the $\pm 3\sigma$ dispersion around the average value plotted as a plain line. Note the jump on day #1175 due to improved performances thanks to the upgrade of the detector thermal link.

Spectrometer sensitivity

The sensitivity of the spectrometer is measured, at a given wavelength, over a spatial interval i.e. a number of pixels along the slit which optimizes the signal-to-noise ratio. The VISIR sensitivities (theoretical and measured) are displayed in Fig.2.15 and 2.16 for the low and medium resolution modes respectively.

Concerning the spectrometer in low-resolution mode, the measured sensitivities clearly deviate from the predictions on several wavelength ranges (e.g. [10-11] μm, see Fig.2.15). It has been identified that this is due to the the order sorting filters that have a degraded transmission at the edges of their bandpasses. This effect was not considered for computing the theoretical sensitivities.

2.7 The VISIR "Pipeline"

A key element for operating VISIR as a VLT instrument is the pipeline. This pipeline is a complex piece of software with a range of tasks :

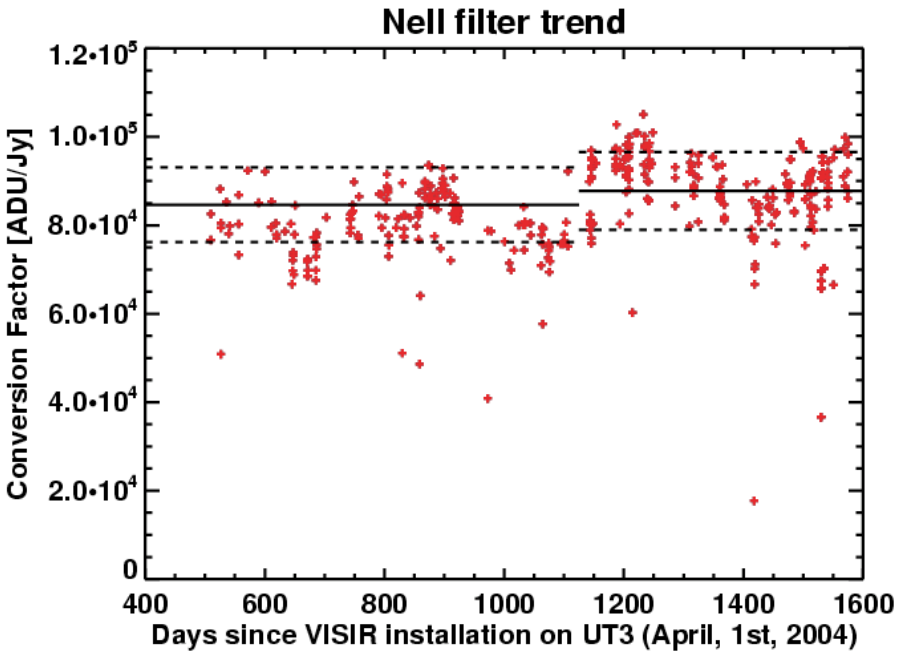

Figure 2.14: Conversion factors for the NeII filter (12.8 μm) in small-field pixel scale. The dashed lines plot the limits of the $\pm 3\sigma$ dispersion around the average value plotted as a plain line. The same jump as for PAH2 filter is noticed on day #1175.

- Reduce the raw data and if possible, calibrate them automatically
- Run in real time as the data are stored in the data repository, in order to allow the night astronomer to assess the data quality and observing conditions
- Provide the observing astronomer with offline processed data with a quality not too far from science grade reduced data.
- Provide the community with online processed data once the proprietary period is over.

At the telescope, this type of software needs to interface smoothly with several sub-systems : the Telescope Control System, the Instrument Control System, the Data Control System. Since the pipeline must run continuously over a night, it must be robust against crashes. This implies handling all types of exceptions that can occur during a night. If some data are corrupted, the pipeline must be able to reduce the non-corrupted part of a dataset. Two VISIR pipelines exist. The first version of the Saclay pipeline was used to prototype the ESO one. The Saclay pipeline, written and maintained by me, has evolved all along these four years of operations of VISIR, and has incorporated almost all the knowledge we have on the instrument. Its products are therefore of higher level than those delivered by the ESO pipeline.

2.7.1 Imager

In imaging mode, the VISIR pipeline performs the following tasks (E:ESO pipeline, S:Saclay pipeline) :

- Sort data between sky and chopped data. Cast them into an easy to handle format (rebuild of individual chopped frames) (E,S).

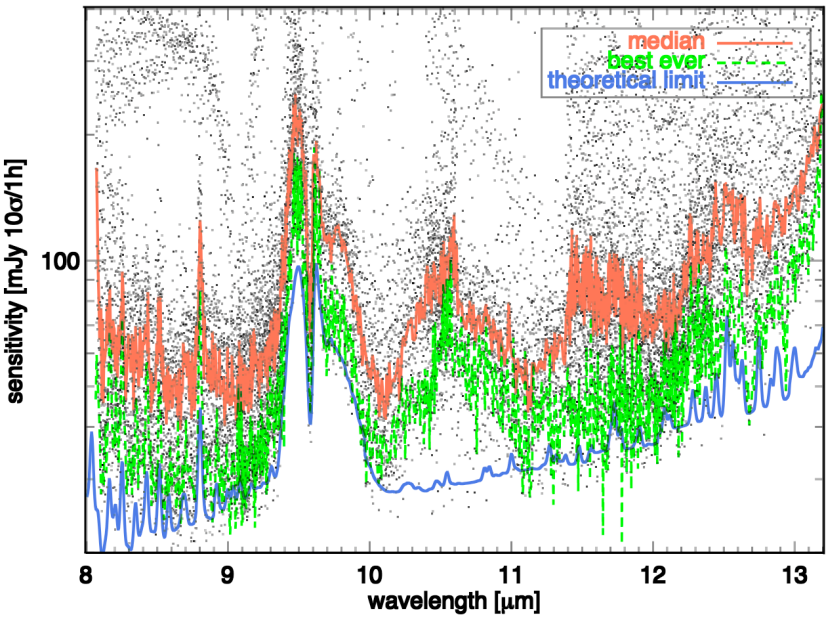

Figure 2.15: Measured sensitivity of the spectrometer in low-resolution mode. The black dots show all the measurements made.

- Allows optional frame selection in chopped frames (S); reject first corrupted frames after detector start (E,S)
- Apply chopping and nodding corrections (E,S)
- Correct or mask bad pixels (E,S)
- Destripe nodded images (see Section 3.2.6) (S).
- Correct for jitter (if set) followed by eventual refining (offsets corrections) (E,S)
- Combine the different beams into one beam if the object can be automatically detected (S).
- Measure the sensitivity/conversion factor on the final image (S).

2.7.2 Spectrometer

In spectroscopic mode, on top on top of the image reduction, the following tasks are performed :

- Correct the image for optical distortions using an optical model (E,S)
- Find wavelength coverage (crude wavelength calibration) on the detector using the optical model and setting parameters (E,S)
- In case of the cross-dispersed mode, extract the useful portion of the detector using the optical model (E,S)
- If the signal is strong enough combine the 3 beams into a single one (S)

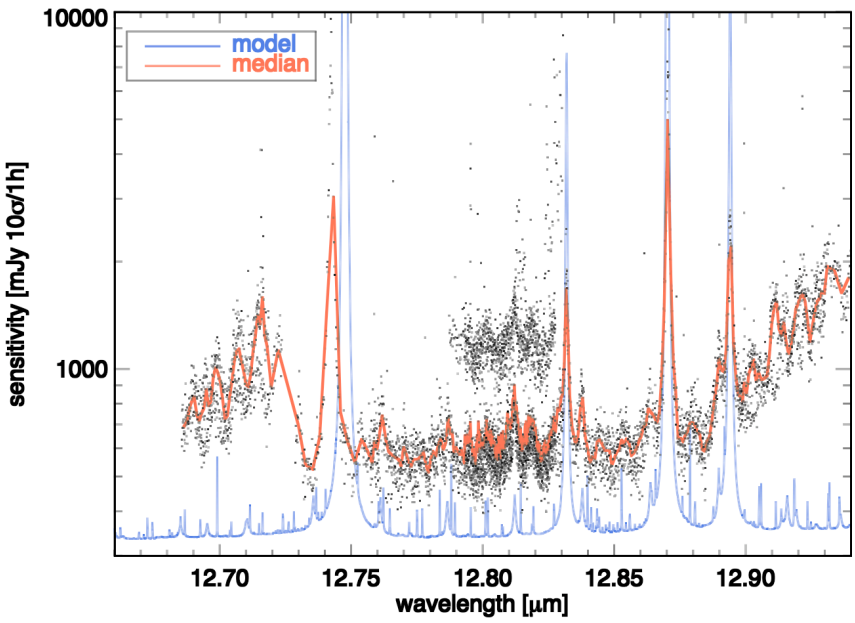

Figure 2.16: Same as Fig.2.15, but for the high resolution mode around 12.8 μm.

- Extract the spectrum (see below) (E,S)
- Refine the wavelength calibration using sky lines (E,S)
- Measure the sensitivity/conversion factor in case in concerns a standard star observation (S).

Spectrum extraction of unresolved sources

The extraction of the spectrum is one of the most difficult tasks while having a considerable impact on the quality of the final product. The goal is to reduce the 2D signal into a 1D spectrum having an optimized signal-to-noise. The reference method in this domain is the optimal spectrum extraction developed by [Horne, 1986] and [Robertson, 1986]. They show that for each wavelength (i.e. column on the detector after optical distortion correction), the spectrum can be optimally extracted (maximum S/N) if the 1D spatial signal is combined using some weights which depend on the signal itself. These weights ideally should be a "clean" (noise-free, sky-free, etc ...) version of the signal profile itself. The situation for VISIR is slightly different from the standard optimum extraction case. We are not dealing with sky background (removed by chopping), and the profile cannot be assumed to be a Gaussian or a low-order polynomium (as for the seeing limited spectra). In our case, the optimal weight is numerically estimated using either a filtered version of the raw profiles (S) or an average profile obtained by collapsing the 2D spectrum in the dispersion direction. In the later case possible changes in the spatial profile are blurred. In both cases, in order to avoid spurious signal from surrounding background, a threshold is applied to null the weights when the signal is too low. The optimally extracted value at wavelength λ_i reads :

$$S_{\lambda_i} = \frac{\sum_x W_x I_{x\lambda_i}}{\sum_x W_x^2}$$

where $I_{x\lambda_i}$ is the 2D image (x: spatial position in the slit, wavelength λ_i) and W_x the estimated weight from the spectrum spatial profile (note that the weights are normalized i.e. $\sum_x W_x = 1$). There are

actually two options to proceed. Either the weights are calculated from and applied to the initial image containing the various positive and negative beams. In this case, the positivity constraint cannot be applied. Alternatively, we can first combine the different beams and apply optimum extraction to the combined beams image. The latter option proved to be much more robust and reliable. One reason for this is that any spurious background residuals are first averaged out in the beam combining process (which avoids the propagation of large errors). The second reason is that the weights are estimated from a signal which has a higher signal-to-noise ratio. Lastly, the "à priori" positivity constraint can be applied. Possible ways of improving the optimum extraction could be impose for instance that the weights contain a single "gauss-like" or "Airy-like" structure. Instead of average over the full wavelength range, a moving box average would produce local profiles better matched to the local spatial extent of a spectrum. Some attempts have also be made to estimate the weights from a wavelets filtering of the local (at wavelength λ_i) profile, but the few spurious wavelets detections have a non-negligible impact on the quality of the result. A newer version of multiresolution filtering based on sparsity properties should be able to solve this problem.

2.7.3 The special case of the Burst Mode

Burst mode data are a particular case for the pipeline because they require the treatment of a large volume of data (previously ∼500 Mb and currently 1.2 Gb per nodding file i.e. about 5-10 Gb in 10 minutes of observations). This large amount of data problem can be tackled by processing the data on a workstation equipped with a fairly large RAM ($\geq$ 1.5 Gb) **and** managing smartly the data when processing them with the pipeline i.e. loading into memory the minimum of data needed for each independent operation, process them, save the partially reduced dataset before reloading them in the final phase to build the final result. The second difficulty lies in the estimation of the phase of the chopper. Indeed, the starting of the exposure is not synchronized with the chopper and the instrument operating system provides no information on the lag between the two. The phase of the chopper must be thus guessed directly from the data by detecting the source.

1) Estimation of the chopper phase

Because of the lack of synchronization between the chopper and the acquisition system, the phase of the chopper is initially not known. The first-order background subtraction using a nodding only correction is first applied. We wish to obtain a precise estimate of the phase of the chopper with a timing accuracy of the order of one DIT (∼10-20 ms). The signal-to-noise ratio of the source in a single DIT is too low to allow an automatic detection. A maximum filter is applied for each pixel of the data cube to detect the 2 positions (corresponding to the two positions of the chopper) of the source on the detector. For each frame the signal at the upper position of the source is then estimated by integrating values of the pixels over a circular aperture of one FWHM (of a source assumed to be point-like) in radius. The result is timing signal which contains the phase of the chopper. However, the crude background cancellation using nodding only leaves a variable background which modulates strongly the signal of the chopper (purple curve Fig.2.17). This extra noise can be controlled by subtracting the median value to each frame to obtain the red curve in Fig.2.17).

The phase of the chopper can be then estimated by a cross-correlation with a synthetic square signal.

2) Background correction using chopping-nodding

Having a full dataset of individual frames taken in burst mode at hand, we can eventually go beyond the standard chopping correction. Indeed, the standard background correction simply **sequentially** averages

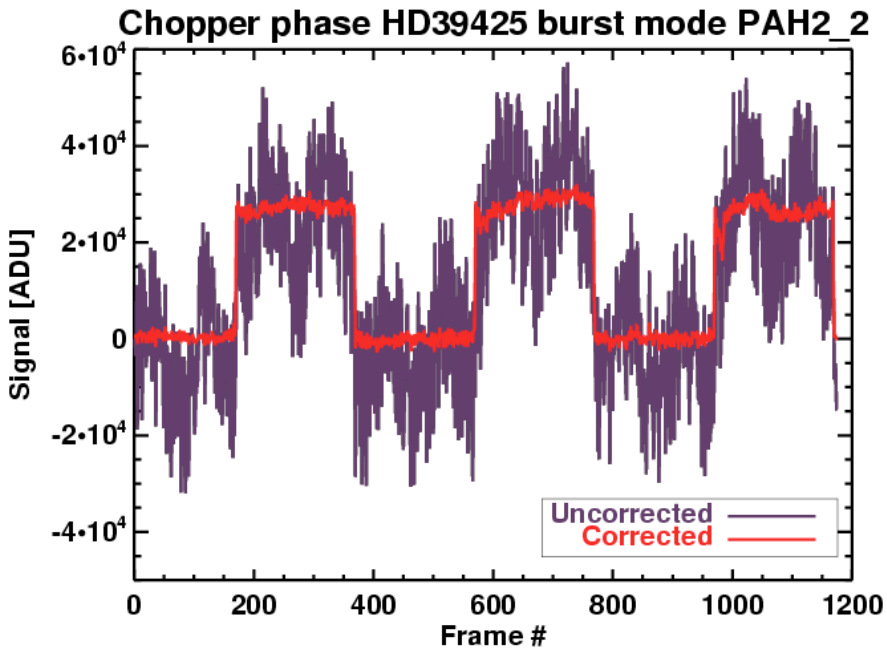

Figure 2.17: The purple curve displays the uncorrected signal in an aperture of radius of one FWHM (which depends on the wavelength). This signal is too noisy for the phase to be identified. The red curve is obtained by correcting the frames using the median value of the background. Now the phase can be easily estimated. This phase is then used as an input for the chopping correction of burst mode data.

the B (background) position and subtract it to the average of the A (on-source) position. In burst mode we can use the individual frames to construct a more representative background. For example:

1. Every experienced mid-infrared observer knows that a few "bad" frames can severely affect the background estimates. It can be then wise to combine more carefully the (B) background frames and build the best estimate of the background by performing some frame selection.
2. As was discussed above the standard background correction in based on an average of the (N) frames following the on-source frames. In the burst mode one can choose a set N frames among the off-source frames that bracket in time the on-source frames. This scheme effectively doubles the chopping frequency which potentially solves the problem of excess of noise at low frequencies (Sec.3.3)

In summary, the steps to reduce a burst mode dataset are the following :

- Loop on pairs of A-B nodding positions
  - Load the first nodding files A and B
  - Make a crude background subtraction by nodding correction A-B
  - Apply a fast destriping to the frames
  - Locate beams positions on the detector using a time maximum filter
  - On one of the beams, analyze the signal to estimate the chopper phase (see below)
  - For each beam, extract it (sub-frame of typical size 64x64) then apply chopping correction using a chosen estimate of background (see below), apply then nodding correction
  - Save each processed beam separately
- End loop on A-B nodding positions
- Load all the files corresponding to one beam position and build a cube of sub-frames
- Apply frames selection on one or many, eventually combined, criteria : cross-correlation value with a reference frame, peak value of source, value of ellipticity of the source, etc
- Shift-and-add the remaining frames
- Eventually combine the (usually 4) different beams

2.8 Conclusions

I have presented in this chapter the VISIR experiment and the associated preparatory work I have done. The installation and the first estimates of the performances could be qualified as a full success. However, when searching deeper and deeper to find the ultimate performances of the VISIR instrument we found some unexpected features that limit these performances especially concerning the case of faint extended sources. The analysis to understand these effects and some proposed solutions by offline processing or observing method are presented in the next chapter.

The article "Successful Commissioning of VISIR: the mid-infrared VLT Instrument" describes VISIR capabilities and performances at the commissioning phase.

The article “VISIR : A taste of scientific potential” published in the review “The Messenger” is based on commissioning and Science Verification results, describes the modes offered by VISIR and illustrate them by some selected scientific results.

Related articles

Annex :

Successful Commissionning of VISIR: the mid-infrared VLT Instrument

published in *The Messenger*, **2004**

Successful Commissioning of VISIR: the mid-infrared VLT Instrument

VISIR is the ESO-VLT instrument dedicated to observations through the two mid-infrared atmospheric windows (the so-called N and Q bands). VISIR was installed in April 2004 at the Cassegrain focus of Melipal, the third of the four 8.2 meter VLT unit telescopes; first light was obtained on May 1st. This cryogenic instrument combines imaging capabilities at the diffraction limit of the telescope (0.3 arcsec at 10 microns) over a field up to 51 arcsec, and long-slit (32 arcsec) grating spectroscopy capabilities with various spectral resolutions up to 25,000 at 10 microns and 12,500 at 20 microns. The instrument will be offered to the community for ESO period 75 (proposal due date: October 1st 2004).

P.O. Lagage[1], J. W. Pel[2,3], M. Authier[1], J. Belorgey[1], A. Claret[1], C. Doucet[1], D. Dubreuil[1], G. Durand[1], E. Elswijk[3], P. Girardot[1], H.U. Käufl[4], G. Kroes[3], M. Lortholary[1], Y. Lussignol[1], M. Marchesi[4], E. Pantin[1], R. Peletier[2,3], J.-F. Pirard[4], J. Pragt[3], Y. Rio[1], T. Schoenmaker[3], R. Siebenmorgen[4], A. Silber[4], A. Smette[4], M. Sterzik[4], C. Veyssiere[1]

[1]DSM/DAPNIA, CEA/Saclay, Saclay, France;
[2]Kapteyn Institute, Groningen University, Groningen, The Netherlands;
[3]ASTRON (Netherlands Foundation for Research in Astronomy), Dwingeloo, The Netherlands;
[4]European Southern Observatory

VISIR stands for VLT Imager and Spectrometer for the mid-InfraRed (mid-IR). This cryogenic instrument, optimised for diffraction-limited performance in both mid-IR atmospheric windows, the *N* and *Q* bands (Fig. 1), combines imaging capabilities with various magnifications, with slit grating spectroscopy with various spectral resolutions, up to R = 25,000 at 10 µm and 12,500 at 20 µm.

The contract to design and build VISIR was signed in November 1996 between ESO and a French-Dutch consortium of institutes led by Service d'Astrophysique of CEA/ DSM/DAPNIA; the Dutch partner is ASTRON, Dwingeloo. One year after the signature of the contract, VISIR passed the *Preliminary Design Review*, which concluded that VISIR was feasible (Rio et al. 1998). The project passed the *Final Design Review* in 1999 (Lagage et al. 2000). The instrument was then manufactured, integrated and suffered from unexpected events, such as fire and then flooding in the Saclay building housing the VISIR laboratory! After extensive tests in the laboratory (Lagage et al. 2003), VISIR was shipped to Paranal in March 2004; after that everything went very smoothly. The instrument was transported fully integrated, so that in April it could be mounted almost right away onto Melipal, the third of the four 8.2-m VLT Unit Telescopes (Fig. 2). First images were obtained on May 1st, a few hours after feeding VISIR with sky light. The second commissioning (from June 30 to July 7) was jeopardized by bad weather conditions (4 nights fully lost and 3 nights rather poor). During the two commissioning runs, several observing modes were sufficiently tested to consider to offer them to the community at the next call for observing proposals (deadline October 1, 2004). To finish commissioning, a third commissioning run took place from August 27 to September 5. All the VISIR modes have now been successfully tested. The results from this last run will be reported later.

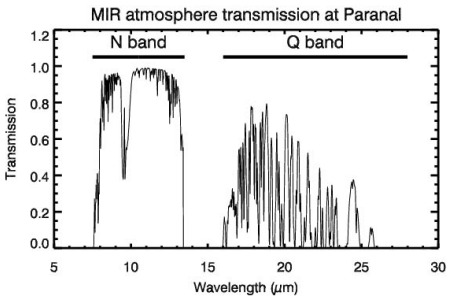

Figure 1: Mid-IR transmission of the atmosphere at Paranal, computed using the HITRAN model. The *N* window (8-13 microns) is a good window, especially in the 11 micron range; the only bad part is around 9.5 microns (ozone band). The *Q* window (17-25 microns) is a poorer window and the transmission depends crucially on the water vapour content of the atmosphere. For the transmission given in the figure, good atmospheric conditions of 1.5 mm of precipitable water vapour were assumed.

Scientific capabilities and observing modes

The mid-IR region is the domain of excellence to study both warm dust and gas (molecular or atomic) in various objects in the Universe, from nearby objects such as comets to quasars. Warm dust at an equilibrium temperature ranging between 80 and 400 K is best detected in the mid-IR through its thermal emission; grains small enough to be transiently heated to high temperature, the so-called VSGs (Very Small Grains), can emit in the mid-IR, even if their "mean" temperature is very low. Broad solid-state dust features (for amorphous or crystalline silicate dust around 10 and 20 microns) are observable from the ground, as well as the so-called PolyAromatic Hydrocarbonates (PAHs) bands at 12.7, 11.3 and 8.6 microns. Concerning gas transitions, two of the three lowest energy (i.e. pure rotational) quadrupole transitions of molecular hydrogen in the vibrational ground state ($H_2(0,0)S(2)$ at 12.28 microns and $H_2(0,0)S(1)$ at 17.03 microns) are observable from the ground, at least using high spectral resolution (>10,000) to find them between atmospheric lines. A variety of atomic lines are accessible from ground-based observations in the mid-IR, such as the forbidden lines of [Ne II] at 12.8 microns, the [S IV] line at 10.5 microns, and [Ar III] at 8.99 microns.

The main advantage when observing from the ground in the mid-IR is the high angular resolution achievable with large telescopes. Indeed, in this wavelength range, the angular resolution is mainly limited by the diffraction of the telescope. Until the launch of the James Webb Space Telescope (JWST), scheduled for 2011, the angular resolution achievable using ground-based facilities will be 10 times higher than from space facilities. With VISIR the diffraction Airy pattern of the Spitzer Space Telescope (formerly known as SIRTF, the Space Infrared Telescope Facility) can be resolved into 100 elements (full width half maximum of 2.6 arcsec at 10 µm for a 80 cm telescope, to be compared to 0.26 arcsec for a 8-meter class telescope). Thus, the top priority in the VISIR specifications has been the image quality.

Of course, the huge atmospheric and telescope background dramatically limits the sensitivity achievable with ground-based mid-IR instruments. Thus the "niche" for ground-based mid-IR astronomy is the observation of relatively bright sources (a few mJy) for which high angular resolution is needed. Examples of such programs are the study of circumstellar environments, the study of multiplicity in early stages of star formation, …

To conduct the various observing programs with VISIR, several observing modes were implemented :

- imaging with a choice of 3 magnifica-

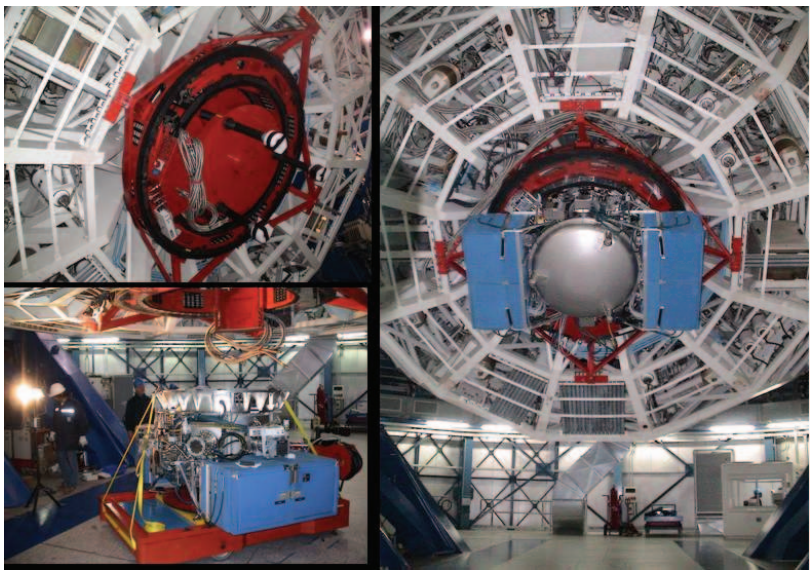

Figure 2: Top left: VISIR cable wrap mounted at the Cassegrain focus of MELIPAL. The cable wrap carries the electrical cables and closed-cycle cooler hoses to the instrument and rotates with it as the telescope tracks objects on the sky. At that time, a mass dummy was mounted on the cable wrap instead of VISIR. Bottom left: the mass dummy has been removed and VISIR, on its carriage, is going to be mounted onto the cable wrap. We can recognize the vacuum vessel (cylindrical shape with a diameter of 1.2 m and a height of 0.7 m) and the blue cabinets containing electronics for controlling and monitoring the instrument functions. Just above the middle of the blue boxes, we can see one of the three cryocoolers, used to cool the instrument to about 20K and the detector arrays to 7K. Right: VISIR fully mounted behind the primary mirror of MELIPAL. The total weight of VISIR is 2.3 tons.

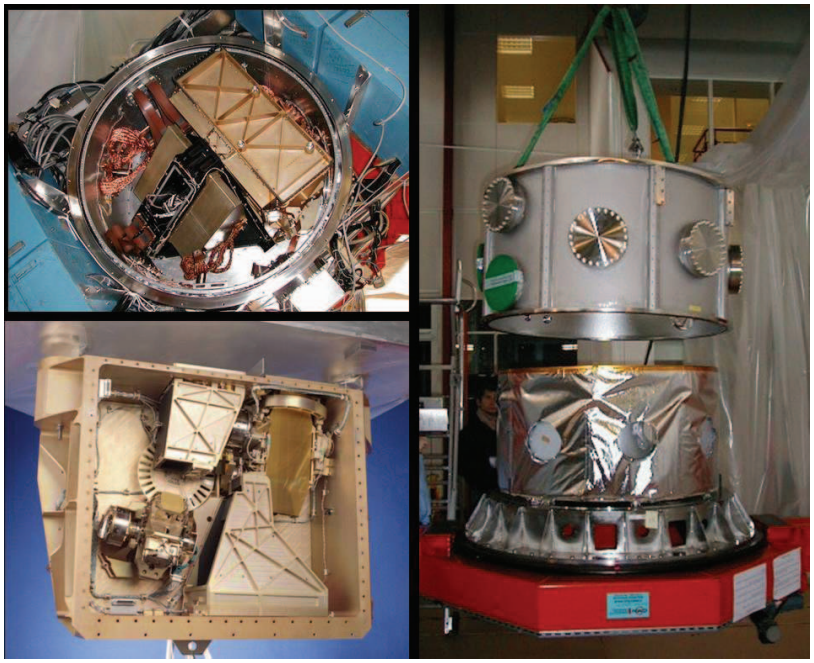

Figure 3: Top left: inside the cryostat; after removing the dome at the back of the cryostat, as shown in Figure 2 (right), one can see two sub-units: the imager (bottom left) and the spectrometer (top right). Bottom left: inside the spectrometer, partly integrated; one can see the slit wheel, the high-resolution duo-echelle grating (top right) and the grating carrousel carrying the 4 gratings including one scanner each for the low- and medium- spectral resolution arm (bottom left). Right: VISIR cryostat being assembled; the cryostat consists of a vacuum vessel and radiation screens; the vessel is composed of a flange to interface VISIR with the telescope adapter rotator (bottom of the image), a cylinder and a dome. The vessel is equipped with a radiation screen with superinsulation to lower the temperature of the surface radiating towards the cold optical bench.

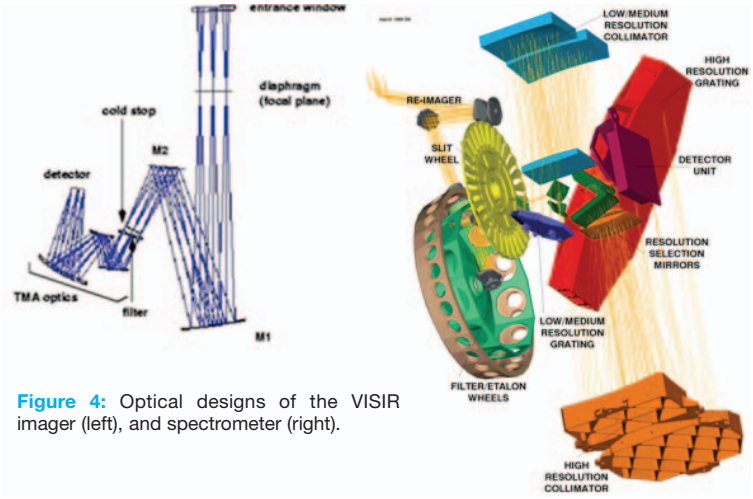

Figure 4: Optical designs of the VISIR imager (left), and spectrometer (right).

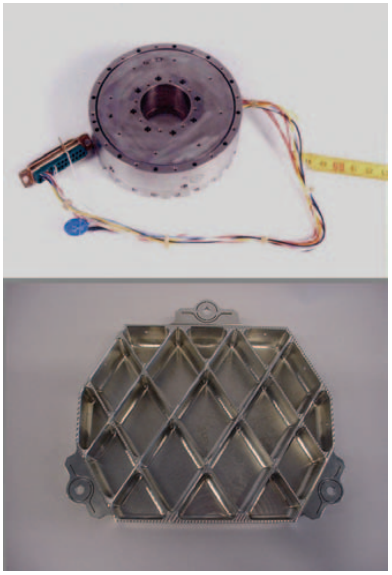

Figure 5: Top: Novel compact, precise and cryogenic motor/clutch unit actuator of VISIR. Such compactness was a key requirement to achieve a very compact mechanical design, imperative for a cryogenic instrument. Bottom: light-weighted structure on the back of one of the mirrors of the spectrometer. Also shown are the special mounting 'ears' for stress-free isostatic mounting.

tions and 24 narrow- and broad-band filters. The three Pixel Fields Of View (PFOV) are 0.075 arcsec, 0.127 arcsec and 0.2 arcsec. The corresponding fields of view are 19.2×19.2 arcsec^2, 32.5×32.5 arcsec^2 and 51.2×51.2 arcsec^2.

• slit grating spectroscopy with various spectral resolutions (R=λ/δλ), given for an entrance slit width set to 2λ/D, (where, as usual, λ is the wavelength and D the telescope diameter). Three spectral resolutions are available in the *N* band: low (R = 350 at 10 μm), medium (R = 3200 at 10 μm) and high (R = 25,000 at 10 μm). Two spectral resolutions are available in the *Q* band: medium (R = 1600 at 20 μm) and high (R = 12,500 at 20 μm). There is also the possibility to have a low resolution mode in *Q* band (R = 175 at 10 μm) but the usefulness of such a mode in the poor *Q* band atmospheric window has to be proven. The PFOV along the slit is 0.127 arcsec. There are 28 slits with selectable width between 0.3″ and 4″. In low and medium resolution the slit length is 32 arcsec. The nominal high-resolution echelle spectroscopy mode is performed with cross-dispersion grisms for order separation. With these low-dispersion grisms four to five echelle orders are imaged simultaneously on the detector. To avoid order overlap the slit length is reduced to 4.5 arcsec for the cross-dispersed mode. Alternatively, for astrophysically important isolated lines, long slit Echelle spectroscopy observations are possible. At the moment four order-selection filters are available to perform long-slit high-resolution echelle spectroscopy: H_2 at 8.02 microns, [Ne II] at 12.81 microns, H_2 at 17.03 microns and [S III] at 18.68 microns.

Design and development

The choice was made in the early stage of the ESO VLT instrumentation plan to have only one VLT instrument in the mid-IR, able to combine imaging and spectroscopy. This decision resulted in VISIR being a rather complex multi-mode instrument. On top of that, in order to limit the contribution of the optical bench to the photon background to less than 1%, the optical bench has to be cooled to a temperature lower than 60 K for the imager and lower than 32 K for the spectrometer. Thus VISIR is a cryogenic instrument (Fig. 3).

VISIR is made of two subsystems: an imager and a spectrometer. Each subsystem has its own detector array. The detectors are both 256×256 Si:As BIB arrays developed by DRS Technologies (Galdemard et al. 2003). The acquisition system is the common-user IRACE system developed by ESO. The software is based on the general VLT software. The detectors have to be cooled down to ~8K to avoid prohibitive dark current.

The optical design of the imager is an all-reflective system made of five mirrors (Fig. 4). The first mirror images the telescope pupil onto a cold stop (18 mm in diameter) to block extra background. The second mirror is a folding flat to ease the mechanical implementation. The last three mirrors form a Three Mirror Anastigmat (TMA) configuration. They ensure the re-imaging of the field onto the detector. The three magnifications of the imager are implemented by a set of three TMA systems mounted on a wheel, named TMA wheel. Near the focal plane another wheel (the diaphragm wheel) is used to adapt the entrance field aperture to the selected magnification, in order to limit possible extra-background. Three positions of the wheel are occupied by aperture masks and folding flats to deflect the telescope beam into the spectrometer. The third wheel of the imager is a filter wheel, which is located just after the cold stop and which can hold up to 40 filters.

In the spectroscopic mode the telescope beam enters the spectrometer via the 're-imager' unit with a cold stop, two filter wheels (with order-selection filters and fixed Fabry-Perot etalons for wavelength calibration) and an entrance slit wheel (Fig. 4). The actual spectrometer has two arms, one for Low- and Medium- Resolutions (LMR) and one for the High-Resolution (HR) mode. Like the imager, the spectrometer makes use of Three Mirror Anastigmat systems, but now in double pass: in the first pass the TMA acts as a collimator, in the second pass as a camera. Each arm has its own TMA, with a collimated beam diameter of 125 mm in the HR arm and 53 mm in the LMR arm. Via switchable folding flats the spectra from both arms are imaged onto the spectrometer detector. The LMR arm gives a choice between four small reflective gratings. All are used in 1st order in the *Q*-band and in 2nd order in the *N*-band. The HR arm is built around the 'duo-echelle': two large echelle gratings mounted back-to-back on an aluminium blank of 350×130 mm. Both echelles have slightly different rulings (80.0 and 77.3 grooves/mm), resulting in two sets of "interlaced" grating orders. By choosing either the 'A' or the 'B' side of the duo-echelle, one can select for each wavelength the grating order with optimum blaze efficiency.

Given that VISIR is a cryogenic instrument and given the number of modes, the leading mechanical design criteria were high

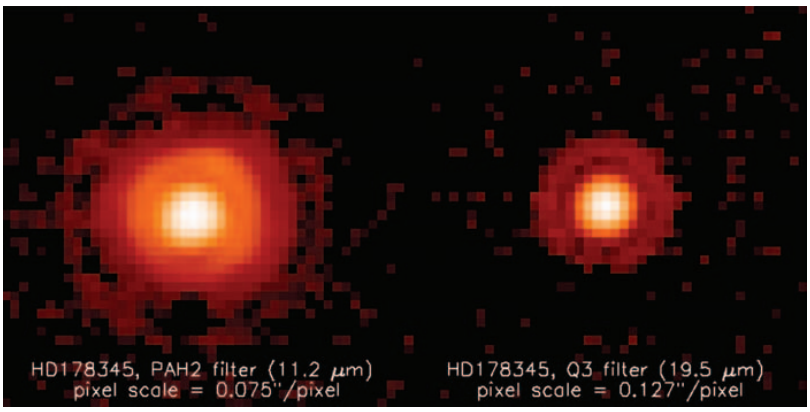

Figure 6: Point source with diffraction rings at 11.2 microns and 19.5 microns.

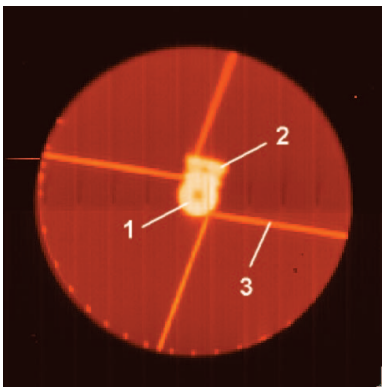

Figure 7: *N*-band pupil image for the spectrometer. In the thermal infrared, the pupil-image is an inverse of an 'optical' pupil image. What would show up dark in an optical image is radiating strongly at 10 microns. We can see thermal emission of 1) the (circular) M3-tower, 2) the rectangular attachment of the M3-tower in the stow-position and 3) the spiders of the VLT-M2 with their V-shaped geometry.

stiffness to weight ratio, low mass and high thermal stability. Such criteria have led to the development of a novel type of cryomechanism by the CEA/DAPNIA (Fig. 5). These devices have to actuate, at cryogenic temperature, optical devices with a very high accuracy and positioning repeatability (5 arcsec). By design, the cryomechanisms are very rigid and can be used in a cantilever position. The concept allows open loop control by use of a stepper motor with high torque and direct drive and includes a zero position switch as well. The power dissipation is zero when the cryomechanism is locked in position. Eleven such cryomechanisms are used in VISIR: three for the imager and eight for the spectrometer. The low mass criterion has also led to light-weighting of the opto-mechanic parts of VISIR, such as the mirrors (Fig. 5).

Performance

The image quality of the imager was checked to be diffraction limited both in *N* and *Q* band (Fig. 6), at least under good seeing conditions. In the mid-IR at 10 microns the influence of atmospheric turbulence on image quality is obviously much less than at optical wavelengths. However, it is important to note that, when the optical seeing is worse than about 0.6 arcsec, a departure from diffraction limited performance at 10 microns is also observed.

The pupil alignment was also checked and found to be correct within a few percent (Fig. 7).

The sensitivity depends considerably on the weather conditions, especially in the *Q* band. While we achieved reasonable sensitivities in the *N* band (for example, down to 3.6 mJy 10σ 1 hour for the 11.3 μm PAH filter in good weather conditions), we were far off (an order of magnitude) in the *Q* band. The origin of such bad sensitivity is probably bad weather conditions.

To achieve the required sensitivity, the huge photon background has to be removed. This is done following the classical chop-

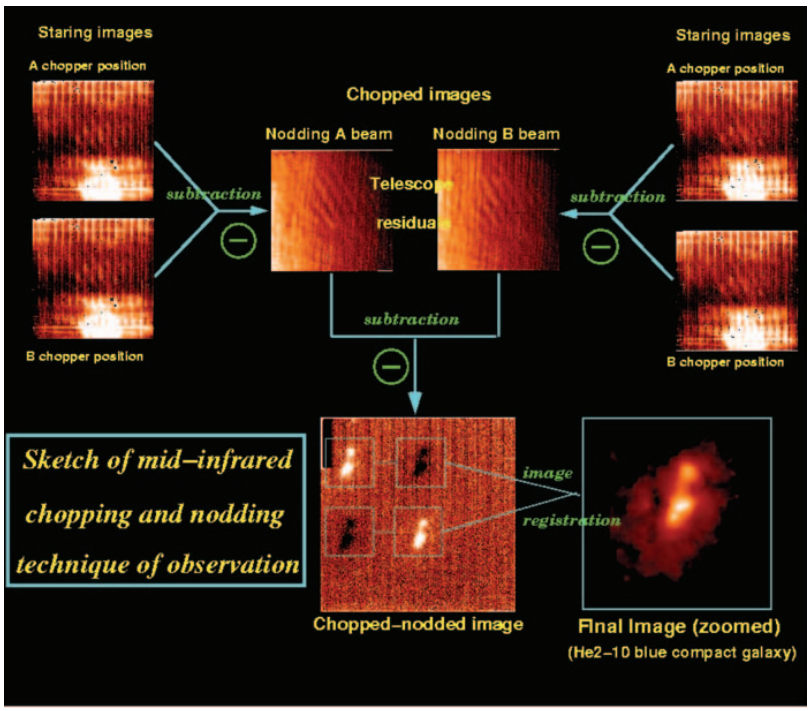

Figure 8: Illustration of the chopping-nodding technique when observing the He2-10 blue compact galaxy (see ESO press release about VISIR for more information about the object). The basic idea to remove the huge photon background generated by the atmosphere and the telescope is to make the difference between two observations: one on-source (background plus source) and the other off-source (background alone). Given the background fluctuation time scale, the on- and off-source measurements have to be done at a rate typically in the Hz range. Such a high rate cannot be achieved by moving the telescope. That is why it is done by moving the secondary mirror of the telescope (positions A and B on the left of the illustration); this is called *chopping*. The chopping technique allows us to remove the sky background and most of the telescope background. However the optical path on the primary mirror is not exactly the same according to the chopper position. That is why a residual background remains after chopping and one cannot detect the galaxy (see image labeled *nodding A beam* in the illustration). The time scale for the fluctuations of the residual background is long and can be monitored by moving the telescope off source and doing the same chopping observation sequence as in the preceding telescope position (resulting in the image labeled *nodding B beam*). After subtracting beams A and B, the galaxy is detected. If the chopping throw and nodding throw are small enough, the source is always present in the field of view of the instrument, so that we end up with four sources on the final image (two positive and two negative).

© ESO - September 2004

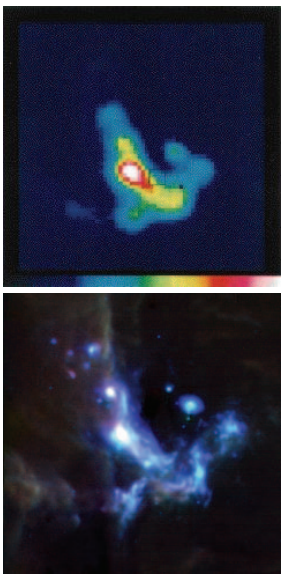

Figure 9: Top : image of the galactic centre obtained with the TIMMI instrument mounted on the 3.6-meter telescope on La Silla (H. Zinnecker et al. 1996). Bottom: image of the galactic centre obtained with VISIR. This illustrates the huge improvement when going from a 3-meter class to a 8-meter class telescope.

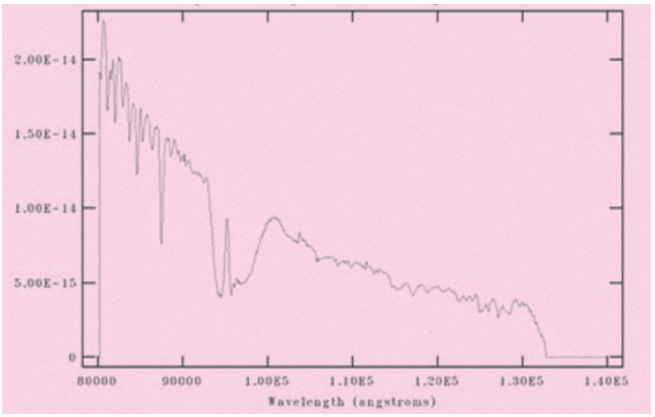

Figure 10: Full low-resolution *N*-band spectrum of standard star HD175775 (20.2 Jy at 12 μm). Note that the spectra have not been corrected for atmospheric effects.

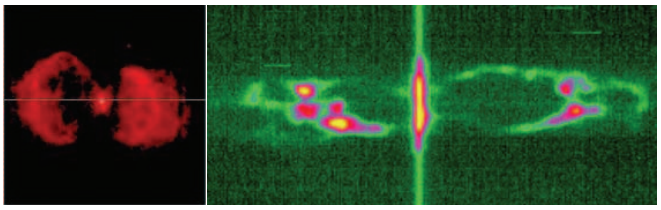

Figure 11: Left: image in the [NeII] line at 12.8 microns of the "Ant" Planetary Nebula (Mz3). Right: long-slit high-resolution spectrum around the [NeII] line; spatial direction is horizontal and spectral direction vertical. The slit was located as indicated by the line on the left image. The velocity resolution is about 17km/s.

ping-nodding technique illustrated in Fig. 8. While the VLT secondary mirror assembly allows chopping up to typically 5 Hz, substantially lower frequencies are being used, so that active field-stabilisation with the VLT-secondary mirror (M2) while chopping becomes possible. This is necessary for ultimate image quality under typical wind conditions. For the commissioning runs chopping frequencies as low as 0.25Hz were used to detect sources at a level of a few tens of mJy in imaging. Further tests are pending, to see whether these low frequencies compromise the sensitivity.

With VISIR a huge hurdle in improving ground-based mid-IR observation has been passed. We knew that with observations on a 3-meter class telescope we were only seeing the "tip of the iceberg" and that improvements should be achieved with VISIR. But, we were surprised by what we saw (Fig. 9)! With VISIR, we can obtain from the ground, mid-IR images with a quality rivalling that of shorter wavelength observations.

The spectrometer is also performing very well. Complete low-resolution *N*-band spectra were taken on July 4 and 6 in four settings (two with the LSW grating and two with the LLW grating) for various standard stars. The result for HD 175775 is shown in Fig. 10. In general the different parts of the spectrum join up quite well. The ratio of the spectra of two standard stars is reasonably close to the ideally flat distribution, except at wavelengths with strong atmospheric features like in the ozone band around 9.5 microns, where the atmospheric contributions do not cancel sufficiently due to difference in air mass and atmospheric variations.

Of special interest is the high spectral resolution mode, which has, so far, no equivalent in the Southern hemisphere (Fig. 11).

Observing with VISIR

VISIR is one of the instruments which will generally be used during bright time. Given the international competition (for example the T-ReCS instrument on Gemini South), VISIR will be offered to the community as soon as possible. The VISIR modes that have been sufficiently tested during the first two commissionings will be offered to the community in the call for proposals for Period 75 (proposal due date: October 1st).

Acknowledgments

VISIR would have not been possible without the contributions of numerous people in the consortium and at ESO. We would like to thank all those who have contributed to this superb instrument:

Staff at Saclay: D. Arranger, A. Bakaou, P. Bargueden, J.C. Barriere, G. Dhenain, A. Donati, B. Duboue, N. Eyrard, Ph. Galdemard, D. Gibier, J.F. Gournay, E. Gregoire, J.M. Joubert, A. Lotode, P. Magnier, P. Mulet, J. NevesDaCosta, D. Nicolleau, F. Nunio, B. Pinvidic, Y. Sauce, Ph. Seguier, A. Sinanna, J.C. Toussaint, C. Walter. Former Saclay staff, N. Bottu, F. Garnier, E. Guelin, C. Lyraud, G. Wang.

Staff at ASTRON: A. van Ardenne, J. Bakker, M. Bakker, R. van Dalen, S. Damstra, J. Dekker, M. Drost, G. Hagenauw, R. ter Horst, J. Idserda, A. de Jong, T. de Jong, G. Koenderink, Y. Koopmans, A. Koster, J. Kragt, S. Kuindersma, J. Nijboer, P. Pul, M. Schuil, J. Tinbergen, N. Tromp.

Staff at ESO headquarters: E. Allaert, P. Ballester, J.L. Beckers P. Biereichel, B. Delabre, G. Finger, Y. Jung, J.-L. Lizon, L. Lundin, W. Nees, L. Mehrgan, M. Meyer, J. Stegmeier, J. Vinther and former ESO staff: N. Devillard, A. Van Dijsseldonk. The support to the project by G. Monnet and A. Moorwood was crucial, especially during difficult phases.

We wish also to thank the ESO staff on Paranal (R. Gilmozzi, J. Spyromilio, A. Kaufer, U. Weilenmann P. Baksai, J. Brancacho, R. Castillo, N. Hurtado, J. Navarrete) for their excellent support during installation and commissioning of VISIR.

References

Ph. Galdemard et al. 2003, SPIE Vol. 4841, 129
P.O. Lagage et al. 2000, SPIE Vol. 4008, 1120
P.O. Lagage et al. 2003, SPIE Vol. 4841, 923
Y. Rio et al. 1998, SPIE Vol. 3354, 615
H. Zinnecker et al. 1996, Messenger 84, 18
ESO press release 13/04, May 2004

Annex :

VISIR, a Taste of Scientific Potential

published in *The Messenger*, **2005**

VISIR, A TASTE OF SCIENTIFIC POTENTIAL

VISIR, THE ESO-VLT INSTRUMENT MADE FOR OBSERVATIONS IN THE TWO MID-INFRARED ATMOSPHERIC WINDOWS (THE SO-CALLED N- AND Q-BANDS), IS NOW PRODUCING SCIENTIFIC RESULTS. SOME FIRST RESULTS ARE DISCUSSED FROM A PEDAGOGIC POINT OF VIEW, EMPHASISING THE VARIOUS MECHANISMS AT WORK THAT PRODUCE MID-INFRARED RADIATION (THERMAL DUST EMISSION, TRANSIENTLY HEATED DUST EMISSION, ION LINE EMISSION, PURE ROTATIONAL LINE EMISSION OF MOLECULAR HYDROGEN, SYNCHROTRON EMISSION). THE TWO KEY ADVANTAGES OF VISIR, I.E., ITS HIGH ANGULAR RESOLUTION AND ITS HIGH SPECTRAL RESOLUTION, ARE ILLUSTRATED RESPECTIVELY BY THE RESULTS FROM THE OBSERVATIONS OF THE BROWN DWARF BINARY SYSTEM ε INDI, AND BY KINEMATIC STUDIES OF THE GALAXY NGC 7582.

ERIC PANTIN[1,4], PIERRE-OLIVIER LAGAGE[1], ARNAUD CLARET[1], CORALIE DOUCET[1], ANDREAS KAUFER[4], HANS-ULRICH KÄUFL[4], JAN-WILLEM PEL[2,3], REYNIER F. PELETIER[2], RALF SIEBENMORGEN[4], ALAIN SMETTE[4,5], MICHAEL STERZIK[4]

[1]DSM/DAPNIA/SERVICE D'ASTROPHYSIQUE, CEA/SACLAY, SACLAY, FRANCE;
[2]KAPTEYN INSTITUTE, GRONINGEN UNIVERSITY, GRONINGEN, THE NETHERLANDS;
[3]ASTRON (NETHERLANDS FOUNDATION FOR RESEARCH IN ASTRONOMY), DWINGELOO, THE NETHERLANDS; [4]EUROPEAN SOUTHERN OBSERVATORY, [5]F.N.R.S. BELGIUM

VISIR, THE VLT MID-INFRARED Imager and Spectrometer, was installed at UT3 (Melipal) in early 2004 and was successfully commissioned between May and August 2004 (Lagage et al., 2004). After this, the time until its planned start of regular science operations in period 75 (April–September 2005) has been used to integrate the instrument into the Paranal operations and maintenance schemes and to carry out some first Guaranteed Time Observations (GTO) by the instrument consortium and Science Verification (SV) observations to demonstrate the scientific capabilities of the instrument. A complete list of GTO and SV programs can be found at *http://www.eso.org/observing/proposals/gto/visir* and *http://www.eso.org/science/vltsv/visirsv*. The data from the Commissioning and SV observations are available to the public and can be retrieved through the ESO science data archive (*http://archive.eso.org*).

Since June 2004, the sensitivities of VISIR were carefully monitored through a systematic program of observations of standard stars as often as possible. Figures 1 and 2 show a compilation of these measured sensitivities both in the imaging and the spectroscopic mode. As seen on these figures, the sensitivities are in reasonable agreement with the predicted ones. However, the last 6 months of monitoring have shown that the sensitivity of VISIR depends quite significantly on the conditions of the weather and the observations conditions (seeing, airmass, amount of Precipitable Water Vapour; the value of the latter can be found at *http://www.eso.org/genfac/pubs/astclim/forecast/meteo/ERASMUS/par_fore.txt*). Mid-infrared observations with VISIR will thus benefit greatly from the flexibility provided by service observing scheduling since the constraints of the observer will be much better matched to weather and observation conditions. One should also note that some spurious effects, such as detector striping, may degrade the sensitivity performance sporadically.

A sample of first scientific results from VISIR has been selected to give a first taste of the overwhelming scientific potential of this latest VLT instrument.

VARIOUS ORIGINS OF MID-INFRARED RADIATION

EMISSION OF LUKEWARM DUST GRAINS IN THERMAL EQUILIBRIUM

Dust grains (silicates, amorphous carbon, graphite ...) immersed in a radiation field reach thermal equilibrium at the temperature that corresponds to the balance between absorbed and re-radiated energy. Depending on the circumstances (orbit, central source luminosity, chemical composition) they can reach a temperature of around 100–500 K. Their re-emitted energy is mostly radiated at infrared wavelengths, such that:

$\lambda_{max} = 2898/T$ μm, T in K (Wien's law).

Hence, a warm dust grain at room temperature (i.e., around 300 K), radiates its maximum energy at around 10 μm. Mid-infrared wavelength (10 and 20 μm) windows are thus well adapted to probe dust grains in orbits around a star, typically in the planetary zone (1–50 AU). As a result, the search for footprints left by planets very close to the star in dusty discs is possible. Figure 3 illustrates this with images of the dust-disc of β-Pictoris observed without coronograph (in contrast to visible and near-infrared observations) allowing one to study structures in the innermost regions; from these observations, the mechanism of disc replenishment can be inferred (collisions of planetesimals producing small particles) (Pantin et al. 1997; Pantin et al. 2005, in preparation) and the structure of the disc gives precious indications about the presence of gravitational perturbers, such as massive planets.

Generally speaking, in the mid-IR one is approaching the Jeans limit. Thus, the contrast between the stellar photospheres and the circumstellar environment is more favorable as compared to the near-IR, where coronography is a must.

EMISSION OF VERY SMALL DUST PARTICLES AND PAH

Very small dust grains (e.g. silicates, graphite, with sizes smaller than 0.01 μm) as well as polycyclic aromatic hydrogenated grains (PAH or "big" molecules formed of benzene rings) can be heated quite far away from a source, provided that the source emits a sufficient number of visible or ultraviolet photons. These photons stochastically heat these small grains (or big molecules) temporarily to temperatures close to 1000 K. The grains then relax through vibrational modes of C-H and C-C bonds, at a few precise wavelengths mainly found in the mid-infrared range (3.3 μm, 6.2 μm, 7.7 μm, 8.6 μm, 11.3 μm ...).

The ISO infrared satellite discovered that some isolated Herbig AeBe (HAEBE) stars

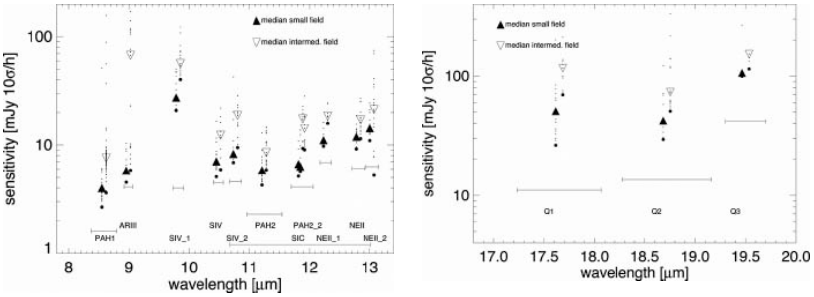

Figure1: Imager sensitivity monitored over 6 months, in *N*-band (left), and *Q*-band (right). The sensitivity is estimated for each standard star observation using the following method. One determines the radius at which the signal-to-noise is maximal. The star signal is integrated within this optimum radius and the corresponding error is computed. The sensitivity is finally deduced from the calibrated flux of the star deduced from Cohen et al. (1999) all sky network database of infrared calibrators. The horizontal bars represent the theoretical limits of VISIR sensitivity, the black dots show the "best ever" value of sensitivity reached. Note that the two pixel scales available ("small field" and "intermediate field") have differing sensitivities. Although not expected when modeling VISIR sensitivity, "small field" sensitivities are systematically better than "intermediate field" ones.

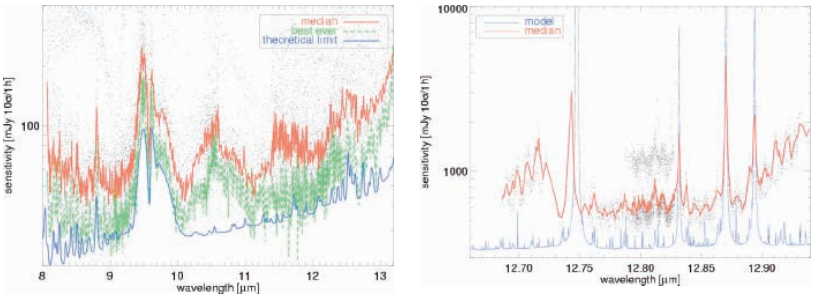

Figure 2: Spectrometer sensitivity monitored over a period of 6 months. The left panel shows the low-resolution mode in all four settings currently offered spanning the full *N*-band. The right panel displays the sensitivity measured in the long-slit [NeII] setting at 12.8 μm.

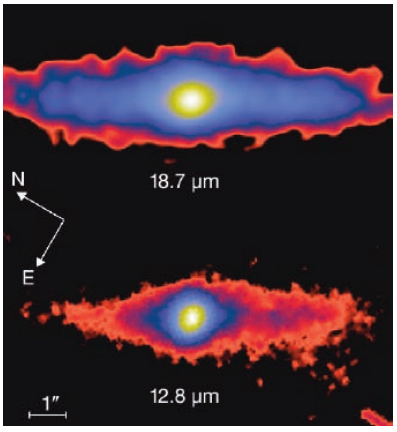

Figure 3: The dust disc of β-Pictoris seen by VISIR at 12.8 and 18.7 μm. The asymmetry (South-West side brighter than North-East side) is clearly seen. As illustrated here, the longer the observing wavelength, the colder the dust probed. However, the spatial resolution is also worse because of the diffraction limit. One key question that will be addressed with the above images is the following: is there an inner tilt in the β-Pictoris dust disc, as claimed from Keck observations (Wahhaj et al. 2003, Weinberger et al. 2003), or not, as claimed from recent Gemini observations (Telesco et al. 2005). Some more data processing (image deconvolution) is needed before having the VLT view!

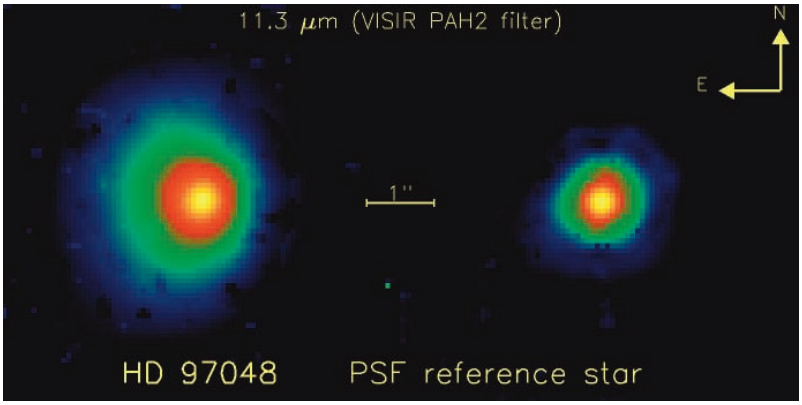

Figure 4: Image of the Herbig Ae star HD 97048. The extension seen in the "PAH" band filter centred on 11.3 μm is clearly visible. Such an extension cannot be explained just by thermal emission of dust grains at an equilibrium temperature and a population of small grains or PAH molecules transiently heated has to be invoked to explain the extension (Doucet et al. 2005). The spectroscopic observations (see Figure 5) indicate that a 11.3 μm feature attributed to PAH is indeed present. As expected the extension at 11.3 μm is larger than that observed recently at 3.3 μm with NACO (Habart et al.,2005, in preparation). A striking feature of the extension is its asymmetry. Sophisticated models including PAH, flaring disc geometry, viewing angle, inclination … are now needed to interpret these observations.

harbour dusty discs in which planetary formation is suspected to take place, and show the signature of such PAH (Waelkens et al. 1997, Waters et al. 1998).

One key programme of the VISIR guaranteed time observations is devoted to the study of a large sample of such HAEBE pre-main-sequence stars. We have observed one of these stars (HD 97048, Figures 4 and 5) using VISIR in imaging mode (PAH2 filter centred on 11.3 µm) and spectrometry mode (low-resolution 11.4 µm setting). The 11.3 µm image shows a quite large extension (2–3 arcsec) that was already suspected from previous observations (van Boekel et al. 2004). The spectrum confirms that PAH emission is indeed prominent in this disc, while the right panel of Figure 5 proves that the PAH emission is indeed spatially extended.

Line emission from ionized gas

Narrow atomic gas emission lines are also powerful probes of the astrophysical conditions. The most famous ones in the *N*-band are [NeII] at 12.8 µm, [ArIII] at 8.992 µm, and [SIV] at 10.485 µm. Narrow band (R = 50–80) filters corresponding to these lines are available in the VISIR imager and long-slit mode of the spectrometer. Concerning other lines (e.g. [HI] at 12.36 µm, forbidden lines such as [NII] at 12.79 µm, or [NaIV] at 9.04 µm), a cross-dispersed mode of the spectrometer will be offered in the future. In Figure 6, we demonstrate the possibility of studying the spatial emission of the [NeII] line in the central regions of the Seyfert 2 galaxy NGC 1068. Indeed, after subtraction the 2D continuum emission interpolated from images taken through reference filters around 12.8 µm, one obtains a map of the pure [NeII] emission (right panel of Figure 6). One can notice that the [NeII] emission is extended and follows the Narrow-Line-Regions, but, most interestingly, unveils the South-East, dust-extincted component of the ionising cone, as predicted by the unified AGN model (Galliano et al. 2005).

Emission lines from pure rotational modes of molecular gas

Although this mode has not been offered to the community yet, VISIR has the capability to obtain spectra at very high resolution (R ~ 15 000 to 30 000) of "cold" molecular Hydrogen H_2 at 12.28 and 17.03 µm. The transitions accessible to VISIR correspond to the lowest lying rotational states of the vibrational ground-state of Hydrogen. This potential is demonstrated in Figure 7 showing the emission line at 17.03 µm produced in the Orion bar (Allers et al. 2004). As shown in the same figure, the velocity structure of this cloud might be inferred from the precise central wavelength of the H_2 emission line. Additional checks are needed, however, before definitely attributing the observed wavelength changes to velocity.

This type of observation from the ground is not easy because of a strong atmospheric emission line very nearby at 17.027 µm; the high spectral resolution of VISIR makes VISIR a powerful instrument to detect the H_2 line.

Precise wavelength calibration is routinely achieved using the sky spectra recorded in the data. The observed atmospheric lines are compared with those predicted from an atmospheric model based on a HITRAN radiation transfer model. Using a cross-correlation method, an accurate wavelength calibration is derived on the fly (see Figure 8).

This observing mode offers great potential for example for the search for cold H_2 in protoplanetary discs.

Synchrotron emission from compact objects

Charged particles rotating in a strong magnetic field generate synchrotron emission. The observed spectrum is usually close to

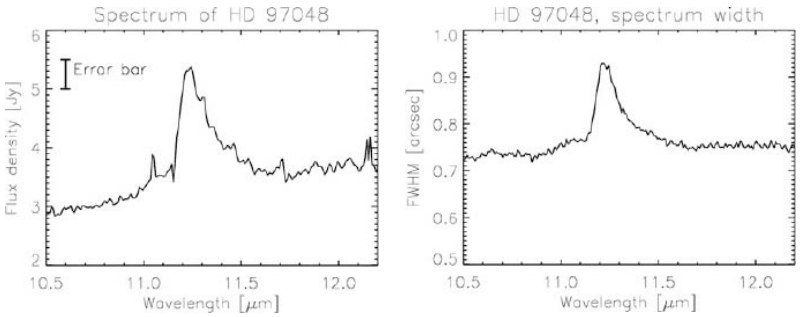

Figure 5: Left: Observed spectrum of HD 97048 around 11.4 µm in the long-slit low-resolution mode of VISIR. Right: The measured spatial full width at half maximum of the HD 97048 spectrum as a function of wavelength. The PAH emission at 11.3 µm is spatially more extended than the continuum and confirms the spatial extension of the image seen in Figure 4.

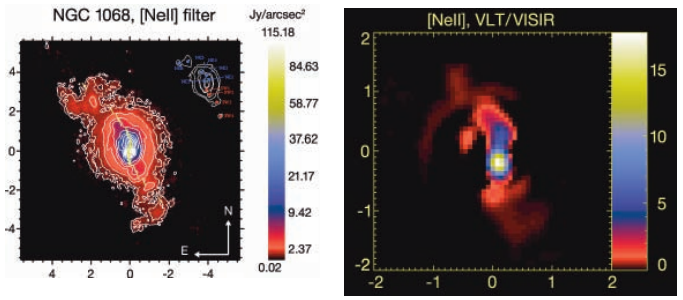

Figure 6: The Seyfert 2 galaxy NGC 1068. The left panel shows the image obtained through the NeII filter centered on 12.8 µm, and contains both the continuum and the gas emission. The yellow ticks overplotted mark the local position angle of the isophotes, showing the symmetrical twisting of the mid-infrared emission from the center to the outer parts of the AGN. Also shown is a sketch of the different knots identified in the image. The right panel shows the atomic emission line of [NeII] once the continuum component has been subtracted. Overplotted scales give the offset coordinates in arcseconds from the central engine position.

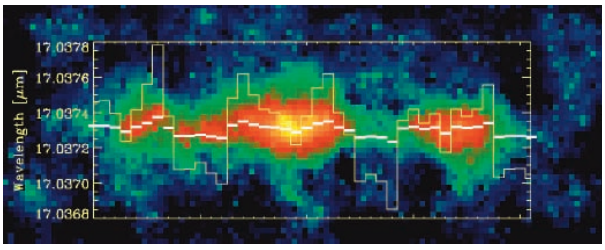

Figure 7: The Orion bar observed using VISIR in a long-slit, high-resolution setting at 17.03 µm. In the background is shown the 2D spectrum (dispersion direction is vertical, spatial direction is horizontal, North is to the left). The horizontal white bars overplotted pinpoint the local maxima of the emission line across the field. The yellow curve displays the corresponding central wavelengths as a function of the position in the field.

© ESO – March 2005

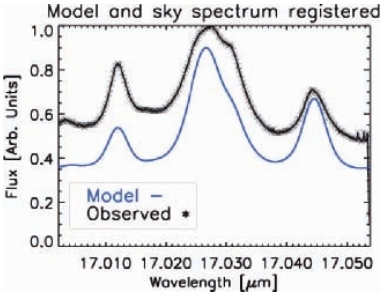

Figure 8: Wavelength calibration of the spectrometer using a cross-correlation method between the observed sky spectrum (black) and a model of atmospheric emission based on HITRAN computations (blue).

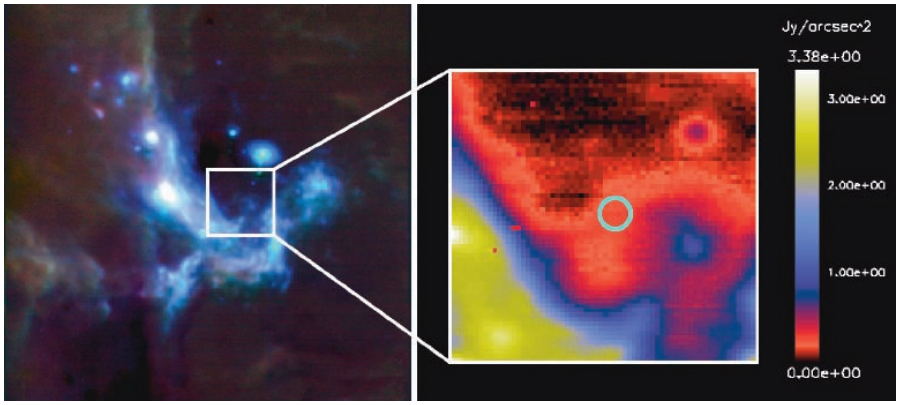

Figure 9: The Galactic Centre observed through the PAH1 (8.6 μm) filter. The goal is to detect the synchrotron emission from the black hole (position shown by the circle) and constrain its emission models.

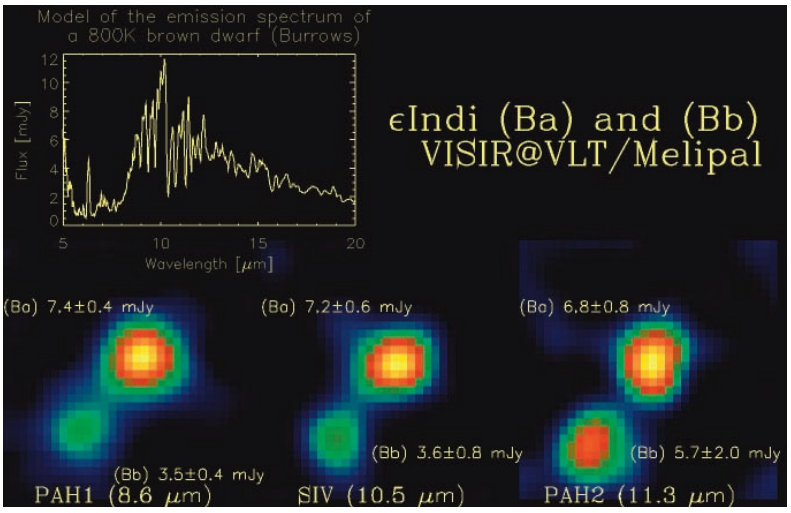

Figure 10: ε Indi, the closest binary brown dwarf, observed with VISIR in three filters (PAH1 (8.6 μm), SIV (10.4 μm), and PAH2 (11.3 μm)). We were able to spatially resolve both components, separated by ~ 0.73 arcsec, and determine accurate mid-infrared photometry for both components independently. In particular, our VISIR observations allowed us to probe the NH_3 features in both of the T1 (component Ba) and T6 (component Bb) cool brown dwarf. For the first time, we could disentangle the contributions of the two components, and find that the cold ε Indi Bb is in reasonable agreement with recent "cloud-free" atmosphere models. On the other hand, the warmer ε Indi Ba deviates significantly from any available atmosphere model calculations. It may or may not have clouds, and we might witness non-equilibrium chemical effects of NH_3 in ε Indi Bb. One should note that SPITZER could only measure a composite spectrum (Roellig et al. 2004).

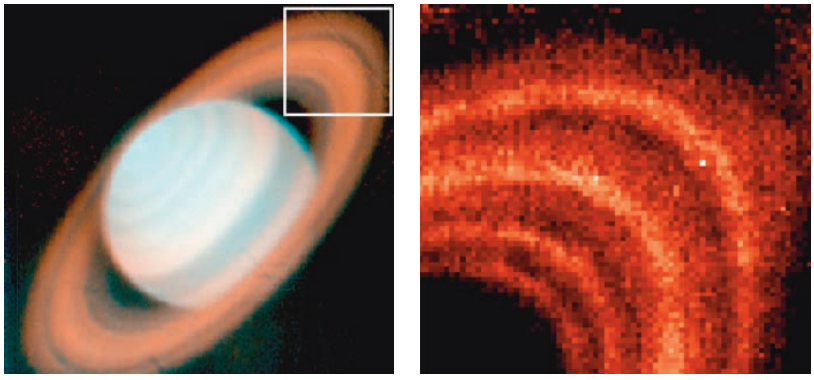

Figure 11: Left: Composite image of Saturn (blue = PAH2 filter at 11.3 μm, red = Q3 filter at 19.5 μm). The "shadow" region on the left side of the planet corresponds to ring particles with lower temperatures after cooling down in Saturn's shadow. Right: A close-up of Saturn's rings showing the D, C, B, and A rings (from left to right), Cassini's division between the B and A rings, and more interestingly, an increase of the particle temperature (hence increasing thermal emission) in the A ring just before entering the shadow of the planet.

a power-law function ($F_\nu \propto \nu^\alpha$ with α in the range 1–2) in the radio domain, peaking sometimes in the mid-infrared range as is the case for the black hole in Sgr A (Galactic Centre).

The very high extinction towards this object (A_V close to 30!) makes Sgr A impossible to detect in the visible range and quite difficult in the near-infrared range (Genzel et al. 2003).

We have monitored the Galactic Centre (see Figure 9) over four periods in order to try to detect the black hole mid-infrared emission. We could not catch it in its excited state (when it produces flares), but we could derive an upper limit of around 15 mJy for the flux in its quiescent state (Lagage et al. 2005, in preparation).

Key VISIR features: high angular resolution, high spectral resolution

High angular resolution: individual emission from a binary brown dwarf, Saturn's rings

One key advantage of VISIR over the SPITZER space observatory is the angular resolution. This is illustrated by two examples, the observations of binary brown dwarfs and Saturn's rings.

Cool stars and L and T brown dwarfs emit their energy maxima at wavelengths from the near-infrared up to 20 µm (Burrows et al., 2003), depending on their structure (dust settling, presence of "clouds", etc.) and effective temperature. We had the possibility to observe a binary brown dwarf during the science verification phase of VISIR in November 2004. As shown in Figure 10, we were able to detect the binary in the three filters with which we observed, and estimated the photometry of each of the components (SPITZER, although more suited to observe such faint objects, could only measure the spectrum of the two components and not distinguish each one separately). One can then put some constraints on the temperature, mass, and radius of each of the components (Sterzik et al. 2005, in preparation).

We observed Saturn's rings in May 2004, when the opening angle of the rings was maximal. VISIR images allow the study of the thermal emission from dust particles, and make it possible to spatially resolve the rings with a precision never reached before (see Figure 11) (Ferrari et al. 2005, in preparation). It is amazing that the resolution obtained with VISIR is equivalent to that obtained with the far-infrared focal plane FP1 of the CIRS (Composite InfraRed Spectrometer) instrument on board the Cassini spacecraft, at a distance of 20 Saturn radii during the CASSINI-HUYGENS Tour around Saturn between 2004 and 2008. CIRS will observe the rings at different wavelengths and under different viewing angles. This makes both instruments complementary. When observing such an extended object it is recommended to observe in imaging mode using jitter mode; i.e. some slight offset is applied between two nodding cycles, to avoid a significant number of bad pixels (~ 1%) affecting the final image.

High spectral resolution: Kinematics of warm gas in NGC 7582

The unique spectral resolution of VISIR in *N*- (R ~ 30 000) and *Q*-band (R ~ 15 000) allows us to resolve kinematically warm or ionized gas down to a limit of ~ 15 km/s. One example is shown in Figure 12. Here the dusty, composite starburst-Seyfert 2 galaxy NGC 7582 reveals its kinematic structure through the high spectral-resolution study of emission of ionized [NeII] gas at 12.8 µm, while the NeII filter image reveals the star-forming, circum-nuclear gas disc in the inner kiloparsec. The precision reached in velocity is around 18 km/s, and the spatial resolution of 0.4 arcsec corresponds to ~ 40 pc. From these data, one can infer an upper limit on the mass of central black hole (Wold et al. 2005, in preparation). This example shows the great potential of VISIR to study gas dynamics at high spatial resolution in the centres of galaxies.

More to come

VISIR will start science operation in visitor and service mode in P75. Only a selected number of instrument modes which could be properly characterised in the early phases of commissioning have been offered for the first proposal period. Additional modes and improved sensitivities in imaging and spectroscopy are planned to be offered for the coming observing periods. It is worth noting here that all offered instrument modes are fully supported by the newly developed VISIR (quick-look) pipeline which is available at the telescope and ESO Garching to process the data obtained in visitor and service mode. The latest information about the availability of the VISIR pipeline can be found at *http://www.eso.org/observing/dfo/quality/pipeline-status.html*. The latest information on the status of the instrument is available at *http://www.eso.org/instruments/visir/*.

Acknowledgements

We would like to thank the VISIR team at CEA, ASTRON and ESO for all their efforts to build and to bring into operation the VISIR instrument. We are further very grateful to C. Ferrari, E. Galliano and M. Wold for making some material available for this article prior to publication.

References

Burrows, A., Sudarsky, D. and Lunine, J. I. 2003, ApJ, 596, 587

Cohen, M. et al. 1999, AJ, 117, 1864

Galliano, E., Pantin, E., Alloin, S. and Lagage P.-O. 2005, MNRAS, submitted

Genzel, R. et al. 2003, Nature, 425, 934

Lagage, P.-O. et al. 2004, The Messenger, 117, 16

Pantin, E. et al. 1997, A&A, 327, 1123

Richter, M. J., Jaffe, D. T., Blake, G. A. and Lacy, J. H. 2002, ApJ, 572, L 161

Roellig, T. L. et al. 2004, ApJS, 154, 418

Telesco, C. et al. 2005, Nature, 433, 133

van Boekel, R. et al. 2004, A&A, 418, 177

Waelkens, C., Malfait, K., and Waters, L. B. F. M., 1997, Ap&SS, 255, 25

Waters, L. B. F. M. and Waelkens, C. 1998, ARA&A, 36, 233

Wahhaj, Z. et al. 2003, ApJ, 584, L 27

Figure 12: NGC 7582. Left panel: Rotation curve derived from the high-resolution spectrum in the 12.8 µm [NeII] mid-infrared line. Right panel: Image of NGC 7582 obtained in the [NeII] filter showing the slit position (top), and a 2D spectrum unveiling the velocity structure (bottom).

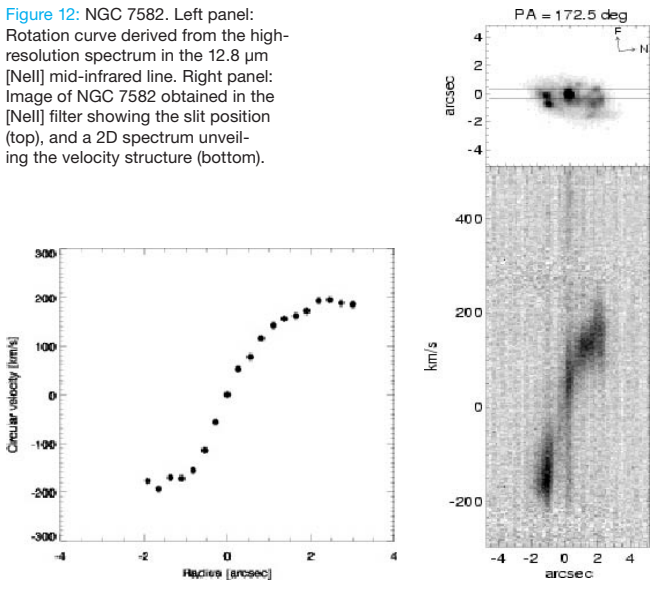

Chapter 3

4 years of experience with VISIR

Résumé

Les instruments infrarouge-moyen de l'ancienne génération, montés sur des télescopes de la classe des 4 m bénéficiaient paradoxalement de meilleures conditions de stabilité (fond thermique, PSF) en majeure partie car ils étaient limités par la diffraction, mais aussi de par la simplicité relative des anciens télescopes (pas d'optique active, pas de dé-rotateur, etc ...). Grâce aux nombreuses observations que nous avons, en tant que constructeur, obtenues sur VISIR, nous avons découvert une certain nombre d'effets inattendus, certain provenant de l'interaction particulière entre un instrument infrarouge moyen observant à des longueurs d'onde "peu classiques" et un télescope de nouvelle génération dont le fonctionnement est basé de plus en plus sur des automatismes (par exemple l'optique active) qui permettent de controler en temps réel la qualité d'image. Ce chapitre décrit l'analyse de problèmes rencontrés et propose éventuellement des méthodes de correction soit par des réglages de paramètres d'observation différents, soit par des méthodes de traitement du signal au niveau des données affectées.

Abstract

Mid-infrared instruments mounted on the "old" generation of 4 m-class telescopes were paradoxically beneficiating of better (because extremely stable) physical (telescope background, telescope PSF) conditions, mainly because they were diffraction limited. Given the substantial amount of guaranteed time we had as the manufacturer on VISIR, we have experienced a number of unexpected effects, some of which originate from the particular interaction between a mid-infrared instrument which observes at wavelengths quite unusual and invisible for the human eye, and one of the representants of the generation of new telescopes which rely on a large number of closed-loop active systems to deliver the best image quality. This chapter describes the analysis of problems and effects encountered and eventually proposes either hardware/operational or offline processing solutions.

Contents

3.1 Background properties and detector gains

Every couple telescope-instrument has in the mid-infrared range its own "signature", i.e. a particular pattern of emission observed in staring frames. On top of that, the detector inprints also its own characteristics in the final pattern observed. It is thus important to study the different components individually to further understand any observed effect. We have conducted a small study of the different effects and try to characterize them individually. The study of the stability of the gains is very important in the context of determining the optimum observing parameters such as the chopping frequency for instance.

3.1.1 The environment thermal background

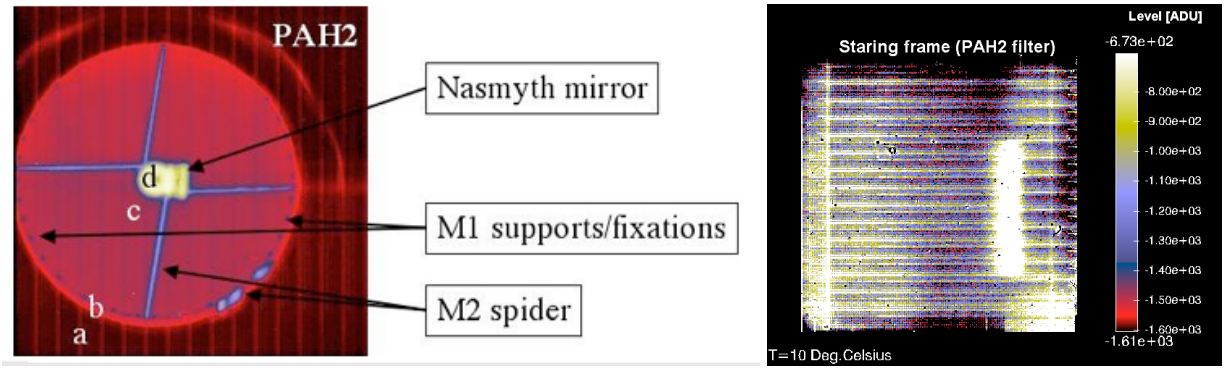

Figure 3.1: VISIR staring frame (left panel) and pupil image in PAH2 filter (right panel).

The telescope, at a mean temperature of ∼280 K emits a featureless thermal background which amount is directly linked (see Chapter 1) to its average emissivity. The average emissivity is composed of the mirror coating emissivity (eventually contaminated by dust particles) combined with structural elements which have either higher emissivities (but occupy a much smaller effective area, e.g. the M2 spider, the M3 structure) or carry misaligned components which point towards warmer surfaces (e.g. the mirror clamps). These elements are illustrated in Fig.3.1 which shows a VISIR pupil image in N band. In principle, since the M1 telescope is very close to a pupil plane, these elements should create at the level of the detector (focal plane) an almost pure flat background emission (unless some unexpected alternative optical path are possible in the instrument, producing straylight but this should in principle be discarded thanks to a careful baffling in the instrument). However, when looking at a typical VISIR staring frame (Fig.3.1, left image), the background is not uniform and shows large scale/low-frequency structures superimposed to a high frequency gains map pattern (low-frequency noise excess, LFNE). These structures originate from a component which must be not too far from a focal plane; a possible

candidate would be the **entrance window**, but this has to be confirmed by making multiple cross-check experiments.
Using the extended simulated source in VISIR, it is possible to vary the background emission (by changing the temperature of the source) and thus disentangle the structured background at low spatial frequencies and the gain map pattern. For a very low temperature of the source (T=-40°C), the observed emission should be dominated by the (simulated) telescope and the instrument (entrance window) backgrounds. For higher temperatures of the flat source, a significant part of the background can be assumed to be flat. The subtraction of two frames (taken in a sufficiently short interval time) corresponding to two different flat source fluxes cancels the structured background and allows to produce a gain map. This process is illustrated in Fig.3.2.

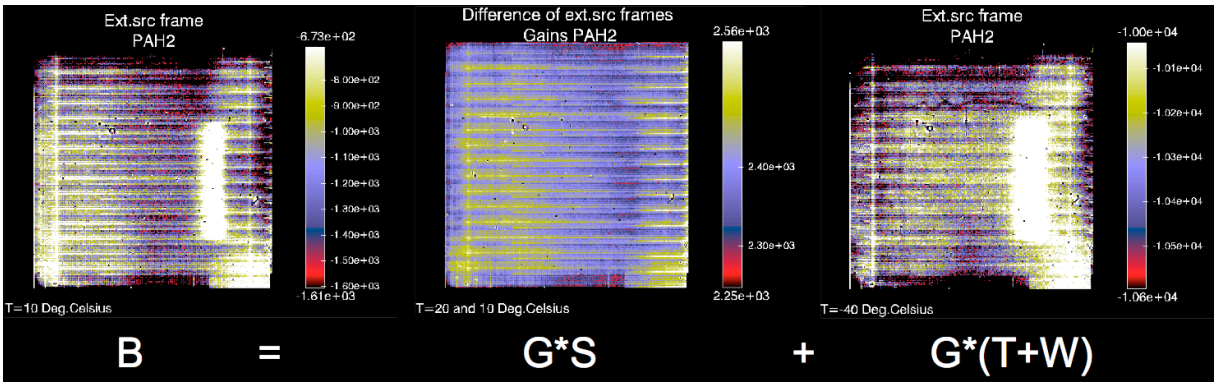

Figure 3.2: VISIR background spatial structures in PAH2 filter (11.2 µm) decomposed into a pure gain map contribution (G*S) and a strongly structured background (G*(T+W)) which probably originates from the entrance window and the telescope.

However, in the decomposition process we had to assume that 1) everything was stable during the experiment 2) there is no mixing of the different contributions. This is probably not true and some "side-effects" (such as detector striping, see Sec.3.2.6) probably contaminate the results. This question about the background decomposition and gain map estimation would deserves a dedicated study which is beyond the scope of the present document.

3.2 Detectors

3.2.1 Gains in imaging mode

Using the decomposition scheme described in the section above, it is possible to obtain, for each instrument setting, an estimate of the gains map. This study focuses on the particular case of the PAH2 filter (11.2 µm) in imaging mode but the observations and conclusions drawn here apply also to the other instrumental settings in imaging mode.

In Fig.3.3, left panel is shown the obtained gain map. One striking feature is we still observe structures at low spatial frequency. The average variation of level between two "zones" is about 6% while the variation of the gains within one zone is of the order 2.5% rms. This is quite unexpected to see such large scale variations since the BIB detectors design, also as tests performed in the lab ([Galdemard et al., 2003]) would predict only pixel-to-pixel variations with a standard variation of ∼2.5%. One (partial) tentative explanation is the following : different illumination levels produced by a structured background set different working points on the pixels.

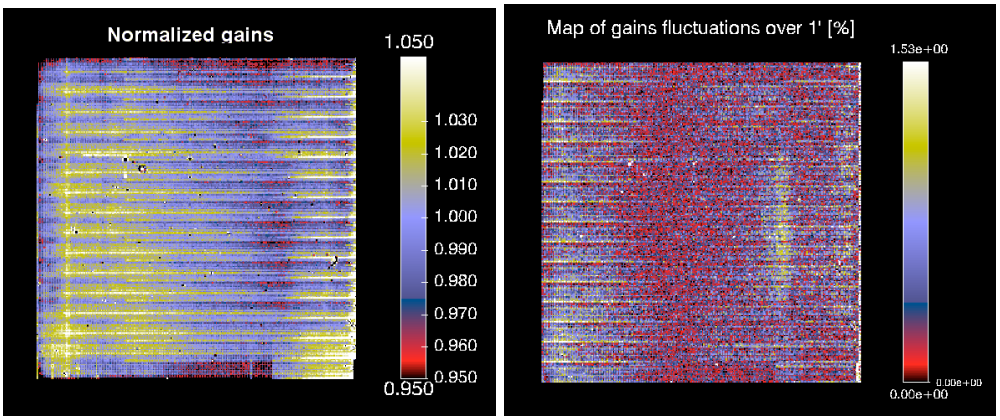

Figure 3.3: Left panel: gain map in PAH2 filter of VISIR imager. Right panel: Relative variation of the gain map in PAH2 filter over 1 min

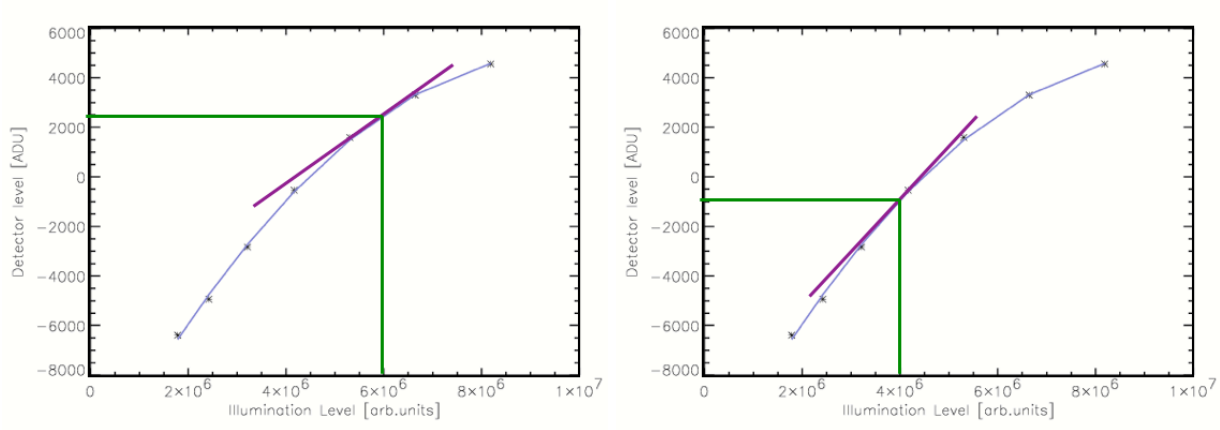

Figure 3.4: Response curve of the detectors. When observing at working at high level (2500 ADU) the differential gain is lower than at lower level working point.

Given the non-linearity of the response of the BIB DRS detector, the differential gain (which is the one we are interested in when performing differential observations) varies significantly with the illumination level, hence explaining the large-scale variations of the gains (see Fig.3.4). For instance, the right side bright "vertical bar" (Fig.3.1, right panel) corresponds to a zone of low average values of the gains (Fig.3.3, left panel).

3.2.2 Gains stability in imaging mode

In the context of assessing the BLIP performances as a function of the parameters such as the chopper frequency, it is interesting to study the temporal stability of the gains. First, it is possible to use two consecutive extended source images, taken at a time interval of 1 min, and in controled conditions of flux (set by the temperature of the Peltier Plate). The relative variation is shown in Fig.3.3, right panel. If the standard deviation of the relative variation of the gains remains reasonable, there is a quite large dispersion in the variations which vary from 0.15% in a majority of the pixels, to up to 1.5 % for a limited

number of them. These pixels are also those which are concerned by fairly high levels of illumination. Once again, their large variation is probably correlated with a modification of the working point.
Unfortunately, we do not have in the VISIR archive enough datasets taken at larger time intervals that would allow to study the gains stability over longer periods. However, thanks to imaging burst mode data which are sampled at a frequency of 40 Hz, it is possible to have accurate enough a time resolution for such a study. Assuming that over a period of $\sim$ 30s (the maximum integration time in burst mode) the telescope and instrument backgrounds are constant, it is possible to study the detector gain/sky background stability. The Fourier transform of the difference between a frame in the sequence and the very first one is shown in Fig.3.5.

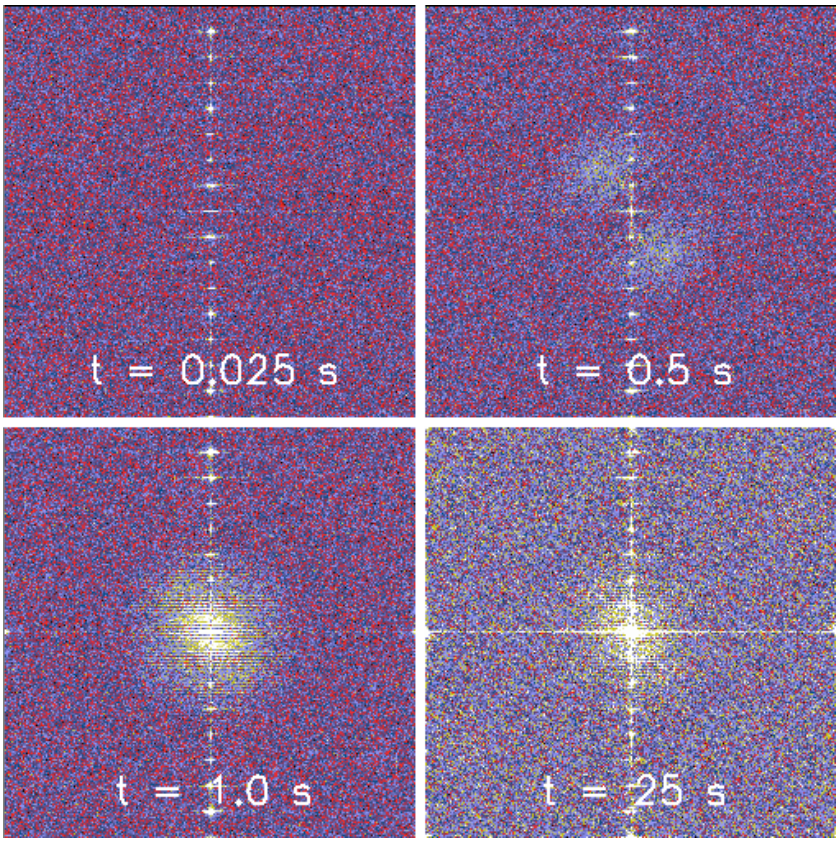

Figure 3.5: Power spectra of the frame subtraction error for different time intervals. See the text for the analysis of the structures.

On a short timescale (25 ms), a pure Gaussian white noise is observed (the vertical 'dots' are produced by a rectangular "dead zone" on the lower right). After 500 ms, some noise excess at mid frequencies is observed. This noise excess corresponds to a variation of the gains. After 1 s, the low-frequencies background error increases and dominates on a 25 s timescale.

3.2.3 Flat-fieldability in imaging mode

The gain map derived from the measurements using the extended source were used to try to improve the photometry of the sources. For instance, when applying the flat-field correction it is expected that dispersion in counts on the 4 beams of a source (in quadrangular chopping-nodding scheme) should be

lowered. The typical dispersion among the photometry of the beams is ∼1.0 %. When applying flat-field correction, the dispersion is only reduced to 0.9 %. This means that either the source of the dispersion is not only the differential gain map but eventually another effect not taken into account or the estimated flat-field is not accurate enough. Current tests do not allow to discriminate between the two.

3.2.4 Gains in spectroscopic mode

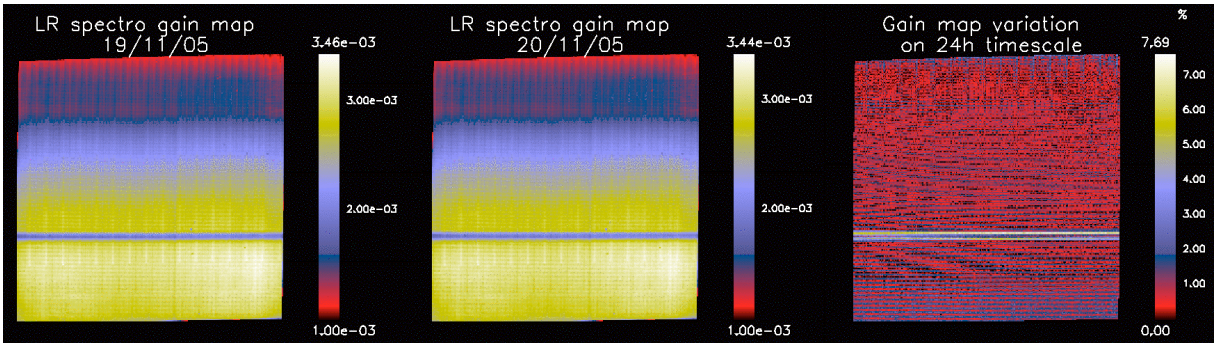

Figure 3.6: Gain maps obtained on different dates and the relative variation (right panel).

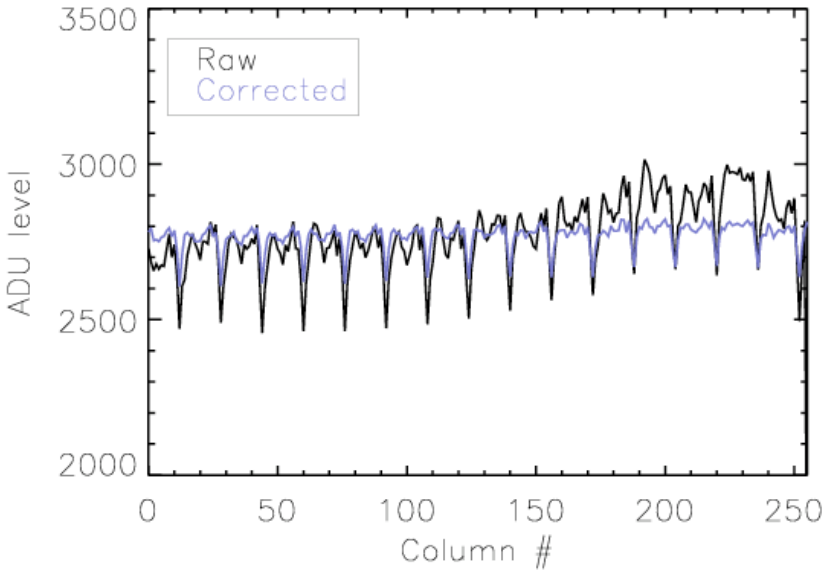

Figure 3.7: Plot of a cut (black line) at constant wavelength (in spectrometer low-resolution mode) through a 2D spectrum of the extended simulated source. After division by the gain map, the relative pixel-to-pixel variations are noticeably reduced.

The same type of measurements can be performed using the spectrometer. Using the extended source which temperature is set to a set of temperatures in order to modify the flux, it is possible to get

an estimate of the gain map using the differential gain map estimation method[1]. However, the main difference with the imaging mode is that the gains are computed and normalized at constant wavelength (i.e. fixed row in Fig.3.6).

The gain map obtained in low-resolution mode around 8.5 µmis shown in Fig.3.6. One first noticeable thing is the absence of low-resolution structures in this gain map. This is because only a very small part of the field (defined by the spectroscopy slit) is only "seen" so that background components such as window emission cannot create low-frequency structures. Concerning the temporal stability, the relative variation of the gains over a period of 24h is shown in the right panel of Fig.3.6. Except for the deep absorption feature which equivalent width seems to have changed (apparently because of an unexpected and unexplained slight change of spectral resolution), the variation of gains is typically in the range [0-2.5]%; some detector structures (6 pixels periodicity on the bottom region, fringing ??) also seem to pop-up which are probably related with the hardware design of the detector. Concerning the practical flat-fieldability of the data although the experiments made do not allow to conclude to an improvement of the photometry after flat-fielding, a simple test on extended source data themself (used to estimate the gain map) show that the relative variations of gains ($\sigma \approx 2\%$) are significantly reduced (to $\sigma \approx 0.25\%$) when applying the flat-field correction; see Fig.3.7.

3.2.5 Detector ghosts

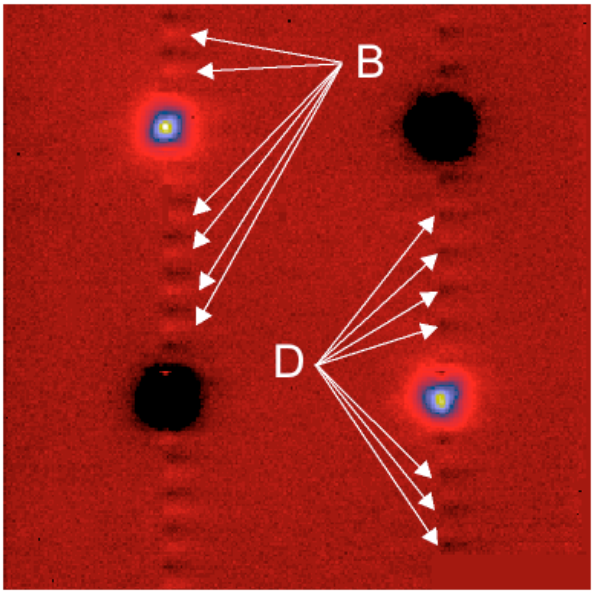

Figure 3.8: Detector ghosts in imaging mode. The negative beams trigger the positive (B) ghosts while the positive one produces the negative ones (D).

When a bright source (which peak is larger than $\sim$ 20 % of the background level) is observed on a DRS-Boeing detector, some ghosts appear repetitively on the array (see Fig.3.8). These ghosts are very similar to the effect also noticed in the Raytheon 320x240 mid-infrared detector ("Hammer Effect", see [Sako et al., 2003]).

[1]The differential gain map estimation method consists in taking several measurements at different flux level and computing for each pixel a linear regression of the observed pixel level as a function of the median level in the full frame

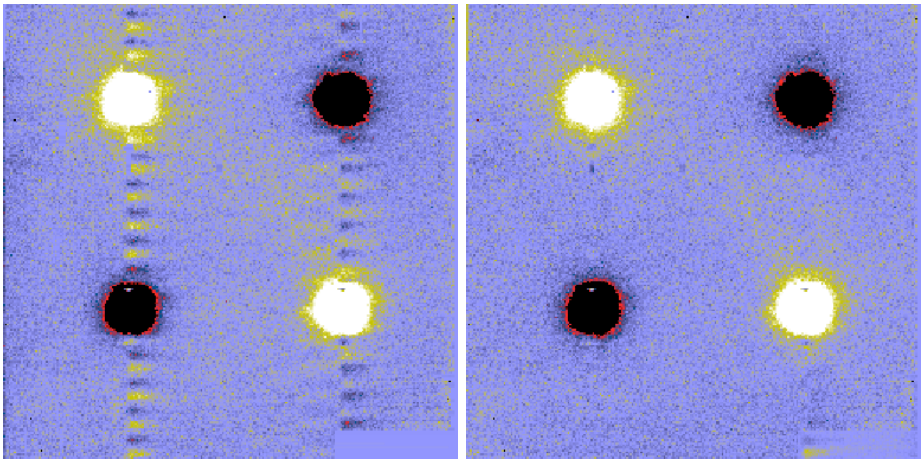

Figure 3.9: Left panel: the hammer effect is clearly evidenced. Right panel: after correction by subtracting the lower area of 256x16 pixels to all the 256x16 sub-frames above.

They are of electronic nature and have been identified as variations (level drop) of the bias voltage in the read-out circuit CRC-774 (ROIC) induced ; in the case of the DRS-Boeing IBC 256x256 detector although being equipped a different ROIC an effect of the same nature probably takes place since the technological principles are used. The same kind of effect appears also in spectroscopic mode as dark stripes around the double positive beam. This effect can be partially corrected for. Since this effect is additive it is possible to correct it by making an estimate of the hammer errors in an region of 256x16 pixels void source (e.g. the lower 256x16 rectangular area) and subtracting it to the remaining fifteen areas above (see Fig.3.9).

3.2.6 Striping

In the laboratory with stable conditions of background and a relatively faint point source, the DRS-Boeing 256x256 Si:As BIB detectors show good performances with an absence of any spurious artifacts. The significantly different conditions once on telescope (varying background and in certain cases, relatively strong sources against the background) produce unexpected effects such as stripes on the detector in a direction perpendicular the read-out stream.

Presentation of the phenomenon

The physical origins of the striping effect are still poorly understood. Our observations of the phenomenon show that one stripe result from an offset at the level of one (out of 16) detectors output. Since the detectors pixels are read sequentially by groups of 16, the additional offset on one of the outputs creates a signal which looks like a periodic stripe (with a period of 16 pixels). Our assumption is that this offset signal is produced by a saturated amplifier of one the outputs. This saturation lasts a “certain time” which probably depends on the level of the initial saturation and the conditions of illumination onto the detector and is very hard to predict. In the same manner, the values of the offsets seem to depend highly on the external conditions and are very difficult model. When the amplifier saturation is triggered by a pixel which has an abnormally high gain, one gets the “detector striping”. When a “normal pixel” (which gain belongs, in the histogram of the gains, to the core of gains centered around the median value) triggers a stripe (e.g. because hit by an astrophysical source stronger than the background, we deal with

"source striping". It can be easily distinguished from the "detector striping" because the stripes start from the precise location of the sources on the detector (see Fig.3.10). The "source striping" is also usually stronger in intensity. Fig.3.11 shows the stripe that produces a "jump" in the signal read by one detector amplifier. This stripe appears on first approximation as a constant offset value. This value can be estimated and corrected for.

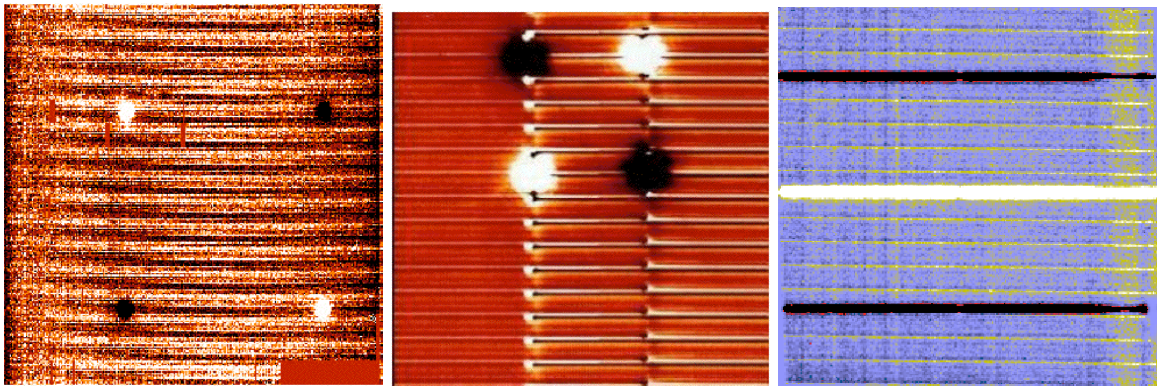

Figure 3.10: Left panel shows the detector striping caused likely by atmosphere emission fluctuations. Middle panel displays the *source striping* which is triggered by strong sources. right panels shows the striping in the case of low-resolution spectroscopic data in which case the stripes are particularly harmful because mixed with the horizontal spectra.

It has been proved that by identifying the pixels having a abnormal behavior which triggers the striping and "masking" them in the read-out sequencer scheme (masking means actually read them very rapidly; it is impossible to physically really mask them out) the striping is significantly reduced (in occurrence and intensity). However, deep (long lasting) integrations on usually faint sources still produce on the stacked image a fairly large number of stripes which render often quite difficult the analysis of a faint object (see e.g. the case of observations of the Eps Indi B binary brown dwarf). In spectrometry mode, this phenomenon is particularly harmful because the stripes are aligned with the spectra and potentially contaminate them heavily.

The striping phenomena could be probably much better understood but at the price of extensive testings in laboratory with dedicated test benches. We are now in a transition phase in which the infrared detector manufacturers are preparing the next generation of much bigger (1kx1k) and announced better (in cosmetics) detectors (Aquarius by Raytheon, MegaMir by DRS/Boeing). These new detectors will be based on completely redesigned multiplexers, it is therefore of weak interest to invest too much time to fully understand the physical origins of the striping. It remains however completely relevant to analyze the phenomenon with the goal of being able to **correct by o -line processing** the $\approx$ 10 Tb of data already present in the archive.

A destriping method

Let us assume that the striping is a constant offset value affecting a group of pixels which are placed periodically somewhere on the detector. The goal is to determine only 3 parameters : the column number (modulo 16), the starting row, and the ending row. It is very complex to determine these parameters accurately directly from the images. I have developed a novel method which consists in projecting the image onto an analyzing space using a bijective transform. This transform is designed to concentrate the

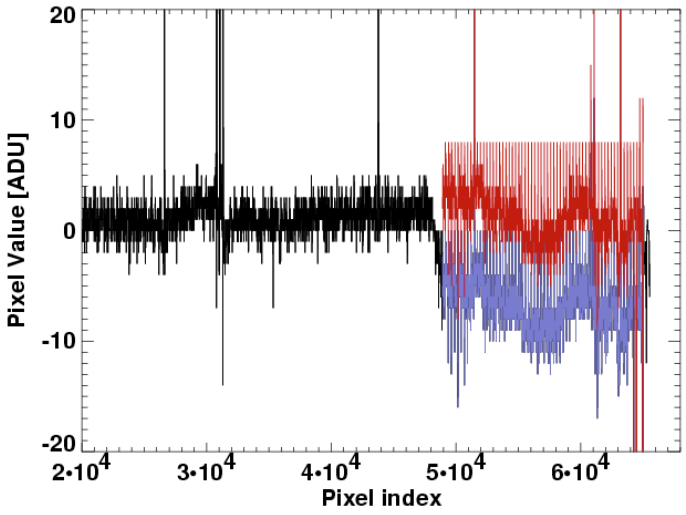

Figure 3.11: The stripe signal along a set of columns on the detector. The red part is the stripe. The blue one is after stripe correction by a constant offset.

signal of a stripe in the dual space (see Fig.3.12). In this three-dimensional space (3 parameters), the detection of a stripe is achieved by a simple peak detection. The stripe is back projected onto the image space and subtracted to the image. Since we deal usually with multiple striping, and with some stripes which are not a pure constant, the process is iterated until no more stripe signal is found in the dual space.

A fast destriping method for compact objects

The method described is relatively heavy and time-consuming because of the iterative process involving back and forth transforms. In the case of *very compact objects* (like point-sources), a simpler scheme can be used. Since a compact source concerns only a limited number of pixels, one can use a statistical approach assuming that the background should be formed by a random white Gaussian noise with a mean value of zero. Considering a set of columns which are read by the same read-out amplifier, the *median value* of pixels at fixed row number shall follow any offset constant due to a stripe. So, by subtracting to each of these group of pixels their median value, any stripe will be eliminated. On top of that any horizontal low-frequency noise (see Sec.3.3) is also eliminated in this process. This type of destriping method can be systematically used for instance in the case of standard star observations.

3.2.7 Detector breathing

When looking at burst mode data on the 25 ms sampling rate, one immediately notices an oscillation of the detector output level. This oscillations appears as a peak in the power spectrum of the signal (see Fig.3.14, left panel). This oscillation centered on 1 Hz frequency, is directly linked to the cryo-coolers which also have a cycle at 1 Hz frequency. This oscillation could be efficiently damped (Fig.3.14, right panel) by improving the thermal link between the head of the cryo-cooler and the detector and slightly heating the detector from 6.5 to 8.0 K. Nevertheless, some residuals oscillations are still present; a proper operational procedure (where the chopping period is forced to be an integer times the cryo-cooler cycle)

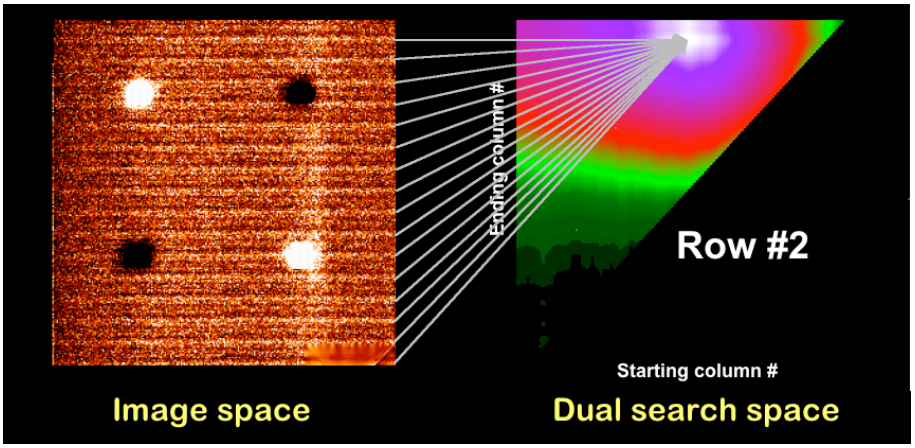

Figure 3.12: Principle of stripe detection. The original dataset (image) is projected onto a dual space in which the stripe is concentrated. A simple peak detection followed by an inverse transform allows to isolate the stripe and subtract it.

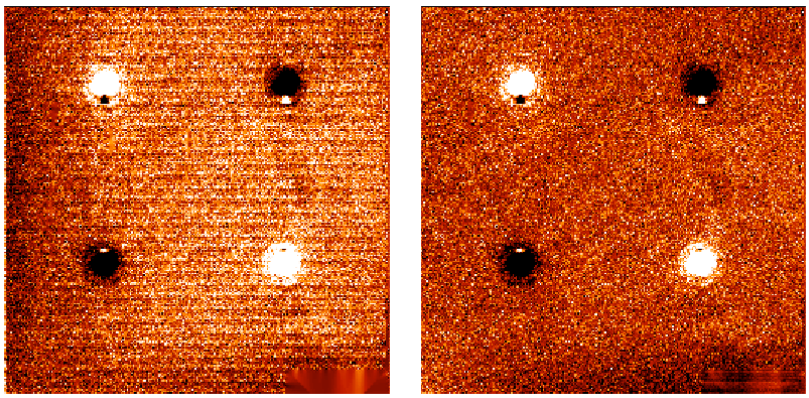

Figure 3.13: Fast destriping. Left panel, the striped image, right side after fast destriping.

allows to damp at a higher level of rejection these residuals.

3.3 The background problem

A very large fraction of VISIR imaging data show unexpected large scale structures in the background, behind the sources. In principle, the chopping/nodding background cancellation should produce a flat background containing only shot-noise. This noise, given the physical processes of thermal emission which create it, is expected to be white (no preferred spatial frequency) and have a Gaussian distribution (because of th large number of statistical events). The observed background (Fig.3.15, right panel) has a spectrum which variance increases dramatically at low spatial frequencies (large spatial scales, see Fig.3.15, right panel).

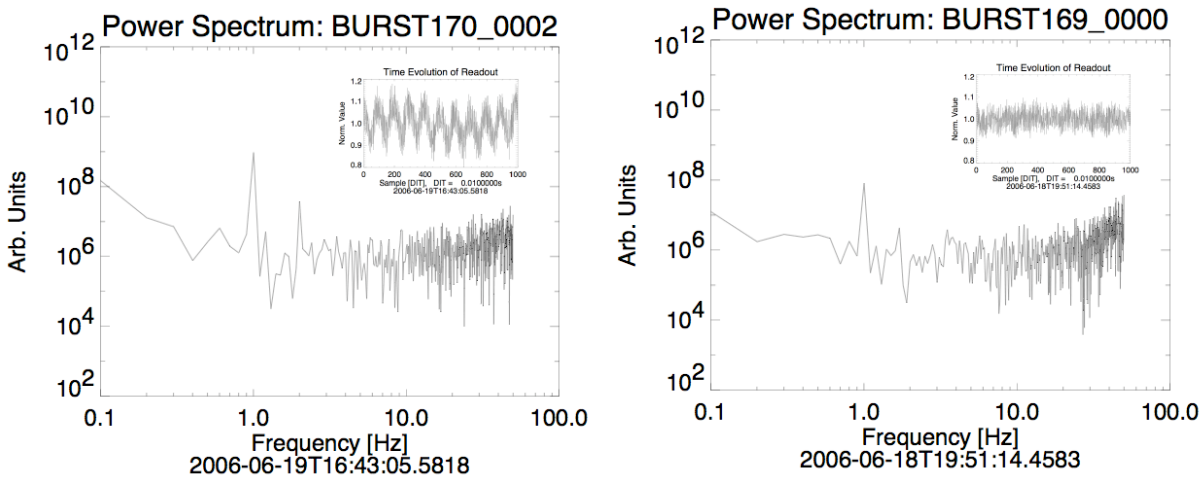

Figure 3.14: Left panel : the power spectrum of a VISIR detector time sequence (6.5 K); inset the corresponding signal. The signal shows a prominent 1 Hz peak which is produced by detector breathing (temperatures fluctuations due to the cryo-coolers). Right panel : same as left panel but at a detector temperature of 8.0 K. The breathing is significantly damped by heating slightly the detector to 8 K.

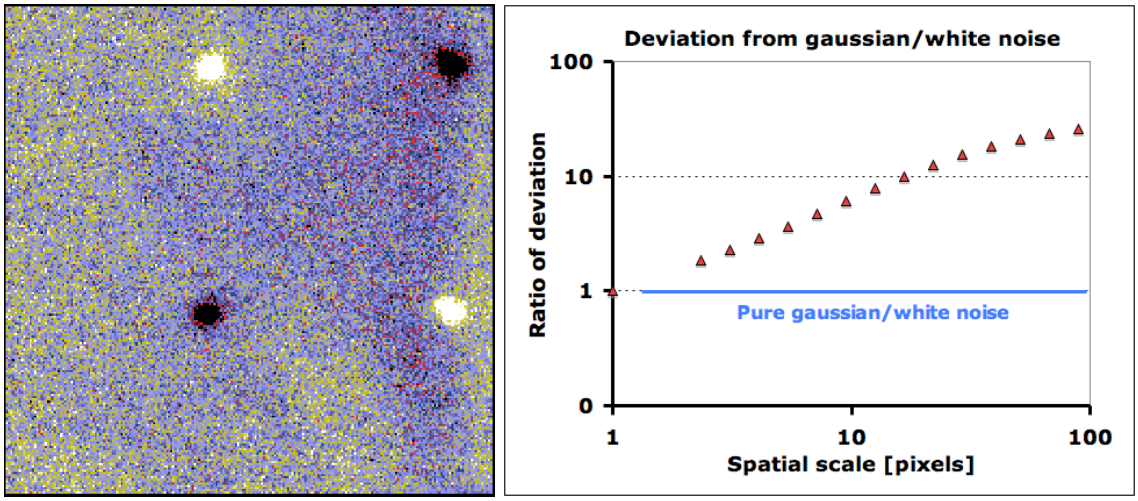

Figure 3.15: Left panel : VISIR image in PAH1 filter of comet Tempel 1. The underlying background which should appear "flat" in case of (expected) white Gaussian noise, features spurious "hills and valleys" which considerably degrades the photometric accuracy. Right panel shows a scale analysis of the left-side image. At high spatial scales (low frequencies), the background variance strongly deviates from the expected values in case of Gaussian white noise.

We identified two possible origins of this low-frequency noise excess. The first one is an inaccurate nodding correction because of the field stabilization process. This field stabilization is undertaken by the secondary mirror: the active optics system analyzes the wave-front on a field guiding star and the tip-tilt error is corrected using a fast adjustment of the M2 secondary mirror (cut-off frequency of 50 Hz). Not only any mechanical vibration can be compensated for (such as those caused by wind gusts) but also the atmospheric turbulence (seeing) is partly corrected. The nodding correction assumes that the difference in optical paths (between the two chopper positions) is strictly conserved from one nodding position the complementary one. When the field stabilization is performing large amplitude on the M2, this is not true any longer. However, if this effect contributes undoubtly to degrade the background cancellation, even in case of strong wind or bad seeing, the background residual structures are barely worse than those observed in good conditions.
The background low-frequency noise can be probably reduced by simply increasing the chopper frequency (which is physically possible) on the VLT; the cost on other performance parameters has still to be assessed thanks to experimental data. Nevertheless, already more than 4 years of VISIR data are already existing in the archive; some offline processing methods were needed to extract the most accurate informations for them. This is the purpose of the next section.

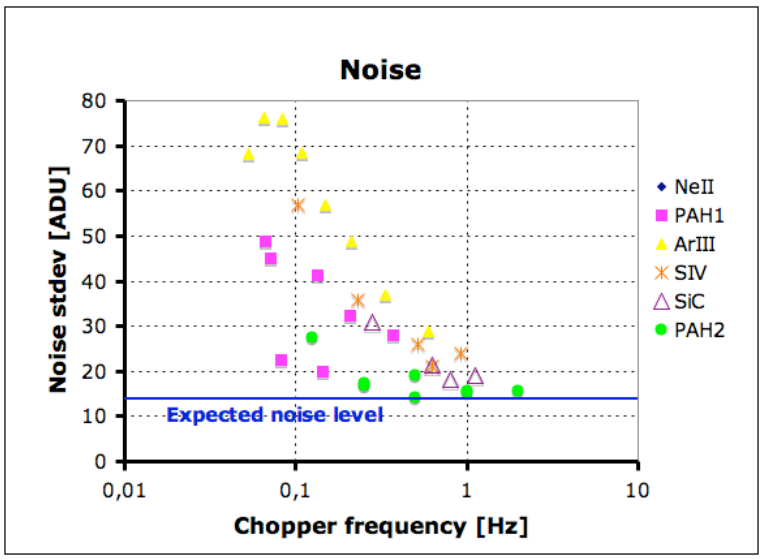

Figure 3.16: Analysis of the background noise as a function of the chopping frequency. For frequencies lower than $\sim$ 1 Hz (depending on the filter used) the background noise stars increasing; the observing conditions are probably not BLIP any longer.

3.3.1 How to recover an accurate photometry ?

Point sources case

Since the excess of noise is mainly concentrated at high frequencies, the first method which comes to the mind is a frequency filtering. Unfortunately since any extended object contains also eventually some low frequencies which overlap with the low-frequency noise, a Fourier filtering would be disastrous for the photometric accuracy. However, in the particular case of **point sources** the filtering impact on the photometry can be controled thanks to a comparison with the PSF. Instead of making a simple Fourier filtering, the use of a wavelets decomposition into frequency bands is a more precise tool. Using the simple

"à trous" wavelets transform ([Starck et al., 2002]), a filtered version is obtained by simply rejecting all wavelet planes but the second to the fourth one. Some of the energy of the object is definitively lost in the process but this the part which is mixed with the low-frequency noise. The same process applied to a PSF allows to correct the photometry for this loss. The photometric measure is a standard aperture photometry but restricted to a radius of **4 pixels, 0.3 arcsec** because beyond this radius the partial reconstruction produces a negative ring. In the photometric measure, the residual sky value is forced to 0.0 since the residual background component is assumed to have been eliminated in the partial wavelets reconstruction process. For the assessment of the resulting photometric errors, a Monte-Carlo bootstrap scheme is used. A known point source (either a measured or a synthetic PSF) is plunged into the real data at different random locations on the detector. The recovered intensity is then compared to the true one to form a statistic distribution (on 250 trials such that the error on the estimate of the standard deviation, assuming a $\mathcal{N}$ormal distribution, is less than 10%). The photometric errors are plotted in Fig.3.17. This analysis allows to typically improve the photometric accuracy by a factor of 1.75

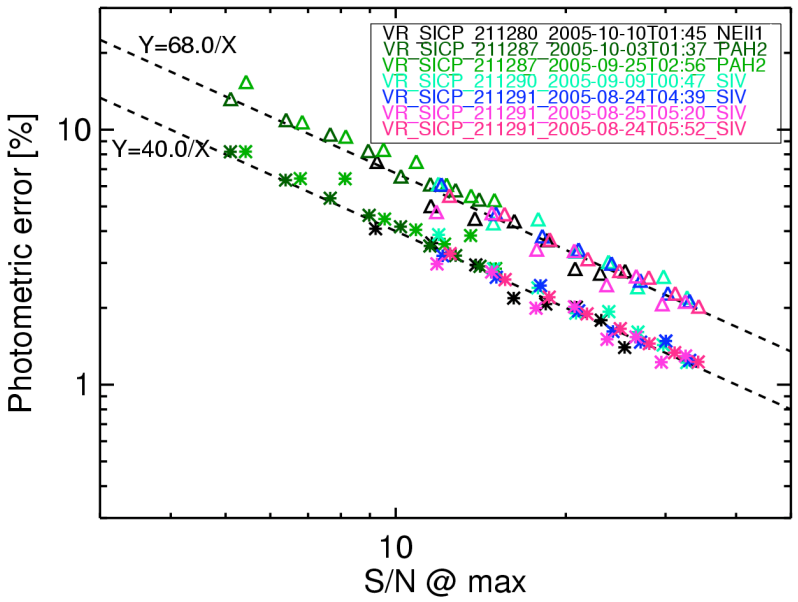

Figure 3.17: Plot of the photometric error as a function of the peak signal-to-noise ratio of the point source. The estimate has been performed on different datasets in different VISIR filters labeled with different colors, and using a Monte-Carlo scheme to place a simulated point source at different locations in the frame. The stars correspond to a wavelets pre-filtering described in the text. The triangles correspond to photometric error on the initial datasets in an aperture of 4 pixels and a residual sky measurement between radii of 6 and 8 pixels. Overplotted (dashed lines) are the best fits using power-law with a index of -1 (see text).

Extended sources case

When the source is extended the method described above is not valid any longer. Another simple idea in this case is to reconstruct the underlying background under the source and remove it afterwards. The first method consists in masking the source (by means of a simple threshold) and interpolate the missing pixels using e.g. a linear or a low-order polynomium. This method presents however some biases (e.g. the à-priori definition of the spatial support of source for masking, the choice of the polynomium degree, etc

...). Using a set of multi-resolution schemes it is possible to find a less biased more accurate method which converges towards the true solution. The idea is to approximatively define first a spatial support of the source and masking it. The missing data are reconstructed using a multi-resolution inpainting method ([Elad et al., 2005]) to form a background which is subtracted to the data. A new updated spatial support of the source can be then estimated and the full process is iterated until the spatial support does not evolve any longer. An example of corrected imaging data using this inpainting method (inpaintBG) is shown in Fig.3.18. Tempel 1 imaging data in this figure are a fairly good example of weak (400 mJy) and extended data for which the background reconstruction is at the limits of the possibilities of the method. In this particular example, the photometric error is decreased from 20% (using a simple interpolation algorithm) to 10% using the inpaintBG method.

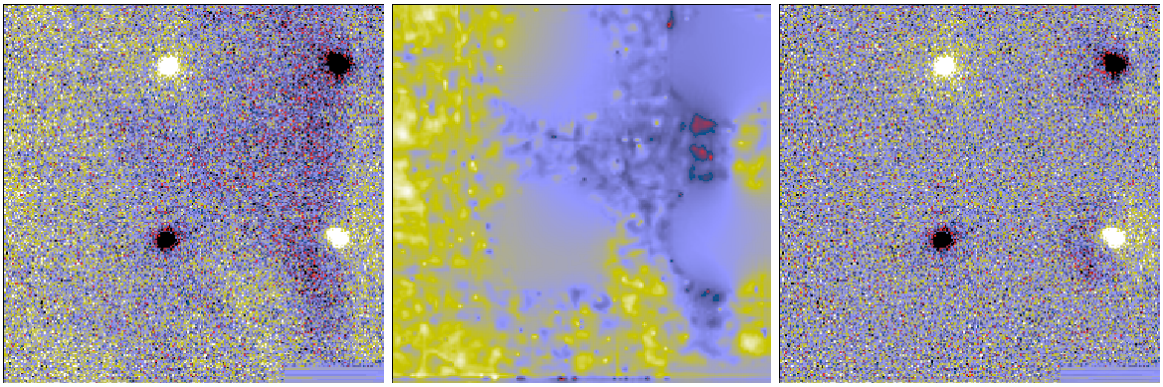

Figure 3.18: The inpaintBG background removal method applied to comet Tempel 1 imaging data. In the left panel, the faint extended source beams are strongly corrupted by a varying background. After iterative estimation of the spatial support of the sources, the background is reconstructed (middle panel) and subtracted to the original data in the right panel.

In the inpainting method described above, the "à priori" information we have i.e. the similarity of the 4 beams within the background noise errors, was not employed. We propose here an extension of the inpainting method, a modified inpainting scheme which takes into account this information (MIMBIR). The method is based on the following iterative process:

$$\begin{aligned} S_{n+1} &= P_{S,\lambda}(S_n + CN_R^{-1}(D - CN_R(S_n) - B_n)) \\ B_{n+1} &= P_{B,\lambda}(B_n + SM(D - CN_R(S_n) - B_n)) \end{aligned}$$

with

- D: observed data (VISIR image)
- S_n: reconstructed source signal at iteration n
- B_n: reconstructed background at iteration n
- CN_R: 4 beams splitting operator

- CN_R^{-1}: 4 beams splitting inverse operator
- SM: 4 beams masking operator
- $P_{S,\lambda}$: Projection operator onto source solution space : positivity, wavelets hard thresholding at λxσ
- $P_{B,\lambda}$: Projection operator onto background solution space : wavelets + curvelets hard thresholding at λxσ

Starting with null images for S_0 and B_0 and λ equal to the maximal signal to noise ratio amidst multi-resolution decompositions, the background and the solution are progressively and simultaneously rebuilt by decreasing the λ threshold factor until a value of 3.0 (to limit retained components to 3.0 times the noise, which corresponds to a probability larger than 99.9 % of being a deterministic signal). Performances estimates based on simulated data (Fig.3.19) show that this method allows to decrease the photometric error from 20 % to 10 % on point sources. A simple background interpolation using a a polynomium of degree 1 leads to a photometric error of 16 %.

Derived application : extraction of sources embedded into an astrophysical background

In the mid-infrared range, we can encounter several cases of very extended astrophysical backgrounds e.g. in star-forming nebulae. This background also strongly limits the photometric precision (see left panels of Fig.3.20 and Fig.3.21). The inpainting method described above can be used also in this case to extract the objects *while preserving the noise properties* and thus being able to evaluate also a photometric error. The extracted objects in the cases of imaging and spectroscopy are shown in the right panels of the same figures.

3.4 The nodding issue

The choice of the nodding parameters impacts also the quality of the data and eventually contribute to the final sensitivity. First, the de-rotating mount of VISIR (at Cassegrain focus of a Ritchet-Chretien type telescope) has the consequence of a rotating pupil at the level of VISIR focus. The rotation speed depends on the telescope altitude and tends theoretically to infinity at zenith; hence the setting of a minimum allowed angle to zenith which defines a zone of avoidance around zenith. The principle of nodding correction assumes that the telescope pattern remains stable over the nodding period. For fairly large velocities of pupil rotation, this assumption is not valid any longer. We found that for zenithal distances in the range 0-30 degrees, the nodding period had to be decreased from 1 min to 30 s to avoid an increase of non properly canceled telescope structures. Another unexpected new effect was experienced with VISIR. Some observations show a semi-regular pattern of lines which are oriented at $\approx$60° one respectively to the other (see Fig.3.22, upper left panel). When analyzing the image in Fourier space (Fig.3.22, upper right panel), the pattern corresponds to the 4 bright spikes (making a cross) seen in the Fourier modulus image. These spikes have the same geometry as the telescope spider. A qualitative tentative explanation is the following. A fairly extended source produces a concentration of the energy a low spatial frequencies. These low-spatial frequencies are particularly strongly impacted by a (potentially fast when close to zenith) rotation of the spider pattern in the pupil plane. The nodding pattern is not conserved and the nodding correction produces the observed spikes which in turn produce the pattern

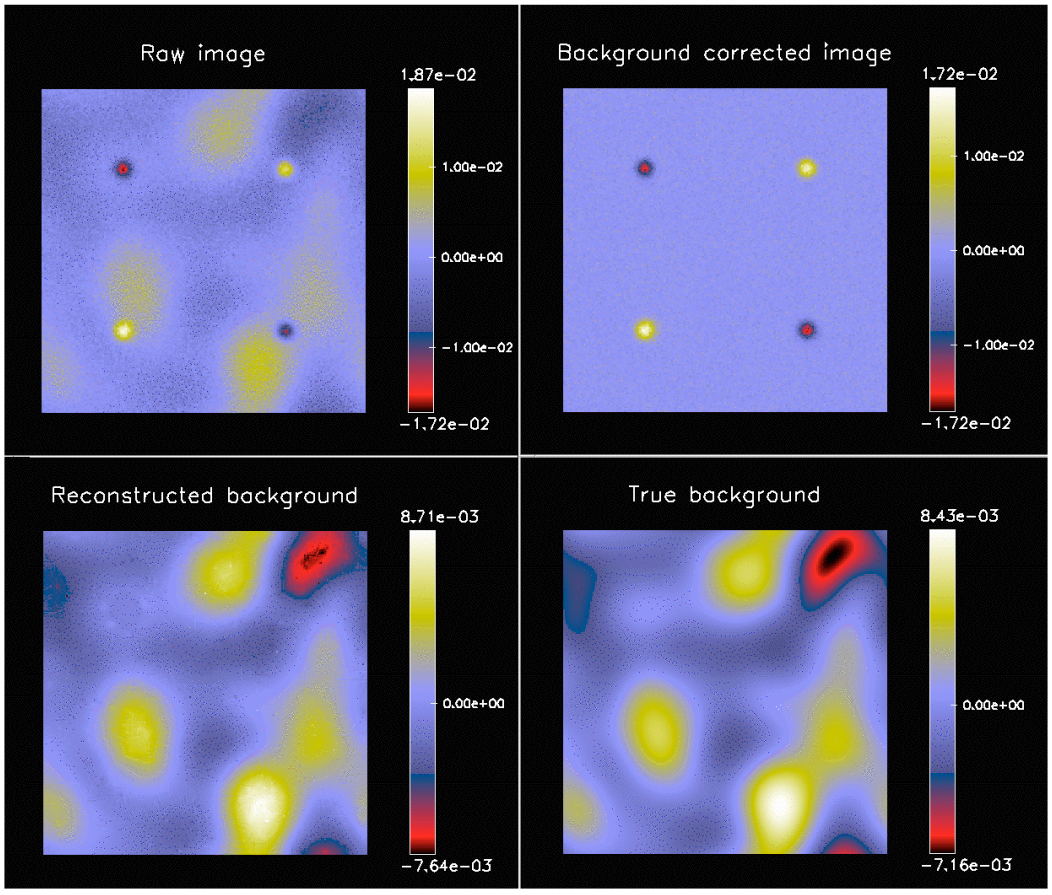

Figure 3.19: Upper left: simulated VISIR image of a point source with a low-frequency noise excess. Upper right: the noise-free simulated image. Lower left: the reconstructed low-frequencies excess of noise using the MIMBIR method. Lower right panel: the original simulated low-frequencies excess of noise

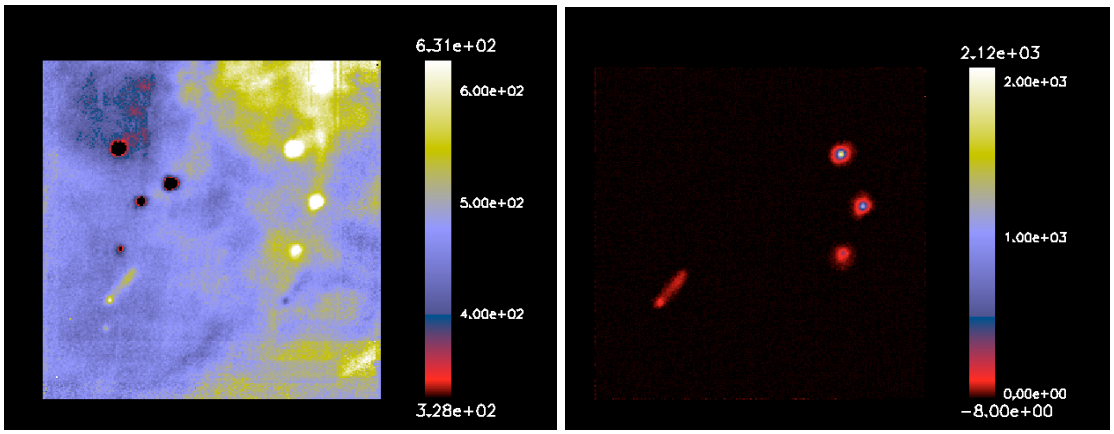

Figure 3.20: The inpaintBG background subtraction method applied to VISIR imaging observations of objects physically sitting in an emission nebulae. After extraction, the photometry of the proplyds is more easily estimated. Another advantage is the preservation of the shot-noise in the extracted image which allows to assess the photometric error.

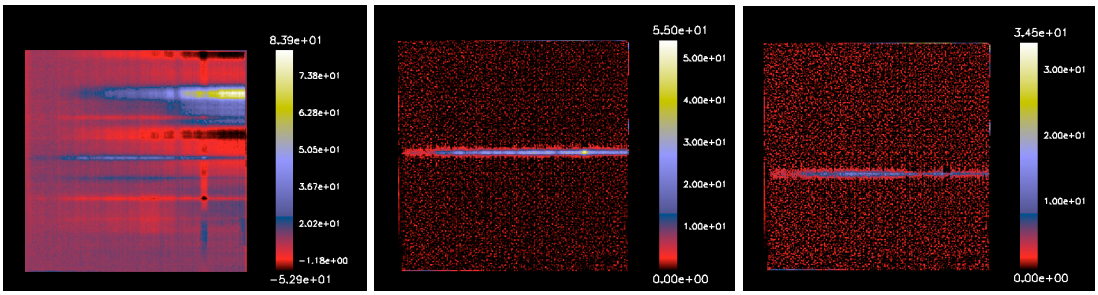

Figure 3.21: Application of inpaintBG method to VISIR low-resolution spectroscopic observations of embedded objects in an astrophysical background.The proplyds spectra are extracted from the surrounding nebulae and their photometry is more easily estimated. Another advantage is that the preservation of the shot-noise in the extracted image in order to assess the spectro-photometric error.

seen in the image plane. The spurious spikes can be eventually masked out in Fourier space but this operation remains delicate since the true signal is also strongly impacted.

3.5 Scanners jitter

VISIR spectroscopic mode were presenting evidence of poor atmospheric features cancelation. This could be possibly be attributed to a very fast change of atmospheric emission at a timescale smaller than the chopping period. If in some cases, this interpretation might hold, some other cases like in Fig.3.23 (left panel), the particular shape of the atmospheric residuals (P-cygni like profiles) shows that the origin of the residuals lies in a spurious jitter of the scanners. This jitter was originally associated with a non-optimal closed-loop control of the scanners which control the gratings (especially concerning the high-resolution mode). However, even after a careful study of the closed-loop parameters and an upgrade of the control boards, still some jitter is present in some cases in low-resolution mode. The only remaining solution was then to include in the pipeline the possibility to register (only in the dispersion direction) the frames using a shift-and-add algorithm applied to the *sky frames* which in the majority of the cases solves almost completely the problem (see Fig.3.23). If some residuals are still present after this process, a modified background suppression method similar to that described in Sec.3.3.1 can be applied. In this case, the multi-resolution basis used is the ridgelets transform which is better matched to describe these horizonthal residual structures.

3.6 The image quality problem

Although in principle diffraction-limited (proportional to λ/D) the main advantage of VISIR should be its sharp angular resolution (0.28 arcsec at 8.6 μm); VISIR has indeed the best angular resolution amidst non adaptative optics assisted instruments at Paranal observatory. However, VISIR imaging data in about 15 % of the cases present PSF ellipticities larger than 10% preferentially around position angles of 50 or 170 degrees (see Fig.3.24).

The exact origin of these PSF sporadic deformations is still not clearly identified, however during the 20s of the burst sequence sequence shown in Fig.3.25 none of the VISIR optical elements is moved nor deformed. Since the atmosphere was also very stable and with a good seeing around 0.7 arcsec during this sequence, we have to infer that the PSF deformations originate from the telescope. We are currently performing some technical tests in burst mode with a parallel analysis of all telescope telemetry parameters to assess this hypothesis.

3.7 Spectrophotometry in the spectrometer LR mode

The spectrophotometric calibration of VISIR spectroscopic data is performed using standard stars observations in the same setting. However, although a careful selection of the standard star is usually made in order to observe it at a similar airmass as the target, some atmospheric absorption mismatch can decrease the accuracy of the calibration. In the particular case in which two calibrators observations at two different airmasses m_1 and m_2 have been obtained, an interpolation-like method can be used. If S_1 and S_2 design the two standard star extracted spectra on the detector, I_1 and I_2 their "true" spectra (i.e. observed in absence of any transmission modulation), $T(\lambda)$ is the overall transmission function (i.e. atmosphere and instrument), and $\alpha(\lambda)$ is the atmospheric extinction per unit of airmass, one writes :

$$S_1(\lambda) = I_1 T(\lambda) e^{-m_1 \alpha(\lambda)}$$

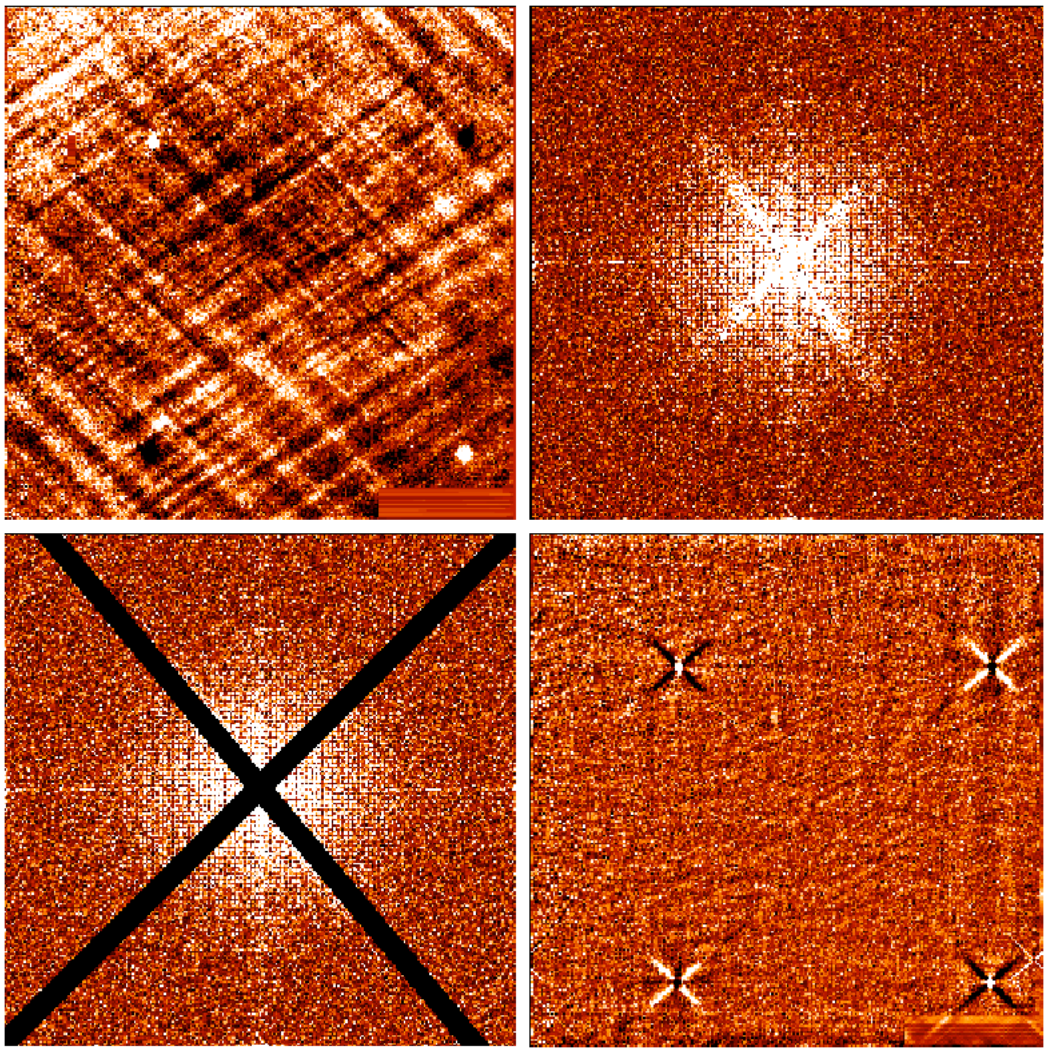

Figure 3.22: Upper left: VISIR image showing the "fence effect" i.e. a spurious pattern (semi-regular grid) superimposed to the image of a standard star. This pattern is clearly evidenced in Fourier space (upper right panel, fourier modulus) as a cross located at low-intermediate frequencies. When playing the game of simply masking out this cross (lower left panel) and going back into the image space, the pattern has indeed disappeared. The crude correction of the masking produces artifacts around the point sources which result from the convolution of the point sources with the inverse fourier transform of the mask.

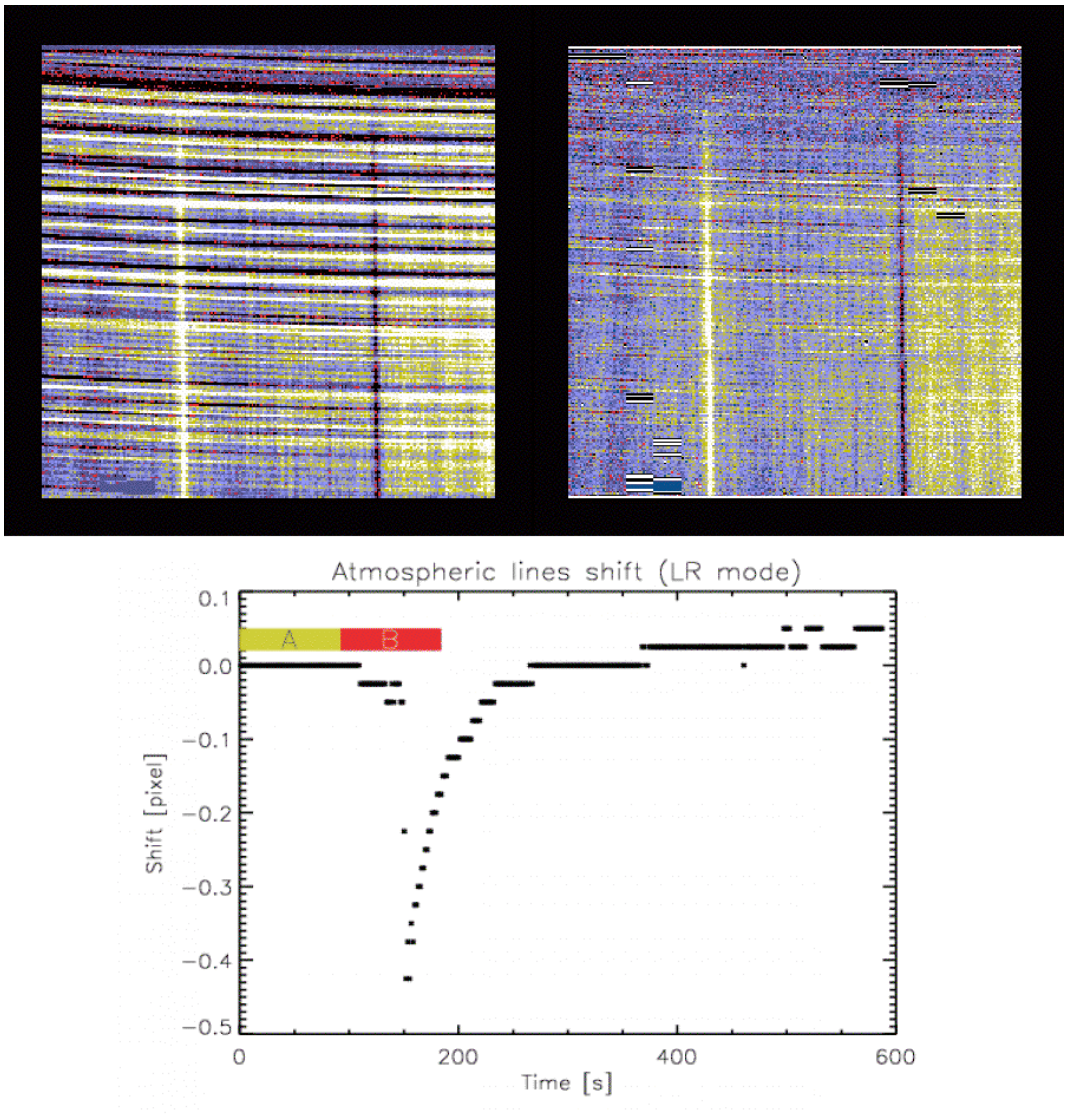

Figure 3.23: Jitter in low-resolution spectroscopy mode. Left panel: the jitter (vertical dispersion direction) produces strong residuals. Middle panel: after a frame-by-frame registering, the jitter is corrected for. Right panel: plot of the offsets found as a function of time (reference: first frame). A strong jump is observed at t≈150 s and does not coincide with a telescope offset which would impose a sudden acceleration to VISIR. After a timescale of $\sim$ 50 s, the closed-loop which controls the LR scanner has recovered the initial position; however some drift is still observed for 360<t<600 s.

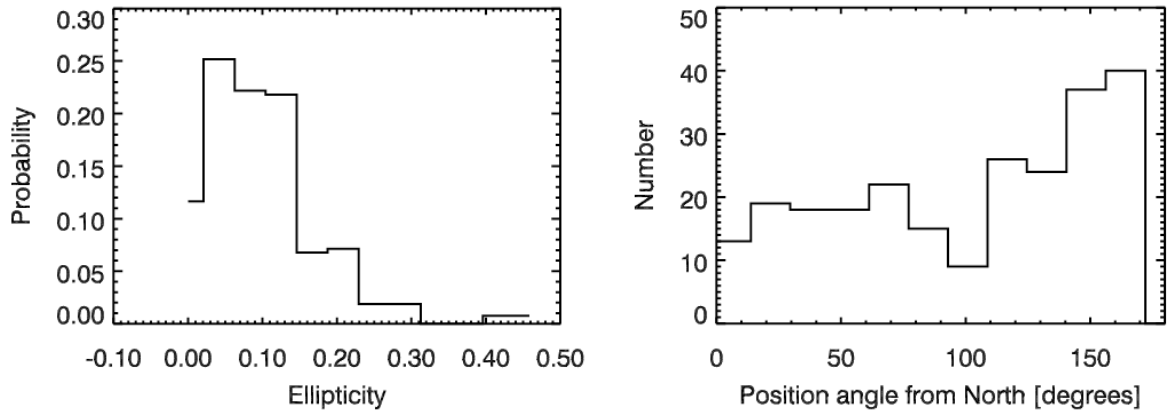

Figure 3.24: Left panel: PSF ellipticities distribution. A 2D Gaussian fit is applied to the PSF and the ellipticity is defined as $|\ \mathrm{FWHM}_1 - \mathrm{FWHM}_2\ |\ /(0.5(\mathrm{FWHM}_1 + \mathrm{FWHM}_2))$ where FWHM_1 and FWHM_2 are the full width at half maximum estimated along the major and minor axis of the ellipse. In the same process, the position angle of the 2D Gaussian shape is also estimated; its distribution is plotted in the right panel.

$$S_2(\lambda) \quad = \quad I_2 T(\lambda) e^{-m_2 \alpha(\lambda)}$$

Solving for α and $T(\lambda)$ one gets:

$$\alpha \quad = \quad \frac{\log(S_1/S_2) - \log(I_1/I_2)}{m_2 - m_1}$$

and

$$T(\lambda) \quad = \quad \frac{O_1}{I_1 e^{-m_1 \alpha(\lambda)}}$$

In the case of 3 or more calibrators, the system is "over-resolved"; the solution is obtained by a best-model fit (regression-like) of the system of equations above. When only one calibration observation has been observed, a method based on extrapolation is used (see Annex 4.3.

Nevertheless even when applying airmass correction some stitching errors are observed between the different low-resolution settings covering the N-band (Fig.3.26).

3.8 Spatial resolution in low-resolution spectroscopic mode

As shown already in Fig.3.26 the spatial scale measurements are affected by a jump between the low-resolution mode setting at 9.5 μm and that at 11.8 μm. When making a more comprehensive study of the spatial resolution in the low-resolution spectroscopic mode on standard stars, one notices that 1) this jump is quasi systematic 2) the jump corresponds in most of the cases to an increase of the FWHM between lower and upper wavelength 3) the expected diffraction-limited spatial resolution is never reached, even in case of good seeing conditions.; a systematic offset of ~ 0.05 arcsec is observed. Fig.3.27 illustrates the above statements. In the case of low seeing values, the FWHM follows the expected variation as a function of the wavelength, but with a systematic offset of at least 0.05 arcsec. In the case of seeing-dominated conditions, the FWHM decreases with the wavelength following quantitatively the expected $\lambda^{-1/5}$ law. See Annex 4.3 for a more complete analysis and description and how a statistical approach can be used to derive physical constraints on the size of the targets as a function of the wavelength.

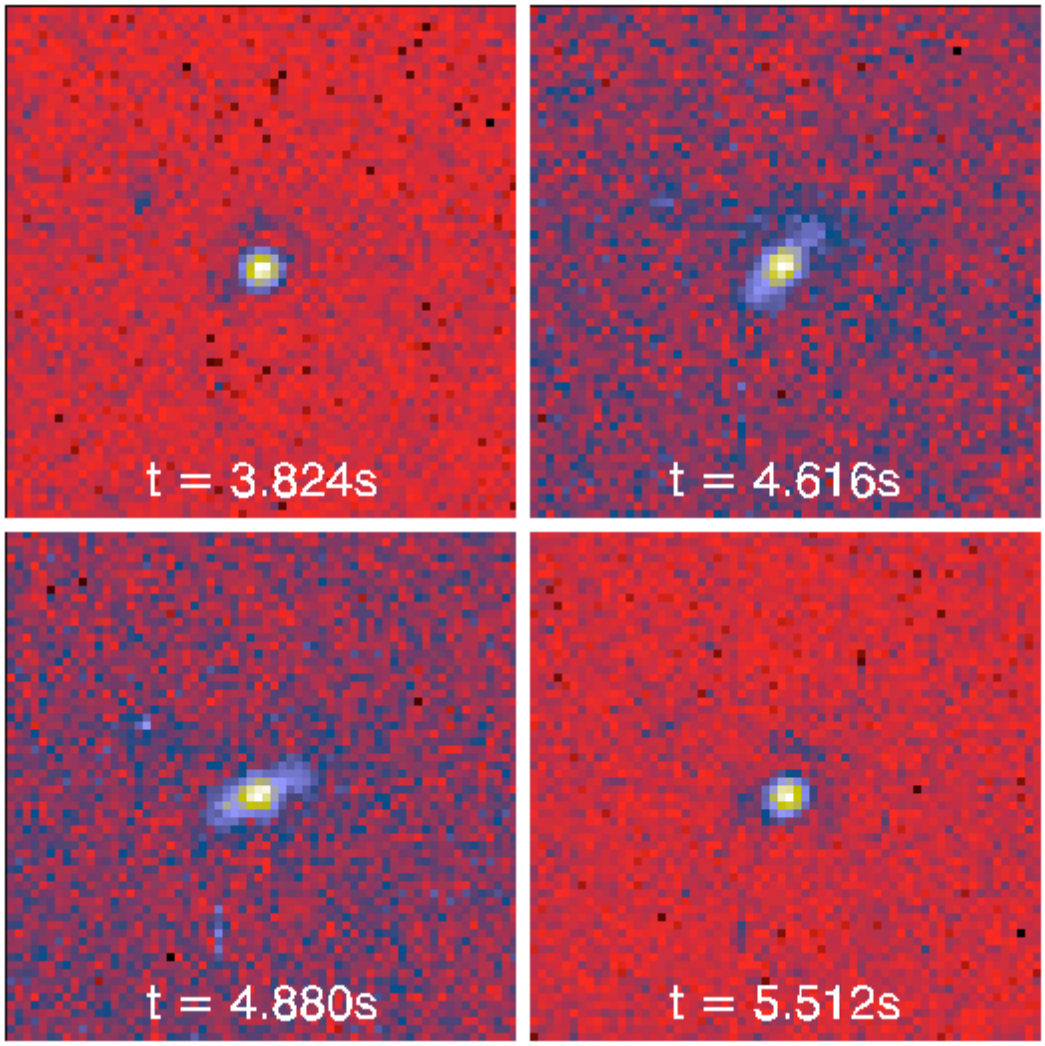

Figure 3.25: Time sequence of VISIR frames. A strong PSF deformation is noticed between t=4.6 and 4.8 s; the position angle of the deformation rotates from -45 to -60 degrees. 1s later, the nominal image quality is recovered.

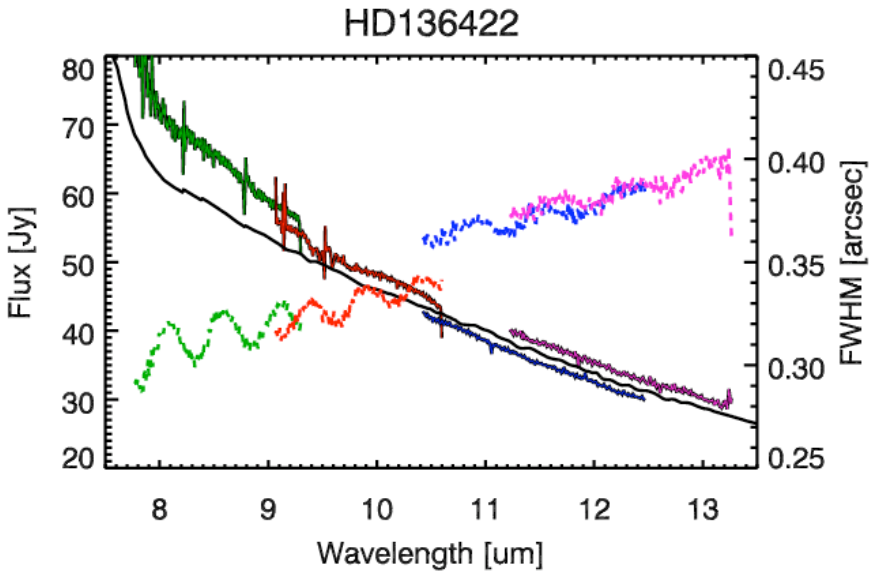

Figure 3.26: Low-resolution spectra of a standard star (HD136422) in the four settings covering the N band. The observation has been corrected for telluric absorption using a second calibration star. The VISIR observed spectra (plain lines) are discontinuous between two adjacent settings, which evidences of a photometric miscalibration. The black line represents the true HD136422 spectrum template ([Cohen et al., 1992a]). The dashed lines display the FWHM measurements of HD136422 low-resolution spectra. Notice the jump of FWHM between settings 2 (orange) and 3 (light blue).

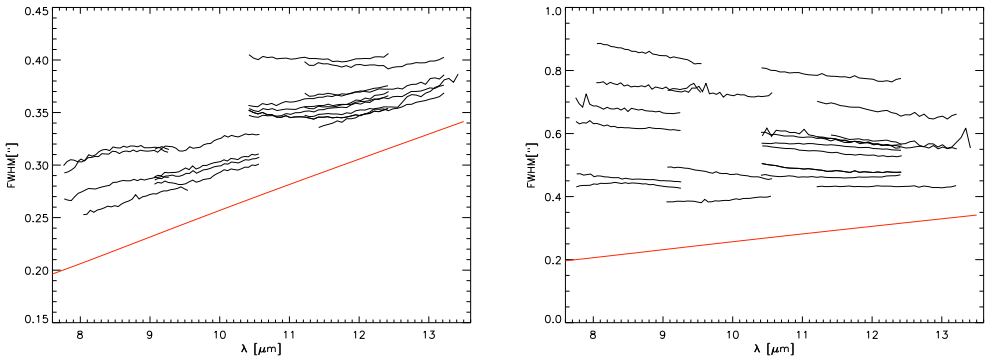

Figure 3.27: Plots of the angular resolution measured on point-like standard stars as a function of the wavelength. In the left panel, the seeing was always lower than 0.6 arcsec; in the right one the seeing was always larger than 1.1 arcsec. The red line draws the expected diffraction-limited FWHM (obscured pupil).

3.9 Image deconvolution

VISIR on a 8.2m telescope reaches the limits of purely diffraction-limited instruments. Assuming an atmospheric turbulence following a Kolmogorov distribution of turbulence cells (seeing $\lambda^{-1/5}$), the seeing value around 10 μm is roughly half of that in the visible range. VISIR mid-infrared data should thus not be longer diffraction limited as soon as the optical seeing becomes larger than 0.7 arcsec. VISIR burst mode data allows to carefully analyze the tip-tilt fluctuations of standard star images, and then derive macroscopic turbulence parameters such as the Fried parameter R_0. Our measurements give $R_0 = 6.23 \pm 0.33$ m at 8.6 μm and $R_0 = 8.76 \pm 0.42$ m at 11.3 μm when the optical is 0.75 arcsec. They confirm that VISIR data become seeing-limited at 10 μm for an optical seeing larger than $\sim$0.75 arcsec. In these conditions, mid-infrared image deconvolution becomes a much more difficult problem to solve. Standard methods which assume an almost perfectly calibrated PSF, such as Landweber, Richardson-Lucy, or more modern wavelets based ones will produce wrong solutions (Fig.3.28). Myopic deconvolution methods are a must in this case but require a large, redundant, dataset.

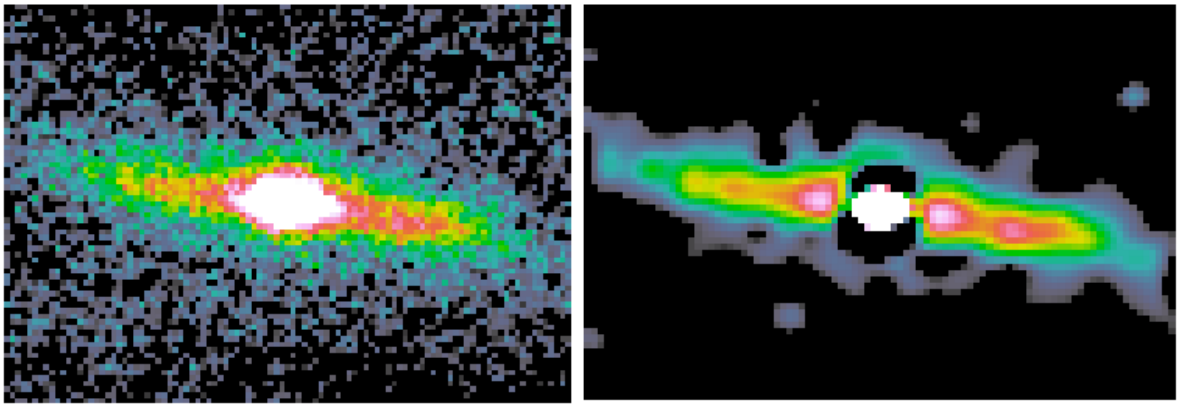

Figure 3.28: VISIR image of the β Pictoris dust disk at 11.2 μm (PAH2 filter) (left panel) has been deconvolved using a standard star observations to estimate the PSF (right panel). This PSF differs slightly from the true one and creates spurious deconvolution artifacts (e.g. and inner dark ring around the star). With such data, myopic deconvolution is compulsory.

3.10 Conclusions and Perspectives

We have described in this section the knowledge we have acquired on VISIR over four years of use. Although a fairly large number of unexpected spurious effects have been found such as detector striping, detector ghosts, etc..., VISIR provides nevertheless since 2004 the science users with high angular resolution mid-infrared data at a level of sensitivity close to theoretical expectations. Still, some good, physically very informative, measurements can be obtained but often at the cost of off-line data processing efforts. As a matter of fact, the mid-infrared data are probably among the most demanding data in terms of processing effort.

Thanks to the analysis of VISIR data, we identified some effects that can or will be corrected either by hardware solutions (e.g. jitter of the scanners, detector breathing), using software post-processing techniques (low-frequency noise excess, PSF deformations in the case of standard observing modes), or a combination of the two (e.g. PSF deformations in Burst mode observations).

Standard image deconvolution which is a technique we were used to apply on 4-m class telescopes in not applicable any longer because of the large sources of PSF variations (e.g. seeing that starts blurring

the images for optical seeing values larger than 0.7 arcsec) on a 8m-class telescope. We thus have to turn towards myopic deconvolution techniques which are much more complex and need larger datasets to constrain the solution.
Rapid imaging burst mode data were not only of large interest because allowing to circumvent spurious effects and increase the quality of the result on bright objects, but also of awesome usefulness to analyze and understand spurious effects. Using these data, it is even possible to partly simulate foreseen new observing modes on the next generation of telescopes (see Chapter 6).
Our global experience experience with VISIR is that the preservation of the high angular resolution (which is the spearhead of mid-infrared astronomy from the ground) will unavoidably require the implementation of new observing modes such as phase-mask coronography (its advantage over Lyot coronography is the absence of strong limitation on minimum distance to the star) or differential imaging, or both combined (see Chapter 6).
In the meantime, I have used the tools and methods presented in this chapter to obtain some scientific results in the domain of dusty disks. These results are presented in the next chapter.

Related articles

Annex :

Some (little) thing(s) about VISIR

published in *2007 ESO Instrument Calibration Workshop*, **2007**

Some (little) thing(s) about VISIR

E. Pantin[1], L. Vanzi[2], and U. Weilenman[3]

[1] DSM/DAPNIA/SAp, CE Saclay, UMR 7158, FRANCE eric.pantin@cea.fr
[2] ESO, Chile lvanzi@eso.org
[3] ESO, Chile uweilenm@eso.org

Summary. VISIR is the VLT mid-infrared Imager and Spectrometer. It offers a comprehensive set of observing modes, imaging in N and Q bands, at the limits of the telescope diffraction, also as spectroscopy in the same bands. In particular, VISIR provides a very high-resolution spectroscopy mode with an achieved resolution up to 30000 in N band; this mode is so far unique in the southern hemisphere. VISIR calibration is quite specific if compared to standard visible/near-infrared ones. Various dedicated methods have to be developed to remove the instrumental signatures and obtain the best scientific return.

1 The instrument

VISIR is mounted on the VLT unit Melipal at Paranal and has been commissioned in April 2004. Since April 2004, it operates routinely to deliver mid-infrared (mid-IR) images and spectra in N and Q bands (atmospheric windows centered on 10 and 20 μm respectively). The Imager and the Spectrograph are two entities physically separated, having each one their own optics and detector. Given the huge background emitted by both the atmosphere and telescope, background cancelling techniques are compulsory (see Fig.1). The instrument itself emits a negligible background since its interior is cryogenically cooled between 50 and 70 K. VISIR Imager uses typical chopping frequencies around 0.25 Hz and nodding period around 1 minute. VISIR spectrometer uses the same parameters in low and medium resolution modes, but given the small number of photons impiging onto the detector at much higher spectral dispersions, 10 times larger periods are set for the high resolution mode.

1.1 The Imager sub-instrument

The imager is equipped with a 3-mirror anastigmat all reflective design collimator, feeding the detector with diffraction-limited performances images. It

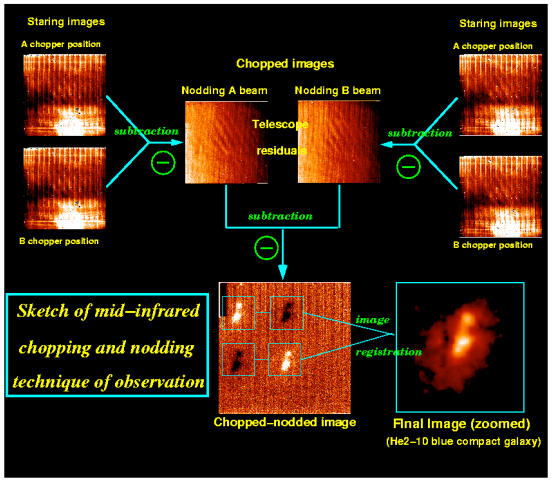

Fig. 1. Scheme of chopping and nodding technique used to suppress the very high mid-IR background. First, the elementary images are averaged (-¿ staring images) over half a chopping period. Then, the chopping is applied for each telescope nodding position. Finally, chopping residuals due to different optical paths in the 2 chopper positions, are canceled by subtracting the two nodding beams.

is equipped with a DRS 256x256 detector designed for high-level fluxes. The imager provides 11 filters (at several wavelength of interest, such as the PAH bands at 8.6 and 11.3 μm) covering the N-band and 3 in Q-band, matched to the atmospheric sub-bands between 17.5 and 19.5 μm. The imager is equipped with calibration devices such as pupil imaging and a pinhole mask, used for measuring the pixel scale and the optical distorsion in the field.

1.2 The Spectrometer sub-instrument

VISIR spectrometer optics have a similar all-reflective design. Various gratings are mounted in the instrument, allowing to perform low (LR mode, R≈300 in N band) and medium resolution (MR mode) spectroscopy (R≈3000 in N band,R≈1500 in Q band). VISIR offers also a high spectral resolution mode (R≈30000 in N band, R≈15000 in Q band) thanks to a duo-echelle grating. Some order-sorting filters are provided allowing to observe spectral lines of physical interest (e.g. H_2, NeII) with a slit length of 32.1″ on the sky (long-slit, HRS mode); a cross-dispersed mode allows to set any central wavelength onto the detector, but with a reduced slit length (about 4″, HRX mode). See [4] for a more complete description of the spectrometer sub-unit.

2 The Warm Calibration Unit (WCU)

On top of VISIR enclosure, lies the Warm Calibration Unit (WCU). This unit comprises a point source (monochromator), and extended source (Peltier plate) presenting an adjustable surface temperature ([-20,50]^{o}C), and a telescope simulator (Offner design). This unit allows to perform daytime checks and calibrations (e.g. image quality, relative sensitivity, flat data measurements).

3 Detector Features

The two detectors that equip VISIR have to be fine tuned for the conditions we are working in. They are cooled by pulsed Sumitomo cryo-coolers. Although much efforts have been devoted to damp temperature oscillations, the detectors still feel periodic (1 Hz) temperature fluctuations inducing slight changes the in detector gain. To minimize this effect, some heaters are glued to the detector sockets, and stabilize the detectors at temperatures between 6.0 and 9.0 K. Residual temperature fluctuations (therefore detector gain variations) are canceled by keeping in phase the chopper with the cryo-coolers.The two DRS detectors have well-capacities around 2.10^7 e^- (large capacity mode) and 2.10^6 e^- (small capacity mode). Quantum efficiency is typically around 50%. For a detailed study of the detectors characteristics, see [3].

The detectors working point is nominally set around +5000 ADU on the sky (1 ADU $\approx$ 275 e^-, given a total range of [-32000,32000] ADU. The detectors start to saturate when the levels reach about 8000 ADU and more (about 2/3 of the total capacity). Some pixels have an abnormal behaviour (gain) and will trigger striping (due to multiplexer amplifiers collapse, see Fig.2) over a usually wide range of rows on the detector. This striping is periodic, with a period of 16 columns, since one amplifier reads every 16 pixels sequentially.

4 Instrument performances

Instrument performances are mainly monitored using standard stars from Cohen's database [1] (see also Sec.4.2) which are systematically observed at the beginning of a VISIR night. The background level, the Point Spread Function (PSF) as a measure of image quality, and the point source conversion factor (between detector ADU and physical units) and sensitivity are estimated. All these values are reported in a Quality Control summary provided by the ESO's Data Processing and Quality Control Group (http://www.eso.org/observing/dfo/quality/VISIR/qc/qc1.html, and also D.Dobrzycka, these proceedings) .

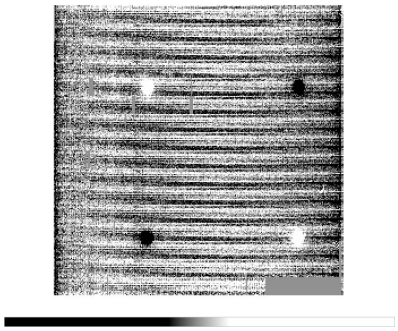

Fig. 2. Imager data showing the "striping effect". This striping is periodic (16 pixels) and depends at first order, on background fluctuations that affect "hot" pixels.

4.1 Sensitivity

Imager

VISIR imager sensitivity over the period Sep04-Dec04 is reported in Fig.3. The median sensitivities are close to expected values within a factor of 2. Elements concerning effects possibly degrading these performances are given in Sec.5. When the point source sensitivities in N band are remarkably stable in time and under various weather conditions, Q band ones are much more sensitive to the precipitable water vapor (PWV) content and airmass.

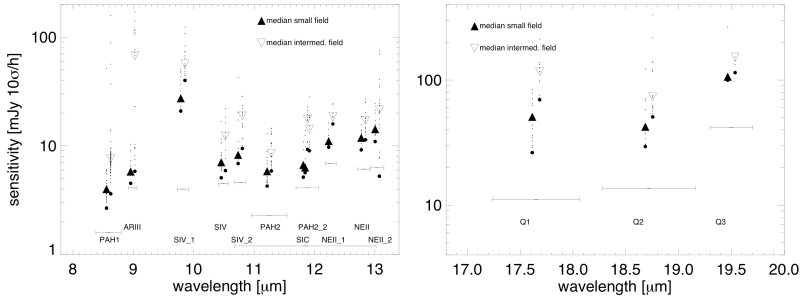

Fig. 3. Sensitivities of the VISIR Imager, for all filters, in N and Q bands. Both pixel scales (small field (0.075″/pixel) and intermediate field (0.127″/pixel) are shown.

Image quality

VISIR imager image quality achieve diffraction-limited performances in N band when the optical seeing is $\leq$ 0.8 arcsec. For instance, in PAH1 filter (8.6 μm), the spatial resolution of VISIR is PSF FWHM is close to 0.25 arcsec. On a 8.2m telescope, the atmosphere turbulence starts to play a significant role, degrading the spatial resolution for standards optical seeings (0.8 arcsec and more). In Q band, diffraction-limited PSF are routinely observed. VISIR images deconvolution is still a challenge since VISIR PSF, half affected by random seeing fluctuations, half by stable diffraction, is varying in time (see Fig.4)

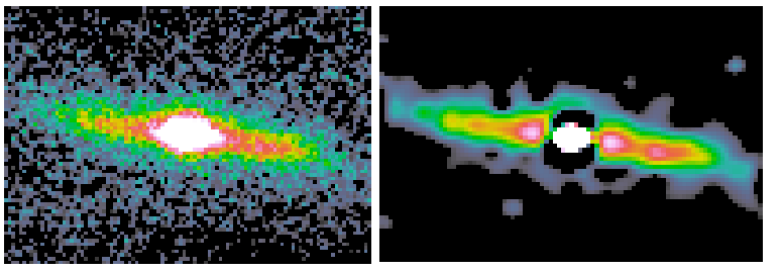

Fig. 4. VISIR image of the β Pictoris dust disk at 11.2 μm (PAH2 filter) (left panel) has been deconvolved using a standard star observations to estimate the PSF (right panel). This PSF differs slightly from the true one and creates spurious deconvolution artefacts (e.g. and inner dark ring around the star). With such data, myopic deconvolution is compulsory.

4.2 Instrument calibration

Photometric and spectrophotometric calibration

Imager photometric and Spectrometer spectrophotometric calibrations are usually performed using standard stars. These calibrators (81 in southern skies) have been chosen among Cohen's radiometric database [1] and adding a selection of A0 type stars for which the spectrum is well-known and relatively free of lines in the mid-IR. The experience over 3 years now shows that derived conversion factors (from ADU to physical Jy units) are quite stable in N-band (15% typical variations), and more variable in Q band (30% and more). In the specific case of high-resolution spectra, it is advised to use also bright asteroids observations to get a more accurate correction of the telluric absorption.

Wavelength calibration of spectra

VISIR data contain both sky-subtracted images and sky data. Sky spectra can be usefully compared to models of mid-IR atmospheric emission to derive a wavelength calibration. In the majority of the cases, except some very "clean" windows in N-band at medium resolution, it is possible therefore to "self-calibrate" the data.

5 Instrument characteristics and signatures

5.1 Detector noise studies

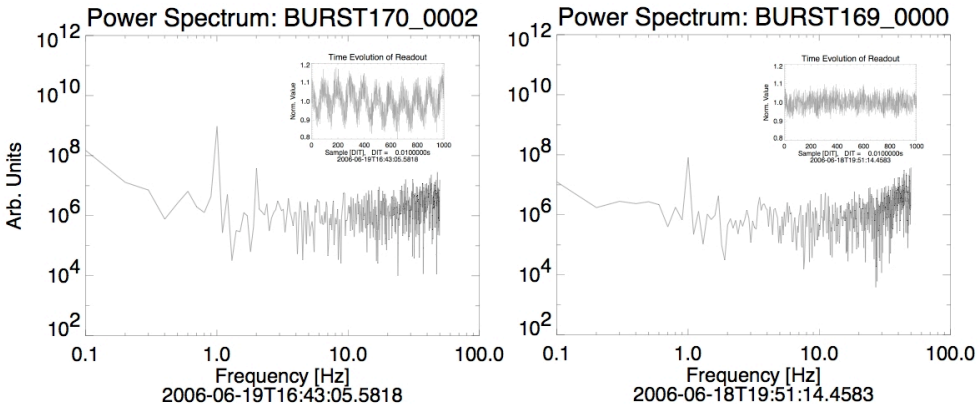

Fig. 5. Detector output power spectrum as a function of the detector temperature (inset are the time signals). At 6.5K, a clear 1Hz fluctuations noise is evidenced. At 8.0K, the 1 Hz noise is significantly reduced, and the time signal does not show any longer periodic modulation.

Given the level of the background, the detector dark current (smaller than 7000 e^-) and readout noises (1771 and 296 e^- in high and low capacity modes) are negligible against the background shot noise. Rapid imaging experiments have been performed in order to study any other source of noise. These experiments show that a too low temperature of the detector (6.5K), a 1 Hz oscillations noise generated by the cryocoolers pulse tube is observed (see Fig.5). When slightly increasing the working temperature of the detector to 8.0K, these thermal oscillations vanish (see Fig.5), but at the cost of deterioration of detector cosmetics (increase of detector "striping", see Sec.5.5). At 8.0K also, the shot noise increases as expected (square-root of impinging number of photons), whereas its behaviour seems more erratic and less easily interpretable at 6.5K.

5.2 Background noise

Once the detector is properly set at a temperature around 8.0K, observation parameters such as the chopping frequency, number of rejected images after a chopper movement, etc, shall be adjusted. A study of the background noise (image in a whole) has been carried out. As seen in Fig.6, for chopping frequencies larger than typically 1 Hz, the background noise is close to the expected noise level. However, for chopping frequencies lower than 1 Hz, the background noise starts to increase in a different way, according to the filter. This degree of noise increase seems to be linked to the quality of the atmospheric transmission in the given filter; the more affected by atmospheric tranmission is a filter, the higher is the increase of background noise.

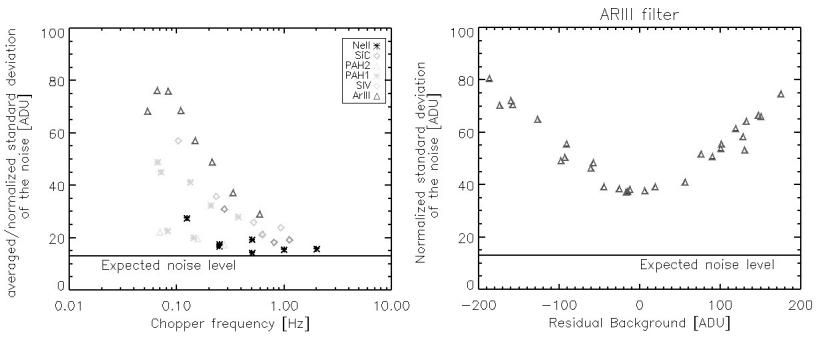

Fig. 6. Left : Background noise as a function of the chopper frequency. Right panel : Background noise as a function of the residual background level after chopping. As evidenced, the noise level is correlated with background fluctuations.

5.3 Background errors and noise

As seen in Fig.7, VISIR background noise deviates from a pure gaussian and white noise behaviour. The excess of noise a low-frequencies degrades VISIR performances for faint extended objects making it particularly difficult to assess the object spatial support and measuring its photometry (e.g. a faint spatially extended comet). This effect is also particularly annoying when trying to extract spectra. On the other hand, the point source performances are only weakly affected by this effect. This excess of low/medium spatial frequencies noise is probably related to the global effects described in sect.5.2. Some measurements of spectral characteristics of VISIR background noise as a function of observing parameters would be helpful.

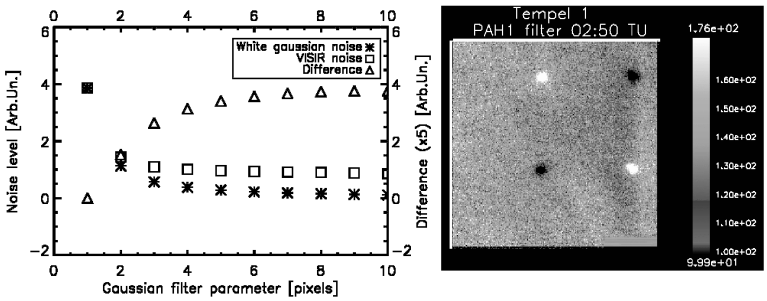

Fig. 7. Plot of the noise level as a function of a low-pass gaussian filter parameter σ. As the cut-off frequencies decrease, **the noise level gets higher than a pure gaussian noise having the same standard deviation than VISIR noise in original image**. This shows that VISIR noise has a different behaviour than a pure gaussian noise, and presents an excess of noise at lower frequencies, as seen visually in right panel image.

5.4 How to correct for this background errors ?

As seen previously, this "extra noise" at medium and low spatial frequencies can be assimilated to a problem of varying background one has to deal with. In order to properly assess some objects photometry, it is possible to mask the observed objects and reconstruct the underlying background. Usual methods are very poor in doing this job. However, using wavelets+curvelets reconstruction [2], it is possible to get reasonable results (see Fig.8).

5.5 Detector striping

As already discussed in Sec.3, VISIR DRS detectors are affected by striping triggered by some abnormal behaviour of some pixels. Although the striping is sensibly reduced thanks to a "masked" read-out scheme by the sequencer, some residual periodic (16 pixels) stripes appear very often. Then, the only method is to suppress the stripes in the off-line processing. The currently adopted method consists in using an "adapted image transform towards a dual space" in which a given stripe starting at line l and row r will produce a peak concentrating the full stripe signal in the dual space (Fig.9).

5.6 Gain map and Flat-fielding

Optical and near-infrared usually include flat-field correction for the data. One can wonder if this is applicable or even compulsory for mid-IR data; there is a long debate in the litterature about this question. Pragmatically, experiments show typical variations of a few percent of photometric estimate on the 4 different beams of a standard star in a VISIR image using the most sensitive

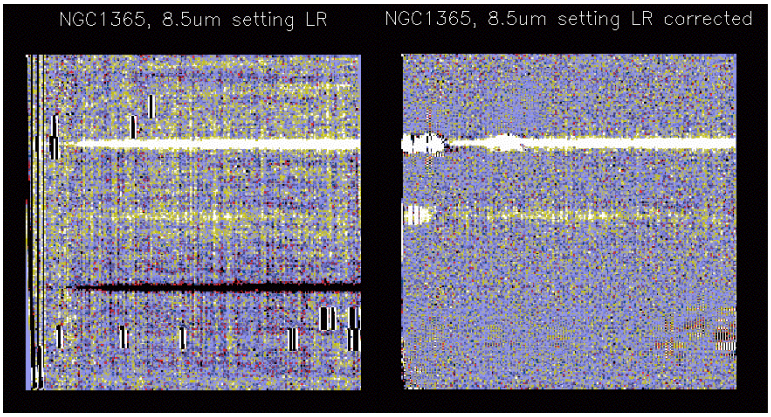

Fig. 8. Left panel : low-resolution VISIR spectrum showing some important background errors from the atmosphere. This extra "noise" cannot be easily filtered in Fourier space because spread over a wide range of frequencies. Right panel, the corrected image (the negative beam has not been reconstructed using the wavelets+curvelets method (see text).

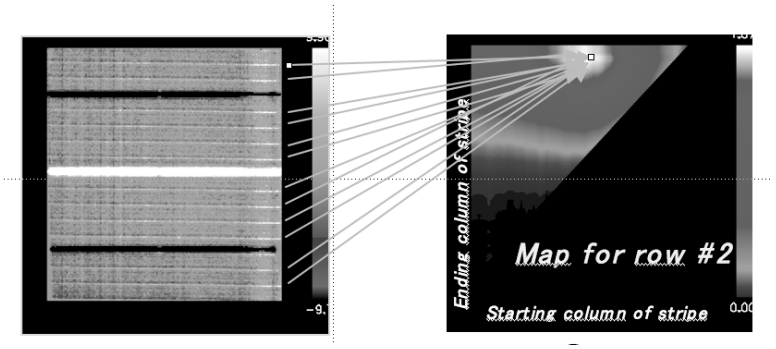

Fig. 9. Periodic stripes (left panel) are "concentrated" via a dedicated image transform, into a dual space (right panel). Once the "stripe" detected in this dual space where is appears as a single peak, the stripe is then reconstructed and subtracted from the original image. Since we usually deal with more than only one stripe, the process is iterated until no more stripes are detected (this threshold is computed based on the noise level in image space).

N-band filter (PAH2), the dispersion having a standard deviation of about 1%. The background shot-noise itself can contribute at most to about typically 0.5 % of photometric error and therefore, cannot explain a few percents of variation peak-to-peak. The observed variations must be then attributed either to background errors (see 5.3), or to a spatially varying differential response of the detector. Using the method described above to correct for background errors, one can discard any predominance of them in the observed variations, on the other hand laboratory measurements of the detectors gain, showed peak-to-peak variations of about 1% of individual pixels gains [3]. To reach the highest photometric accuracy, it would be probably interesting to be able to correct for individual gain response. Estimating this response is not an easy task. On one hand, sky dips can be affected by instrument flexures, on the other hand, observations of the extended source of the WCU and varying the plate temperature can be corrupted by any warm element on the light path. So far, flat-fielding attemps did not improve the photometric accuracy.

6 Conclusions

VISIR offers to the ESO community the possibility to obtain valuable infrared data in N and Q bands. Although its sensitivity, limited by the background shot noise, remains two to three orders of magnitude worse than a space observatory (e.g. SPITZER), its high spatial resolution, typically 10 times better, provides mid-IR imaging with a unprecedent sharpness. In addition, the VISIR spectrometer sub-unit with spectral resolution up to 30 000, opens a new "window" for resolved both spatially **and** spectrally the mid-IR emission. However, on a 8.2m telescope, the spatial resolution degradation due to the atmospheric turbulence is not negligible any longer, and usual deconvolution techniques are useless. There is then a need for simple pre-focal adaptive optics systems that would allow to reconver purely diffraction limited data and stabilize the PSF.

References

1. M. Cohen, R.G. Walker, B. Carter et al.: AJ **117**, 1864 (1999)
2. M. Elad, J-L. Starck, D. Donoho et al. **19**, 340 (2005)
3. P. Galdemard, F. Garnier, and P. Mulet : Characterisation of DRS Technologies 256x256 mid-IR arrays for VISIR. In: *Proceedings SPIE*, vol 4841, 129 (2002)
4. VISIR users manual, www.eso.org/instruments/visir

Annex :

The experience from VISIR on the design of and ELT mid-infrared instrument

Published in *Science with the VLT in the ELT Era*, 2009.

The experience from VISIR and the design on an ELT mid-infrared instrument

E. Pantin[1] and R.Siebenmorgen[2]

[1] DSM/DAPNIA/SAp, CE Saclay, UMR 7158, FRANCE eric.pantin@cea.fr
[2] ESO Garching, GERMANY rsiebenm@eso.org

Summary. VISIR is the VLT mid-infrared (mid-IR) Imager and Spectrometer. It offers the possibility to obtain data at high spatial (0.27") and spectral(R=30000) resolution in the N (8-13 μm) and Q (16-28 μm) atmospheric windows. VISIR observations have provided unique constraints on targets such as central regions of AGNs, or protoplanetary disks. Its successor on an ELT will provide data with a unique sharpness (0.05") and sensitivity (50 μJy source detectable in 1 hour), thus allowing to characterize exoplanetary disks and exoplanets. In this paper, we review a selection of scientific contributions thanks to VISIR, then, a the light of VISIR experience, we discuss the stakes for the future mid-IR instrument of the European ELT.

1 VISIR instrument

VISIR is mounted on the VLT unit Melipal at Paranal and has been commissioned in April 2004. Since April 2004, it operates routinely to deliver mid-infrared (mid-IR) images and spectra in N (R=300,3000,30000) and Q (R=1500,15000) bands (atmospheric windows centered on 10 and 20 μm respectively) ([4]). The data are diffraction limited if the optical seeing is below $\sim$ 0.8 arcsec. The high spectral resolution mode remains unique in the southern hemisphere, and allows for instance to observe the H_2 ro-vibrationnal emissions at 8.02, 9.66, 12.28 and 17.03 μm.

2 A VISIR pot-pourri of scientific results

2.1 Extragalatic astronomy

A prime category of targets for VISIR are galaxies hosting active galactic nuclei (AGN). AGNs contain usually a massive compact object (black hole) surrounded by either accreted or ejected material. Studying these materials provides us strong constraints on the physical mechanisms acting at the level

of the inner black hole. The dust close-by environment of the AGN is usually heated to 100K and more, while being, in some cases, relatively embedded is dust. Mid-IR observations are then adapted to study this kind of object. NGC1068 is a famous and well studied object belonging to this family. Left panel of Fig. 1 shows the very inner regions as observed in the mid-infrared range. MIDI interferometric data are interpreted in terms of a 3 components model : one unresolved source, on elongated source (500 mas scale), and one "extended" component on a $\sim$ 2 arcsec scale ([8]). VISIR observations are complementary to MIDI ones, providing the information at intermediate scales (0.3 arcsec) and showing that the "extended" component is actually made of several knots [1].
NGC7582 is another AGN. VISIR observations in high-resolution (R=25000) spectroscopy allowed [10] to derive an accurate estimate of mass of the black hole (5.5 10^7 $M_\odot$) (Fig. 1, right panel).
Some active galaxies host embedded young massive clusters (YMC) which typically contain 10^6 $M_\odot$ and believed to be the progenitors of super star-clusters. These YMC are usually opaque to the visible radiation. On the other hand, VISIR low-resolution spectroscopy allows, to determine physical quantities such as mass and age, as in the case of NGC1365 [2].

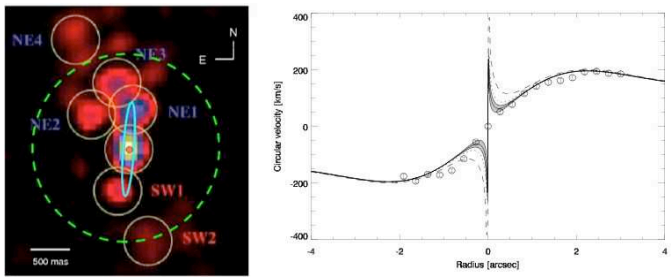

Fig. 1. Left panel : NGC1068 as observed with VISIR (underlying image) and MIDI (red dot, green and blue contours). MIDI detects an intermediate scale (2") mid-IR emission; VISIR shows it is actually composed on several knots. Right panel : velocity resolved VISIR data of the active galaxy NGC7582 using the high-resolution spectrograph of VISIR at 12.8 μm (NeII line). The variation of the velocity curve allows to determine the mass of the central black hole.

2.2 Low-mass companions and dusty disks

The sub-stellar mass system ϵ Indi B is the closest brown dwarf binary system known. Their separation is only 0.73". SPITZER observatory is thus unable to physically separate the emission of each of the components. VISIR observations, although penalized by a much lower sensitivity, are able to put

constraints on the physical characteristics of both components ([9]).
HD97048 is a young (3 Myr) intermediate-mass Herbig star (Ae) in the Chameleon cloud, surrounded by protoplanetary disk of dust and gas. VISIR observations in PAH bands (8.6 and 11.3 μm) could resolve the structure of the disk. For the first time, direct imaging shows that this disk is thick, dense, and has a flared structure as predicted by [3]. The measured flaring index (1.26 $\pm$ 0.05, [5]) is strikingly close to the expected value of 9/7= 1.28 assuming hydrostatic equilibrium of the disk (see Fig.2). VISIR high spectral resolution observations ([6]) confirmed then the presence of large quantities of gas; the detected H_2 emission line at 17.035 μm (see Fig.2) shows that 0.01 to 1 Jupiter masses (depending on hypothesis on the gas temperature) of warm H_2 are confined in the inner 35 AU, and maybe more important, that the gas to dust mass ratio (3000 to 14000) deviates significantly from the canonical value of 100.

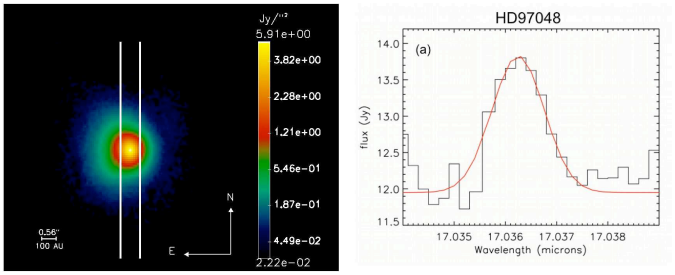

Fig. 2. Left panel : the HD97048 dust disk resolved in VISIR image at 8.6 μm. The measure of the decentering of the isophotes as a function of the distance to the star allows to precisely measure the flaring index of the disk. Right panel : the 0-0 S(1) H_2 emission line detected in HD97048. This detection confirms that at 3 Myr, relatively large amounts of gas are still present.

3 Limitations of current VISIR observations

VISIR suffers from various limitations and errors, such as detector striping, flat-fieldability, stitching of consecutive low-resolution spectroscopy settings, background errors. See [7] for a detailed description of these effects. Various measurements tend towards an interpretation of background errors as an excess of noise at mid and low spatial frequencies (see Fig.3). This excess is probably linked to a too small chopping frequency of 0.25 Hz. Future mid-infrared instruments should benefit from large format (1kx1k) and flat-fieldable detectors better stability of the gains). In an ideal case, detectors with a gain known

at a 10^{-5} level of accuracy would permit to get rid of chopping/nodding techniques of background cancelation, thus relaxing largely the constraints on the ELT designs.

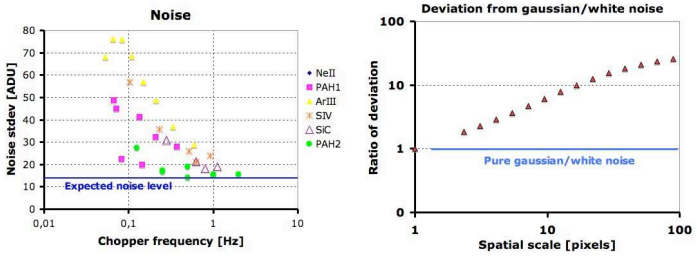

Fig. 3. Left panel : measurements of the background noise as a function of the chopping frequency, for various N-band filters of VISIR. One can notice the sudden increase of noise for chopping frequencies smaller than $\sim$ 1 Hz. Note also the correlation between the noise excess and the presence of atmospheric lines in the filter (e.g. ArIII filter (9 μm) spans a large number of atmospheric lines, while PAH2 one (11.25 μm) depends much less on the chopping frequency. Righ panel : analysis of the excess noise in PAH1 filter (8.6 μm) as a function of the spatial frequency. At a spatial scale of 10 pixels, the noise is about 10 times larger than expected if the noise had a white spatial distribution.

4 Calibration of mid-IR instruments

Based on our experience with VISIR, we realized that : 1) Relevant quality control parameters are the pwv (precipitable water vapour content), the background level, and conversion factor. 2) The data themself contain valuable informations to calibrate the data (e.g. sky lines for wavelength calibration) 3) Weather observational parameters are relatively stable over few hours, thus only a limited number of standard star interlaced observations are really needed.

5 Observing in the mid-infrared range on an ELT

The awaited sensitivity of a mid-IR on an ELT opens some new perspectives in the field of exoplanetary sciences. Low-resolution spectroscopy of giant planets on orbits of a few AUs from the parent star would allow to better characterize their atmospheric composition and mass (see Fig. 4). A proto-planetary nebulae able to form extreme (1 Jupiter radius) super-Earth planets would

be probably gravitationally unstable, and thus only brown dwarfs would born in such an environment. Let's anyway imagine that nature would invent some smart mechanism to create such monsters. In that case, such a planet, placed on a ??? orbit would be directly observable, up to a distance of ?? pc. Finally, a ELT mid-IR instrument is a perfect tool to accurately study protoplanetary and debris disks. As shown in Fig.4, their structures (e.g. embedded planets digging gaps) would be easily revealed.

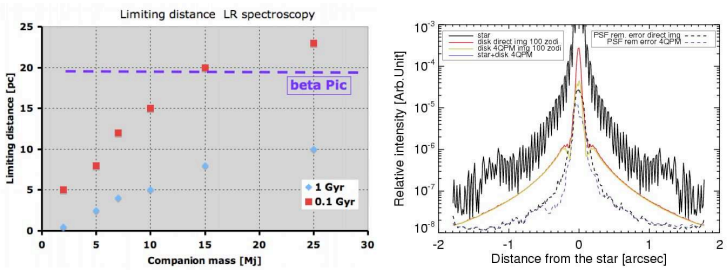

Fig. 4. Left panel : Limiting distances when characterizing in low-resolution (R=100) spectroscopy on an ELT a giant exoplanet, as a function of planet mass. Two cases are considered : an age of 0.1 Gyr (more favourable because young planets are intrinsically hotter), and and age of 1 Gyr. Right panel : profiles of debris disks emission when observed in mid-IR on an ELT. The use of a 4 QPM coronograph strengthen by 30% the contrast of a gap made by a planet, almost smeared out otherwise when observing without 4 QPM. Note also the reduction of residuals when making compulsory PSF subtraction, assuming a variation of seeing of 0.1 arcsec (0.7 to 0.8 arcsec).

The predicted performances of a mid-IR instrument depend significantly on the observatory site. If N band observations are quite insensitive to the altitude, Q band sensitivity and spectral coverage are highly dependant (e.g. 24 μm atmospheric transmission (T$\sim$1) is twice higher at 4500m than at Paranal altitude).
In order to be competitive with space-born infrared observatories, high spatial and spectral resolutions shall be the drivers to build ground-based mid-IR instruments. The ELT theoretical diffraction limit can be maintained in the mid-IR range at a moderate cost, i.e. using relatively simple adaptive optics system when compared to near-IR ones. However, the number of "warm" mirrors (increasing the background) on the lightpath shall also be limited to its minimum set.
Most of the science cases described in this paper deal with targets angularly very close to a stronger source (star, central engine of an AGN); differential observing techniques are a must. These conditions imply very high constraints

on the temporal stability of the components (telescope, AO front-end, instrument). Some higher accuracy could be gained when using coronographic devices (4) of differential imaging (recall that a 1 Jy source would be 3 times the background level; spurious saturation effects would probably then arise) that would be very useful to correct for PSF variations due to seeing variations.

6 Conclusions and perspectives

Important science cases, requiring either high spatial or spectral resolution, can be uniquely addressed by ground-based mid-IR astronomy. Although mid-IR data are generally very demanding in terms of data reduction efforts, the results can lead to unique scientific break-through, unachievable at any other wavelength. The step when going from 4m-class telescope to 8m-class ones has resulted in the apparition of a certain number of uncertainties on the results, mainly because the intrinsic higher accuracy reveals now a certain number of defects hidden in the past, but also because modern large telescope unavoidably contain several closed-loop systems which need to be very carefully tuned w.r.t. mid-Ir observing constraints. This statement will be even more true on a future ELT; the influence of all the telescope sub-system on mid-IR data quality shall be carefully studied, and the resulting effects anticipated well before the instrument commissioning. A mid-IR ELT instrument would largely increase its sharpness (especially concerning differential measurements) if devices such as four quadrants coronographs, or dual-band imaging would be implemented. In such conditions, not only such an instrument would be "the perfect machine" to study dusty disks, but direct characterization of exoplanetary systems would be achievable.
The niche for mid-IR astronomy from the ground clearly lies on the specificity of "high resolutions" : spatial and spectral. The question whether a future ELT mid-IR shall be split into two specific instruments (one imager and one spectrograph) is open, but our experience on former instruments pleads in favour of 2 specialised, separate instruments to ensure the best scientific return of each of them.

References

1. E. Galliano, E. Pantin, D. Alloin et al: MNRAS,**363**, L1 (2005)
2. E. Galliano, D. Alloin, E. Pantin et al: submitted to A&A
3. S.J. Kenyon and L. Harmann **323**, 714 (1987)
4. P.O. Lagage, J.W. Pel, M. Authier et al: The messenger **117**, 12 (2004)
5. P.O. Lagage, C. Doucet, E. Pantin et al: Science **314**, 621 (2006)
6. C. Martin-Zaïdi, P.O. Lagage, E. Pantin et al: ApJ **666**, L117 (2007)
7. Pantin, E., L. Vanzi, and U. Weilenman : Some (little) things about VISIR. In *2007 ESO Instrument Calibration Workshop*, Springer Verlag
8. A. Poncelet, C. Doucet, G. Perrin et al: A&A **472**, 823 (2007)

9. M. Sterzik, E. Pantin E., M. Hartung et al: A&A **436**, L39 (2005)
10. M. Wold, M. Lacy, H. U. Käufl et al: A&A **460**, (2006)

Annex :

Lessons learned from VISIR

Published in *Society of Photo-Optical Instrumentation Engineers (SPIE) Conference Series*, 2008.

Lessons learned from VISIR

E. Pantin[a] and C. Doucet[a] and H.U. Käufl[b] and P.O. Lagage[a] and R. Siebenmorgen[b] and M. Sterzik[c]

[a]DSM/DAPNIA/SAp, CE Saclay, UMR 7158, FRANCE;
[b]ESO Garching, GERMANY;
[c]ESO Chile, Chile;

ABSTRACT

VISIR is the VLT mid-infrared (mid-IR) Imager and Spectrometer. Since 2004, it provides data at high spatial and spectral resolutions in the N (8-13 μm) and Q (16-24 μm) atmospheric windows. VISIR observations have provided unique constraints on targets such as central regions of nearby galaxies, or protoplanetary disks. We review here VISIR Imager and Spectrometer characteristics, emphasizing on some current limitations because of various undesirable effects. Its successor on an ELT will provide data with a unique sharpness (0.05") and sensitivity (35 μJy source detectable in 1 hour at 10 σ level), thus allowing a characterization of exoplanetary disks and inner exoplanets with an unprecedent precision. At the light of VISIR experience, we discuss how the lessons learned from VISIR can be turned to good account for designing and operating the future mid-IR instrument on the European ELT.

Keywords: Mid-infrared, VISIR

1. VISIR INSTRUMENT

VISIR is mounted on the VLT unit Melipal at Paranal and has been commissioned in April 2004. Since April 2004, it operates routinely to deliver mid-infrared (mid-IR) images and spectra in N (R=300 to 30000) and Q (R=1500,15000) atmospheric bands[1] , (see Fig.1). The data are diffraction limited in the N band if the optical seeing is below $\sim$ 0.8 arcsec (see Sec.4.1); Q band imager data are almost always diffraction limited. The high

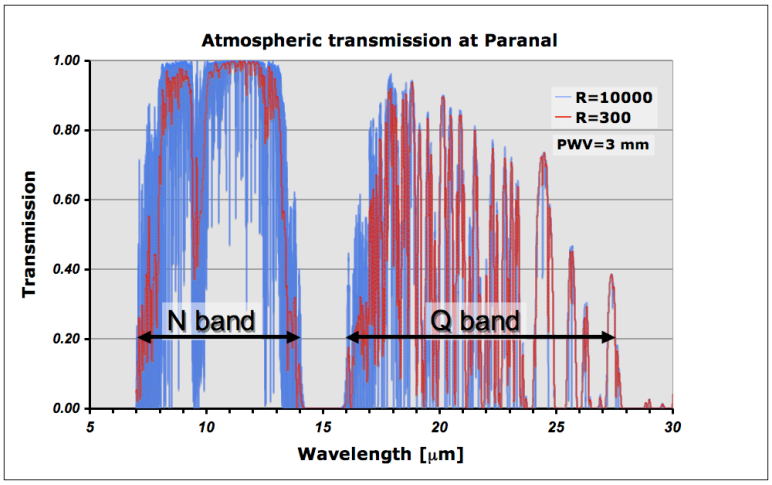

Figure 1. Mid-IR atmospheric transmission at Paranal site for medium weather conditions. The transmissions at two spectral resolutions are displayed.

Further author information: (Send correspondence to E.P.)
E-mail: eric.pantin@cea.fr, Telephone: 33 1 69 08 71 31

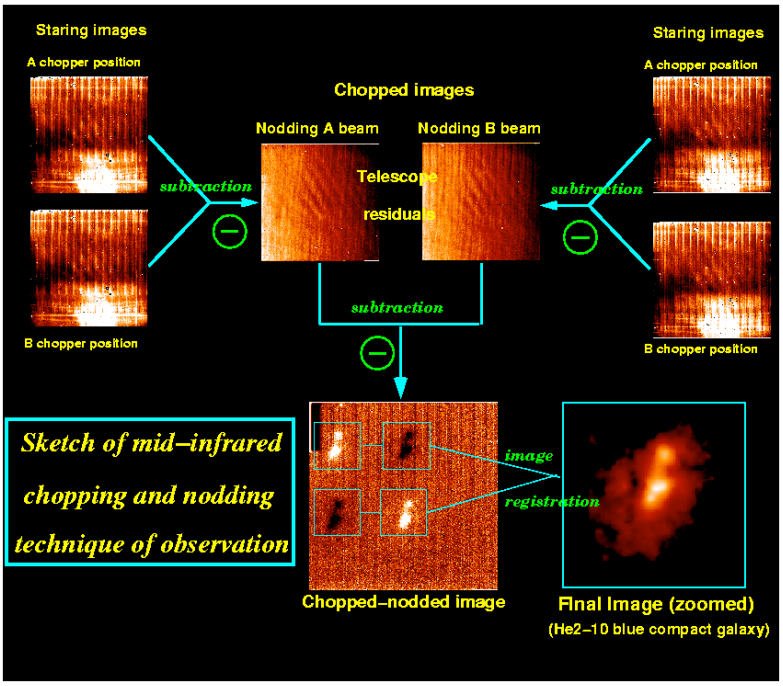

Figure 2. Scheme of chopping and nodding technique used to suppress the high mid-IR background. First, the elementary (staring frames) images are averaged over half a chopping period. Then, the chopping correction is applied for each telescope nodding position. Finally, chopping residuals due to different optical paths in the 2 chopper positions, are canceled by subtracting the two nodding beams. If the field on the detector is large enough, the four beams can be maintained in the field of view and, apart from beam switching overheads, no telescope time is loss.

spectral resolution mode is unique in the southern hemisphere; it offers for instance the possibility to perform observations of the warm H_2 pure vibrational modes at 8.02, 9.66, 12.28, 17.03 μm or the NeII line at 12.81 μm. Given the overwhelming background emitted by both the atmosphere and telescope, background canceling techniques are compulsory (Fig.2). The instrument itself emits a negligible background since its interior is cryogenically cooled between 50 and 70 K. VISIR Imager uses typical chopping frequencies around 0.25 Hz and nodding period around 1 minute.

1.1 Detectors

VISIR contains two DRS detectors, one in the imager, one in the spectrometer. They have well-capacities around 2.10^7 e^- (large capacity mode) and 2.10^6 e^- (small capacity mode). Quantum efficiency is typically around 50%. A detailed study of the detectors characteristics can be found in Ref.2. The detectors working point is nominally set around +5000 ADU on the sky (1 ADU $\approx$ 275 e^-, given a total range of [-32000,32000] ADU. The detectors start to saturate at levels higher than 8000 ADU and more (about 2/3 of the total capacity). Some pixels have an abnormal behavior (gain) and will trigger striping (detector striping, due to multiplexer amplifiers collapse, see Fig.3) over a usually wide range of rows on the detector. This striping is periodic, with a period of 16 pixels, since one amplifier reads every 16 pixels sequentially. A strong source on the detector will also produce (although at a higher level) the same type of effect, the source striping, on any pixel. A first order correction of source striping can be achieved by estimating the stripes pattern in a 256x16 sub-frame free of any source, and subtracting this pattern to all other (15) 256x16 sub-frames. See Ref.3 for a more complete description of all possible (including more evolved) methods. Given the level of the background, the detector dark current (smaller than 7000 e^-) and readout noises (1771 and 296 e^- in high and low capacity modes) are negligible against the background shot noise. Rapid imaging experiments have been performed in order to study any other source of noise. These

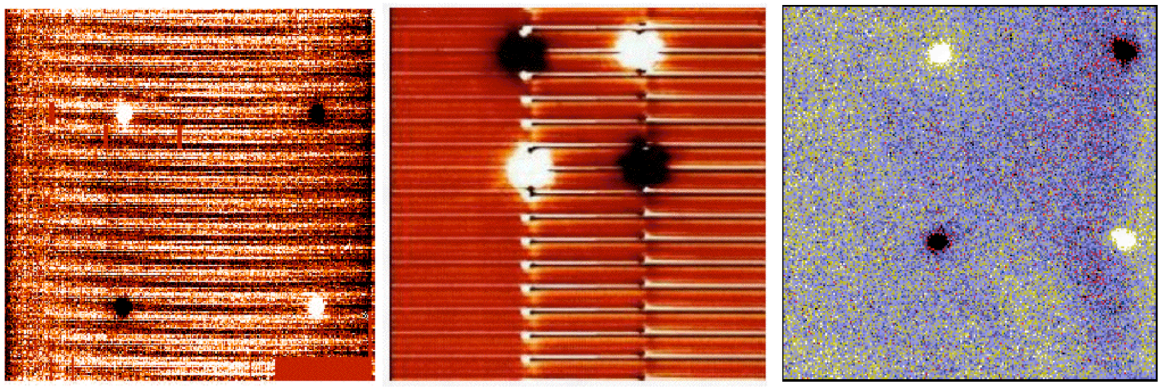

Figure 3. Left and middle panels : Imager data showing the "striping effect". On the left side, the "detector striping" at low level on top of a faint point source is shown. This striping is periodic (16 pixels) and depends at first order, on background fluctuations that affect "hot" pixels. On the middle panel is shown the "source striping", triggered by the a strong source. Right panel shows the background residuals underneath a relatively faint source (Comet Tempel 1). The background excess excess of noise at low spatial frequencies appears as "valleys and hills" (see Sec.3)

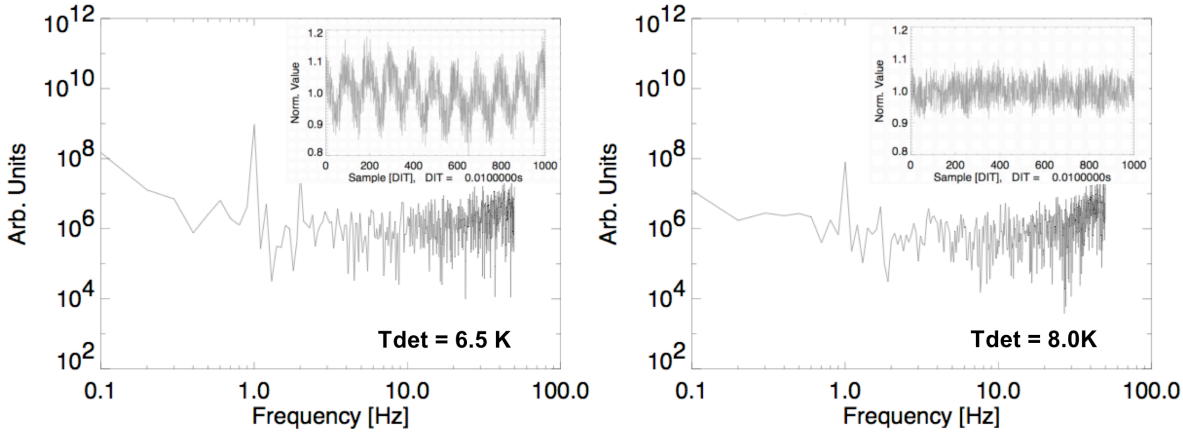

Figure 4. Detector output power spectrum as a function of the detector temperature (inset are the time signals). At 6.5K, a clear 1Hz fluctuations noise is evidenced. At 8.0K, the 1 Hz noise is significantly reduced. In both cases, no other obvious periodic noise is evidenced; above few Hertz, the noise is almost white as expected.

experiments show that a too low temperature of the detector (6.5 K), a 1 Hz periodic noise generated by the cryocoolers pulse tube is appears (see Fig.4). When slightly increasing the working temperature of the detector to 8.0K, these thermal oscillations vanish (see Fig.4), but at the expense of the detectors cosmetics (increase of detector striping). At 8.0 K also, the shot noise increases as expected (square-root of impinging number of photons), whereas its behavior seems more erratic and less easily interpretable at 6.5 K. A detectors upgrade for the Raytheon 1kx1k Aquarius detectors is planned in a near future.

1.2 Warm Calibration Unit (WCU)

On top of VISIR enclosure lies the Warm Calibration Unit (WCU). This unit comprises a point source (monochromator), and extended source (Peltier plate) presenting an adjustable surface temperature ([-20,50]^{o}C) and a

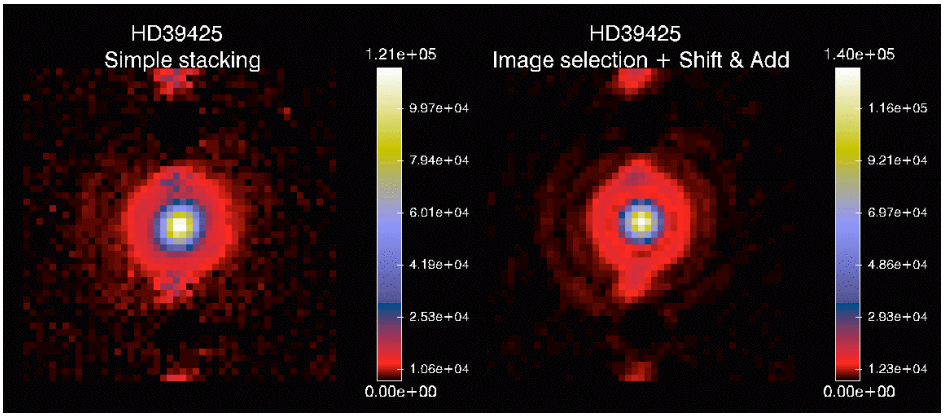

Figure 5. Left panel : simple stack of burst mode frames of the standard star HD39425, simulating a classical observation. Right panel, shift-and-add and image selection are applied to burst mode data. The average FWHM is decreased by 15% and the Strehl ratio is improved from 0.52 to 0.65. Note also the two unveiled diffraction rings (dark red) appearing in right panel.

telescope simulator (Offner design). This unit allows to perform daytime checks and calibrations (e.g. image quality, relative sensitivity, flat-field measurements, filter transmission curves).

1.3 "Burst Mode"

The burst mode is a fast readout mode in which all the elementary (DIT) frames are recorded. Obtained at frame rates in the range 10-100 Hz (T=10-100 ms), they offer various possibilities over standard data : speckle imaging (complementary to MIDI4), shift-and-add to correct for turbulence tip-tilt or any external PSF deformation/tilt and recover diffraction-limited data[5] , see Fig.5. However, 1) the source has to be clearly detectable (e.g. a source flux larger than 1 Jy in PAH2 filter) to properly shift-and-add (after eventual frames selection) the frames. 2) Since the chopper is not synchronized with the instrument operating system, the data reduction is rather complex; in particular, the chopper phase has to be estimated. 3) The instrument efficiency is quite affected in this mode; the ratio total time/time shutter open increases from ∼1.5 to ∼2.5.

2. OBSERVING AND CALIBRATING MID-INFRARED DATA

Relevant quality control parameters are the precipitable water vapor content (PWV), the background level, and the sensitivity. The data themself contain valuable informations to calibrate the data (e.g. sky lines for wavelength calibration). Weather observational parameters are relatively stable over few hours, thus only a limited number of standard star interlaced observations are really needed for photometric calibration purpose.

2.1 Sensitivity

VISIR imager measured sensitivities over the period Sep. 04-May 08 are reported in Fig.6. The median sensitivities (∼ 4-5 mJy/10σ/1h in the best N-band filter, ∼ 50 mJy/10σ/1h in Q-band) are close, within a factor of 2, to expected theoretical values. The point source sensitivities in N band are remarkably stable in time and under various weather conditions; Q band ones are much more sensitive to the precipitable water vapor content and airmass. The same conclusions apply to the spectrometer data. See Ref.6 for a detailed analysis of spectrometer sensitivities.

2.2 Photometry

Imager conversion factors (which allows to convert from ADU to physical units (e.g. Jy)) are frequently monitored on a selection of standard stars from Cohen's radiometric catalogue. The value depends mainly on the external conditions (pwv, dust content and temperature of the atmosphere, telescope temperatures), but shows very small

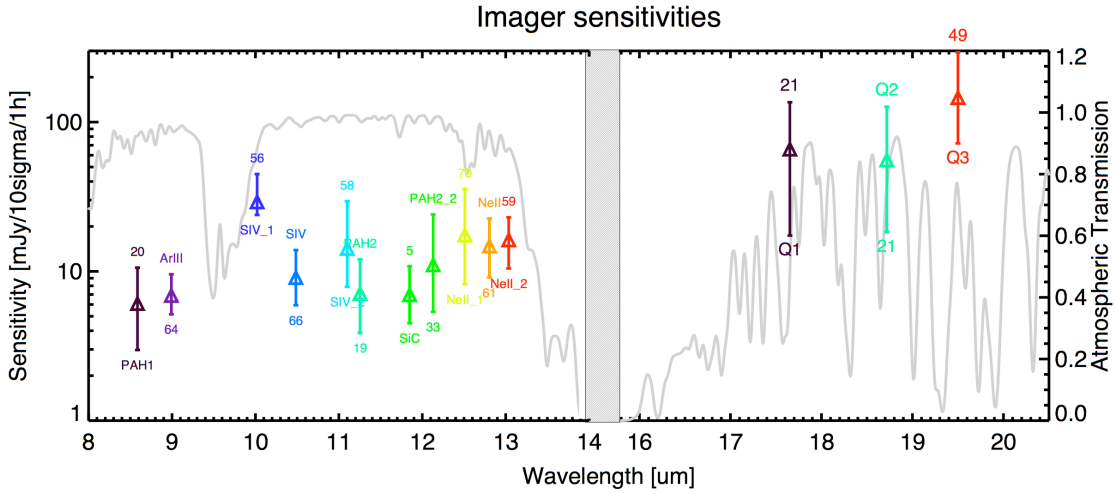

Figure 6. Sensitivities of the VISIR Imager, for all filters, in N and Q bands, for the smallest field of view (75 mas/pixel). The triangles mark the median sensitivities over the period 2004-2008; the vertical bars are bounded by the values of the first and fourth quartiles of measured sensitivities. The spectral resolutions for each of the filters are also given. In gray is overlplotted a low-resolution atmospheric transmission model for Paranal (3mm PWV).

variations ($\leq 10\%$ in N band) from one night to another. This means that a decent photometry at a 10% precision level can be obtained on a "standard conditions" night by using simply the median value of monitored conversion factors over one year. Recent observations of asteroids (bright point sources) using VISIR show that a careful photometric analysis of data taken under fairly good conditions lead to typical $\sim$3% and $\sim$4.5% photometric error levels in N and Q bands respectively[7] . However, the final photometric precision on faint, slightly extended sources becomes extremely limited not any longer by the background shot noise, but by the background residuals shown in Sec.3.

Spectrophotometric calibration is also achieved on the same standard stars, but in the specific case of high-resolution spectra data, the use of bright asteroids leads to a better telluric calibration.

2.3 PSF calibration

Thanks to the relatively low impact of the seeing on the angular resolution of N-band data, the spatial accuracy, mainly diffraction-limited as long as the optical seeing is lower than 0.8 arcsec(FWHM$\sim$0.25-0.3 arcsec), should be in principle easily calibratable using interlaced observations of standard PSF stars. Q-band imager data are almost always diffraction-limited (FWHM$\sim$0.5-0.6 arcsec). However in practice, even if the optical seeing has often a median value close or lower the above limit, its possible rapid variations render the PSF calibration difficult. On top of that, the uncertainty on the PSF calibration is strengthened by a variable in time (and unpredictable) ellipticity. The same effect seems altering also the FWHM measurements as a function of wavelength in spectrometer low-resolution mode, because the N-band is sliced into four settings (thus potentially 4 different PSFs). See Fig.7 for further details. VISIR image deconvolution is consequently very challenging. With such conditions, standard PSF deconvolution methods (such as Richardson-Lucy, and any wavelets based by-products[8]) become unapplicable. One alternative to recover a diffraction-limited PSF is to use the Burst Mode followed by a careful data reduction in which the PSF-degraded frames are discarded and the retained frames are stacked using a good shift-and-add algorithm (see Fig.5).

2.4 Spectrometer specificities

VISIR data contain both sky-subtracted images and sky data. Sky spectra can be usefully compared to models of mid-IR atmospheric emission to derive in most of the cases an accurate enough wavelength calibration. In the

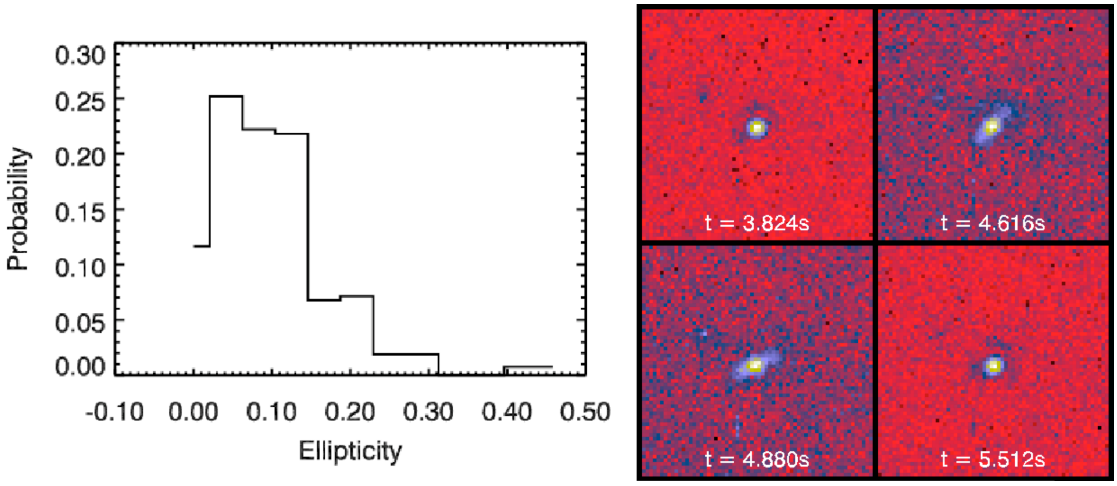

Figure 7. Left panel : histogram of observed PSF standard stars ellipticities. According to this analysis, about 20% of VISIR observations shall have distorded PSFs with ellipticities larger than 0.15 (the ellipticity is defined as 1-fwhm$_{min}$/fwhm$_{max}$); in other words, an ellipticity of 0.15 reflects a difference of 0.15% in FWHM between the horizontal and the vertical axis). Typical PSF distortions on a 2s timescale are evidenced in real time when examining burst mode data in which the data are recorded at a frame rate of 125 Hz.

majority of the cases, except some very "clean" windows in N-band at medium and high resolution, it is possible therefore to "self-calibrate" the data.
N-band low-resolution spectra (R∼300) often suffer from significant photometric absolute errors. A full N-band spectrum can be only obtained through a sequence of 4 low-resolution settings, stitching errors between the different settings are often observed (Fig.8). An correct absolute spectrophotometry of the individual settings can be however obtained if some narrow-band imaging data have been taken in each of the spectrometer settings. A similar problem is evidenced with full-with at half maximum measurements of an target as a function of the wavelength.

2.5 Flat-fieldability

Photometric standard stars observations show typical photometric variations of a few percent on the 4 different beams in the most sensitive N-band filter (PAH2), the dispersion has a standard deviation of about 1%. The background shot-noise contributes to about typically 0.5% in the photometric error and therefore, cannot explain a few percents of variation peak-to-peak. The observed variations must be then attributed either to background errors (see 3), or to a spatially varying differential response of the detector. Background errors (Sec.3) cannot account for the full photometric variations observed; on the other hand laboratory measurements of the detectors gains show peak-to-peak variations of about 1% on individual pixels gains.[2] To reach the highest photometric accuracy, it would be probably interesting to correct for individual pixels responses, however, estimating them is not an easy task. On one hand, sky dips are affected by instrument flexures, on the other hand, observations of the extended source of the warm calibration unit and varying its plate temperature can be corrupted by temperatures variations on the light path. So far, flat-fielding attempts did not improve the photometric accuracy.

3. BACKGROUND CANCELLATION AND ERRORS

The background errors appear as residual, non flat, slowly varying structures in VISIR images (Fig.3, rightmost panel). On the other hand, background noise measurements on the sky show a departure from the expected noise levels as soon as the chopping frequency is lower than ∼1 Hz (Fig.9, left panel). A spatial scale analysis finally shows that the noise excess is mainly located a mid- and low-spatial frequencies (Fig.9, right panel). A natural interpretation is that a too low chopping frequency (0.25 Hz) produces the observed residual background

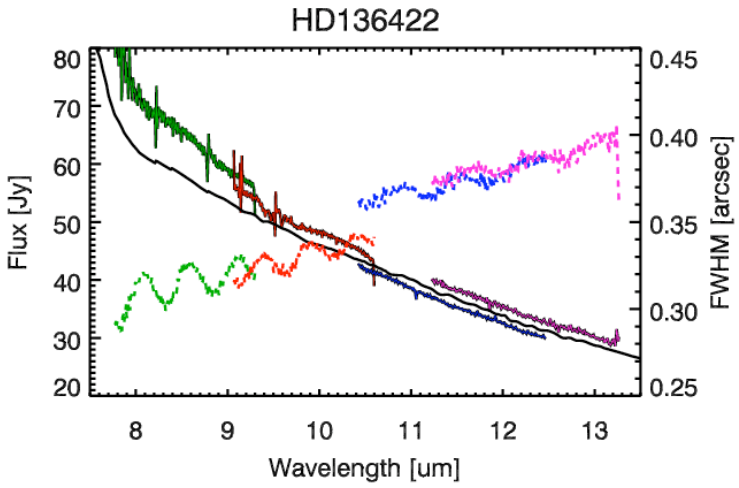

Figure 8. Low-resolution spectra of a standard star (HD136422) in the four settings covering the N band. The observation has been corrected for telluric absorption using a second calibration star. The VISIR observed spectra are discontinuous between two adjacent settings, which evidences of a photometric miscalibration. The black line represents the true HD136422 spectrum. The dashed lines display the FWHM measurements of HD136422 low-resolution spectra.

structures in VISIR images. This background error limits severely the achievable photometric accuracy on faint, extended sources (the more extended, the higher the uncertainty). A first order correction can be "manually" made by hiding the source in VISIR images and reconstructing underlying background using 2D spline or bilinear interpolation on the nearest source neighbors pixels. However, this method is highly biased by the *a-priori* definition of the source support. Alternative methods, based on multiresolution inpainting scheme, provide much better results.[3]

Future mid-infrared instruments should benefit from large format (1kx1k) and flat-fieldable detectors better stability of the gains). In an ideal case, detectors with a gain known at a $10^{-(4-5)}$ level of accuracy would significantly decrease the constraints concerning the background cancellation techniques, especially on an ELT.

4. HIGH LEVEL PROCESSING

4.1 Image deconvolution

VISIR on a 8.2m telescope reaches the limits of purely diffraction-limited instruments. Assuming an atmospheric turbulence following a Kolmogorov distribution of turbulence cells (seeing $\lambda^{-1/5}$), the seeing value around 10 μm is roughly half of that in the visible range. VISIR mid-infrared data should thus not be longer diffraction limited as soon as the optical seeing becomes larger than 0.7 arcsec. Burst VISIR data allows to carefully analyze the tip-tilt fluctuations of standard star images, and then derive macroscopic turbulence parameters such as the Fried parameter R_0. Our measurements give $R_0 = 6.23 \pm 0.33$ m at 8.6 μm and $R_0 = 8.76 \pm 0.42$ m at 11.3 μm when the optical is 0.75 arcsec. They confirm that VISIR data become seeing-limited at 10 μm for an optical seeing larger than $\sim$0.75 arcsec. In these conditions, mid-infrared image deconvolution becomes a much more difficult problem to solve. Standard methods which assume an almost perfectly calibrated PSF, such as Landweber, Richardson-Lucy, or more modern wavelets based ones will produce wrong solutions. Myopic deconvolution methods are a must in this case but require a large, redundant, dataset.[8]

5. MAIN RESULTS BY ASTRONOMY DOMAIN

Several key questions in astronomy are best tackled by observations in the Mid-IR. In the following we present two recent achievements which are based on VISIR data, a first one is concerned with properties of galactic nuclei and a second one with the structure of proto-planetary disks.

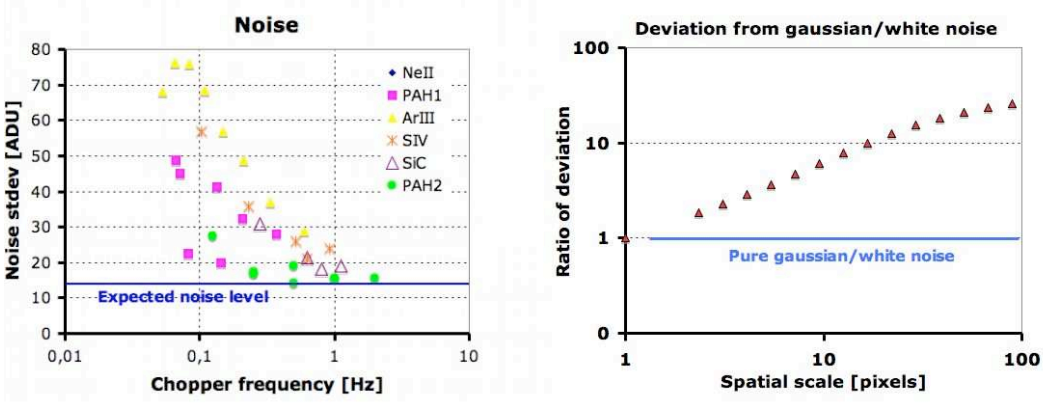

Figure 9. Left panel : measurements of the background noise as a function of the chopping frequency, for various N-band filters of VISIR. Depending on the filter, an increase of noise for chopping frequencies smaller than $\sim$ 1 Hz is evidenced. Note also the correlation between the noise excess and the presence of atmospheric lines in the filter (e.g. ArIII filter (9 μm) spans a large number of atmospheric lines, while PAH2 one (11.25 μm) depends much less on the chopping frequency). Righ panel : analysis of the excess noise in PAH1 filter (8.6 μm) as a function of the spatial frequency. At a spatial scale of 10 pixels, the noise is about 10 times larger than expected if the noise had a white spatial distribution.

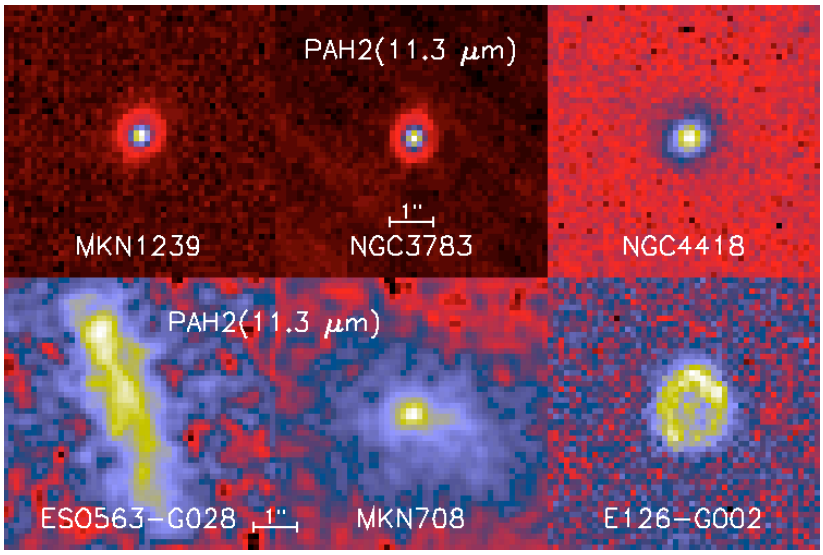

Figure 10. Nuclear MIR emission of nearby galaxies as revealed by VISIR (spatial resolution: 0.35" (FWHM), 11.3 μm filter). While AGNs (top) remain unresolved at high surface brightness, starbursts (bottom) show extended emission of up to a few arcsec at much lower surface brightness[9] .

5.1 Extragalactic infrared astronomy

The Mid-IR luminosity of the central region of galaxies has long been known to be a reliable indicator of activity and is much less affected by dust extinction than optical and NIR observations. The Mid-IR emission traces thermal radiation from hot dust ($\sim$100K) heated either by OB stars or black hole activity. Many diagnostics have been proposed to quantify which of the two activity types, starburst (SB) or active galaxies nuclei (AGN), is dominant. At the spatial resolution of VISIR it is found that AGN and SB can now be clearly separated using the nuclear Mid-IR surface brightness, S, as criterion: AGNs appear to be dominated by an unresolved core at

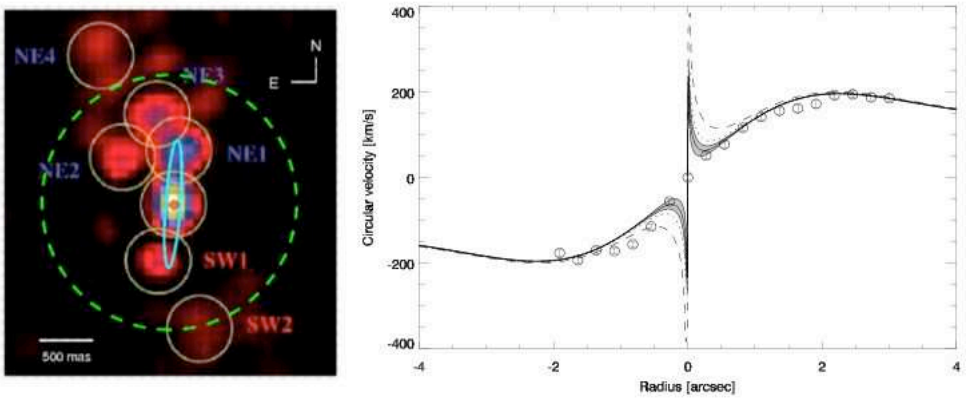

Figure 11. Left panel : NGC1068 as observed with VISIR (underlying image) and MIDI (red dot, green and blue contours). MIDI detects an intermediate scale (2") mid-IR emission (green dashed contour); VISIR resolves it into several knots. Right panel : velocity resolved VISIR data of the active galaxy NGC7582 using the high-resolution spectrograph of VISIR at 12.8 μm (NeII line). The velocity curve of inner obscured regions allows to determine an upper limit on the mass of the central black hole.

S $\geq$ 10,000 $L_\odot/pc^2$ whereas SB show extended structure of the nucleus of several arcsec at S $\sim$ 1000 $L_\odot/pc^2$ (see Fig.10). A few examples are shown in Fig.11. This technique to separate AGN - SB activity requires the resolving power of an 8m class telescope and is still limited to distances of up to 100 Mpc or at an ELT to $\leq$ 500 Mpc, respectively. It cannot be applied to data obtained from the ground by a 4m class telescope or using space-born telescopes.

A key question in modern astronomy is the formation of galaxy and related to this is the process of black hole formation and growth. To advance knowledge good observational techniques are required to estimate the black hole mass. One method is to apply the tight correlation between black hole mass and stellar velocity dispersion as derived from optical data. Unfortunately such direct measurements of black hole mass are challenging because of the high spatial resolution required and the high dust enshrouding of the nucleus. Both limitations could be overcome by recent VISIR MIR high resolution (R$\sim$16000) spectroscopy of the [NeII] 12.8 μm line. The VISIR data provided for the first time a black hole mass estimate in an external galaxy by MIR observations and from the rotational potential of the stellar bulge a central black hole mass of $\leq$ 5.5 x 10^7 M$\odot$ was found in NGC7582 (see Fig. 11 right panel, and Ref.10).

5.2 Low-mass companions and protoplanetary disks

ϵ Indi B is the closest brown dwarf binary system known. The sources separation is only 0.73". SPITZER observatory is thus unable to study individually each of the components. VISIR observations, although penalized by a much lower sensitivity, resolved them and put constraints on the physical characteristics of both components (see Ref.11).

HD97048 is a young (3 Myr) intermediate-mass Herbig star of the Chameleon cloud, surrounded by a protoplanetary disk of dust and gas. VISIR direct imaging in PAH bands (8.6 and 11.3 μm) have resolved for the first time the structure of the disk (Ref.12 and Fig.12). The disk is thick, dense, and has a flaring upper surface as predicted by Kenyon & Hartmann[13] . The measured flaring index (1.26 $\pm$ 0.05) is strikingly close to the expected value of 9/7= 1.28 obtained when assuming hydrostatic equilibrium of the disk. VISIR high spectral resolution observations confirmed the presence of warm gas (0.01 to 1 Jupiter masses) by detecting the H_2 emission line at 17.035 μm (see Fig.12). Maybe more important, the gas to dust mass ratio measured in the inner 35 AU (3000 to 14000) significantly departs from the canonical value of 100 (Martin-Zaïdi et al.[14]); maybe due to planet formation inducing dust depletion.

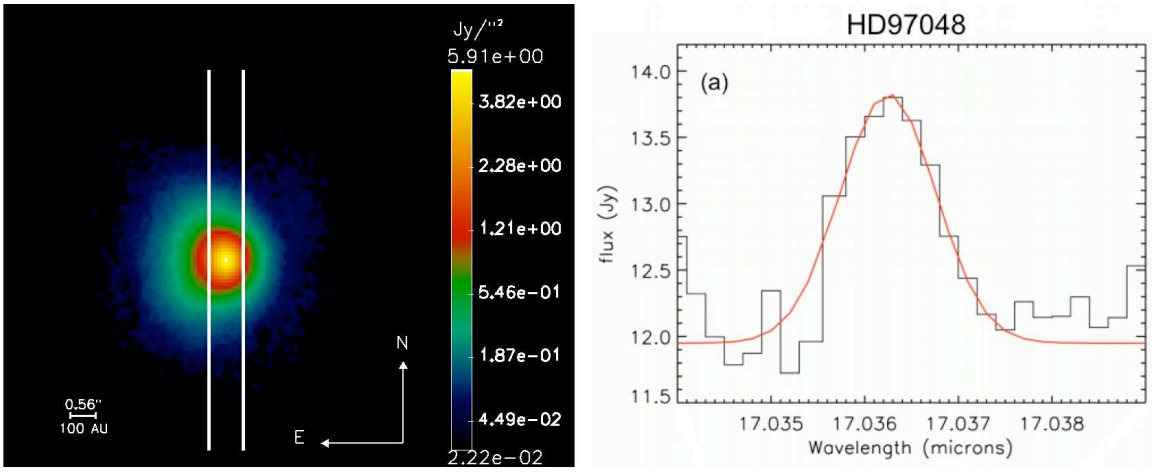

Figure 12. Left panel : the HD97048 dust disk resolved in VISIR image at 8.6 μm. For the first time, a precise measure of the flaring index β (H$\propto$r$^{\beta}$, where H is the scale height of the disk at a distance r from the star) of a proto-planetary disc around an intermediate-mass star has been achieved. Right panel : the 0-0 S(1) H_2 emission line detected in HD97048 (0.75 arcsec wide slit overplotted on left panel).

6. OBSERVING IN THE MID-INFRARED RANGE ON AN ELT

The expected sensitivities in the mid-IR on an ELT open some new perspectives in the field of exoplanetary sciences. Low-resolution spectroscopy of giant planets on orbits of a few AUs from the parent star would allow to better characterize their atmospheric composition and mass. Inner (r$\leq$0.4 AU) "super-Earth" massive telluric exoplanets radii would be marginally directly detected around the closest stars (d$\leq$3pc). Finally, a ELT mid-IR instrument, given its sensitivity and spatial resolution is a perfect tool to accurately study protoplanetary and debris disks. In particular, structures such as gaps would be quite easily revealed.

The awaited performances of a mid-IR instrument depend critically on the observatory site. N-band observations are [1.2-1.3] times more sensitive at a high altitude site (4500 m) than at Paranal. This factor reaches even a value of 5 for Q-band observations (see Fig.13). In addition, the Q-band extends further at higher wavelength as the precipitable water vapor (PWV) content in the atmosphere (highly reduced at higher altitudes) decreases. In particular, quite clean intermediate band windows (R$\sim$30) open at 24.5 and 27.3 μm (see Fig.13). In combination with the angular resolution provided by an extremely large telescope, we get a unique instrument able to study circumstellar/circumnuclear materials at intermediate temperatures (T=100K), bridging the gap between the well studied characteristics of the targets around 10 μm and far-infrared/sub-millimetric observations.

In order to be competitive with space-born infrared observatories, high spatial and spectral resolutions shall be the drivers to build ground-based mid-IR instruments. The ELT theoretical diffraction limit can be maintained in the mid-IR range at a moderate cost, i.e. using relatively simple adaptive optics system when compared to near-IR ones. Most of the science cases described in this paper deal with targets angularly very close to a stronger source (star, central engine of an AGN); this implies very tight constraints on the temporal stability of the components (telescope, AO front-end, instrument). Moreover, the peak value of a typical 1 Jy source observed with an ELT will be three times larger the background level; spurious detector saturation effects will probably arise. Stability and accuracy can be recovered by using coronagraphic devices in combination with simultaneous differential imaging.

7. CONCLUSIONS AND PERSPECTIVES

Important science cases, requiring either high spatial or spectral resolution, can be uniquely addressed by ground-based mid-IR astronomy. Although mid-IR data are generally very demanding in terms of data reduction efforts,

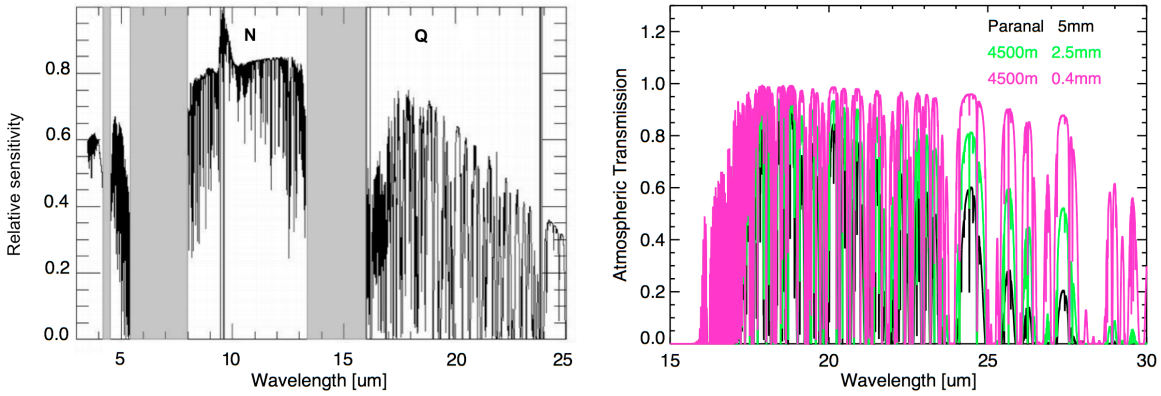

Figure 13. Left panel : ratio of ground-based mid-IR point-source sensitivity between Paranal and a site at an altitude of 4500 m. right panel : atmospheric transmissions in Q band as a function of the site/altitude. Paranal site (altitude = 2450 m) with a PWV of 5 mm (poor conditions) is taken as the reference. A higher altitude site (4500 m) is considered, in 2 cases : poor PWV conditions (2.5 mm) and good ones (0.5 mm). Note the large gains in transmissions at highest wavelength.

the results can lead to unique scientific break-through, sometimes unachievable at any other wavelength. VISIR on the VLT offers to the astronomers a very large palette of observing modes, some of which are unique in the Southern hemisphere. VISIR potentialities are still affected by restrictive factors such as detector striping or PSF stability. However, hardware (detectors upgrades) or operational (burst mode) solutions are foreseen to obtain the best scientific return from VISIR.

A mid-IR ELT instrument will have unique combination of spatial resolution and point source sensitivity (0.05 arcsec/35 μJy in 1h), but such an instrument would largely increase in sharpness (especially concerning differential measurements) if devices such as four quadrants coronagraphs, or dual-band imaging would be implemented. In such conditions, not only such an instrument would be "the perfect machine" to study dusty disks, but direct characterization of exoplanetary systems would be achievable.

ACKNOWLEDGMENTS

The authors thanks the scientific and technical staff of Paranal for their valuable help and their strong involvement in setting VISIR into operations. The author thanks T. Müller for allowing to report his results on asteroids observations with VISIR.

REFERENCES

[1] Lagage, P. O., Pel, J. W., Authier, M., Belorgey, J., Claret, A., Doucet, C., Dubreuil, D., Durand, G., Elswijk, E., Girardot, P., Käufl, H. U., Kroes, G., Lortholary, M., Lussignol, Y., Marchesi, M., Pantin, E., Peletier, R., Pirard, J.-F., Pragt, J., Rio, Y., Schoenmaker, T., Siebenmorgen, R., Silber, A., Smette, A., Sterzik, M., and Veyssiere, C., "Successful Commissioning of VISIR: The Mid-Infrared VLT Instrument," *The Messenger* **117**, 12–16 (Sept. 2004).

[2] Galdemard, P., Garnier, F., Mulet, P., and Reynolds, D., "Characterization of DRS Technologies' 256x256 mid-IR arrays for VISIR," in [*Instrument Design and Performance for Optical/Infrared Ground-based Telescopes. Edited by Iye, Masanori; Moorwood, Alan F. M. Proceedings of the SPIE, Volume 4841, pp. 129-140 (2003).*], Iye, M. and Moorwood, A. F. M., eds., *Presented at the Society of Photo-Optical Instrumentation Engineers (SPIE) Conference* **4841**, 129–140 (Mar. 2003).

[3] Pantin, E., "VISIR data processing and enhancement," In preparation (Sept. 2008).

[4] Poncelet, A., Doucet, C., Perrin, G., Sol, H., and Lagage, P. O., "An original interferometric study of NGC 1068 with VISIR BURST mode images," A&A **472**, 823–831 (Sept. 2007).

[5] Doucet, C., Lagage, P., and Pantin, E., "High resolution Mid-Infrared Imaging of Dust Disks Structures around Herbig Ae Stars with VISIR," in [*Visions for Infrared Astronomy, Instrumentation, Mesure, Métrologie*], Coudé Du Foresto, V., Rouan, D., and Rousset, G., eds., 25–30 (2006).

[6] Smette, A. and L.Vanzi, [*VISIR Users Manual*], ESO, ESO (2008).

[7] Müller, T., Pantin, E., Kaasalainen, M., Durech, J., Hormuth, F., and Sterzik, M., "Thermophysical characterisation of 16 main-belt asteroids with VISIR," In preparation (Sept. 2008).

[8] Pantin, E. and Starck, J.L. Murtagh, F., "Deconvolution and blind deconvolution in Astronomy," in [*Blind Image deconvolution : Theory and Applications*], Campisi, P. and Egiazarian, K., eds., 100–138, CRC Press (May 2007).

[9] Siebenmorgen, R., Haas, M., Pantin, E., Krügel, E., Leipski, C., Kaüfl, H., Lagage, P., Moorwood, A., Smette, A., and Sterzik, M., "Nuclear activity in nearby galaxies," Submitted (May 2008).

[10] Wold, M., Lacy, M., Käufl, H. U., and Siebenmorgen, R., "The nuclear regions of NGC 7582 from [Ne II] spectroscopy at 12.8 μm - an estimate of the black hole mass," A&A **460**, 449–457 (Dec. 2006).

[11] Sterzik, M. F., Pantin, E., Hartung, M., Huelamo, N., Käufl, H. U., Kaufer, A., Melo, C., Nürnberger, D., Siebenmorgen, R., and Smette, A., "The cool atmospheres of the binary brown dwarf ϵ Indi B," A&A **436**, L39–L42 (June 2005).

[12] Lagage, P.-O., Doucet, C., Pantin, E., Habart, E., Duchêne, G., Ménard, F., Pinte, C., Charnoz, S., and Pel, J.-W., "Anatomy of a Flaring Proto-Planetary Disk Around a Young Intermediate-Mass Star," *Science* **314**, 621–623 (Oct. 2006).

[13] Kenyon, S. J. and Hartmann, L., "Spectral energy distributions of T Tauri stars - Disk flaring and limits on accretion," ApJ **323**, 714–733 (Dec. 1987).

[14] Martin-Zaïdi, C., Lagage, P.-O., Pantin, E., and Habart, E., "Detection of Warm Molecular Hydrogen in the Circumstellar Disk around the Herbig Ae Star HD 97048," ApJ **666**, L117–L120 (Sept. 2007).

Part II

Science applications

Chapter 4

Infrared observations of circumstellar disks

Résumé

L'une des découvertes majeures de la précédente décennie fut l'universalité de la présence de disques autour d'étoiles. On retrouve des disques autour d'étoile jeunes, d'étoiles de séquence principale, et même d'étoiles évoluées (pulsars). Les disques autour d'étoiles jeunes permettent de créer les conditions physiques favorables (surtout de densité de matière) à la formation des planètes. Dans un contexte large de compréhension de la formation planétaire et sa fréquence, il est donc important d'étudier les disques autour d'étoiles jeunes mais il est aussi possible de détecter de manière indirecte la présence de planètes grâce aux structures que forment les planètes dans ces disques. Un phénomène similaire se produit dans les disques de débris régénérés à partir de collisions de planètésimaux. Dans ce chapitre, je montre que l'infrarouge moyen est un outil de choix pour étudier les disques. Je montre notamment comment l'on peut déduire certaines propriétés physiques des disques à partir d'observations en bandes N et Q. Une attention particulière est apportée au disque protoplanétaire autour de l'étoile HD 97048 qui présente une géométrie évasée particulièrement marquée, et que nous avons étudiée en tant que prototype des disques jeunes autour d'étoiles de masse intermédiaire.

Abstract

One of the main discovery of the last decade in this domain is that disks are ubiquitous around stars, either as protoplanetary disks (see e.g. [Megeath et al., 2005] or [Haisch et al., 2001]), or as remnants debris disks ([Meyer et al., 2006]) or even around evolved stars like pulsars ([Wang et al., 2006]). Favorable physical conditions for planetary formation such as density of material are found in young disks around pre-main sequence stars. In the general context of understanding planet formation it is also important then to study these disks around young stars. Moreover, it is also possible to indirectly detect planets in protoplanetary disks thanks to the structures the planets produce through gravitational interactions. The same kind of situation also happends in the case of second generation debris disk (replenished by means of collisions of planetesimals). In this chapter we show the assets from mid-infrared imaging at high angular resolution from the ground. In particular, we show how N and Q band observations are valuable to constrain the physical (mostly geometrical) properties of the disks. A more particular attention is paid to the case of the disk around HD 97048 which presents a particularly impressive flared geometry and is studied here as a prototype of protoplanetary disks around intermediate-mass stars.

Contents

4.1 Protoplanetary disks

4.1.1 Introduction : disks as a natural outcome of stellar formation

Disks are the natural outcome, due to the combination of angular momentum conservation and vertical energy dissipation, of the gravitational collapse of a clump in a dense molecular cloud. As the cloud (initial size ∼20 000 AU[1]) shrinks, the matter concentrates into a geometrically thinner and thinner disk. The initial composition of this protostar nebula is that of the parent cloud, i.e. mainly gas (hydrogen and helium in majority) and dust (typical sizes 0.01-0.1 μm, 1% in mass). This concentration of matter brings together dust particles that would otherwise have had no chance to stick together to form larger particles. In addition, the loss of gravitational energy in the process is converted through viscosity into heat which also creates favorable physical conditions for the planet formation process to take place. In ∼100 000 years a geometrically thin dense proto-planetary disk is formed. It has a typical size of few hundreds of AUs and contains at its center a dense and hot core, the protostar in which hydrogen fusion has not yet started. As the disk evolves with time, the dust particles grow from 0.1 μm to few centimers, first thanks to the electrostatic force, then by gravitational attraction. In a very short time (1 000 years, [Dullemond and Dominik, 2004a]) in a "quiet" (non turbulent) disk, large particles (boulders) settle in the disk midplane. It is however debated if this process is really that fast and efficient; some theoretical works predict that the process of particle growth could even be completely inhibited by the turbulence (either of hydrodynamic or magneto-rotational origin), see e.g. [Nomura and Nakagawa, 2006, Weidenschilling and Cuzzi, 1993, Dominik et al., 2007]. Indeed, some signatures of turbulence are indirectly evidenced by the observed accretion of disk material onto the star (see e.g. [D'Alessio, 2001]). The step from these ∼1 m sized boulders to the real building bricks of the planets, the planetesimals (with sizes in the range 1-100 km) has remained for a long time unexplained. As a matter of fact, these boulders do not stick together easily; moreover they face a headwind produced by the slower rotating gas. They are consequently expected spiral very rapidly onto the protostar in a few hundred of orbits (1000-10000 yr, [Weidenschilling, 1977]). A very recent work by [Johansen et al., 2007] suggests that these boulders could efficiently and rapidly undergo a gravitational collapse in locally overdense regions in the disks midplane (vortices). In their numerical simulation, the boulders accrete in few

[1] Astronomical Units

orbital periods to form larger bodies having a mass comparable to that of CERES. These building blocks have a sufficiently long period of "rest" to slowly gravitationally accrete on timescales of about 10^5 yr to form the embryos of telluric planets and the cores of the giants planets ([Wetherill, 1990]) by the process of runaway growth.
Our solar system most probably went through the same stages. A significant part of the planetesimals (up to ∼60%) which were far enough from the larger bodies or have been ejected into the Oort cloud have not participated to the building phase of the planets. They have been "stored" over billions of years in the Oort cloud, in the Kuiper belt and in the asteroid belt; we observe them nowadays either as asteroids or as trans-neptunian objects and comets.
The branch of research which studies the disks has pratically exploded in the past 20 years. The yearly average number of articles on the subject around 1990 was 100. In 2008 this number had increased by a factor of 5.3. This reflects the considerable progress that we made in the detailed understanding of these objects that allow us to understand the very early phases of the solar system evolution.

4.1.2 Classification of young stellar objects, evolutionary sequence

Young stellar objects with masses ranging from 0.03 to 8 $M_\odot$ can be classified into classes according to the shape of the SED[2]. Each class reflects the degree of youth and embedding in optically thick matter composed of dust and gas. In the class 0 phase (10 000 year), a proto-star is still embedded into a very thick cloud of dust and gas which contains about the same mass as the proto-star. These objects emit most of their light in the millimetre range and often have collimated jets and molecular flows. It is not clear whether a disk has already formed at that stage but some observations support this idea ([Rodríguez et al., 2005]). In the class I (100 000 year) phase the mass ratio between the envelope and the star has decreased significantly; the embedded star still accretes matter through a thick disk; powerful jets and flows are observed. Most of the flux is emitted in the mid- and far-infrared range. Class II objects are objects more evolved with a typical age of ∼1 000 000 year. The envelope is almost completely dissipated and the star is directly visible. The SED contains two main components : the starlight distribution of energy which peaks in the visible range and the disk emission which emits predominantly in the mid-infrared range (10-50 µm). Class III objects (∼10 000 000 years) show a weak infrared excess due to an optically thin disk probably at a transitional stage between the protoplanetary disk and the debris disks. At this stage, the gravitational interaction between the dust particles and giant planets (e.g. in resonances), potentially create structuring of the disk ([Ozernoy et al., 2000, Lagage and Pantin, 1994]). T-tauri stars are class II low-mass stars ($1 \leq m \leq 3$ $M_\odot$) and are the progenitor of sun-like main sequence stars. Herbig Ae stars are the intermediate-mass (3-8 $M_\odot$) equivalents of T-tauri stars. The present study focuses on the Herbig Ae (HAe) stars surrounded by dense and relatively massive protoplanetary disks.

4.1.3 Structure of Herbig Ae protoplanetary disks

Numerous observational constraints obtained in the last 10 years concerning Herbig Ae protoplanetary disks have allowed to build a sketch of the disks structure. First, ISO/SWS observations have shown that HAe sources can be subdivided into two groups based on the shape of their SED. Group I objects have a rising SED in the range 5-30 µm and contain Polycyclic Aromatic Hydrocarbon (PAH) features while group II contains sources with monotonically falling spectra beyond 10 µm ([Meeus et al., 2001]). The groups are sub-divided into two sub-groups. The groups Ia and IIa contains the sources showing solid state bands (e.g. the silicates) while the groups Ib and IIb sources don't. These differences have been interpreted as differences in the geometry of the disks surfaces. Group I stars are believed to be surrounded by flared disks whereas group II disks would have much flatter geometries (Fig.4.2). It is also believed that group II sources exhibit a particular disk geometry. Their disk features a *puffed-up* inner

[2]Source Energy Distribution i.e. the source brightness as a function of the wavelength over a broad range

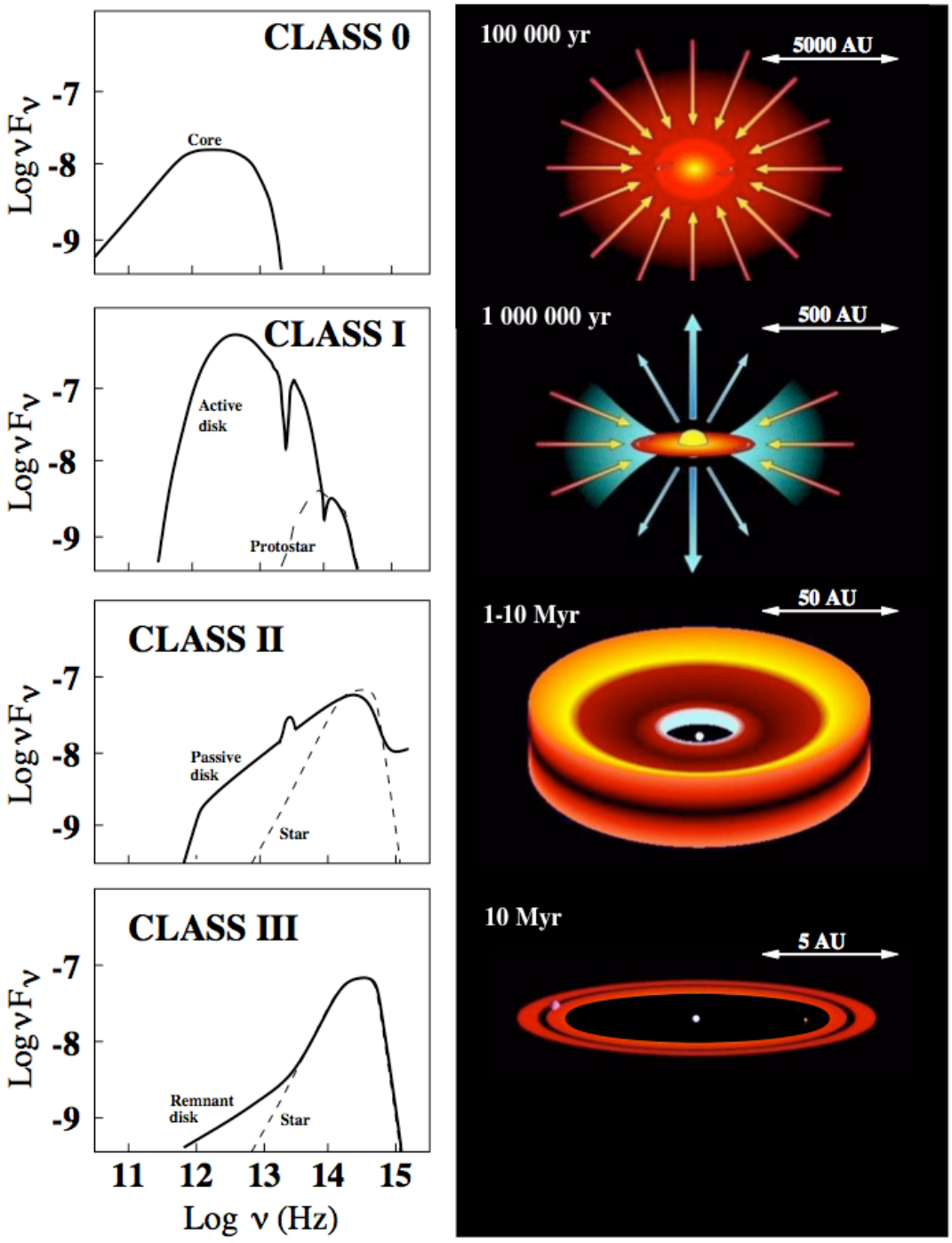

Figure 4.1: Schematic representation of the formation and evolution of a star. On the right side is shown the SED of the objects, the right panel displays a pictural representation of the objects at different ages. On the left are shown the typical SEDs at each stage (From Acke, PhD.Thesis, sources : A. Natta, M.McCaughrean, C.Dominik and V.Icke)

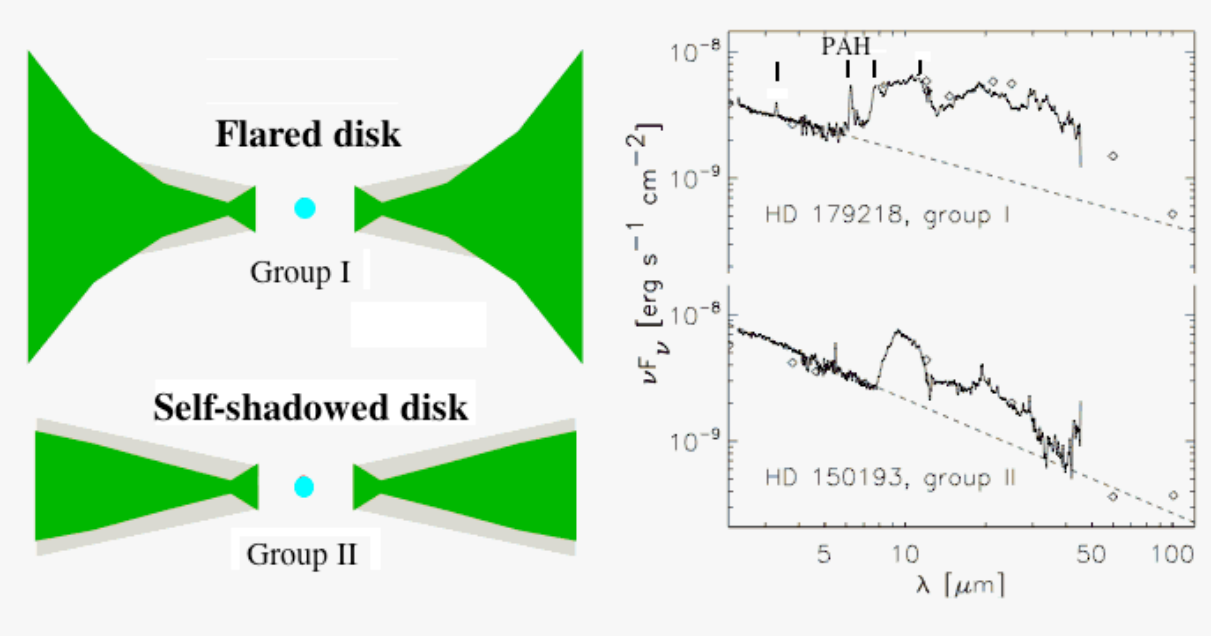

Figure 4.2: Left panel sketches our current view of HAe sources depending on the group they belong to. On the right is illustrated the corresponding SEDs which the sorting is based on. The PAH emission bands in group I SED are marked by small vertical ticks.

rim which produces a *self-shadowing* of the disk ([Dullemond et al., 2001]). Scattered light observations with the HST ([Grady et al., 2005]) seem to confirm this hypothesis since group I sources are observed to be systematically more extended in scattered light than group II ones.

[Chiang and Goldreich, 1997] have presented the first model of radiative transfer in flared T-Tauri disks which can also be applied in our present case to group I sources. Their model is based on a passive disk which re-processes the starlight. A thin surface layer sitting at the surface of the disk (the disk atmosphere) is optically thin to the UV-visible radiation; strongly heated by the star it emits most of the extended flux in the mid-infrared range. About half of this flux is emitted towards space (and a possible observer !) while the other half heats the interior of the disk. Given the very high optical thicknesses of the disks interior, only the sub-millimetre (and beyond) radiation reaches the disk mid-plane. A consequence of this is that a temperature gradient is established. Taking into account the equation of state of the gas (which represents 99% of the mass in the inner regions of the disks), the predicted disk geometry has a *flaring structure* i.e. a scale height which increases with the distance to the star following a power-law which index is 9/7 (Fig.4.3).
The composition of the disks is also an important question in the context of the planetary formation. As a matter of fact, the formation and composition of the planets, built from the constituents of the protoplanetary disk, is highly dependant on the nature of the materials present in the disk. For instance, the formation and the composition of giant gaseous planets depends critically on the the nature and the amounts of gas present at the moment of the gravitational collapse. In the core-accretion model a solid core is first formed ([Pollack et al., 1996]); the planet contains then a fraction of its mass in solids (up to 3%). In the formation model *ab-initio* because of disk instabilities ([Boss, 2001])) the planet is built from the gravitational collapse of a region of the disk. In the later case the proportion of solids is less than 1%. The gas phase of the protoplanetary disks will be more developed in Sec. 4.1.6. Concerning the solid phase made of refractory species usually called “dust”, most of the discussion

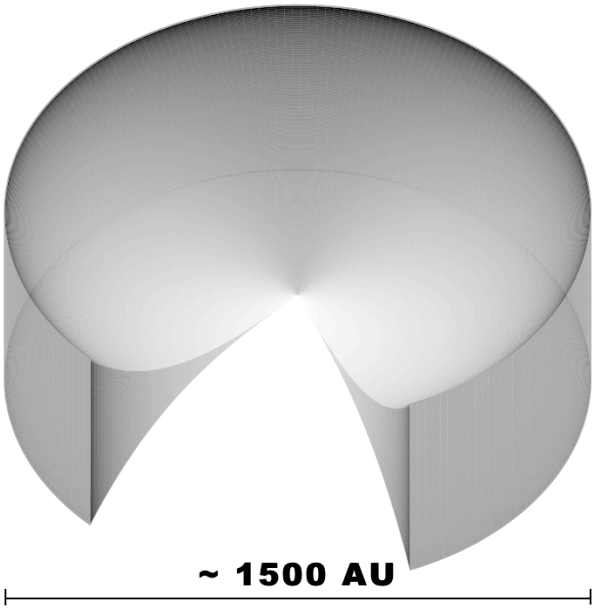

Figure 4.3: 3D synthetic view of a flared protoplanetary disk. The star sits at the center of the disk.

will be found in Sec. 4.1.4. However, we already mention here an interesting point concerning the crystallinity of the dust. The matter of the protoplanetary disk derives mainly from the interstellar medium (ISM) phase. In the ISM the dust is mostly in the amorphous form (less than 0.2% of degree of cristallinity [Kemper et al., 2004]). ISO/SWS spectra of Herbig Ae disks display a very large variety of dust compositions, starting form ISM-like amorphous very small grains to grown and crystalline ones (see e.g. [Acke and van den Ancker, 2004]). The same applies to SPITZER observation concerning the fainter and less massive T-tauri stars ([Bouwman et al., 2008]). The mechanism(s) at the origin of the "crystallization" phenomenon is not very clear but the observational facts tend to show that it is a slowly evolutionary process. The older the system, the more crystalline is the dust. We can thus infer that the "crystallization" process proceeds inside-out. Indeed the dust found in inner parts of the systems shows much higher degrees of crystallinity than in the outer parts (see e.g. [van Boekel et al., 2004]). The common interpretation is that the amorphous silicate dust is vaporized/recondensed or annealed in the regions of the disk close to the silicate sublimation radius to form crystalline dust. Radial-mixing mechanisms (e.g. turbulent flows ([Gail, 2001])) will then transport the crystallized dust (mainly forsterite) outwards. Finally the forsterite will eventually react with the gas-phase silicon to produce the observed crystalline enstatite at larger distances in the disks ([Gail, 2004]); a gradient of crystallinity and iron stochiometry is thus expected in the disks. MIDI interferometric observations of protoplanetary disks at very high angular resolutions qualitatively support this interpretation ([van Boekel et al., 2004]). Througout this chapter, the inner disk will refer to a region in the disk which is located between the inner radius (usually defined by the sublimation of the most refractory species, usually the silicates) and a distance of 50 AU from the star. This region can be also be quoted here the "planetary region" because this is the part of the disk where there enough material and the physical timescales a short enough to form telluric and giant planets.

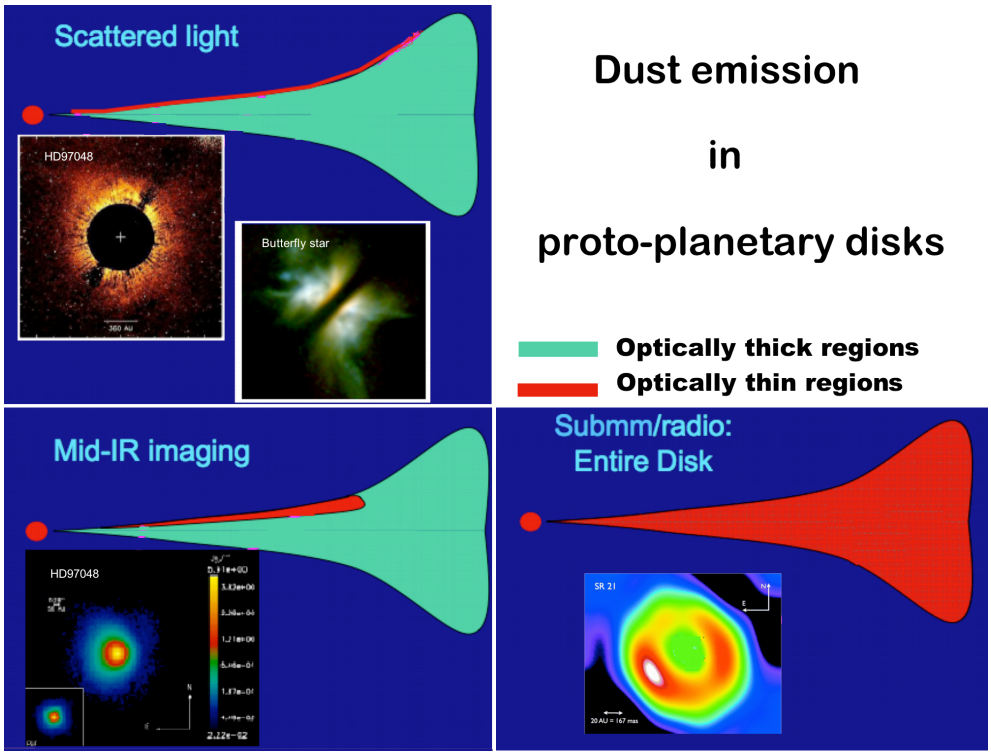

Figure 4.4: Sketch of the emission at different wavelength of protoplanetary disks. Scattered originates from a very thin layer of dust at the surface of the disks. Given the high dust surface densities and the $r^{-}2$ (r: distance to the star) dilution factor, the scattered emission can be observed up to fairly high distances from the star. Lower left panel: the mid-infrared emission comes from a slightly thicker layer, but given a dust temperature that varies roughly as $T \propto r^{-3/2}$ for large grains in thermal equilibrium, the emission which is en exponential function of the temperature drops very fast with r. Very small grains such as PAH which are not in thermal equilibrium obey more simply to the dilution factor $r^{-}2$. Finally, optically thin sub-millimetric emission (e.g. ^{13}CO or 850 μm continuum emission) comes from the entire volume of the disk except maybe the very densest inner parts.

4.1.4 Observations of protoplanetary disks at various wavelength

Current astronomical observation means offers now a fairly large panel of possibilities to probe the different parts/layers of protoplanetary disks. First, the maximum of thermal emission of dust or gas is linked to the wavelength through the Wien's law. Cold matter is more easily detected at long wavelength (sub-millimetric and millimetric ranges) while hot circumstellar solid matter is preferentially observed in the near-infrared range while the hot gas and the plasma are eventually detected in the UV or X-ray regimes. Second, because the matter has different opacities at different wavelengths, longer wavelengths are more adapted to study the deeply embedded parts of optically thick disks. Fig.4.6 schematically decompose the emission from dust in circumstellar optically thick disks as a function of the wavelength range into different regions of the disk. Fig.4.4 sketches the emission from the dust spatially speaking while Fig.4.7 sketches the emission from the gas as a function of the distance to the star. Scattered light observations in the visible (e.g. HST [Grady et al., 2005]) or in the near-infrared range (J, H , K bands see e.g. [Pantin et al., 2000, Boccaletti et al., 2004]) trace a very thin skin at the surface of the disks. Given the relatively high sensitivities achieved in these bands, the disks can be traced up to fairly high distances from the star. However, the high contrast ratio between the star and the disk imposes the use of coronographic techniques which limits the minimum distance from the star that can be imaged. The inner parts of the disks cannot be usually observed at these wavelength unless interferometric techniques are used ([Monnier et al., 2005, van Boekel et al., 2004]). In 2000, we have obtained the **very first** coronographic images of a protoplanetary disk in J and Ks bands (scattered light) around the star HD100546 (Fig.4.5). Using the ADONIS adaptive optics system mounted on the ESO 3.6m telescope of the La Silla observatory, the SHARP II+ camera, and a pre-optics Lyot coronograph, we were able to study the structure of the disk down to a distance of $\sim$40 AU from the star and up to a limiting distance (because of sensitivity) of $\sim$200 AU from the star. The position angle and inclination of the disk have been tightly constrained (37 $\pm$ 5 degrees from the North and 40 $\pm$ 5 degrees from face-on). The main results are reported in paper 4.3.

Mid-infrared observations trace the heated dust surface layer. 90% of the emission comes only a 1/10 of the thickness at a distance of 20 AU from the star and much less in terms of dust mass. The particles in direct view to the star are heated and either reach an equilibrium temperature in the case of large particles (i.e. in the range 0.01-10 µm) or have a fluctuating temperature (stochastic heating, [Puget et al., 1985]) for sizes in the range 10-100 Å) through single-photon or multiple-photon excitation. Note also that the turn-over size of particle (where the excitation regime changes) depends also on the intensity of the local radiation field; the larger the intensity, the higher the turn-over size. The Polyclic Aromatic Hydrogenated (PAH) are a particular type of carbonaceous very small particles. The PAH are large (more than 50 carbon atoms, sizes in the range 10-100 Å) organic molecules which are believed to contain a significant fraction of the available carbon of the universe. They are easily excited by visible/UV photons; their temperatures can be raised stochastically to very high levels (1000 K) up to large distances around UV-emitting stars. The N-band contains three PAH emission bands which are centered at 8.6, 11.2, 12.7 µm. The rest of the species (e.g. silicate, carbon) are gathered under the generic naming of Very Small Grains (VSG). Mid-infrared continuum observations, or pseudo-continuum observations in the case of the VSGs, can be obtained in the N-band or in the Q-band. The advantage of the N-band is the larger sensitivity (by a factor of $\sim$10) and the better resolution (around 0.3 arcsec on a 8m-class telescope). Q-band observations benefit from higher flux levels (the SED is usually rising between 10 and 20 µm, especially in the case of Group I sources) and intrinsically more extended emission (because probing lower dust temperatures) but the achievable angular resolution is also reduced. The PAHs and the VSGs are thus a potentially very interesting tracer of the disk geometry up to very large distances from the stars where they easily dominate the thermal continuum produced by "large" particles. The turn over distance depends on the luminosity of the star but is roughly located around 50 AU from the star.

In the same line of thoughts the gas phase can be observed under different states. Electronic transitions

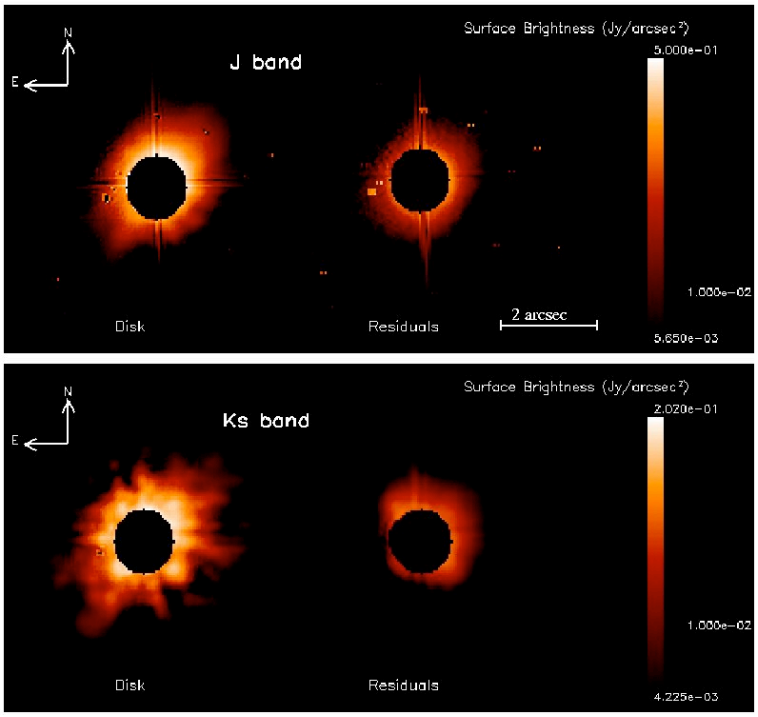

Figure 4.5: The HD100546 protoplanetary disk observed with ADONIS in coronographic mode. It has been detected both in J and Ks bands. This is the very first detection of a protoplanetary disk around an Herbig Ae star in scattered light emission.

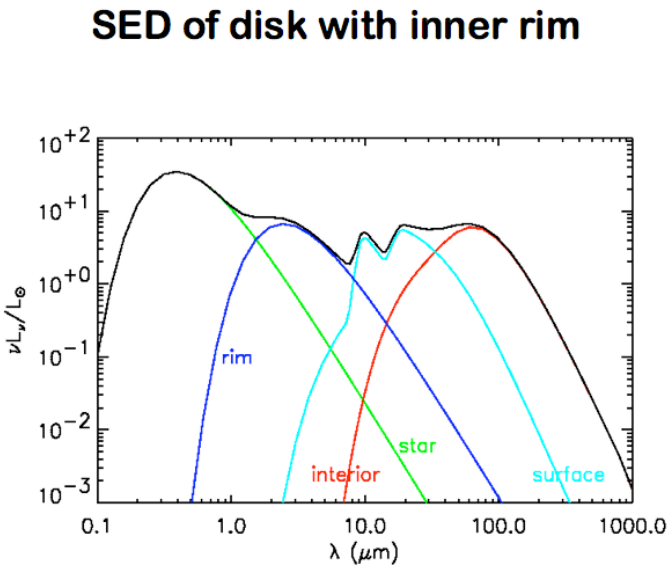

Figure 4.6: Sketch of the different disks components building the integrated SED of a HAe protoplanetary disk with inner rim. We see here that the surface emission is mainly concentrated in the mid-infrared range (10-20 μm).

of the very hot molecular hydrogen produce UV emission lines. The far-UV flux from the star (including Ly α emission which is probably linked to accretion of matter onto the star, see [Blondel et al., 1993]) raises the temperature of the molecular hydrogen H_2 in the inner [0.1-1] AU regions of the disk, which in turn produces the near-infrared ro-vibrational lines. Other mechanisms are also proposed to excite this emission (shocks, X-rays). Non thermal excitation mechanisms are also possible such as absorption of a UV photon in the Lyman-Werner band ([Regan and Haehnelt, 2008]) or the collision with a fast electron produced by X-ray ionization ([Weintraub et al., 2000]). Rotational lines from warm H_2 are observed e.g. at 8.0250 μm(S(4), ν=0-0, J=6-4), 9.66 μm(S(3), ν=0-0, J=5-3), 12.2278 μm(S(2), ν=0-0, J=4-2), 17.035 μm(S(1), ν=0-0, J=3-1) and 28.218 μm(S(0), ν=0-0, J=2-0); the last one is unfortunately unobservable from the ground. These lines are of high importance because the H_2 molecule is the dominant component in the gas phase. They provide a direct and (almost) unbiased estimate of the mass reservoir of warm gas in the regions of the protoplanetary disks where the planets form. Unfortunately, H_2 transitions are of quadrupolar nature which implies small Einstein coefficients. The lines are rather weak and their detection challenging. Only high spectral resolution and sensitive instruments have the potential to detect them.

CO lines can be observed either in the warm phase in the near-infrared or in the cold phase in the sub-mm range. The ν=2-0 bandhead is observed around 2-3 μm . It requires a gas which is hot and dense i.e. in the very inner parts where the dust is sublimated. These lines require a non-thermal pumping mechanism for excitation (strong UV, X-rays). In the rare cases that the profiles have been observed, they are often strongly distorted because convolved with a large velocity field. This "dilution" makes it very difficult and unaccurate to derive a structure in velocity from the observations. The CO ro-vibrational lines are observed around 4.7 μm (P and R branches). They are produced in the regions of the disks around 5 AU where the density and the temperatures are still high (500-1500 K and more). These lines have been successfully observed both in low-mass stars protoplanetary disks (T-Tauri, e.g. [Brittain et al., 2005]) and around intermediate-mass Herbig Ae stars ([van der Plas et al., 2008]). Given the large number of lines observable from the ground and the avent of adaptive optics assisted high-resolution spectrographs on large telescopes, these lines offer the possibility to get very precise informations regarding the gas compositions, the gas temperature and the velocity structure of the inner disks (3-10 AU), where the telluric planetary formation is assumed to take place. A very recent work by [Pontoppidan et al., 2008] shows that a spectroastrometric method (differential spectroscopy based on two opposed slit orientations and the measure of the barycenter to a sub-pixel precision) allows to get an equivalent spatial resolution of 1 mas (or ∼0.15 AU for Ae disks) ! The velocity structure of the disks around SR 21, HD135344, and TW Hya, is finely resolved and brings strong constraints on the density structure and the position angle/inclination of the disks.

Water vapor exhibits also numerous lines in the infrared range. These have been detected e.g. using the SPITZER spectrograph IRS in protoplanetary disks around T-Tauri stars AS 205A and DR Tau ([Salyk et al., 2008]). These detections allows a complex chemistry to take place in the region 0.5-5 AU. It should be noted that water is not expected to be initially present below the snow line, this is a strong indication of an innerward transport of the icy components.

Sub-millimetric observations of cold (temperatures in the range 20-50 K) ^{12}CO and ^{13}CO pure rotation emission lines is common in protoplanetary disks ([Qi et al., 2004, Thi et al., 2004, Ceccarelli et al., 2002, Dutrey et al., 1998, Piétu et al., 2005]). These lines allow to probe the dense and embedded regions of the disks up to fairly large distances ($\geq$ 50 AU). They cal also provide some useful informations of the disk's velocity structure. Non-keplerianities have, for instance, been evidenced in the AB Auriga protoplanetary disk ([Piétu et al., 2005]). The disks inclination is also well constrained by these heterodyne submillimetric data.

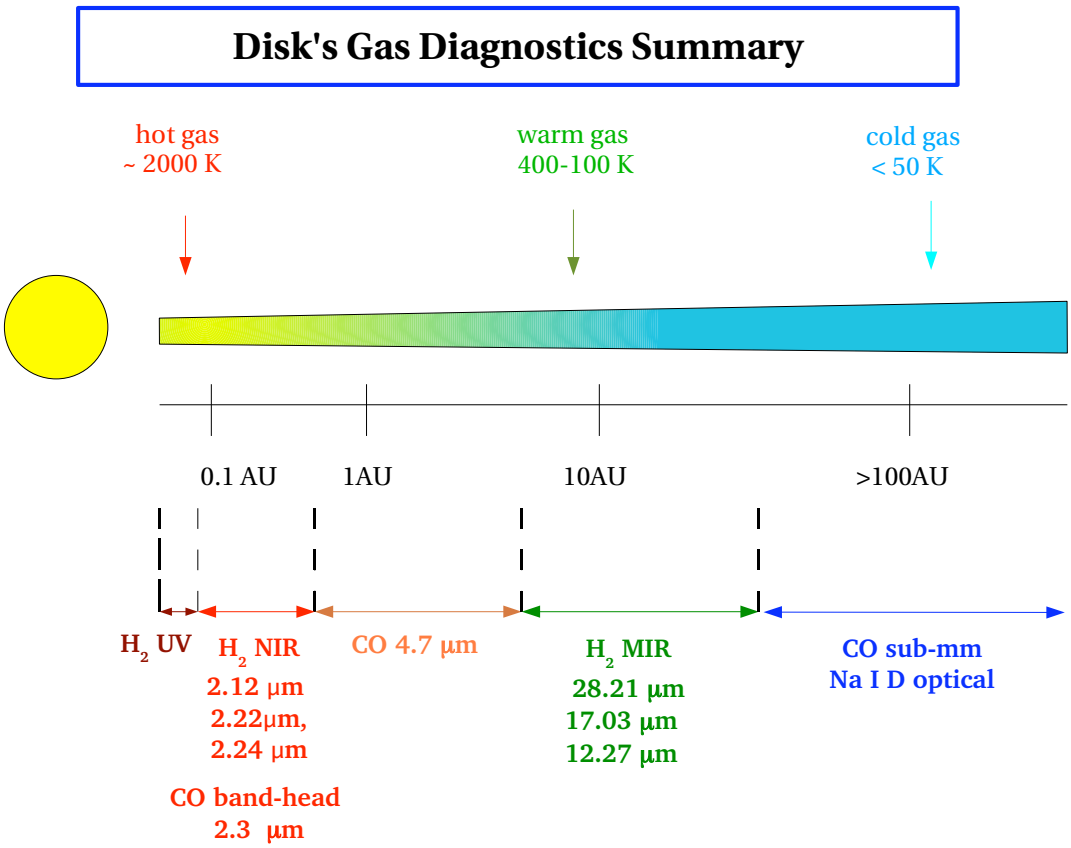

Figure 4.7: Sketch of the infrared emission from the gas in a HAe proto-planetary disk (From Carmona, 2007)

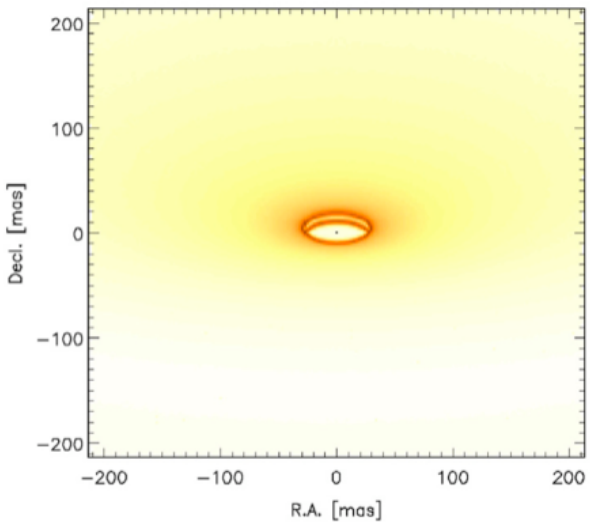

Figure 4.8: Simulated emission at 10 µm of a protoplanetary disk with an inner cavity at r=4 AU (From Wolf et al. 2007). This type of structure will be resolved by ground-based mid-infrared interferometers like MIDI or MATISSE.

4.1.5 Mid-infrared observations of the dust phase in HAe protoplanetary disks

As explained above, mid-infrared observations are expected to essentially probe a thin layer in the atmosphere of the disk (and trace thus the geometry of the surface of the disks). However, any discontinuity in the region [3≈500] AU might also produce a bright detectable structure at 10 or 20 μm(see e.g. [Wolf et al., 2007] and Fig.4.8). Mid-infrared (simple) imaging observations from the ground are currently able, given their performances in angular resolution and sensitivity to detect **and** resolve the intermediate regions i.e. 30-400 AU, the upper limit in distance depending mostly on the distance from the Sun and the luminosity of the star (and to certain extent also on the composition of the dust).

AB Auriga

In 1999 and 2000 we have used the mid-infrared imager CAMIRAS ([Galdemard et al., 1998]) optimized for Q band on CFHT 3.6m telescope for studying the spatial extent of Herbig Ae protoplanetary disks. Several objects were spatially resolved at 20.5 μm, one of which is around the PMS star AB Auriga. AB Auriga is one of the nearest, brightest and best studied Herbig Ae stars. It is of spectral type A0-A1 ([Hernández et al., 2004]) and is located at a distance 144^{+23}_{-17} pc according to Hipparcos measurements ([van den Ancker et al., 1998]). Near-infrared imaging with the HST-STIS ([Grady et al., 1999]) shows a large envelope which surrounds the star and which scatters the starlight. This apparently flattened reflection nebulae is seen close to pole-on, up to more than 5000 AU from the star. More recent near-infrared observations, performed with the Subaru telescope using the CIAO instrument ([Fukagawa et al., 2004]) detected a disk up to 580 AU and showed the presence of a spiral structure in the outer disk at distances in the range ∼250-400 AU. AB Auriga has been also observed in MID-IR spectroscopy with ISO ([Bouwman et al., 2000, Meeus et al., 2001]). These data constrain the dust composition out to several tens of AUs from the star. The modelling of the SED in this wavelength range also shows that this object belongs to the group I ([Meeus et al., 2001]). Finally, the surrounding material was also observed at millimeter wavelengths by [Mannings and Sargent, 1997].
CAMIRAS 20.5 μm deconvolved image shown in Fig.4.10 displays an unexpected structure. A central core is marginally resolved (0.9 arcsec w.r.t a deconvolved spatial resolution of 0.6 arcsec) but much more striking is the presence of a ring (slightly elliptic) of emission at a median distance of 1.94 arcsec with a thickness which is unresolved and maybe more interesting, *which center is offset w.r.t. the star*. The 20.5 μm image has been modeled using a simple geometric model which contains a central extended core and an ring of emission (produced by some discontinuity in the disk, e.g. an abrupt and local change of the flaring angle) which is placed at the surface of a flaring disk observed under a certain inclination. The geometrical parameters are given in Table 4.1. Note that a flaring structure is essential for reproducing accurately the observed asymmetries.

One of the most interesting points here is that the global variations of intensity along the ring (azimuthal variations) are fairly well reproduced by the geometrical model containing a flaring surface (Fig.4.10, upper right panel).

This image has provided the very first direct evidence of a flaring structure of a protoplanetary disk, at least at a radius of 280 AU from the star. The measured flaring angle is 0.23 rad (13 degrees) which is modest in comparison to the extreme flaring derived in HD 97048 (see 4.1.5). Nevertheless, this disk is likely to have a thickness which is increasing with the distance to the star but in this case (when compared to HD 97048, see 4.1.5) the thickness could be observed only at a specific distance of 280 AU thanks to this bright emitting region at 20.5 μm. The relatively "flattened" geometry with respect to an expected flaring predicted by the theory ([Chiang and Goldreich, 1997]) or simply in comparison with (the extreme flaring of) HD 97048 might be interpreted in terms of disk evolution. Protoplanetary disks

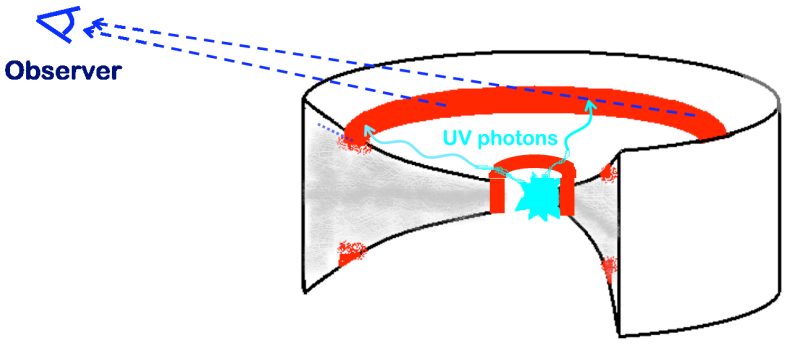

Figure 4.9: Sketch of the mid-infrared emission at 20.5 µm from the AB Auriga disk

tend to flatten with time because of energy and gas dissipation (hence probably the group I to group II transition). The disk around AB Auriga could have started flattening; it would be then in a transitional state, mixing both group I and group II characteristics. On the other hand, the integrated SED shows, contrarily to other disks e.g. HD 100546, a 10 µm silicate feature whose shape is characteristic of small pristine interstellar dust grains thus arguing in favor of a rather young system. However, the SED is an integrated measurement over the whole disk; some inner regions might have begun their evolution while the outer ones remain in a more pristine state.

This observation raises (at least) two questions. The first one is how is it possible to create such a discontinuity in the structure of the disk at such a large distance (280 AU) in the disk ? The second concerns the origin of the 20 µm emission itself: standard models based on dust particles in thermal equilibrium predict a continuum emission far too weak to be detected. Dust grains in thermal equilibrium have too low temperatures to produce a detectable continuum emission at such large distances from the star; transiently heated very small particles (1-10 nm) marginally do the job (Habart, priv.comm.). The first question is usually linked to the presence of massive compact bodies (giant planets or brown dwarves) which perturb sufficiently the structure of a disk initially in hydrostatic equilibrium to create gaps and walls. These structures in turn create secondary structures (e.g. rims by puffing up of heated "walls" and thinner disk regions in the shadow of the rim, see e.g. [Dullemond et al., 2001]). It is therefore very tempting to associate the bright ring with the presence a massive body. However, in absence of any other information, one has to be very careful because mother nature probably disposes also of some undiscovered yet instability mechanisms able to produce such a structure. The second question addresses more our understanding of the composition and the mechanisms of dust heating in these protoplanetary disks. Recent observations e.g. of the gas phase raise also a lot of questions concerning the excitation mechanisms, these questions should be addressed in detail in a mid-term future using forthcoming "disk observing machines" like ALMA, JWST/MIRI or METIS on the E-ELT.
In any case, concerning the AB Auriga disk structure, a confirmation on larger telescopes and at complementary wavelengths are definitively needed to assess the nature and the origin of this bright ring.

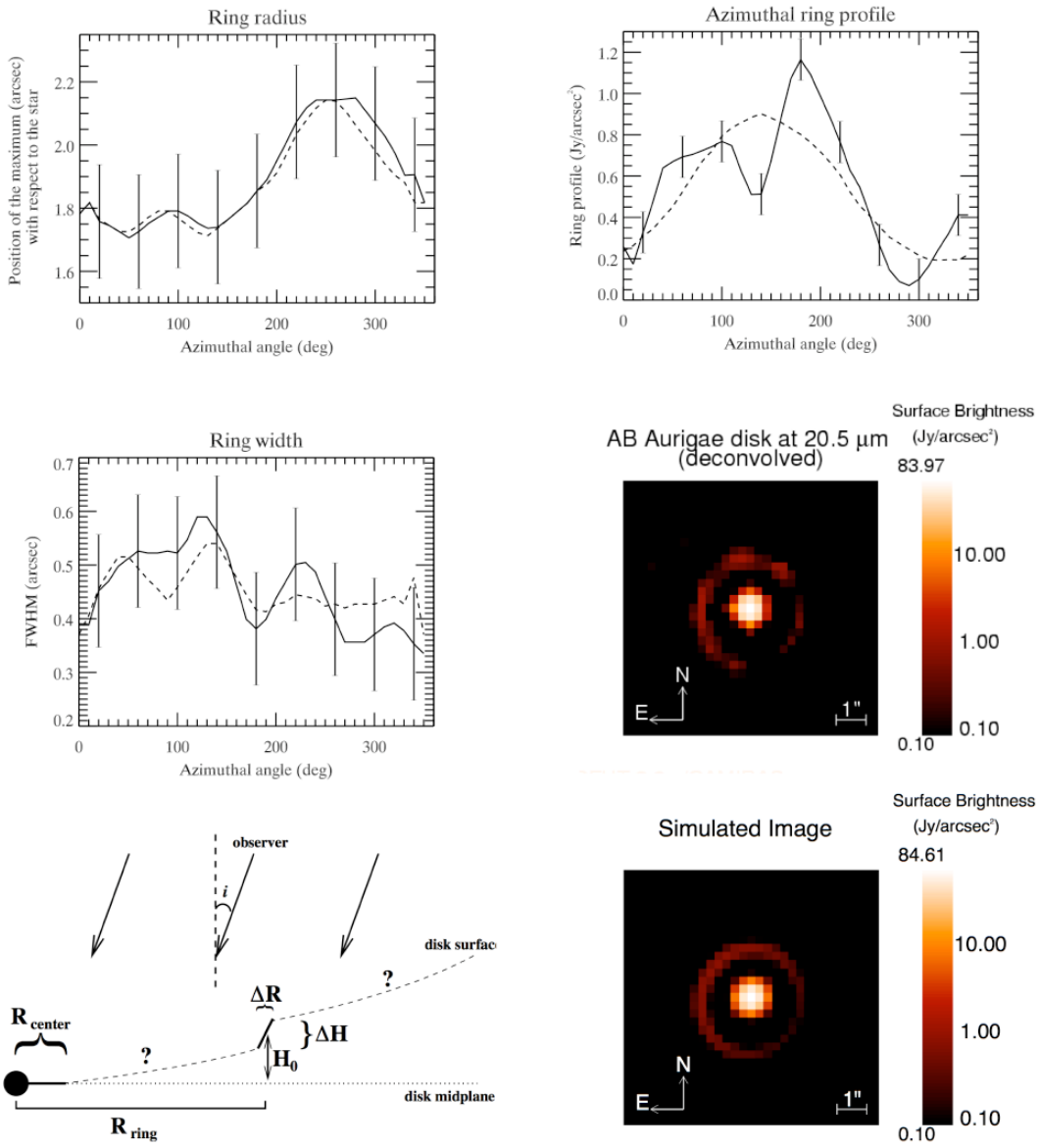

Figure 4.10: Observed data and model fit of the 20.5 μm CAMIRAS image of AB Auriga. Center right image: The 20.5 μm image observed by the CAMIRAS instrument on the CFHT. After image deconvolution, a bright ring is observed at a mean distance of 280 AU. This structure is observed in 2 independant datasets taken in 2000 and 2001. The model described in the text and sketched in the lower left frame is fitted to several measures in the observed image. The model assumes an emission ring of constant intensity and width placed at the surface of a thick disk inclined by 21 degrees. Upper right: azimuthal brightness variations of the ring. The general brightness structure of the ring is fairly well reproduced, but some local variations are however missing in the model reproduced. These maxima, which are significant gicen the sensitivity achieved, could reflect the presence of inhomogeneities at the surface of the disk. The upper left plot shows the apparent (projected) distance to the star as a function of the azimuthal angle. This quantity is very well reproduced by the model and confirms the hypothesis of a ring structure at the surface of a circumstellar disk. Center left: the ring width (or thickness) as a function of the azimuthal angle.

Table 4.1: Best fit model parameters of AB Aur. Listed are the model parameters defining the system orientation, the ring emission and central emission region.

Parameter	Value	±	1σ error
system orientation†:			
Θ	65.699 °	±	1.565 °
i	-20.904 °	±	1.002 °
ring parameters:			
e	0.135	±	0.0063
a	1.955 ″	±	0.0079″
Φ	123.46 °	±	2.65°
ΔR	0.122 ″	±	0.0086 ″
H_0	0.469 ″	±	0.0563 ″
ΔH	0.177 ″	±	0.0158 ″
I_{ring}	2.371 Jy arcsec^{-2}	±	0.116 Jy arcsec^{-2}
parameters central emission:			
R_{center}	0.427 ″	±	0.00122 ″
I_{center}	89.035 Jy arcsec^{-2}	±	0.409 Jy arcsec^{-2}

†angles are given in degrees counter clockwise with respect to the west direction (right direction)

CQ Tau, HD163296, HD135344

In the same observing campain focused on 20 µm observations of protoplanetary disks using CAMIRAS mounted on the CFHT, a full set of disks was observed. Among this list, some objects, albeit in a less spectacular manner, were also resolved.

Using the [Dullemond and Dominik, 2004b] radiative transfer model, we were able to reproduce the observed profiles and constrain the inclination, the position angle (see annex 4.3); but the most important physical constraint brought by these 20.5 µm observations is undoubtly a lower limit on the outer radius (450 AU in the case of CQ Tau in this study). Although classified as a group Ia source ([Grady et al., 2005]), the flaring of CQ Tau protoplanetary disk seems also relatively small when compared to typical values of flared disks. This tends to classify CQ Tau into the category of "intermediate stage" disks for which the geometry of the inner disk has already started to flatten; this is consistent with a (old) 10 Myr system already evolving towards the "planetary phase" i.e. a dissipating disk. An interesting point which deserves some attention here is the inclination of the disk. CQ Tau has been classified as an UX Ori type object which is usually linked to an fairly inclined disks w.r.t. to the line of sight. This observation is supported also by the conclusions from VLA interferometric data obtained by [Testi et al., 2001] who found an inclination of 63° w.r.t. the face-on geometry. We found here a quite modest inclination of 33 ± 5 ° which is coherent with the image seen in Fig.4.11. This rather large discrepancy can be interpreted at first glance by the fact that the inner regions of the disk (1-10 AU) have a geometry which differs significantly from that of the outer regions. These results are presented in details in annex 4.3.
We note that there is a group of observed sources which are unresolved with CAMIRAS. Among them the disk around HD179218 presents many similarities with CQ Tau or HD 97048 (distance, SED, group I, expected inclination, ...) and would have been expected to be resolved by CAMIRAS. 20.5 µm CAMIRAS data are however definitively unresolved (see annex 4.3). In this context we shall also mention that HD35187 (group II), HD36112 (group Ia) and HD150193 (group II) were also observed with CAMIRAS at

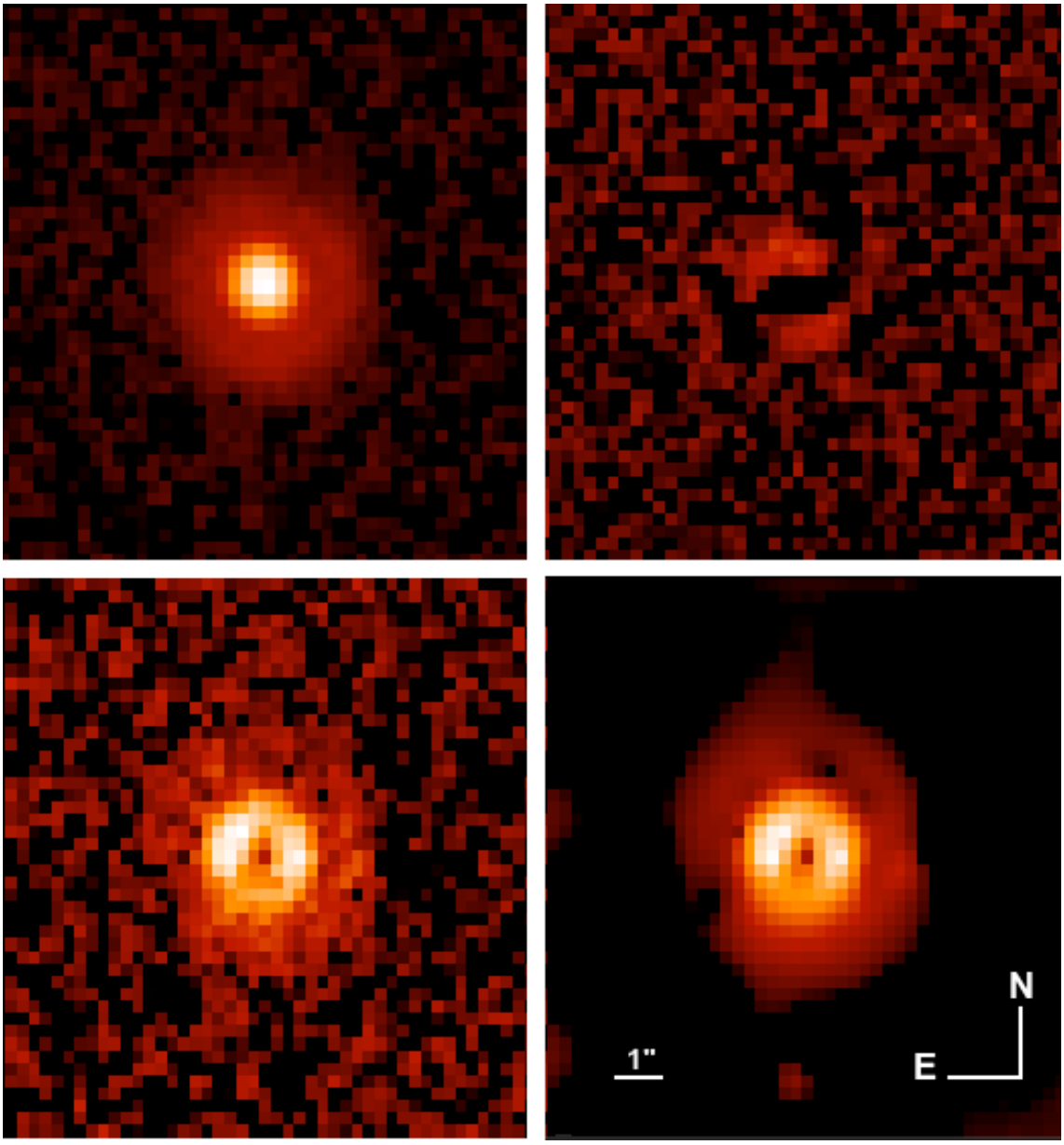

Figure 4.11: 20.5 μm observation of the CQ Tau protoplanetary disk with CAMIRAS on the CFHT 3.6m telescope. Upper left panel displays the original image. Upper right panel shows the residuals of two PSF over two consecutive nights (upper limit on the residuals) using the same display scale as that of the lower panels. Lower left panel displays the extended emission of the disk after subtraction of a rescaled PSF, the energy of the extended part is ∼6 times that of the PSF residuals. Lower right: same as lower left but filtered using the MEM-MS method ([Pantin and Starck, 1996]).

20.5 µm. HD36112 and HD150193 are definitively unresolved. HD35187 disk might have been marginally resolved ([Doucet et al., 2004]).

The prototype of HAe flaring disks around HD 97048

HD 97048 is also a group Ib Herbig Ae star. It is located at a distance of ∼180 pc from Earth and surrounded by an optically thick protoplanetary disk. This disk has been marginally resolved around 10 µm with low-resolution spectroscopic mid-infrared observations with the instrument TIMMI2 ([van Boekel et al., 2004]). We have observed this disk with VISIR on the VLT in the framework of a guaranteed time key-project on protoplanetary disks. It has been observed in N and Q bands, in PAH bands and adjacent continua (8.6 and 11.2 µm). PAH bands images reveal a fairly extended structure up to distances of ∼400 AU from the star. This structure is asymmetric with respect to the star (see Fig.4.12) yelding a potential information on the geometry of the disk. HD 97048 has been found to show strong PAH emission bands and also resolved spatially by ISOCAM CVF ([Siebenmorgen et al., 2000]) over a 5-10 arcsec spatial scale depending on the wavelength (6-13 µm). At such a large distance from the star (more than 1000 AU), the extended structure observed by ISOCAM is probably an envelope, remnant of the dense core which gave birth to the star. One could therefore argue that the shape seen in the mid-infrared image is simply produced by an asymmetric envelope surrounding the star. However, this is quite an unsatisfactory interpretation. First, the star is known to be surrounded by a thick and dense protoplanetary disk which produces a large infrared excess starting from 2 µm (see [The et al., 1986] for the first photometric and spectroscopic study) and observed later in details by ISO/SWS. Besides, the disk has already been spatially resolved in the 3.3 µm feature (L band) with the adaptive optics instrument NACO ([Habart et al., 2004]).

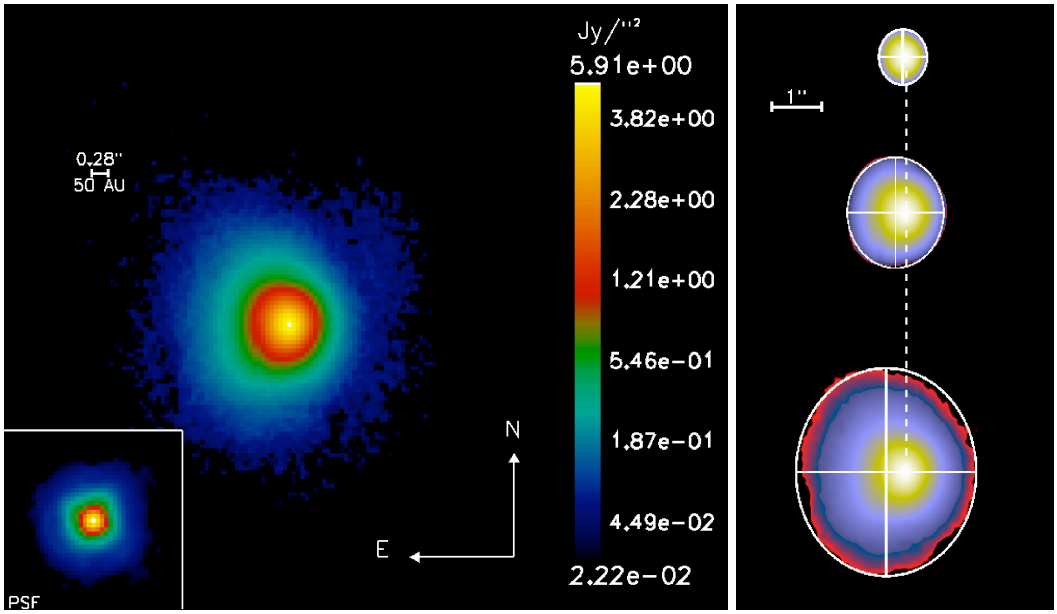

Figure 4.12: Left panel: the protoplanetary disk around HD 97048 observed at 8.6µm by VISIR. The inset image shows the PSF measured on a reference star. Right panel shows the same image but thresholded at different intensity levels. The isophotes are fit with an ellipse. A remarquable offset between the location of the star (dashed line) and the center of fit ellipses is clear. This offset increases as the threshold level decreases (further regions of the disk are probed).

One has therefore some good reasons to believe that the observed structure at 8.6 µm is emitted

at the surface of a disk. The peculiar shape and the observed trends of the isophotes have a natural explanation in the framework of an inclined flaring disk. Indeed, considering an inclined disk (from the face-on case), if the star is not in the plane of the emitting region (e.g. because the disk has a non negligible thickness). By projection the star will be offset with respect to the center of the isophotes (see Fig.4.13) that correspond to regions of equal temperature (and therefore equal distance to the star). The higher the distance to the star, the larger will be the the offset.

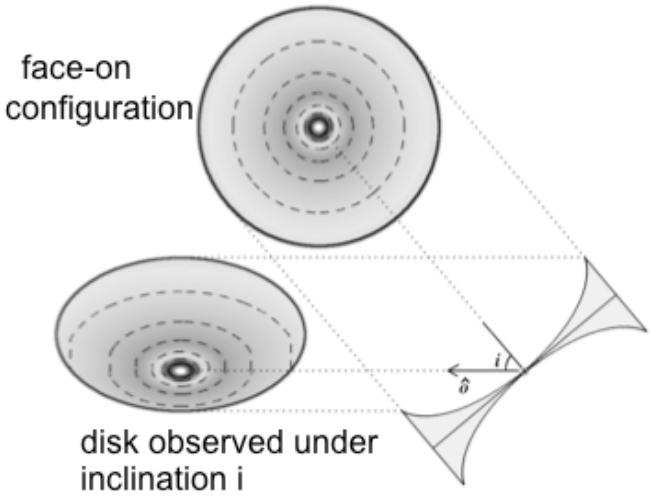

Figure 4.13: Sketch of the projection effect described in the text. In the face-on case, no offset between the star and the center of the isophotes is observed. At an inclination different from zero, the projection effect induces an offset.

This tells us that first that the disk has an non-negligible thickness. Secondly, the offset between the star and the center of the isophotes increases with the distance to the star (Fig.4.16, left panel). Consequently, the thickness of the disk increases also with the distance to the star. At this stage any monotonically increasing function (linear, quadratic, square root, etc...) is possible.
We developped a simple geometrical model of mid-infrared emission in order to constrain more accurately the geometric parameters. This simple model assumes that the emittance of the surface of the disk follows a power-law function, $I = I_0(r/r_0)^\gamma$ where r_0 is a reference distance to the star (135 AU in the present case) and I_0 is the emittance at this reference distance. The "à priori" assumption of pure surface emission is supported by advanced radiative transfer models which show that given the densities of material expected the 8.6 µm emission originates from a layer which is thin compared to the geometrical thickness of the disk. This remains true even for large distances (350 AU) at which the density has dramatically decreased (see Fig.4.14).

The disk is assumed to have a flared geometry with a flaring index δ. Figure 4.15 displays sketches the assumptions and displays the variables used in the analytical model. Assuming that de disk scale-height and surface flux density are following power-laws:

$$\begin{aligned} H(r) &= H_0(r/r_0)^\delta \\ I(r) &= I_0\left(\frac{r}{r_0}\right)^{-\gamma} \end{aligned}$$

on the west (front) side, the apparent surface brightness S_b reads

$$S_b(x_p \geq 0) = I_0\left(\frac{r_p}{r_0}\right)^{-\gamma} \frac{1}{\cos(i+\beta(r_p))}$$

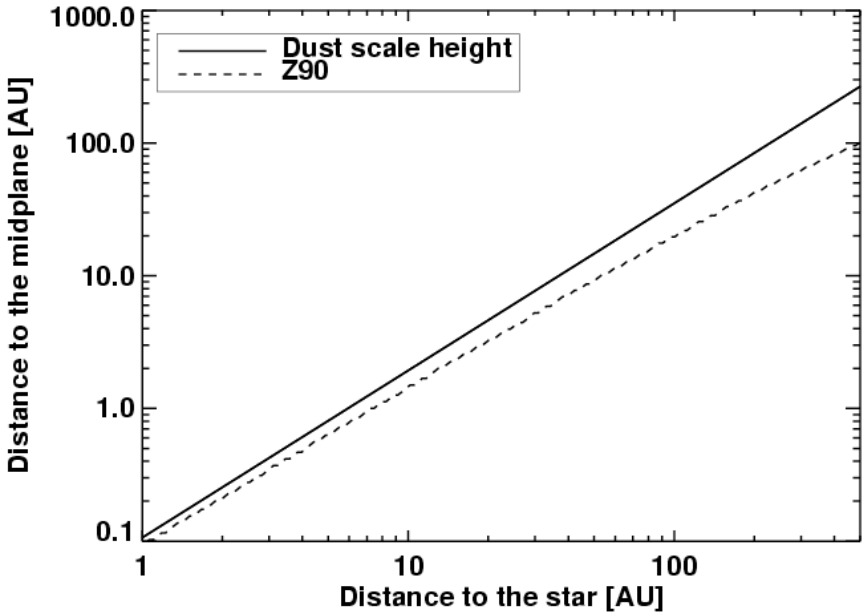

Figure 4.14: Plot of the dust scale height (plain line) and the limits of the volume which emits at 8.6 μm 90% of the emission (optical thickness $\tau = 2$) in dashed line.

$$
\begin{aligned}
& & \text{with} \\
r_p &= x_p \frac{\cos(\alpha(r_p))}{\cos(i + \alpha(r_p))} \\
& & \text{and} \\
\tan(\beta(r_p)) &= \frac{H_0}{r_0} \delta \left(\frac{r}{r_0} \right)^{\delta - 1} \\
\tan(\alpha(r_p)) &= H_0 \left(\frac{r^{\delta - 1}}{r_0^{\delta}} \right) \\
& & \text{On the east side, the apparent surface brightness } S_b \text{ reads} \\
S_b(x_p \leq 0) &= I_0 \left(\frac{r_p}{r_0} \right)^{-\gamma} \frac{1}{\cos(i - \beta(r_p))} \\
& & \text{with} \\
r_p &= x_p \frac{\cos(\alpha(r_p))}{\cos(i - \alpha(r_p))}
\end{aligned}
$$

where

- $I(x)$ is the flux density of the disk at the radius r from the star
- β(r) is the flaring angle at the distance r from the star
- i is the inclination angle

- α(r) is the opening angle at distance r from the star
- $S_b(x)$ is the observed surface brightness at an projected distance x from the star
- r_p is the radial distance to the star corresponding to the point P at the surface of the disk.
- x_p is the corresponding abscissae and also the projected distance from the star on the sky.

Starting from x_p:

1. r_p is computed by solving the implicit equation numerically
2. β and α are computed for the distance r_p

finally, the distance r_{max} for which this is still valid reads:

$$r_{max} = r_0 \left(\frac{r_0 \tan(\pi/2 - i)}{H_0 \delta} \right)$$

and corresponds to the distance at which the surface of the disk is perpendicular to the line-of-sight. In this case, the model presents a singularity and is no longer valid.

Best fit (Fig.4.16, right panel) parameters obtained by minizing the χ^2 in the region [1-350] AU show that the disk is rather thick ($51.3^{+0.7}_{-3.3}$ at a distance of 135 AU) and its scale-height increases exponentially with the distance to the star with a (flaring) index of δ=1.26 ($\pm$0.05). The surface intensity at 8.6 µm decreases as a power-law with an index of -$2.3^{+0.2}_{-0.06}$, very close to the expected value of -2 for PAH emission in the case of the surface of an optically thick medium (pure radial dilution). It is interesting to notice here the remarquable agreement between the measured value of 1.26 for the flaring index and the value of 9/7 (1.285) predicted by hydrostatic equilibrium models ([Chiang and Goldreich, 1997]). Fig.4.17 plots the scale height of the distance as a function of the distance to the star. It can be noticed that although the flaring index is close to the expected value of 9/7, the measured absolute scale height is twice lower than the expected value. Since the PAH1 filter traces the almost pure PAH emission (especially for distances larger than 100 AU) and assuming that the PAH particles are strongly coupled with the gas phase, this factor of 2 difference cannot be explained by a possible effect of dust sedimentation towards the midplane.

Beyond a distance of about 350 AU from the star, the measured star-disk offsets display a different behaviour since the offset reaches a maximum and decreases with the distance to the star beyond. This change can be interpreted in two possible ways. The first would be that the disk starts to be optically transparent to the mid-infrared radiation and thus the "pure surface emission" assumption is no longer valid. When starting to mix the infrared radiation from both surfaces (frontside and backside) the corresponding offsets tend to cancel each other. The second explanation is simply that beyond 400 AU the mid-infrared emission is not purely produced by the disk the the emission of the envelope starts to dominate at these wavelengths. Since the remnant envelope has a likely inhomogeneous and clumpy structure, any kind of situation can occur. There is a quite simple manner to distinguish between these two interpretations. It consists in observing the disk in the dust continuum emission. Indeed, at the very large distances from the star where the envelope is probably located (500 AU and more), only PAH excitation can occur. The N-band continuum emission is highly peaked at the center of the disk because the inner rim dominates the flux at these wavelengths; the disk emission drops very rapidly and the

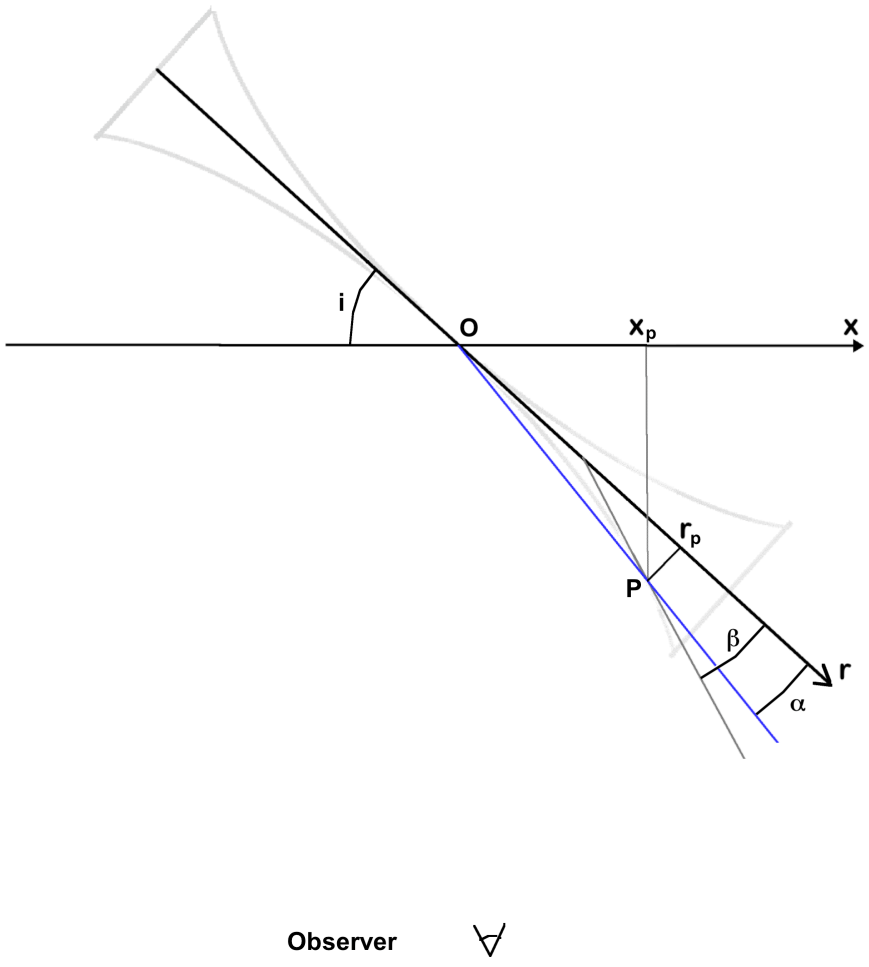

Figure 4.15: Sketch of the model and the corresponding variables. The star is located at the origin O.

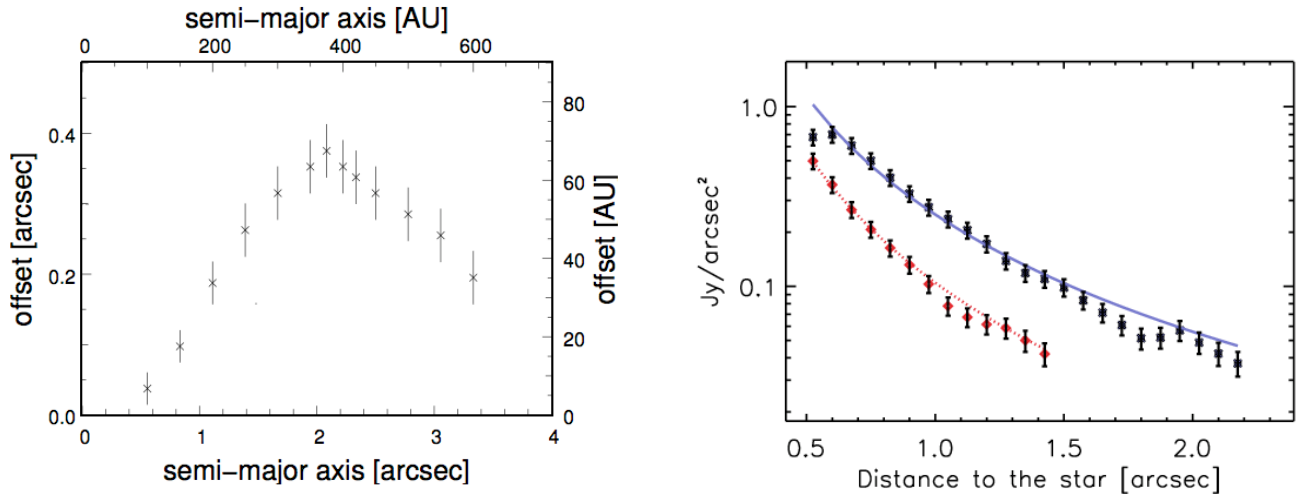

Figure 4.16: Left panel: plot of the measured (on the 8.6 μm image) offset between the center of the isophotes and the star as a function of the distance to the star. Right panel: the observed profiles on the east and west side are fitted by a purely geometrical model of thermal emission. The red colors labels the west side, blue color labels the east side. Note that the continuum emission, which has a completely different behavior, has been removed from the total emission in the PAH filter using the 9.0 μm continuum images extrapolated to 8.6 μm.

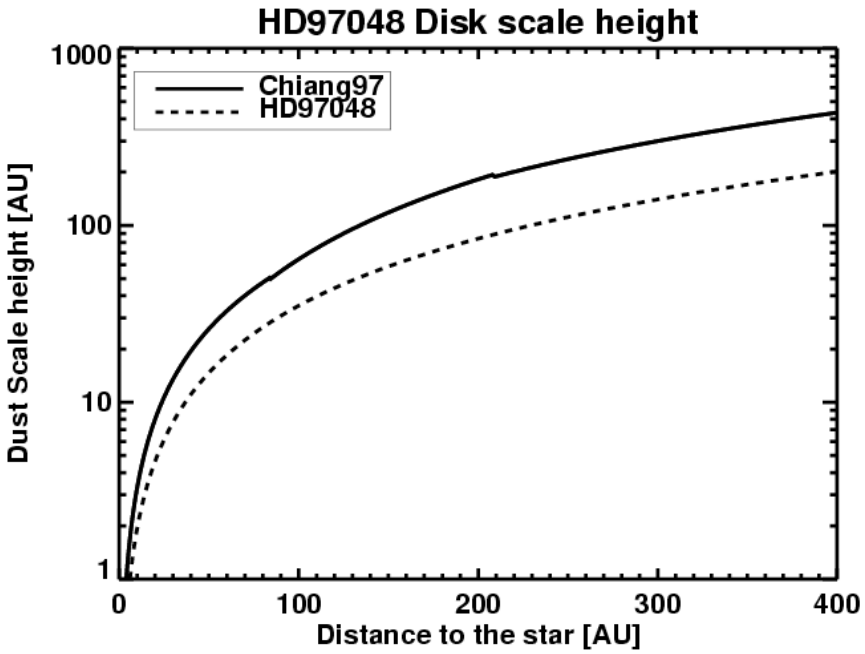

Figure 4.17: Plot of the dust scale height measured in the PAH1 filter, this study (dashed line). For comparison, the scale height predicted by the model of Chiang & Goldreich ([Chiang and Goldreich, 1997]) is overplotted (plain line).

detection limits of VISIR are reached at moderate distances (∼200 AU) from the star. However, Q-band observations sensitive to colder dust, although penalized by a reduced sensitivity, can potentially trace the disk continuum emission out to larger distances. Fig.4.18 shows the Q2 image (18.7 μm) of the disk.

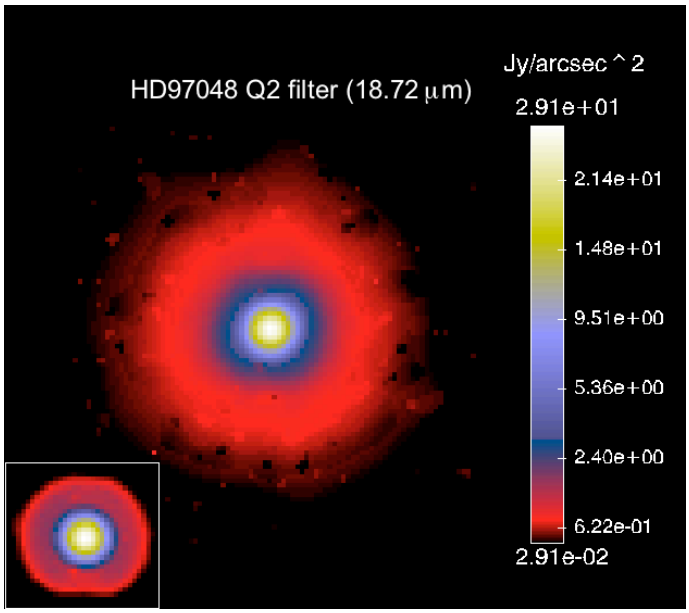

Figure 4.18: VISIR image of the HD 97048 protoplanetary disk observed at 18.72 μm. The inset shows the PSF. The disk is clearly resolved spatially and detected up to very large distances from the star (500 AU).

This very deep image (3h of total integration time) detects the disk in continuum radiation over 3 orders of magnitude down to a level of 30 mJy/arcsec^2. This level is reached at a distance of 2.7 arcsec (about 500 AU) from the star. The isophotes are more symmetric than the N-band ones. This is not simply an effect of degradation of the spatial resolution (from 0.26 to 0.54 arcsec) but is caused by observing at a different wavelength (hence different dust opacities). Indeed if in the N-band one observes essentially the surface of the disk up to fairly large distances from the star, the reduced dust opacity in Q band (about 3 times smaller) allows the opposite disk surface to produce a siginificant flux at shorter distances (about 200 AU assuming that the surface density varies as $r^{-3/2}$ as found in [Doucet et al., 2007] when fitting N-band data with a comprehensive radiative transfer model). At such a large distance of 500 AU from the star, one may wonder what kind of dust can still emit at 18 μm. Grains with sizes in the range 0.1-10 μm are heated to only ∼70 K and are unable to produce any significant 18 μm radiation. We thus infer the presence of very small grains transiently heated to produce the 18 μm radiation. Their nature and size is unknown but should they be composed of silicate, some prominent 10 and 18 μm silicate features would probably be observed. This is not the case. Featureless material like amorphous carbon or coals would be a good candidate. What is also striking in the Q-band image is its relative circular symmetry (see Figures 4.12 and 4.18). On the other hand, the PAH1 image is relatively asymmetric between the East and the West side which is interpreted in terms of a flaring geometry. This pronounced geometric difference between the images at the two wavelength cannot be explained only by change of spatial resolution; the emission at 18.72 μmis thus intrinsically more symmetric than at 8.6 μm. A possible partial interpretation is that the radiation emitted by the disk is produced at scale heights smaller than the radiation produced at 8.6 μm. Another alternative would be that the disk becomes optically thin at 18.72 μmbeyond distances of ∼200 AU. These hypotheses need to be tested by making radiative transfer models; this is a currently on-going work.

The results concerning the N-band data and the geometry of the disk have been published in the *Science* report (see annex 4.3). A complete radiative transfer model of the disk has been built based on all the existing constraints (including the source spectrum) (annex 4.3). One of the most difficult observable to reproduce, when assuming a single and homogeneous dust composition throughout the disk, is the absence of a silicate feature at 10 µm. Silicates are indeed among the most abundant materials in the dust phase and are observed in emission at 18 µm. It is possible to "hide" the 10 µm silicate feature by assuming that the dust grains are physically decoupled between the carbon and the silicate phase. Amorphous carbon grains, heated to larger temperatures in this hypothesis, would produce a strong continuum emission that dominates the silicate emission. However, since the 10 µm silicate feature arises from the innermost regions ([3-50] AU) alternative interpretations such as a change of dust properties in the inner regions such as grains growth (larger grains have a reduced 10 µm feature contrast), a different of inner disk geometry (e.g. a flatter disk), or a smaller surface density are also possible intepretations. Only very high spatial resolution observations such a interferometric ones will be able to bring constraints strong enough to remove this degeneracy. The comprehensive physical model we have built allows to confirm the results found in annex 4.3 and justifies the assumptions made in the later article. It concludes also that a large reservoir of large grains (1 mm and larger) must be present in the disk given a sub-millimetric/millimetric predicted flux which is is by far too weak with respect to the observed flux ([Henning et al., 1998] (1.3 mm), p-ArTéMIS at 450 µm(see Fig.4.19). 18 µmobservations are currently being interpreted and will be part of a forthcoming publication.

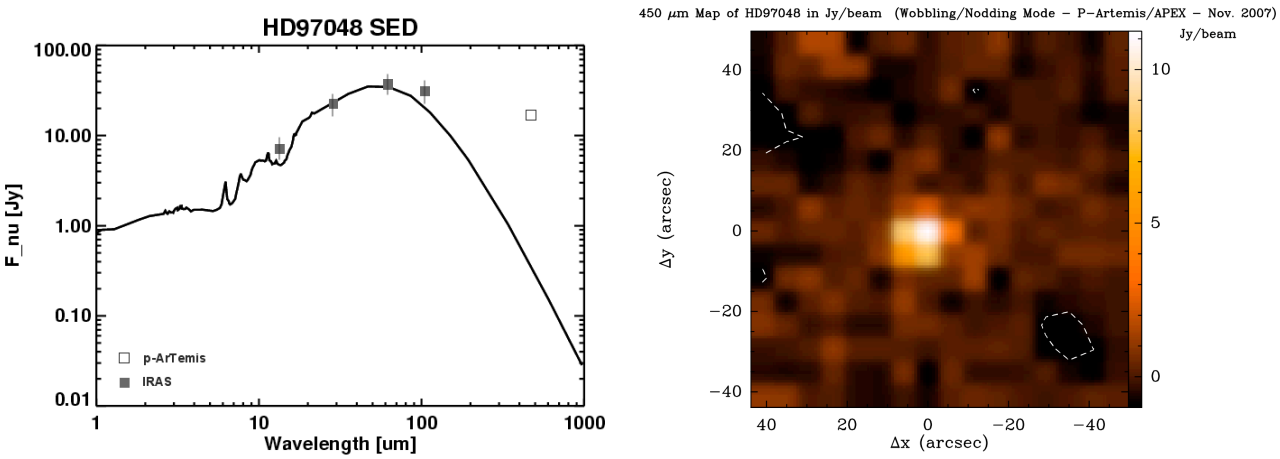

Figure 4.19: Left side: the HD 97048 sed modeled. Right side: HD 97048 at 450 µm mapped by the p-ArTéMis instrument on the APEX telescope. The integrated photometry is 15±0.5 Jy and is shown on the left plot.

A gas to dust transition disk around 95881

HD95881 is also a southern hemisphere HAe star located at a distance of 170 pc. This A2III/IVe type star is surrounded by a group II protoplanetary disk ([van den Ancker et al., 2004]). This disk is relatively evolved since its SED displays relatively strong crystalline forsterite features. Its SED almost flat in the range 10-35 µmshows that the disk is probably self-shadowed and that the dust particles are located in a relatively flat disk. The spectrum also displays prominent PAH and [OI] (6300 A) line emission. VISIR burst mode imaging in the PAH2 filter does not display any extended structure that can be identified with the disk resolved emission. However, as seen in Fig.4.20, the level of the residuals for angular distances to the star lower than ∼0.4 is too high to have a reasonable physical constraint. The corresponding

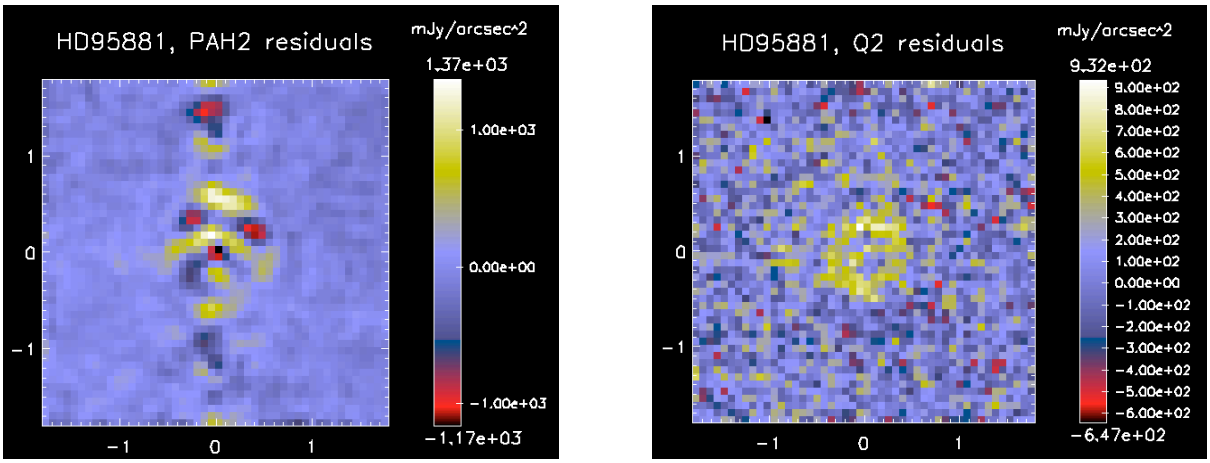

Figure 4.20: VISIR imaging data of HD 95881. Left panel displays the residuals in the PAH2 filter (11.3 µm, burst mode) after subtraction of a scaled reference star (HD 97576). Because of a relatively strong variation of the seeing during the observation, the level of the residuals is very high within a radius of 0.4 arcsec from the star. Right panel shows the residuals in Q2 band (18.72 µm) after PSF subtraction. A slight spatial extension attributed to an extended spatial emission of the disk is detected.

sensitivity upper limits are plotted in Fig.4.21. In the Q band (Q2 filter, standard imaging mode) the disk is marginally extended on a scale of ∼0.45 arcsec from the star. The corresponding azimuthally averaged profile is shown in Fig.4.21. While it is difficult with VISIR imaging modes (standard and burst) to detect relative extensions smaller than ∼0.15 arcsec in radius around bright stars, the use of a differential spatial extent measurement using spectroscopic is able to detect extensions of an emission feature with respect to the continuum with an accuracy of about 10 mas. This analysis has been performed on HD 95881 N-band low-resolution spectrum. We find that the PAH features are slightly extended : $0.34"^{+0.05}_{-0.08}$ and $0.40"^{+0.04}_{-0.06}$ respectivily at 8.6 and 11.25 µm(see Fig.4.22). These extensions correspond to spatial emission of the PAH on absolute scales of 58 and 68 AU from the star respectively.

The article 4.3 presents all the available observables of the disk including VISIR low-resolution spectra and imaging. This fairly comprehesive set of data is interpreted as a disk having a flat dusty self-shadowed part and a flared gaseous component (see sketch in Fig.4.22). Recalling that the PAH particules are so small that they are strongly coupled to the gas, a flared gaseous disk explains the strong PAH and [OI] features which are produced in the upper layers of the surface in direct view to the star radiation. We propose that the disk around HD 95881 would be a transition disk in which the dust content has already settled in the midplane while the gas phase has still the original flaring geometry.

Low-resolution spectroscopy of Herbig Ae dusty disks

Up to now, we have mainly focused on mid-infrared imaging but spectrometry brings also valuable spatial informations. In collaboration with our colleagues from the university of Amsterdam (Nederlands), we have obtained with VISIR a set of ∼25 low-resolution spectra of Herbig Ae stars. This set has been reduced and analyzed using mainly the pipeline that I have developed. The advantage of the low-resolution spectroscopy is the possibility to get a lower-limit on the disk extension as a function of the wavelength independently of any source of bias on the extension such as PSF instabilities (see Sec.3.6). For instance a disk which contains PAH features, usually more extended than the continuum is, will present a FWHM as a function of the wavelength which has some maxima in the PAH bands. The continuum FWHM can be used a simultaneous reference FWHM measurement which allows to obtain

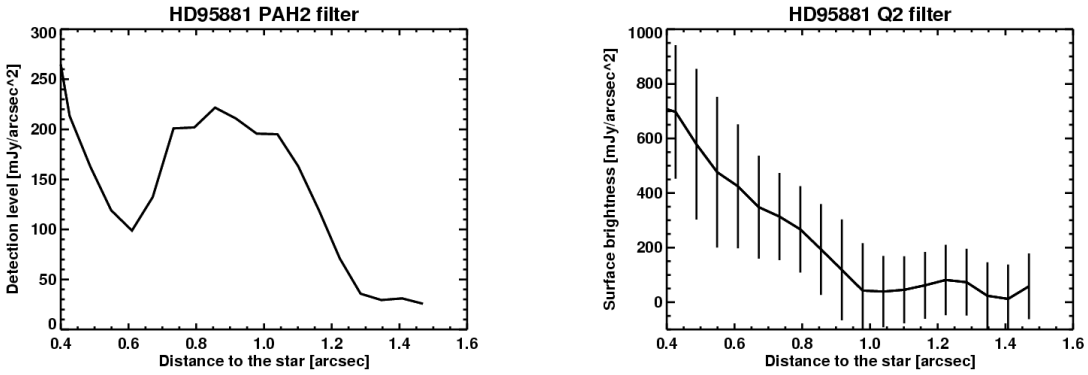

Figure 4.21: Analysis of VISIR imging data of HD 95881. In the left panel are shown the detection limits in the PAH2 filter (11.3 μm) to an extended disk emission as a function of the angular distance to the star. The right panel plots the azimuthally averaged spatial emission in the Q2 band (18.72 μm) as a fonction of the angular distance to the star. The averaging has been performed in a set of concentric ellipses that correspond theoretically to the isophotes of a disk inclined at 55 degrees and having a position angle of 103° from the North.

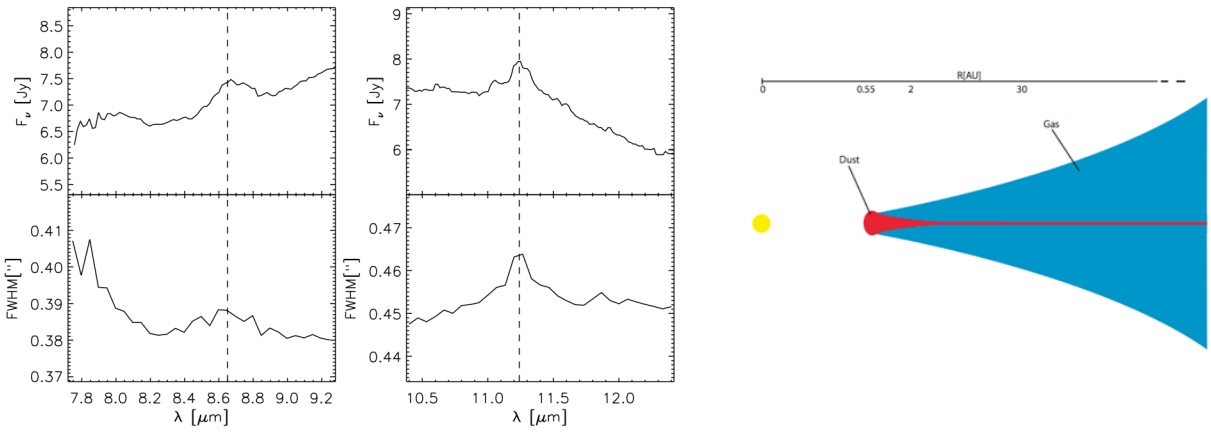

Figure 4.22: Left panel: VISIR N-band low-resolution spectra of HD 95881 and their corresponding FWHM as a function of the wavelength. The positions of of the PAH features are marked by a dashed line. Right panel presents a sketch of the HD 95881 system derived from the analysis of the observational constraints.

an accurate differential measurement of the FWHM (following the same idea as differential imaging), see e.g. [van Boekel et al., 2004]. The comprehensive set of Ae disks we have observed using the same VISIR settings allows to obtain a global view of phenomenon and at the same time, the extract some characteristics of a particular objects in comparison with the other ones. Some evolutionary sketches can be then drawn. The submitted version of the paper reporting these results is shown in annex 4.3.

4.1.6 Observations of the molecular hydrogen warm gas phase

First as explained above, although the molecular hydrogen is the most abundant molecule in the gas phase (which already represents 99% of the mass in the interstallar medium), its detection is challenging because of the quadrupolar nature of the transitions. VISIR is equipped with a high-resolution spectrometer (see Sec.2.2) which is a sensitive tool to detect the emission of warm (T=100-1500K) H_2 pure rotational transitions. Preliminary estimates fix the sensitivity levels around 0.1-1 Jupiter masses depending on the temperature of the optically thin (at 10 μm) molecular hydrogen. We have conducted a key-program aimed at detecting the molecular hydrogen around Herbig Ae stars. The idea was to constrain the amounts of mass of gas available for giant (gaseous) planet formation around B9-A8 stars. Other tracers such as CO are probably inaccurate either because of assumed relative compositions which are wrong or because of physical effects affecting the exact measure of the mass of CO (self-shielding, optically thick line). On one hand [Hollenbach et al., 2005, Takeuchi et al., 2005, Gorti and Hollenbach, 2008] predict a very fast inner gaseous disk clearing timescale of 10^4 yr at 30 AU for a typical HAe star of 2.5 $M_\odot$, much shorter than most of the Ae stars ages. On the other hand, [Thi et al., 2001] have successfully detected CO gas emission from similar, although probably slightly older, disks around intermediate-mass stars. Warm molecular hydrogen has been already detected in the mid-infrared range around several T-Tauri stars (e.g. T-Tau, [Richter et al., 2005]). However, concerning the more massive and luminous Ae star, how much cold gas is present in their protoplanetary disks and at which distance is a remaining question that can be adressed through observations of the emission of warm molecular hydrogen. We have observed a ten of HAe disks over 3 periods and spent about 4 nights on this program. In most of the cases, both the 17.03 S(1) and 12.28 S(2) features were observed. In parallel, another team has also conducted the same type of observations on a complementary set of targets ([Carmona et al., 2008]). With the exceptions of HD 97048 and AB Auriga, none of the observations gave a positive detection. [Carmona et al., 2008] interpret these non-detections simply by an effect of opacity. Only a very thin surface layer on the disk in the [5-30] AU region (where the temperatures are high enough to excite the rotational emission) can be detected at 10 μm. Assuming a [Chiang and Goldreich, 1997] structure for the disk, this layer contains an estimated mass of only 10^{-5} M_j of molecular hydrogen. The current detection limits from the ground on large telescopes (around 0.5-1 10^{-14} erg.s^{-1}.cm^2) are transposed into 0.01 (300K) or 0.1 (200K) Jupiter masses of warm gas depending on the temperature of the gas. Fig.4.23 plots the sensitivity in mass of gas as a function of the temperature of the gas for a line having an integrated flux of 10^{-14} erg.s^{-1}.cm^2.

HD 97048 and AB Auriga are therefore two exceptions concerning the detection of the H_2 among intermediate-mass protoplanetary disks. In the case of AB Auriga, [Bitner et al., 2007] argue that an additional heating mechanism (UV or X-rays heating [Glassgold et al., 2007, Nomura et al., 2007]) is needed to increase sufficiently the temperature of the hydrogen (670K) well above the dust temperature, at the constrained distance of 18 AU (obtained by line profile fitting). Another interpretation is based on a decreased opacity of the surface layer e.g. because dust settling is occuring in the disk. Indeed, in the case of HD 97048, although the S(1) line is clearly detected (see Fig.4.24) the temperature is not very well constrained because of non-detections of the S(2) and S(4) emission lines[3], nevertheless this upper limit constrains the gas-to-dust ratio (in mass) to be well above 1 000 and lower than 10 000 inside a radius of 35 AU from the star. This number, extremely high in comparison the canonical value of 100

[3]only an upper limit of 920 K can be estimated, [Martin-Zaidi et al., 2009]

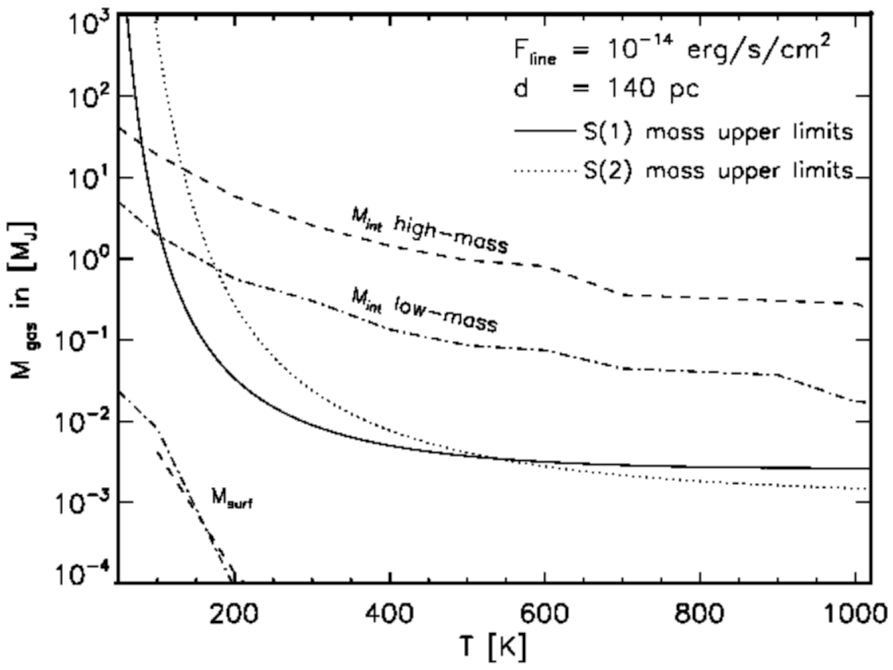

Figure 4.23: Plot of the sensitivity in mass of gas as a function of the temperture of the gas in 2 lines observable from the ground (S(1) at 17.035 μm and S(2) at 12.285 μm) The S(1) line is more sensitive for gas temperatures lower than ∼500K. The expected *total amounts* of mass of gas at the same temperatures (including the optically thick parts) are overplotted in dashed lines (M_{int}) in two extreme cases of disk masses. However, the optically thin parts (M_{surf}) at S(1) and S(2) wavelengths are only a tiny part of that (from Carmona 2008).

is maybe a hint that dust settling has already started in HD 97048. In that respect, AB Auriga and HD 97048 could be 2 "transitional" in which the dust settling has just begun just before the unprotected gas is photodissociated. The articles 4.3 and 4.3 present our results concerning the detection of the warm molecular hydrogen in the protoplanetary disk around HD 97048.

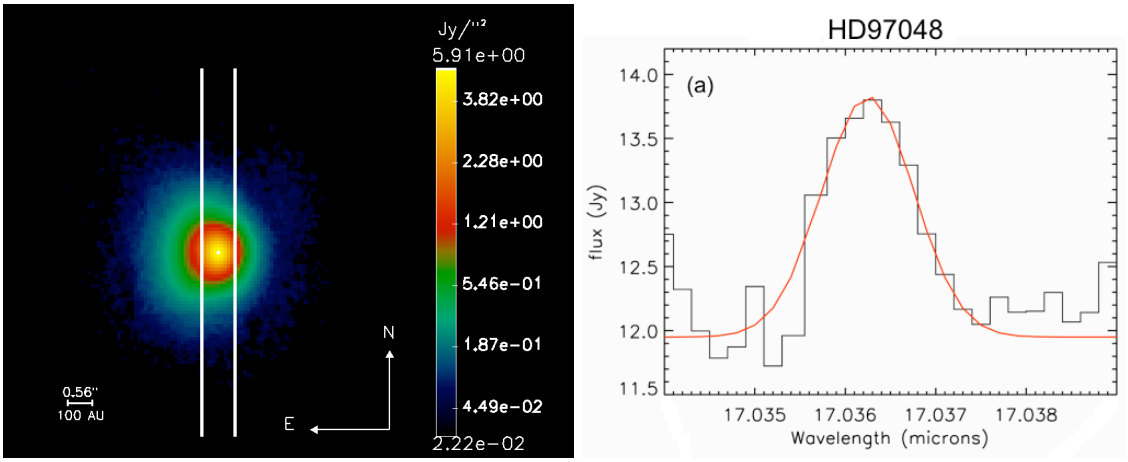

Figure 4.24: Left side: The PAH1 (8.6µm) image of HD 97048 with the 0.75 arcsec slit overplotted. Right side, the H_2 emission line detected at 17.0365 µm. The Full Width at Half Maximum of the lines corresponds to 30 km.s^{-}1 i.e. the measured spectral resolution of the spectrometer. The line is thus unresolved. It is however spatially located inside a raduis of 35 AU.

4.2 Perspectives : follow-ups of HD97048

The results on HD 97048 are the very first direct evidence of the flaring geometry of a protoplanetary disk. I have no doubts that future observations with more and more accurate instruments, especially in the mid-infrared range on large telescopes, will probably bring valuable insights in this domain (see Sec.6.4). In the meantime, several follow-ups can be performed already to test some hypothesis and obtain a better knowledge of this disk.

4.2.1 The warm CO and H_2 phase using CRIRES observations

We have proposed and obtained follow-up observations using CRIRES, the high-resolution near-infrared spectrograph on the VLT. The goal is twofold. First, we can probe the ro-vibrational H_2 emission line at 2.12 µm with an excellent spectral resolution and thus not only constraint the amount of hot gas, but also potentially measure its velocity structure. Fig.4.25 shows the spectrum of HD 97048 around 2.12 µm. The measured spectral resolution is about R∼60000 which corresponds to a speed of 5 km/s. The H_2 line is clearly detected and resolved. A simple gaussian fit of the line gives an equivalent width of 17 km/s (χ^2 =7.64 10^{-6}). However, given the asymmetric shape of the line, a better fit (χ^2 =4.95 10^{-6}) can be obtained by using a combination of 3 gaussian unresolved in velocity. The results are summarized in Tab.4.2. In any case, the line is resolved in velocity. In the first case (single gaussian fit) we would simply observe a single region within a radius of ∼40 AU. In the second case, the line would be built in 2 distinct regions. One would be very far away (1000 AU) and the second one would be a kind of "ring" at a distance of 45 AU from the star. However, in the later case, the questions of the asymmetry in amplitude between the red and the blue-shifted components remains open. The integrated flux is 1.427

$10^{-14} \pm 3\ 10^{-17}$ erg.cm^{-2}.s^{-1} which corresponds, when using the relation found in [Thi et al., 2001] to a mass of gas of ∼0.04 Earth masses when assuming a temperature of the gas of 1500 K. Whatever is the true situation, the most striking point here is the *strong* emission of hot H_2 at orbital distances larger than 10 AU. Indeed, in the context of a standard passive model ([Dullemond et al., 2001]) the H_2 gas at temperatures of few thousand K, necessary to emit the near- IR lines, it is expected to be confined in the inner parts of the disk only up to a few AU. This detection tells us that non-standard disk models have to be considered, e.g. with large disks atmospheres in which the dust and the gas components are decoupled and additional heating mechanisms are considered.

Table 4.2: Best fits of 2.12 µm H_2 emission line

Model	Amplitude (A.U.)	Center (nm)	Width (km/s)	χ^2
1 gaussian	0.01788	2121.8746±2e-4	17(2)	7.64 10^{-6}
3 gaussians	0.0239	2121.8781±2e-4	5(1)	4.95 10^{-6}
	0.0129	2121.8296±2e-4	5(1)	
	0.01089	2121.93±2e-4	5(1)	

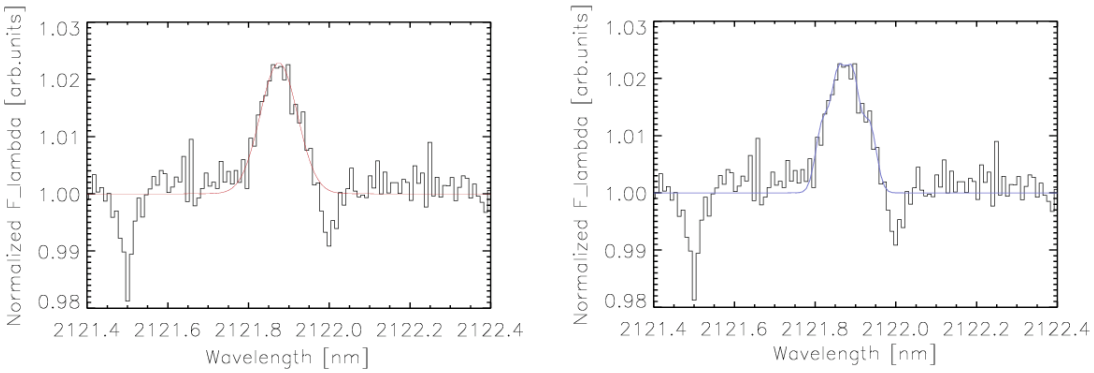

Figure 4.25: Upper right panel shows the PAH1 VISIR image (8.6µm) with overplotted the location of the 200 mas slit used for CRIRES observations. Upper left panels displays the 2.12µm ro-vibrational H_2 emission line detected in HD 97048. The spectral resolution of CRIRES at this wavelength is overplotted. Lower left: fit of the emission line using a single gaussian shape (χ^2=7.6e-6). Lower right: same as lower left but using a combination of 3 gaussian shapes (χ^2=5e-6). Errors in the widths are indicated in parenthesis.

4.2.2 Imaging in scattered light

As explained above, scattered light images are well suited to observe the external parts of the disks. Fig.4.26 shows in the middle panel the image of HD 97048 obtained with the HST/ACS coronograph. As seen, only the very outer parts can be observed. However, the use of a four-quadrants coronographic mask on large ground-based telescope allow to significantly extend the domain towards the star ([Boccaletti et al., 2004]). Moreover, the possibility to observe at different wavelength (J,H,K,L bands) allows a multi-wavelength analysis. Indeed, if dust seetling is occuring in the disk, the observed morphology shall change with the wavelength (because different wavelength as more sensitive to different

grains sizes). Following the same philosophy as [Duchêne et al., 2004] we have shown that in the context of dust settling, multi-wavelength observations between H and L band are an efficient and sensitive tool to assess dust settling and sedimentation in the HD 97048 disk. We have proposed therefore to make H, Ks, L' bands coronographic observations of HD 97048 (H and Ks using a four-quadrants phase mask). We have performed end-to-end state-of-art simulations of these observations by first simulating images at these wavelength thanks to the radiative transfer code MCFOST ([Pinte et al., 2006]). NACO coronographic observations have been then numerically simulated. Finally, representative noise corresponding to 30 minutes of observation has been included. The simulated Ks image is shown in the right panel of Fig.4.26. A combined analysis of H, Ks, L' bands has been performed on the simulated observations and is displayed on the lower plots. These plots show that this combination allows to disantangle between geometry, dust sizes and settling effects.

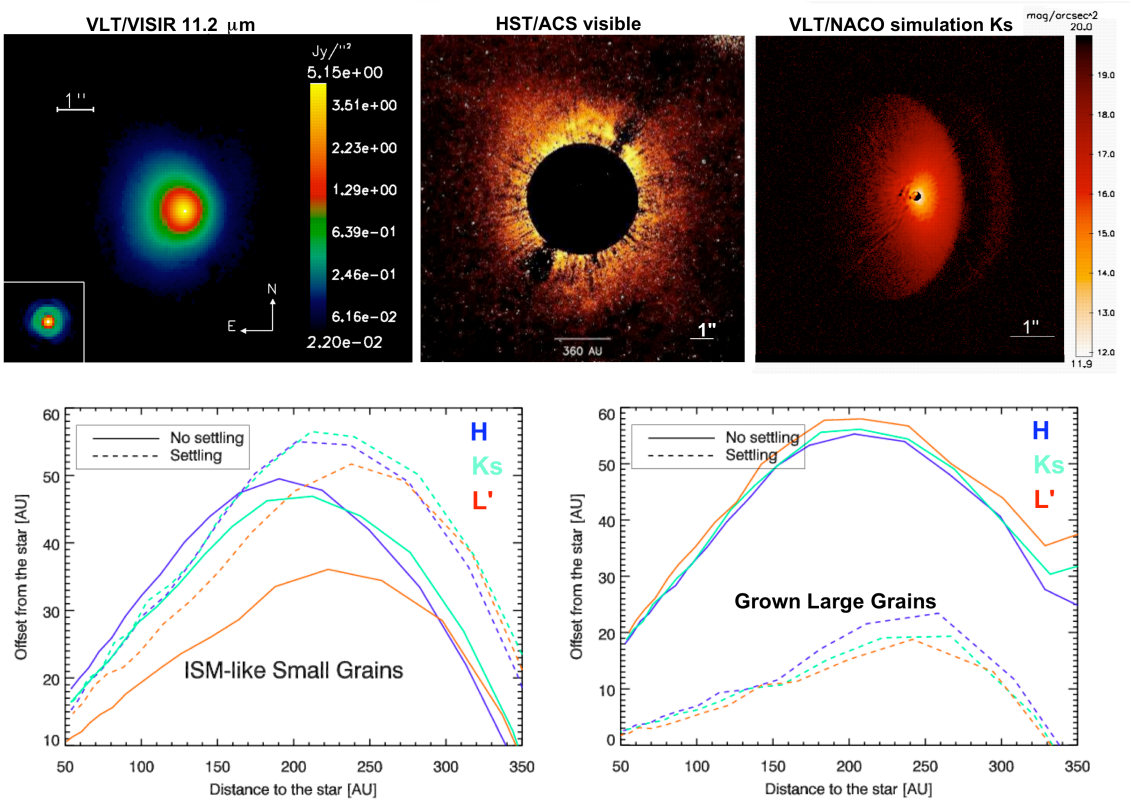

Figure 4.26: HD 97048 imaging. Upper panels from left to the right: PAH1 VISIR observed image, HST/ACS coronographic image in the visible range of the outer parts (r¿400 AU, [Doering et al., 2007]). VLT/NACO simulated coronographic image in Ks band. The linear scales in arcsec are indicated on each image for comparison. In the lower plots two cases are considered. In the first case, small ISM-like grains of maximum size of 0.1 µm are considered. In this case, the 3 bands H, Ks, L' are mandatory to disantangle between the settling and no settling case. In the case of "large" grains (up to 3 µm), a single observation would be sufficient.

4.2.3 The cold CO phase

As stated above [Thi et al., 2001] have successfully detected CO gas emission from similar, although probably slightly older, protoplanetary disks around intermediate-mass star. How much cold gas is

present in the HD 97048 disk, and at which distance is a question that can be first adressed through CO molecular emission observations in the sub-millitric range probing the midplane, cold regions, containing the bulk mass of gas. The flaring geometry of the HD 97048 disk indicates that large amount of gas are still present, suggesting that at an age of 1-3 Myr, the gas phase is not significantly depleted yet at large scales (more than 50 AU). The total amount of cold gas located in the disk midplane can be efficiently and **directly** studied using ^{12}CO combined with ^{13}CO observations. As shown in the case of similar objects ([Thi et al., 2001]), the CO lines can be resolved in velocity in some cases, allowing then to estimate the distance of the CO gas emission from the star. Combined with continuum millimeter observations (see above) these sub-millimetric CO observations will allow to estimate the gas-to-dust ratio of the dense midplane regions in the disk. A proposal has been submitted to ESO to use the APEX-2A facility to observe the CO emission. It had been ranked B and could not have been executed because of technical problems. This proposal has been re-submitted in period 83.

4.3 Conclusions

Our understanding on the protoplanetary disks has made very large progresses in the past 10 years. From a knowledge which was limited to detected infrared excesses interpreted as the presence of circumstellar matter we have reached a point where we are able to apprehend not only the fine details of the geometry of the disks geometry but also their composition that can vary with the distance to the star. Modern space-born or ground-based instruments are now achieving outstanding spatial resolutions which are so performant that we can nowadays discuss the existence of very fine details in the structure of protoplanetary disks ([Acke et al., 2005]).
We have shown in this chapter different aspects of possible contributions from mid-infrared observations in this field. However, the measurements we can make with mid-infrared instruments on 8m-class telescopes are somewhat limited both by the sensitivity and the angular resolution. The resolution needed to confortably study the finest details in these disks is around 5-10 AU (the typical size of a gap produced by giant planets has a width of the order of the orbital distance) which corresponds to an angular accuracy of $\sim$50 mas for typical distances of the nearest Ae stars (100-180 pc). Such angular resolutions will be achieved on extremely large telescopes (e.g. the European E-ELT of 42m, see Sec.6) at the explicit condition that considerations of costs do not shrink their sizes to “larger VLTs”.

Related articles

Annex

ADONIS observations of the HD 100546 circumstellar dust disk

published in the journal *A&A*, September 2000

Astron. Astrophys. 361, L9–L12 (2000)

ASTRONOMY AND ASTROPHYSICS

LETTER

Letter to the Editor

ADONIS observations of the HD 100546 circumstellar dust disk⋆

E. Pantin[1], **C. Waelkens**[2], **and P.O. Lagage**[1]

[1] DSM/DAPNIA/Service d'Astrophysique, CEA/Saclay, 91191 Gif-sur-Yvette, France
[2] Instituut voor Sterrenkunde, Celestijnenlaan 200B, 3001 Leuven, Belgium

Received 29 June 2000 / Accepted 15 July 2000

Abstract. We report in this letter the first resolved images of the circumstellar dust disk around the Pre-Main-Sequence star HD 100546. These near-infrared images were obtained in J and short K bands with the adaptive optics system ADONIS at the ESO observatory. A bright disk extending 2 arcsec (200 AU) far from the star and viewed with an inclination with respect to the line of sight around 50 degrees is revealed by the observations. Using a simplified model of light scattering, we find that the dust disk density peaks at a distance of 40 AU from the star, and the FWHM of this dense ring is typically 20 AU. This type of disk is believed to be a denser precursor of β Pictoris-like main-sequence disks. The structure of the disk is compared with the best known example of the class of "debris disks", the disk surrounding β Pictoris.

Key words: scattering – methods: data analysis – stars: binaries: eclipsing

1. Introduction

The discovery of infrared excesses around an important fraction of main-sequence stars (Aumann et al. 1984; Plets & Vynckier 1999) and attributed to the presence of cool dust grains orbiting the star and geometrically arranged in a disk, has triggered a lot of studies because these disks may be linked to planetary formation. For a long time the disk around the star β Pictoris was the only example to be resolved both in the visible (Smith & Terrile 1984) and in the mid-infrared range (Lagage & Pantin 1994). Recent discoveries of young "debris" circumstellar disks around relatively "old" and isolated (i.e. not associated to any star forming region) stars have shown that this phenomenon extends towards Pre-Main-Sequence stars (cf the photometric survey by Malfait et al. 1998a). The detection and resolution of disk around stars such as HD 141569 (Weinberger et al. 1999; Augereau et al. 1999) or HR 4796A thanks to high-resolution observations in the visible/near-infrared range (Schneider et al. 1999; Augereau et al. 1999) or mid-infrared images (Koerner et al. 1998; Jayawardhana et al. 1998) have shown the possibility to observe and study precursors to main-sequence dust disks. These so-called "baby-β Pic" dust disks are the denser precursors to main-sequence debris disks. IRAS and ISO/SWS observations have shown that they usually produce a huge infrared excess (typically 250 times the infrared excess produced by the β Pic disk); some of them, as HD 100546 for instance, showing prominent signatures of crystalline water ice (Waelkens et al. 1996, Malfait et al. 1998b), are particularly interesting targets in the visible/near-infrared because of high particle albedo. Observing this class of disks at various stages of evolution will help in finding a comprehensive scenario for the origin, the evolution, and the lifetime of the Vega phenomenon, i.e. how these disks form, how long they last, and how they disappear.

We report in this paper the first images of the disk around HD 100546, an isolated young main-sequence star. Using a model of scattering by dust grains, we derive the morphology of the disk outwards 10 AU and show evidence for a density maximum around 40 AU. The structure of the disk is compared to the best known example of the Vega Phenomenon, the disk around β Pic.

2. Observations

We observed the HD 100546 star (m_V=6.7) using the SHARP II+ camera coupled with the adaptative optics system ADONIS, and mounted on the ESO 3.6m telescope at La Silla, Chile. A pre-focal optics coronograph (Beuzit et al. 1997) was used to reject the direct starlight and increase the integration time in each elementary exposure. The mask size we used has a diameter of 0.74″. J (1.25 μm) and Ks (2.15 μm) band exposures were obtained on nights 23 and 24 of June, 1999. The seeing was quite variable the first night, but had decreased to a value of 0.7″ at the time of the J and Ks observations. It was stable at a value around 0.85″ during the second night. We spent a total observing time of 1550 s in the Ks band and 2600 s in the J band. The Point Spread Function (PSF) was frequently monitored thanks to interlaced observations of two reference stars, HD 97218 and HD 101713. These reference stars were used later in the reduction process to remove the wings of the stellar PSF and

Send offprint requests to: E. Pantin

⋆ based on observations collected on the ESO 3.6m telescope at La Silla, proposal 63.H-0239

Correspondence to: epantin@cea.fr

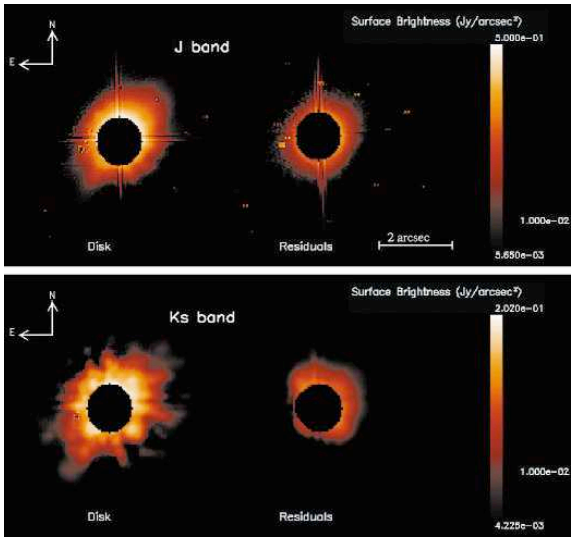

Fig. 1. Upper left: the disk seen in the J band, North is to the top, East to the left. The pixel scale is 0.035 arcsec/pixel. Upper right, the corresponding residuals obtained when applying the reduction method described in the text to two reference stars. Lower frame: same as upper frame but in the Ks filter. The "cross-like" pattern (with fingers orientations at 45,135,225, and 315 degrees) superimposed to the disk emission is produced by astigmatism residuals not corrected by the adaptive optics loop, showing that, contrarily to J band where the correction residuals are still dominated by the seeing, in Ks band under good conditions, one can reach high Strehl ratio values (i.e. system residuals dominating the uncorrected part of the seeing)

for photometric calibration. Observations of empty fields were also performed to estimate and remove the background flux which can be important in the Ks band.

3. Reduction procedure

First, standard reduction techniques were applied to the data: bias subtraction, flat-field correction. For each filter, we obtained a set of HD 100546 observations and corresponding PSFs. In spite of the use of a coronograph mask, the disk surface brightness is still dominated by the stellar emission at any distance from the star. In order to retrieve the disk image, one has to remove numerically the starlight wings. The rough substraction of a scaled PSF to HD 100546 images gives poor results because of slight shifts in position on the array between the reference and the object, uncertainties on the fluxes (given by the literature), and a residual background (ADONIS bench emission, different airmasses). We developed a specific method to get an optimum subtraction. For each couple of HD 100546 image (Obj) and corresponding Psf, we have to find 3 parameters: a shift (δx,δy) between the two images, a scaling factor R, and a residual background Bg. These parameters are estimated by minimizing the following error functional:

$$J = \sum |\mathrm{Obj} - S(\mathrm{Psf}/R, \delta x, \delta y) - Bg| \quad (1)$$

where the S function stands for image shift. The sum is performed on a set of pixels (typically 1000) located in a region of the images where no disk emission is expected, and from which non accurate ones are excluded (bad pixels, pixels belonging to area contaminated by diffracted light from the coronograph support). The functional minimum is found using a 0-order minimization algorithm called Powell method (Press 1996). The method was first checked on simulated data whose input parameters (shifts, scaling factor) were recovered with an accuracy better than 5%. In order to evaluate the errors in the subtraction process, test the stability of the PSF, and make sure that the disk obtained is not an artifact created by the process, the same substraction process was applied to the two different PSFs. Fig. 1 shows the resulting images in the J and Ks filters of the disk and the corresponding residuals between the two reference stars. The position of the star under the mask, and therefore the disk center is also carefully determined in this procedure thanks to offset observations (out of the coronograph mask) of the reference stars and the object.

4. Results

Since the dataset in J band is more accurate (because of a larger integration time, better observing conditions, and a better sensitivity of the whole system) than in Ks band, the geometrical parameters and the disk model are based on the J band image. We checked in a second step that the results are compatible with the Ks band data.

4.1. Disk geometrical parameters

Given a disk inclination with respect to the line of sight which is $\approx 45°$, we expect to observe some deviations from the perfect ellipse case. Indeed, particles relatively large with respect to the wavelength produce non-isotropic scattering. One simple way to reduce this effect is to symmetrize the disk i.e. construct an isotropic-like virtual disk by averaging the original disk image and its symmetrical image with respect to the major axis. Best ellipse fitting on this symmetrized images gives the following results:

- disk position angle on the sky of **37 ± 5** degrees with respect to east direction.
- ellipse major to minor axis ratio of 1.2 implying a disk inclination of **50 ± 5** degrees with respect to the line of sight (or from the edge-on case).
- disk extension: $\approx$ 2.0 arcsec from the star corresponding to a distance to the star around 200 AU (assuming a distance to the Earth of 103 parsecs (van den Ancker et al. 1998) and a limiting sensitivity of 5 mJy/arcsec^2.

4.2. Photometry

Using the stars HD 101713 (B9V) and HD 97218 (G8) as references whose V magnitude is known and using appropriate V-J and V-Ks color indices, we derived the following photometry for the disk in J and Ks band: a disk flux in J band of

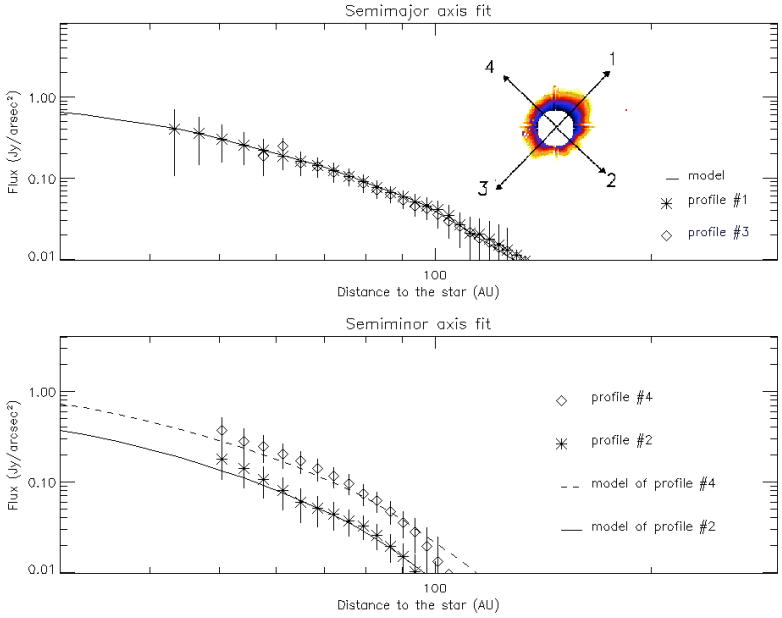

Fig. 2. Fit of the data profiles. Upper plot, full lines: the modeled profiles, stars and diamonds represent the data profiles 1 and 3 defined on the disk image inserted. Lower plot, dashed line: model of profile 4 (dominant forward scattering), plain line: model of profile 2. As seen on the lower plot, the scattering asymmetry is well reproduced by an anisotropic phase function (Henyey-Greenstein, see the text) with $g = 0.2$, corresponding to a particle size around 0.1 μm.

0.32 ± 0.06 Jy outside the coronograph mask and a maximum surface brightness of **0.5 ± 0.1** Jy/arcsec^2. From images of HD 100546 and corresponding reference star images (HD 101713 and HD97218) obtained when shifting the targets outside of the mask, we can deduce a total of scattered flux in the J band around 1 Jy; note that we get also a disk-shaped emission when removing a scaled reference to the HD 100546 image obtained outside the mask, but its signal to noise is very low. This result is compatible with the infrared excess computed considering a Kurucz model of the star (B9V spectral type). Consequently, the disk flux outside the coronograph mask represents roughly 30% of the total disk emission.

In the Ks band, we find an emission of **0.25 ± 0.1** Jy outside the coronograph mask and a maximum surface brightness of **0.25 ± 0.1** Jy/arcsec^2

4.3. Model and observation fit

In order to derive physical parameters of the disk, we built a numerical model of starlight scattering by an optically thin disk made of dust particles. Assuming that no multiple scattering is occurring in the disk, and since the exact physical properties of the particles are poorly known (composition, shape, size distribution), we chose to use a global, single-parameter, scattering phase function. The most practical one, although not realistic, is the Henyey-Greenstein phase function (Henyey & Greenstein 1941). The disk is assumed to be seen with an inclination derived above, and to have a proper thickness similar to the one of β Pic parameterized following Artymowicz et al. 1989. The disk midplane density is described by a scattering area which follows a series of broken power laws. We start with a first guess deduced from the radial surface brightness, and we iterate on the parameters until we obtain a satisfactory fit along the four directions defined on Fig. 2.

4.4. Fit results

The best fit model provides the following parameters (one must keep in mind that they are model-dependent):

- The Henyey-Greenstein phase function parameter found is g = **0.2** corresponding to dominant spherical particles with size around 0.1 micron.
- A radial normal optical thickness fitted by a series of broken power laws whose exponents are: 0.6 in the range [10,45]AU, −0.4 in the range [45,70]AU, −1.35 in the range [70,100]AU, −5 outwards from 100 AU, see Fig. 3.
- An exponentially decreasing vertical profile, and an opening angle around 0.1 radian.
- A total scattering area of 10^{29} cm^2 and a dust mass of 0.02 $M_\oplus$.
- An approximate disk surface density at maximum around **3 × 10^{14}** particles/m^2 assuming single-sized particles of 0.1 μm, or an equivalent maximum scattering area of the order of the unity/m^2.

5. Discussion

The radial surface brightness distribution shows that the disk density peaks at a distance of 40 AU from the star corresponding to the edge of the planetary zone in our solar system. The normal optical thickness found is more than 100 times larger than in the case of the β Pic disk. Simultaneously, the presence of sub-micronic particles sizes, well below the radiation pressure cut-off in sizes, suggests that huge quantities of very small

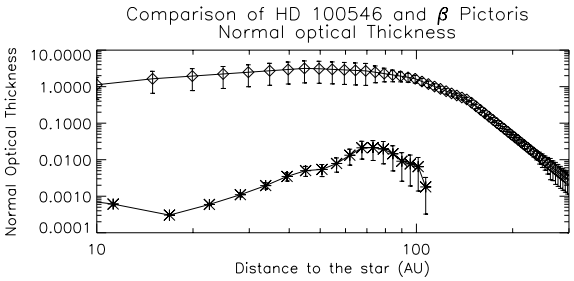

Fig. 3. The normal optical thickness of the disk deduced from model fitting of the data (diamonds). We have overplotted (stars) the normal optical thickness found in the case of the disk around β Pictoris (Pantin, Lagage & Artymowicz 1998)

particles are produced continuously by evaporation or collisions of planetesimals. We are probably witnessing a analogue of the young Kuiper belt with planetesimals undergoing violent agitation. If the dust particles are the result of collisions, a high rate is required to produce the observed disk. This implies that gravitational perturbations occur frequently in this disk, maybe because of giant planets. If the disk is replenished by planetesimal evaporation as suggested by Lecavelier des Etangs (1998) in the case of the β Pic disk, 10^9 planetesimals (40 km size) whose orbits were recently perturbed by planet migration are required to maintain the disk. Some of them which orbits are gravitationally perturbed might be the origin of the casual redshifted absorption profiles observed in some of the spectra of HD 100546 (Grady et al. 1997), a phenomenon highly similar to what is observed in the system of β Pictoris (Lagrange-Henry et al. 1987, Beust et al. 1996).

6. Conclusion

Thanks to coronograph adaptive optics observations we could detect the disk surrounding the PMS star HD 100546. This detection of a disk which is believed to represent a class of precursors to β Pic-like disks adds a new clue in the understanding of the formation and evolution of these debris disks. Other imaging observations of disks at various stage of evolution are necessary to sketch more closely the possible scenario of such a disk creation and evolution. This should be achieved by next generation instruments such as the VLT/NAOS (adaptive optics) and VLT/VISIR (mid-infrared) instruments or the NGST.

Acknowledgements. We would like to express our warm gratitude to the persons who helped in achieving these observations: D. Le Mignant, F. Marchis, O. Marco, V. Meriño, E. Wenderoth, and the whole 3.6m team.

References

Augereau, J. C., Lagrange, A. M., Mouillet, D., Papaloizou, J. C. B. & Grorod, P. A., 1999, A&A, 348, 557
Artymowicz, P., Burrows, C., & Paresce, F., 1989, ApJ, 337, 494
Augereau, J. C., Lagrange, A. M., Mouillet, D. & Ménard, F., 1999, A&A, 350, 51
Aumann, H. H. et al., 1984, ApJ, 278, L23
Beust, H., Lagrange, A.M., PLazy, F., & Mouillet, D., 1996, A&A, 310, 181
Beuzit, J.-L., Mouillet, D., Lagrange, A.-M. & Paufique, J., 1997, A&AS, 125, 175–182
Jayawardhana, R. et al., 1998, ApJ, 503, L79
Koerner, D. W., Ressler, M. E., Werner, M. W. & Backman, D. E., 1998, ApJ, 503, L83
Henyey, L.G. & Greenstein, J.L., 1941, ApJ, 93, 70
Lagage, P. O. & Pantin, E., 1994, Nature, 369, 628
Lagrange-Henry, A.M., Ferlet, R., & Vidal-Madjar, A., 1987, A&A, 173, 289
Lecavelier Des Etangs, A., 1998, A&A, 337, 501
Malfait, K., Bogaert, E. & Waelkens, C., 1998a, A&A, 331, 211
Malfait, K., Waelkens, C., Waters, L. B. F. M., Vandenbussche, B., Huygen, E. & de Graauw, M. S., 1998b, A&A, 332, L25
Pantin, E., Lagage, P. O. & Artymowicz, P., 1997, A&A, 327, 1123
Plets, H. & Vynckier, C., 1999, A&A, 343, 496
Press, W. H., 1996, in *Numerical Recipes*, Cambridge University Press
Schneider, G. et al., 1999, ApJ, 513, L127
Smith, B. A. & Terrile, R. J., 1984, Science, 226, 1421
van den Ancker, M. E.,de Winter, D. & Tjin A Djie, H. R. E., 1998, A&A, 330, 145
Waelkens et al., 1996, A&A, 315, L245
Weinberger, A. J. et al., 1999, ApJ, 525, L53

Annex

The AB Aurigae protoplanetary disk unveiled at 20.5 μm

published in the journal *A&A*, July 2005

A&A 437, 525–530 (2005)
DOI: 10.1051/0004-6361:20040448
© ESO 2005

Astronomy & Astrophysics

An emission ring at 20.5 μm around the HAEBE star AB Aurigæ: Unveiling the disk structure

E. Pantin[1], J. Bouwman[1,2], and P. O. Lagage[1]

[1] CEA/Saclay, DSM/DAPNIA/Service d'Astrophysique, 91191 Gif-sur-Yvette, France
e-mail: epantin@cea.fr
[2] Max-Planck-Institut für Astronomie, Königstuhl 17, 69117 Heidelberg, Germany

Received 14 October 2003 / Accepted 25 January 2005

Abstract. Isolated Herbig Ae/Be stars are believed to be a class of objects at an intermediate stage between young stellar objects surrounded by massive, optically thick, gaseous and dusty disks and Vega like stars surrounded by debris disks. The Herbig Ae star AB Aurigæ is already known for being surrounded by an intermediate-stage dust disk emitting a fairly large infrared and (sub-)millimetric excess. Until now, its outer disk structure has only been resolved at millimeter wavelengths and at optical and near infrared wavelengths with coronographic imaging. We have obtained 20.5 μm images which show an unexpected elliptical ring-like emission structure in the disk around AB Aurigæ at a distance of about 280 AU from the central star. This structure is characterized by a large azimuthal asymmetry in its brightness profile and an off-centered position with respect to the central star. To explain the observations, we propose a simple, purely geometrical model based on an emission ring with an uniform surface brightness, but having an intrinsic eccentricity. Our modeling of this ring-like structure provides valuable constraints on the inclination and the dust composition of the disk. Given the large distance from the central star, only transient heating of very small particles can explain the occurrence of the bright emission ring at mid-infrared wavelengths. Our observations point towards an unexpected geometry of the pre-main-sequence disk. In contrast to the usual sketch of a disk having a constant flaring angle, we argue that the circumstellar disk has a sudden, non uniform increase in the disk thickness. This sudden increase in the disk thickness as inferred by our modeling could be caused by disk instabilities. This suggests, together with the derived intrinsic eccentricity of the emission ring, the presence of a still undetected massive planetary type object, in an orbit at the outer-parts of the disk, disturbing the disk structure through gravitational interaction.

Key words. circumstellar matter – stars: formation – stars: pre-main-sequence

1. Introduction

Herbig Ae/Be (HAEBE) stars represent a class of intermediate mass, pre-main-sequence (PMS) stars, first described as a group by Herbig (1960). The circumstellar (CS) disks found around these stars are believed to be the sites of on-going planet formation. By studying the characteristics and evolution of the CS disk and its dust composition, valuable insights can be obtained into the processes leading to the formation of planets, and put constraints on disk and planet formation models. Infrared spectroscopy obtained with the Infrared Space Observatory (ISO) has given us insight into the dust composition of a sample of isolated HAEBE systems (e.g. Bouwman et al. 2000a, 2001; Meeus et al. 2001). While these spectra reveal a rich mineralogy, no direct information concerning the spatial distribution of the different dust species can be inferred from the ISO data. Most studies so far have used the available spectral energy distributions (SEDs) to put constraints on the spatial distribution of the CS material. Models for passively heated disks surrounding PMS stars are successful in reproducing the ISO spectra (e.g. Dullemond et al. 2001; Dominik et al. 2003), but these models cannot be uniquely constrained from SED fitting alone (e.g. Bouwman et al. 2000b). For this, spatially resolved imaging as presented in this paper is required.

Among the isolated HAEBE systems, the disk around AB Aurigæ is one of the most interesting and well studied objects. Its star has a probable age of 2 Myr (van den Ancker et al. 1997), indicating that, according to current planet formation theories, planet building could still being ongoing in this system. ISO spectra show strong emission bands from polycyclic aromatic hydrocarbons (PAH) molecules, and emission from various dust species such as silicates, and carbonaceous dust grains (van den Ancker et al. 2000; Bouwman et al. 2000a). Though the inferred grain sizes are differing from interstellar grains, the dust around AB Aur seems to be relatively unprocessed, indicating an evolutionary young system. This is also suggested by the combined ISO-SWS and submillimeter observations of H_2 and CO rotational lines, which demonstrate that the disk still has a large gas content (Thi et al. 2001). The AB Aurigæ disk has been resolved in the millimeter range by Mannings & Sargent (1997), showing a structure consistent with a Keplerian disk. Its surrounding nebulae and outer disk structure were also studied in the visible range

Article published by EDP Sciences and available at http://www.edpsciences.org/aa or http://dx.doi.org/10.1051/0004-6361:20040448

using broad-band coronographic observations (Grady et al. 1999), showing a disk with spiral-shaped structures. Similar spiral-like structures can also be seen in near-IR coronographic observations obtained with the Subaru telescope (Fukagawa et al. 2004). Near-IR interferometric observations (Millan-Gabet et al. 1999, 2001; Eisner et al. 2003) have resolved the inner parts of the disk. These observations are consistent with the model of a passive disk with an inner hole, seen at a low ($\leq$40°) inclination angle. Recent mid-IR imaging (Chen & Jura 2003), has also resolved the inner disk structure, showing it to originate from thermal emission from dust grains heated by the stellar radiation field near the central star. Here we present mid-IR imaging, not only resolving the thermal emission from dust close to the central star, but also showing an emission structure at the outer parts of the disk. In the next sections we will describe these observations, and propose a simple geometrical model explaining our results.

2. Data collection and reduction

The observations were performed using the CEA mid-IR camera CAMIRAS (Lagage et al. 1992), equipped with a Boeing 128 × 128 pixels BIB detector sensitive up to a wavelength of $\approx$28 μm. AB Aurigæ was observed from the CFH 3.6 m telescope on 1999 August 1 and between 2000 March 16 and March 20. During these two runs, seeing and weather conditions – humidity and amount of atmospheric precipitable water – were particularly favorable and extremely stable in time. We spent a total integration time on AB Aurigæ of 2 h split into several nights. Each dataset was reduced independently in order to avoid any erroneous conclusion due for instance to some corrupted dataset; it permits also to evaluate error bars on our results. The orientation of the array on the sky was carefully determined at the start of each observing run. The pixel size was 0.29″. In the 20 μm window, we used a filter centered at 20.5 μm and with a bandpass (*FWHM*) $\Delta\lambda$ = 1.11 μm. This filter is free of any important atmospheric line contribution. The source was always observed at an airmass of less than 1.3. Standard chopping and nodding techniques were applied with a chopping throw of 16″ North and nodding amplitude of 20″ West. A shift-and-add procedure was applied to each final cube of images using a correlation based method with a re-sampling factor of 4:1. In order to get the best spatial resolution in the dataset, the nodding direction was perpendicular to the chopping direction, resulting in an image containing four times the image of the source. The four sources were extracted and co-added using a cross-correlation method. Finally, each independent dataset was deconvolved separately before co-addition to produce the final image. The peak signal-to-noise ratio in the various datasets ranges from 225 to 255. The standard star α Tau was frequently monitored for further data photometric calibration and for PSF measurements. Because final co-added images are strongly limited in spatial resolution by the seeing and above all by the 3.6 m telescope diffraction-pattern (*FWHM* of 1.4″ at 20.5 μm), the use of deconvolution techniques is mandatory in order to recover the best spatial resolution in mid-IR images. We used the Multiscale Maximum Entropy Method developed by Pantin & Starck (1996) based upon wavelet analysis based on the concept of multiscale information. Shannon theorem prescription allows to pursue the deconvolution down to twice the pixel size, in this case down to $\approx$0.6″, and iterations are stopped according to the residual map (i.e. the data minus the re-convolved solution), which properties should be consistent with noise characteristics. Each epoch dataset was processed (including image deconvolution) independently in order to check the consistency of the results.

3. Results and discussion

3.1. Emission structures and photometry

After deconvolution, the 20.5 μm image of AB Aurigæ shows two main structures, as can be seen in the left panel of Fig. 1. The most striking one is a narrow ring-like structure slightly open (i.e. the flux is decreased by an order of magnitude) in the SW direction. It has a total flux of 2.7 ± 0.3 Jy (taking into account deconvolution errors) and is located at an average distance of 1.94″ (280 AU, assuming a distance of 144 pc) and with a typical width *FWHM* of 0.45″ (65 AU). The ring structure isophotes can be fitted by an ellipse with an eccentricity of 0.3 and position angle (with respect to the west direction) of 85°, offset by 0.2″ along the major axis in southward direction, compared with the central emission. The second structure, and brightest, with a total flux of 48.7 ± 5 Jy, is concentrated in the close vicinity of the star. By comparing AB Aurigæ and PSF profiles we find that the central emission is also resolved with a *FWHM* (diameter) of 3 pixels or 0.9″ (130 AU), probably due to thermally emitting dust grains in the inner regions of the circumstellar disk (note that the star emission ($\approx$4 mJy) is negligible at that wavelength).

3.2. Interpretation: Disk structure and the nature of the emitting grain population

Our images show in the inner parts of the disk a similar structure as reported by Chen & Jura (2003), which can be explained by thermal emission from either a disk and/or an envelope. In our schematic view of the disk thermal emission, the resolved inner structure corresponds to thermal emission of hot dust grains between about 10 AU to 65 AU from the star. At these distances the temperature of the dust grains is such that they emit efficiently thermal radiation at wavelengths around 20 μm. Table 1 list the emission properties of this central emission, assuming that it can be represented by a uniform brightness disk. We stress that our approach is only an approximation, and that we will discuss and model this emission from the inner regions extensively in a forthcoming paper.

Here we will concentrate on the intriguing ring-like structure at about 280 AU from the star. The first thing one can note is that thermal emission from grains in radiative equilibrium with he stellar radiation field can be discarded at such a large distance from the star. In these outer regions of the disk, the stellar radiation field will heat dust grains to temperatures of around a 100 K or less. Reproducing the observed flux from the emission ring with grains at these low temperature, would

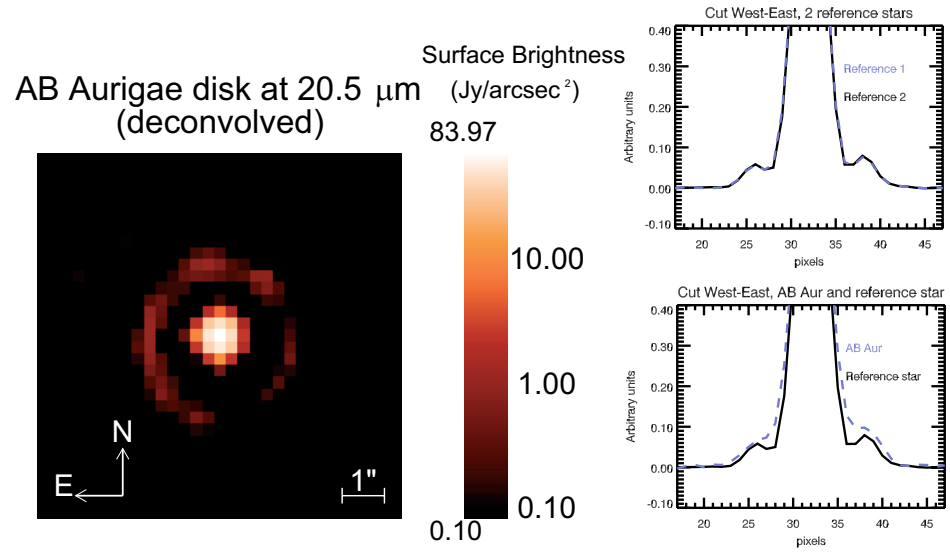

Fig. 1. Image of the AB Aurigae disk at 20.5 μm. The left figure shows the deconvolved image, with a pixel scale of 0.3″/pixel. Clearly visible is a resolved central emission region surrounded by a ring like structure. The panels on the right show the normalized intensity profiles along a cut through the CAMIRAS images of 2 reference stars and AB Aur. The upper right panel shows the comparison between two observations of reference stars, demonstrating the stability of the PSF. The panel on the lower right shows a comparison of AB Aur with the PSF, clearly showing that the central emission is extended and that a ring-like emission structure is also detected in non deconvolved data.

produce such a large flux at wavelengths in the range from 30 to 60 μm that it would be inconsistent with the spectrum as measured by ISO-SWS. Therefore, we must infer stochastically heated very small grains or big molecules like PAHs as the source of the ring-like emission. PAH molecules can be exited at large distances from the central star depending on the the stellar UV field. PAH bands were already found in the ISO-SWS spectrum of AB Aurigæ (van den Ancker et al. 2000; Bouwman et al. 2000a). According to Schutte et al. (1993) and Draine & Li (2001), large PAH molecules (or very small grains), consisting of a few thousand carbon atoms, can efficiently emit infrared radiation with a "plateau"-like spectral shape at around 20 μm. This would be a natural explanation for the observed narrow-band emission of ≈3 Jy at 280 AU from the star. Also, the relative band strength between the emission seen in our images and the PAH bands at shorter wavelengths as observed in the ISO-SWS spectra, is also consistent with the PAH emission models cited above.

The fact that the emission is arranged in a ring puts strong constraints on the disk geometry. In the following we call apparent or projected ellipse the ellipse directly seen on the 20.5 μm image. The most constraining feature of this ring-like elliptical structure is that it is *off-centered along the major axis of the projected ellipse*. In principle, inclining a circular structure leads to a projected elliptical structure that can be off-centered but always *along the apparent minor axis*. Also the systematic brightness variation along the ring is not symmetric with respect to the minor axis of the apparent ellipse (see also the left bottom panel in Fig. 2). This means that either this brightness variation is intrinsic to the ring or that the orientation of the inclination axis is not the same as the major axis of the apparent ellipse. This leads unavoidable to the conclusion that we are looking at an intrinsically elliptical structure seen under a small inclination angle.

Table 1. Best fit model parameters of AB Aur. Listed are the model parameters defining the system orientation, the ring emission and central emission region.

Parameter	Value	±	1σ error
System orientation†:			
Θ	65.699°	±	1.565°
i	−20.904°	±	1.002°
Ring parameters:			
e	0.135	±	0.0063
a	1.955″	±	0.0079″
Φ	123.46°	±	2.65°
ΔR	0.122″	±	0.0086″
H_0	0.469″	±	0.0563″
ΔH	0.177″	±	0.0158″
$I_{\rm ring}$	2.371 Jy arcsec^{-2}	±	0.116 Jy arcsec^{-2}
Parameters central emission:			
$R_{\rm center}$	0.427″	±	0.00122″
$I_{\rm center}$	89.035 Jy arcsec^{-2}	±	0.409 Jy arcsec^{-2}

† Angles are given in degrees counter clockwise with respect to the west direction (right direction).

To determine the main characteristics of the ring structure as seen in the CAMIRAS image of AB Aurigæ, we constructed a simple, geometrical model based on the deconvolved image. Since the inferred very small grains need stellar UV or visible

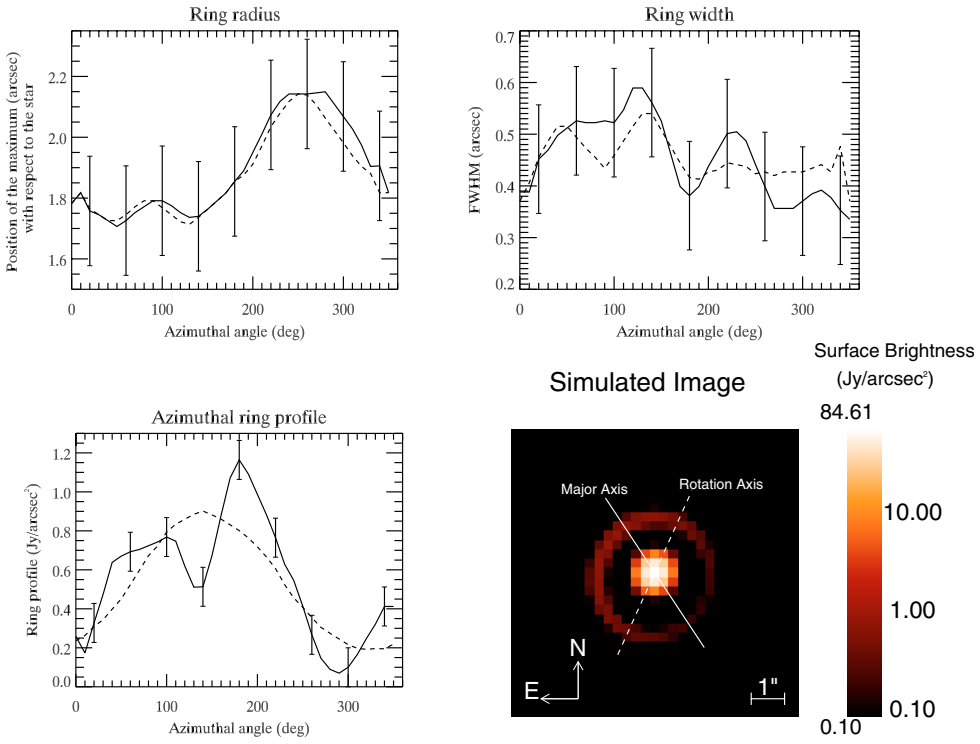

Fig. 2. The structure of the emission ring as an function of azimuth, compared with our best-fit model. Plotted are, *from left to right, top to bottom*, with the solid lines, the ring radius, its width (*fwhm*), and its intensity profile as a function of azimuthal angle (from the west direction, going counter clock wise). Over-plotted with dashed lines are the modeled ring radius, width and intensity profile. For the three solid line plots (data), the profiles have been smoothed by a 5 points (number of angle points being 36) boxcar in order to smooth high frequencies variations. The error bars indicate the formal 1σ error. Also shown is the best fit model image (*bottom right*) with overlaid the rotation axis (link to the disc inclination) and the major axis of the intrinsic ellipse described in Sect. 3.

photons to be excited, their emission most likely originates from the disk surface layer, i.e. the disk photosphere, being directly illuminated by the central star. To mimic this emission from the disk surface layer, we used a uniform brightness ring, with an eccentricity e, semi major axis a, and orientation Φ, radial width ΔR, scale-height H_0, vertical width ΔH, and surface brightness $I_{\rm ring}$. The ring model is positioned such that the central emission is in the focus of the ellipse. The central emission is modeled with a uniform brightness disk with radius $R_{\rm center}$ and surface brightness $I_{\rm center}$. Further, the disk model has a overall inclination i and orientation Θ. The thus constructed projection from this "infinite resolution" model is then convolved with a $\sigma = 0.15$ Gaussian filter to take into account the limited resolution of the deconvolved image (0.6″). Our best-fit model (using the 2D fitting procedure MPFIT2DFUN of IDL package written by Markwardt 2002) is shown in Fig. 2 and the resulting fit parameters are listed in Table 1. The parameter values and 1σ errors have been obtained using a so called "boot-strap" method. From the image shown in Fig. 1 we generated 100 additional images by adding Gaussian noise with a distribution corresponding to $1\sigma = 0.1$ Jy/arcsec^2 at each pixel. By performing the identical fitting procedure, resulting each time in slightly different model parameters, a distribution of fitted values for each of the model parameters is thus obtained. The resulting mean and standard deviation of these distributions are quoted in Table 1. We checked that the overall inverse modeling is correct by verifying that our solution also corresponds to a minimum of χ^2 in raw data (non deconvolved) space. Examples of the remaining residuals after subtracting model images from the raw data can be seen in Fig. 3. This excellent agreement between our model with both the deconvolved images as well as the raw data, shows the strength of modern deconvolution techniques. We would like to stress that in many cases model parameters can be degenerated, and many solutions are, therefore, possible. The only solution is to start with a model close to the real solution to avoid falling in a local minimum. In the case of AB Aurigæ this means that without image deconvolution, it would have been impossible to guess that are dealing with a narrow ring at 1.94″ from the star. The large intrinsic width of the PSF would have prevented this when using solely non-deconvolved images.

A sketch of the derived disk structure is shown in Fig. 4. The appearance of an emission ring can be linked to the disk geometry as follows: in a flaring disk model the amount of radiation intercepted, and thus emitted, is proportional to the angle at which the stellar light impinges onto the disk surface. This

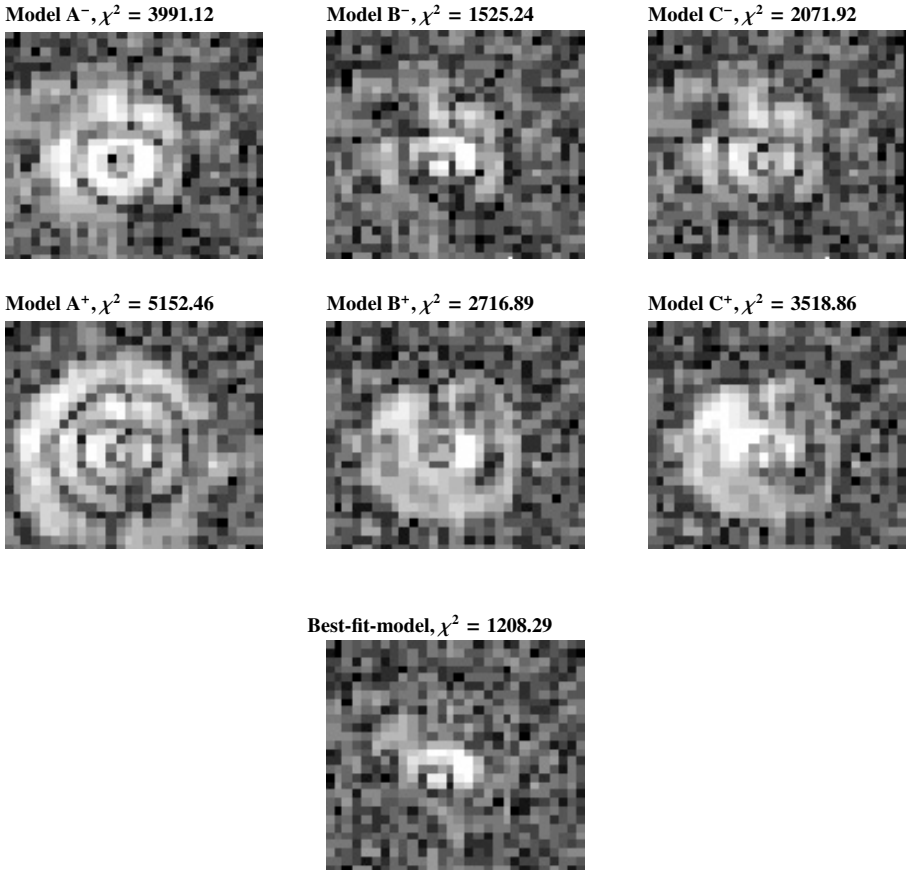

Fig. 3. Residual images of the (non deconvolved) AB Aurigæ observation minus model images. Shown are the residuals for three models (A, B, C), having identical model parameters as listed in Table 1 but with one parameter varied by 20%. The varied parameters for the three models are, respectively, the major axis a, the ring width ΔR and the ring intensity $I_{\rm ring}$. *The top panels* show the models with a minus 20% variation, the lower with a plus 20% variation. Also indicated above each figure is the resulting chi-square value. *The bottom panel* shows the residual for the best-fit model. One can notice that the residuals of the best-fit model still show some structures in the central regions of the disk. This means that our simple model (uniform disk) is not describing perfectly this region; more complex structures with possible offsets from the star will be investigated in a forthcoming paper.

angle is a factor of 15 (with the parameters found in the case of AB Aurigæ) larger at the ring surface compared to a uniform flaring (wedge) disk. This implies that a factor of 15 more light is intercepted and consequently emitted at the disk surface, lifting it above the detection limit of the CAMIRAS instrument. This large flaring angle of the disk surface can also explain the gap in the SW direction, as the disk surface becomes self shadowed when seen under a small inclination of $-20°$. This kind of "puffed-up" structure might be the result of gravitational disk instabilities like those suggested by Boss (2001, 2004) or the result of shadowing instabilities as reported by Dominik et al. (2003). Other possibilities to explain a sudden increase in brightness at a distance of 280 AU, could be:

- dust sizes segregation (Takeuchi & Lin 2003) but one must infer a very peculiar structure of the gaseous disk to reproduce the observations;
- PAH photo-dissociation, but it is unlikely to occur to the inferred population of large PAH molecules (e.g. Allain et al. 1996);
- an hollow spherical shell and its limb brightening, but it is difficult to explain the off-centering with this model.

Any proposed model must be able to explain the origin of the intrinsic eccentricity and off-centering of the emission ring A natural explanation for this could be the presence of a massive perturber on an eccentric orbit. Such an object might produce the detected deformations of the disk trough gravitational interaction. This could also be the explanation for the spiral-like structures seen in optical and near-IR coronographic imaging (Grady et al. 1999; Fukagawa et al. 2004). Given the large distance from the central star at which the emission ring occurs, it is unlikely for the perturbing companion to be a giant planet.

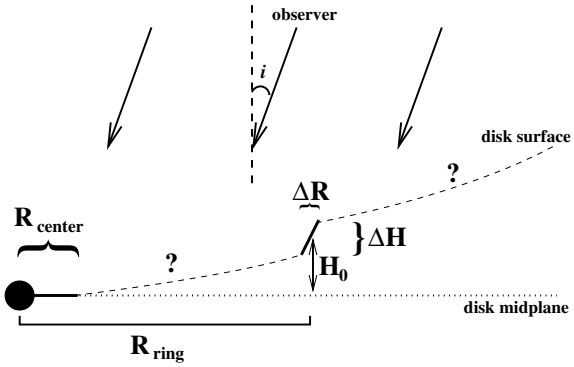

Fig. 4. Schematic representation of the disk structure in the AB Aur system. Drawn is the derived geometry of the disk surface. Indicated in the figure are the model parameters defining this geometry as listed in Table 1. $R_{\rm ring}$ is the distance to the star and varies between $a(1-e)$ and $a(1+e)$.

If the companion hypothesis is correct, it will most likely be a not yet detected brown dwarf.

4. Conclusions

We have presented in this paper a thermal infrared image at 20.5 μm of the AB Aurigæ dusty disk. The deconvolved image shows an inner resolved structure containing the majority (95%) of the thermal flux at this wavelength, together with an unexpected ellipsoidal, ring-like structure at an average distance of 280 AU from the central star. This large distance implies that this emission originates from stochastically heated, PAH like grains. The most interesting features of the ring are the large scale azimuthal asymmetry in its intensity profile and its off-centered position with respect to the position of the central star. When modeling the ring structure using a purely geometrical model (in which asymmetries are essentially produced by inclination and self shadowing effects in a flared disk), we have to conclude that we are observing an *intrinsically ellipse-shaped* ring. The appearance of the ring can be explained by a sudden increase in the scale height of the disk photosphere in an otherwise uniform flaring disk, leading to a kind of "wall-like" structure. This sudden increase of the flaring angle causes the disk to intercept more stellar light and consequently to emit more IR radiation, lifting the emission from the disk surface at the position of the ring above the detection limit of our observations. Disk instabilities perturbing the disk vertical thickness might produce such a structure. However, the origin of its intrinsic eccentricity and off-centered position remains unclear. A natural explanation could be the presence of a massive planetary object or brown dwarf on an elliptical orbit structuring the disk trough gravitational interaction. More detailed modeling and further observations, including higher resolution imaging in several PAH bands and spatially resolved mid-IR spectroscopy, are needed to fully understand the physics of this intriguing structure.

Acknowledgements. We are gratefully indebted to P. Masse, R. Jouan and M. Lortholary for their efficient assistance with the CAMIRAS instrument, A. Claret in efficiently supporting us in our observations, as well as to the staff of CFHT/Hawaii for their support during the observing runs. JB acknowledges financial support by the EC-RTN on "The Formation and Evolution of Young Stellar Clusters" (RTN-1999-00436, HPRN-CT-2000-00155) The observations preparation was done using the SIMBAD database.

References

Allain, T., Leach, S., & Sedlmayr, E. 1996, A&A, 305, 602
Boss, A. P. 2001, ApJ, 563, 367
Boss, A. P. 2004, ApJ, 610, 456
Bouwman, J., de Koter, A., van den Ancker, M., & Waters, L. 2000a, A&A, 360, 213
Bouwman, J., de Koter, A., van den Ancker, M., & Waters, L. 2000b, in Thermal Emission Spectroscopy and Analysis of Dust, Disks, and Regoliths, ASP Conf. Ser., 196, 63
Bouwman, J., Meeus, G., de Koter, A., et al. 2001, A&A, 375, 950
Chen, C. H., & Jura, M. 2003, ApJ, 591, 267
Dominik, C., Dullemond, C. P., Waters, L. B. F. M., & Walch, S. 2003, A&A, 398, 607
Draine, B. T., & Li, A. 2001, ApJ, 551, 807
Dullemond, C. P., Dominik, C., & Natta, A. 2001, ApJ, 560, 957
Eisner, J. A., lane, B. F., Akeson, R. L., Hillenbrand, L. A., & Sargent, A. I. 2003, ApJ, 588, 360
Fukagawa, M., Hayashi, M., Tamura, M., et al. 2004, ApJ, 605, L53
Grady, C. A., Woodgate, B., Bruhweiler, F. C., et al. 1999, ApJ, 523, L151
Herbig, G. H. 1960, ApJS, 4, 337
Lagage, P. O., Jouan, R., Masse, P., Mestreau, P., & Tarrius, A. 1992, in Progress in Telescope and Instrumentation Technologies, 601
Mannings, V., & Sargent, A. I. 1997, ApJ, 490, 792
Markwardt, C. 2002, Markwardt IDl programs, `http://cow.physics.wisc.edu/~craigm`
Meeus, G., Waters, L., Bouwman, J., et al. 2001, A&A, 365, 476
Millan-Gabet, R., Schloerb, F. P., Traub, W. A., et al. 1999, ApJ, 513, L131
Millan-Gabet, R., Schloerb, F. P., & Traub, W. A. 2001, ApJ, 546, 358
Pantin, E., & Starck, J.-L. 1996, A&AS, 118, 575
Schutte, W. A., Tielens, A. G. G. M., & Allamandola, L. J. 1993, ApJ, 415, 397
Takeuchi, T., & Lin, D. N. C. 2003, ArXiv Astrophysics e-prints
Thi, W. F., van Dishoeck, E. F., Blake, G. A., et al. 2001, ApJ, 561, 1074
van den Ancker, M., Bouwman, J., Wesselius, P., et al. 2000, A&A, 357, 325
van den Ancker, M. E., The, P. S., Tjin A Djie, H. R. E., et al. 1997, A&A, 324, L33

Annex

Mid-infrared imaging of the circumstellar dust around three Herbig Ae stars: HD 135344, CQ Tau, and HD 163296

published in the journal *A&A*, December 2006

A&A 460, 117–124 (2006)
DOI: 10.1051/0004-6361:20054371
© ESO 2006

Astronomy & Astrophysics

Mid-infrared imaging of the circumstellar dust around three Herbig Ae stars: HD 135344, CQ Tau, and HD 163296⋆

C. Doucet[1], E. Pantin[1], P. O. Lagage[1], and C. P. Dullemond[2]

[1] AIM, Unité Mixte de Recherche CEA – CNRS – Université Paris VII – UMR 7158, DSM/DAPNIA/Service d'Astrophysique, CEA/Saclay, 91191 Gif-sur-Yvette, France
e-mail: doucetc@cea.fr
[2] Max-Planck-Institut fur Astronomie Heidelberg, Konigstuhl 17, Heidelberg, Germany

Received 18 October 2005 / Accepted 22 August 2006

ABSTRACT

Aims. Planet formation has been known for many years to be tied to the spatial distribution of gas and dust in disks around young stars. To constrain planet formation models, imaging observations of protoplanetary disks are required.
Methods. Given this, we have undertaken a mid-infrared imaging survey of Herbig Ae stars, which are pre-main sequence stars of intermediate mass still surrounded by a large amount of circumstellar material. The observations were made at a wavelength of 20.5 μm with the CAMIRAS camera mounted at the Cassegrain focus of the Canada France Hawaii Telescope.
Results. We report the observations of three stars, HD 135344, CQ Tau, and HD 163296. The circumstellar material around the three objects is spatially resolved. The extensions feature a disk-like shape. The images provide direct information on two key parameters of the disk: its inclination and its outer radius. The outer radius is found to be quite different from the one deduced from disk models, which is only constrained by fitting the Spectral Energy Distribution of the object. Other parameters of the disk, such as flaring and dust mass have been deduced from fitting both the observed extension and the spectral energy distribution with sophisticated disk models.
Conclusions. Our results show how important imaging data are to tighten constraints on the disk model parameters.

Key words. circumstellar matter – stars: formation – stars: pre-main-sequence – stars: individual: HD 163296 – stars: individual: CQ Tau, stars: individual: HD 135344

1. Introduction

The formation of circumstellar disks is a natural outcome of the star formation process by which a molecular core collapses to form a star (Shu et al. 1987). Circumstellar disks can outlive the period during which stars form and still be present when the star is in its Pre-Main-Sequence (PMS) phase. In these disks, composed of gas and dust, various physical processes can lead to the growth of dust grains and eventually to the formation of planets. Understanding the physical conditions that prevail in these objects is of crucial importance when studying planet formation.

The study of circumstellar disks is a rapidly developing field, both from the observational and the modeling points of view (e.g., Natta 2004, and references there-in). The Infrared Space Observatory (ISO) has given clues about the dust composition of a sample of isolated HAeBe systems (Bouwman et al. 2001; Meeus et al. 2001). While these spectra reveal the composition of the dust, no direct information concerning the spatial distribution of the different dust species can be inferred from the ISO data. Most studies so far have used the Spectral Energy Distributions (SEDs) to put constraints on the spatial distribution of the circumstellar material.

Models of protoplanetary disks are increasingly successful at accounting for much of the observed properties. For instance, they can justify that disks' SEDs are generally rather flat in νF_ν, where ν is the frequency and F_ν the flux (Kenyon & Hartmann 1987). Furthermore, models can explain that dust features are almost all seen in emission (Calvet et al. 1991; Chiang & Goldreich 1997, hereafter CG97), reveal the presence of a near-infrared excess in the SEDs of Herbig Ae stars (Natta et al. 2001; Dullemond et al. 2001, hereafter DDN01), and interpret the differences observed in the far-IR excesses (Dullemond et al. 2002; Dullemond & Dominik 2004). Fitting the SED only allows us to make conjectures about the disks' geometrical apparearance; spatially resolved imaging data of those disks are absolutely necessary to verify theories and models' assumptions. For instance, key parameters, such as the disk surface density profile with radius, are still very poorly constrained when fitting SEDs.

Mid-infrared imaging observations from a large ground-based telescope are potentially well suited to bringing spatial information on disks around Herbig Ae (HAe) stars. HAe stars represent the middle stage of PMS evolution of intermediate-mass stars (~2–3 $M_\odot$); they are bright enough to heat sub-micron dust grains at 100 AU to a temperature of about 150 K. Grains at such a temperature have their peak of thermal emission in the mid-InfraRed (mid-IR). The diffraction limited angular resolution achievable with a 3.6 m class telescope in the mid-IR, 0.6/1.2 arcsec at 10/20 μm, corresponds to a distance of 60/120 AU for a star located at a typical distance of 100 pc,

⋆ Based on observations obtained at the Canada France Hawaii Telescope (CFHT), which is operated by the national Research Council of Canada, the Institut National des Sciences de l'Univers of the Centre National de la Recherche Scientifique of France, and the University of Hawaii.

Article published by EDP Sciences and available at http://www.aanda.org or http://dx.doi.org/10.1051/0004-6361:20054371

Table 1. Properties of the three Herbig Ae stars observed with the CAMIRAS mid-InfraRed camera. First two columns: coordinates of the objects (right ascension and declination); third column: their spectral type; fourth column: their distance, as deduced from Hipparcos data; fifth column: flux in the IRAS 25 μm band; sixth column: flux at 20 μm obtained in this paper; seventh column: age of the objects in Myr.

Object	RA (2000)	Dec (2000)	Spectral type	Distance (pc)	F_{25} (Jy)	F_{20} (Jy)	Age (Myr)	References
HD 135344	15 15 48.4	–37 09 16	F4V	140^{+42}_{-42}	6.7	5 ± 1	8 ± 4	1, 2, 4, 8, 10, 11
HD 163296	17 56 21.4	–1 57 20	A3Ve	122^{+13}_{-16}	21	18 ± 4	7 ± 5	3, 4, 5, 11, 12
CQ Tau	05 35 58.4	+24 44 54	A1-F5IVe	100^{+25}_{-17}	20.6	23 ± 3	10	6, 7, 9, 12

References: (1) Coulson et al. (1998); (2) Dominik et al. (2003); (3) Jayawardhana et al. (2001); (4) Meeus et al. (2001); (5) Mannings & Sargent (1997); (6) Mannings & Sargent (2000); (7) Natta et al. (2001); (8) Sylvester et al. (1996); (9) Testi et al. (2001); (10) Thi et al. (2001); (11) van Boekel et al. (2005); (12) van den Ancker et al. (1998).

and thus allows for a relatively good sampling of disks whose sizes range up to several hundreds of AU. The first attempts to resolve the spatial structure of the circumstellar material around HAe stars were performed with multi-aperture observations with a single bolometer; emissions extending up to large distances from the star (more than 5 arcsec) were found around 3 objects HD 97048, HD 97300, and HD 176386 (Prusti et al. 1994). Such extended emissions were attributed to the emission from large molecules and small grains transiently heated by starlight and distributed in a dust shell with a large inner radius, probably a remnant from the cloud from which the star was born. It is only with the advent of mid-IR cameras that the full potential of mid-IR observations to study disk structures was achieved. Single dish observations have revealed the disk structure in the 500 AU (Astronomical Units) range around two HAe stars: AB Aur (Marsh et al. 1995; Pantin et al. 2005) and HD 100546 (Grady et al. 2001; Liu et al. 2003). Interferometric observations have allowed for the probing of the innermost regions of the disk (1–10 AU), and numerous objects have been observed (Millan-Gabet et al. 2001; Tuthill et al. 2002; Wilkin & Akeson 2003; Leinert et al. 2004; Liu et al. 2005). Mid-IR single dish observations have now clearly demonstrated in a few examples that they can provide unique information on the disk structure, although the constraints brought on the disk modeling by such spatial information have not yet been fully exploited.

In this paper, we are interested in both increasing the number of HAe for which information on the mid-IR spatial extension is available, and in using this information, in combination with the already existing SED measurements between 1 and 100 μm, to constrain the parameters of the disk models developed these last years. The paper is organized as follows: the observations and data reduction are described in Sect. 2. Section 3 deals with the results, in terms of spatial extensions. In Sect. 4, a first, simple approach is used to establish the disk inclination, and in Sect. 5, we describe the 2-D radiative transfer code used to reproduce the observations. A discussion of the results follows in Sect. 6. Conclusions are drawn in Sect. 7.

2. Observations and data reduction

We have observed a sample of three Herbig Ae stars: HD 135344, CQ Tau, and HD 163296. Table 1 presents the main stellar parameters of the sample. The objects were selected from the catalogue of Thé et al. (1994) and Malfait et al. (1998) according to the following criteria: the objects are bright in the mid-IR, relatively close, and isolated, i.e., not associated with extended diffuse emission due to the parental cloud.

CQ Tau is located at a distance of 100^{+25}_{-17} pc and has an age of 10 Myr (Natta et al. 2001; van den Ancker et al. 1998). HD 163296 is at a distance of 122^{+13}_{-16} pc and has an age of 7 ± 5 Myr (van Boekel et al. 2005). The distance and age of HD 135344 are more controversial. Until 2001, a distance of 84 pc (Meeus et al. 2001) with an age of 17 ± 3 Myr (Thi et al. 2001) were used for this object. But, in a recent paper (van Boekel et al. 2005), the distance was re-evaluated to 140 ± 42 pc and the age to 8 ± 4 Myr; these latter values will be used in the following.

The observations were performed with the mid-IR camera CAMIRAS (Lagage et al. 1992) installed as a visiting instrument at the Cassegrain focus of the Canada France Hawaii Telescope (CFHT). The camera is equipped with a Boeing 128 × 128 pixels Blocked Impurity Band (BIB) detector sensitive up to a wavelength, λ, of ∼27 μm. A filter centered at 20.5 μm with a Full Width Half Maximum (FWHM) bandpass, $\Delta\lambda$, of 1.11 μm was used. The Pixel Field of View (PFoV) on the sky was 0.29 arcsec; such a PFoV provides a good sampling of the diffraction pattern, which is of 1.5 arcsec FWHM.

The objects were observed between March 18, 2000 and March 24, 2000. During the run, seeing and weather conditions were extremely favorable and stable in time. HD 163296 and CQ Tau were observed at a median airmass of 1.4, and HD 135344 at an airmass around 1.9, which is the best achievable when observing from CFHT. Standard chopping and nodding techniques were applied to suppress atmosphere and telescope background emissions; the chopping throw was 16 arcsec to the North and the frequency used was 3.33 Hz; the nodding amplitude was 20 arcsec to the West. The nodding direction was perpendicular to the chopping direction, to get the best spatial resolution; given the low chopping and nodding throw and the field of view of the camera, the source always remained within the detector field of view and the obtained images thus contain 4 beams (2 positive, 2 negative). Given the huge photon background in the mid-IR, the elementary integration time was set to 15 ms, and the images were co-added in real time to store only two co-added images (one for each chopping position) every second.

The basic data reduction is standard. The data cubes of one observation are carefully stacked with the rejection of corrupted planes. A shift-and-add procedure is applied to each cube of images using a correlation based method with a re-sampling factor of 8:1. The four beams are then combined in one image by a source extraction algorithm followed by a shift-and-add procedure. Finally, flux calibration is achieved via aperture photometry of a set of photometric standard stars such as αTau, αBoo, βGem, or γDra (Cohen et al. 1999). The photometry gives a total flux of 6.3 ± 0.6 Jy for HD 135344, 23 ± 3 Jy for CQ Tau, and 18 ± 4 Jy for HD 163296, in good agreement with the IRAS values (Table 1).

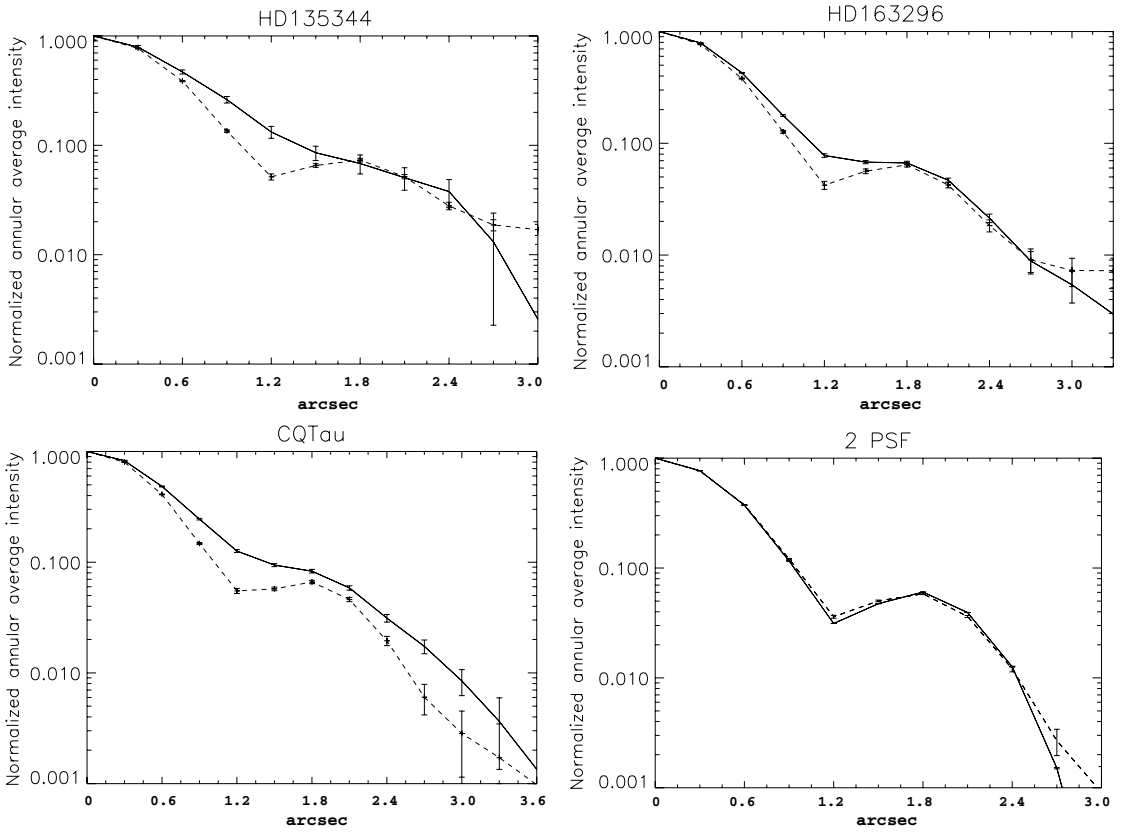

Fig. 1. Annular averages intensity aperture for the source (solid line) and PSF (dashed line) normalized to the peak value, as a function of radius. The errors drawn are 1 σ-errors rms. The reference star for HD 135344 is α Boo, for HD 163296 γ Dra, and for CQ Tau, β Gem. The plot labeled "2 PSF" shows two reference stars, α Boo and γ Dra, as observed on the March 24, 2000. Although the two reference stars have very different fluxes (γDra with 43 Jy and α Boo with 170 Jy, Van Malderen et al. 2004), the two profiles are similar.

3. Extended emission

The three objects of the sample are spatially resolved. This can be seen in Fig. 1 where we have compared the average annular profile of the object with those of the Point Spread Function (PSF), obtained from the observation of a reference point-like star. Extended emission is detected up to 100–300 AU.

We carefully checked that the observed extensions are not artifacts, but the result of true extended emission from the objects. Several arguments lead us to reject explanations of the extensions in terms of temporal variations of the PSF between the observation of the object and the observation of the reference star. One possible cause of such temporal PSF variations could be variations of the seeing. This hypothesis is however rejected for the following reasons. First, concerning the limitations of the spatial resolution, the seeing contribution at 20.5 μm is negligible with respect to the diffraction: for a typical seeing value of 0.8″ FWHM in the visible range, one can estimate a seeing contribution at 20.5 μm around 0.4″, when using the $\lambda^{(-1/5)}$ scaling law; thus, seeing induces PSF changes of the order of 1 pixel FWHM, which is much smaller than the widths of observed extensions. Secondly, the seeing was quite stable during the observations; thus we estimated seeing variation effects to be much lower than one pixel. Note also that two of the objects were observed during different nights. HD 135344 was observed for four different nights: on March 18, 2000 (exposure time 6 mn), on March 19 (exposure time: 3 mn), on March 21 (exposure time: 6 mn), and on March 24, (exposure time: 2 mn 30). Its extension is confirmed over the 4 nights. CQ Tau was observed during 2 different nights on March 20, and on March 21 (respectively, with 3 and 6 mn of integration time) and is spatially extended in both datasets. HD 163296 was observed only once (exposure time: 3 mn) on March 24.

Another possible source of fake extensions could be chromatic effects. Indeed, HAe stars have large infrared excesses, and thus have SEDs quite different from that of the PSF reference stars. Any filter leak, either on the blue or on the red side of the nominal filter bandpass, would then potentially lead to PSF variations between point-like HAe objects and PSF reference stars. We double-checked the filter transmission at the operating temperature of the filter (10 K) using a Fourier Transform Spectrometer with a spectral resolution of 4 cm^{-1}. The rejection rate outside the filter bandpass is typically better than 10^{-3}. We simulated the PSF variations due to such a filter using the mid-IR spectra of the objects obtained with ISO (Meeus et al. 2001) for two of the three extended objects; (CQ Tau was not observed by ISO SWS). The simulated PSF variations lead to some extended emission, but much fainter than observed, both in intensity and in spatial extension. Thus, an explanation of the

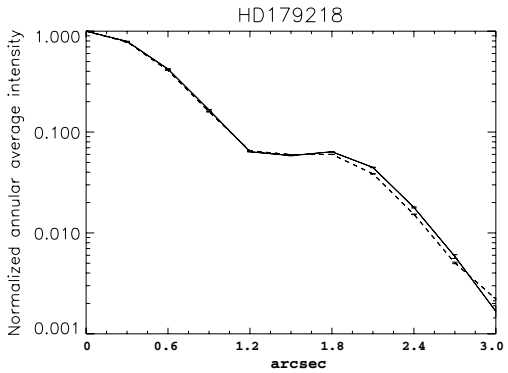

Fig. 2. Same as Fig. 1, to make a comparison with HD 179218 for which there is no extended emission detected.

observed extensions in terms of chromatic variations of the PSF can be discarded.

Note also that not all the HAe stars observed are extended. To make a comparison, a far away HAe star, with a similar (even greater) IR excess, HD 179218 located at 240 pc (Meeus et al. 2001), was observed. This object does not show extended emission at 20.5 μm (Fig. 2). This is an additional argument to conclude that the extension observed in HD 135344, CQ Tau, and HD 163296 is really due to an extended emission from the objects.

4. Inclination of the disk

Extensions around two out of the three objects, namely CQ Tau and HD 163296, were already observed at other wavelengths. Testi et al. (2001) have resolved the emission around CQ Tau at 7 mm and concluded that it was compatible with a disk-like geometry. Grady et al. (2001) have obtained coronographic images of HD 163296 with the Space Telescope Imaging Spectrograph on board the *Hubble Space Telescope*, which revealed a circumstellar disk with a radius of 450 AU. Therefore, our modeling of the extensions seen in the mid-IR range assumes a priori a disk-like geometry.

Disks inclinations can be relatively easily determined if their emissions are spatially resolved. However, HAe disks are generally dominated in the mid-IR by the innermost regions (1–30 AU). Our goal was to detect the emission from the *intermediate* regions of the disks (30–200 AU). The disk emission can be decomposed, in our image, into a central *unresolved* component plus an extended one (whose geometry should reflect the true disk geometry at the distance scales achievable for our data). We first removed the "point-like" central emission component by subtracting a scaled PSF from the image of the object. The parameters of the point-like component (intensity, position) were computed automatically using a penalty functional (to avoid any visual bias) and then cross-checked visually using a dedicated graphical interface built in IDL. The resulting image, called *residuals*, is free from the central emission, so that the extended emission is enhanced and it is easier to determine the disk geometry. For each target, this processing was done using all available PSF measurements. The errors on the putative extensions were assessed when applying the same procedure to two PSF reference stars and, when possible, when comparing the extensions obtained from different nights. The results are shown in Figs. 6–8.

Table 2. Parameters of the elliptical fit of the image. In the first column, the inclination of the disk (0 degree means a faced-on disk). The position angle (PA) of the disk on the sky is measured counter-clockwise from the North. The distance corresponds to the maximum distance at which the disk is detected in the 20 μm observations. The brightness level in the last column corresponds to the brightness of the maximum distance at which the disk is detected here.

	i (deg)	PA (deg)	Distance (AU)	Brightness level (mJy/″2)
HD 135344	46 ± 5	100 ± 10	210	170
HD 163296	60 ± 5	105 ± 10	215	135
CQ Tau	33 ± 5	120 ± 10	290	129

The first result is the elliptical shape of the extensions, which is characteristic of the emission of disks inclined with respect to the line of sight. An ellipse fit of the residuals gives an estimate of the disks' inclinations and position angles. The results in terms of inclination and position angles are shown in Table 2.

The inclination of 33° ± 5 found here for CQ Tau is in the middle range of values found in the literature, which range from 63° (Testi et al. 2001) to 14° (Dent et al. 2005); in between we can find $48^{\circ}{}^{+4^{\circ}}_{-3^{\circ}}$ (PA = 105° ± 5) (Eisner et al. 2004).

For HD 163296, the disk inclination of 60° ± 5° is in good agreement with that found by Mannings & Sargent (1997) of 58°. Concerning the position angle of the disk, Mannings & Sargent (1997) found 126° ± 3 with CO observations, and Grady et al. (2000) found 140° ± 5 thanks to optical coronographic images. We found a value of 105° ± 10 when fitting our mid-IR data. This difference in the position angle could be related to the fact that our data are only sensitive to warm dust whose geometry could slightly differ from that seen at shorter or longer wavelengths, if the disk contains, for instance, non axisymmetric structures.

5. Modeling

We used a relatively simple parameterized model to investigate the dependence of the emission in the mid-IR on each parameter. We consider disks heated by irradiation from the central star. The density profile of the gas is parameterized as a function of r (radius) and z (vertical height above the disk mid-plane):

$$\rho(r,z) = \frac{\Sigma(r)}{\sqrt{2\pi}H_p(r)} \exp\left(-\frac{z^2}{2H_p(r)^2}\right) \quad (1)$$

and it is assumed that the dust is well mixed with the gas. The surface density is assumed to follow a power-law in radius: $\Sigma(r) = \Sigma_0(r/r_0)^{-p}$, with r_0 a fiducial radius. The scale height of the disk $H_p(r)$ is also assumed to be a power-law: $H_p(r) = H_0(r/r_0)^q$. The inner radius of the disk ($r = R_{\rm in}$) is located at the dust evaporation radius (1400–1500 K for silicate dust). The inner boundary (rim) is directly exposed to the stellar flux and is puffed up since it is hotter than the rest of the disk. Here, we mimic the puffing-up of the rim predicted by DDN01 by a specified value of $H_{p,\rm in}$ at $r = R_{\rm in}$, which is a parameter of the model. It should be noted that whether such an inner rim is indeed puffed-up is still a matter of debate. Moreover, Isella & Natta (2005) have shown that the rim is probably rounded-off due to the density-dependence of the dust sublimation temperature. This effect is not included here.

For the dust opacities, we use those of Draine & Li (2001). We use a MRN (Mathis et al. 1977) distribution of grains

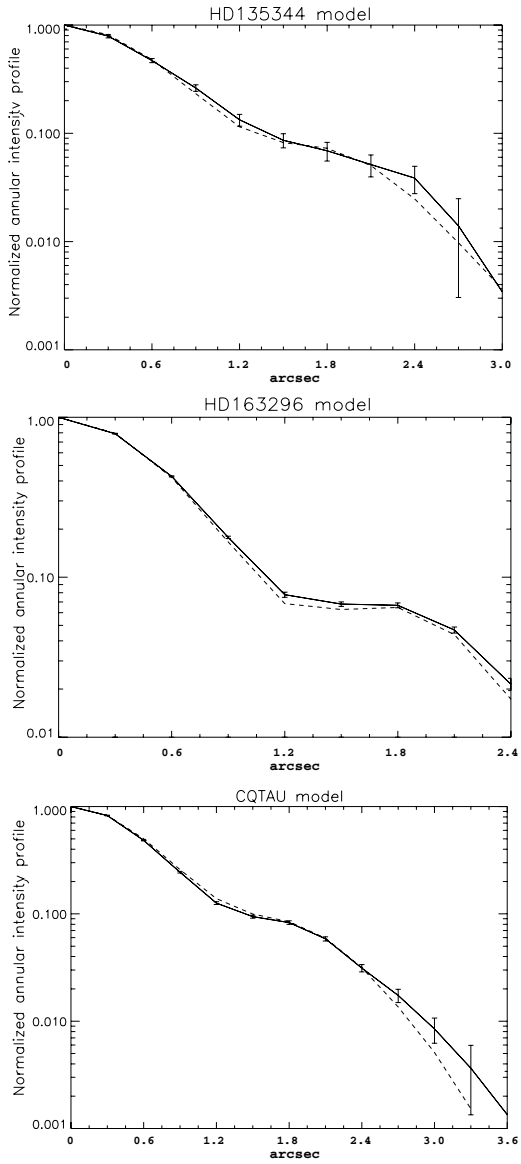

Fig. 3. Annular average intensity aperture normalized to the peak for the observations (*full line*), model (*dashed line*), and the PSF associated (*dot-dashed line*). We have constructed an image with the DD04 model that we have convolved with the PSF of the associated night. The error in the profile comes from the noise rms in the image.

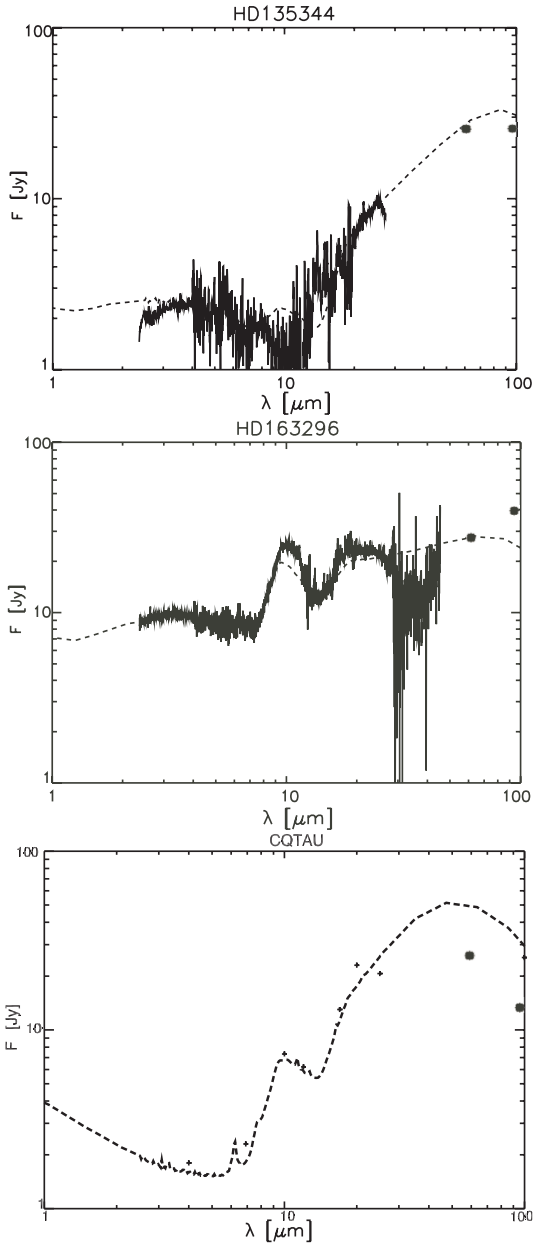

Fig. 4. Modeled spectrum (dashed line) between 1 and 100 μm. For HD 135344 and HD 163296, the ISO spectrum is overplotted by a bold line. For CQ Tau, there are some photometric points from Grady et al. (2005); we have added the one from this study at 20.5 μm and IRAS points at 60 and 100 μm (filled circles).

($n(a) \propto a^{-3.5}$) with a size between 0.01 and 0.3 μm. It is the disk surface layer that dominates the SED in the mid-IR range. The emission of the surface is made by small grains that trace the disk geometry. We will focus on this component in this paper. Since the objects have no PAH (Polycyclic Aromatic Hydrocarbon) emission (or only a weak one in the case of HD 135344), we do not take into account this population of grains.

Once the density profile is set, and the dust opacities and stellar parameters are given, the code `RADMC` (Dullemond & Dominik 2004; Pontoppidan & Dullemond 2005) solves the temperature structure of the disk with a Monte-Carlo method using a variant of the algorithm of Bjorkman & Wood (1997). This Monte-Carlo code also produces the source terms for scattering, in the isotropic-scattering approximation. With a ray-tracing tool (which is part of the code `RADICAL`, see Dullemond & Turolla (2000) for a detailed description) the SED and images can then be produced and compared to the observations. Comparative

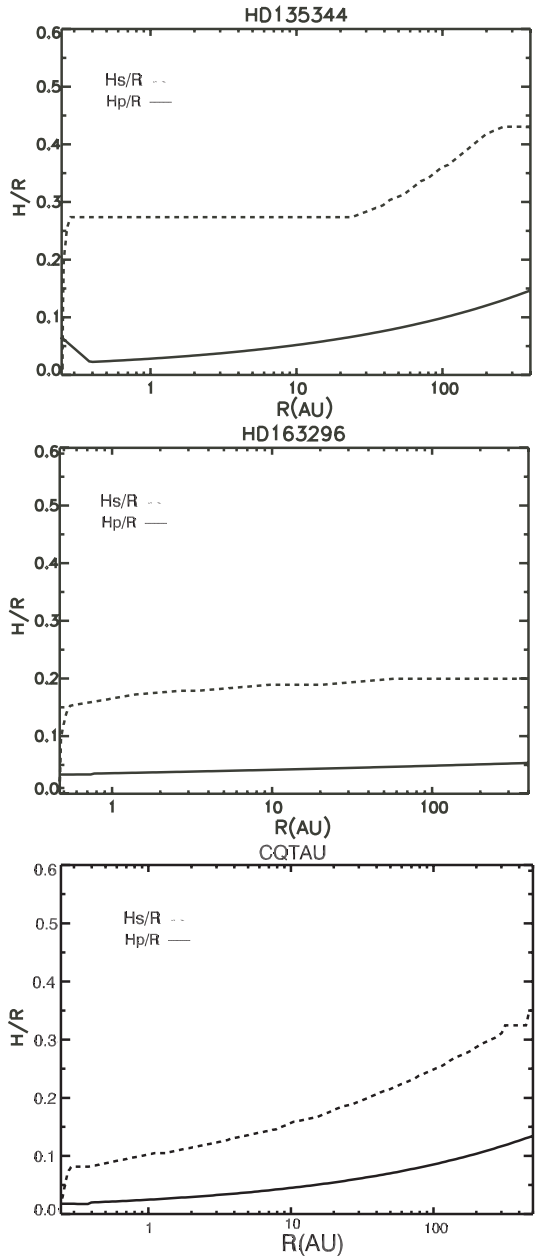

Fig. 5. Modelized vertical structure versus the radius. The pressure height scale (H_p/R) is the solid line and the surface height scale (i.e., the height of the disk photosphere above the mid-plane H_s/R) is the dashed line.

images are obtained by first resampling the maps to the CAMIRAS sampling and then by convolving them with the PSF.

6. Comparison model versus observation

For each object, the best model should simultaneously fit the SED (Fig. 4) and the extension found at 20.5 μm with our observations (Fig. 3). Concerning HD 135344 and HD 163296, we

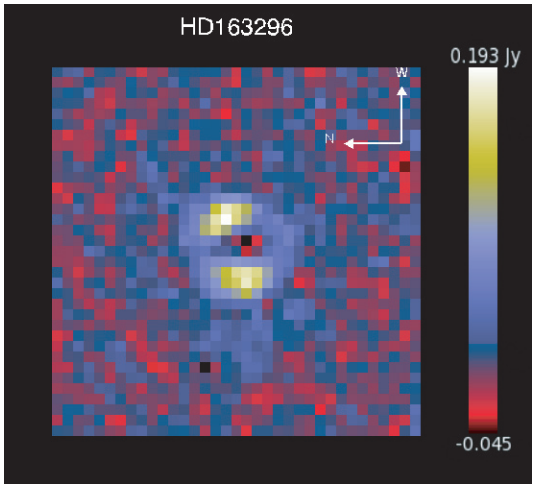

Fig. 6. HD 163296 extended emission (central point source removed). West is up, north on the left. The pixel size is 0.29 arcsec. The disk has a surface brightness of 0.59 Jy/$''^2$ (S/N = 27 for $\sigma \sim$ 0.002 Jy) for the brightness part in the direction east/west and 0.23 Jy/$''^2$ (S/N = 11) for the less bright part in the direction north/south. The noise is calculated using a sigma-clipping technique.

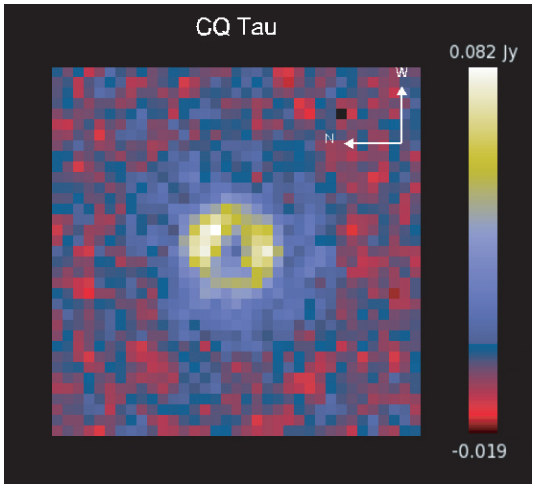

Fig. 7. CQ Tau extended emission (central point source removed). The same orientation as Fig. 6. The pixel size is 0.29 arcsec. At 0.9″ from the center, the surface brightness is 0.94 Jy/$''^2$ (S/N = 15 for $\sigma \sim$ 0.004 Jy). At 2″ from the center, the surface brightness is 0.23 Jy/$''^2$ (S/N = 5).

used mainly the ISO spectrum to constrain the SED; as far as CQ Tau is concerned, IRAS photometry and BASS points obtained by Grady et al. (2005) are used. Figure 5 shows the structure of the disk in terms of pressure and surface scale height.

Multiple runs of the model are performed until a satisfactory fit to the observed spectrum and the extension found at 20.5 μm is obtained. In the fitting procedure, the stellar parameters ($T_{\rm eff}$, $M_\star$, $R_\star$, see Table 3), the dust evaporation temperature (i.e., the position of the inner rim) at 1400 K, the outer radius and the inclination of the disk, and the dust composition and size distribution are fixed. Other parameters, such as the pressure scale height for the inner rim (possibly puffed-up), the outer

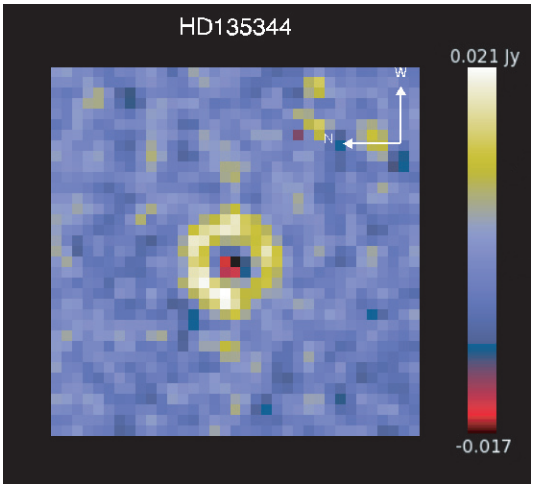

Fig. 8. HD 135344 extended emission (central point source removed). The same orientation as Fig. 6. The pixel size is 0.29 arcsec. At 0.9″ from the center, the surface brightness is 0.25 Jy/″^{2} (S/N = 15 for $\sigma \sim 0.0015$ Jy).

pressure scale height (H_0), the power-law index of the pressure scale height (i.e., q, which has been fixed in the case of flared disk to 9/7, a value determinated by hydrostatic equilibrium, Chiang & Goldreich 1997), the mass of the disk, and the power-law index of the surface density (i.e., p) are estimated. Fitting the SED gives one solution among several degenerate combinations. A minimum value of the outer radius is derived from 20 μm observations, which is a very strong constraint on the true disk size, thus largely removing the degeneracy of the set of model parameters.

As first guesses, we used those parameters found when fitting the SED by Dominik et al. (2003) for HD 135344 and HD 163296, and those by Chiang et al. (2001) for CQ Tau. Trying to fit the SED, we focused mainly on the Near-IR and mid-IR regions. Indeed, those regions are the regions where most of the reprocessed stellar energy (by the disk's surface layer) emerged, and therefore are the most strongly affected by the model and the geometry of the disk. Not all the parameters are sensitive to the spatial distribution at 20.5 μm (Table 4). The CAMIRAS images put a strong constraint on the minimum outer radius, and we have to find a solution with all the free parameters to reproduce the shape of the SED, the extension and the total flux at 20.5 μm.

For HD 135344, the disk parameters deduced from fitting only the SED of HD 135344 were close to those that allow us to fit both the SED and our observations. For CQ Tau, in addition to previous studies fitting only the SED, we had to take into account the fact that the disk is quite extended at 20 μm (about 300 AU) and is observed with an inclination of 33°±5. The fast increase of the disk emission in the [10–30] μm range can be modeled only with a flared disk (with $H_p^{\rm out}/R_{\rm out} > 0.1$). In the framework of our modeling, we found that the only manner to simultaneously obtain a quite low far-IR excess (as seen in the spectrum) with the observed extended 20 μm emission is a low-mass disk of only 0.005 $M_\odot$ with a pressure scale height of 58 AU at 450 AU. The total flux in the infrared excess compared to the stellar flux is determinated by the fraction of the central star energy intercepted by the disk. This covering fraction is linked to $H_{\rm p}^{\rm out}/R_{\rm out}$, where the disk geometry thickness is maximum. Here, this parameter is the same as the previous study (energy conservation), but for a different outer radius. That means that the disk is less flared than deduced earlier. For CQ Tau we obtain a disk mass 10 times smaller than that already found (Testi et al. 2003; Chiang et al. 2001), and this mass only traces the small grains. The disk emission at mm wavelength is determined by the mid-plane grain and disk properties, and it is not affected by the nature of the surface dust. Consequently, in this paper, we have not tried to select the best parameters for the mid-plane dust to fit mm observations. Our underestimated flux at mm wavelength suggests that there must be big grains in the disk mid-plane of CQ Tau to recover the measured flux at these wavelengths (Testi et al. 2003).

HD 163296 is classified as a group II object (interpreted as being surrounded by a flat or self-shadowed disk); it should in principle be much more difficult to resolve the disk in the mid-IR range. Surprisingly, some extended mid-IR emission at 20 μm, although less prominent than for group I objects, is however observed. In the modeling, we used the parameter found in Dominik et al. (2003), who modeled the SED with a flared disk cut at 50 AU, as a first guess. Here, we modified the large-scale pressure scale-height to mimic a weakly flared disk. The SED is well reproduced with a disk having little flaring (Fig. 4 and Table 3), while the extension at 20 μm (Fig. 3) constrains the disk to have a minimum outer radius of 200 AU with a disk mass of 0.01 $M_\odot$.

7. Conclusions and future work

We have shown the strength of mid-IR imaging to constrain the disk properties. There are still a very limited number of objects with spatially resolved extended emission, and it is not yet possible to draw statistical conclusions about the spatial structure of disk around HAe stars. With the advance of mid-IR instruments on 8-m class telescopes, such as the VISIR (Lagage et al. 2004) instrument available on the MELIPAL Very Large Telescope (VLT) at the European Southern Observatory (ESO), higher angular resolution will be available and the field will further develop; more quantitative studies will be possible and the goal of retrieving detailed disk surface density profiles from the observations should be achievable.

Observations should not be limited to the 20 μm atmospheric window; observations in the 10 μm atmospheric window are also very promising, especially for those HAe stars whose spectra feature the so-called PAH bands' features at 3.3, 6.2, 7.7, 8.6, 11.2, 12.7 μm. PAH bands are attributed to vibrational relaxation of UV-pumped Polycyclic Aromatic Hydrocarbon molecules containing about 50–100 carbon atoms (Allamandola et al. 1989; Puget & Leger 1989). Their emission, as a function of the distance r to the star, drops with a r^{-2} power-law, much slower than thermal emission from large grains in thermal equilibrium. PAH's emission is thus a promising probe for studying flaring disks at large distances from the star, with the good angular resolution now achieved on large ground-based telescopes at 10 microns. One clear method of improving the field over the next few years would be to use sophisticated models to fit a combination of interferometric and single dish observations in the near- and mid-IR, which probe the innermost and intermediate disk regions, respectively.

Acknowledgements. We are gratefully indebted to P. Masse, R. Jouan, and M. Lortholary for their assistance with the CAMIRAS instrument, A. Claret in efficiently supporting us in our observations, as well as to the staff of CFHT/Hawaii

Table 3. Stellar properties and fit parameters. The stellar parameters of CQ Tau are taken in Chiang et al. (2001). For HD 135344 and HD 163296, the parameters are taken from Meeus et al. (2001) and van Boekel et al. (2005). $H_p^{\rm in}/R_{\rm in}$ characterizes the puffed inner rim. q is the power-law index of the scale height and p that of the surface density. $H_{\rm p}^{\rm out}/R_{\rm out}$ characterizes the flaring angle of the disk. The last column is the flux at 20.5 μm calculated from the modeled image.

Object	Distance (pc)	$M_\star$ ($M_\odot$)	$T_{\rm eff}$ (K)	$R_\star$ ($R_\odot$)	$R_{\rm in}$ (AU)	$H_p^{\rm in}/R_{\rm in}$	$R_{\rm out}$ (AU)	$H_p^{\rm out}/R_{\rm out}$	p	q	i (degrees)	F (20.5 μm) (Jy)
HD 135344 (DDN03)	84	1.3	6750	2.1	0.24	0.065	800	0.21	0.8	9/7	60	–
HD 135344 (in this study)	140	1.3	6750	2.1	0.24	0.065	200	0.12	0.8	9/7	45	5.7
HD 163296 (DDN03)	122	2.5	10500	1.7	0.45	0.033	50	0.07	0.2	9/7	65	–
HD 163296 (in this study)	100	2.5	10500	1.7	0.45	0.033	200	0.05	1.	1.07	60	16.6
CQ Tau (Chiang2001)	100	1.7	7130	1.3	0.23	0.0002	180	0.13	1.5	9/7	–	–
CQ Tau (in this study)	100	1.7	7130	1.9	0.23	0.018	450	0.13	0.3	9/7	33	20

Table 4. Effects of the free parameters of the model on the SED and spatial distribution of the 20.5 μm emission in the CAMIRAS image.

Parameter	Influence on SED	Spatial distribution at 20.5 μm
Σ_0	Influence on the total flux in the mid-IR and more strongly for $\lambda \geq 60\,\mu$m	No influence
p	No influence in the mid-IR	Little influence
$H_p^{\rm in}/R_{\rm in}$	Modifies contrast mid-/near-IR (structure inner rim/shadow)	No influence (inner rim + shadow in the first pixel)
q	Modifies the whole shape of the SED	Large influence
$H_p^{\rm out}/R_{\rm out}$	Modifies flux in the mid- and far-IR	Little influence
$R_{\rm out}$	Modifies far-IR emission	Large influence

for their support during the observing runs. CD wishes to thank J. Bouwman and E. Habart for very helpful discussions and advice.

References

Allamandola, L. J., Tielens, G. G. M., & Barker, J. R. 1989, ApJS, 71, 733
Bouwman, J., Meeus, G., de Koter, A., et al. 2001, A&A, 375, 950
Calvet, N., Patino, A., Magris, G. C., & D'Alessio, P. 1991, ApJ, 380, 617
Chiang, E. I., & Goldreich, P. 1997, ApJ, 490, 368
Chiang, E. I., Joung, M. K., Creech-Eakman, M. J., et al. 2001, ApJ, 547, 1077
Cohen, M., Walker, R. G., Carter, B., et al. 1999, AJ, 117, 1864
Coulson, I. M., Walther, D. M., & Dent, W. R. F. 1998, MNRAS, 296, 934
Dent, W. R. F., Greaves, J. S., & Coulson, I. M. 2005, MNRAS, 359, 663
Dominik, C., Dullemond, C. P., Waters, L. B. F. M., & Walch, S. 2003, A&A, 398, 607
Draine, B. T., & Li, A. 2001, ApJ, 551, 807
Dullemond, C. P., & Turolla, R. 2000, A&A, 360, 1187
Dullemond, C. P., & Dominik, C. 2004, A&A, 417, 159
Dullemond, C. P., van Zadelhoff, G. J., & Natta, A. 2002, A&A, 389, 464
Eisner, J. A., Lane, B. F., Hillenbrand, L. A., Akeson, R. L., & Sargent, A. I. 2004, ApJ, 613, 1049
Grady, C. A., Devine, D., Woodgate, B., et al. 2000, ApJ, 544, 895
Grady, C. A., Polomski, E. F., Henning, T., et al. 2001, AJ, 122, 3396
Grady, C. A., Woodgate, B. E., Bowers, C. W., et al. 2005, ApJ, 630, 958
Isella, A., & Natta, A. 2005, A&A, 438, 899
Jayawardhana, R., Fisher, R. S., Telesco, C. M., et al. 2001, AJ, 122, 2047
Kenyon, S. J., & Hartmann, L. 1987, ApJ, 323, 714
Lagage, P. O., Jouan, R., Masse, P., Mestreau, P., & Tarrius, A. 1992, in Progress in Telescope and Instrumentation Technologies, ed. M.-H. Ulrich, 601
Lagage, P. O., Pel, J. W., Authier, M., et al. 2004, The Messenger, 117, 12
Leinert, C., van Boekel, R., Waters, L. B. F. M., et al. 2004, A&A, 423, 537
Liu, W. M., Hinz, P. M., Meyer, M. R., et al. 2003, ApJ, 598, L111
Liu, W. M., Hinz, P. M., Hoffmann, W. F., et al. 2005, ApJ, 618, L133
Malfait, K., Bogaert, E., & Waelkens, C. 1998, A&A, 331, 211
Mannings, V., & Sargent, A. I. 1997, ApJ, 490, 792
Mannings, V., & Sargent, A. I. 2000, ApJ, 529, 391
Marsh, K. A., Van Cleve, J. E., Mahoney, M. J., Hayward, T. L., & Houck, J. R. 1995, ApJ, 451, 777
Mathis, J. S., Rumpl, W., & Nordsieck, K. H. 1977, ApJ, 217, 425
Meeus, G., Waters, L. B. F. M., Bouwman, J., et al. 2001, A&A, 365, 476
Millan-Gabet, R., Schloerb, F. P., & Traub, W. A. 2001, ApJ, 546, 358
Natta, A., Prusti, T., Neri, R., et al. 2001, A&A, 371, 186
Pantin, E., Bouwman, J., & Lagage, P. O. 2005, A&A, 437, 525
Pontoppidan, K. M., & Dullemond, C. P. 2005, A&A, 435, 595
Prusti, T., Natta, A., & Palla, F. 1994, A&A, 292, 593
Puget, J. L., & Leger, A. 1989, ARA&A, 27, 161
Shu, F. H., Lizano, S., & Adams, F. C. 1987, in Star Forming Regions, ed. M. Peimbert, & J. Jugaku, IAU Symp., 115, 417
Sylvester, R. J., Skinner, C. J., Barlow, M. J., & Mannings, V. 1996, MNRAS, 279, 915
Testi, L., Natta, A., Shepherd, D. S., & Wilner, D. J. 2001, ApJ, 554, 1087
Testi, L., Natta, A., Shepherd, D. S., & Wilner, D. J. 2003, A&A, 403, 323
Thé, P. S., de Winter, D., & Perez, M. R. 1994, A&AS, 104, 315
Thi, W. F., van Dishoeck, E. F., Blake, G. A., et al. 2001, ApJ, 561, 1074
Tuthill, P. G., Monnier, J. D., Danchi, W. C., Hale, D. D. S., & Townes, C. H. 2002, ApJ, 577, 826
van Boekel, R., Min, M., Waters, L. B. F. M., et al. 2005, A&A, 437, 189
van den Ancker, M. E., de Winter, D., & Tjin A Djie, H. R. E. 1998, A&A, 330, 145
Van Malderen, R., Decin, L., Kester, D., et al. 2004, A&A, 414, 677
Wilkin, F. P., & Akeson, R. L. 2003, Ap&SS, 286, 145

Annex

Anatomy of a Flaring Proto-Planetary Disk Around a Young Intermediate-Mass Star

published in the journal *Science*, October 2006

EXTENDED PDF FORMAT
SPONSORED BY
usb
www.usbweb.com

Anatomy of a Flaring Proto-Planetary Disk Around a Young Intermediate-Mass Star
Pierre-Olivier Lagage, *et al.*
Science **314**, 621 (2006);
DOI: 10.1126/science.1131436

The following resources related to this article are available online at www.sciencemag.org (this information is current as of September 18, 2008):

Updated information and services, including high-resolution figures, can be found in the online version of this article at:
http://www.sciencemag.org/cgi/content/full/314/5799/621

Supporting Online Material can be found at:
http://www.sciencemag.org/cgi/content/full/1131436/DC1

A list of selected additional articles on the Science Web sites **related to this article** can be found at:
http://www.sciencemag.org/cgi/content/full/314/5799/621#related-content

This article **cites 25 articles**, 3 of which can be accessed for free:
http://www.sciencemag.org/cgi/content/full/314/5799/621#otherarticles

This article has been **cited by** 5 article(s) on the ISI Web of Science.

This article appears in the following **subject collections**:
Astronomy
http://www.sciencemag.org/cgi/collection/astronomy

Information about obtaining **reprints** of this article or about obtaining **permission to reproduce this article** in whole or in part can be found at:
http://www.sciencemag.org/about/permissions.dtl

Downloaded from www.sciencemag.org on September 18, 2008

Science (print ISSN 0036-8075; online ISSN 1095-9203) is published weekly, except the last week in December, by the American Association for the Advancement of Science, 1200 New York Avenue NW, Washington, DC 20005. Copyright 2006 by the American Association for the Advancement of Science; all rights reserved. The title *Science* is a registered trademark of AAAS.

Anatomy of a Flaring Proto-Planetary Disk Around a Young Intermediate-Mass Star

Pierre-Olivier Lagage,[1]* Coralie Doucet,[1] Eric Pantin,[1] Emilie Habart,[2] Gaspard Duchêne,[3] François Ménard,[3] Christophe Pinte,[3] Sébastien Charnoz,[1] Jan-Willem Pel[4,5]

Although planets are being discovered around stars more massive than the Sun, information about the proto-planetary disks where such planets have built up is sparse. We have imaged mid-infrared emission from polycyclic aromatic hydrocarbons at the surface of the disk surrounding the young intermediate-mass star HD 97048 and characterized the disk. The disk is in an early stage of evolution, as indicated by its large content of dust and its hydrostatic flared geometry, indicative of the presence of a large amount of gas that is well mixed with dust and gravitationally stable. The disk is a precursor of debris disks found around more-evolved A stars such as β-Pictoris and provides the rare opportunity to witness the conditions prevailing before (or during) planet formation.

Based on the growing number of known planetary systems (*1*) and on the wealth of observations of disks around young stellar objects (*2*, *3*), it is now well established that planets around main-sequence solar-type stars form in massive, gaseous, and dusty proto-planetary disks that survive for several million years around the nascent stars (*4*). The situation is less clear for stars of more than ≈2 solar masses. Such stars have a much higher luminosity than solar-type stars, and, according to models, processes such as photoevaporation may be at work clearing the inner disk in a few million years (*5*). Whereas radial velocity surveys have just started to reveal planets around stars about twice as massive as the Sun (*6*), current imaging observations of proto-planetary disks around stars with such a mass remain very sparse (*3*). Most resolved disks are debris disks around A-type stars that are on the main sequence (*3*, *7*). In such disks, the gas has been dispersed, and planets have probably formed already, as indicated by asymmetries and ring-like structures in the disks (*4*). The lack of well-resolved images of proto-planetary disks around much younger A stars, still on the pre–main sequence, is due to the fact that such stars are less numerous than their solar-type equivalents, the T-Tauri stars, and in general are located farther away from Earth. As a result, the fallback option to estimate the properties of the disks around these stars has been to fit their spectral energy distribution (SED). By doing so, the pre–main sequence stars of intermediate mass (≈2 to 4 solar masses), the so-called Herbig Ae (HAe) stars, have been classified in two groups: Group I members feature a rising SED in the 10- to 60-micrometer (μm) wavelength range [mid- and far-infrared (IR)], whereas group II members feature a flatter SED (*8*). The preferred physical interpretation is that group I disks are flared and group II disks are geometrically flatter. A flaring disk is a disk in which the ratio of disk thickness to the distance to the star, H/r, increases with r; then, any point at the surface of such disks receives direct light from the star, and the disk intercepts a substantial part of the stellar radiation out to large distances. Half of the intercepted light is reradiated away from the disk, and the other half is reradiated down into the disk's deeper layers, providing additional heating to the dust in the optically thick disk interior, which reradiates in the mid-IR, far-IR, and submillimeter wavelengths. The information provided by SED fitting remains limited, because numerous disk parameters are assumed or have not been conclusively determined (*9*). Direct measurements from imaging are therefore required to unambiguously constrain more parameters, such as the overall shape (outer radius and height) of the disk, which determines the amount of starlight captured by the disk. Imaging of disks has been obtained either by observations of the starlight dust scattering (in the visible and near-IR radiation) or of dust thermal emission or by CO lines in the millimeter observations (*3*, *10*, *11*). Scattered starlight observations suffer from the limited contrast offered by imaging devices, and millimeter observations suffer from limited spatial resolution.

A new approach to image disks around HAe stars exploits the fact that about half of them have prominent IR emission bands (IEBs) at 3.3, 6.2, 7.7, 8.6, and 11.3 μm (*12*). These IEBs are believed to arise from the cooling of transiently heated polycyclic aromatic hydrocarbons (PAHs),

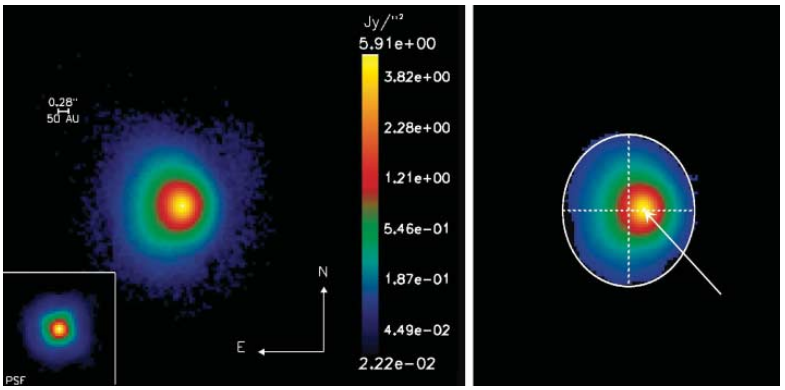

Fig. 1. (**Left**) VISIR false-color image of the emission from the circumstellar material surrounding the HAe star HD 97048 after a deep exposure (36 min). VISIR's PAH1 filter was used; it is centered on the IEB at 8.6 μm and has a full width at half maximum (FWHM) of 0.42 μm. The emission is widely extended, as compared with the point spread function (PSF) (inset) obtained from the observation of the pointlike reference star HD 102964, which was made 15 min before the observation of HD 97048. The measured FWHM of 0.33″ is close to the diffraction limit of 0.28″, also indicated on the figure. The pixel size is 75 milli–arc sec. The noise level is 1.6 millijansky (mJy)/arc sec^2. The photometry, calibrated with HD 102964, yields a total flux of 5.75 (±0.2) Jy. (**Right**) Same image but with a cut at the brightness level of 4.4×10^{-3} Jy/arc sec^2 and a fit of the edge of the image by an ellipse. The dashed lines show the ellipse axis; the ellipse center is offset eastward from the peak flux, as indicated by the arrow.

[1]Laboratoire de l'Astrophysique des Interactions multi-échelles, Unité Mixte de Recherche N° 7158 [Commissariat à l'Energie Atomique (CEA), CNRS, Université Paris 7], Direction des Sciences de la Matière (DSM)/Laboratoire de recherches sur les lois fondamentales de l'Univers (DAPNIA)/Service d'Astrophysique, CEA Saclay, F-91191 Gif-sur-Yvette Cedex, France. [2]Institut d'Astrophysique Spatiale, F-91405, Orsay Cedex, France. [3]Laboratoire d'Astrophysique de Grenoble, CNRS/Université Joseph Fourier, Unité Mixte de Recherche N° 5571, Boîte Postale 53, F-38041 Grenoble Cedex 9, France. [4]Netherlands Foundation for Research in Astronomy, Dwingeloo, Netherlands. [5]University of Groningen, Groningen, Netherlands.

*To whom correspondence should be addressed. E-mail: Pierre-Olivier.Lagage@cea.fr

Downloaded from www.sciencemag.org on September 18, 2008

which can be excited by the intense stellar ultraviolet radiation (*13*). For a flaring disk, the PAHs at the surface of the disk are in direct view of the central star and can be excited; the resulting IEB emission provides distinguishing information on the disk structure up to large distances from the star. In addition, observing in the mid-IR wavelength alleviates the problem of too much contrast between the photospheric and disk emission. We have thus undertaken a program of imaging "nearby" HAe stars with VISIR (very large telescope imager and spectrometer in the mid-IR) at the European Southern Observatory (ESO) (*14*). One of the first targets was HD 97048, a nearby group I HAe star of spectral type Be9.5/A0 located in the Chameleon I dark cloud, at a distance of 180 parsecs (*15*). The star has a temperature of 10,000 K, a luminosity ($L_\odot$) of 40 solar luminosities, and a mass ($M_\odot$) of 2.5 solar masses (*15*). It is surrounded by a large amount of circumstellar material left from the star formation process, as indicated by the large IR excess (L_{IR}) observed in the SED [L_{IR}~0.40$L_\odot$ (*16*)]. Mid-IR–extended emission has been detected on scales of a few thousand astronomical units and modeled as originating from a dust shell with an inner cavity radius of 180 AU (*17*). Recent long-slit mid-IR spectroscopic observations have revealed a strong resolved emission from the inner region (*18*). Imaging this region with the high-angular resolution offered by a 8-m-size telescope would be a direct way to assess whether HD 97048 is surrounded by a flaring disk, as expected from its rising mid-IR and far-IR SED (*12*).

The observations of HD 97048, conducted on 17 and 19 June 2005, were performed with filters centered on the IEB at 8.6 μm and on the adjacent continuum at 9 μm. The classical mid-IR observing technique of "chopping and nodding" was used, with a chopper throw of 10″ (north-south) and a nodding throw of 8″ (east-west). The 8.6-μm image (Fig. 1) reveals a large extended emission with a strong east-west asymmetry; the brightness isophotal contours

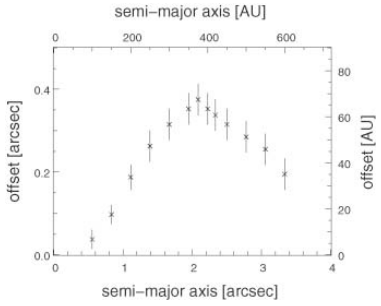

Fig. 2. Offset from the peak flux of the center of the ellipses fitting the image of HD 97048 at various brightness level cuts, as a function of the length of the ellipse semi-major axis (fig. S1). Error bars indicate the uncertainties from ellipse fitting.

are elliptical in shape, and the ellipse centers are offset from the peak of emission. The offset increases when lowering isophotal contours up to a semi-major axis of 2.1″, (Fig. 2 and fig. S1). Such features are characteristic of a flaring disk, vertically optically thick at the wavelength of the observations and inclined to the line of sight (Fig. 3). Beyond 2.1″, the offsets decrease. One possible explanation is that the disk then becomes vertically less optically thick. However, as an alternative explanation, the increasing contribution from the shell emission cannot be disregarded (*17*). We therefore restricted our study to the regions <2.1″, corresponding to an astrocentric distance of 370 AU.

To retrieve quantitative information about the disk flaring in these regions, we have fitted the east and west brightness profiles with a simplified model. In this model, the PAH-emitting region is only located at the surface of the disk, whose surface scale height H_s varies with the astrocentric distance following a power law $H_s(r) = H_0.(r/r_0)^\beta$, where H_0 is the disk surface height at the astrocentric distance r_0 and β is the

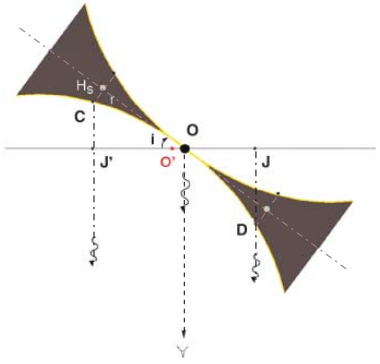

Fig. 3. Sketch of a slice of a flaring disk. The observer is viewing the disk from below (eye symbol). The disk is inclined, from pole-on, by an angle *i*. The disk is optically thick to the ultraviolet and visible starlight along its midplane so that the PAH emission only arises from the disk "surfaces," indicated in yellow. When the disk is also optically thick vertically at the wavelengths of the observations (here in the mid-IR), only the front disk surface is seen by the observer. Consider two points C and D of the front disk surface, located at equal distances from the star (black circle at O). Because of projection effects, the observer views the center of emission from C and D at O′ (red circle), between J and J′, which is offset from O. For a flaring disk, the disk height H_s increases with the distance *r* to the star, so that the apparent offset increases, as observed for HD 97048. When the disk is vertically optically thin, the front and bottom disk surfaces are both observable, and the disk appears symmetrical with respect to the star. Curved arrows indicate that electromagnetic radiation is emitted toward the observer; gray circles indicate the projection of point C or D onto the disk midplane.

flaring index. We further assumed that the spatial variation of the flux intensity *I* follows a power law $I(r) = I_0.(r/r_0)^\delta$, where I_0 is the intensity at r_0 and δ is the power law index. This hypothesis is only valid once the continuum emission contribution in the filter at 8.6 μm has been removed, which we have done by extrapolating the continuum emission observed at 9 μm (fig. S2). The result of the fit is shown in Fig. 4; δ for the intensity is found to be –2.3 (+0.2/–0.06), close to the expectation of an index value of –2 for PAH emission (fig. S2), and the disk inclination is 42.8 (+0.8/–2.5) degrees from pole-on. The scale height H_0 is 51.3 (+0.7/–3.3) AU at r_0 = 135 AU and β is 1.26 (±0.05), in agreement with the value expected from hydrostatic, radiative equilibrium models of passive flared disks (*9*). In these models, the flaring structure is supported by the gas, whose vertical scale height H_g is governed by the balance between gas pressure and gravitational pull; the dust plays the key role to capture the starlight and then heat the gas collisionally. H_s corresponds to the upper layers of the disk, where the starlight is intercepted by dust, and is about four times as large as the gas height (*9*). Given the disk's outer radius and scale height, the calculated amount of starlight captured by the disk is 43%, in good agreement with the observed IR excess (*16*).

Our observations also provide information about the disk mass. From the observed west-east asymmetry, we can infer that the vertical optical thickness τ at 370 AU is at least 1, implying that, at 370 AU, the dust mass surface density Σ_o is at least $^1/_{1600}$ g cm^{-2} (*19*). Assuming that the astrocentric variation of mass

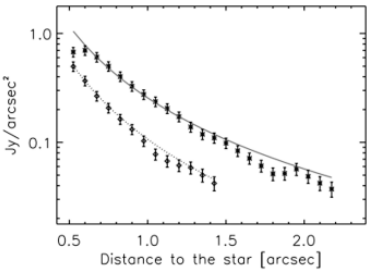

Fig. 4. Fit of the observed east (upper data and solid curve) and west (lower data and dotted line) intensity profiles with a simple flaring disk model. The reduced χ^2 value of the fit is 0.3, well below 1. The error bars indicate the uncertainties in the data due to the background noise and photometric uncertainties from the continuum subtraction (±5% for each image). The range in model parameters has been calculated by exploring the parameter space, which leads to a reduced $\chi^2 < 1$. Below 0.5″, there is no data point, because it is impossible to disentangle reliably the IEB emission from the much larger continuum thermal emission. The angular distance to the star refers to the projected distance on the plane of the sky.

Downloaded from www.sciencemag.org on September 18, 2008

surface density Σ follows a power law $\Sigma(r) = \Sigma_o (r_{AU}/370)^q$, with an index q equal to $-3/2$, as the one inferred for the solar nebula or for extrasolar nebulae (*20*, *21*), we derived a disk dust mass of 40 Earth masses within 370 AU. This lower limit is compatible with the mass of 500 Earth masses derived from the observed 1.3-mm flux (*22*). The dust mass derived here is three to four orders of magnitude larger than the dust mass observed in debris disks and Kuiper belt–like structures found around more-evolved A stars such as β-Pictoris, Vega, Fomalhaut, and HR 4796 (*4*). The dust around these Vega-like stars is thought to be produced by collisions of larger bodies, whose total mass in the case of β-Pictoris has been estimated to be on the order of 100 Earth masses (*23*). Therefore, the dust mass observed around HD 97048 is similar to the mass invoked for the (undetected) parent bodies in more-evolved systems. HD 97048's disk is thus most likely a precursor of debris disks observed around more-evolved A stars. This finding is coherent with the HD 97048 age of ~3 million years, estimated from evolutionary tracks. Another argument in favor of the early evolutionary stage of the system is the presence of a large amount of gas required to support the flaring structure revealed by our observations. Part of the gas has been recently detected, thanks to observations of the molecular hydrogen emission at 2.12 μm (*24*). Assuming that the canonical interstellar gas-to-dust mass ratio of 100 holds, we estimate a total minimum disk mass of 0.01 solar masses, like the estimated minimum mass for the proto-planetary disk around the Sun (*20*).

Because the disk surrounding HD 97048 has a mass surface density comparable to that of the minimum proto-planetary nebula around the Sun, it is worth studying the prospects for planet formation in this environment. Planet formation models are divided into two categories: gravitational instabilities (*25*) and core accretion (*26*). It seems improbable that giant planets will form by means of gravitational instabilities, because the Toomre stability criterion coefficient, equal to $H_g/r\ M_\odot/(r^2\Sigma)$, is >> 1 (*27*). Considering the alternative core accretion scenario by which planets coagulate from initially μm-sized dust (*28*, *29*), it also appears improbable that cores of giant planets are present in the outer regions because of the very long local orbital time scales. Although regions within 40 AU have not been resolved by our observations, it is tempting to extrapolate the surface density from the outer regions and investigate the predictions of planet formation models for the inner regions; inside 10 AU, planetary embryos may be present. Follow-up observations at higher angular resolution with the mid-IR instrument of the ESO Very Large Telescope interferometer will allow probing these regions.

References and Notes

1. The Extrasolar Planet Encyclopaedia presents a comprehensive list of all known exoplanets (www.obspm.fr/planets).
2. C. R. O'Dell, S. V. W. Beckwith, *Science* **276**, 1355 (1997).
3. A comprehensive list of spatially resolved disks is available (www.circumstellardisks.org).
4. J. S. Greaves, *Science* **307**, 68 (2005).
5. T. Takeuchi, C. J. Clarke, D. N. C. Lin, *Astrophys. J.* **627-1**, 286 (2005).
6. J. Setiawan *et al.*, *Astron. Astrophys.* **437**, L31 (2005).
7. B. A. Smith, R. J. Terrile, *Science* **226**, 1421 (1984).
8. G. Meeus *et al.*, *Astron. Astrophys.* **365**, 476 (2001).
9. E. I. Chiang *et al.*, *Astrophys. J.* **547**, 1077 (2001).
10. V. Mannings, A. I. Sargent, *Astrophys. J.* **529**, 391 (2000).
11. C. Grady *et al.*, *Astrophys. J.* **630**, 958 (2005).
12. B. Acke, M. E. van den Ancker, *Astron. Astrophys.* **426**, 151 (2004).
13. J. L. Puget, A. Leger, *Annu. Rev. Astron. Astrophys.* **27**, 161 (1989).
14. P.-O. Lagage *et al.*, *The Messenger* **117**, 12 (2004).
15. M. E. van den Ancker, D. de Winter, H. R. E. Tjin A Djie, *Astron. Astrophys.* **330**, 145 (1998).
16. C. Van Kerckhoven, A. G. G. Tielens, C. Waelkens, *Astron. Astrophys.* **384**, 568 (2002).
17. T. Prusti, A. Natta, F. Palla, *Astron. Astrophys.* **292**, 593 (1994).
18. R. van Boekel *et al.*, *Astron. Astrophys.* **418**, 177 (2004).
19. V. Ossenkopf, Th. Henning, *Astron. Astrophys.* **291**, 943 (1994).
20. S. J. Weidenschilling, *Astrophys. Space Sci.* **51**, 153 (1977).
21. M. J. Kuchner, *Astrophys. J.* **612**, 1147 (2004).
22. Th. Henning, A. Burkert, R. Launhardt, Ch. Leinert, B. Stecklum, *Astron. Astrophys.* **336**, 565 (1998).
23. P. Artymowicz, *Annu. Rev. Earth Planet. Sci.* **25**, 175 (1997).
24. J. S. Weintraub, J. S. Bary, J. H. Kastner, S. J. Shukla, K. Chynoweth, in *Proceedings of the Protostars and Planets V Conference*, Waikoloa, HI, 24 to 28 October, 2005, B. Reipurt, D. Jewitt, K. Keil, Eds. (LPI Contribution Number 1286, Univ. Arizona Press, Tucson, 2006), p. 8197.
25. R. H. Durisen *et al.*, in *Protostars and Planets V*, B. Reipurt, D. Jewitt, K. Keil, Eds. (Univ. of Arizona Press, Tucson, 2006), in press; preprint (www.ifa.hawaii.edu/UHNAI/ppv.htm).
26. J. J. Lissauer, *Annu. Rev. Astron. Astrophys.* **31**, 129 (1993).
27. A. Toomre, *Astrophys. J.* **139**, 1217 (1964).
28. S. Ida, D. N. C. Lin, *Astrophys. J.* **604-1**, 388 (2004).
29. P. Goldreich, Y. Lithwick, R. Sari, *Astrophys. J.* **614-1**, 497 (2004).

30. This work was based on observations carried out at the ESO, Paranal, Chile. The VISIR could not have been built without contributions from many people, including G. Durand, Y. Rio, M. Authier, C. Lyraud, and J. Pragt. We also thank A. Palacio, P. Nghiem, and C. Martin for discussions about the age of HD 97048, as well as F. Masset for discussions about gravitational instabilities.

Supporting Online Material

www.sciencemag.org/cgi/content/full/1131436/DC1
Figs. S1 and S2

19 June 2006; accepted 12 September 2006
Published online 28 September 2006;
10.1126/science.1131436
Include this information when citing this paper

Downloaded from www.sciencemag.org on September 18, 2008

The Phase-Dependent Infrared Brightness of the Extrasolar Planet υ Andromedae b

Joseph Harrington,[1,2] Brad M. Hansen,[3]* Statia H. Luszcz,[2,4] Sara Seager,[5] Drake Deming,[6] Kristen Menou,[7] James Y.-K. Cho,[8] L. Jeremy Richardson[9]

The star υ Andromedae is orbited by three known planets, the innermost of which has an orbital period of 4.617 days and a mass at least 0.69 that of Jupiter. This planet is close enough to its host star that the radiation it absorbs overwhelms its internal heat losses. Here, we present the 24-micrometer light curve of this system, obtained with the Spitzer Space Telescope. It shows a variation in phase with the orbital motion of the innermost planet, demonstrating that such planets possess distinct hot substellar (day) and cold antistellar (night) faces.

Last year, two independent groups (*1*, *2*) reported the first measurements of the infrared light emitted by extrasolar planets orbiting close to their parent stars. These "hot Jupiter" (*3*) planets have small enough orbits that the energy they absorb from their hosts dominates their own internal energy losses. How they absorb and reradiate this energy is fundamental to understanding the behavior of their atmospheres. One way to address this question is to monitor the emitted flux over the course of an orbit to see whether the heat is distributed asymmetrically about the surface of the planet.

We have observed the υ Andromedae system with the 24-μm channel of the Multiband Imaging Photometer for Spitzer (MIPS) (*4*) aboard the Spitzer Space Telescope (*5*). We took 168 3-s images at each of five epochs spread over 4.46 days (97% of the 4.617-day orbital period of υ Andromedae b) beginning on 18 February 2006 at 12:52 UTC. After rejecting frames with bad pixels near the star and those with Spitzer's "first frame effect" (*1*) (2% to 8% of the data, depending on epoch), we measured the flux of the system and that of the surrounding sky by using both subpixel, interpolated aperture photometry and optimal photometry (*6*, *7*) on each frame.

The detection of eclipses (*8*) from the hot Jupiter planetary systems HD 209458b (*1*), TrES-1 (*2*), and HD 189733b (*9*) demonstrate that a small fraction (~0.1%) of the total infrared light we observe from these systems is actually emitted from the planet rather than the

Annex

HD 97048: a closer look at the disk

published in the journal *A&A*, August 2007

Astronomy & Astrophysics manuscript no. HD97048˙Doucet˙version˙100407
April 11, 2007
© ESO 2007

HD 97048 : a closer look to the disk ⋆

C. Doucet[1,2], E. Habart[3], E. Pantin[1,2], C. Dullemond[4], P. O. Lagage[1,2], C. Pinte[5], G.Duchêne[5], and F. Ménard[5]

[1] AIM, Unité Mixte de Recherche CEA - CNRS - Université Paris VII -UMR 7158 ,France
[2] DSM/DAPNIA/service d'Astrophysique, CEA/Saclay, F-91191 Gif-sur-Yvette, France
[3] Institut d'Astrophysique Spatiale (IAS), 91405 Orsay cedex, France
[4] Max-Planck-Institut fur Astronomie Heidelberg, Konigstuhl 17, Heidelberg, Germany
[5] Laboratoire d'Astrophysique Observatoire de Grenoble CNRS/UJF UMR 5571

Preprint online version: April 11, 2007

ABSTRACT

Aims. Today, large ground-based instruments, like VISIR on the VLT, providing diffraction-limited (∼0.3 arcsec) images in the mid-infrared where strong PAH features appear enable us to see the flaring structure of the disks around Herbig Ae stars. Although great progress has been made in modelling the disk with radiative transfer models able to reproduce the spectral energy distribution (SED) of Herbig Ae stars, the constraints brought by images have not been yet fully exploited. Here, we are interested in checking if these new observational imaging constraints can be accounted by predictions based on existing models of passive centrally irradiated hydrostatic disks made to fit the SEDs of the Herbig Ae stars.
Methods. The images taken by VISIR in the 8.6 and 11.3 μm aromatic features reveal a large flaring disk around HD97048 inclined to the line of sight. In order to analyse the spatial distribution of these data, we use a disk model which includes the most up to date understanding of disk structure and physics around Herbig Ae stars with grains in thermal equilibrium in addition to transiently-heated PAHs.
Results. We compare the observed spatial distribution of the PAH emission feature and the adjacent continuum emission with predictions based on existing full disk models. Both SED and spatial distribution are in very good agreement with the model predictions for common disk parameters.
Conclusions. We take the general agreement between observations and predictions as a strong support for the physical pictures underlying our flared disk model.

Key words. Circumstellar matter – Stars : formation – Stars : pre-main-sequence – Stars: individual (HD 97048)

1. Introduction

Herbig Ae/Be stars are thought to be the intermediate mass (∼ 2-10 $M_\odot$) counterparts of T Tauri stars (Waters & Waelkens 1998). They have a strong infrared (IR) excess coming from warm circumstellar dust. Similar to T Tauri stars, this dust is believed, due to the interpretation of spectral energy distributions (SEDs), to reside in a flared/flat circumstellar disk (Meeus et al. 2001).

PAHs (Polycyclic Aromatic Hydrocarbons) undergo transient heating : they do not reach thermal equilibrium with the radiation field but absorb individual photons, experiencing a rapid increase in temperature, slowly cool, thus re-radiating the absorbed energy in the infrared (IR). This radiation allows to see much further in the disk since these grains can reach high temperatures far away from the star. As a result, PAHs emission can be used to probe the external region of disks around HAe stars (Lagage et al. 2006). Another point of interest is that, if present, PAHs can constitute an important source of opacity and are likely to play a key role in the thermal budget and chemistry of the gas, as they do in the interstellar medium. The thermal coupling between PAHs and gas via the photoelectric effect will, for example, determine the gas temperature in the upper layer of the disk where the gas and dust temperatures are not well coupled (Jonkheid et al. 2004; Kamp & Dullemond 2004). Furthermore, PAHs are also good tracers of the presence of very small particles in the surface layers of disks and their emission can tell if and where very small particles survive settling and coagulation processes that cause the majority of the original grain population to grow to larger sizes in the same objects.

We have started a program of imaging nearby HAe stars with VISIR, the new mid-infrared instrument attached to the third 8-m unit of ESO's Very Large Telescopes located at Cerro Paranal, Chile. One of the first targets was HD 97048 which has a strong IR excess, characteristic of a flared disk, and strong PAH features.

In a previous work, we were able for the first time to constrain the geometry of the disk, thanks to PAH emission (Lagage et al. 2006). Lagage et al. (2006) found there is a large flaring disk around HD97048 extending at least up to 370 AU, vertically optically thick at the observed wavelength (8.6 μm) and inclined to the line of sight by $42.8^{+0.8}_{-2.5}$ degree. Morever, with a very simple model, we were able to measure the flaring index which was found to be $1.26^{+0.05}_{-0.05}$. In this model, the PAH-emitting region is only located at the surface of the disk, whose surface scale height H_s varies with r^q (q is the flaring index) and whose flux intensity I

Send offprint requests to: C.Doucet, e-mail: doucetc@cea.fr
⋆ Based on observations obtained at VLT (Paranal) with VISIR. Program number 075.C-0540(C)

follows r^{-p}. It is only recently that there are some images of the flaring structure of the disk around Herbig Ae objects (Perrin et al. 2006; Lagage et al. 2006). It is now primordial to confront the spatial distribution constraints with existing full disk models only based on fitting the SEDs of the Herbig Ae stars.

In this paper, we are interested in particular to check if these new observational spatial constraints can be accounted by predictions based on existing models of passive centrally irradiated hydrostatic disks made to fit the SEDs of the Herbig Ae stars. We wonder if a more accurate model of disk could explain the SED of HD 97048 and at the same time, the spatial distribution of the circumstellar material with little free parameters. To the best of our knowledge, few tests like that (Doucet et al. 2006) have been done yet for disks around pre-main sequence stars of intermediate mass. To do that, we used the model of Dullemond et al. (2001); Dullemond & Dominik (2004a) which could already account for the global shape of the SED of a quite large number of Herbig Ae stars. The dust model takes into account grains at thermal equilibrium and stochastically-heated PAH. The structure of the disk is calculated with hydrostatic equilibrium and a radiative transfer in two dimensions is used to calculate the emission of the different grains population.

The paper is organized as follows. In Sect. 2, we present the knowledge on HD 97048 and its circumstellar material. In Sect. 3, we describe the observations and the data results. In Sect. 4, we describe the disk model and in Sect. 5, we compare the observed SED and spatial distribution of the circumstellar material to the model predictions.

2. HD97048

HD97048 is a nearby HAe star of spectral type Be9.5/A0 located in the Chameleon I dark cloud, at a distance of 180 pc (van den Ancker et al. (1997), Whittet et al. (1997)). It is surrounded by a large amount of circumstellar material left from the star formation process, which produces a large IR excess (LIR) over the stellar emission (LIR$\sim$0.35-0.40$L_\star$, Acke & van den Ancker (2004); Van Kerckhoven et al. (2002)). HD 97048 has been classified as a HAe star of group I with evidence of flared disk (Meeus et al. 2001), since its SED is rising in the IR (Acke & van den Ancker 2004). Spectroscopic observations of the IR excess have also revealed the presence of strong PAH features at 3.3, 6.2, 7.7, 8.6, 11.3 microns and nano-diamonds features in the 3.4-3.5 μm region (Siebenmorgen et al. 2000; Van Kerckhoven et al. 2002). No silicate emission band at 10 μm appears in the spectra of HD 97048. Recent mid-IR long slit spectroscopic observations with TIMMI2 show that the aromatic emission features at long wavelength (i.e., 8.6 and 11.3 μm) are extended and come mostly from a region of 200-300 AU, likely a disk (van Boekel et al. 2004). These results have been confirmed recently by imaging data taken in the PAH band at 8.6 μm (Lagage et al. 2006). The large extended part of the mid-IR emission seen on scales of 5 to 10 arcsec by Prusti et al. (1994) and Siebenmorgen et al. (2000) is most likely due to an extended envelope of transiently heated very small grains and PAHs surrounding the star and the disk system. Using Adaptive Optics high angular resolution ($\sim$0.1 arcsec) spectroscopic observations, Habart et al. (2004, 2005) were also able to spatially resolve the emission in the aromatic and diamond features around 3 μm and found that the emission must be within 30 AU closely related to the star-disk system. Finally, Weintraub et al. (2005) have recently reported near-IR molecular hydrogen emission for this object.

3. VISIR observations

3.1. Observations

The observations were performed using the ESO mid-infrared instrument VISIR installed on the VLT (Paranal, Chili), equiped with a DRS (former Boeing) 256×256 pixels BIB detector. The object was observed on 2005, January 25^{th} and June 17^{th}. It was observed in the PAH bands at 8.6 and 11.3 μm and in the adjacent continuum. The data at 8.6 μm were already used in Lagage et al. (2006). In this paper, we focus on the data obtained at 11.3 μm. A summary of the observations is given in Table 1. These data were taken with an imaging mode of VISIR which allows diffraction-limited image in the N band: the BURST mode.

Under good seeing ($\leq$ 0.5 arcsec in the visible), the images in the mid-IR are diffraction-limited even on a 8 meter class telescope. Unfortunately, the median seeing experienced at Paranal is rather of 0.8 arcsec, which degrades the angular resolution. Indeed, for a seeing of 0.8 arcsec in the visible, assuming that the wavelength dependence of the seeing follows a $\lambda^{-1/5}$ law, the seeing value at 10 μm is 0.4 arcsec, which is larger than the diffraction limit of 0.3 arcsec. This represents a 5 pixels movement on the detector with the smallest field of view of VISIR (0.075"/pixel). In order to get the best spatial resolution with VISIR, we experiment a new imaging mode on bright objects, the *BURST mode*. The principle is to take short enough exposure images ($\lesssim$ 50 ms) to freeze the turbulence; the coherence time of the atmosphere at 10 μm is around 300 ms at Paranal for a good seeing. In order to correct for the turbulence by offline processing, the data are stored every 1000 elementary images in one nodding position for a chopping frequency of 0.25 Hz in the direction north/south. The nodding direction is perpendicular to the chopping direction with an amplitude of 8". After classical data reduction in mid-IR, a cube of 500[1] images chopped and nodded (4 beams/image) is obtained. Because of the turbulence, each source on an image moves independently and as a result, we have to extract individually the 4 sources in each image (4 quarters) of the cube and shift and add the image with the ones corresponding to the same quarter. Finally, we shift and add the four final images of the four quarters.

3.2. Results

In this section, we present the images of HD 97048 obtained in the PAH emission filter, as well as in the adjacent continuum emission, and compared it with the standard star in the same filters.

Fig. 1 shows the image of HD 97048 in the PAH filter centered at 11.3 μm and compared with the standard star HD85503. HD 97048 is quite extended - up to 2 arcsec

[1] 1000 divided by 2 because of the 2 chopper positions

Table 1. Observations of HD 97048 in the different VISIR filters in imaging BURST mode. The sensitivity were calculated for each night in the BURST mode. The filter are free of any strong atmospheric line contribution.

Filter	Central wavelength (μm)	half band width (μm)	Sensitivity (mJy/10σ/1h)	Elementary exposure time (ms)	Total time on source (s)	Date	Seeing (arcsec)	Airmass	Standard star
SIV	10.49	0.16	5.6	25	600	17/06/2005	0.80	1.74	HD91056
PAH2	11.26	0.59	4.5	50	800	25/01/2005	0.55	1.66	HD85503
NeII	12.27	0.18	7.7	16	320	17/06/2005	0.80	1.74	HD91056

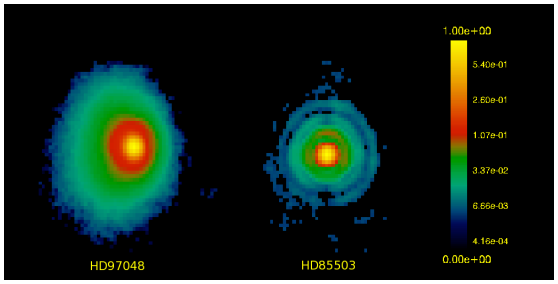

Fig. 1. *On the left*, HD 97048 in the PAH2 filter (centered at 11.3 μm) with VISIR camera. *On the right*, PSF reference (HD85503) with the same filter. The two object are normalized in order to see the extension. The object is more extended than the reference with an asymmetry east/west in the emission.

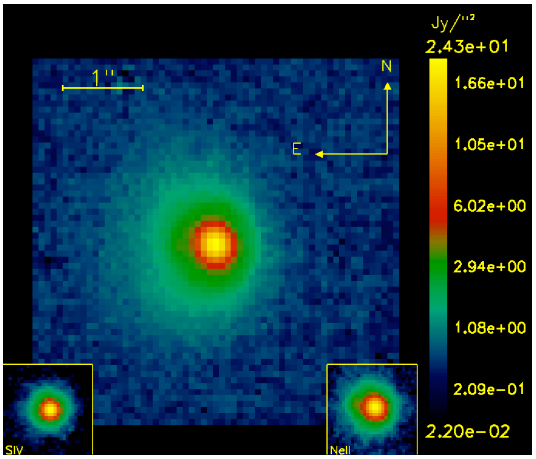

Fig. 2. HD 97048 in the PAH2 filter (*image in the middle*), and in the adjacent continuum (SIV *on the left*, NeII *on the right*). The images have the same signal-to-noise so that it is possible to compare the extension.

- compared to the reference star. The full-width at half-maximum (FWHM) of HD 97048 is 1.2 times that of the standard star, close to the diffraction-limit, for almost all filters (Tab. 2). In addition, comparing the emission in the PAH band and in the adjacent continuum (Fig. 2), the emission in PAH is much more extended than in the continuum. Fig. 3 shows the brightness spatial distribution along a cut in the north/south and east/west direction in the PAH filter and in the adjacent continuum (SIV) compared to the standard star in SIV filter. In the PAH filter, the disk is extended in the direction north/south up to 320 AU (surface brightness of 53 mJy/"^{2}) whereas the extension in the continuum at 10.5 μm goes to 135 AU (surface brightnesss of 110 mJy/"^{2}). These results are in agreement with those already found in the previous study at 8.6 μm (Lagage et al. 2006). Furthermore, it is also interesting to point out that the continuum is extended, when comparing the object and the reference star in the SIV filter. Finally, by comparing the VISIR and ISO (Infrared Space Observatory) fluxes, we found that the PAH emission peak to the continuum is stronger in the ISO spectrum. This is certainly due to the surrounding nebula, as already suggested by van Boekel et al. (2004). Based on the fluxes measured in the wavelength bands at 8.6 and 11.3 μm, we estimate that the nebula contamination is about 40%, in agreement with that found by van Boekel et al. (2004).

4. Disk model

In order to analyse the observations, we use the disk model described in Dullemond et al. (2001); Dominik et al. (2003); Dullemond & Dominik (2004a), including the most up to date understanding of disk structure and physics around Herbig Ae/Be stars. In the following, we describe the disk structure and the radiation transfer used and give the details of the adopted dust model.

4.1. Disk structure

We consider disks heated by irradiation from the central star, in hydrostatic equilibrium in the vertical direction, with dust and gas well mixed (flared disks, Chiang & Goldreich (1997)). In this model, the stellar flux impinging with flaring angle α upon the disk is absorbed in the upper layers of the disk, which will reradiate half of the flux away from the disk and half down into its deeper layers. The inner boundary (rim) is directly exposed to the stellar flux and is puffed up since it is hotter than the rest of the disk. The model computes how much the inner rim puffs up, and how much of the disk behind it will be shadowed by this puffed-up rim (Dullemond et al. 2001). Once the star is given, the disk structure (i.e pressure scale height and flaring angle) is completely defined after specifying the inner and outer radii, the surface density distribution ($\Sigma = \Sigma_0(R/R_0)^{-p}$,with R_0 a fiducial radius) and the dust model. The models are appropriate for disks that are optically thick to the stellar radiation. It is the case for disks around pre-main sequence stars, up to very large radii (e.g., 5000 AU for a disk mass $M_d \sim 0.2 M_\odot$, p=1).

Table 2. Comparaison of the FWHM for the object and the reference star (PSF) in the different filters. We also mentionned the theorical value of the FWHM in order to show that the diffraction-limit is obtained with the BURST mode. In order to see the spatial extension, we notice in the third and fourth columns the distance from the star at 10 σ above the noise in the east/west direction.

		HD97048					PSF		
Filter	Central wavelength (μm)	Flux measured (Jy)	East (10 σ) (arcsec)	West (10 σ) (arcsec)	FWHM (east/west) (mas)	FWHM (north/south) (mas)	FWHM (east/west) (mas)	FWHM (north/south) (mas)	FWHM (diffraction) (mas)
SIV	10.49	4.2 ± 0.1	0.67	0.60	322 ± 15	337 ± 15	277 ± 15	262 ± 15	262
PAH2	11.26	7.7 ± 0.1	1.60	0.90	337 ± 15	360 ± 15	300 ± 15	285 ± 15	285
NeII	12.27	6.7 ± 0.2	0.67	0.60	390 ± 15	412 ± 15	300 ± 15	307 ± 15	307

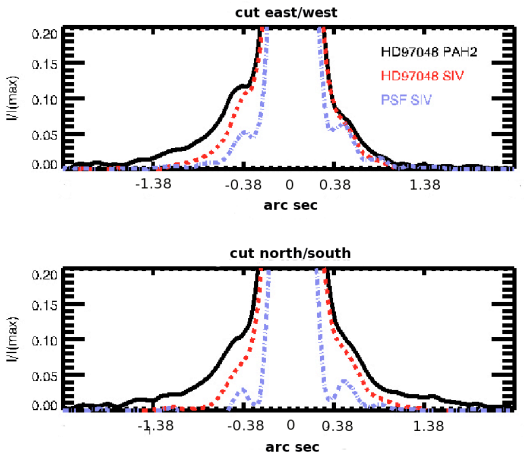

Fig. 3. Normalized intensity profiles along a cut through the VISIR images of HD 97048 in the PAH band (full line) and in the continuum SIV (dashed line) superimposed on a reference star (dashed-dot line) in SIV band. Direction East/West is in the upper panel and above, it represents the direction South-North. Comparing the PAH band and the adjacent continuum (for a same signal-to-noise), HD 97048 is much more extended in the PAH band. Comparing the PSF and the object in SIV, we see that HD 97048 is also extended in the continuum.

4.2. Radiative transfer

We use the 3-dimensional Monte Carlo radiative transfer code `RADMC` (Dullemond & Dominik 2004a), for which a module to treat the emission from quantum-heated PAH molecules has been included. This module will be described in detail in Dullemond et al. (in prep.), but a rough description has been given by Pontoppidan et al. (2006) and for a recent publication using it, see Geers et al. 2006. The code `RADMC` (Dullemond & Dominik 2004a; Pontoppidan & Dullemond 2005) solves the temperature structure of the disk in a Monte-Carlo way using a variant of the algorithm of Bjorkman & Wood (1997). This Monte-Carlo code also produces the source terms for scattering, in the isotropic-scattering approximation.

4.3. Dust model and PAH properties

The dust is a mixture of grains in thermal equilibrium and transiently heated PAHs.

- **Thermal grains**: The grains are composed of graphite and silicate with optical constants from Draine (1985). They have a MRN (Mathis et al. 1977) size distribution ($n(a) \propto a^{-3.5}$) with a size between 0.01 μm and 0.3 μm. Since no silicate emission features have been detected in HD97048 (see Sect. 2), we have considered the hypothesis of thermal decoupling carbon and silicate grains (see Sect. 5). But this effect could be due to a geometrical effect or less silicate abundance in the inner regions.
- **Transiently heated grains** (PAH): We can explain the observed PAH spectra, at least of the isolated HAe stars, with PAH abundances and qualitative properties similar to those of PAHs in the ISM (Habart et al. 2004a). In the ISM, PAHs are made up of a few tens up to a few hundreds of carbon atoms; for reasons of simplicity, we take only one PAH size in our model, $N_C = 100$. The hydrogen to carbon ratio is $H/C = f_H \times (6/N_C)^{0.5}$ (case of compact symmetric PAHs, see Omont (1986)) with f_H - the hydrogenation fraction of the molecule. Here, we consider f_H equal to 1 (i.e., essentially fully hydrogenated PAHs) or 0.5 (partially hydrogenated PAHs). We take the absorption cross section from Li & Draine (2001) based on both laboratory data and astrophysical spectra. Those authors consider the bands at 3.3, 8.6, 11.3, 11.9 and 12.7 μm from vibrational modes of the aromatic C-H bond; the strong bands at 6.2 and 7.7 μm due to vibrations of the aromatic C-C bonds; and a few weak features probably caused by C-C bending modes at 16.4, 18.3, 21.2 and 23.1 μm. With respect to the charge, in order to keep the model simple, we ignore that we have probably in disks a mixture of neutral and charged PAHs and we assume that PAHs are mostly neutral. Simple determination of the ratio between the photoionisation rate of the grain to the electron-grain recombination rate suggests that this is probably the case in the outer regions ($R \geq 150$ AU) of a disk heated by a typical HAe star (see Habart et al. (2004b) for more details). Finally, we do not take into account photo-destruction of PAHs in a strong FUV radiation field.

In summary, we adopt a dust model with large thermal grains of graphite and silicate and small transiently heated aromatic particles. The silicate abundance in dust

is $[Si/H] = 3.10^{-5}$, and the total carbon abundance in dust is $[C/H] = 2.2\ 10^{-4}$. Of this 10% are in PAH and 90% in large grains.

5. Comparison between model and observations

In this section, we compare the model's predictions to the observations. In the following, we first describe the adopted stellar and disk parameters for HD 97048 and thus discuss the results of the calculation and the confrontation to the observations.

5.1. Stellar and disk parameters

A Kurucz model spectrum is taken for the central star with T_{eff} = 10000 K. The stellar parameters ($L_\star = 32 L_\odot$, $M_\star = 2.5 M_\odot$) were chosen from stellar evolutionary tracks by Siess et al. (2000) for an age of 3 Myr (Lagage et al. 2006). Once the stellar flux has been redenned, the resulting SED is in agreement with the photometry extracted from Hillenbrand et al. (1992) in the UV and near-IR. To correct for extinction, we used the method of Cardelli et al. (1989) where we adopt A_V=1.24 (van den Ancker et al. 1998) and E(B-V)=0.36 (Davies et al. 1991; The et al. 1986).

Concerning the disk's parameters, the surface density is taken equal to $\Sigma = \Sigma_0\ (r/R_{in})^{-q}$ with q the power law index equal to 3/2 inferred for the solar nebula (Weidenschilling 1977) and $\Sigma_0 = 444\ g.cm^{-2}$ a minimum value deduced from VISIR observations (Lagage et al. 2006). The inner radius R_{in} is at the dust (silicate) evaporation radius at 0.4 AU from the central star and the outer radius is at 370 AU as deduced from observations (Lagage et al. 2006). Finally, as the disk is vertically optically thick at the wavelength of observation, a minimum mass of 0.01 $M_\odot$ (gaz + dust) can be derived (Lagage et al. 2006). We take this minimum disk mass as a first guess.

5.2. Disk's structure

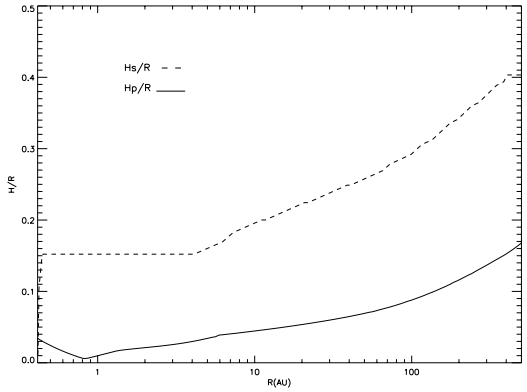

Fig. 4. Structure of the disk for the template model. The surface (dashed line) and pressure (full line) scale height of the flared disk versus the distance from the central star.

Figure 4 shows the run with radius of the pressure (H_p) and photospheric (H_s) scale height. The disk is flaring with H_s increasing with radius as $R^{9/7}$ (Chiang & Goldreich 1997). At a radius of 135 AU, H_s= 51 AU.

In a previous work, we used the VISIR PAH band image to constrain the parameters of the disk structure around HD 97048 (Lagage et al. 2006). Using a very simple model, Lagage et al. (2006) measured an flaring index of $1.26^{+0.05}_{-0.05}$ and H_s=$51.3^{+0.7}_{-3.3}$ AU at 135 AU. Both values are very close to those expected from our hydrostatic, radiative equilibrium models of passive flared disks (Chiang & Goldreich 1997; Dullemond et al. 2001).

Concerning the structure of the inner region, VISIR has clearly not enough spatial resolution to constrain it. The puffed inner rim and the shadow region lie within the central pixel of VISIR (1 pixel is equivalent to 13.5 AU for a distance of 180 pc) and the two effects[2] compensate each other in terms of resulting mid-IR emission. Finally, we would like to underline that as soon as the disk is vertically optically thick in the mid-IR, the change of the slope of the surface density in the model does not have any influence on the structure of the disk or its mid-IR emission and cannot be constrained here.

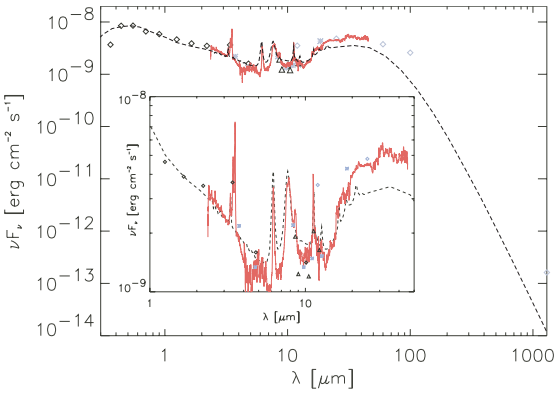

Fig. 5. SED calculated with the template model (dashed line). The disk is inclined by 43 ° and the system is situated at a distance of 180 pc. A Kurucz model spectrum is taken for the central star with T_{eff} = 10000 K. The luminosity is $L_\star = 32 L_\odot$ and the mass $M_\star = 2.5 M_\odot$. The disk is flared with a total mass of 0.01 $M_\odot$, R_{in}=0.41 AU and R_{out}=370 AU. Full red line shows ISO SWS spectrum of HD 97048. Points of photometry are taken from Hillenbrand et al. (1992) (open diamond black), IRAS (open diamond blue), Prusti et al. (1994) (blue crosses) and VISIR measurement (black triangle)

5.3. Spectral energy distribution

Figure 5 shows the calculated spectrum in the 0.1-1300 μm range for a star/disk system inclined by 43 degree and situated at 180 pc. At short wavelength between 0.1 to $\sim$1μm, the emission is made by the stellar photosphere. The near-IR emission (around 3 μm) is induced by the puffed inner rim. The region which emits between 5 and 8 μm corresponds to the shadow region. In this part, the disk is not in sight of the star itself, but it receives flux from the inner rim,

[2] Increasing the height of the inner rim augments the shadow region.

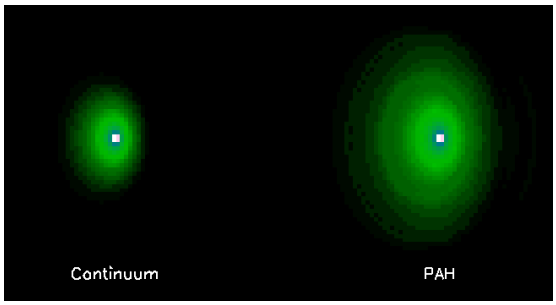

Fig. 6. The non PSF-convolved predicted image for our template model in the adjacent continuum (at 10.5 μm on the left) and in the PAH band at 11.3 μm (on the right).

which is sufficiently strong to keep the disk up. At larger radii, the flaring disk reappears from the shadow, and produces the rise observed in the spectrum around 20-30 μm. Concerning the dust spectroscopic features, the PAH emission features are clearly visible, and some of them at 3.3, 6.2, 7.7 and 11.3 μm are very strong. Strong ratio between 30 and 10 μm and PAH features show that the disk intercepts a large fraction of energy in the outer part and are indeed evidence of a flared disk geometry. For geometrically flat disks, PAH features are predicted to be very weak, even when PAH with standard properties are present on the disk surface (Habart et al., 2004). The infrared emission under the narrow PAH features is mostly due to the large thermal grains which are very hot in the inner regions. For the model in which carbon and silicate grains are thermally coupled, it is possible to see, for example, the strong broad feature due to silicate emission peaking at about 10 μm. On the other hand, for the model in which the grains are decoupled, one can see (Fig.5) that this feature almost disappears.

In Figure 5, we also compare the predicted SED to one of HD 97048 constructed with different sets of data. Photometric points from the visible to the mid-IR were taken from Hillenbrand et al. (1992) and Prusti et al. (1994). To that we have added IRAS and VISIR photometric measurements. Spectroscopic observations were obtained with ISO-SWS (Short Wavelength Spectrometer) (Acke & van den Ancker 2004). The model reproduces roughly well the global shape of the observed SED of HD97048. The agreement between predicted slopes and absolute fluxes from the near- to mid-IR waves with observed ones is rather acceptable (differences $\leq$20-40%). Moreover, our model reproduces also well the observed intensity of the most commonly observed PAH features, i.e., 3.3, 6.2, 7.7 and 11.3 μm, especially if we correct for contamination by the associated reflection nebula (about 40%, see Section 3). This is in agreement with previous comparisons made by Habart et al. (2004) between flared disk model results and observed PAH emission features with ISO and ground-based telescopes of some thirty HAeBe stars, including HD 97048.

Nevertheless, one can note that there is some mismatch between the predicted and observed PAH spectra; the strength of the 8.6 μm feature is, for example, significantly underestimated by the model. However, this is not surprising considering the uncertainties on the PAH absorption cross section (Li & Draine 2001) and our simple hypothesis that PAH are characterized by a single charge state, size or hydrogenation parameter along the disk. This is unlikely to be the case and is briefly discussed in this section. Also, one can note that HD 97048 presents peculiar strong features that peaks at 3.43 and 3.53 μm not predicted by our model. Several studies have proposed attributing these features to surface C-H stretching modes on nanodiamond particles (e.g., Guillois et al. 1999; Van Kerckhoven et al. 2002; Sheu et al. 2002; Jones et al. 2004). Because of the good match between laboratory and observed spectra, this identification is very convincing.

In addition, the absence of the small grains of silicate features in the HD 97048 spectra could appear intriguing since they are the most abundant dust species in interstellar space. However, in ISO spectra, Acke & van den Ancker (2004) reported non detection of silicate feature for 16 objects out of 46 showing that the absence of the silicate feature is a common phenomenon among HAeBe stars. The silicate emission at 10 μm is arising from grains with a size of 0.1 μm thermally heated in the inner region ($1 < r < 10$ AU) from direct and/or indirect irradiation by the central star. The absence of this emission could probably result from various effects concerning either the dust properties either the disk geometry. But this issue could not be invistigated with the resolution of VISIR observations.

Finally, concerning the longer wavelength, we find that the submm flux is too low by a factor 70 compared to observations (Henning & Launhardt 1998). This shows that a large reservoir of large grains (around a millimeter size) must exist in the outer regions of the disk. These grains would naturally reside close to the midplane and therefore do not affect the shape of the disk. They are therefore not within the focus of this paper, and for this reason we do not include them in our model. If we would have included them, they would only affect these long-wavelength fluxes, because the disk has a flaring geometry (see e.g. Dullemond & Dominik 2004a, Figs. 6 and 7).

5.4. Imaging

Figure 6 shows the modelled disk image in the PAH band at 11.3 μm and the adjacent continuum. These emissions both originate from the optically thin surface of the disk but the PAH emission is much more extended than the adjacent continuum. The continuum reaches 50 % of its integrated intensity at a very small radius (about 2 AU), while the PAH feature does so at large radii (about 100 AU). This behaviour basically reflects the different excitation mechanisms of grains in thermal equilibrium and PAHs transiently heated. Only grains very near the star are warm enough to emit at 11 μm whereas PAHs farther away can be excited and emit in the 11.3 μm feature. The emission at 11.3 μm (band + continuum), in the central part of the disk (< 2 AU) is dominated by the thermal emission from silicate and carbon grains, whereas in the outer regions of the disk, the emission is dominated by the PAH feature. Morever, among the PAH features, the 11.3 μm is one of the most extended spatially. Indeed, as discussed in Habart et al. (2004b), the features at shorter wavelengths are in fact stronger in the inner part of the disk (where PAHs are hotter because multiphoton events occur where the radiation field is most intense), decreasing rapidly in the outer cold part. On the other hand, the features at longer wavelengths are more extended.

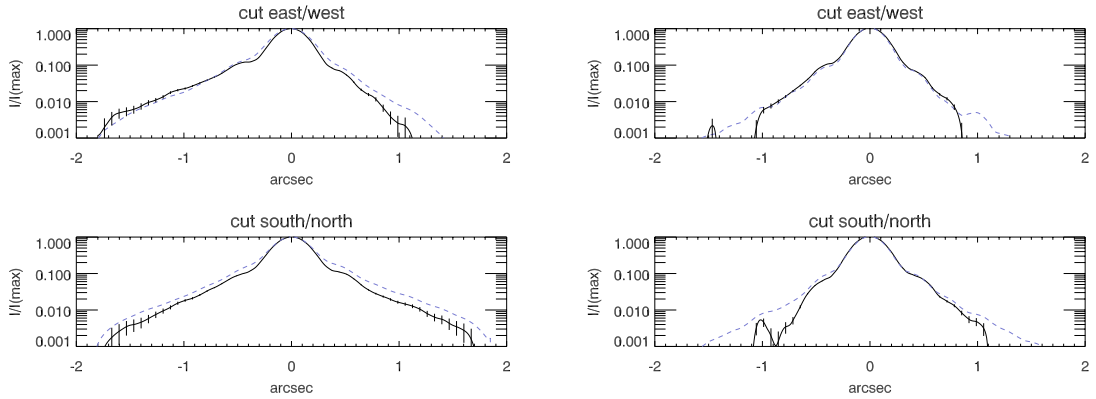

Fig. 7. *On the left*, cut in north/south and east/west (up panel) for the template model of the PAH band at 11.3 μm convolved with VISIR PSF (dashed line) compared to the observation (full line). *On the right*, the same as on the left with the adjacent continuum at 10.5 μm.

Fig 7 shows the brightness emission profiles of the PAH feature and the adjacent continuum obtained by convolving the model with the corresponding PSF observed by VISIR. The model predicts a spatial distribution of the PAH emission very similar to that observed. The predicted FWHM and wings extension are in fact very closed to the observed ones (differences $\leq$20%). Moreover, our disk model predicts, as in the observations, an asymetry east/west, which only results from the inclination of a flared disk optically thick at the observed wavelength. This acceptable agreement gives a strong support for the physics underlying in our flared disk model. The disk parameter that most affects the PAH emission is in fact the disk flaring angle, which determines at each radius the fraction of FUV intercepted by the disk surface. Lower values of the flaring could be caused by a variety of reasons, for example if the dust settles toward the disk midplane (Dullemond & Dominik 2004b). If the disk is less flared, the PAH emission which directly tracks the illumination of the disk surface will strongly reduce in the outer disk region. Less flared disks will have less extended PAH emission features and weaker. This will be particularly true for the features at long wavelength, such as the 11.3 μm one, which have a large contribution from the outer disk. In the extreme case of a fully self-shadowed disks, the PAH feature strenghts should decrease by orders of magnitude and the spatial distribution should be similar to one of the adjacent continuum.

In addition, it is remarkable to note that, as predicted by the model, the observed spatial extension of the 11.3 μm feature is much larger than that observed for PAH feature at the 3.3 μm, which are extended on a scale of (several) 10 AU (Habart et al. 2004a). This has the interesting implication that PAHs appears to be present over a large range of radius; in other words, PAHs can survive over a wide range of physical conditions. Finally, concerning the spatial extent of the 10 μm adjacent continuum emission, the model predicts that it is slighlty broader than the PSF but still agrees with the observations.

It must be emphasized here that there are several complications which we have neglected. The most obvious is that we have assumed that PAHs can be characterized by a single size, hydrogenation and charge state. This is unlikely to be the case, and one can expect variations as a function of radius and depth in the disk. For example, PAHs are likely to be more positively ionized in the inner disk regions. Moreover, processes such as photo-evaporation or coagulation could affect the abundance and size of PAHs. In order to get some insight into the specific PAH properties, one needs spatial information of several band strength ratios. We are developing this study in a forthcoming paper.

.

6. Summary and conclusions

In a former paper (Lagage et al. 2006), we were able to constrain for the first time the flaring geometry of a disk around an intermediate-mass young star HD97048. These results were based on a very simple model making several assumptions such as a surfacic PAH emission, an optically thick disk, and a power-law function for the surface height and the intensity. In the present paper, using a full radiative transfer model based on predicted disk geometries assuming hydrostatic equilibrium (Dullemond et al. 2001; Dominik et al. 2003; Dullemond & Dominik 2004a), we could:

- justify the hypothesis made in the previous paper (Lagage et al. 2006), and therefore confirm the results, e.g., the images calculated with a different code (Pinte et al. 2006).
- show that both SED and spatial distribution of the PAH emission and the adjacent continuum are in very good agreement with the model predictions for common disk parameters.
- take the general agreement between observations and predictions as a strong support for the physical pictures underlying our flared disk model.

References

Acke, B. & van den Ancker, M. E. 2004, A&A, 426, 151
Cardelli, J. A., Clayton, G. C., & Mathis, J. S. 1989, ApJ, 345, 245
Chiang, E. I. & Goldreich, P. 1997, ApJ, 490, 368

Davies, J. K., Evans, A., Bode, M. F., Whittet, D. C. B., & Kilkenny, D. 1991, MNRAS, 252, 271
Dominik, C., Dullemond, C. P., Waters, L. B. F. M., & Walch, S. 2003, A&A, 398, 607
Doucet, C., Pantin, E., Lagage, P.-., & Dullemond, C. P. 2006, A&A, in press
Dullemond, C. P. & Dominik, C. 2004a, A&A, 417, 159
Dullemond, C. P. & Dominik, C. 2004b, A&A, 421, 1075
Dullemond, C. P., Dominik, C., & Natta, A. 2001, ApJ, 560, 957
Guillois, O., Ledoux, G., & Reynaud, C. 1999, ApJL, 521, L133
Habart, E., Natta, A., & Krügel, E. 2004a, A&A, 427, 179
Habart, E., Testi, L., Natta, A., & Carbillet, M. 2004b, ApJL, 614, L129
Henning, T. & Launhardt, R. 1998, A&A, 338, 223
Hillenbrand, L. A., Strom, S. E., Vrba, F. J., & Keene, J. 1992, ApJ, 397, 613
Jones, A. P., d'Hendecourt, L. B., Sheu, S.-Y., et al. 2004, A&A, 416, 235
Lagage, P.-., Doucet, C., Pantin, E., et al. 2006, Science express, 10.1126/science.1131436
Li, A. & Draine, B. T. 2001, ApJL, 550, L213
Mathis, J. S., Rumpl, W., & Nordsieck, K. H. 1977, ApJ, 217, 425
Meeus, G., Waters, L. B. F. M., Bouwman, J., et al. 2001, A&A, 365, 476
Omont, A. 1986, A&A, 164, 159
Perrin, M. D., Duchêne, G., Kalas, P., & Graham, J. R. 2006, ApJ, 645, 1272
Pinte, C., Ménard, F., Duchêne, G., & Bastien, P. 2006, A&A, 459, 797
Pontoppidan, K. M. & Dullemond, C. P. 2005, A&A, 435, 595
Prusti, T., Natta, A., & Palla, F. 1994, A&A, 292, 593
Sheu, S.-Y., Lee, I.-P., Lee, Y. T., & Chang, H.-C. 2002, ApJL, 581, L55
Siebenmorgen, R., Prusti, T., Natta, A., & Müller, T. G. 2000, A&A, 361, 258
The, P. S., Tjin, H. R. E., Steenman, H., & Wesselius, P. R. 1986, A&A, 155, 347
van Boekel, R., Waters, L. B. F. M., Dominik, C., et al. 2004, A&A, 418, 177
van den Ancker, M. E., de Winter, D., & Tjin A Djie, H. R. E. 1998, A&A, 330, 145
van den Ancker, M. E., The, P. S., Tjin A Djie, H. R. E., et al. 1997, A&A, 324, L33
Van Kerckhoven, C., Tielens, A. G. G. M., & Waelkens, C. 2002, A&A, 384, 568
Waters, L. B. F. M. & Waelkens, C. 1998, Annual Review of Astron and Astrophys, 36, 233
Weidenschilling, S. J. 1977, Astrophysics and Space Science, 51, 153
Weintraub, D. A., Bary, J. S., Kastner, J. H., Shukla, S. J., & Chynoweth, K. 2005, in Protostars and Planets V, 8197–+
Whittet, D. C. B., Prusti, T., Franco, G. A. P., et al. 1997, A&A, 327, 1194

Annex

Detection of warm molecular hydrogen in the circumstellar disk around the Herbig Ae star HD 97048

published in the journal *ApJ*, September 2007

The Astrophysical Journal, 666: L117–L120, 2007 September 10
© 2007. The American Astronomical Society. All rights reserved. Printed in U.S.A.

DETECTION OF WARM MOLECULAR HYDROGEN IN THE CIRCUMSTELLAR DISK AROUND THE HERBIG Ae STAR HD 97048

C. Martin-Zaïdi,[1] P.-O. Lagage,[1] E. Pantin,[1] and E. Habart[2]
Received 2007 July 6; accepted 2007 July 26; published 2007 August 24

ABSTRACT

We present high-resolution spectroscopic mid-infrared observations of the circumstellar disk around the Herbig Ae star HD 97048 with the VLT Imager and Spectrometer for the mid-InfraRed (VISIR). We detect the $S(1)$ pure rotational line of molecular hydrogen (H_2) at 17.035 μm arising from the disk around the star. This detection reinforces the claim that HD 97048 is a young object surrounded by a flared disk at an early stage of evolution. The emitting warm gas is located within the inner 35 AU of the disk. The line-to-continuum flux ratio is much higher than expected from models of disks at local thermodynamic equilibrium. We investigate the possible physical conditions, such as a gas-to-dust mass ratio higher than 100 and different excitation mechanisms of molecular hydrogen (e.g., X-ray heating, shocks), that would explain the detection. We tentatively estimate the mass of warm gas to be in the range from 10^{-2} to nearly 1 $M_{\rm Jup}$. Further observations are needed to better constrain the excitation mechanisms as well as the mass of gas.

Subject headings: circumstellar matter — infrared: stars — planetary systems: protoplanetary disks — stars: individual (HD 97048) — stars: pre–main-sequence

1. INTRODUCTION

Circumstellar (CS) disks surrounding pre–main-sequence stars are supposed to be the location of planet building. The characterization of the gaseous component, which initially represents 99% of the total disk mass, is a key research question toward an understanding of protoplanetary disks and planet formation. However, from previous observations, little is known about the gas compared to the dust. Major questions concerning planet formation remain. How massive are the disks? Can giant planets form in every disk? How long does the planet formation process take? Detailed information is required about the gas in disks in order to address these questions. In particular, characterizing the warm gas phase in the inner disk ($R < 50$ AU), where planet formation is supposed to take place, is an essential step.

Molecular hydrogen (H_2) is the main constituent of the molecular cloud from which the young star is formed and is also expected to be the main component of the CS disk. It is expected to be at least 10^4 times more abundant than other gas tracers such as carbon monoxide (CO) (e.g., Bell et al. 2006), since it self-shields very efficiently against photodissociation by far-ultraviolet (FUV) photons and does not freeze effectively onto grain surfaces. H_2 is the only molecule that can directly constrain the mass reservoir of warm and hot molecular gas in disks. Indeed, the detection of H_2 excited by collisions allows us to measure the temperature and density of the warm gas. Unfortunately, direct observation of H_2 is difficult. Electronic transitions occur in the ultraviolet to which the Earth's atmosphere is opaque, and rotational and rovibrational transitions at infrared (IR) wavelengths are faint because of their quadrupolar origin. FUV absorption lines have been observed with the *FUSE* satellite in the spectrum of some Herbig Ae stars and show the presence of warm ($T_{\rm gas} > 300$ K) molecular hydrogen gas in the CS environment of these stars (Martin-Zaïdi et al. 2007). However, absorption observations require specific configurations to observe the gas within the disks, i.e., nearly edge-on. Due to the high inclination angles to the lines of sight estimated for the disks observed by Martin-Zaïdi et al. (2007) the detected H_2 is not in the disk. Those authors concluded that the lines of sight probably pass through a thin layer of warm/hot gas above the surface of the disk that is produced by the photoevaporation of the disk. Searches for mid-IR H_2 rotational emission lines have been performed using different space- and ground-based instruments. Space-based instruments on *ISO* and *Spitzer* have low spectral and spatial resolution, and therefore have not yielded an unambiguous detection of H_2 line emission from protoplanetary disks (Thi et al. 2001; Pascucci et al. 2006). Indeed, when detections of H_2 toward a few pre–main-sequence stars have been claimed with *ISO* SWS (Thi et al. 2001), ground-based observations showed that contamination from surrounding cloud material was important and that *ISO* detections were likely not dominated by the emission of the disk gas (e.g., Richter et al. 2002; Sako et al. 2005). Recently, Carmona et al. (2007) estimated the line-to-continuum ratio that should be observed for H_2 transitions in the mid-IR. They used a two-layer model (Chiang & Goldreich 1997; Dullemond et al. 2001) of a gas-rich disk [column density of $N(H_2) = 10^{23}$ cm^{-2}] seen face-on, located at 140 pc from the Sun, with local thermodynamics equilibrium (LTE) for the gas and dust, $T_{\rm gas} = T_{\rm dust}$, and assuming a gas-to-dust mass ratio of about 100. Those authors concluded that the expected peak flux of the $S(1)$ line at 17.035 μm, observed at a spectral resolution of 20,000, should be less than 0.3% of that of the continuum at temperatures higher than 150 K, and thus should not be observable with the existing instruments. Indeed, they did not detect any H_2 mid-IR emission line in their sample of six Herbig Ae stars.

However, H_2 rotational lines have been recently detected in the disk around one Herbig Ae star, namely AB Aur, with the high spectral and spatial resolution TEXES spectrometer (Bitner et al. 2007). These detections imply that H_2 can be observed in the mid-IR domain when particular physical conditions exist in disks.

The VLT Imager and Spectrometer for the mid-InfraRed (VISIR; Lagage et al. 2004) has the high spectral ($10{,}000 < R$

[1] Laboratoire AIM, CEA/DSM–CNRS–Université Paris Diderot; and DAPNIA/Service d'Astrophysique, Bat. 709, CEA/Saclay, 91191 Gif-sur-Yvette Cedex, France; claire.martin-zaidi@cea.fr, pierre-olivier.lagage@cea.fr, epantin@cea.fr.

[2] Institut d'Astrophysique Spatiale, 91405 Orsay, France; emilie.habart@ias.u-psud.fr.

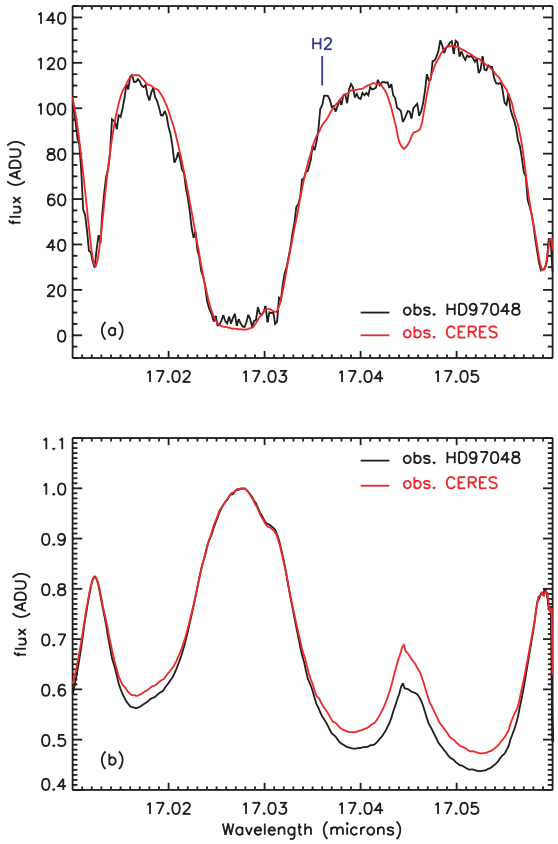

FIG. 1.—(*a*) VISIR spectrum of the Ceres asteroid (*red*) overplotted on the HD 97048 spectrum (*black*). (*b*) Spectrum of the sky during the observations of HD 97048 and Ceres.

< 30,000) and spatial resolution necessary to pick up such narrow gas lines from the disks. In addition, high spectral resolution is a key element to disentangle the H_2 line from the absorption lines due to the Earth's atmosphere. The spectral ranges covered by VISIR offer access to the most intense pure rotational lines of molecular hydrogen: $S(1)$ ($v = 0$–0, $J = 3$–1) at 17.0348 μm, $S(2)$ ($v = 0$–0, $J = 4$–2) at 12.2786 μm, $S(3)$ ($v = 0$–0, $J = 5$–3) at 9.6649 μm, and $S(4)$ ($v = 0$–0, $J = 6$–4) at 8.0250 μm. The $S(0)$ ($v = 0$–0, $J = 2$–0) transition near 28 μm is not observable from the ground due to the Earth's atmospheric absorption.

A particularly interesting object to study the CS material around a pre–main-sequence intermediate-mass star is HD 97048. HD 97048 is a nearby, relatively isolated Herbig A0/B9 star located in the Chamaeleon cloud at a distance of 180 pc (van den Ancker et al. 1998). Its age has been estimated from evolutionary tracks to be of the order of 3 million years (kindly computed by L. Testi and A. Palacios). This star is known to be surrounded by an extended CS disk. The VISIR imaging observations of this star conducted on 2005 June 17 and 19 have revealed an extended emission of PAHs (polycyclic aromatic hydrocarbons) at the surface of a flared disk inclined to the line of sight by $42.8^{+0.8}_{-2.5}$ deg (Lagage et al. 2006). This is the only Herbig star for which the flaring of the disk has been observed by direct imaging. The flaring index has been measured to be 1.26 ± 0.05, in good agreement with hydrostatic flared disk models (Lagage et al. 2006; Doucet et al. 2007). This geometry implies that a large amount of gas should be present to support the flaring structure and that the disk is at an early stage of evolution. This star is thus one of the best candidates to study the gas component in the disks of Herbig Ae stars.

In this Letter, we present VISIR observations of the $S(1)$ pure rotational emission line of molecular hydrogen at 17.03 μm arising from the disk of HD 97048.

2. OBSERVATIONS AND DATA REDUCTION

HD 97048 was observed for 1800 s with the high spectral resolution long-slit mode of VISIR on 2006 June 22. The central wavelength of the observation was set to 17.035 μm. We used the 0.75″ slit, providing a spectral resolution of about 10,000, i.e., $\Delta v = 30$ km s^{-1}.

The weather conditions were very good and stable during the observations; the optical seeing was less than 0.66″ and the air mass (<1.8) was close to the minimum air mass accessible when observing this object from the Paranal ESO observatory. The standard "chopping and nodding" technique was used to suppress the large sky and telescope background dominating at mid-infrared wavelengths. Secondary mirror chopping was performed in the north-south direction with an amplitude of 8″ at a frequency of 0.025 Hz. The nodding technique, necessary to compensate for chopping residuals, was applied using a telescope offset of 8″ in the south direction, every 3 minutes. The pixel scale was 0.127″ pixel^{-1}, resulting in a total field of view along the slit of about 32.5″. The elementary frames were combined to obtain chopping/nodding corrected data. The VISIR detector is affected by stripes randomly triggered by some abnormal high-gain pixels. A dedicated destriping method has been developed to suppress them (E. Pantin 2007, in preparation). In order to correct the spectrum from the Earth's atmospheric absorption and obtain the absolute flux calibration, we observed the Ceres asteroid and the standard star HD 89388 just before and after observing HD 97048. HD 89388 and Ceres were observed at nearly the same air mass and seeing conditions as the object. As shown in Figure 1*b*, air masses are slightly different between the observation of Ceres and that of HD 97048. However, the discrepancy between the two spectra of the sky cannot be responsible for the emission feature we observe in the HD 97048 spectrum around 17.035 μm, i.e., the H_2 line (Fig. 1*a*). We thus have divided the spectrum of HD 97048 by that of Ceres (which has a much better signal-to-noise ratio than that of the standard star HD 89388) to correct for the telluric absorption, and used the HD 89388 observed and modeled spectra (Cohen et al. 1999) to obtain the absolute flux calibration. The wavelength calibration is done by fitting the observed sky background features with a model of Paranal's atmospheric emission.

We note that Valenti et al. (2000) found $A_v = 0.24$ mag from the fit of the *IUE* spectrum of HD 97048; thus we have not corrected the spectrum for dust extinction, since it is negligible in our wavelength range for $A_v < 40$ mag (Fluks et al. 1994).

3. RESULTS

As shown in Figure 2*a*, we have detected the H_2 pure rotational $S(1)$ line near 17.03 μm. In the flux-calibrated spectrum, the standard deviation (σ) of the continuum flux was calculated in regions less influenced by telluric absorption, and close to the feature of interest. We deduced a 6 σ detection in amplitude for the line, corresponding to a signal-to-noise ratio of about 11 σ

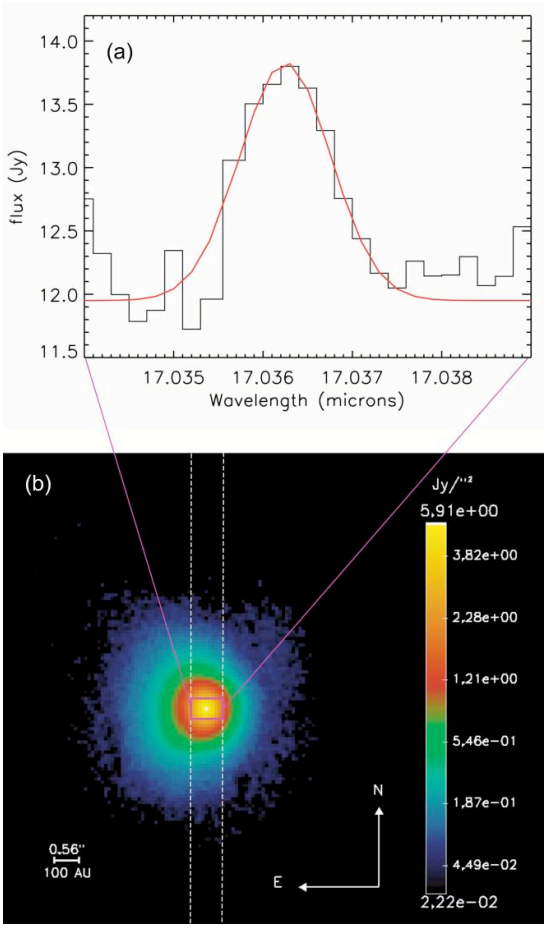

FIG. 2.—(*a*) *S*(1) H_2 emission line from HD 97048 disk, observed with the high spectral resolution mode of VISIR. *Black line*: Observed spectrum corrected for telluric absorption. *Red line*: Fit of a Gaussian with FWHM equal to a spectral resolution element. Here the spectrum has not been corrected for the Earth's rotation. (*b*) VISIR false-color image of the emission from the CS material surrounding HD 97048 (Lagage et al. 2006). *White dotted lines*: Position of the 0.75″ slit of the spectrograph during the observation of H_2 emission. *Purple rectangle*: One element of spatial resolution (diffraction limited). As the line is not spatially resolved, the H_2 emission arises within this element.

for the line, when integrating the signal over a resolution element (6 pixels). The line is not resolved as we can fit it with a Gaussian with a full width at half-maximum equal to a spectral resolution element of 30 km s^{-1} (see Fig. 2*a*). From our fit, assuming the emission arises from an isothermal mass of optically thin H_2, we derived an integrated flux in the line of 2.4×10^{-17} W m^{-2} or 2.4×10^{-14} ergs s^{-1} cm^{-2}.

Once the spectrum is corrected for the Earth's rotation, and knowing the heliocentric radial velocity of HD 97048 (+21 km s^{-1}; Acke et al. 2005), we estimated, from the wavelength position of the Gaussian peak, the radial velocity of H_2 to be about 4 ± 2 km s^{-1} in the star's rest frame. We thus considered that the radial velocity of the H_2 is similar to that of the star, implying that the emitting gas is bound to the star. The H_2 line is not resolved spatially. Given the VISIR spatial resolution of about 0.427″ at 17.03 μm, and the star distance (180 pc from the Sun), we can assess that the emitting H_2 is located within the inner 35 AU of the disk (Fig. 2*b*). We estimated the corresponding column densities and masses as a function of prescribed temperatures (Table 1). For this purpose, we first assumed that the line is optically thin and that the radiation is isotropic. In this context, assuming that the first rotational levels (up to $J = 3$) of H_2 are thermalized, and thus that their populations follow the Boltzmann law for a given temperature (LTE), the column densities are derived from the following formula:

$$I_{ul} = \frac{hc}{4\pi\lambda} N_u(H_2) A_{ul} \text{ ergs s}^{-1} \text{ cm}^{-2} \text{ sr}^{-1}, \quad (1)$$

where I_{ul} is the integrated intensity of the line, λ is the wavelength of the transition $J = u$–l, A_{ul} is the spontaneous transition probability, and $N_u(H_2)$ is the column density of the upper rotational level of the transition. Since the line is not spatially resolved, we calculated a lower limit on I_{ul} by dividing the integrated flux value by the solid angle of the point spread function, and thus obtained lower limits on the total column densities. Under the same assumptions as used for the calculations of the column densities and assuming that the medium we observe is homogeneous, the mass of warm H_2 is given by (Thi et al. 2001)

$$M_{\text{gas}} = f \times 1.76 \times 10^{-20} \frac{F_{ul} d^2}{(hc/4\pi\lambda) A_{ul} x_u(T)} \; M_\odot, \quad (2)$$

where F_{ul} is the line flux, d the distance in parsecs to the star, $x_u(T)$ is the fractional population of the level u at the temperature T in LTE (for details on the calculation method, see van Dishoeck 1992), and f is the conversion factor required for deriving the total gas mass from the H_2-ortho or H_2-para mass. Since $M_{H_2} = M_{H_2}(\text{ortho}) + M_{H_2}(\text{para})$, $f = 1 + 1/(\text{ortho/para})$ for the *S*(1) line (a H_2-ortho transition). The equilibrium ortho-para ratio at the temperature T was computed using Takahashi & Uehara (2001).

We also estimated the dust mass producing the flux level of the continuum in the spectrum. We used a simple model of optically thin emission of a given mass of dust at the surface of a disk. The grains have sizes between 0.01 and 100 μm and a size distribution following a power law with an index of −3.5. A fixed-composition mixture of amorphous silicates (50%) and amorphous carbon (50%) is assumed. For different temperatures (150, 300, 1000 K) assigned to the dust, we computed the corresponding mass of dust and derived gas-to-dust mass ratios. Our results are tabulated in Table 1.

TABLE 1

TOTAL COLUMN DENSITY AND MASS OF H_2, MASS OF DUST, AND GAS-TO-DUST MASS RATIO AS A FUNCTION OF THE TEMPERATURE

Parameter	150 K	300 K	1000 K
$N(H_2)$ (cm^{-2})	$>2.19 \times 10^{23}$	$>1.41 \times 10^{22}$	$>3.27 \times 10^{21}$
$M(H_2)$ (M_{Jup})	7.37×10^{-1}	4.51×10^{-2}	1.33×10^{-2}
M_{dust} (M_{Jup})	2.23×10^{-4}	1.03×10^{-5}	9.39×10^{-7}
Gas-to-dust mass ratio	3260	4378	14164

4. DISCUSSION

Our high-resolution spectroscopic observation of the *S*(1) pure rotational line of H_2 at 17.03 μm of HD 97048 has revealed the presence of significant amounts of warm gas in the inner

35 AU of the disk. From a Gaussian fit of the emission line, we derived very high column densities of warm gas, which are more than 2 orders of magnitude higher than those generally observed in the CS environment of Herbig Ae stars (Martin-Zaïdi et al. 2007). This confirms that HD 97048 is a young object surrounded by a circumstellar disk at an early stage of evolution. Indeed, photoevaporation of the gas is expected to clear up the inner part of the disk within 3 million years (Takeuchi et al. 2005).

We derived masses of the warm gas in the range from 10^{-2} to nearly 1 $M_{\rm Jup}$ (1 $M_{\rm Jup} \sim 10^{-3}$ $M_{\odot}$), depending on the adopted temperature and assuming LTE. The masses derived here are lower than those of Lagage et al. (2006), who have estimated a minimum mass of gas in the inner disk to be of the order of 3 $M_{\rm Jup}$. But it should be pointed out that mid-IR H_2 lines are only probing warm gas located in the surface layer of the disk, when a higher mass of colder gas is expected to be present in the interior layers of the disk. In any case, the finding of warm molecular hydrogen reinforces the claim that a large amount of cold gas is present in the disk to support its flaring geometry (Lagage et al. 2006).

It is generally accepted that the first rotational levels (J) of H_2 are populated by thermal collisions, an excitation mechanism that requires kinetic temperatures higher than 150 K to produce the $S(1)$ transition. Assuming equal dust and gas temperatures, we estimated dust masses responsible for the continuum emission and derived gas-to-dust mass ratios in the range from 3260 to 14,164 (Table 1), much larger than the canonical value of 100. These crude estimates are in agreement with more sophisticated models such as two-layer LTE disk models (Carmona et al. 2007). Indeed, by scaling the gas-to-dust mass ratio found here to the canonical value of 100, we obtained a peak line flux of about 0.46% of that of the continuum at 150 K, decreasing to 0.1% of the continuum at 1000 K, which is close to the line-to-continuum ratios calculated in disk models by Carmona et al. (2007). Thus one possible interpretation of our observation is that the dust is partially depleted from the disk surface layer, where the H_2 emission originates. The spatial decoupling between the gas and the dust may be due to dust settling or dust coagulation into larger particles.

However, other excitation mechanisms cannot be excluded. Several competing mechanisms could contribute to the excitation of molecular hydrogen, such as UV pumping, shocks, or X-rays (see review papers by Habart et al. 2004; Snow & McCall 2006), and could be responsible for the observed emission. Weak X-ray emission has been detected from HD 97048 by *ROSAT* (Zinnecker & Preibisch 1994). X-rays and UV photons are likely candidates to heat the gas to temperatures significantly higher than those of the dust (Glassgold et al. 2007) and could partly explain a high line-to-continuum ratio. According to radiative transfer models of disks around T Tauri stars (Nomura & Millar 2005; Nomura et al. 2007), X-ray heating could significantly increase the line-to-continuum flux ratio, but, applying the same increase factor to Herbig Ae stars, the $S(1)$ H_2 line would still be below the detection limit of VISIR.

Note that the present VISIR observation does not allow us to discriminate between the different possible physical origins of the emission of H_2. New observations of HD 97048 will be performed with VISIR in order to observe the other pure rotational lines of H_2. The detection of these lines would help to better constrain the temperature (and thus the mass) of the warm gas.

Our results are very similar to those obtained by Bitner et al. (2007) for AB Aur with the TEXES instrument. Indeed, those authors have shown that the emitting warm gas is located in the inner 18 AU of the disk around AB Aur. For the two stars, the gas has not completely dissipated in the inner region of the disk in a lifetime of about 3 Myr. HD 97048 and AB Aur have nearly identical astrophysical parameters ($T_{\rm eff}$, age, mass, distance). Their disks are flared (Pantin et al. 2005; Lagage et al. 2006) and seem to be in similar evolutionary states, which could well be a disk old enough that the dust sedimentation/coagulation has already been at work, but young enough that the gas has not yet been photoevaporated. It is not possible to draw definite conclusions with only two examples, and it would be interesting to observe other Herbig Ae stars similar to AB Aur and HD 97048. The high angular resolution and high spectral resolution available with ground-based instruments are key advantages over space-based instruments such as *ISO* SWS in obtaining firm detections of H_2 from disks.

This work is based on observations obtained at the ESO VLT (Paranal) with VISIR, program 077.C-0309(B). We would like to thank S. Madden for her careful reading of the manuscript. C. M. Z. warmly thanks C. Gry, C. Doucet, P. Didelon, and A. Carmona for fruitful discussions.

REFERENCES

Acke, B., van den Ancker, M. E., & Dullemond, C. P. 2005, A&A, 436, 209
Bell, T. A., Roueff, E., Viti, S., & Williams, D. A. 2006, MNRAS, 371, 1865
Bitner, M. A., et al. 2007, ApJ, 661, L69
Carmona, A., et al. 2007, A&A, submitted
Chiang, E. I., & Goldreich, P. 1997, ApJ, 490, 368
Cohen, M., Walker, R. G., & Witteborn, F. C. 1999, LPI Contrib., 969, 5
Doucet, C., et al. 2007, A&A, 470, 625
Dullemond, C. P., Dominik, C., & Natta, A. 2001, ApJ, 560, 957
Fluks, M. A., et al. 1994, A&AS, 105, 311
Glassgold, A. E., Najita, J. R., & Igea, J. 2007, ApJ, 656, 515
Habart, E., et al. 2004, A&A, 414, 531
Lagage, P.-O., et al. 2004, Messenger, 117, 12
———. 2006, Science, 314, 621
Martin-Zaïdi, C., et al. 2007, A&A, submitted
Nomura, H., et al. 2007, ApJ, 661, 334
Nomura, H., & Millar, T. J. 2005, A&A, 438, 923
Pantin, E., Bouwman, J., & Lagage, P. O. 2005, A&A, 437, 525
Pascucci, I., et al. 2006, ApJ, 651, 1177
Richter, M. J., Jaffe, D. T., Blake, G. A., & Lacy, J. H. 2002, ApJ, 572, L161
Sako, S., et al. 2005, ApJ, 620, 347
Snow, T. P., & McCall, B. J. 2006, ARA&A, 44, 367
Takahashi, J., & Uehara, H. 2001, ApJ, 561, 843
Takeuchi, T., Clarke, C. J., & Lin, D. N. C. 2005, ApJ, 627, 286
Thi, W. F., et al. 2001, ApJ, 561, 1074
Valenti, J. A., Johns-Krull, C. M., & Linsky, J. L. 2000, ApJS, 129, 399
van den Ancker, M. E., de Winter, D., & Tjin A Djie, H. R. E. 1998, A&A, 330, 145
van Dishoeck, E. F. 1992, in Infrared Astronomy with *ISO*, ed. Th. Encrenaz & M. F. Kessler (Commack: Nova Science Publishers), 283
Zinnecker, H., & Preibisch, T. 1994, A&A, 292, 152

Annex

Molecular hydrogen in the disk of the Herbig star HD 97048

published in the journal *ApJ*, April 2009

The Astrophysical Journal, 695:1302–1307, 2009 April 20 doi:10.1088/0004-637X/695/2/1302
© 2009. The American Astronomical Society. All rights reserved. Printed in the U.S.A.

MOLECULAR HYDROGEN IN THE DISK OF THE HERBIG Ae STAR HD 97048

C. Martin-Zaïdi[1], E. Habart[2], J.-C. Augereau[1], F. Ménard[1], P-.O. Lagage[3], E. Pantin[3], and J. Olofsson[1]
[1] Laboratoire d'Astrophysique de Grenoble, CNRS/UJF - UMR 5571, 414 rue de la Piscine, DU Saint Martin d'Hères, 38041 Grenoble cedex 9, France; claire.martin-zaidi@obs.ujf-grenoble.fr, augereau@obs.ujf-grenoble.fr, menard@obs.ujf-grenoble.fr, olofsson@obs.ujf-grenoble.fr
[2] Institut d'Astrophysique Spatiale, 91405 Orsay, France; emilie.habart@ias.u-psud.fr
[3] Laboratoire AIM, CEA/DSM, CNRS, Université Paris Diderot, DAPNIA/Service d'Astrophysique, Bat. 709, CEA/Saclay, 91191 Gif-sur-Yvette Cedex, France; pierre-olivier.lagage@cea.fr, epantin@cea.fr
Received 2008 December 19; accepted 2009 January 22; published 2009 April 7

ABSTRACT

We present high-resolution spectroscopic mid-infrared observations of the circumstellar (CS) disk around the Herbig Ae star HD 97048 obtained with the *VLT Imager and Spectrometer for the Mid-InfraRed*. We conducted observations of mid-infrared pure rotational lines of molecular hydrogen (H_2) as a tracer of warm gas in the disk surface layers. In a previous paper, we reported the detection of the S(1) pure rotational line of H_2 at 17.035 μm, and argued that it is arising from the inner regions of the disk around the star. We used the VISIR on the VLT for a more comprehensive study based on complementary observations of the other mid-infrared molecular transitions, namely S(2) and S(4) at 12.278 μm and 8.025 μm respectively, to investigate the physical properties of the molecular gas in the CS disk around HD 97048. We do not detect either the S(2) line or the S(4) H_2 line from the disk of HD 97048, but we derive upper limits on the integrated line fluxes which allows us to estimate an upper limit on the gas excitation temperature, $T_{ex} < 570$ K. This limit on the temperature is consistent with the assumptions previously used in the analysis of the S(1) line, and allows us to set stronger constraints on the mass of warm gas in the inner regions of the disk. Indeed, we estimate the mass of warm gas to be lower than 0.1 M_{Jup}. We also discuss the probable physical mechanisms which could be responsible for the excitation of H_2 in the disk of HD 97048.

Key words: circumstellar matter – infrared: stars – planetary systems: protoplanetary disks – stars: individual (HD97048) – stars: pre-main sequence

1. INTRODUCTION

Disks around young stars are a natural outcome of the star formation process and the place for planet formation. At the present time, significant effort has been put into the study of the dust in disks. However, the dust only represents a tiny fraction of the disk mass (∼1%), and it is thus mandatory to deeply study the gas phase in disks in order to set stronger constraints on the giant planets formation process. Molecular hydrogen (H_2) is the most abundant molecule in the circumstellar (CS) environments of young stars and is supposed to be the key element of giant planet formation; thus its diagnostics are promising. Indeed, the detection of H_2 provides the most direct information about the gaseous content of disks, setting limits on the timescales for the dissipation of CS matter and possibly planet building. H_2 has been observed in CS environments at ultraviolet (e.g., Johns-Krull et al. 2000; Martin-Zaïdi et al. 2008) and near-infrared (e.g., Bary et al. 2003) wavelengths. These observations trace hot CS gas, or gas excited by fluorescent processes, or require specific spatial distributions for the gas to be detectable. They are therefore difficult to translate into gas masses. The pure rotational mid-infrared H_2 lines are useful probes because the level populations are expected to be in local thermodynamic equilibrium (LTE) at the local gas temperature, and so line ratios allow the determination of the excitation temperature and mass of the warm gas.

HD 97048 is a nearby, relatively isolated Herbig A0/B9 star, surrounded by a CS disk, located in the Chameleon cloud at a distance of 180 pc (van den Ancker et al. 1998). Its age has been estimated from evolutionary tracks to be on the order of 3 Myr (kindly computed for us by L. Testi and A. Palacios). The VISIR (VLT Imager and Spectrometer for the mid-infraRed; Lagage et al. 2004) imaging observations of this star have revealed emission of Polycyclic Aromatic Hydrocarbons (PAHs) at the surface of a flared disk extending at least up to 370 AU (Lagage et al. 2006). The flaring index has been measured to be 1.26 ± 0.05, which is in good agreement with hydrostatic flared disk models (Lagage et al. 2006; Doucet et al. 2007). This is the only Herbig star for which the flaring of the disk has been observed by direct imaging. This geometry implies that a large amount of gas should be present to support the hydrostatic structure, and that the disk is at an early stage of evolution. This star is thus one of the best candidates to study the gas component in the disks of HAes.

In a previous paper (Martin-Zaïdi et al. 2007, hereafter Paper I), we presented VISIR high-resolution spectroscopic mid-infrared observations of the CS disk around the Herbig Ae (HAe) star HD 97048 near 17.03 μm. Although Carmona et al. (2008) suggested, from their disk model with the assumptions of LTE conditions and a gas-to-dust ratio of about 100, that mid-IR H_2 lines should not be detected with the existing instruments, we detected the S(1) pure rotational line of molecular hydrogen at 17.035 μm arising from the disk around HD 97048. In addition, Bitner et al. (2007) have detected mid-IR H_2 rotational lines in the disk of another Herbig star, namely AB Aur, using the high spectral and spatial resolution TEXES spectrometer. These detections demonstrate that H_2 can be observed in the mid-IR domain when particular physical conditions exist in disks.

Despite the fact that the line is neither spatially nor spectrally resolved, the detection of the S(1) line in the disk of HD 97048 revealed the presence of significant amounts of warm gas in the inner 35 AU of the disk. CS gas had been previously detected in the disk of HD 97048 by Acke & van den Ancker (2006), who showed that the [O I] emission arises at radii between 0.5 and 60 AU from the central star. Very recently, modeling of near-infrared CO emission showed that the inner radius of

the CO emitting region is located at 12 AU from the star (van der Plas et al. 2008). These observations reinforced the claim that the disk of HD 97048 contains large amounts of gas both at small and large radii, as suggested by the flaring geometry, and that HD 97048 is a young object surrounded by a disk at an early stage of evolution. Indeed, photoevaporation of the gas and planet formation clear up the inner part of the disk in timescales expected to be lower than 3 million years (Takeuchi et al. 2005; Gorti & Hollenbach 2008, 2009). The H_2 S(1) line detection also implies that particular physical conditions for H_2 are present in the inner disk surface layer. The analysis of these data usually assumes that the H_2 excitation is in LTE, and can itself thus be characterized by a single excitation temperature, which should be close to the gas temperature because of the low critical densities. As shown by the AB Aur observations (Bitner et al. 2007, 2008), the H_2 gas temperature could be significantly higher than the dust temperature in the disk surface layers of HD 97048, due to the dust settling or coagulation, for example. However, several competing mechanisms could contribute to the excitation of molecular hydrogen such as UV and X-rays heating, shocks, etc (see the review papers by Habart et al. 2004; Snow & McCall 2006), and could be responsible for the observed emission. We refer the reader to Paper I for a complete discussion about the different possible explanations.

The detection of the other pure rotational lines of H_2 is a potentially powerful tool to determine the excitation temperature (and thus the mass) of the warm gas, and better constrain the excitation of H_2. In this paper, we thus present VISIR high-resolution spectroscopic observations of the two other pure rotational lines of H_2 observable from the ground: the S(2) line at 12.2786 μm, and the S(4) line at 8.0250 μm. We also recall the main results obtained from the S(1) line detection (detailed in Paper I).

2. OBSERVATIONS AND DATA REDUCTION

HD 97048 was observed at three different epochs. The observations at 17.035 μm presented in the Paper I were performed on 2006 June 22, the 8.025 μm observations on 2007 April 7, and the 12.278 μm observations on 2007 July 3. The three sets of observations were obtained with the high-resolution spectroscopic mode of the VISIR. The exposure time, slit width, and atmospheric conditions during the observations for the target star and standard references are presented in Table 1.

For all the three observations, the standard chopping and nodding technique was used to suppress the large sky and telescope background dominating at mid-IR wavelengths. Asteroids and standard stars were observed just before and after observing HD 97048, at nearly the same airmass and seeing conditions as the object. In order to correct the spectra from the Earth's atmospheric absorption, we divided each spectrum of HD 97048 by that of the corresponding asteroid (which has a much better signal-to-noise ratio than that of the standard star), and used the standard stars observed and modeled spectra (Cohen et al. 1999) to obtain the absolute flux calibration. In order to verify our flux calibration, we checked the *Spitzer Space Telescope* archives. HD 97048 was observed with the IRS spectrograph installed onboard the *Spitzer Space Telescope* as part of the "Cores to Discs" (c2d) legacy program (AOR:0005644800, PI: Evans). The data reduction was performed using the c2d legacy team pipeline (Lahuis et al. 2006) with the S15.3.0 pre-reduced (BCD) data. The absolute flux calibration of our VISIR data in the three wavelength ranges has been performed in order to be consistent with the *Spitzer* flux measurements. We estimate the error on the absolute flux calibration to be lower than 10%, a value which does not affect our analysis.

The wavelength calibration is done by fitting the observed sky background features with a model of Paranal's atmospheric emission (for more details on the observation and data reduction techniques, see Paper I). We note that $A_v = 0.24$ mag for HD 97048 (Valenti et al. 2000); thus we have not corrected the spectra for dust extinction, since it is negligible in our wavelength range for any $A_v < 40$ mag (Fluks et al. 1994).

3. RESULTS

3.1. Non-Detection of the S(2) and S(4) Lines

HD 97048 spectra show no evidence for H_2 emission either at 12.278 μm or at 8.025 μm (Figure 1, middle and bottom panels). For each flux-calibrated spectrum, we calculated the standard deviation (σ) for wavelength ranges relatively unaffected by telluric absorption, and close to the wavelength of interest. The 3σ upper limits on the integrated line fluxes were calculated by integrating over a Gaussian of FWHM equal to a spectral resolution element (21 km s^{-1}) and an amplitude of about 3σ flux (Figure 1). We assumed the same radial velocity for the S(2) and S(4) lines than that observed for the S(1) line and corrected appropriately for each epoch of observation. We thus centered the Gaussian on the expected wavelengths for the S(2) and S(4) lines, respectively (see Table 2). From the limits on integrated intensities, we estimated the upper limits on the column densities of the corresponding upper rotational levels of each H_2 transition (see Table 2). For this purpose, we first assumed that the line is optically thin and that the radiation is isotropic. In this context, the column densities are derived from the following formula (van Dishoeck 1992):

$$I_{ul} = \frac{hc}{4\pi\lambda} N_u(H_2) A_{ul} \text{erg s}^{-1} \text{ cm}^{-2} \text{ sr}^{-1}, \quad (1)$$

where I_{ul} is the integrated intensity of the line, λ is the wavelength of the transition $J = u - l$, A_{ul} is the spontaneous transition probability, and $N_u(H_2)$ is the column density of the upper rotational level of the transition.

Table 1
Summary of the Observations

λ (μm)	t_{exp} (s)	Airmass	Optical seeing ($''$)	Slit ($''$)	R	Stand. Star	Airmass	Optical seeing ($''$)	Asteroid	Airmass	Optical seeing ($''$)
17.0348	1800	1.72–1.79	0.52–0.66	0.75	14 000	HD89388	1.90–1.94	0.60–0.72	CERES	1.68–1.82	0.58–0.69
12.2786	960	1.81–1.87	1.97–2.16	0.4	13 600	HD91056	1.82–1.87	1.39–1.82	VESTA	1.03–1.04	1.67–2.23
8.0250	1872	1.66–1.69	0.51–0.65	0.4	13 300	HD92305	1.69–1.70	0.64–0.65	VESTA	1.54–1.59	0.75–0.79

Note. The airmass and seeing intervals are given from the beginning to the end of the observations.

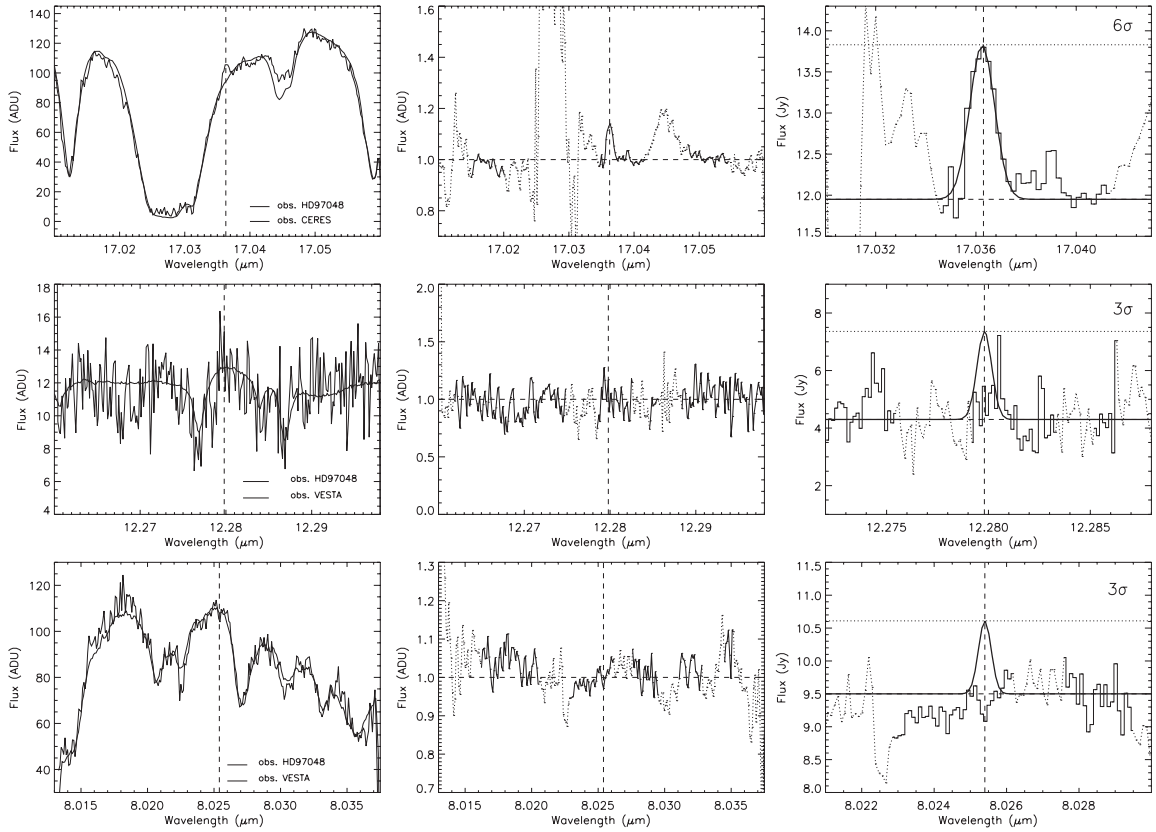

Figure 1. VISIR spectra of HD 97048 at 17.035 μm (top panel), 12.278 μm (middle panel) and 8.025 μm (bottom panel). Left panel: continuum spectra of the asteroid and of the target before telluric correction. Central panel: full corrected spectra: dotted lines show spectral regions strongly affected by telluric features. Right panel: zoom of the region where the H_2 lines should be observed (dashed vertical lines). The spectra were corrected neither for the radial velocity of the targets nor for the Earth's rotation velocity.

Table 2
Fluxes, Intensities, Luminosities, and Column Densities of Each Observed Mid-IR Transitions of H_2

λ_{obs} (μm)	Transition	v_{up}	J_{up}	Continuum flux[a] (Jy)	Integrated line flux (erg s^{-1} cm^{-2})	Line intensity (erg cm^{-2} s^{-1} sr^{-1})	Line luminosity log($L/L_\odot$)	$N_{J_{up}}(H_2)$ (cm^{-2})	M(H_2) (M_{Jup})
17.03625	S(1)	0	3	11.95 ± 0.94	$(2.4 \pm 0.2) \times 10^{-14}$	$(5.7 \pm 0.5) \times 10^{-3}$	-4.61 ± 0.04	$(1.29 \pm 0.12) \times 10^{21}$	$(1.6 \pm 0.1) \times 10^{-2}$
12.2798	S(2)	0	4	4.3 ± 3.0	$<5.5 \times 10^{-14}$	$<2.6 \times 10^{-2}$	< -4.25	$<7.46 \times 10^{20}$	$<1.0 \times 10^{-1}$
8.0254	S(4)	0	6	9.5 ± 1.1	$<4.7 \times 10^{-15}$	$<5.1 \times 10^{-3}$	< -5.32	$<9.80 \times 10^{18}$	$<1.0 \times 10^{-2}$

Notes. The mass of H_2 is calculated for a temperature of about 570 K. λ_{obs} is the wavelength of the centroid of the line. v_{up} and J_{up} are, respectively, the vibrational and rotational upper levels of the transition of interest.
[a]The error bars on the continuum fluxes are 3σ error bars.

3.2. Detection of the S(1) Line at 17.035 μm

We recall here the results of our analysis of the S(1) line. For more details, we refer the reader to the Paper I. As shown in Figure 1 (top panel), we have detected the H_2 pure rotational S(1) line near 17.03 μm. In the flux-calibrated spectrum, the standard deviation (σ) of the continuum flux was calculated in regions less influenced by telluric absorption, and close to the feature of interest. We deduced a 6σ detection in amplitude for the line, corresponding to a signal-to-noise ratio of about 11σ for the line, when integrating the signal over a resolution element (6 pixels). The line is not spectrally resolved as we can fit it with a Gaussian with a full width at half maximum (FWHM) equal to a spectral resolution element of 21 km s^{-1} (Figure 1). From our fit, we derived the integrated flux in the line (see Table 2). Once the spectrum is corrected from the Earth's rotation, and knowing the heliocentric radial velocity of HD 97048 (+21 km s^{-1}; Acke et al. 2005), we estimated, from the wavelength position of the Gaussian peak, the radial velocity of H_2 to be about 4 ± 2 km s^{-1} in the star's rest frame. We thus considered that the radial velocity of the H_2 is compatible with zero (at the VISIR resolution) and therefore similar to that of the star, implying that the emitting gas is gravitationally bound to the star, and likely arising from the disk and not from an outflow.

H_2 outflows from T Tauri stars usually have (blueshifted) velocities of a few tens up to a hundred of km s^{-1} when a clear outflow is identified. Otherwise, when the line is detected at zero systemic velocity and is narrow or unresolved as is the case here, it is generally attributed to the disk (e.g., Herczeg et al. 2006; Bitner et al. 2008). The H_2 line is not resolved spatially either. Given a VISIR spatial resolution of about 0.″427 at 17.03 μm, and the star distance (180 pc from the Sun), we can assess that the emitting H_2 is located within the inner 35 AU of the disk. Assuming that the H_2 gas follows the same (Keplerian) kinematics as the disk, the emitting gas observed with VISIR is likely not concentrated significantly in the innermost AU of the disk (< 5 AU) otherwise rotational broadening would be observed. Indeed, near the central star, the rotational velocity of the disk is on the order of a hundred of km s^{-1}, to be compared to the spectral resolution of VISIR, 21 km s^{-1}. The emitting H_2 is thus more likely distributed in an extended region within the inner disk, between 5 AU and 35 AU of the disk. Assuming the emission arises from an isothermal mass of optically thin H_2, we estimated the corresponding column densities and masses of H_2 as a function of prescribed temperatures (for 150 K, 300 K and 1000 K; see Paper I for details about the method). In Table 2 are reported the integrated flux of the S(1) line, its intensity, and the corresponding column density for the $J = 3$ rotational level. Since we have a signal-to-noise ratio of about 11σ for the line, we can deduce 9% error bars on theses values (see Table 2).

3.3. Physical Properties of H_2

The estimates of the column densities of the $J = 3$, $J = 4$, and $J = 6$ rotational levels of H_2 allowed us to plot an excitation diagram of H_2 (see Figure 2). Assuming that all three levels are populated by thermal collisions (LTE), we estimated the excitation temperature of the observed gas. The upper limit on the column density of the $J = 6$ level strongly constrains the value of the column density of the $J = 4$ level. Indeed, the population of the $J = 4$ level should correspond to the excitation temperature given by the ratio of the column densities of the $J = 3$ and $J = 6$ levels. We assumed that the population of the $J = 3$ and $J = 6$ levels follow the Boltzmann law, which corresponds to a linear fit to the points on the excitation diagram (Figure 2):

$$\frac{N(H_2)_{J=3}}{N(H_2)_{J=6}} = \frac{g_3}{g_6} \times \exp\Big(-\frac{E_3 - E_6}{kT_{\rm ex}}\Big), \qquad (2)$$

where $N(H_2)_{J=i}$ is the column density, g_i is the statistical weight, E_i is the energy of the $J = i$ level, k is the Boltzmann constant, and $T_{\rm ex}$ is the temperature defined as the excitation temperature. Since we only have upper limits on the column densities of the $J = 4$ and $J = 6$ levels, only an upper limit on the excitation temperature is relevant. Since the temperature is inversely proportional to the slope on the excitation diagram, in order to obtain the upper limit on the excitation temperature, we considered the lower value of the column density of the $J = 3$ level (i.e., the measured value minus 1σ) and the upper limit on the $J = 6$ population level (that procedure yields the minimum slope/maximum temperature and corresponds to the solid line in Figure 2). We thus find that the excitation temperature of H_2 should be lower than 570 K. In this case, the column density of the $J = 4$ level should be lower than 1.6×10^{20} cm^{-2} which is lower than the value obtained from the 3σ upper limit (see Table 2).

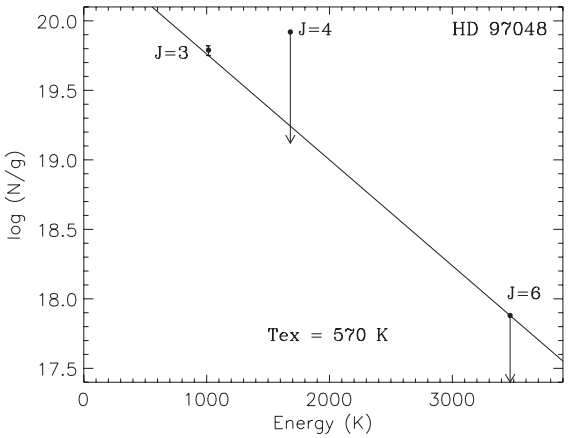

Figure 2. Excitation diagram for H_2 toward HD 97048. If the three rotational levels are populated by thermal collisions, their populations follow the Boltzmann law, and the upper limit on the excitation temperature is given by considering the lower limit on the column density of the $J = 3$ level and the upper limit on the $J = 6$ population level (solid line). Thus, in this case, the gas temperature should be lower than 570 K.

Under the assumption that the H_2 emission is optically thin, that the emitting H_2 is in LTE at a temperature of about 570 K, and that the source size is equal or smaller than VISIR's beam size, we derived upper limits on the H_2 mass (see Table 2):

$$M_{\rm gas} = f \times 1.76 \times 10^{-20} \frac{F_{ul} d^2}{(hc/4\pi\lambda) A_{ul} x_u(T)} M_\odot, \qquad (3)$$

where F_{ul} is the line flux, d the distance in pc to the star, $x_u(T)$ is the fractional population of the level u at the temperature T in LTE (for details on the calculation method, see van Dishoeck 1992), and f is the conversion factor required for deriving the total H_2 gas mass from the H_2-ortho or H_2-para mass. Since $M_{H2} = M_{H2}$(ortho)+M_{H2}(para), then f =1+1/(ortho/para) for the S(1) line (a H_2-ortho transition) and f =1+ortho/para for the S(2) and S(4) lines (H_2-para transitions). The equilibrium ortho-para ratio at the temperature T was computed using Equation (1) from Takahashi (2001).

4. DISCUSSION

Our previous high-resolution spectroscopic observations with VISIR of the S(1) pure rotational line of H_2 at 17.035 μm of HD 97048 revealed the presence of significant amounts of warm gas in the surface layer of the disk in the inner 35 AU from the central star (Paper I). This detection confirmed that HD 97048 is a young object surrounded by a CS disk at an early stage of evolution, still rich in gas.

In the present paper, we report the non-detections of the S(2) and S(4) lines of H_2 in the disk of the Herbig Ae star HD 97048. Using VISIR high-resolution spectra, we compute upper limits for the column densities of the $J = 4$ and $J = 6$ rotational levels. Using the results obtained from the analysis of the S(1) line (column density of the $J = 3$ level), and assuming that the $J = 3$ to $J = 6$ levels are excited by thermal collisions, we derive an upper limit on the excitation temperature of H_2 of about 570 K.

This constraint on a temperature lower than 570 K for the gas allows us to set a stronger constraint on the mass of warm H_2 (< 0.1 $M_{\rm Jup}$; 1 $M_{\rm Jup} \sim 10^{-3}$ $M_\odot$) in the inner 35 AU of the disk

than that estimated in Paper I. Indeed, in Paper I, we derived the masses of the warm gas in the range from 10^{-2} to nearly 1 $M_{\rm Jup}$, for temperatures in the range from 150 K to 1000 K and assuming LTE. The mass of warm gas we estimate is also lower than that we derived from the paper by Lagage et al. (2006) who estimated the mass of H_2 in the disk to be of about 0.01 $M_\odot$. By assuming that the surface density Σ follows a power law $\Sigma(r) = \Sigma(r/370)^q$ with an index q equal to $-3/2$ (Lagage et al. 2006), we estimated in Paper I a minimum mass of gas in the inner 35 AU of the disk to be on the order of 3 $M_{\rm Jup}$. But it should be pointed out that mid-IR H_2 lines are only probing warm gas located in the surface layer of the disk, when a higher mass of colder gas is expected to be present in the interior layers of the disk.

However, from their disk model, Carmona et al. (2008) concluded that the expected peak flux of the S(1) line at 17.035 μm, observed at a spectral resolution of 20,000, should be less than 0.3% of that of the continuum at temperatures higher than 150 K, and thus should not be observable with the existing instruments. Those authors used a two-layer model (Chiang & Goldreich 1997; Dullemond et al. 2001) of a gas-rich disk (column density of $N(H_2) = 10^{23}$ cm^{-2}) seen face-on, located at 140 pc from the Sun, with LTE for the gas and dust, $T_{\rm gas} = T_{\rm dust}$, and assumed a constant gas-to-dust mass ratio of about 100.

As shown in Paper I from the observation of the S(1) line in the disk of HD 97048, such a detection can only be explained if the physical conditions of the gas differ from those used by Carmona et al. (2008). In Paper I, we proposed several ways to explain our detection. First, assuming equal dust and gas temperatures (LTE), we estimated gas-to-dust mass ratios much larger than the canonical value of 100. This hypothesis cannot be ruled out by the non-detections of the S(2) and S(4) lines. One possible interpretation to explain a very high gas-to-dust ratio is that the dust is partially depleted from the uppermost disk surface layer, where the H_2 emission originates. The spatial decoupling between the gas and the dust may be due to low densities in the surface layers, or dust settling and coagulation into larger particles. The physical conditions may thus rapidly differ from the LTE ones, i.e., $T_{\rm gas} > T_{\rm dust}$. In the upper disk surface layers, photoelectric heating can thus play a significant role in the gas heating process (Kamp & Dullemond 2004; Jonkheid et al. 2007). In addition, photoelectric heating will be much efficient on small grains, such as PAHs, which show significant features in the different observations of HD 97048 (e.g., Doucet et al. 2007, and reference therein). Our upper limit on the excitation temperature is consistent with photoelectric heating. Indeed, as shown by Kamp & Dullemond (2004), photoelectric heating is characterized by a temperature limit ($\sim$1000 K) since for high stellar UV flux, grain ionization can be so large that the photoelectric effect is less efficient and $T_{\rm gas}$ does not increase any more.

However, our observations do not allow us to rule out the possibility of a gas heating due to other excitation mechanisms such as UV pumping or X-ray heating. Indeed, UV and X-ray heating are likely possibilities that can heat the gas to temperatures significantly hotter than the dust. Nomura & Millar (2005) modeled UV heating of CS disks around T Tauri stars and the resulting H_2 emission. In their model the temperature can be of about 1000 K at 10 AU from the central star, and the predicted H_2 S(2) line flux is about 2×10^{-15} erg s^{-1} cm^{-2}. This value is lower than our upper limit on the S(2) line flux, but their model was for a less massive star and disk.

The upper limit on the excitation temperature of about 570 K we found for H_2 in the disk of HD 97048, could also be consistent with X-ray heating. Very recently, Ercolano et al. (2008) demonstrated from their two-dimensional photoionization and dust radiative transfer models of a disk irradiated by X-rays from a T Tauri star, that the uppermost layers of gas in the disk could reach temperatures of 10^6 K at small radii (<0.1 AU) and 10^4 K at a distance of 1 AU. The gas temperatures decrease sharply with depth, but appear to be completely decoupled from dust temperatures down to a column depth of $\sim 5 \times 10^{21}$ cm^{-2}. These results are consistent with those of Glassgold et al. (2007) who computed that at 20 AU from the central star, the temperature can reach 3000 K at the surface of the disk before dropping to 500–2000 K in a transition zone and then to much cooler temperatures deep in the disk. By extrapolation, these models suggest that in the inner 35 AU from the central star, the upper layers of the disk could reach temperatures consistent with the upper limit of about 570 K we find for HD 97048.

The kinetic temperature of the gas is generally supposed to be given by the population of the first rotational levels (namely $J = 0$ and $J = 1$) since their critical densities are relatively low, and cannot be higher than the excitation temperature given by the higher energy levels. Thus, in any case, even if the H_2 we observe around HD 97048 is not essentially excited by thermal collisions, the populations of the three levels derived from our observations give strong constraints on the gas kinetic temperature. Our upper limit on the temperature of about 570 K is thus reliable whatever the mechanisms responsible for the excitation of the observed gas may be. We stress that the excitation temperature we find for H_2 from the VISIR observations of HD 97048 is close to that derived from the TEXES observations of AB Aur (670 K) by Bitner et al. (2007), which reinforces the similarities between the two stars (see Paper I).

In order to better constrain the physical conditions of H_2, high-sensitivity and high-resolution space-based spectrographs in the mid-IR would be required (e.g., Boulanger et al. 2009). In particular, only the observation of the S(0) emission line near 28 μm would allow us to clearly constrain both the kinetic temperature of the observed gas and the physical mechanisms responsible for its excitation.

This work is based on observations obtained at the ESO/VLT (Paranal) with the VISIR, programs' number 079.C-0839A and 079.C-0839B. C.M.Z. is supported by a CNES fellowship. This work was supported by the Agence Nationale de la Recherche (ANR) of France through contract ANR-07-BLAN-0221. We also thank the Programme National de Physique Stellaire (PNPS) of CNRS/INSU, France, for supporting part of this research.

Facilities: ESO/VLT VISIR

REFERENCES

Acke, B., & van den Ancker, M. E. 2006, A&A, 449, 267
Acke, B., van den Ancker, M. E., & Dullemond, C. P. 2005, A&A, 436, 209
Bary, J. S., Weintraub, D. A., & Kastner, J. H. 2003, ApJ, 586, 1136
Bitner, M. A., et al. 2007, ApJ, 661, L69
Bitner, M. A., et al. 2008, ApJ, 688, 1326
Boulanger, F., et al. 2009, Experimental Astronomy, 23, 277
Carmona, A., et al. 2008, A&A, 477, 839
Chiang, E. I., & Goldreich, P. 1997, ApJ, 490, 368
Cohen, M., Walker, R. G., & Witteborn, F. C. 1999, LPI Contrib., 969, 5
Doucet, C., et al. 2007, A&A, 470, 625
Dullemond, C. P., Dominik, C., & Natta, A. 2001, ApJ, 560, 957

Ercolano, B., Drake, J. J., Raymond, J. C., & Clarke, C. C. 2008, ApJ, 688, 398
Fluks, M. A., et al. 1994, A&AS, 105, 311
Glassgold, A. E., Najita, J. R., & Igea, J. 2007, ApJ, 656, 515
Gorti, U., & Hollenbach, D. 2008, ApJ, 683, 287
Gorti, U., & Hollenbach, D. 2009, ApJ, 690, 1539
Habart, E., Boulanger, F., Verstraete, L., Walmsley, C. M., & Pineau des Forêts, G. 2004, A&A, 414, 531
Herczeg, G. J., Linsky, J. L., Walter, F. M., Gahm, G. F., & Johns-Krull, C. M. 2006, ApJS, 165, 256
Johns-Krull, C. M., Valenti, J. A., & Linsky, J. L. 2000, ApJ, 539, 815
Jonkheid, B., Dullemond, C. P., Hogerheijde, M. R., & van Dishoeck, E. F. 2007, A&A, 463, 203
Kamp, I., & Dullemond, C. P. 2004, ApJ, 615, 991
Lagage, P. O., et al. 2004, Messenger, 117, 12
Lagage, P.-O., et al. 2006, Science, 314, 621
Lahuis, F., et al. 2006, c2d Spectroscopy Explanatory Supplement, Tech. rep. (Pasadena, CA: Spitzer Science Center)
Martin-Zaïdi, C., et al. 2008, A&A, 484, 225
Martin-Zaïdi, C., Lagage, P.-O., Pantin, E., & Habart, E. 2007, ApJ, 666, L117
Nomura, H., & Millar, T. J. 2005, A&A, 438, 923
Snow, T. P., & McCall, B. J. 2006, ARA&A, 44, 367
Takahashi, J. 2001, ApJ, 561, 254
Takeuchi, T., Clarke, C. J., & Lin, D. N. C. 2005, ApJ, 627, 286
Valenti, J. A., Johns-Krull, C. M., & Linsky, J. L. 2000, ApJS, 129, 399
van den Ancker, M. E., de Winter, D., & Tjin A Djie, H. R. E. 1998, A&A, 330, 145
van der Plas, G., et al. 2008, arXiv:0810.3417
van Dishoeck 1992, in Infrared Astronomy with ISO, ed. Th. Encrenaz & M.F. Kessler (Commack, NY: Nova Science Publisher), 283

Annex

VISIR spectroscopic and spatial survey of Herbig Ae stars

submitted to the journal *A&A*, January 2009

Astronomy & Astrophysics manuscript no. HAEBE
November 7, 2008
© ESO 2008

VISIR spectroscopic and spatial survey of Herbig Ae stars ⋆

A.P. Verhoeff[1], L.B.F.M. Waters[1,2], H. Veerman[1], E. Pantin[3], M. Min[1], J.W. Pel[4], A.G.G.M. Tielens[5], M. van den Ancker[6], R. van Boekel[7], C. Boersma[5], J. Bouwman[7], C. Dominik[1], A. de Koter[1], P.-O. Lagage[3], and R.F. Peletier[4]

[1] Astronomical Institute "Anton Pannekoek", University of Amsterdam, Kruislaan 403, NL-1098 SJ Amsterdam, The Netherlands
[2] Institute for Astronomy, Catholic University Leuven Celestijnenlaan 200D, B-3001 Heverlee, Belgium
[3] CEA/DSM/DAPNIA/Service d'Astrophysique, CE Saclay F-91191 Gif-sur-Yvette, France
[4] Kapteyn Astronomical Institute, University of Groningen, 9700 AV Groningen, The Netherlands
[5] Space Science and Astrobiology Division, NASA Ames Research Center, MS 245-3, Moffet Field, CA 94035, US
[6] European Southern Observatory, Karl-Schwarzschild-Str2 D85748 Garching bei München, Germany
[7] Max Planck Institut für Astronomie Königstuhl 17, 69117 Heidelberg, Germany

Received ....; accepted .....

ABSTRACT

Context. Herbig Ae stars are intermediate mass pre-main-sequence stars surrounded by gas-rich disks that are the remnant of the star formation process. These disks are sites of on-going planet formation, which affects their geometry and composition.
Aims. We map the spatial distribution of warm circumstellar dust in a sample of 17 Herbig Ae stars. We put our results into a multi wavelength context and investigate possible links between disk size and other quantities such as chemistry, geometry and the spectral energy distributions.
Methods. We use the N-band long-slit spectrometer of VISIR to spatially and spectroscopically resolve our targets. The spectra are Gaussian-fitted to obtain the FWHM-sizes as a function of wavelength and we have deconvolved with a PSF derived from a sample of ~130 calibrators.
Results. We spatially resolve 9 of the 17 stars in the continuum and/or in the 8.6 and 11.2 μm PAH features. Typical spatial scales of the PAH emission are 50–100 AU FWHM. We find that disks with a flaring geometry (group I) are more often spatially resolved than disks with a "self-shadowed" geometry (group II). The disks are more extended in the PAH bands than in the continuum, with the notable exception of HD169142. Sources with strong PAH emission tend to be larger than sources with weak PAH emission. The continuum emission of a few sources is considerably more extended (up to ~60 AU) than expected from thermal emission modeling. This may be due to the presence of very small grains in the disk surface layers, and/or the presence of inner holes or disk gaps. The latter explanation is supported by the negative trend we found between the continuum sizes and the NIR excess flux.

Key words. star formation - protoplanetary disks - Herbig Ae stars

1. Introduction

There is growing evidence that the gas- and dust rich disks that surround virtually all young low- and intermediate mass pre-main-sequence stars are the sites of on-going planet formation. These disks form due to conservation of angular momentum in the collapse phase of a molecular cloud core. Once accretion has stopped, the disk dissipates on time-scales of 5-10 Myrs, leaving a gas-poor dusty debris disk in which the dust is formed by collisions of larger bodies (see Hillenbrand 2008 and references therein for a recent review).

Herbig Ae/Be stars, first described as a group by Herbig (1960), are intermediate mass pre-main-sequence stars that possess a passive proto-planetary disk, i.e. the disk is heated by stellar photons only. They are often, but not always, associated with reflection nebulosities and have both permitted and forbidden emission lines in their spectra (see e.g. Waters & Waelkens 1998 or Natta et al. 2000 for reviews). In this paper we focus mostly on the late B and A-F type Herbig stars, which we will refer to as Herbig Ae stars. The disks surrounding these stars share many properties with those of lower mass T Tau stars.

The Spectral Energy Distribution (SED) of Herbig Ae stars is characterized by a large infrared (IR) and millimeter flux excess due to the thermal radiation of dust grains in the disk. The SEDs can roughly be divided into two groups, based on the slope of the spectrum from 10 to 60 μm (Meeus et al. 2001). Group I sources have a rising spectrum, while group II sources have a flat or decreasing spectral slope. These groups were further subdivided into 'a' and 'b' according to the presence or absence of the 10 μm amorphous silicate band. No group IIb sources were found, i.e. group II sources are all dominated by silicate emission. Meeus et al. (2001) and Acke & van den Ancker (2004) show that group I sources have on average strong emission bands from Polycyclic Aromatic Hydrocarbons (PAHs), while group II sources have weak or no PAH emission. These trends are confirmed by recent studies of a large *Spitzer* spectral survey of Herbig Ae stars (Bouwman et al, in preparation). The SED classification and PAH correlations can be understood if the group I sources have flaring outer disk geometries, and group II sources have flat disks.

The SEDs of Herbig Ae stars have been interpreted with physical disk models such as those of Chiang & Goldreich (1997), Dullemond et al. (2001), Dominik et al. (2003) and Dullemond & Dominik (2004). The near-IR excess in the 1-

Send offprint requests to: A.P. Verhoeff, e-mail: verhoeff@uva.nl

⋆ Based on observations collected at the European Southern Observatory, Chile. Under program IDs: 074.A-9016A, 075.C-0540A, 075.C-0540C, 075.C-0620A, 075.C-0687A, 076.C-0159A, 077.C-0367A, 079.C-0602A.

5 μm wavelength range is due to hot dust located in a puffed-up inner rim. The 10-60 μm range is dominated by small warm dust grains in the upper disk layers. The slope of the SED, and hence the classification into group I or II, can be understood by the shadow which the inner rim casts on the outer disk regions (Dullemond & Dominik 2004). Disks with a large mass in small dust grains flare and as such the dust in the outer disk regions receives direct starlight (group I). Disks with a low mass in small dust grains have their radial $\tau = 1$ surface in the shadow of the inner rim, and have a flat or decreasing 10-60 μm spectrum (group II). Note that the scale-height of the *gas*, that is set by the mid-plane gas temperature, need not differ between group I and group II sources (see also Dullemond et al. 2007).

In this paper, we will study the spatial structure and dust composition of Herbig Ae disks at mid-IR wavelengths, using ground-based VISIR spectra, backed up with spectra from the literature of the Spitzer and ISO space telescopes. We will focus on the 10 μm atmospheric window which gives access to warm silicate emission (both amorphous and crystalline) as well as some prominent PAH bands at 8.6, 11.2 and 12.7 μm and we will use the space-based data as a reference. Mid-IR imaging using 4 and 8 meter class telescopes has proven to be an essential tool to determine the spatial distribution of different dust species and to constrain disk geometries, because the disk geometry cannot uniquely be constrained by the SED. This is particularly true when planet formation affects the large-scale disk geometry, by creating disk gaps and/or inner holes. Such "transitional" disks may show a large diversity in properties, reflected in the SED (e.g. Furlan et al. 2006).

Many observational studies in the mid-IR have been published that show evidence for disk gaps, inner holes, and sometimes unexpected spatial distributions of dust species (e.g. Liu et al. 2003; Honda et al. 2005; Pantin et al. 2005; Fujiwara et al. 2006; Lagage et al. 2006; van Boekel et al. 2005; Doucet et al. 2006b; Doucet et al. 2007; Mariñas et al. 2006; Geers et al. 2007a). This motivates the present study, in which we use VISIR at the VLT to spatially and spectrally resolve the mid-IR emission of a sample of bright, nearby Herbig Ae stars. We will study the relation between the dust composition, SED shape, and mid-IR spatial scales detected with VISIR. This paper is organized as follows: In Sect. 2 we present the sample of stars. Section 3 describes the observations, Sect. 4 the data reduction, and Sect. 5 addresses the derivation of the telescope point spread function. In Sects. 6 and 7 we show the results of the observations and derive deconvolved sizes of the disks. Section 8 is devoted to a discussion of the individual objects and Sect. 9 of the general trends observed in our data set. Section 10 contains the main conclusions of this study.

2. Sample

2.1. Selection

To fully cover the spectral type A of the Herbig Ae/Be stars we selected a list of sources with spectral type later than B8 from the catalog of Herbig Ae/Be stars presented by Thé et al. (1994). These sources all contain an IR excess and emission-lines. They are associated with an obscured star forming region, but they are not all shrouded in a reflection nebula. This list was supplemented with more recently found Herbig Ae stars by Malfait et al. (1998). From this combined list, sources were selected that display emission features of PAHs. For these sources it was known from studies like Habart et al. (2004) that the specific excitation mechanism of the PAH bands leads to spatially more extended emission in the PAH bands than in the surrounding continuum, which is dominated by thermal emission from dust grains. To secure a balanced sample we also selected sources with weak or absent PAH emission.

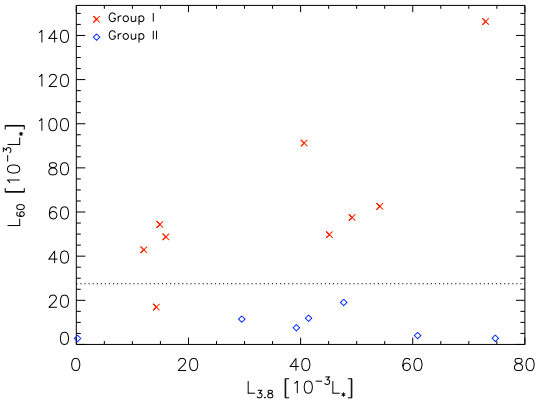

Fig. 1. The 3.8 and 60 μm excess luminosities of the sample stars, expressed in units of the stellar flux. The quantities represent the energy output of the hot and cold circumstellar dust respectively. The dotted line accentuates a rough division between group I and II sources.

The choice of unobscured objects leads to a sample of sources which are seen under small inclinations ($i \lesssim 70°$), which means relatively face on. This choice also leads to more isolated objects, which are thus less under influence of the radiation of neighboring stars. The choice of PAH sources is likely to introduce more group I sources, since recent surveys suggest the existence of a correlation between the presence of PAH-emission and the flaring geometry of the disks (e.g. Meeus et al. 2001, Acke & van den Ancker 2004 or Lagage et al. 2006). Even though we have added a few other Herbig Ae stars, we should be careful with statistical statements based on our sample.

2.2. Stellar parameters

Most of the general characteristics of our sample stars have been discussed in the literature. See for instance the surveys by van den Ancker et al. (1998), Acke & van den Ancker (2004), van Boekel et al. (2005) or Bouwman et al. (in prep). The distances have been determined mostly by association with star formation regions and span a range of ~100-400 pc. Luminosities were determined to be in between 0.6-100 $L_\odot$. Together with the effective temperatures, which are in a range from 6600 to 10500 K, the masses and ages could then be determined from comparing their positions in the Hertzsprung-Russell diagram with pre-main-sequence evolutionary tracks (Palla et al. 1993). The masses vary from ~1 to ~5 $M_\odot$ and the ages from $10^{5.5}$ to 10^7 yr. The stars have also been the subject of many specific studies at different wavelengths, some of which will be addressed in Sect. 8. Table 1 displays the stellar parameters for the entire sample.

2.3. SEDs and IR-excess

We have taken SEDs of the target stars from Acke & van den Ancker (2004) (see also references therein). These data-sets have been updated and these revisions will be published in Bouwman

Table 1. Stellar parameters of our sample of targets. The distance is indicated with d, the effective temperature with $T_{\rm eff}$ and the optical extinction with $A_{\rm V}$, which has an absolute error of 0.06 mag. L stands for the stellar luminosity, R for the stellar radius and SFR for the association with a particular star formation region. Data was taken from Acke & van den Ancker (2004) and van Boekel et al. (2005) and updated, these updates will be published in Bouwman et al. (in prep.). For CQ Tau, refer to Doucet et al. (2006b) and references therein. For HD95881 we state the updated parameters as derived in a separate paper (see Verhoeff et al. in prep.).

Name	Sp.Type	Group	d [pc]	$T_{\rm eff}$ [K]	$A_{\rm V}$	L [$L_\odot$]	R [$R_\odot$]	Mass [$M_\odot$]	log Age [yr]	SFR
AB Aur	A0Vpe	Ia	144±14	9520	0.50	49.2±6.8	2.6±0.2	2.4±0.2	6.3±0.2	L1519
HD34282	A3Vne	Ib	400±40	8720	0.28	19.0±2.7	1.9±0.1	2.1±0.2	6.5	
CQ Tau	F3e	Ia	100±20	6740	0.87	0.57±0.16	0.55±0.08	0.21±0.04	10	Tau T4
HD95881	A2III/IVe	IIa	170±50	8990	0.25	15.4±8.0	1.6±0.5	2.0±0.4	>6.5	
HD97048	B9.5Ve	Ib	175±18	10010	1.27	43.5±6.3	2.2±0.2	2.5±0.2	>6.3	Ced 111
HD100453	A9Ve	Ib	111±11	7390	0.02	7.9±1.1	1.7±0.1	1.7±0.2	7.0±0.1	
HD100546	B9Vne	Ia	103±6	10500	0.26	32.9±2.7	1.7±0.1	2.4±0.1	>7.0	Sco OB2-4?
HD135344B	F4Ve	Ib	140±14	6590	0.31	8.2 ±1.1	2.2±0.2	1.6±0.2	6.9±0.3	Sco OB2-3
HD141569	A0Ve	IIa	99±10	9520	0.37	19.5±2.8	1.6±0.1	1.1±0.1	>7.0	(L169)
HD142666	A8Ve	IIa	145±15	7580	0.93	14.0±2.0	2.2±0.2	1.8±0.3	6.8±0.4	Sco OB2-2
HD142527	F7IIIe	Ia	145±15	6257	0.64	15.4±2.2	3.3±0.2	2.0±0.2	6.3±0.4	Sco OB2-2
HD144432	A9IVev	IIa	145±15	7345	0.17	10.4±1.5	2.0±0.1	1.8±0.2	7.0±0.3	Sco OB2-2
HD144668A	A7IVe	IIa	210±21	7925	0.49	90±13	5.0±0.4	3.2±0.5	5.7±0.3	Lupus 3
HD150193A	A2IVe	IIa	150±30	8990	1.46	24.6±7.0	2.0±0.3	2.3±0.2	>6.3	Sco OB2-2
HD163296	A3Ve	IIa	122±12	8720	0.09	24.2±3.4	2.2±0.2	2.0±0.2	6.7±0.4	
HD169142	A5Ve	Ib	145±15	8200	0.43	14.8±2.1	1.9±0.1	2.0±0.3	6.9±0.3	Sco OB2-1
HD179218	B9e	Ia	243±24	10500	0.56	104±15	3.1±0.2	2.9±0.5	6.1±0.4	(L693)

et al (in prep.). The SEDs have been de-reddened, after which a Kurucz model was fit to identify the photosphere.

In order to quantify the shape of the SEDs we have calculated the excess IR luminosity ($L_{\rm E}$) and the excess energy over the photospheric flux at 3.8 and 60 μm ($L_{3.8}$ and L_{60} respectively). These quantities are listed in table 7. It shows that group I and group II sources have a similar range in total excess luminosity $L_{\rm E}$. Recall that the distinction between group I and II is only based on the slope of the spectrum from 10 to 60 μm (Meeus et al. 2001). In Fig. 1 we plotted $L_{3.8}$ against L_{60}. The plot shows that the group I and II sources of our sample are nicely separated in L_{60} space. The only exception to this is HD179218, which is a group I source according to the definition of (Meeus et al. 2001) and is categorized as flaring with [OI] observations (see van der Plas et al. 2008). The high luminosity seems to be the obvious peculiarity of HD179218 compared to what is typical for the sample, but it is not clear how this would influence its 60 μm luminosity.

The value of $L_{3.8}$ is an indication of the amount of hot dust near the star. For example for HD141569, having almost no excess luminosity, the lack of this emission is generally interpreted as the presence of an inner dust-free cavity. Note in Fig. 1 that besides HD141569 only group I sources have very low values of $L_{3.8}$.

3. Observations

3.1. VISIR

VISIR is the VLT Imager and Spectrometer for mid Infrared (see Lagage et al. 2004). It is mounted at the Cassegrain focus of ESO's VLT telescope Melipal at Paranal. Under good seeing conditions it provides diffraction-limited imaging and spectroscopy in the N and Q-band, which is ∼0.3″ at 10 μm. The spectrometer offers a range in spectral resolution of 150 to 30000 and it has a pixel-scale of 127 mas/pix. In order to get rid of the high atmospheric background the instrument employs standard chopping and nodding techniques.

Our observations were obtained between December 2004 and July 2007 as part of the VISIR GTO program on circumstellar disks. For all our observations the low resolution spectroscopic mode of VISIR was used. The full N-band can be mapped by performing 4 wavelength settings at 8.5, 9.8, 11.4 and 12.2 μm. VISIR offers a choice in slit-width, slit-rotation and chopping throw. The standard orientation of the slit is North-South, but for a few observations a different orientation was chosen. This was done with the goal of tracing the expected extended emission along the slit. We note that the limited knowledge of the IR position angle leads to a small systematic underestimate of the disk sizes in IR emission. For all the observations chopping and nodding was performed parallel to the slit. Since our targets were known to have angular sizes of 1″ and lower, a chopping throw of 8″ was appropriate. This allowed the sources to remain inside the detector field of view at all times and thus to maintain the best integration efficiency. A log of our observations can be found in table 2 and table 3.

Table 4. Instrument specification of the different data types. Stated are the typical values of the data used. The parameters specified from left to right are: the slit width, the theoretical diffraction limit, the spectroscopic resolution, the sensitivity and the wavelength range.

Instrument	Slit [″]	θ [″]	R	S [mJy/10σ/h]	$\Delta\lambda$ [μm]
VISIR	0.75	0.3	250	100	7.9-13.2
Spitzer	3.6	3	70	185	5.5-37
ISO	14x20	4	250	2000	2.4-200
TIMMI2	1.2	0.7	160	250	7.9-13.2

3.2. ISO, Spitzer & TIMMI2

In order to compare, verify and flux-calibrate our VISIR data, we will also employ ISO, Spitzer and TIMMI2 data of the stars. Both ISO and Spitzer have a much lower spatial resolution than VISIR, but their space-based unobscured view of the stars and wider slits gives them superior wavelength coverage and flux-calibration. TIMMI2 is VISIR's predecessor, it's a ground-based mid-IR spectrometer, which is operated at ESO's 3.6 m telescope at La Silla. In table 4 we list the used instrument specifications for comparison. For the details regarding the observations and

data reduction, we refer the reader to Acke & van den Ancker (2004) for ISO, Bouwman et al. (in prep.) for Spitzer and van Boekel et al. (2005) for the TIMMI2 data.

4. Data Reduction

4.1. Spectral extraction

An IDL pipeline written by one of us (E. Pantin) was used to perform the first steps of the spectral data processing. It stacks the data in the proper order, subtracts the atmospheric and telescope backgrounds and suppresses the detector striping (Pantin et al. 2007). A correction for slit curvatures and optical distortion is then applied. The 1D spectrum is obtained with a optimal extraction method by Horne (1986). Subsequently, the spectrum is wavelength calibrated by correlating the simultaneously measured sky spectrum with a ATRAN/HITRAN model. See Pantin (in prep.) for a more detailed description of the reduction process.

Some secondary processing methods were devised to refine the results. Small wavelength mismatches between the objects and the photometric calibrators were corrected. The correction shift was obtained by correlating the stacked sky-frames of science and calibration measurements. To correct for atmospheric extinction we used the formalism described in van Boekel et al. (2005), which requires two calibration measurements, at differing airmass, and interpolates the extinction to the airmass of the science target. Unfortunately, for roughly half of our science observations we obtained only a single suitable calibration measurement. To correct for the extinction of the science observation we used the following formalism:

$$I_{\lambda,\mathrm{s}} = S_{\lambda,\mathrm{s}} \frac{1}{R} \left(\frac{R I_{\lambda,\mathrm{c}}}{S_{\lambda,\mathrm{c}}} \right)^{\frac{m_\mathrm{s}}{m_\mathrm{c}}} \quad (1)$$

The intrinsic spectrum of a science target, $I_{\lambda,\mathrm{s}}$, is calculated by taking the observed spectra of science and calibrator $S_{\lambda,\mathrm{s}}$ and $S_{\lambda,\mathrm{c}}$, the airmass values of these observations, m_s and m_c, the model spectrum of the calibrator $I_{\lambda,\mathrm{c}}$ and the responsivity of the system, R. The latter was assumed to be a constant and was obtained by taking the cross-section with the y-axis in a $\ln(S/I)$ versus airmass diagram containing all wavelength averaged calibration measurements.

For the error determination we went back to the raw data. We split every observation up into 10 or more subsets of equal integration time. Next, we performed a simplified extraction on the central beam in all sets creating a distribution of spectra for each observation. After normalizing these spectra with their median level, we determined the standard deviation as a function of wavelength, which left us with the fractional error of the observed spectra. To obtain the error-spectrum of the final calibrated spectrum we used standard differential error-propagation. We find that typical sensitivities are around 100 mJy/10σ/1h.

4.2. FWHM extraction

To obtain the size of the sources as a function of wavelength we looked at every individual nod position and considered only the beam in the center of the detector. This approach allows for a determination which is independent of how well the A-A chop-nod-position coincides with the B-B chop-nod position. In order to increase the Signal to Noise Ratio (SNR) we rebinned the data in the wavelength direction, merging 8 pixels. Then we did a Gaussian fit to get the Full Width at Half Maximum (FWHM) of every wavelength bin. After repeating this for every individual nod position we obtained a distribution of wavelength dependent sizes. The final wavelength-dependent width of a target is then the 'nod' average of this distribution. For HD34282 and HD141569 the SNR's were too low to obtain meaningful results with this method. For these sources the total stack of all nod positions was used, just as was done to extract the spectra. The final width was then obtained by treating the central beam with the same regridding and gauss-fitting as described above. The combined measurement error and fitting error was determined by taking the same total 2D spectrum, but this time we only merged 4 pixels in the wavelength direction to retain significant wavelength resolution. Subsequently, the error could be retrieved by subtracting a spline from the wavelength dependent FWHM and then calculating the standard deviation. Note that this is the measurement error of a 4 pixel wavelength bin. When we use an entire setting as a single measurement of size the error is decreased by the root of the number of bins used.

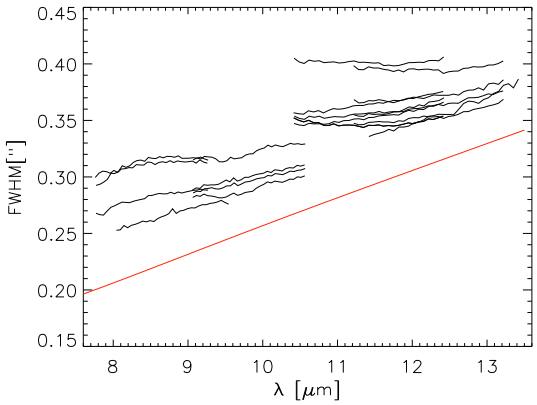

Fig. 2. The 20 calibration measurements with the best optical seeing (< 0.6″). The straight (red) line is the simulated diffraction limit of the instrument. Since all these calibrations measurements are close to or in the diffraction-limited regime, the variety of the signal is due to artifacts of the telescope and instrument. Here we can identify a broadening, time-dependent variations and a jump going from the 9.8 to the 11.4 setting.

5. The PSF

Measuring the FWHM as a function of wavelength for ~130 calibrators reveals a great level of variety. To start classifying this variety we plotted the 20 calibrators taken during optimal optical seeing (Fig. 2) and the 20 calibrators observed during worst seeing (Fig. 3). Also plotted in red is the simulated diffraction limit, calculated by considering an obscured pupil in analogy with Brown & Burrows (1990) to simulate the effect of the telescope optics. Then we applied a spatial sampling to simulate the effect of VISIR's pixel grid, followed by a Gaussian fit to obtain the FWHM. Figure 2 allows us to address the diffraction-limited behavior of the telescope, since the seeing can be assumed to be negligible in the mid-IR as soon as the optical seeing drops below 0.7″ (see Doucet et al. 2006a). The slope of the measurements is in general agreement with theory, but we can see that there is an overall offset. There is also a spread between measurements taken at different times. A third effect, that remains

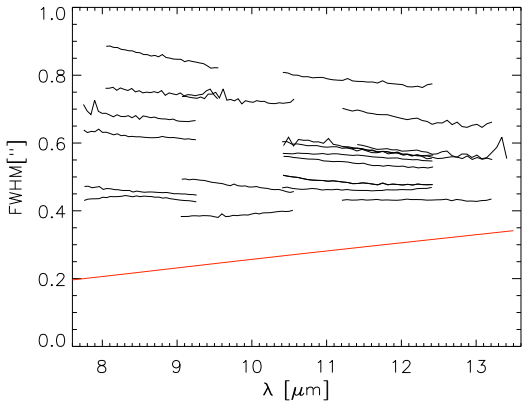

Fig. 3. The 20 calibration measurements with the highest optical seeing (> 1.1″). The straight red line is again the simulated diffraction limit of the instrument. Notice that the FWHM values are larger, the spread between measurements is larger and the slopes are negative.

unexplained, is the jump observed between the 9.8 μm setting and the 11.4 μm setting. In the seeing limited regime (Fig. 3) we observe much more broadened signals, which decrease with wavelength. Again there is a substantial spread between measurements at different times.

We know from Burst Mode data in which all individual ∼20 ms integrations are stored, that the VISIR imaging data present sporadic PSF distortions on a 3s timescale (Brandl et al. 2008). We therefore infer that these PSF variations might produce the spread observed in Fig. 2. However, the FWHM discrepancy between the simulated diffraction limit and the 'best' calibration measurements (i.e. with the lowest FWHM values), remains unexplained. The offset between second and third setting could be caused by the instrument going slightly out of focus when the filter is changed from N_SW to N_LW. In the seeing-limited regime the slope generally agrees with the Roddier formula (FWHM $\propto \lambda^{-0.2}$). The found spread in sizes is in first order explained by the correlation between optical and IR-seeing. Then there are second order effects like the airmass (m) dependence of seeing, which is roughly FWHM $\propto m^{0.6}$ according to Sarazin (2003).

The non-uniformity of the calibration measurements prompted us to deviate from the usual deconvolution procedure. That is, we do not consider the calibrators taken before or after the science measurement as good enough to define the PSF. A single, or even two calibrators would underestimate the true uncertainty in the PSF during the science observation. To solve this problem we can either (a): still use the spectral calibrator, but assign a larger error bar to its PSF than on the basis of Gaussian error estimates; or (b): use the sample as a whole. In the second approach we assume that the PSF depends on 3 variables, i.e. wavelength, seeing and airmass. We use the observed spread in the calibrator signals to measure the statistical error on an individual science observation. Careful inspection of individual cases showed that non of the calibration measurements were a completely reliable representation of the PSF during the science measurement. There were either large FWHM differences between consecutive calibrations or large differences between science and calibration in the optical seeing, the airmass or the time of measurement. Therefore we defined the PSF and its error using the entire sample of calibrators.

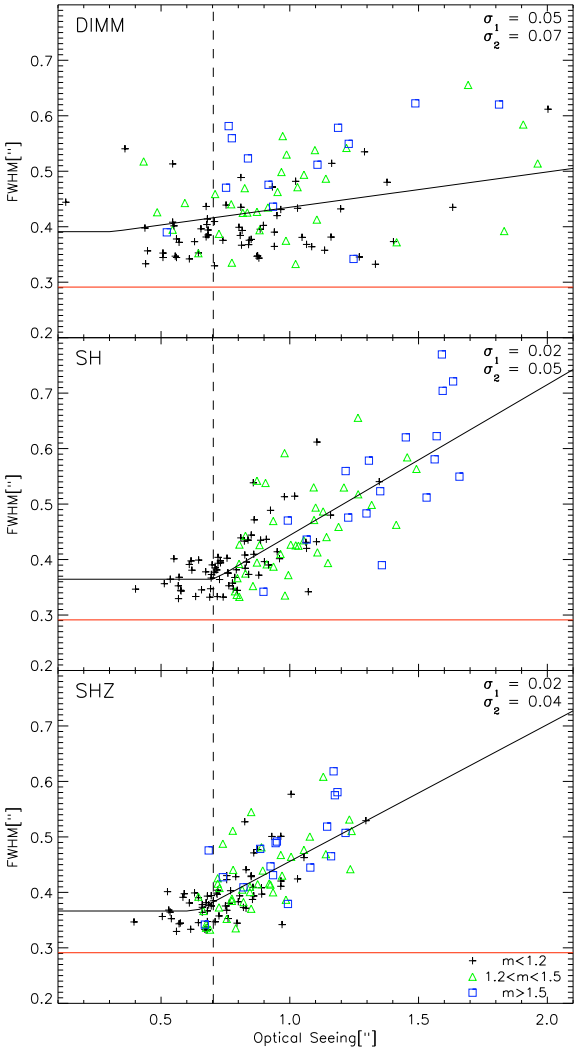

Fig. 4. The correlation between the size of a point source on the detector and the optical seeing. In the top panel we plotted the wavelength-median of the measured IR-size of the 11.4 μm setting against the optical seeing as measured by the Differential Image Motion Monitor (DIMM, see Sarazin & Roddier 1990). In the middle panel we plotted the same values against the optical seeing as measured by the Shack-Hartmann wavefront sensor of the telescope's active optics system (SH). The SHZ label in the bottom panel stands for the same optical seeing, but as it would be in the zenith. The quantities on both axes have been transformed to zenith, via the airmass-corrections given in the text. All displayed measurements are separated in 3 airmass categories as indicated in the bottom right corner. The measurement uncertainties are negligible compared to the scatter. The straight (red) line is the simulated diffraction limit of the instrument. The dotted line displays the assumed border between the diffraction limited and the seeing-limited regimes (see text). The data on the left of this line is fit with a constant and to the right we have fit a linear relation. Indicated in the top right we indicated the standard deviation around the fit for both regimes, σ_1 and σ_2 respectively.

We know that the measured PSF has contributions from three sources, which are the diffraction limit, the telescope-broadening

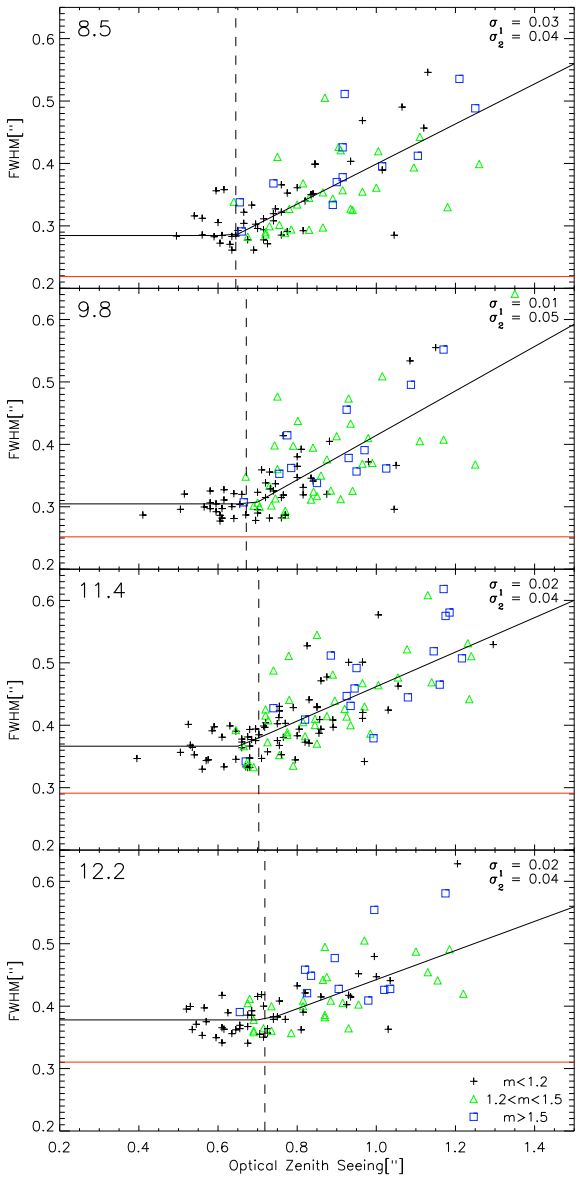

Fig. 5. The measured size of a point source as a function of optical zenith seeing for the four different observational settings. The central wavelength of each setting is indicated in the top left in μm. All the measurements are separated in 3 airmass (m) categories as indicated in the bottom right corner. The measurement uncertainties are negligible compared to the scatter. The straight (red) line is the simulated diffraction limit of the instrument. The dotted line displays the assumed border between the diffraction-limited and the seeing-limited regimes (see Sect. 5). The data left of this line is fit with a constant and to the right we have fit a linear relation. The final function (given in black) is the upper value of both fits. Indicated in the top right is the standard deviation around the fit for both regimes, σ_1 and σ_2 respectively.

and the atmospheric seeing. In order to quantify these terms we correlated the measured size of the sample of calibrator stars on the detector with the optical seeing. Figure 4 displays the wavelength-median values of the calibrators observed with the 11.4 μm setting. When we use the optical seeing as measured with the Differential Image Motion Monitor (DIMM, see Sarazin & Roddier 1990) we get a poor correlation, because the DIMM measures from a different physical location and it observes a different part of the sky. We checked with the optical seeing as measured with the Shack-Hartmann wavefront sensor of the telescope active optics system (SH). This is a measurement of the guidestar that was used during our science measurements, thus in the same location and direction. The improved correlation is clear from figure 4. In the bottom panel it shows the zenith or airmass corrected version (SHZ), using an airmass dependence of the seeing of $m^{-0.6}$ (Sarazin 2003).

The optical seeing could directly be corrected with this dependence, but the correction of the IR size is less straight forward, because both the diffraction limit and the seeing have to be taken into account (in the optical, seeing dominates over telescope diffraction). We first empirically determined the diffraction limit, $\theta_{\rm exp}$. This was done by separating the data by eye in diffraction limited (seeing-independent) and seeing-limited regimes, and determining the median value of the diffraction-limited measurements. Then we quadratically subtracted this value from all measurements above the median value to isolate the seeing contribution. This seeing part was then corrected with the $m^{-0.6}$ factor. Subsequently, the experimental diffraction limit was quadratically added again. In formula form:

$$\Sigma_{\rm c} = \sqrt{(\Sigma_{\rm m}^2 - \theta_{\rm exp}^2) \cdot m^{-1.2} + \theta_{\rm exp}^2} \qquad (2)$$

In which $\Sigma_{\rm m}$ and $\Sigma_{\rm c}$ represent the measured and the airmass corrected IR-size respectively. We plotted the data-points with symbols corresponding to their original airmass values. This shows that there is still correlation left between airmass and seeing. Whether this is due to an incorrect correction factor or due to an observational bias remains unclear.

At this stage the data points have all been transformed to their zenith values and can be internally compared. The fit for the diffraction-limited regime was assumed to be constant and equal to $\theta_{\rm exp}$. For the seeing-limited regime we assumed a linear function. The final function was then obtained by taking the highest value of both fits. With this resulting function we have obtained a statistical or average PSF, which accounts for the effect of seeing. In addition the standard deviation of the data-points around the function gives the statistical dispersion of the data and thus the FWHM error of the PSF estimation for a random measurement. Figure 5 displays the result for the four different settings. To apply this PSF to our measurements we extended the statistical analysis to all wavelength bins and transformed the PSF to the airmass of measurement with an inversion of formula 2.

6. Results

6.1. Spectra

In order to obtain a continuous wavelength scale in our spectra the four different wavelength settings were spliced together. The third setting was scaled at 10.6 μm to the Spitzer spectrum when available, otherwise the ISO spectrum was used. The choice of 10.6 μm as the point of scaling was motivated by the overall lower atmospheric transmission in the first, second and fourth setting. The other settings were scaled to connect with the third in a continuous way. The scaling factor was found by clipping 10 pixels of the edges of both settings, taking the mean of the fixed setting in the remaining overlapping wavelength domain

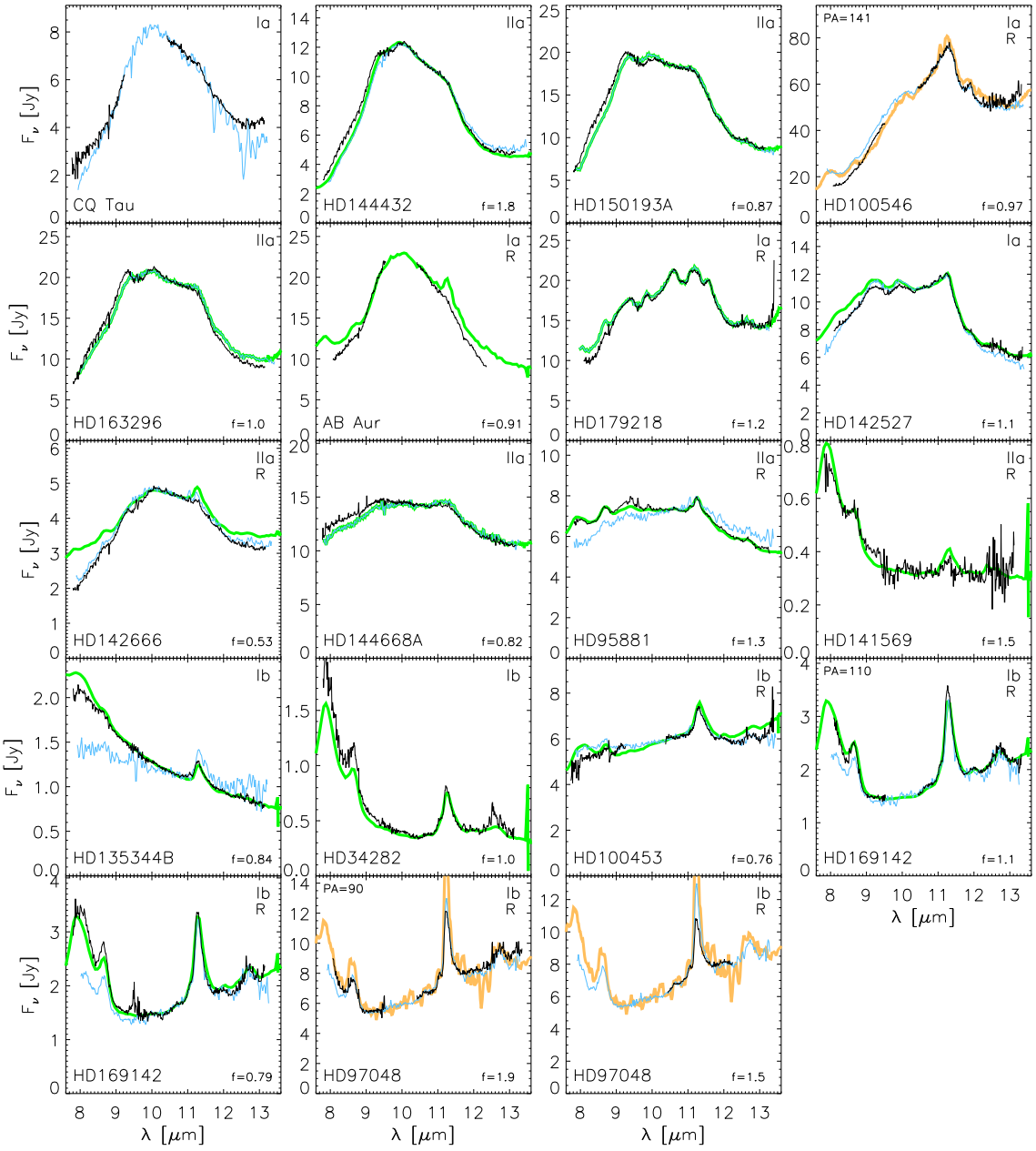

Fig. 6. The N-band spectra of our targets. Our VISIR spectra are plotted with the fine black line. Overplotted in thick green are the Spitzer spectra obtained in the legacy program, see Bouwman et al. (in prep). For HD97048 and HD100546 the ISO spectrum was overplotted with thick orange. Indicated in the bottom right is the scaling factor needed to bring our VISIR spectra to the same flux-level as the alternative spectrum. Also overplotted with the medium thick blue lines are the TIMMI2 spectra, where available. The default orientation of the VISIR slit is North-South, where a different rotation was used this is indicated in the upper left corner, with the position angle running East from North. In the upper right corner we indicated the group classification and an optional 'R', which indicates that either the continuum or the PAH band is resolved in our analysis.

and dividing this by the mean of the next setting in the same domain. When the second setting was not present in the observation the first setting was independently scaled to the Spitzer or ISO spectrum. The resulting spectra are plotted in Fig. 6. Overplotted

Table 5. All solid state and PAH features discernible by eye in the spectra in Fig. 6.

Name	Amorphous Silicate	Forsterite	Enstatite	PAH 8.6	PAH 11.2
AB Aur	✓	-	-	-	✓
HD34282	-	-	-	✓	✓
CQ Tau	✓	-	-	-	-
HD95881	✓	✓	✓	✓	✓
HD97048	-	-	-	✓	✓
HD100453	-	-	-	✓	✓
HD100546	✓	✓	-	-	✓
HD135344B	-	-	-	✓	✓
HD141569	-	-	-	✓	✓
HD142666	✓	-	✓	✓	✓
HD142527	✓	✓	✓	-	-
HD144432	✓	-	✓	-	-
HD144668A	✓	✓	✓	-	-
HD150193A	✓	✓	✓	-	-
HD163296	✓	✓	✓	-	-
HD169142	-	-	-	✓	✓
HD179218	✓	✓	✓	-	-

with green thick lines are the Spitzer spectra, thick orange are the ISO spectra and intermediate thickness blue are the TIMMI2 spectra.

The first thing to notice when looking at Fig. 6 is the diversity of morphology. There's the typical PAH sources such as HD169142. There are sources showing mainly small amorphous silicate-grains like HD144432 or bigger silicate grains like in HD144668. Then there are sources with crystalline silicates like HD179218. And of course there are sources that display a mixed chemistry like HD95881. In table 5 we indicated all the features that we can distinguish by eye from the spectra.

Another interesting finding is the difference in flux level between the VISIR and Spitzer/ISO spectra. In the bottom right corners of the spectra we stated the factor needed to scale the VISIR spectrum to the alternative spectrum. For the continuum the difference is understood with the 10 to 20 % uncertainty in VISIR's absolute flux calibration. This uncertainty is mainly caused by the change in atmospheric transmission with time, airmass, and azimuth. Another part of the uncertainty stems from slit-loses: To obtain optimal spectral resolution VISIR employs a long narrow slit that cuts away spatially extended flux in the dispersion direction. This effect occurs with spatially extended sources, but also when there are seeing differences between science and calibration measurements.

The relatively smaller contributions in the PAH features (8.6 and 11.2 μm or the shoulder of 7.7 μm) of the VISIR spectra are real and most likely caused by the large spatial scale of this emission. With the Spitzer slit-width of 3.6″ it is likely to pick up emission from the entire disk and any additional extended emission from surrounding molecular cloud material, whereas VISIR with a slit-width of 0.75″ focuses on the disk. Some interesting examples that illustrate this are AB Aurigae, HD97048 and HD142666. The cases in which the PAH features appear identical in the VISIR and Spitzer/ISO spectra are also interesting. In these cases the PAH emission most likely originates from the protoplanetary disk. The differing slopes observed in some cases (e.g. HD144668) are most likely an artifact of the atmospheric correction. The exact origin remains unclear.

Table 6. List of all targets from our sample that have been resolved, either in the continuum or in the PAH-band. For the 8.6 and 11.2 μm PAH-bands we give the significance level of the increase in spatial extent (FWHM) with respect to the continuum, except for HD169142 which displays no variation.

Name	Resolved in continuum?	Significance 8.6 increase [σ]	Significance 11.2 increase [σ]
AB Aur	yes	10	35
HD95881	no	7	32
HD97048	yes	24	76
HD100453	no	7	13
HD100546	yes	27	41
HD141569	yes	7	13
HD142666	no	16	13
HD169142	yes	-	-
HD179218	yes	86	39

6.2. Spatial extension of science targets

In Fig. 7 we displayed the resulting angular sizes of our science targets as a function of wavelength. In red we overplotted the simulated diffraction limit. Also we plotted in green any calibration measurements taken within 3 hours before or after the science observation, all corrected for airmass differences. Likewise we plotted in blue the statistical calibrator appropriate for the optical seeing at the time of measurement and transformed to the airmass of measurement. In addition we plotted the error of the PSF, as determined in Sect. 5.

The behavior of our science targets is significantly different from that of the calibrators. For several sources the continuum is more extended than that of the calibrators. For some sources there is a relative increase at the 8.6, 11.2 or the 12.7 μm PAH features. This relative increase in FWHM(λ) can be measured with high precision because the same observing conditions and instrumental effects apply to all wavelengths within one spectral setting. Moreover, an upturn with decreasing wavelength is seen in the first setting, which also coincides with a PAH opacity-increase, i.e. the red wing of the 7.7-7.9 μm PAH complex. Table 6 summarizes the results. For HD97048 we have observations in two orientations and we can see that at least in the PAH-band the target is more extended in the North-South direction.

6.3. Comparing flux and extent

In Fig. 8 we zoom in on the extended PAH features. It demonstrates unambiguously how the relatively extended emission is related to PAH-features in the spectra. This is in agreement with previous findings by Habart et al. (2004), van Boekel et al. (2004) and Geers et al. (2007a), that in Herbig Ae/Be stars PAH emission is more extended than thermal silicate emission. This is explained with the fact that PAH molecules are transiently heated and can thus radiate at large distance from the star where thermal equilibrium temperatures are too low to cause a significant emission at 10 μm. Sources that deviate from the observed trend are HD34282 and HD169142, which show clear presence of all PAH features in the spectrum, but no increase of the extent at any of these wavelengths.

7. Analysis

7.1. Feature strength

From the VISIR spectra we measured the strength of the 8.6 and 11.2 μm PAH features. This was done by interpolating the con-

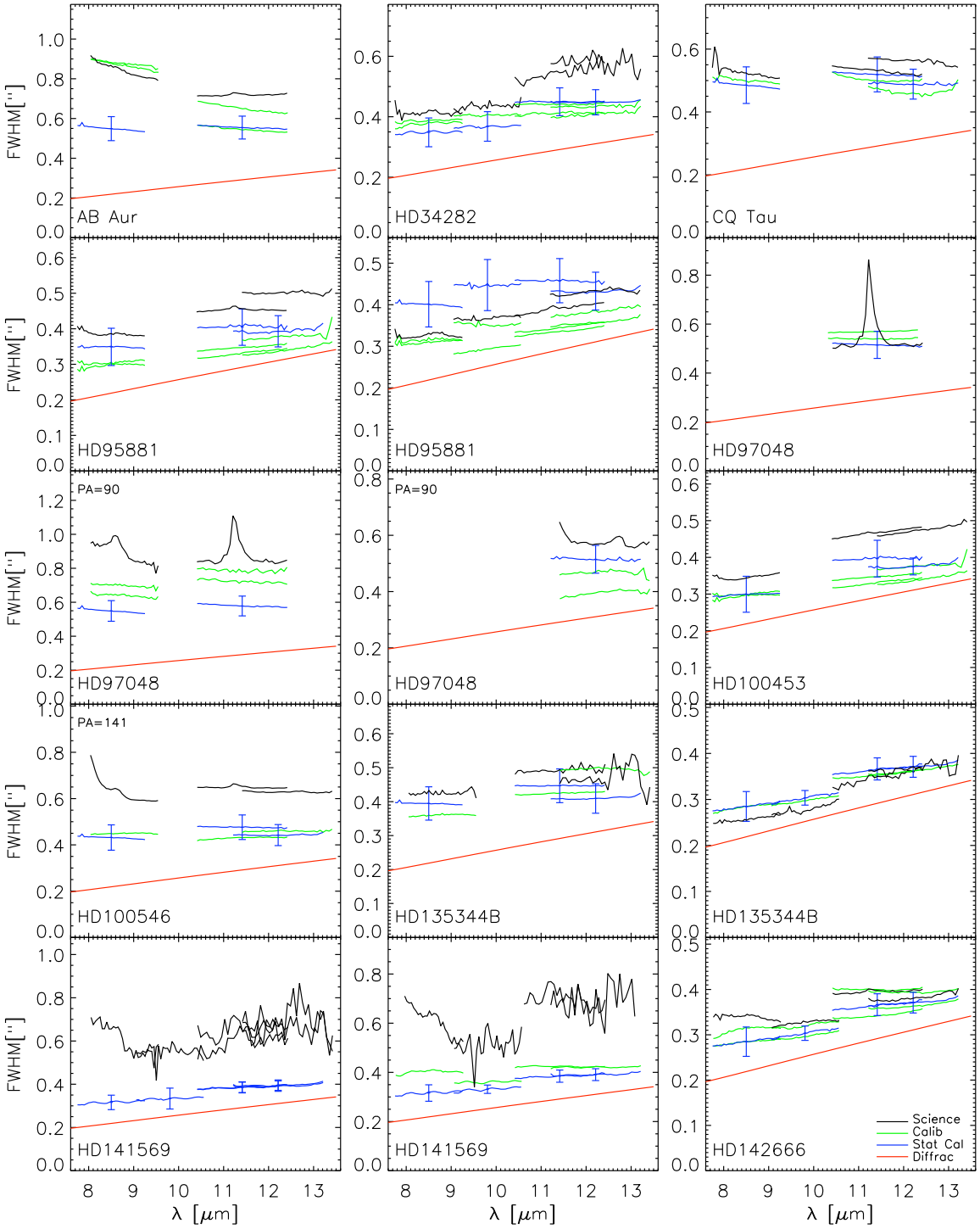

Fig. 7. Size of all our targets as a function of wavelength (Science). Plotted in green are calibration measurements taken right before or after the science exposures (Calib). Plotted in blue is the statistical calibrator as determined from the entire sample of calibrators (Stat Cal). The straight red line is the simulated diffraction limit (Diffrac).

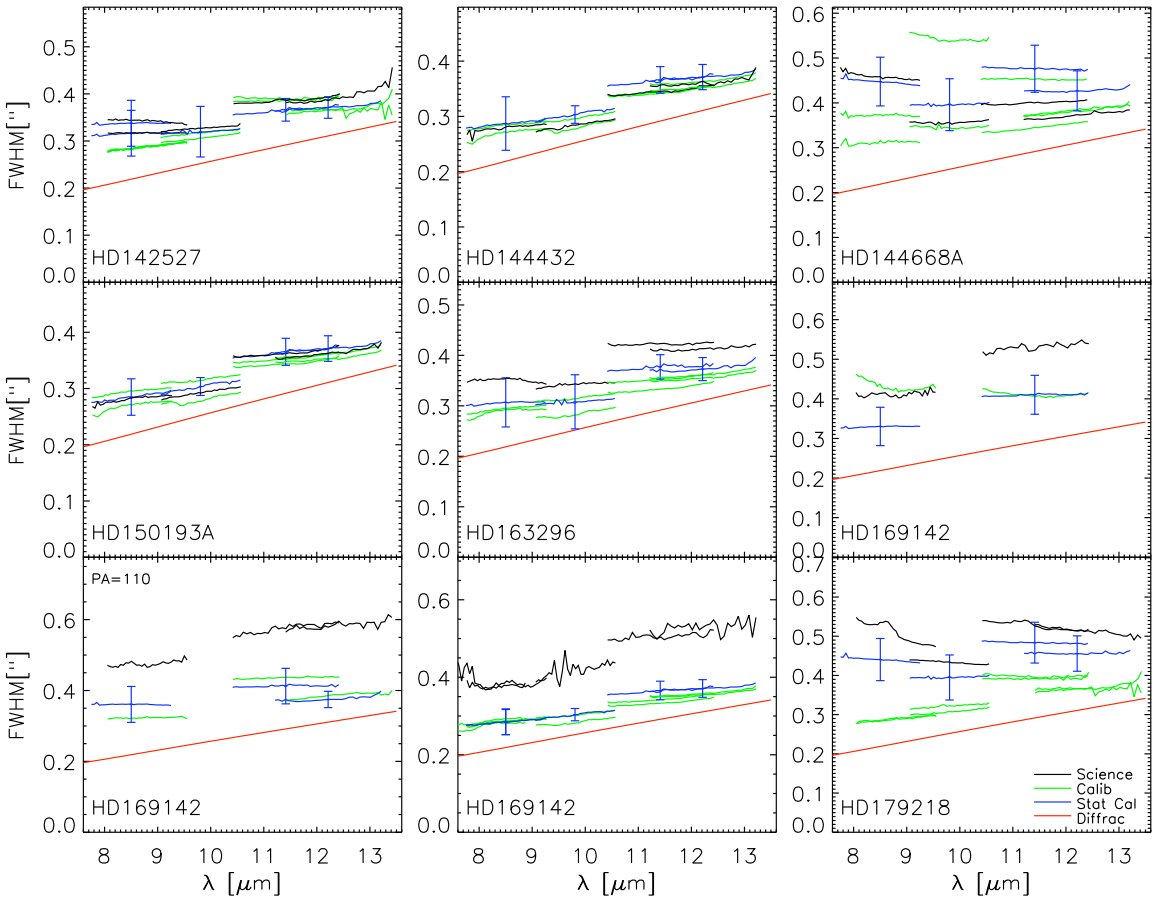

Fig. 7. Continued

tinuum between two wavelength bins of 0.1 μm, just next to the features. For the 8.6 μm feature we used 8.4 and 8.85 μm and for the 11.2 μm feature we used 10.9 and 11.7 μm. The height of the PAH peak and the corresponding continuum level could then be measured by taking a 5 pixel average. The continuum subtracted PAH strength was then expressed as a fraction of the continuum. We estimated the continuum flux determination relative to the total flux to have an accuracy of ~1%. However, for the sources that blend forsterite and PAH emission at 11.2 μm, this method systematically overestimates the PAH strength.

We also measured the strength of the 8.6, 11.2 μm PAH, and silicate features from the Spitzer spectra, where the silicate feature was defined as the sum of all silicate species. For the targets for which we did not have Spitzer data the ISO or TIMMI2 spectra were substituted. To find the contribution of the individual species we performed a mineralogical fit, similar to the one described in van Boekel et al. (2004). The difference being that the PAH features were allowed to vary independently. The extracted features could then be integrated within the respective boundaries 8.2-9.0, 10.9-11.8 and 8.0-13.2 μm. For the silicate feature we also integrated the continuum and expressed the feature as a fraction of the sum of silicate feature and continuum (i.e. total thermal radiation). Table 7 displays the resulting values. The silicate strength was used to sort the spectra in Fig. 6. The sources dominated by PAH emission were sorted using the 11.2 μm strength.

7.2. Deconvolution of the continuum

In order to obtain the intrinsic angular size of the sample sources, we deconvolved the results of Fig. 7. We assumed the spatial distribution of the light of our science targets as well as that of our PSF to be Gaussian. This simplifies the deconvolution to a quadratic subtraction. To select the appropriate PSF we evaluated the quality of the calibrators taken before and after the science measurement, by considering differences in airmass, seeing and time, but also the wavelength-dependent behavior of the calibrator. In most cases, we preferred the statistical PSF as described in Sect. 5. The deconvolution was then performed for every wavelength bin separately. Figure 9 displays the result of the analysis for the resolved sources.

The error-bars were obtained by propagating the PSF error derived in Sect. 5 and the measurement error derived in 4.2. This was done by numerically perturbing the science and PSF signals with random offsets within their Gaussian distributions. Evaluating the standard deviation of the resulting distri-

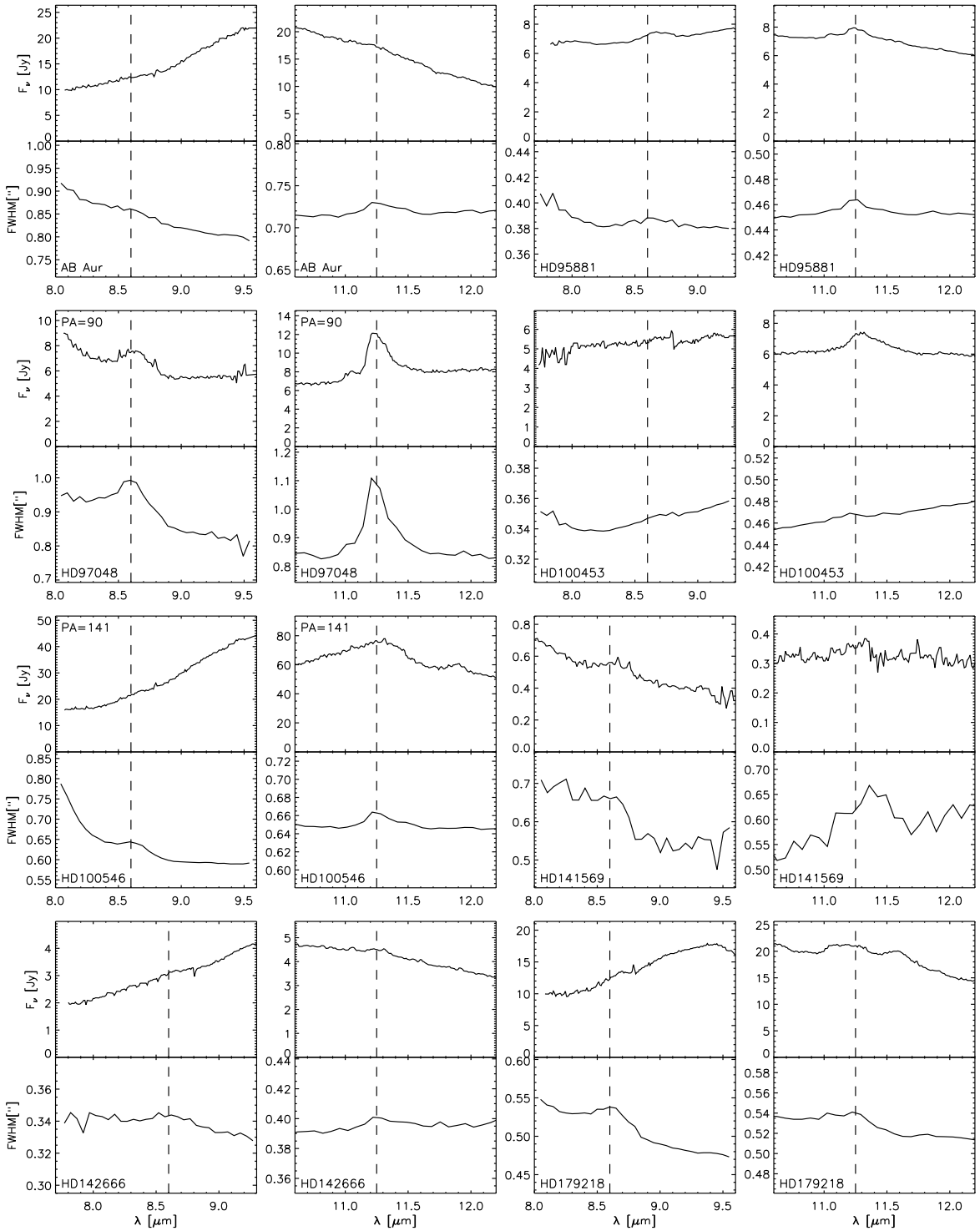

Fig. 8. Comparing the flux of our sources with the angular size of their signal. The dashed lines indicate the position of PAH-features at 8.6, 11.25 and 12.7 μm. Note that HD169142 shows no significant bump in FWHM.

Table 7. Feature strengths and excess luminosities. The feature strengths as determined from the VISIR spectra are expressed as the ratio of continuum subtracted peak flux over continuum flux times 100%. The features as measured from the Spitzer spectra are expressed as integrated flux under the continuum subtracted features. The silicate feature is defined as the sum of all silicate species. For HD100546 and HD97048 the ISO spectrum was used and for CQ Tau the TIMMI2 spectrum (see Sect. 7.1 for more details). The excess luminosities at 3.8 ($L_{3.8}$) and 60 μm (L_{60}) and the overall infrared excess ($L_{\rm E}$) were determined from the SEDs (see Sect. 2.3).

	VISIR			Spitzer			SED		
Name	8.6/cont	11.2/cont	12.7/cont	Sil	8.6	11.2	$L_{3.8}$	L_{60}	$L_{\rm E}$
	[%]	[%]	[%]	[%]	[10^{-15}Wm^{-2}]	[10^{-15}Wm^{-2}]	[10^{-3} L$_*$]	[10^{-3}L$_*$]	[10^{-2} L$_*$]
AB Aur	0.0	5.1	0.0	$44^{+2.6}_{-2.1}$	$7.8^{+2.1}_{-2.4}$	$16^{+7.6}_{-9.1}$	45	49	51
HD34282	30	92	8.8	$49^{+5.7}_{-5.7}$	$2.1^{+0.2}_{-0.2}$	$2.9^{+0.4}_{-0.3}$	40	91	54
CQ Tau	0.0	0.0	0.0	$101^{+9.4}_{-8.0}$	$2.9^{+1.0}_{-1.0}$	$0.0^{+0.0}_{-0.0}$	315	385	476
HD95881	5.9	12	2.9	$15^{+0.6}_{-0.6}$	$7.2^{+0.3}_{-0.3}$	$7.1^{+1.7}_{-1.1}$	74	2.7	54
HD97048	18	62	9.9	$8.5^{+2.3}_{-1.7}$	$21^{+2.2}_{-2.0}$	$52^{+3.8}_{-4.5}$	15	48	33
HD100453	3.1	19	4.1	$20^{+2.0}_{-1.7}$	$3.4^{+0.6}_{-0.6}$	$10^{+0.7}_{-0.4}$	54	62	56
HD100546	1.1	22	0.1	$64^{+1.6}_{-1.6}$	$36^{+2.5}_{-3.4}$	$58^{+7.2}_{-7.2}$	14	54	58
HD135344B	3.2	19	0.0	$0.9^{+4.4}_{-0.5}$	$0.0^{+0.0}_{-0.0}$	$1.7^{+0.0}_{-0.1}$	49	57	43
HD141569	8.8	10	0.0	$27^{+4.3}_{-6.4}$	$0.6^{+0.0}_{-0.0}$	$0.6^{+0.1}_{-0.1}$	0.2	2.7	0.8
HD142666	5.0	7.1	0.0	$26^{+1.5}_{-1.1}$	$2.2^{+0.2}_{-0.1}$	$3.9^{+1.5}_{-1.5}$	29	11	32
HD142527	0.0	17	0.3	$34^{+1.8}_{-1.4}$	$2.6^{+0.7}_{-0.9}$	$10^{+3.0}_{-1.9}$	73	146	82
HD144432	0.0	6.9	0.0	$76^{+1.1}_{-1.2}$	$0.2^{+0.3}_{-0.1}$	$1.3^{+1.1}_{-0.7}$	41	11	47
HD144668A	0.6	6.9	0.0	$25^{+1.5}_{-2.1}$	$0.0^{+0.0}_{-0.0}$	$1.3^{+1.3}_{-0.8}$	60	4.0	44
HD150193A	0.0	8.0	0.9	$67^{+1.5}_{-1.5}$	$0.0^{+0.0}_{-0.0}$	$0.0^{+0.0}_{-0.0}$	39	7.5	42
HD163296	1.1	7.8	0.0	$59^{+1.3}_{-1.5}$	$2.1^{+1.7}_{-1.4}$	$3.4^{+2.2}_{-1.6}$	47	19	46
HD169142	24	90	13	$25^{+7.1}_{-4.5}$	$3.5^{+0.5}_{-0.4}$	$12^{+1.5}_{-2.1}$	12	42	26
HD179218	4.5	10	2.2	$41^{+1.4}_{-1.3}$	$21^{+1.1}_{-1.4}$	$12^{+2.2}_{-1.5}$	14	16	27

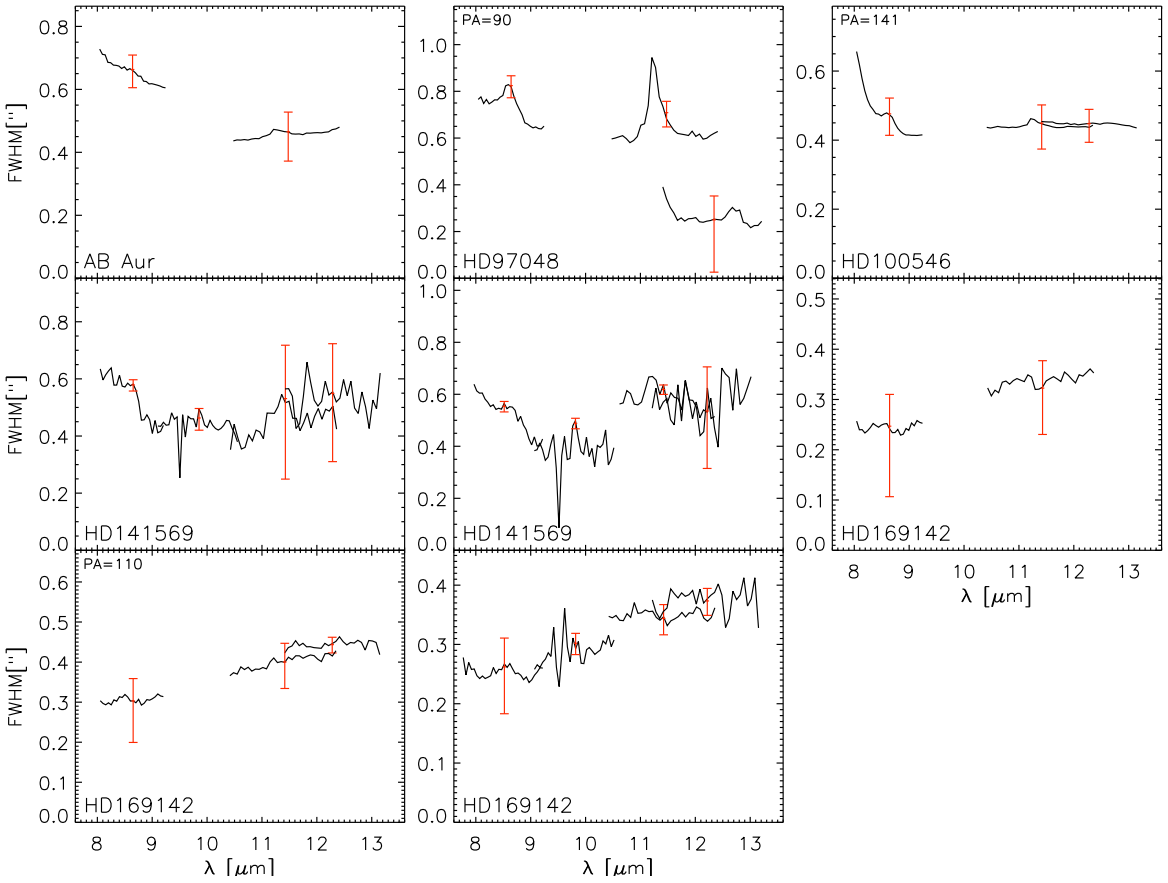

Fig. 9. The deconvolved sizes of the sources that were resolved in the continuum.

Table 8. Deconvolved sizes (FWHM) of our resolved targets. The 8.6 and 11.2 μm Cols. contain the continuum subtracted extent of the respective PAH features. The 3.3 μm feature was obtained from the literature as a comparison: Geers et al. (2007b) (*a*) give the size of the PAH and continuum emission with respect to the continuum, so we quote it as a lower-limit, Habart et al. (2006) (*b*) used a similar analysis. The size of our continuum is the mean of all our measurements. For the sources that were not resolved we give the 3 σ upper-limit. For all our results we also give the absolute sizes in AU, which assume the distance given in table 1. The Col. next to it are the 10 μm sizes stated in the literature: Liu et al. (2007) (*c*) with interferometric nulling, Weinberger et al. (2004) (*d*) determined the outer radius with spatially resolved N-band spectroscopy, Doucet et al. (2007) (*e*) used burst-mode imaging with VISIR and Doucet et al. (2006b) (*f*) obtained outer radii at 20.5 μm. The outer diameter of CO-gas was taken from Dent et al. (2005). The FWHM width of the [OI] 6300 Å emission line was quoted from Acke et al. (2005). Coronagraphic scattering light imaging is also indicated, where available an outer radius is quoted: Liu et al. (2003) (*g*), Grady et al. (2000) (*h*), Ardila et al. (2007) (*i*), Grady et al. (2005) (*j*), Fukagawa et al. (2006) (*k*), Doering et al. (2007) (*l*), Grady et al. (2007) (*m*) and Mouillet et al. (2001) (*n*).

Name	3.3 μm	8.6 μm		11.2 μm		Continuum		Lit.	CO D_{out}	OI	Scat.	Group
	[″]	[″]	[AU]	[″]	[AU]	[″]	[AU]	[AU]	[″]	[km s^{-1}]	[AU]	
CQ Tau	-	-	-	-	-	< 0.40	< 40	450[f]	0.7	-	no[j]	Ia
HD144432	-	-	-	-	-	< 0.19	< 27	-	0.6	-	-	IIa
HD150193A	-	-	-	-	-	< 0.18	< 28	-	-	-	190[g]	IIa
HD100546	$>0.24\pm0.06$[a]	$1.92^{+0.56}_{-0.58}$	198	$0.60^{+0.03}_{-0.04}$	62	$0.45^{+0.02}_{-0.03}$	46	24 ± 3[c]	-	25	824[i]	Ia
HD163296	-	-	-	-	-	< 0.19	< 24	< 12[c]; 200[f]	4.0	-	450[h]	IIa
AB Aur	-	$1.06^{+0.33}_{-0.42}$	153	$0.79^{+0.05}_{-0.06}$	115	$0.46^{+0.06}_{-0.09}$	66	27 ± 3[c]	8.4	20	yes[j]	Ia
HD179218	-	$0.92^{+0.08}_{-0.09}$	225	$0.48^{+0.04}_{-0.06}$	117	< 0.31	< 75	-	1.9	43	-	Ia
HD142527	-	< 0.21	< 31	< 0.21	< 31	< 0.21	< 31	-	-	-	490[k]	Ia
HD142666	-	$0.30^{+0.03}_{-0.04}$	44	$0.34^{+0.04}_{-0.04}$	49	< 0.18	< 26	-	0.8	-	no[j]	IIa
HD144668A	-	-	-	-	-	< 0.25	< 53	-	-	-	no[j]	IIa
HD95881	-	$0.33^{+0.05}_{-0.09}$	57	$0.38^{+0.04}_{-0.06}$	65	< 0.18	< 31	-	-	76	no[j]	IIa
HD141569	-	$0.68^{+0.03}_{-0.03}$	68	$1.50^{+0.12}_{-0.12}$	149	$0.51^{+0.03}_{-0.05}$	50	< 90[d]	5.0	154	325[n]	IIa
HD135344B	-	< 0.17	< 24	< 0.17	< 24	< 0.17	< 24	200[f]	1.8	-	no[j]	Ib
HD34282	-	< 0.45	< 180	< 0.45	< 180	< 0.45	< 180	-	1.8	-	-	Ib
HD100453	0.18 ± 0.02[b]	$0.31^{+0.04}_{-0.07}$	34	$0.27^{+0.06}_{-0.13}$	30	< 0.26	< 29	-	-	-	-	Ib
HD169142†	-	$0.30^{+0.03}_{-0.05}$	44	$0.30^{+0.03}_{-0.05}$	44	$0.30^{+0.03}_{-0.05}$	44	-	1.8	22	200[m]	Ib
HD169142	0.3 ± 0.05[b]	$0.35^{+0.01}_{-0.02}$	50	$0.35^{+0.01}_{-0.02}$	50	$0.35^{+0.01}_{-0.02}$	50	< 11[c]	1.8	22	200[m]	Ib
HD97048†	-	$1.27^{+0.03}_{-0.03}$	223	$1.29^{+0.02}_{-0.02}$	226	$0.41^{+0.05}_{-0.10}$	72	4[e]	-	24	720[l]	Ib
HD97048	>0.2[b](?)	-	-	$1.46^{+0.02}_{-0.02}$	256	< 0.64	< 113	4[e]	-	24	720[l]	Ib

bution of deconvolved signals then gives the final error. Table 8 sums up the results and includes the derived sizes in AU, assuming the distances as displayed in table 1. The number given for the continuum is extracted from figure 9 by taking the median value of the wavelength domain for all the measurements. For the measurements that contained the 7.7-7.9 PAH complex or a broad 11.2 component, we first selected the wavelength domain of the continuum and then a median value was determined. Subsequently, we averaged over all measurements and obtained the error as the quadratic sum of errors divided by the number of measurements.

7.3. Deconvolution of the PAH-features

The spatial emission profiles of our sources are a composition of continuum emission and emission from PAH molecules. Often the PAH component is found to be more extended, see for instance figure 8. To find the intrinsic extension of the PAH emission we need to first disentangle the PAH emission profile from the underlying continuum profile. A first order approximation of the composed spatial emission profile is the sum of two Gaussian distributions with different widths and heights. To isolate the spatial flux distribution of the PAH emission we first subtracted an estimated continuum profile and then analyzed the residual.

We took the 2D spectrum that we obtained for the spectral extraction (see Sect. 4.1) and did a telluric correction. The composed spatial emission profile was then measured at the wavelength of the PAH feature. The shape of the continuum profile was determined by taking the average of the two wavelength bins just next to the PAH-band. The flux in the continuum profile was established by taking the flux contribution of the PAH feature relative to the other emission components, determined in Sect. 7.1 using the VISIR spectra. At this stage we isolated the emission profile of the PAH component by simply subtracting the derived continuum-profile. Subsequently, we fitted a Gaussian to the isolated PAH profile, to obtain the FWHM. To deconvolve this result we did a quadratic subtraction of the statistical PSF just like in Sect. 7.2. For HD95881 the width of the continuum was smaller then the statistical PSF, this means the latter was an overestimate of the true PSF and so we used the continuum as the PSF.

Table 8 contains all the resulting values of our PAH size analysis. The absolute sizes in AU were obtained by multiplying with the distances as indicated in table 1. The targets CQ Tau, HD150193, 144668A, HD144432 and HD163296 were omitted because the PAH contribution in their spectra is negligible. For HD142527, HD135344B, HD169142 and HD34282 we have substituted the size of the continuum. Their PAH features have significant flux contributions and their FWHM shows no variation at the wavelengths of the PAH bands. By looking at AB Aurigae we know that PAH emission leaves a significant signature in the FWHM before it is significant in the flux levels.

The stated errors on the PAH extent were established in the following manner. In the feature the error in the continuum flux relative to the total flux is typically 1 %. We converted this to an error in the width of the PAH profile by applying numerical error propagation. The resulting error was then quadratically added to the relative measure error (see Sect. 4.2). Finally, the effect of the deconvolution taken into account by adding the error of the PSF through another numerical error propagation, which then gave the final error.

Note that this spectroscopic technique of determining the extension of the PAH emission leads to higher values compared to a similar measurement with image filters would, because we

minimized and shifted our passband to the peak of the PAH emission. Furthermore, the sources that blend forsterite and PAH emission at 11.2 μm will have a systematic under-estimation of the 11.2 PAH size, as a result of the systematic over-estimation of the feature strength (see Sect. 7.1).

8. Discussion of individual stars

CQ Tau: We did not resolve CQ Tau in the N-band and give an upper-limit of the FWHM of 40 AU. Thanks to imaging at 20.5 μm Doucet et al. (2006b) found a disk with an inclination of ~33° and an outer radius of 450 AU. This enormous size difference between 10 and 20 μm is puzzling. The fact that the 20 μm emission originates from colder dust which is thus further away from the star only contributes marginally to solving this discrepancy, unless the disk contains a gap between the dust responsible for the 10 and 20 μm emission. The size *definition* however can also lead to substantially differing results. We can think of a spatial emission profile which could by itself entirely explains the size discrepancy. Take for example the case where the profile consists of a bright spatially unresolved component and a lower intensity extended plateau. The FWHM value would then result in an unresolved source, but the outer radius would be quite large.

HD144432: We did not resolve the source in the N-band, and find a 3 σ upper-limit of FWHM < 27 AU.

HD150193A: Our measurements give FWHM < 28 AU. Also interferometric nulling at 10 μm by Liu et al. (2007) led to an upper-limit of FWHM < 12 AU. Scattered NIR light extends out to ~190 AU and deviates from axi-symmetry (Liu et al. 2003). This is remarkable because scattered light is rarely observed in group II sources (see Grady et al. 2005). With submillimeter imaging, Mannings & Sargent 1997 found a total disk mass of ~0.01 $M_\odot$.

HD100546: For this source we found a continuum size of FWHM = 46±3 AU. The PAH features are more extended than the continuum: 198 and 62 AU. The spectrum shows a very dominant silicate feature, however the FWHM(λ) plot does not display a wavelength dependence of the silicate feature. Apparently the small warm silicate grains have the same spatial distribution as the continuum emission. Our continuum size is larger than that of Liu et al. (2007), who found a FWHM of 24±3 AU at 10 μm with interferometric nulling. However, Liu et al. (2003) derived a FWHM at 11.7 μm of 30 AU and a disk inclination of 45°±15°. In order to explain the similar sizes they find at longer wavelengths they infer the presence of a large inner gap.

Another interesting finding is the difference between the VISIR, TIMMI2 and ISO spectra. The different slit sizes put a lower limit on the spatial scale of the excess PAH emission seen in the TIMMI2 spectrum and even more so in the ISO spectrum. From this we estimate the PAH emission to reach up to at least a 100 AU in diameter, which is in agreement with the sizes we find for the 8.6 and 11.2 μm PAH features. Geers et al. (2007b) looked at the 3.3 μm PAH feature and found a smaller FWHM of 0.24″±0.06″ (35 AU at 144 pc). However, they evaluated the size with respect to the continuum and did not subtract the spatial emission profile of the continuum (see Sect. 7.3). Any remaining intrinsic size difference can be attributed to the fact that the 3.3 feature is more energetic than the 8.6 band and thus emits stronger in regions with higher probability of a multi-photon excitation. At other wavelengths the object proves to be interesting as well. Bouwman et al. (2003) modeled the ISO spectrum and found a relatively large mid-IR excess and deviating dust distribution and composition. They speculate on the presence of a proto-Jupiter in the inner disk. Ardila et al. (2007) determine that the disk stretches out to 8″ (824 AU at 103 pc) with HST ACS coronagraphic imaging.

HD163296 : We resolved the continuum of this target with a 2.7 σ certainty. Therefore it is very close to being resolved. However, we provide the 3 σ upper-limit of FWHM < 24 AU. Also Liu et al. (2007) found an upper limit of FWHM < 11 AU at 10 μm with interferometric nulling. This value forms an amazing contrast to the 200 AU outer radius found at 20.5 μm by Doucet et al. (2006b) who also report a disk inclination of 60°. This size difference could be due to the definition of the measured quantity, but it could also be an indication of a disk gap (see the comments for CQ Tau). The finding of an extended disk in scattered light is unusual for a group II source (see Grady et al. 2005). Still Grady et al. (2000) observed a disk with radius of 450 AU, inclination of 60° and a dark lane at ~325 AU, which they linked to planetary disk-clearing. Furthermore, they detected a nebulosity, which appears to be a Herbig-Haro outflow. Isella et al. (2007) found a Keplerian disk from millimeter imaging with an outer radius of ~200 AU, inclination of 46° and CO emission up to 540 AU from the star, which they also consider an indication of a planet forming in the outer disk. They also find a spectral slope between 0.87 and 7 mm which reveals mm/cm-sized grains and flux-levels from which they derive a total disk mass of ~0.12 $M_\odot$.

AB Aurigae: We found a size in the continuum of AB Aurigae of FWHM = 66±10 AU. Both 8.6 and 11.2 μm PAH features are more extended than the continuum; we find 153 and 115 AU respectively. Caution is needed for the continuum size, since we have a number of reasons to doubt the measurements. First, both observations were done at high airmass. Second, the size as derived from our pre-imaging is substantially smaller than our spectroscopic result. Also the 2 settings seem inconsistent with each other. Finally, the measured calibrators give reason to assume that the PSF was larger than estimated by our statistical method. We conclude that we have probably over-estimated the absolute size of AB Aur. The PAH emission however is extended on such a scale that PSF uncertainties are less relevant. The stronger PAH flux as observed with the wider slit of Spitzer (see Fig. 6) also gives confidence that the PAH emission indeed extends out to a radius of more than ~100 AU.

Mariñas et al. (2006) looked at AB Aur with the Gemini North and found a FWHM of 17±4 AU at 11.6 μm. Liu et al. (2007) did 10 μm interferometric nulling and found a FWHM of 27±3 AU. With 21 μm imaging Pantin et al. (2005) found a resolved source of 130 AU (FWHM) and a ring of emission at 280 AU. Comparison of these sizes with a model for the thermal emission leads to the suspicion that the inner-disk is strongly evolved (see Sect. 9.2).

From SED considerations Dominik et al. (2003) have shown that the NIR excess of AB Aur is too high to solely be explained by a puffed up inner rim. Tannirkulam et al. (2008) find that part of the NIR flux stems from inside the dust-sublimation radius. They suggest dense opacity features from molecular gas as the most plausible origin of this emission. Brittain et al. (2003) found two separate concentrations of CO gas around this star between radii of ~0.5 and 50 AU. While Piétu et al. (2005) observe an inner hole of 70 AU in radius in CO-emission. Polarimetric measurements by Oppenheimer et al. (2008) reveal the presence of a disk gap at ~100 AU from the star and an apparent gas-depletion inside 130 AU.

HD179218: We didn't resolve the source in the continuum: FWHM < 75 AU. The PAH-features are resolved however and show a large difference in FWHM: ~225 and ~117 for the 8.6 and 11.2 μm features respectively. This is likely an artifact of the

method used to measure the 11.2 μm PAH strength since here its feature blends with forsterite leading to an overestimate of the PAH strength and subsequently to an under-estimate of the PAH size. Liu et al. (2007) did 10 μm interferometric nulling and found a FWHM of 20±4 AU. Van der Plas et al. (2008) found [OI]-gas in emission from 0.3 to 65 AU pointing to a flaring geometry. Based on submillimeter observations of the CO-gas, Dent et al. (2005) find an outer radius of 120±20 AU and an inclination of 40±10°.

HD142527: Our N-band spectra are unresolved, which puts a limit on the size of FWHM < 31 AU. This is in agreement with imaging at 10 μm with VISIR that we will present in a future paper (Verhoeff et al. in prep.). Nevertheless HD142527 is a very interesting object. Imaging at 18.8 and 24.5 μm by Fujiwara et al. (2006) displays bright arcs at 0.85″ from the star. They explain the observed morphology with an inclined flared disk. The SED of HD142527 is remarkable in that it has an excess IR luminosity which is almost equal to the stellar luminosity: L_E = 0.8 L_*. Dominik et al. (2003) have shown that such an excess is too large to be understood with a simple passive disk model. Furthermore, Malfait et al. (1999) have demonstrated, using fits to the ISO spectrum, that the star possesses two distinct dust populations with different temperatures and compositions. In NIR scattered light Fukagawa et al. (2006) observed a 'banana-split' structure, which consists of 2 arcs at 100-400 AU and 150-490 AU from the star.

HD142666: We did not resolve this source in the continuum and derive an upper-limit of FWHM < 22 AU. However, the PAH features are extended. We measured widths of 44 and 49 AU for the 8.6 and 11.2 μm features, therefore this emission originates from the disk. A comparison of VISIR, TIMMI2 and Spitzer spectra (figure 6) leads us to believe that the star is surrounded by PAH molecules and material responsible for the continuum emission on a scale larger than ∼100 AU (see Sect. 9.2). However, a nebula is not detected in HST scattering images (Grady et al. 2005). Hales et al. (2006) confirm this with near-IR imaging polarimetry with the UKIRT. They found no extended structure, but a degree of polarization, which at least confirms the presence of circumstellar material.

HD144668A: We didn't resolve this source and give an upper-limit of FWHM < 53 AU. This is in agreement with Liu et al. (2007), who determine its FWHM at 10 μm to be < 19 AU with interferometric nulling.

HD95881: We give an upper limit for the continuum of this source of FWHM < 26 AU. The PAH bands were resolved: 57 and 65 AU for the 8.6 and 11.2 μm bands respectively. This object was classified as a group II source, based on it's IR-SED. HST coronagraphic imaging by Grady et al. (2005) led to a non-detection, which confirms its compact dust geometry. We know however from our data and from [OI]-emission that the source contains PAH molecules and gas at an abundance that is unusually high for a group II source (see e.g. Meeus et al. 2001 and Acke et al. 2005). Self-consistent passive disk modeling, taking PAHs into account, actually predicts that dust-settling will leave PAH and gas signatures intact (see Dullemond et al. 2007). We suspect that HD95881 is in an intermediate state between a flaring and flat geometry.

HD141569: We measured a continuum FWHM size of 50±6 AU. Also the PAH-features are more extended than the continuum: 68 and 149 AU for the 8.6 and 11.2 μm respectively. Our continuum value is consistent with that of Weinberger et al. (2004), who detected the disk out to 90 AU with spatially resolved N-band spectroscopy. In any case both values are larger than what is to be expected from standard models. Of course HD141569 is not a typical disk. Based on the SED Merín et al. (2004) state that this protoplanetary disk contains a small amount of dust and is on its way to become a debris disk. In scattered light Mouillet et al. (2001) observed a geometrically thin disk with ringlike structures at 200 and 325 AU and an empty region between 125 and 175 AU. The central region ($\lesssim$17 AU) seems to be cleared of cold CO (Brittain et al. 2003). Measurements of [OI] by Acke et al. (2005) however indicate a central concentration of hot gas, which is in agreement with the smaller size we found for the more energetic one of the two measured PAH bands (i.e. the 8.6 μm band). Even though the disk is in an advanced state of evolution, gas in the inner disk regions has not yet dispersed.

HD135344B : We did not resolve the source in the N-band and give an upper-limit of FWHM < 24 AU. While at 20.5 μm Doucet et al. (2006b) observe an outer radius of 200 AU and an inclination of 45°. The large difference between the size at 10 and 20 μm is very surprising. A possible explanation is that a disk gap separates the 10 μm emission coming from the hot, inner dust rim and the 20 μm emission coming from a colder outer disk. However, the size definition could also play a role (see the comments for CQ Tau). At 20 μm the SED is rising, which means that the 20 μm flux is dominated by cold dust further out in the disk. This by itself suggests the presence of a disk gap, since otherwise a gradual decrease of flux with wavelength was expected. Brown et al. (2007) modeled the Spitzer spectrum and found an inner rim starting at 0.18 AU, a gap from 0.45 to 45 AU and a gas rich outer disk. This nicely agrees with the picture that emerges from our data. Furthermore, Grady et al. (2006) suggest the presence of a planet in the inner disk to explain the lack of shadowing of the relatively flat outer disk as perceived from the IR SED. Finally van der Plas et al. (2008) find a complex gas structure in [OI], which stretches up to 90 AU.

HD34282: We find an upper-limit to the FWHM of 180 AU. It was expected that VISIR could not resolve the source in the continuum, since it is at 400 pc. We also do not observe an increase of the extent in the PAH features, which was unforeseeable because almost all other sources with PAH emission do contain these. However, the large distance to HD34282 could be the reason we do not resolve the mid-IR emission at any wavelength.

HD100453: We resolved the continuum of this target with a 2.7 σ certainty. Therefore it is very close to being resolved. However, we provide the 3 σ upper-limit of FWHM < 29 AU. The FWHM seems to be increasing with wavelength faster than the calibrators. It is plausible that this is caused by colder dust at larger distance contributing to the emission profile. We also find that the PAH emission features are more extended than the continuum. Habart et al. (2006) looked at the 3.3 μm PAH feature and found a FWHM of 0.18″. Based on the deficit of warm dust and gas as derived from the IR-SED, Collins et al. (2007) suggest the presence of a planet in the inner-disk. Chen et al. (2006) suggest that the gravitational influence of the companion of HD100453 caused the evolved state in the inner disk.

HD169142: Our VISIR observations display a resolved source which is dominated by PAH emission. The continuum has a FWHM of 50±3 AU in the North-South direction and a FWHM of 44±4 AU with the slit in a position angle of a 110°. At the wavelengths of the PAH bands we do not find a relative increase of the spatial extent, while most other PAH sources do show such an increase. This absence can be explained if the continuum is produced by a non-thermal, optically thin, featureless component (see Sect. 9.2).

Habart et al. (2006) looked at the 3.3 μm PAH feature and measured a FWHM of 0.3″, which is again the same as our

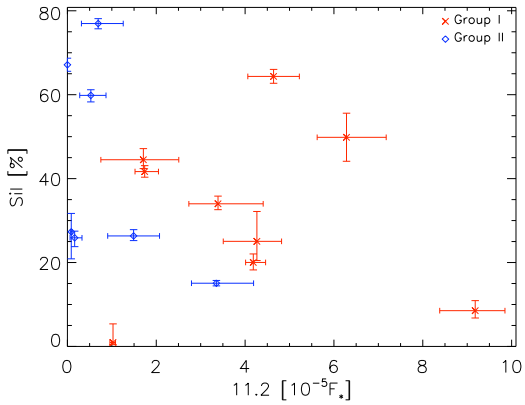

Fig. 10. The chemistry of our targets. The strength 11.2 μm PAH feature as a fraction of stellar flux is plotted on the x-axis and the silicate strength as a fraction of the local thermal emission is plotted on the y-axis.

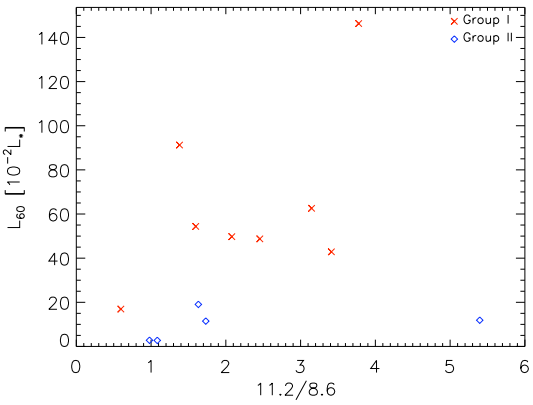

Fig. 11. The strength ratio of the 11.2 over 8.6 μm PAH features against the 60 μm excess luminosity. The diagram displays a clear difference between group I and II sources.

continuum value. Based on coronagraphic imaging Grady et al. (2007) propose a strongly evolved inner disk, which is detached from the outer disk. They suggest the presence of a planet as the most likely explanation for the observed structure. Such a central cavity may also diminish the size difference between the continuum and the PAH bands. Millimeter observations by Panić et al. (2008) display a Keplerian disk with a 13° inclination. They estimate a total disk mass of (0.6-3)·10^{-2} M$_\odot$.

HD97048: This is a group Ib source with strong emission from PAH molecules. Our measurements show a continuum size of FWHM = 72±12 AU and PAH sizes of 223 and 256 AU for the 8.6 and 11.2 μm bands respectively. We do not consider the estimate of the continuum size as reliable, since all measurements were taken at high airmass and seeing values. Also the calibrators of one of the observing nights show that we are underestimating the PSF. Furthermore, the settings vary a fair deal among each other. The calibration seems to be less of a problem for the measurement with the N-S orientation. The corresponding PAH estimate is also of such a magnitude that the PSF uncertainty should become negligible. Another problem with this source is that the spatial emission profile is quite complex and only considering the FWHM gives only limited information on the object's dimensions.

Lagage et al. (2006) and Doucet et al. (2007) took burst-mode imaging with VISIR at 8.6 and 11.3 μm and found a slightly resolved continuum and a 11.3 μm size of FWHM = 200 AU. Their modeling shows that the emission can best be explained with a flaring disk with North-South alignment and an inclination of $42.8^{+0.8}_{-2.5}$ degree and a flaring index of β = 1.26±0.05, which is in agreement with the value expected from hydrostatic, radiative equilibrium models of passive flared disks. Ignoring the continuum size, our results agree with those of Lagage et al. (2006), although the PAH size we derive is slightly larger.

Habart et al. (2006) studied the spatial extent of the continuum subtracted 3.3 μm PAH-feature and found that it originates at distances > 0.2″ away from the star. Doering et al. (2007) observed scattered light up to 720 AU from the star with HST coronagraphy.

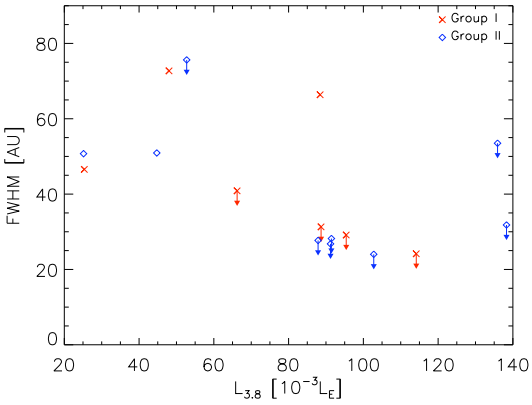

Fig. 12. The size of the continuum as a function of the 3.8 μm excess luminosity. Note that the $L_{3.8}$ is expressed as a fraction of the total excess luminosity L_E.

9. Discussion

We will now consider the correlation or trends between the spatial extent of our sample and other parameters that characterize the disk and the dust properties. For the determination of the numbers we refer to Sect. 7. We will first discuss the relation between PAH strength, the silicate strength and the SEDs. Second, we address the relation between the spatial extent of the continuum and the disk geometry. Third, we consider the relation between the spatial extent of the PAH features and their emission strength.

9.1. PAH and silicate strength

The mid-IR spectra of our sample show a wide range of PAH and silicate band strengths (see Fig. 6). We considered the silicate strength as the most characterizing parameter of our objects, which is why we displayed the sample in the order of decreasing silicate strength. In doing so a division into two groups becomes

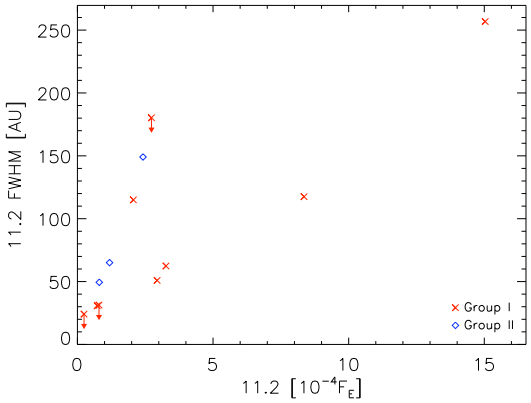

Fig. 13. The spatial extent of the 11.2 μm PAH emission as a function of its flux strength in the Spitzer/ISO spectrum. Where the feature strength is expressed as a fraction of the total infrared excess.

apparent. There are sources, which are dominated by silicates and there are sources dominated by PAH emission. We sorted the latter in order of increasing strength of the 11.2 μm PAH feature. The question then arose whether the silicate and PAH feature strengths are anti-correlated, so we plotted in Fig. 10 the silicate strength versus the 11.2 μm PAH strength as measured by Spitzer (see Sect. 7.1). We expressed the PAH strength as a fraction of the stellar flux, to represent the reprocessing power of the PAH population. The silicate feature is expressed as a fraction of the local thermal emission (feature+continuum). Figure 10 displays no trends, which indicates that all combinations of silicate and PAH strength are possible. The apparent division must thus be caused by a contrast effect, i.e. it is harder to discern the PAH features when the silicate feature is stronger.

We note that there is no relation between the 11.2 μm PAH strength and stellar luminosity, except that at high luminosity there are no strong PAH sources. Such a trend has also been found for the 3.3 μm PAH band by Habart et al. (2004). This is remarkable since the PAH strength is expected to scale with the UV-flux.

Figure 11 shows the ratio of 11.2 over the 8.6 μm PAH feature strengths as a function of L_{60}. The group II sources of our sample display a smaller 11.2/8.6 μm band ratio than group I sources. We suggest that the 8.6 μm feature is in general produced closer to the star, where there is a higher probability of multi photon capture events. The 11.2 μm feature is then naturally suppressed relative to the 8.6 μm band, because of the shadowed geometry of group II sources.

9.2. Disk sizes in the continuum

We resolved 4 out of 10 group I objects and only 1 out of 7 group II objects. The only resolved group II source is HD141569, for which we know that it is in an advanced stage of evolution, and may soon evolve to a debris disk. We note that the group I/group II classification is affected by the absence of dust near the dust sublimation temperature. Setting aside HD141569 for the moment, the size difference we found for the group I and II sources is remarkable. It cannot be explained with the differing excess luminosity at 60 μm, since that parameter shows no relation with continuum size. Modeling by Meijer (2007) predicts that there are no observable size differences at 10 μm between group I and II sources. The segregation is on the other hand in agreement with other differences found between the two groups. That is, Acke & van den Ancker (2004) found that group I sources are more likely to contain PAH emission, Acke et al. (2005) found that group I sources have stronger [OI] emission, and Grady et al. (2005) found that group I sources are more likely to be detected in scattering light imaging.

Assuming the distances of table 1 we derived FWHM sizes of our targets reaching upto FWHM~40-60 AU. This is significantly larger than the ~25 AU predicted by the passive disk model of Meijer (2007) that considers the thermal emission of small dust particles in the disk. With the exception of AB Aur and HD97048 that were observed at high airmass and seeing, we believe the continuum sizes derived above are reliable. So the question is what makes these disks appear so large? We discuss two possibilities, (i) the contribution of very small grains, and (ii) the presence of disk gaps and/or inner holes.

Very small grains. Non-thermal equilibrium emission of very small grains can contribute to the continuum at spatial scales larger than the continuum produced by the thermal equilibrium grains considered in the model of Meijer (2007). Obvious candidates are very small carbonaceous grains (Draine & Lee 1984), but in principle any material that produces a featureless continuum and that can be "super-heated" by the absorption of a single photon can be responsible. Such grains would only be heated when in direct view of the stellar radiation field (similar to the PAHs), and so their spatial signature is only expected in the group I sources, as is observed.

Disk gaps/inner holes. A lack of hot/warm dust in the inner disk regions caused by a disk gap or an inner hole will lead to the suppression of the central peak of the mid-IR emission profile. In this case, the spatial scale will be dominated by emission from regions further out, thus resulting in a larger FWHM. Note that this does not imply that the outer dimensions of these disks are different.

The 3.8 μm excess luminosity can be used to further investigate the second possibility, because it traces the amount of warm dust close to the star and as such is a measure of how centrally peaked the mid-IR emission actually is. We plotted the ratio of 3.8 μm over total excess luminosity against the continuum size in figure 12. The negative trend confirms the picture of the central peak of the emission profile setting the apparent size of the disk.

9.3. Disk sizes in PAH emission

We resolved 6 out of 10 group I objects and 3 out of 7 group II objects in the 8.6 and 11.2 μm PAH features. The size difference noted in Sect. 9.2 between group I and II sources is thus less clear when we look at PAH emission in stead of continuum emission. However, the two added group II sources that display an increase in the FWHM of the PAH bands, but are unresolved in the continuum are HD95881 and HD142666, for which we have suggested that they are in an intermediate stage between group I and group II. The FWHM size range ~30-250 AU is in agreement with the prediction made by Habart et al. (2004).

Interestingly, HD169142 shows no difference in size between the PAH bands and the adjacent continuum, while in e.g. HD97048 and HD100546 the PAH emission is more extended than the continuum. This difference in behaviour is even more remarkable considering the strength of the PAH emission bands in HD169142. This suggests a different spatial distribution between the PAHs and the continuum emitting dust grains in HD169142

compared to other stars. A possible explanation is that a substantial part of the PAH emission comes from the *inner* disk regions, while the continuum is more dominated by grains at larger distance from the star. A similar case was noted by Geers et al. (2007a), who find that the PAH emission in IRS48 originates from closer to the star than the (cold, 20 μm) continuum.

In Sect. 7.1 we determined the strength of the PAH features in the Spitzer or ISO spectra and in Sect. 7.3 we determined the continuum subtracted spatial extent (FWHM) of the PAH features with the VISIR spectra. In Fig. 13 we plotted these quantities against each other for the 11.2 μm feature. The feature strength is expressed as a fraction of the total IR-excess and the spatial extent of the feature is in units of AU (again assuming the distances from table 1). The positive trend in Fig. 13 can mean two things. Either that disk sizes are linked to the PAH abundances. Or that disks are truncated on the outside and then decrease their total 11.2 μm PAH flux. The underlying idea here is that strong PAH features are produced with large illuminated disk-surfaces. This is also consistent with the absence of sources with a high 3.8 μm excess luminosity and a high PAH strength. Also the relatively lower 11.2 over 8.6 μm band strength ratio for self-shadowed disks (see Fig. 11) can be understood in the context of this idea.

Another interesting question is how the sizes of the 8.6 and 11.2 μm PAH features compare. Recall that VISIR maps the N-band spectrum in four separate observations. This means that a comparison of the size of the different features can only be done based on the absolute errors, which are rather large because of the uncertainty in the PSF as described in Sect. 5. Nevertheless, as displayed in table 8, the extent of the 8.6 and 11.2 features does vary greatly for HD179218 and HD141569. For HD179218 we suspect it to be caused by a over-estimation of the 11.2 strength, since it blends with forsterite. For HD141569 however we think the analysis is reliable. The smaller size of the 8.6 feature was interpreted as an indication of the presence of a hot gas in the inner disk region, which is also what Acke et al. (2005) found by looking at [OI] gas.

10. Conclusions

We performed 10 μm long slit spectroscopy on 17 Herbig Ae stars with VISIR at the VLT and obtained the following results:

- We spatially resolved the emission from 9 of the stars, 6 of these were resolved in the continuum and 8 were significantly larger in the 8.6 and 11.2 μm PAH-bands than in the continuum.
- We find that group I sources are more liable to be resolved than group II sources, both in the continuum (4 out of 10 versus 0 out of 6) and in the PAH bands (6 out of 10 versus 2 out of 6).
- We performed Gaussian fits and quadratic subtraction of the PSF and found FWHM disk sizes up to ~60 AU in the continuum and up to ~250 AU in the PAH bands.
- The apparent division between silicate and PAH sources in the spectra is caused by a contrast effect, i.e. the PAH features are less apparent when the silicate feature is stronger.
- At least for the 3 sources, HD100546, HD141569, and HD169142, we found continuum sizes that are considerably larger than predicted on the basis of the thermal emission from protoplanetary disks (Meijer 2007).
- The large continuum size of HD169142 can be explained with non-thermal equilibrium emission of very small grains.
- The large continuum sizes of HD100546 and HD141569 can also be understood with the advanced evolutionary state of the inner disk resulting in the lack of a central peak of the emission profile. In other words, disks with inner cavities or gaps appear bigger.
- The latter explanation is supported by the negative trend we find between the absolute size of the continuum and the 3.8 μm excess luminosity.
- We find that group II sources display relatively more 8.6 than 11.2 μm PAH emission than do group I sources. This is understood with the 8.6 μm feature being generated closer to the star where the probability of multi-photon capture is higher.
- We find a positive trend of PAH emission strength with its spatial extent. Truncation of the irradiated PAH distribution could account for this correlation.
- The sizes we find for the continuum subtracted PAH emission profiles are in good agreement with predictions by Habart et al. (2004).

Acknowledgements. This research was sponsored by NWO under grant number C.2320.0020. It's a pleasure to thank the VISIR instrument team for ...

References

Acke, B. & van den Ancker, M. E. 2004, A&A, 426, 151
Acke, B., van den Ancker, M. E., & Dullemond, C. P. 2005, A&A, 436, 209
Ardila, D. R., Golimowski, D. A., Krist, J. E., et al. 2007, ApJ, 665, 512
Bouwman, J., de Koter, A., Dominik, C., & Waters, L. B. F. M. 2003, A&A, 401, 577
Brandl, B. R., Lenzen, R., Pantin, E., et al. 2008, in Presented at the Society of Photo-Optical Instrumentation Engineers (SPIE) Conference, Vol. 7014, Society of Photo-Optical Instrumentation Engineers (SPIE) Conference Series
Brittain, S. D., Rettig, T. W., Simon, T., et al. 2003, ApJ, 588, 535
Brown, J. M., Blake, G. A., Dullemond, C. P., et al. 2007, ApJ, 664, L107
Brown, R. A. & Burrows, C. J. 1990, Icarus, 87, 484
Chen, X. P., Henning, T., van Boekel, R., & Grady, C. A. 2006, A&A, 445, 331
Chiang, E. I. & Goldreich, P. 1997, ApJ, 490, 368
Collins, K., Grady, C., Wisniewski, J. P., et al. 2007, in American Astronomical Society Meeting Abstracts, Vol. 210, American Astronomical Society Meeting Abstracts, #87.14
Dent, W. R. F., Greaves, J. S., & Coulson, I. M. 2005, MNRAS, 359, 663
Doering, R. L., Meixner, M., Holfeltz, S. T., et al. 2007, AJ, 133, 2122
Dominik, C., Dullemond, C. P., Waters, L. B. F. M., & Walch, S. 2003, A&A, 398, 607
Doucet, C., Habart, E., Pantin, E., et al. 2007, A&A, 470, 625
Doucet, C., Lagage, P., & Pantin, E. 2006a, in Visions for Infrared Astronomy, Instrumentation, Mesure, Métrologie, ed. V. Coudé Du Foresto, D. Rouan, & G. Rousset, 25–30
Doucet, C., Pantin, E., Lagage, P. O., & Dullemond, C. P. 2006b, A&A, 460, 117
Draine, B. T. & Lee, H. M. 1984, ApJ, 285, 89
Dullemond, C. P. & Dominik, C. 2004, A&A, 417, 159
Dullemond, C. P., Dominik, C., & Natta, A. 2001, ApJ, 560, 957
Dullemond, C. P., Henning, T., Visser, R., et al. 2007, A&A, 473, 457
Fujiwara, H., Honda, M., Kataza, H., et al. 2006, ApJ, 644, L133
Fukagawa, M., Tamura, M., Itoh, Y., et al. 2006, ApJ, 636, L153
Furlan, E., Hartmann, L., Calvet, N., et al. 2006, ApJS, 165, 568
Geers, V. C., Pontoppidan, K. M., van Dishoeck, E. F., et al. 2007a, A&A, 469, L35
Geers, V. C., van Dishoeck, E. F., Visser, R., et al. 2007b, A&A, 476, 279
Grady, C. A., Devine, D., Woodgate, B., et al. 2000, ApJ, 544, 895
Grady, C. A., Schneider, G., Hamaguchi, K., et al. 2006, in Bulletin of the American Astronomical Society, Vol. 38, Bulletin of the American Astronomical Society, 1203
Grady, C. A., Schneider, G., Hamaguchi, K., et al. 2007, ApJ, 665, 1391
Grady, C. A., Woodgate, B. E., Bowers, C. W., et al. 2005, ApJ, 630, 958
Habart, E., Natta, A., & Krügel, E. 2004, A&A, 427, 179
Habart, E., Natta, A., Testi, L., & Carbillet, M. 2006, A&A, 449, 1067
Hales, A. S., Gledhill, T. M., Barlow, M. J., & Lowe, K. T. E. 2006, MNRAS, 365, 1348
Herbig, G. H. 1960, ApJS, 4, 337
Hillenbrand, L. A. 2008, ArXiv e-prints, 805

Honda, M., Kataza, H., Okamoto, Y. K., et al. 2005, in Protostars and Planets V, 8090
Horne, K. 1986, PASP, 98, 609
Isella, A., Testi, L., Natta, A., et al. 2007, A&A, 469, 213
Lagage, P.-O., Doucet, C., Pantin, E., et al. 2006, Science, 314, 621
Lagage, P. O., Pel, J. W., Authier, M., et al. 2004, The Messenger, 117, 12
Liu, W. M., Hinz, P. M., Meyer, M. R., et al. 2007, ApJ, 658, 1164
Liu, W. M., Hinz, P. M., Meyer, M. R., et al. 2003, ApJ, 598, L111
Malfait, K., Bogaert, E., & Waelkens, C. 1998, A&A, 331, 211
Malfait, K., Waelkens, C., Bouwman, J., de Koter, A., & Waters, L. B. F. M. 1999, A&A, 345, 181
Mannings, V. & Sargent, A. I. 1997, ApJ, 490, 792
Mariñas, N., Telesco, C. M., Fisher, R. S., Packham, C., & Radomski, J. T. 2006, ApJ, 653, 1353
Meeus, G., Waters, L. B. F. M., Bouwman, J., et al. 2001, A&A, 365, 476
Meijer, J. 2007, http://dare.uva.nl/en/record/259498
Merín, B., Montesinos, B., Eiroa, C., et al. 2004, A&A, 419, 301
Mouillet, D., Lagrange, A. M., Augereau, J. C., & Ménard, F. 2001, A&A, 372, L61
Natta, A., Grinin, V., & Mannings, V. 2000, Protostars and Planets IV, 559
Oppenheimer, B. R., Brenner, D., Hinkley, S., et al. 2008, ApJ, 679, 1574
Palla, F., Stahler, S. W., & Parigi, G. 1993, in Astronomical Society of the Pacific Conference Series, Vol. 40, IAU Colloq. 137: Inside the Stars, ed. W. W. Weiss & A. Baglin, 437
Panić, O., Hogerheijde, M. R., Wilner, D., & Qi, C. 2008, ArXiv e-prints, 806
Pantin, E., Bouwman, J., & Lagage, P. O. 2005, A&A, 437, 525
Pantin, E., Vanzi, L., & Weilenman, U. 2007, in 2007 ESO Instrument Calibration Workshop, ed. A. Kaufer & F. Kerber, ESO workshop Symposia, Springer-Verlag eds
Piétu, V., Guilloteau, S., & Dutrey, A. 2005, A&A, 443, 945
Sarazin, M. 2003, http://www.eso.org/gen-fac/pubs/astclim/paranal/asm/ps/spe-17410-1174-13.pdf
Sarazin, M. & Roddier, F. 1990, A&A, 227, 294
Tannirkulam, A., Monnier, J. D., Millan-Gabet, R., et al. 2008, ApJ, 677, L51
Thé, P. S., de Winter, D., & Perez, M. R. 1994, A&AS, 104, 315
van Boekel, R., Min, M., Waters, L. B. F. M., et al. 2005, A&A, 437, 189
van Boekel, R., Waters, L. B. F. M., Dominik, C., et al. 2004, A&A, 418, 177
van den Ancker, M. E., de Winter, D., & Tjin A Djie, H. R. E. 1998, A&A, 330, 145
van der Plas, G., van den Ancker, M. E., Fedele, D., et al. 2008, A&A, 485, 487
Waters, L. B. F. M. & Waelkens, C. 1998, ARA&A, 36, 233
Weinberger, A. J., Becklin, E. E., & Zuckerman, B. 2004, in Bulletin of the American Astronomical Society, Vol. 36, Bulletin of the American Astronomical Society, 1367

Table 2. Log of the science observations ordered on right ascension. The Cols. from left to right give the target name, the wavelength setting, the slit-width, the orientation of the slit (rotating from North to West), the chopper throw, the date and time, the airmass and seeing, and the integration time.

Target	Setting [μm]	Slit [$''$]	Orient. [$^\circ$]	Chop [$''$]	Date [y-m-d]	Time [h:m]	Airmass	Seeing [$''$]	Int.time [s]
ABAur	11.4	0.3	0	9	2004-12-02	05:00	1.77	1.45	1799
ABAur	8.8	1	0	10	2005-01-25	01:17	1.75	1.58	1236
HD34282	8.5	0.75	0	8	2005-12-14	05:31	1.09	0.78	828
HD34282	9.8	0.75	0	8	2005-12-14	05:51	1.12	0.84	846
HD34282	11.4	0.75	0	8	2005-12-14	06:11	1.18	0.94	862
HD34282	12.2	0.75	0	8	2005-12-14	06:40	1.26	1.02	874
CQTau	8.5	0.75	0	8	2005-12-16	03:00	1.70	1.39	496
CQTau	11.4	0.75	0	8	2005-12-16	03:13	1.65	1.32	517
CQTau	12.2	0.75	0	8	2005-12-16	03:26	1.62	1.33	524
HD95881	8.5	0.75	0	8	2005-12-17	07:04	1.64	1.02	658
HD95881	11.4	0.75	0	8	2005-12-17	07:21	1.60	0.97	513
HD95881	12.4	0.75	0	8	2005-12-17	07:33	1.58	0.99	526
HD95881	8.5	0.75	0	8	2006-04-08	23:49	1.63	1.15	162
HD95881	9.8	0.75	0	8	2006-04-08	23:53	1.62	1.25	165
HD95881	11.4	0.75	0	8	2006-04-08	23:57	1.61	1.12	168
HD95881	12.2	0.75	0	8	2006-04-09	00:02	1.60	1.13	171
HD97048	11.4	0.75	0	10	2005-01-26	07:57	1.67	1.31	517
HD97048	11.4	0.75	270	8	2005-06-17	00:18	1.76	1.52	524
HD97048	8.8	0.75	270	8	2005-06-17	00:34	1.78	1.58	517
HD97048	12.4	0.75	270	8	2005-06-17	00:54	1.81	1.44	179
HD97048	12.4	0.75	270	8	2005-06-19	00:39	1.81	1.46	538
HD100453	8.5	0.75	0	8	2005-12-17	07:54	1.31	0.80	658
HD100453	11.4	0.75	0	8	2005-12-17	08:11	1.28	0.85	513
HD100453	12.4	0.75	0	8	2005-12-17	08:23	1.26	0.82	526
HD100546	8.8	0.75	219	8	2005-03-26	02:04	1.50	1.21	341
HD100546	11.4	0.75	219	8	2005-03-26	02:14	1.49	1.16	345
HD100546	12.4	0.75	219	8	2005-03-26	02:23	1.48	1.13	354
HD135344	8.8	1	0	10	2005-03-25	08:48	1.06	1.00	529
HD135344	11.4	1	0	10	2005-03-25	09:01	1.07	0.96	538
HD135344	12.4	1	0	10	2005-03-25	09:30	1.12	0.90	543
HD135344	8.5	0.4	0	8	2007-07-10	23:33	1.06	0.58	294
HD135344	9.8	0.4	0	8	2007-07-10	23:41	1.05	0.53	322
HD135344	11.4	0.4	0	8	2007-07-10	23:48	1.04	0.55	322
HD135344	12.2	0.4	0	8	2007-07-10	23:56	1.04	0.52	331
HD141569	8.8	0.75	0	8	2005-03-28	08:24	1.07	0.65	334
HD141569	11.4	0.75	0	8	2005-03-28	08:41	1.08	0.67	513
HD141569	12.4	0.75	0	8	2005-03-28	08:55	1.10	0.70	526
HD141569	9.8	0.75	0	8	2005-03-28	09:09	1.12	0.72	513
HD141569	11.4	0.75	0	8	2005-03-28	09:22	1.14	0.71	520
HD141569	12.4	0.75	0	8	2005-03-28	09:35	1.16	0.76	534
HD141569	8.5	0.4	0	8	2007-07-11	00:38	1.08	0.64	588
HD141569	9.8	0.4	0	8	2007-07-11	00:53	1.07	0.62	483
HD141569	11.4	0.4	0	8	2007-07-11	01:34	1.07	0.66	483
HD141569	12.2	0.4	0	8	2007-07-11	01:45	1.08	0.62	496
HD142666	8.5	0.4	0	8	2007-07-11	02:26	1.04	0.61	147
HD142666	9.8	0.4	0	8	2007-07-11	02:31	1.04	0.58	161
HD142666	11.4	0.4	0	8	2007-07-11	02:35	1.05	0.60	161
HD142666	12.2	0.4	0	8	2007-07-11	02:39	1.05	0.59	165
HD142527	8.8	0.4	0	10	2005-04-28	05:50	1.05	0.82	161
HD142527	8.8	0.4	0	8	2005-04-28	05:58	1.05	0.76	644
HD142527	9.8	0.4	0	8	2005-04-28	06:13	1.05	0.76	644
HD142527	11.4	0.4	0	8	2005-04-28	07:01	1.07	0.67	644
HD142527	12.4	0.4	0	8	2005-04-28	07:17	1.09	0.67	517
HD144432	8.5	0.4	0	8	2007-07-11	03:18	1.09	0.69	147
HD144432	9.8	0.4	0	8	2007-07-11	03:22	1.10	0.69	161
HD144432	11.4	0.4	0	8	2007-07-11	03:26	1.11	0.68	161
HD144432	12.2	0.4	0	8	2007-07-11	03:31	1.12	0.67	165
HD144668	8.5	0.75	0	8	2006-04-09	04:10	1.43	1.24	162
HD144668	9.8	0.75	0	8	2006-04-09	04:15	1.41	1.07	165
HD144668	11.4	0.75	0	8	2006-04-09	04:19	1.39	1.13	168
HD144668	12.2	0.75	0	8	2006-04-09	04:24	1.37	1.05	171
HD150193	8.5	0.4	0	8	2007-07-11	04:03	1.12	0.63	147

Continued on next page...

Table 2. Continued.

Target	Setting [μm]	Slit [$''$]	Orient. [$^\circ$]	Chop [$''$]	Date [y-m-d]	Time [h:m]	Airmass	Seeing [$''$]	Int.time [s]
HD150193	9.8	0.4	0	8	2007-07-11	04:08	1.13	0.65	161
HD150193	11.4	0.4	0	8	2007-07-11	04:12	1.14	0.68	161
HD150193	12.2	0.4	0	8	2007-07-11	04:17	1.15	0.69	165
HD163296	8.5	0.4	0	8	2007-07-11	05:03	1.09	0.74	147
HD163296	9.8	0.4	0	8	2007-07-11	05:07	1.10	0.74	161
HD163296	11.4	0.4	0	8	2007-07-11	05:11	1.11	0.73	161
HD163296	12.2	0.4	0	8	2007-07-11	05:16	1.12	0.75	165
HD169142	11.4	0.75	0	8	2005-03-27	09:49	1.02	0.82	524
HD169142	8.8	0.75	0	8	2005-03-27	10:02	1.02	0.79	345
HD169142	12.4	0.75	250	8	2005-06-19	07:30	1.17	0.78	538
HD169142	11.4	0.75	250	8	2005-06-19	07:43	1.21	0.88	524
HD169142	8.8	0.75	250	8	2005-06-19	07:55	1.25	0.95	517
HD169142	8.1	0.4	0	8	2007-07-11	06:05	1.16	0.67	147
HD169142	8.5	0.4	0	8	2007-07-11	06:09	1.17	0.70	147
HD169142	9.8	0.4	0	8	2007-07-11	06:13	1.18	0.66	161
HD169142	11.4	0.4	0	8	2007-07-11	06:17	1.20	0.70	161
HD169142	12.2	0.4	0	8	2007-07-11	06:21	1.21	0.71	165
HD179218	8.8	0.4	0	8	2005-04-28	08:04	1.40	1.21	644
HD179218	9.8	0.4	0	8	2005-04-28	08:21	1.36	1.05	644
HD179218	11.4	0.4	0	8	2005-04-28	09:00	1.32	1.14	644
HD179218	12.4	0.4	0	8	2005-04-28	09:16	1.31	1.14	517

Table 3. Log of the calibration observations ordered on observation date. The Cols. from left to right give the target name, the wavelength setting, the slit-width, the orientation of the slit (rotating from North to West), the chopper throw, the date and time, the airmass and seeing, and the integration time.

Target	Setting [μm]	Slit [$''$]	Orient. [$^\circ$]	Chop [$''$]	Date [y-m-d]	Time [h:m]	Airmass	Seeing [$''$]	Obs.time [s]
HD9362	11.4	0.3	0	9	2004-12-02	05:49	1.81	1.66	341
HD59717	11.4	0.4	0	8	2004-12-02	06:39	1.07	1.35	171
HD40091	11.4	0.4	0	14	2004-12-02	08:42	1.32	1.46	870
HD82434	8.8	0.4	0	10	2005-01-23	08:20	1.20	0.99	51
HD82434	9.8	0.4	0	10	2005-01-23	08:22	1.20	0.90	56
HD82434	11.4	0.4	0	10	2005-01-23	08:25	1.21	0.87	57
HD82434	12.4	0.4	0	10	2005-01-23	08:28	1.22	0.89	60
HD9138	8.8	1	0	10	2005-01-25	00:51	1.71	1.79	529
HD59294	8.8	1	0	10	2005-01-25	02:01	1.40	1.48	677
HD100407	11.4	0.4	0	10	2005-01-25	08:26	1.02	0.71	56
HD100407	12.4	0.4	0	10	2005-01-25	08:29	1.02	0.71	54
HD113996	11.3	0.75	0	10	2005-01-26	08:34	1.67	1.38	513
HD113996	11.3	0.75	180	10	2005-01-26	08:56	1.64	1.33	108
HD113996	11.3	0.75	0	10	2005-01-26	09:07	1.63	1.32	108
HD50310	11.4	0.75	202	10	2005-01-27	02:07	1.13	0.96	172
HD102964	9.8	0.75	0	10	2005-01-28	03:44	1.73	1.42	172
HD102964	11.4	0.75	0	10	2005-01-28	03:50	1.68	1.36	168
HD136422	8.8	1	0	8	2005-03-25	09:57	1.16	1.00	353
HD136422	11.4	1	0	8	2005-03-25	10:05	1.17	1.06	179
HD136422	12.4	1	0	8	2005-03-25	10:19	1.21	1.34	181
HD91056	8.8	0.75	0	8	2005-03-26	00:37	1.42	1.01	168
HD91056	8.8	0.75	0	8	2005-03-26	00:37	1.42	1.01	172
HD91056	11.4	0.75	0	9	2005-03-26	00:59	1.38	0.88	171
HD91056	12.4	0.75	0	9	2005-03-26	01:04	1.37	0.93	175
HD73603	11.0	1	0	8	2005-03-27	02:17	1.06	0.98	176
HD73603	11.0	1	0	8	2005-03-27	02:23	1.06	0.78	176
HD73603	11.0	1	126	8	2005-03-27	02:28	1.07	0.81	176
HD73603	11.0	1	233	8	2005-03-27	04:08	1.39	1.12	176
HD169916	11.4	0.75	0	8	2005-03-27	10:20	1.01	0.86	174
HD73603	12.4	1	233	8	2005-03-28	00:04	1.03	0.68	175
HD73603	12.4	1	233	8	2005-03-28	00:50	1.00	0.52	347
HD73603	8.8	1	233	8	2005-03-28	01:02	1.00	0.53	333
HD73603	9.8	1	233	8	2005-03-28	03:47	1.32	0.99	333
HD73603	12.4	1	233	8	2005-03-28	03:58	1.37	1.06	347
HD73603	8.8	1	233	8	2005-03-28	04:08	1.42	1.07	333
HD152880	8.8	0.75	0	8	2005-03-28	10:03	1.04	0.69	217
HD152880	11.4	0.75	0	8	2005-03-28	10:13	1.05	0.77	224
HD73603	8.8	1	270	8	2005-03-29	00:28	1.01	0.95	341
HD73603	8.8	1	270	8	2005-03-29	00:28	1.01	0.95	345
HD73603	9.8	1	270	8	2005-03-29	00:37	1.00	0.88	341
HD73603	9.8	1	270	8	2005-03-29	00:37	1.00	0.88	345
HD73603	11.0	1	270	8	2005-03-29	00:46	1.00	0.89	345
HD73603	11.0	1	270	8	2005-03-29	00:46	1.00	0.89	349
HD73603	12.4	1	270	8	2005-03-29	00:55	1.00	0.93	175
HD73603	12.4	1	270	8	2005-03-29	00:55	1.00	0.96	358
HD73603	8.8	1	270	8	2005-03-29	03:54	1.37	1.16	345
HD73603	9.8	1	270	8	2005-03-29	04:04	1.42	1.21	345
HD73603	11.0	1	270	8	2005-03-29	04:13	1.47	1.12	349
HD73603	12.4	1	270	8	2005-03-29	04:22	1.53	1.03	358
HD92682	11.4	0.75	270	8	2005-06-16	23:56	1.66	1.59	174
HD92682	8.8	0.75	270	8	2005-06-17	00:01	1.67	1.62	172
HD105340	11.4	0.75	0	8	2005-06-17	01:11	1.67	1.59	174
HD105340	8.8	0.75	0	8	2005-06-17	01:17	1.68	1.54	172
HIP90185	12.4	0.75	0	8	2005-06-19	01:04	1.68	1.14	534
HD177716	12.4	0.75	0	8	2005-06-19	08:16	1.18	0.79	175
HD177716	11.4	0.75	0	8	2005-06-19	08:22	1.19	0.84	171
HD177716	8.8	0.75	0	8	2005-06-19	08:26	1.21	0.86	168
HD2261	8.8	0.75	0	8	2005-06-29	07:48	1.28	0.94	169
HD2261	9.8	0.75	0	8	2005-06-29	07:53	1.26	0.96	169
HD2261	11.4	0.75	0	8	2005-06-29	07:58	1.25	0.94	172
HD2261	12.4	0.75	0	8	2005-06-29	08:03	1.24	0.94	176
HD211416	8.8	0.75	0	8	2005-06-29	10:35	1.34	0.90	110

Continued on next page...

Table 3. Continued.

Target	Setting [μm]	Slit [$''$]	Orient. [°]	Chop [$''$]	Date [y-m-d]	Time [h:m]	Airmass	Seeing [$''$]	Obs.time [s]
HD211416	9.8	0.75	0	8	2005-06-29	10:39	1.35	0.90	110
HD211416	11.4	0.75	0	8	2005-06-29	10:42	1.35	0.94	112
HD211416	12.4	0.75	0	8	2005-06-29	10:46	1.36	1.06	115
HD123139	8.8	0.75	0	8	2005-06-30	02:05	1.12	0.95	29
HD123139	9.8	0.75	0	8	2005-06-30	02:07	1.12	0.87	29
HD123139	11.4	0.75	0	8	2005-06-30	02:08	1.12	0.92	30
HD123139	12.4	0.75	0	8	2005-06-30	02:11	1.13	0.85	30
HD198542	8.8	1	0	8	2005-07-02	04:58	1.10	1.05	172
HD198542	11.4	1	0	8	2005-07-02	05:03	1.09	1.02	174
HD1522	11.4	1	0	8	2005-07-02	06:40	1.69	1.57	174
HD187642	8.5	0.4	0	8	2005-11-18	00:34	1.37	1.21	144
HD187642	9.8	0.4	0	8	2005-11-18	00:39	1.39	1.17	157
HD187642	11.4	0.4	0	8	2005-11-18	00:44	1.40	1.19	157
HD187642	12.2	0.4	0	8	2005-11-18	00:48	1.42	1.09	162
HD1255	8.5	0.4	0	8	2005-11-18	02:15	1.28	1.08	144
HD1255	9.8	0.4	0	8	2005-11-18	02:20	1.29	1.00	157
HD1255	11.4	0.4	0	8	2005-11-18	02:35	1.33	1.11	157
HD1255	12.2	0.4	0	8	2005-11-18	02:40	1.34	1.14	162
HD39425	8.5	0.4	0	8	2005-11-18	04:05	1.22	0.94	144
HD39425	9.8	0.4	0	8	2005-11-18	04:10	1.21	0.79	157
HD39425	9.8	0.4	0	8	2005-11-18	04:10	1.21	0.79	157
HD39425	11.4	0.4	0	8	2005-11-18	04:22	1.18	0.73	157
HD39425	11.4	0.4	0	8	2005-11-18	04:22	1.18	0.73	157
HD39425	12.2	0.4	0	8	2005-11-18	04:27	1.16	0.75	162
HD39425	12.2	0.4	0	8	2005-11-18	04:27	1.16	0.75	162
HIP109268	8.5	0.75	0	8	2005-11-19	00:59	1.20	1.19	165
HIP109268	11.4	0.75	0	8	2005-11-19	01:04	1.21	1.26	172
HIP109268	12.2	0.75	0	8	2005-11-19	01:09	1.22	1.33	174
HIP21281	8.5	0.75	0	8	2005-11-19	03:11	1.28	1.01	165
HIP21281	12.2	0.75	0	8	2005-11-19	03:21	1.26	0.94	174
HIP109268	8.5	0.75	0	8	2005-11-20	00:59	1.20	1.08	165
HIP109268	11.4	0.75	0	8	2005-11-20	01:04	1.21	1.13	172
HIP109268	12.2	0.75	0	8	2005-11-20	01:09	1.22	1.10	174
HD11353	8.5	0.75	0	8	2005-11-20	03:51	1.09	0.82	165
HD11353	11.4	0.75	0	8	2005-11-20	03:56	1.10	0.93	172
HD11353	12.2	0.75	0	8	2005-11-20	04:01	1.10	0.99	174
HIP109268	8.5	0.75	0	8	2005-11-21	00:23	1.15	1.10	165
HIP109268	11.4	0.75	0	8	2005-11-21	00:42	1.18	1.06	172
HIP109268	12.2	0.75	0	8	2005-11-21	00:47	1.19	1.06	174
HD2261	8.5	0.75	0	8	2005-11-21	02:40	1.12	1.20	108
HD2261	11.4	0.75	0	8	2005-11-21	02:44	1.12	1.10	112
HD2261	12.2	0.75	0	8	2005-11-21	02:47	1.13	1.11	114
HD30080	8.5	1	0	8	2005-12-14	03:26	1.05	0.86	165
HD30080	11.4	1	0	8	2005-12-14	03:32	1.06	0.83	171
HD30080	12.2	1	0	8	2005-12-14	03:50	1.07	0.78	172
HD35536	8.5	0.75	0	8	2005-12-14	07:09	1.30	1.07	165
HD35536	9.8	0.75	0	8	2005-12-14	07:15	1.33	1.04	169
HD35536	11.4	0.75	0	8	2005-12-14	07:23	1.36	1.05	172
HD35536	12.2	0.75	0	8	2005-12-14	07:27	1.39	1.11	174
HD22663	8.5	1	212	10	2005-12-15	03:24	1.05	0.77	169
HD22663	11.4	1	212	10	2005-12-15	03:29	1.06	0.83	174
HD13596	8.5	0.75	0	8	2005-12-16	03:49	1.75	1.55	165
HD13596	11.4	0.75	0	8	2005-12-16	03:54	1.79	1.53	172
HD13596	12.2	0.75	0	8	2005-12-16	03:59	1.83	1.49	174
HD30080	8.5	0.75	0	8	2005-12-17	06:36	1.03	0.71	162
HD102964	8.5	0.75	0	8	2005-12-17	08:42	1.18	0.72	162
HD102964	11.4	0.75	0	8	2005-12-17	08:47	1.17	0.78	168
HD102964	12.4	0.75	0	8	2005-12-17	08:53	1.16	0.76	172
HD71701	8.5	0.75	0	8	2005-12-17	09:06	1.72	1.73	162
HD71701	11.4	0.75	0	8	2005-12-17	09:10	1.72	2.17	168
HD71701	12.4	0.75	0	8	2005-12-17	09:15	1.73	1.76	172
HD82668	8.5	0.75	0	8	2006-03-18	00:44	1.26	1.36	60
HD82668	8.5	0.75	0	8	2006-03-18	01:31	1.21	1.02	60
HD82668	9.8	0.75	0	8	2006-03-18	01:34	1.20	1.05	61

Continued on next page...

Table 3. Continued.

Target	Setting [μm]	Slit [″]	Orient. [°]	Chop [″]	Date [y-m-d]	Time [h:m]	Airmass	Seeing [″]	Obs.time [s]
HD82668	11.4	0.75	0	8	2006-03-18	01:36	1.20	1.03	62
HD82668	12.2	0.75	0	8	2006-03-18	01:39	1.20	0.98	62
HD92305	8.5	0.75	0	8	2006-03-18	03:08	1.70	1.24	57
HD92305	9.8	0.75	0	8	2006-03-18	03:11	1.70	1.28	58
HD92305	11.4	0.75	0	8	2006-03-18	03:13	1.70	1.22	60
HD92305	12.2	0.75	0	8	2006-03-18	03:16	1.70	1.15	60
HD92305	8.5	0.75	0	8	2006-03-18	04:30	1.71	1.27	57
HD92305	8.5	0.75	0	8	2006-03-18	04:30	1.71	1.27	57
HD92305	9.8	0.75	0	8	2006-03-18	04:33	1.72	1.31	58
HD92305	9.8	0.75	0	8	2006-03-18	04:33	1.72	1.31	58
HD92305	11.4	0.75	0	8	2006-03-18	04:35	1.72	1.31	60
HD92305	11.4	0.75	0	8	2006-03-18	04:35	1.72	1.31	60
HD92305	12.2	0.75	0	8	2006-03-18	04:38	1.72	1.25	60
HD92305	12.2	0.75	0	8	2006-03-18	04:38	1.72	1.25	60
HD123139	8.5	0.75	0	8	2006-03-18	05:54	1.06	0.66	57
HD123139	8.5	0.75	0	8	2006-03-18	05:54	1.06	0.66	57
HD123139	9.8	0.75	0	8	2006-03-18	05:57	1.06	0.66	58
HD123139	9.8	0.75	0	8	2006-03-18	05:57	1.06	0.66	58
HD123139	11.4	0.75	0	8	2006-03-18	05:59	1.05	0.63	60
HD123139	11.4	0.75	0	8	2006-03-18	05:59	1.05	0.63	60
HD123139	12.2	0.75	0	8	2006-03-18	06:02	1.05	0.63	60
HD123139	12.2	0.75	0	8	2006-03-18	06:02	1.05	0.63	60
HD146051	8.5	0.75	0	8	2006-03-18	07:58	1.12	1.00	57
HD146051	8.5	0.75	0	8	2006-03-18	07:58	1.12	1.00	57
HD146051	9.8	0.75	0	8	2006-03-18	08:01	1.12	1.05	58
HD146051	11.4	0.75	0	8	2006-03-18	08:04	1.12	0.95	60
HD146051	12.2	0.75	0	8	2006-03-18	08:07	1.11	0.99	60
HD80007	11.4	0.75	0	8	2006-03-19	03:33	1.46	1.02	60
HD80007	11.4	0.75	0	8	2006-03-19	03:33	1.46	1.02	60
HD80007	8.5	0.75	0	8	2006-03-19	03:36	1.46	1.02	57
HD80007	8.5	0.75	0	8	2006-03-19	03:36	1.46	1.02	57
HD146791	8.5	0.75	0	8	2006-03-19	05:34	1.78	1.29	58
HD146791	8.5	0.75	0	8	2006-03-19	05:34	1.78	1.29	58
HD146791	9.8	0.75	0	8	2006-03-19	05:36	1.75	1.36	60
HD146791	9.8	0.75	0	8	2006-03-19	05:36	1.75	1.36	60
HD146791	11.4	0.75	0	8	2006-03-19	05:39	1.73	1.30	60
HD146791	11.4	0.75	0	8	2006-03-19	05:39	1.73	1.30	60
HD146791	12.2	0.75	0	8	2006-03-19	05:42	1.70	1.40	61
HD146791	12.2	0.75	0	8	2006-03-19	05:42	1.70	1.40	61
HD146791	8.5	0.75	0	8	2006-03-19	07:53	1.13	0.88	57
HD146791	8.5	0.75	0	8	2006-03-19	07:53	1.13	0.88	57
HD146791	9.8	0.75	0	8	2006-03-19	07:55	1.12	0.90	58
HD146791	9.8	0.75	0	8	2006-03-19	07:55	1.12	0.90	58
HD146791	11.4	0.75	0	8	2006-03-19	07:58	1.12	0.91	60
HD146791	11.4	0.75	0	8	2006-03-19	07:58	1.12	0.91	60
HD146791	12.2	0.75	0	8	2006-03-19	08:00	1.11	0.92	60
HD82308	12.2	0.75	0	8	2006-03-21	01:19	1.54	1.06	174
HD82308	12.2	0.75	0	8	2006-03-21	01:19	1.54	1.06	174
HD82308	9.8	0.75	0	8	2006-03-21	01:24	1.53	1.01	169
HD82308	9.8	0.75	0	8	2006-03-21	01:24	1.53	1.01	169
HD75691	9.8	0.75	0	8	2006-03-21	01:43	1.00	0.61	169
HD75691	9.8	0.75	0	8	2006-03-21	01:43	1.00	0.61	169
HD75691	11.4	0.75	0	8	2006-03-21	01:47	1.00	0.58	172
HD75691	11.4	0.75	0	8	2006-03-21	01:47	1.00	0.58	172
HD75691	12.2	0.75	0	8	2006-03-21	01:52	1.00	0.66	174
HD75691	12.2	0.75	0	8	2006-03-21	01:52	1.00	0.66	174
HD102461	11.4	1	0	8	2006-03-21	02:05	1.35	0.80	60
HD102461	11.4	1	0	8	2006-03-21	02:05	1.35	0.80	60
HD102461	12.2	1	0	8	2006-03-21	02:08	1.35	0.81	61
HD102461	12.2	1	0	8	2006-03-21	02:08	1.35	0.81	61
HD102461	8.5	1	0	8	2006-03-21	03:26	1.22	0.81	58
HD102461	8.5	1	0	8	2006-03-21	03:26	1.22	0.81	58
HD102461	9.8	1	0	8	2006-03-21	03:29	1.22	0.79	60
HD102461	9.8	1	0	8	2006-03-21	03:29	1.22	0.79	60

Continued on next page...

Table 3. Continued.

Target	Setting [μm]	Slit [$''$]	Orient. [$^\circ$]	Chop [$''$]	Date [y-m-d]	Time [h:m]	Airmass	Seeing [$''$]	Obs.time [s]
HD102461	11.4	1	0	8	2006-03-21	03:32	1.22	0.87	60
HD102461	12.2	1	0	8	2006-03-21	03:35	1.22	0.92	61
HD102461	8.5	1	0	8	2006-03-21	04:40	1.19	0.70	58
HD102461	9.8	1	0	8	2006-03-21	04:43	1.19	0.66	60
HD136422	8.5	0.75	0	8	2006-03-21	05:00	1.34	0.92	57
HD136422	9.8	0.75	0	8	2006-03-21	05:02	1.33	0.91	58
HD136422	11.4	0.75	0	8	2006-03-21	05:06	1.31	0.79	60
HD136422	12.2	0.75	0	8	2006-03-21	05:09	1.30	0.86	60
HD136422	11.4	0.75	0	8	2006-03-21	05:12	1.29	0.80	60
HD136422	9.8	0.75	0	8	2006-03-21	05:15	1.28	0.85	58
HD136422	8.5	0.75	0	8	2006-03-21	05:17	1.27	0.87	57
HD136422	8.5	0.75	0	8	2006-03-21	06:09	1.13	0.88	28
HD136422	9.8	0.75	0	8	2006-03-21	06:11	1.13	0.82	29
HD136422	11.4	0.75	0	8	2006-03-21	06:13	1.12	0.83	30
HD136422	11.4	0.75	0	8	2006-03-21	06:26	1.10	0.88	30
HD136422	11.4	0.75	0	8	2006-03-21	06:33	1.09	0.98	30
HD136422	11.4	0.75	0	8	2006-03-21	06:39	1.08	0.90	30
HD136422	11.4	0.75	0	8	2006-03-21	06:45	1.07	0.82	30
HD157999	8.5	1	0	8	2006-03-21	08:27	1.28	0.90	58
HD157999	9.8	1	0	8	2006-03-21	08:29	1.27	0.84	60
HD157999	11.4	1	0	8	2006-03-21	08:32	1.26	0.83	60
HD157999	12.2	1	0	8	2006-03-21	08:34	1.26	0.79	61
HD168723	8.5	1	0	8	2006-03-21	09:50	1.14	0.66	58
HD168723	9.8	1	0	8	2006-03-21	09:52	1.13	0.64	60
HD168723	11.4	1	0	8	2006-03-21	09:55	1.13	0.57	60
HD168723	12.2	1	0	8	2006-03-21	09:57	1.13	0.57	61
HD91056	8.5	0.75	0	8	2006-04-08	23:33	1.44	0.91	25
HD91056	9.8	0.75	0	8	2006-04-08	23:35	1.44	0.96	25
HD91056	11.4	0.75	0	8	2006-04-08	23:37	1.44	0.98	26
HD91056	12.2	0.75	0	8	2006-04-08	23:39	1.43	0.97	26
HD75691	8.5	0.75	0	8	2006-04-09	00:15	1.00	0.70	162
HD75691	9.8	0.75	0	8	2006-04-09	00:20	1.00	0.82	165
HD75691	11.4	0.75	0	8	2006-04-09	00:24	1.00	0.80	168
HD75691	12.2	0.75	0	8	2006-04-09	00:29	1.00	0.77	171
HD123139	8.8	0.75	0	8	2006-04-09	01:49	1.54	1.21	165
HD149447	8.5	0.75	0	8	2006-04-09	04:35	1.46	1.12	25
HD149447	9.8	0.75	0	8	2006-04-09	04:37	1.45	1.16	25
HD149447	11.4	0.75	0	8	2006-04-09	04:39	1.44	1.14	26
HD149447	12.2	0.75	0	8	2006-04-09	04:41	1.43	1.08	26
HD178345	8.8	1	0	8	2006-06-20	06:18	1.04	0.88	168
HD178345	8.8	1	0	8	2006-06-20	06:18	1.04	0.88	172
HD178345	11.4	1	0	8	2006-06-20	06:27	1.04	0.85	171
HD178345	11.4	1	0	8	2006-06-20	06:27	1.04	0.85	174
HD178345	12.2	1	0	8	2006-06-20	06:32	1.04	0.82	172
HD178345	12.2	1	0	8	2006-06-20	06:32	1.04	0.82	176
HD178345	8.8	1	0	8	2006-06-20	07:54	1.14	0.76	168
HD178345	8.8	1	0	8	2006-06-20	07:54	1.14	0.76	172
HD178345	9.8	1	0	8	2006-06-20	07:59	1.15	0.78	168
HD178345	9.8	1	0	8	2006-06-20	07:59	1.15	0.78	172
HD178345	11.4	1	0	8	2006-06-20	08:03	1.16	0.76	171
HD178345	11.4	1	0	8	2006-06-20	08:03	1.16	0.76	174
HD178345	12.2	1	0	8	2006-06-20	08:07	1.17	0.80	172
HD178345	12.2	1	0	8	2006-06-20	08:07	1.17	0.80	176
HD6805	8.5	1	0	8	2006-06-22	08:56	1.36	1.04	165
HD6805	11.4	1	0	8	2006-06-22	09:02	1.33	1.00	171
HD6805	12.4	1	0	8	2006-06-22	09:08	1.31	0.94	175
HD6805	8.5	1	0	8	2006-06-22	10:48	1.06	0.77	165
HD6805	11.4	1	0	8	2006-06-22	10:53	1.06	0.71	171
HD6805	12.4	1	0	8	2006-06-22	10:58	1.05	0.72	175
HD6805	8.5	1	0	8	2006-06-23	07:40	1.94	1.51	169
HD6805	11.4	1	0	8	2006-06-23	07:45	1.88	1.35	174
HD6805	12.2	1	0	8	2006-06-23	07:50	1.83	1.41	176
HD6805	8.5	1	0	8	2006-06-23	09:41	1.18	1.07	165
HD6805	8.5	1	0	8	2006-06-23	09:41	1.18	1.07	169

Continued on next page...

Table 3. Continued.

Target	Setting [μm]	Slit [″]	Orient. [°]	Chop [″]	Date [y-m-d]	Time [h:m]	Airmass	Seeing [″]	Obs.time [s]
HD6805	11.4	1	0	8	2006-06-23	09:45	1.17	1.16	171
HD6805	11.4	1	0	8	2006-06-23	09:45	1.17	1.16	174
HD6805	12.2	1	0	8	2006-06-23	09:50	1.16	1.09	172
HD6805	12.2	1	0	8	2006-06-23	09:50	1.16	1.09	176
HD32887	8.5	0.4	0	8	2007-01-06	05:18	1.22	0.94	67
HD32887	9.8	0.4	0	8	2007-01-06	05:21	1.23	1.00	73
HD32887	11.4	0.4	0	8	2007-01-06	05:23	1.25	0.96	73
HD32887	12.2	0.4	0	8	2007-01-06	05:27	1.26	0.93	75
HD42995	8.5	0.4	0	8	2007-01-06	06:24	1.97	1.37	67
HD42995	9.8	0.4	0	8	2007-01-06	06:26	2.00	1.40	73
HD42995	11.4	0.4	0	8	2007-01-06	06:29	2.02	1.45	73
HD42995	12.2	0.4	0	8	2007-01-06	06:32	2.05	1.53	75
HD48915	8.5	0.4	0	8	2007-01-06	06:51	1.22	1.13	67
HD48915	9.8	0.4	0	8	2007-01-06	06:54	1.23	1.12	73
HD48915	11.4	0.4	0	8	2007-01-06	06:56	1.24	1.10	73
HD48915	12.2	0.4	0	8	2007-01-06	06:59	1.25	1.32	75
HD48915	8.5	0.4	0	8	2007-01-06	08:08	1.66	1.64	67
HD48915	9.8	0.4	0	8	2007-01-06	08:11	1.68	1.60	73
HD48915	11.4	0.4	0	8	2007-01-06	08:14	1.71	1.63	73
HD48915	12.2	0.4	0	8	2007-01-06	08:17	1.73	1.63	75
HD42995	8.5	0.4	0	8	2007-01-08	05:12	1.61	0.88	75
HD42995	9.8	0.4	0	8	2007-01-08	05:15	1.62	0.89	77
HD42995	11.4	0.4	0	8	2007-01-08	05:18	1.63	0.90	77
HD42995	12.2	0.4	0	8	2007-01-08	05:21	1.64	0.88	78
HD32887	8.5	0.4	0	8	2007-01-08	05:52	1.41	0.79	67
HD32887	9.8	0.4	0	8	2007-01-08	05:55	1.42	0.83	73
HD32887	11.4	0.4	0	8	2007-01-08	05:57	1.44	0.80	73
HD32887	12.2	0.4	0	8	2007-01-08	06:01	1.46	0.85	75
HD136422	8.5	0.4	0	8	2007-07-10	23:11	1.09	0.59	70
HD136422	9.8	0.4	0	8	2007-07-10	23:13	1.09	0.61	77
HD136422	11.4	0.4	0	8	2007-07-10	23:16	1.08	0.57	77
HD136422	8.5	0.4	0	8	2007-07-11	00:17	1.03	0.50	70
HD136422	9.8	0.4	0	8	2007-07-11	00:20	1.03	0.51	77
HD136422	11.4	0.4	0	8	2007-07-11	00:22	1.03	0.51	77
HD146051	8.5	0.4	0	8	2007-07-11	01:11	1.08	0.62	70
HD146051	9.8	0.4	0	8	2007-07-11	01:14	1.08	0.61	77
HD146051	11.4	0.4	0	8	2007-07-11	01:17	1.08	0.62	77
HD146051	12.2	0.4	0	8	2007-07-11	01:19	1.07	0.59	79
HD146051	8.5	0.4	0	8	2007-07-11	02:06	1.08	0.56	70
HD146051	9.8	0.4	0	8	2007-07-11	02:08	1.08	0.54	77
HD146051	11.4	0.4	0	8	2007-07-11	02:11	1.08	0.55	77
HD146051	12.2	0.4	0	8	2007-07-11	02:14	1.08	0.55	79
HD152786	8.5	0.4	0	8	2007-07-11	02:59	1.18	1.15	70
HD152786	9.8	0.4	0	8	2007-07-11	03:01	1.18	1.15	77
HD152786	11.4	0.4	0	8	2007-07-11	03:04	1.18	1.07	77
HD152786	12.2	0.4	0	8	2007-07-11	03:07	1.18	1.14	79
HD167618	8.5	0.4	0	8	2007-07-11	03:44	1.02	0.61	70
HD167618	9.8	0.4	0	8	2007-07-11	03:46	1.02	0.61	77
HD186791	8.5	0.4	0	8	2007-07-11	04:37	1.24	0.89	70
HD186791	9.8	0.4	0	8	2007-07-11	04:39	1.24	0.85	77
HD186791	11.4	0.4	0	8	2007-07-11	04:42	1.24	0.86	77
HD186791	12.2	0.4	0	8	2007-07-11	04:45	1.23	0.78	79
HD167618	8.1	0.4	0	8	2007-07-11	05:29	1.11	0.76	70
HD167618	8.5	0.4	0	8	2007-07-11	05:31	1.11	0.83	70
HD167618	9.8	0.4	0	8	2007-07-11	05:34	1.12	0.78	77
HD167618	11.4	0.4	0	8	2007-07-11	05:36	1.12	0.72	77
HD167618	12.2	0.4	0	8	2007-07-11	05:39	1.13	0.76	79
HD168454	8.1	0.4	0	8	2007-07-11	06:35	1.26	0.83	70
HD168454	8.5	0.4	0	8	2007-07-11	06:37	1.27	0.83	70
HD168454	9.8	0.4	0	8	2007-07-11	06:40	1.28	0.80	77
HD168454	11.4	0.4	0	8	2007-07-11	06:42	1.29	0.79	77
HD168454	12.2	0.4	0	8	2007-07-11	06:45	1.30	0.81	79
HD140573	8.5	0.4	0	8	2007-07-30	00:11	1.17	1.24	67
HD140573	9.8	0.4	0	8	2007-07-30	00:13	1.17	1.19	73

Continued on next page...

Table 3. Continued.

Target	Setting [μm]	Slit [$''$]	Orient. [°]	Chop [$''$]	Date [y-m-d]	Time [h:m]	Airmass	Seeing [$''$]	Obs.time [s]
HD140573	11.4	0.4	0	8	2007-07-30	00:16	1.17	1.11	73
HD140573	12.2	0.4	0	8	2007-07-30	00:19	1.17	1.33	75
HD140573	8.5	0.4	0	8	2007-07-30	01:35	1.29	1.12	67
HD140573	9.8	0.4	0	8	2007-07-30	01:37	1.30	2.25	73
HD140573	11.4	0.4	0	8	2007-07-30	01:40	1.31	1.96	73
HD139127	8.5	0.4	0	8	2007-07-30	02:24	1.25	1.40	144
HD139127	9.8	0.4	0	8	2007-07-30	02:28	1.26	1.55	157
HD139127	11.4	0.4	0	8	2007-07-30	02:33	1.27	1.47	157
HD139127	12.2	0.4	0	8	2007-07-30	02:37	1.29	1.46	162
HD178345	8.8	1	0	8	2007-08-30	01:08	1.03	0.76	172
HD178345	9.8	1	0	8	2007-08-30	01:12	1.03	0.72	172
HD178345	11.4	1	0	8	2007-08-30	01:16	1.03	0.67	174
HD178345	12.2	1	0	8	2007-08-30	01:21	1.03	0.70	176
HD178345	8.8	1	0	8	2007-08-30	02:37	1.08	0.71	172
HD178345	9.8	1	0	8	2007-08-30	02:41	1.08	0.69	172
HD178345	11.4	1	0	8	2007-08-30	02:45	1.09	0.70	174
HD178345	12.2	1	0	8	2007-08-30	02:50	1.10	0.68	176
HD218670	12.4	1	0	8	2007-08-30	04:08	1.10	0.80	179
HD218670	11.4	1	0	8	2007-08-30	04:13	1.10	0.76	174
HD218670	8.8	1	0	8	2007-08-30	04:17	1.09	0.71	172
HD218670	9.8	1	0	8	2007-08-30	04:22	1.09	0.77	172
HD218670	12.4	1	0	8	2007-08-30	05:21	1.07	0.83	179
HD218670	11.4	1	0	8	2007-08-30	05:26	1.07	0.86	174
HD218670	8.8	1	0	8	2007-08-30	05:30	1.07	0.83	172
HD218670	9.8	1	0	8	2007-08-30	05:35	1.07	0.84	172
HD218670	12.4	1	0	8	2007-08-30	06:41	1.12	0.81	179
HD218670	11.4	1	0	8	2007-08-30	06:46	1.12	0.81	174
HD218670	8.8	1	0	8	2007-08-30	06:50	1.13	0.89	172
HD218670	9.8	1	0	8	2007-08-30	06:54	1.14	1.13	172
HD218670	9.8	1	0	8	2007-08-30	09:37	1.76	1.09	172
HD167618	8.5	0.4	0	8	2007-09-10	00:09	1.03	0.74	67
HD167618	9.8	0.4	0	8	2007-09-10	00:12	1.03	0.71	73
HD167618	11.4	0.4	0	8	2007-09-10	00:15	1.03	0.69	73
HD167618	12.2	0.4	0	8	2007-09-10	00:18	1.03	0.67	75
HD167618	8.5	0.4	0	8	2007-09-10	01:40	1.13	0.72	67
HD167618	9.8	0.4	0	8	2007-09-10	01:43	1.14	0.71	73
HD167618	11.4	0.4	0	8	2007-09-10	01:46	1.14	0.70	73
HD167618	12.2	0.4	0	8	2007-09-10	01:49	1.15	0.78	75
HD200914	8.5	0.4	0	8	2007-09-10	02:04	1.01	0.56	144
HD200914	9.8	0.4	0	8	2007-09-10	02:09	1.00	0.57	157
HD200914	11.4	0.4	0	8	2007-09-10	02:13	1.00	0.54	157
HD200914	12.2	0.4	0	8	2007-09-10	02:18	1.00	0.57	162
HD169916	11.4	0.4	0	8	2007-09-10	23:28	1.00	0.86	157
HD169916	12.2	0.4	0	8	2007-09-10	23:33	1.00	0.82	162
HD167618	8.5	0.4	0	8	2007-09-10	23:50	1.02	0.60	67
HD167618	9.8	0.4	0	8	2007-09-10	23:53	1.02	0.42	73
HD167618	11.4	0.4	0	8	2007-09-10	23:56	1.02	0.40	73
HD167618	12.2	0.4	0	8	2007-09-10	23:59	1.03	0.62	75
HD168454	8.5	0.4	0	8	2007-09-11	01:09	1.06	0.88	67
HD168454	9.8	0.4	0	8	2007-09-11	01:12	1.07	0.83	73
HD168454	11.4	0.4	0	8	2007-09-11	01:15	1.07	0.89	73
HD168454	12.2	0.4	0	8	2007-09-11	01:18	1.08	0.79	75
HD177716	11.4	0.4	0	8	2007-09-11	23:31	1.02	0.57	157
HD177716	12.2	0.4	0	8	2007-09-11	23:35	1.02	0.60	162
HD167618	8.5	0.4	0	8	2007-09-11	23:52	1.02	0.67	67
HD167618	9.8	0.4	0	8	2007-09-11	23:55	1.03	0.61	73
HD167618	11.4	0.4	0	8	2007-09-11	23:58	1.03	0.62	73
HD167618	12.2	0.4	0	8	2007-09-12	00:01	1.03	0.64	75
HD168454	8.5	0.4	0	8	2007-09-12	00:56	1.05	0.87	67
HD168454	9.8	0.4	0	8	2007-09-12	00:59	1.05	0.87	73
HD168454	11.4	0.4	0	8	2007-09-12	01:02	1.06	0.79	73
HD168454	12.2	0.4	0	8	2007-09-12	01:06	1.06	0.85	75
HD165135	8.5	0.4	0	8	2007-09-13	00:17	1.03	0.73	67
HD165135	9.8	0.4	0	8	2007-09-13	00:20	1.03	0.71	73

Continued on next page...

Table 3. Continued.

Target	Setting [μm]	Slit [″]	Orient. [°]	Chop [″]	Date [y-m-d]	Time [h:m]	Airmass	Seeing [″]	Obs.time [s]
HD165135	11.4	0.4	0	8	2007-09-13	00:22	1.04	0.69	73
HD165135	12.2	0.4	0	8	2007-09-13	00:26	1.04	0.69	75
HD169916	8.5	0.4	0	8	2007-09-13	01:26	1.09	0.72	67
HD169916	9.8	0.4	0	8	2007-09-13	01:29	1.10	0.74	73
HD169916	11.4	0.4	0	8	2007-09-13	01:32	1.10	0.72	73
HD169916	12.2	0.4	0	8	2007-09-13	01:35	1.11	0.72	75
HD200914	8.5	0.4	0	8	2007-09-13	01:51	1.01	0.76	144
HD200914	9.8	0.4	0	8	2007-09-13	01:56	1.00	0.77	157
HD200914	11.4	0.4	0	8	2007-09-13	02:01	1.00	0.72	157
HD200914	12.2	0.4	0	8	2007-09-13	02:05	1.00	0.74	162
HD140573	8.5	0.4	0	8	2007-09-13	23:40	1.59	0.98	67
HD140573	9.8	0.4	0	8	2007-09-13	23:43	1.61	1.00	73
HD140573	11.4	0.4	0	8	2007-09-13	23:46	1.63	0.99	73
HD140573	12.2	0.4	0	8	2007-09-13	23:50	1.65	1.21	75
HD140573	8.5	0.4	0	8	2007-09-14	00:56	2.50	1.14	67
HD140573	9.8	0.4	0	8	2007-09-14	00:59	2.56	1.10	73
HD140573	11.4	0.4	0	8	2007-09-14	01:02	2.64	1.23	73
HD140573	12.2	0.4	0	8	2007-09-14	01:05	2.71	1.10	75
HD189319	8.5	0.4	0	8	2007-09-14	01:29	1.40	1.11	144
HD189319	9.8	0.4	0	8	2007-09-14	01:34	1.40	1.03	157
HD189319	11.4	0.4	0	8	2007-09-14	01:39	1.41	1.09	157
HD189319	12.2	0.4	0	8	2007-09-14	01:44	1.41	1.07	162
HD183799	8.5	0.4	0	8	2007-09-14	02:06	1.06	0.66	67
HD183799	9.8	0.4	0	8	2007-09-14	02:09	1.06	0.66	73
HD183799	11.4	0.4	0	8	2007-09-14	02:12	1.07	0.79	73
HD183799	12.2	0.4	0	8	2007-09-14	02:15	1.07	0.77	75
HD183799	8.5	0.4	0	8	2007-09-14	03:07	1.19	0.89	67
HD183799	9.8	0.4	0	8	2007-09-14	03:10	1.19	0.80	73
HD183799	11.4	0.4	0	8	2007-09-14	03:12	1.20	0.80	73
HD183799	12.2	0.4	0	8	2007-09-14	03:16	1.21	0.82	75
HD8512	8.5	0.4	0	8	2007-09-14	03:30	1.45	1.00	144
HD8512	9.8	0.4	0	8	2007-09-14	03:35	1.42	1.11	157
HD8512	11.4	0.4	0	8	2007-09-14	03:39	1.40	1.09	157
HD8512	12.2	0.4	0	8	2007-09-14	03:44	1.37	1.05	162
HD146051	8.5	0.4	0	8	2007-09-14	23:38	1.29	0.86	67
HD146051	9.8	0.4	0	8	2007-09-14	23:41	1.30	0.74	73
HD146051	11.4	0.4	0	8	2007-09-14	23:43	1.31	0.78	73
HD146051	12.2	0.4	0	8	2007-09-14	23:47	1.32	0.90	75
HD152786	8.5	0.4	0	8	2007-09-15	00:39	1.35	1.51	67
HD152786	9.8	0.4	0	8	2007-09-15	00:42	1.35	1.40	73
HD152786	11.4	0.4	0	8	2007-09-15	00:45	1.36	1.49	73
HD152786	12.2	0.4	0	8	2007-09-15	00:48	1.37	1.33	75
HD152161	8.5	0.4	0	8	2007-09-18	01:01	1.38	0.91	67
HD152161	9.8	0.4	0	8	2007-09-18	01:04	1.39	0.91	73
HD152161	11.4	0.4	0	8	2007-09-18	01:06	1.40	0.91	73
HD152161	12.2	0.4	0	8	2007-09-18	01:10	1.41	0.75	75
HD168454	8.5	0.4	0	8	2007-09-18	02:00	1.25	1.25	67
HD168454	9.8	0.4	0	8	2007-09-18	02:03	1.26	1.28	73
HD168454	11.4	0.4	0	8	2007-09-18	02:06	1.27	1.32	73
HD168454	12.2	0.4	0	8	2007-09-18	02:10	1.28	1.31	75
HD33684	8.5	0.4	0	8	2007-12-19	03:13	1.29	1.01	70
HD33684	9.8	0.4	0	8	2007-12-19	03:16	1.29	1.06	77
HD33684	11.4	0.4	0	8	2007-12-19	03:19	1.29	1.15	77
HD33684	12.2	0.4	0	8	2007-12-19	03:22	1.29	1.08	79
HD32887	8.5	0.4	0	8	2007-12-19	04:18	1.00	0.72	70
HD32887	9.8	0.4	0	8	2007-12-19	04:21	1.01	0.74	77
HD32887	11.4	0.4	0	8	2007-12-19	04:24	1.01	0.76	77
HD32887	12.2	0.4	0	8	2007-12-19	04:27	1.01	0.81	79
HD33684	8.5	0.4	0	8	2007-12-19	04:43	1.29	1.10	70
HD33684	9.8	0.4	0	8	2007-12-19	04:46	1.30	1.10	77
HD33684	11.4	0.4	0	8	2007-12-19	04:49	1.30	0.99	77
HD33684	12.2	0.4	0	8	2007-12-19	04:53	1.30	1.02	79
HD32887	8.5	0.4	0	8	2007-12-19	05:48	1.11	0.81	70
HD32887	9.8	0.4	0	8	2007-12-19	05:51	1.12	0.82	77

Continued on next page...

Table 3. Continued.

Target	Setting [μm]	Slit [″]	Orient. [°]	Chop [″]	Date [y-m-d]	Time [h:m]	Airmass	Seeing [″]	Obs.time [s]
HD32887	11.4	0.4	0	8	2007-12-19	05:54	1.12	0.78	77
HD32887	12.2	0.4	0	8	2007-12-19	05:57	1.13	0.78	79
HD32887	9.8	0.4	0	14	2007-12-21	02:44	1.03	0.71	77
HD32887	11.4	0.4	0	14	2007-12-21	02:47	1.03	0.66	77
HD32887	12.2	0.4	0	14	2007-12-21	02:50	1.03	0.62	79
HD42995	9.8	0.4	0	14	2007-12-21	03:48	1.56	1.11	77
HD42995	11.4	0.4	0	14	2007-12-21	03:51	1.55	1.07	77
HD42995	12.2	0.4	0	14	2007-12-21	03:54	1.54	1.07	79
HD54605	8.5	0.4	0	8	2007-12-21	06:35	1.02	0.68	70
HD54605	9.8	0.4	0	8	2007-12-21	06:38	1.02	0.64	77
HD54605	11.4	0.4	0	8	2007-12-21	06:41	1.02	0.76	77
HD54605	12.2	0.4	0	8	2007-12-21	06:44	1.02	0.64	79
HD54605	8.5	0.4	0	8	2007-12-21	07:35	1.09	0.63	70
HD54605	9.8	0.4	0	8	2007-12-21	07:38	1.10	0.65	77
HD54605	11.4	0.4	0	8	2007-12-21	07:41	1.10	0.72	77
HD54605	12.2	0.4	0	8	2007-12-21	07:44	1.11	0.76	79
HD81797	8.5	0.4	0	8	2007-12-22	07:43	1.04	0.63	70
HD81797	9.8	0.4	0	8	2007-12-22	07:46	1.04	0.63	77
HD81797	11.4	0.4	0	8	2007-12-22	07:49	1.04	0.65	77
HD81797	12.2	0.4	0	8	2007-12-22	07:52	1.04	0.63	79
HD89388	8.5	0.4	0	8	2007-12-22	08:48	1.25	0.77	70
HD89388	9.8	0.4	0	8	2007-12-22	08:51	1.25	0.81	77
HD89388	11.4	0.4	0	8	2007-12-22	08:54	1.25	0.83	77
HD89388	12.2	0.4	0	8	2007-12-22	08:57	1.25	0.82	79
HD45348	8.5	0.4	0	8	2007-12-23	05:48	1.15	0.78	70
HD45348	9.8	0.4	0	8	2007-12-23	05:52	1.15	0.73	77
HD45348	11.4	0.4	0	8	2007-12-23	05:55	1.15	0.74	77
HD45348	12.2	0.4	0	8	2007-12-23	05:58	1.16	0.74	79
HD54605	8.5	0.4	0	8	2007-12-23	06:48	1.03	0.76	70
HD54605	9.8	0.4	0	8	2007-12-23	06:51	1.04	0.78	77
HD54605	11.4	0.4	0	8	2007-12-23	06:54	1.04	0.84	77
HD54605	12.2	0.4	0	8	2007-12-23	06:57	1.04	0.73	79
HD45348	8.5	0.4	0	8	2008-02-24	03:01	1.26	1.27	70
HD45348	9.8	0.4	0	8	2008-02-24	03:05	1.26	0.91	77
HD45348	11.4	0.4	0	8	2008-02-24	03:08	1.27	0.61	77
HD45348	12.2	0.4	0	8	2008-02-24	03:11	1.28	0.67	79
HD48915	8.5	0.4	0	8	2008-02-25	00:37	1.02	1.16	70
HD48915	9.8	0.4	0	8	2008-02-25	00:40	1.02	1.16	77
HD48915	11.4	0.4	0	8	2008-02-25	00:43	1.01	1.01	77
HD48915	12.2	0.4	0	8	2008-02-25	00:47	1.01	1.01	79
HD45348	8.5	0.4	0	8	2008-02-25	01:41	1.15	0.56	70
HD45348	9.8	0.4	0	8	2008-02-25	01:44	1.16	0.50	77
HD45348	11.4	0.4	0	8	2008-02-25	01:47	1.16	0.61	77
HD45348	12.2	0.4	0	8	2008-02-25	01:50	1.16	1.09	79
HD112142	9.8	0.4	0	8	2008-02-25	05:22	1.17	1.21	77
HD112142	11.4	0.4	0	8	2008-02-25	05:25	1.16	1.24	77
HD112142	12.2	0.4	0	8	2008-02-25	05:28	1.15	1.24	79
HD112142	8.5	0.4	0	8	2008-02-25	06:21	1.06	1.92	70
HD112142	9.8	0.4	0	8	2008-02-25	06:24	1.06	4.37	77
HD112142	12.2	0.4	0	8	2008-02-25	06:30	1.06	3.09	79

Annex

HD 95881: a gas rich to gas poor transition disk

submitted to the journal *A&A*, June 2009

Astronomy & Astrophysics manuscript no. HD95881
June 8, 2009
© ESO 2009

HD 95881: A gas rich to gas poor transition disk? ⋆

A.P. Verhoeff[1], M. Min[2], B. Acke[3,⋆⋆], R. van Boekel[4], E. Pantin[5], L.B.F.M. Waters[1,3], A.G.G.M. Tielens[6], M. van den Ancker[7], G.D. Mulders[1], A. de Koter[1,2], and J. Bouwman[4]

[1] Astronomical Institute "Anton Pannekoek", University of Amsterdam, P.O. Box 94249, 1090 GE Amsterdam, The Netherlands
[2] Astronomical Institute Utrecht, University of Utrecht, P.O. Box 80000, 3508 TA Utrecht, The Netherlands
[3] Institute for Astronomy, KU Leuven Celestijnenlaan 200B, B-3001 Leuven, Belgium
[4] Max Planck Institut für Astronomie, Königstuhl 17, 69117 Heidelberg, Germany
[5] CEA/DSM/DAPNIA/Service d'Astrophysique, CE Saclay F-91191 Gif-sur-Yvette, France
[6] Leiden Observatory, Niels Bohrweg 2, 2300 RA Leiden, The Netherlands
[7] European Southern Observatory, Karl-Schwarzschild-Str2, D85748 Garching bei München, Germany

Received ....; accepted .....

ABSTRACT

Context. Based on the far infrared excess the Herbig class of stars is divided into a group with flaring circumstellar disks (group I) and a group with flat circumstellar disks (group II). Dust sedimentation is generally proposed as an evolution mechanism to transform flaring disks into flat disks. Theory predicts however that during this process the disks preserve their gas content, while observations of group II Herbig Ae stars demonstrate a lack of gas.
Aims. We map the spatial distribution of the gas and dust around the group II Herbig Ae star HD 95881.
Methods. We analyze optical photometry, Q-band imaging, infrared spectroscopy, and K and N-band interferometric spectroscopy. We use a Monte Carlo radiative transfer code to create a model for the density and temperature structure which quite accurately reproduces all the observables.
Results. We derive a consistent picture in which the disk consists of a thick puffed up inner rim and an outer region which has a flaring gas surface and is relatively void of small dust grains.
Conclusions. HD 95881 is in a transition phase from a gas rich flaring disk to a gas poor self-shadowed disk.

Key words. star formation - protoplanetary disks - Herbig Ae stars - HD 95881

1. Introduction

Herbig Ae (HAe) stars are known to have gas-rich, dusty disks that are the remnant of the star formation process. These disks are most likely the sites of ongoing planet formation. The processes leading to and associated with planet formation modify both the composition and the geometry of the disk. Grain growth and grain settling are expected to result in large spatial variation of the grain size distribution and the gas to dust mass ratio within the disk. The gravitational interaction of proto-planets with the disk can create gaps/holes. Also the gas and the dust chemistry is expected to vary spatially. In order to understand planet formation, it is thus important to establish the spatial distribution of gas and dust in proto-planetary disks independently.

Observationally, the Spectral Energy Distributions (SEDs) of HAe stars have been divided into two groups, that reflect differences in the slope of the mid-IR (10-60 μm) spectral range (Meeus et al., 2001). Group I sources have red SEDs, while group II sources have blue SEDs. These differences can be interpreted in terms of the geometry of the disk. The direct irradiation of the inner rim of a disk with an inner hole causes it to be puffed up (Dullemond et al., 2001). This puffed up inner rim casts a shadow, and only the outer disk surface regions emerge from the shadow and receive direct stellar light. Depending on the dust opacity, some disks may never emerge from the shadow of the inner rim (Dullemond & Dominik, 2004). This provides an elegant explanation for the observed two types of SEDs: group I sources being *flaring*, and group II sources *self-shadowed*. This interpretation has been confirmed using spatially resolved mid-infrared (IR) imaging with the *Very Large Telescope Interferometer* (e.g. Leinert et al. 2004).

A difference between group I and group II sources was also found for the strength of the mid-IR emission bands attributed to Polycyclic Aromatic Hydrocarbons (PAHs; Meeus et al. 2001; Acke & van den Ancker 2004): flaring disks tend to show strong PAH emission while self-shadowed sources show weaker or no PAH emission. A similar difference was found for the strength of the [O I] 6300 Å line (Acke et al., 2005). However, there is significant scatter in these trends (see below). Both the PAHs and the [O I] line strength probe the *gas* in the upper disk layers, and both require direct irradiation of the disk surface by stellar photons to be excited. PAHs mainly probe the disk on scales of several tens to 100 AU (e.g. van Boekel et al. 2004; Lagage et al. 2006; Geers et al. 2007; Verhoeff et al. 2009), i.e. similar scales as the dust continuum emission in the 10-60 μm wavelength range. These observations suggest that the spatial distribution of gas in group II sources is different from that of group I sources: apparently, in group II sources the gas in the surface of the outer disk does not receive direct stellar photons.

In a theoretical study, Dullemond et al. (2007) show that for disks in which the dust settles but the scale-height of the gas

Send offprint requests to: A.P. Verhoeff, e-mail: verhoeff@uva.nl

⋆ Based on observations collected at the European Southern Observatory, Chile. Under program IDs: 060.A9234A, 076.C-0159A, 077.C-0367A, 078.C-0281

⋆⋆ Postdoctoral Fellow of the Fund for Scientific Research, Flanders.

Table 1. Characterizing parameters of HD 95881. The second Col. lists parameters as given by Acke & van den Ancker (2004), where SFR stands for the star formation region. New values for some of the parameters are given in the third Col.

Parameter	Value	New
Right Ascension	$11^h\ 01^m\ 57\overset{s}{.}62$	
Declination	-72° 30′ 48″.4	
Spectral Type	A2III/IVe	
$T_{\rm eff}$ [K]	8990	
Distance [pc]	118±12	170±30
Luminosity [$L_\odot$]	6.9±1.0	15.4±6
A_V [mag]	0.25	
Radius [$R_\odot$]	1.1±0.1	1.6±0.3
Mass [$M_\odot$]	-	2.0±0.2
SFR	Sco OB2-4?	?
Group	IIa	

does not change, both group I and group II sources should show prominent PAH emission from gas directly exposed to the stellar radiation field, contrary to the observed trend. However, some disks classified as group II sources (i.e. with a self-shadowed dust geometry) are observed to show prominent PAH emission and [O I] line emission; examples are HD 98922 and HD 95881 (Acke et al., 2005; Acke & van den Ancker, 2004). Verhoeff et al. (submitted to A&A) show that for HD 95881 the PAH emission is extended at a scale similar to those of group I sources. Fedele et al. (2008) study the spatial distribution of gas and dust in three HAe stars and show that the gas and dust in these stars may be decoupled. In the case of the group II source HD 101412, PAH and [O I] emission were detected and found to be more extended than the dust continuum at 10 μm. These observations suggest that disks exist in which *the dust has settled but the scale-height of the gas is still large enough at several tens of AU distance from the star to produce substantial PAH and [O I] line emission*. Such disks may provide important clues as to how gas-rich disks evolve to gas-poor debris disks.

In this paper, we study the spatial distribution of the gas and dust in the disk of HD 95881. This star was part of a larger study of spatially resolved mid-IR spectroscopy of HAe stars (Verhoeff et al. 2009, submitted to A&A). We use optical spectroscopy of the [O I] line, the SED, infrared spectra as well as near-IR and mid-IR interferometric observations to constrain the geometry of the gas and dust in the disk. We use a hydrostatic equilibrium disk model to fit the SED and compare the predicted spatial distribution of the near-IR and mid-IR emission of the best fitting disk model to the interferometric observations. We find convincing evidence that the dust in the disk of HD 95881 has settled but that the gas still has a significant scale-height. We derive an estimate on the total disk mass by fitting the strength of the PAH bands.

2. Stellar parameters

There is little information to be found on HD 95881 in the literature. From optical photometry the spectral type was determined to be A2III/IVe (Houk & Cowley 1975), which was translated into an effective temperature of 8990 K (Acke & van den Ancker 2004). The distance was established by a relatively uncertain association with the star formation region Sco OB2-4 (Acke & van den Ancker 2004). The distance to this region was previously determined by de Zeeuw et al. (1999). When we take these parameters to pinpoint HD 95881 in the Hertzsprung-Russell-diagram, we find that it is situated to the left of the Zero Age Main Sequence (ZAMS), which is unphysical. Since we consider the determination of $T_{\rm eff}$ as reliable, we adopted a luminosity of 15.4 $L_\odot$ assuming the ZAMS luminosity from Meynet et al. (1994) at the given $T_{\rm eff}$. The corresponding ZAMS mass was adopted as the stellar mass. From the new luminosity, new estimates for the radius and distance follow. Table 1 lists the basic characteristics and our new estimates. To double check the new distance we looked at the Tycho parallax, which gave a lower limit of 80 pc. We also consulted the Hipparcos catalog for spectral types and $(B-V)$ photometry of stars within 1° from HD 95881 and compared the distance to the color excess $E(B-V)$ for the region (de Zeeuw et al. 1999). For HD 95881 the color excess of $E(B-V) = 0.08$ leads to an upper limit on the distance of ~200 pc. The derived distance interval of 80-200 pc is consistent with both distance estimates, but because of the argument given above we adopt a distance estimate as derived from the ZAMS of 170±30 pc.

3. Observations

3.1. AMBER

Spectrally dispersed K-band interferometric observations of HD 95881 were obtained with VLTI/AMBER on the UT1-UT3-UT4 baseline setting during the night of February 4, 2007. The weather conditions were excellent, with the optical seeing as low as 0.5″. The data have been reduced according to the standard AMBER data reduction procedure described in Tatulli et al. (2007). AMBER observations of a standard star (HD100901, K0/K1III) were performed directly before the science measurement and used to calibrate the raw visibilities.

3.2. VISIR imaging

Q band imaging data were obtained on the 14th of December 2005 using the *VLT Imager and Spectrometer for mid-Infrared* (VISIR; see Lagage et al. 2004). Standard "chopping and nodding" mid-infrared observational technique was used to suppress the background dominating at these wavelength. The Q2 filter was chosen, which has a central wavelength of 18.72 μm and a half-band width of 0.88 μm. The pixel field of view was 0.075″ and the orientation was standard (north up, east to the left). The total integration time spend on HD 95881 was 680 s. The reference star, HD 1024601 (10.6 Jy in the Q2 filter), was chosen from the database of VISIR standard stars based on criteria of flux and distance on the sky to the target. 456 s of integration time was spent on HD 102461. The airmass of both sources was always below 1.5. The sensitivity achieved was estimated to be 57 mJy / 10σ 1h and the optical seeing was moderately fluctuating in the range 0.75-0.85″.

3.3. VISIR spectroscopy

Long slit N-band spectra were obtained with VISIR in the low resolution (LR) mode. A sample of 17 HAe stars was observed under the VISIR GTO program on circumstellar disks (Verhoeff et al. submitted to A&A). During the nights of December 16, 2005 and April 8, 2006 we observed HD 95881. Standard parallel chop-nodding was used with a chopper throw of 8″, a slit-width of 0.75″, and a standard North-South orientation. After and before the science measurements bright standard stars were observed. The airmass of the observations was ~1.6 and the optical seeing was around 1.0″ during the first night and around 1.2″ during the second night.

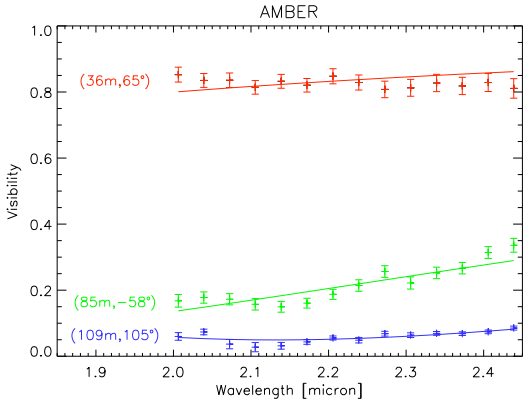

Fig. 1. The AMBER K-band visibilities of HD 95881. The projected length and position angle of the baselines is indicated on the left. Overplotted is the best-fit ring+point-source model (solid lines; see text).

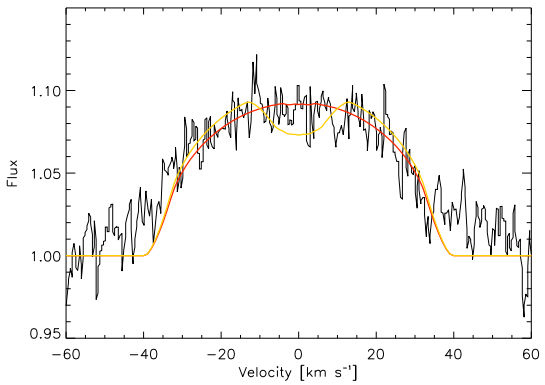

Fig. 2. The continuum-normalized [O I] 6300 Å emission line of HD 95881 (Acke et al. 2005). The velocity axis has been centered on the centroid position of the feature, i.e. the radial velocity of the central star. Line profiles corresponding to a surface brightness proportional to r^{-3} are overplotted. Red represents a model with an outer radius beyond 31 AU; yellow is used for the model with an outer radius equal to 11 AU. See text for details.

3.4. MIDI

HD 95881 was observed with the *MID-infrared Interferometric instrument* (MIDI; see Leinert et al. 2003), the 10 μm instrument of the VLTI, during the night starting June 6 2004, as part of the "science demonstration" program. The UT1-UT3 baseline was used, resulting in a projected baseline length of 65m at a position angle of 81° east of north. The grism was used to spectrally disperse the signal at a resolution of R $\approx$ 230. This ensures that relatively narrow "dusty" emission features such as those of crystalline silicates and PAHs are well resolved spectrally. The seeing was constant at a value of 0.″6 and the atmospheric transparency was excellent.

We performed observations in "High-Sens" mode, i.e. we took an interferometric measurement combining the light from both telescopes, and subsequent photometric measurements measuring the signal from one telescope at a time. Stars of known brightness and angular diameter were observed, using the same procedure, for photometric calibration and monitoring system coherence losses (interferometric "transfer function"). We found our interferometric measurement of HD 95881 to be of significantly higher quality than the corresponding photometric measurements, and chose to directly calibrate the correlated flux rather than converting to interferometric visibility by division over the photometry.

3.5. Additional data

A low resolution Spitzer-IRS spectrum is used to compare and flux-calibrate the VISIR spectrum. For the acquisition and reduction of the Spitzer data we refer to Bouwman et al. (in preparation). Photometric data points were taken from Acke & van den Ancker (2004). Together with the Spitzer spectrum they make up the SED, which allows us to constrain the disk geometry (see Sect. 5). Finally, [O I] data were taken from an earlier study, see Acke et al. (2005).

4. Analysis

4.1. AMBER

A good fit ($\chi^2/\nu = 1.8$) to the AMBER data could be obtained with an inclined uniformly emitting ring surrounding a point-like source representing the star (Fig. 1). The inner and outer radius of this ring are 2.2±0.2 mas (0.37 AU) and 2.7±0.3 mas (0.46 AU). The disk inclination is 60°±10° and its position angle is 102°±2°. The mean radius of the ring is 2.4 mas (~0.4 AU). This is similar to the values found by Eisner et al. (2004) for a group of Herbig Ae/Be stars. The fraction of the K-band flux that is ascribed to the star by the fit of a Kurucz model to the optical photometry (~20%) is not exactly equal to the AMBER estimate of 32±4%. It may be that this discrepancy is due to the presence of an unresolved disk component, e.g. hot gas inside the dust sublimation radius, that contributes to the K-band emission. The latter has been claimed for quite a number of pre-main-sequence stars (Eisner et al. 2007; Kraus et al. 2008; Acke et al. 2008; Tannirkulam et al. 2008b; and Isella et al. 2008)

4.2. [O I] data

Acke et al. (2005) have investigated the [O I] 6300 Å emission line in a large sample of Herbig stars. The authors argue that the emission is non-thermal and originates from the disk surface of a flared circumstellar disk. This is consistent with the large detection rate of [O I] emitters among the group I sources in the sample. Roughly half of the group II sources, however, display the [O I] 6300 Å line in emission as well, albeit less strong. HD 95881 is one of these targets.

In Fig. 2, the [O I] 6300 Å line profile is shown. We have fitted a generic model to the data, assuming that the intensity drops off with radius as a power law and that the disk is in Keplerian rotation. We adopt the disk inclination derived from the AMBER fit. An acceptable fit in terms of reduced χ^2 was achieved with a power index of −3.0±0.2, an inner radius of 0.9±0.2 AU and an outer radius larger than 11 AU. The best fit has an outer radius beyond 31 AU. In the figure we show the best-fit profile, as well

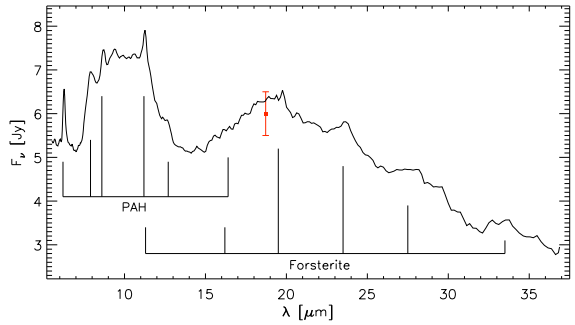

Fig. 3. The Spitzer LR spectrum of HD 95881 (SNR ≈ 500). The left rake points at the PAH bands at 6.2, 7.9, 8.6, 11.2, 12.7, and 16.4 μm. The right rake points at the forsterite bands at 11.3, 16.2, 19.5, 23.5, and 33.5 μm. The red square is the photometry from the VISIR Q-band imaging (see Sect. 4.4).

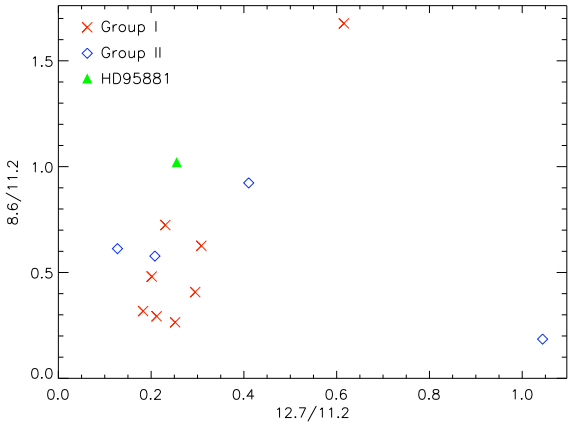

Fig. 4. The ratios of the integrated PAH band strengths for a sample of Herbig Ae stars. The ratio of the 8.6 over 11.2 μm feature is relatively high for HD 95881.

as the profile that corresponds to the model with an 11 AU outer radius. Decreasing the outer radius of the model to even lower values would further deteriorate the fit quality. We can therefore conclude that a significant fraction of the [O I] emission comes from a region at tens of AU from the star. Note that our model does not account for the 15% of [O I] flux which is emitted in the blue- and red wings of the profile. In these regions, close to the star, the power law approximation fails.

4.3. Spitzer

The Spitzer-IRS spectrum is given in Fig. 3. It displays a rich mineralogy, there is emission of amorphous and crystalline silicates as well as emission of various PAH bands. The blue slope at longer wavelengths is typical for group II sources.

We have taken 6.2, 7.7, 8.6, 11.2 and 12.7 μm PAH band strengths from Verhoeff et al. (submitted to A&A) and Bouwman et al. (in prep.) and looked at the ratios of their continuum subtracted and integrated strengths. Compared to other HAe stars HD 95881 appears very ordinary in this aspect. The only exception is the 8.6 μm PAH feature, which is relatively strong. We show this in Fig. 4, where we plotted the 12.7 over 11.2 μm

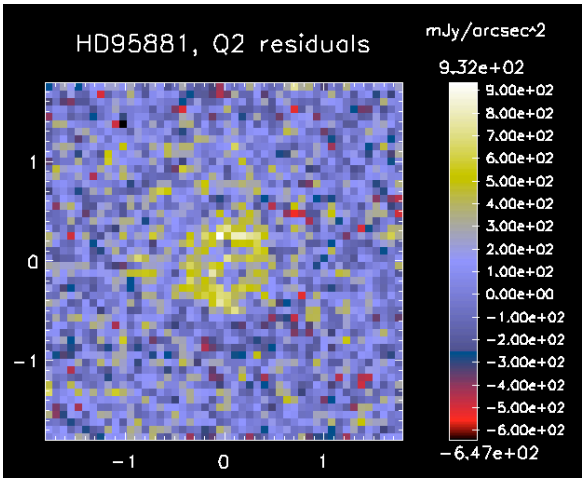

Fig. 5. The residuals of the VISIR Q2 image after point source subtraction. The spatial scale is in arcseconds.

against the 8.6 over 11.2 μm PAH feature ratios. The 8.6 μm feature pops out as being rather strong.

4.4. VISIR imaging

A dedicated data reduction pipeline was used for the imaging. It features a comprehensive set of methods to correct for instrumental signatures such as detector striping or background low-frequencies excess of noise (Pantin et al. 2008, 2009). A photometric analysis gives an integrated flux for HD 95881 of 6.0±0.5 Jy in the Q2 filter (18.72 μm). This is in fair agreement with the Spitzer data (see Fig. 3). Since the emission of the star is negligible at this wavelength, this flux can be attributed to the disk. We searched for an extended emission component using PSF subtraction at a sub-pixel (1/10) precision level. The PSF was derived from the observation of the standard star. The resulting residuals shown in Fig. 5 display an excess of signal that is roughly axi-symmetric and decreases gradually as a function of distance from the star.

Assuming that the disk has the geometric parameters given in Tab. 2, we divided the residuals in a series of concentric ellipses having a separation of 0.075″ along the semi-major axis of the disk. We assumed an aspect ratio corresponding to a flat disk inclined at 55°, and a position angle of 103° from North. We used these elliptic annuli to numerically estimate the surface brightness distribution and the corresponding uncertainty levels.

Our statistical analysis confirms we have a true detection since for distances in the range 0.4-0.85″ from the star the average values in each of the elliptical annuli are well above the detection limits set at 99% confidence. The measured average surface brightness in elliptic annuli as a function of the semi-major axis distance to the star are plotted in Fig. 6. The 3σ uncertainties are displayed as bars on the plot. The total flux in the resolved component is 0.7±0.1 Jy.

4.5. VISIR spectroscopy

The general reduction and analysis strategy of the spectroscopic VISIR data is described in detail in Verhoeff et al. (submitted to A&A). For HD 95881 the telluric correction was done by means

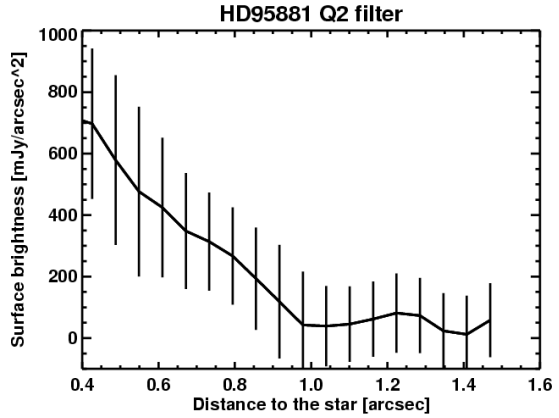

Fig. 6. Surface brightness levels as a function of distance from the star in the Q2 image after point source subtraction.

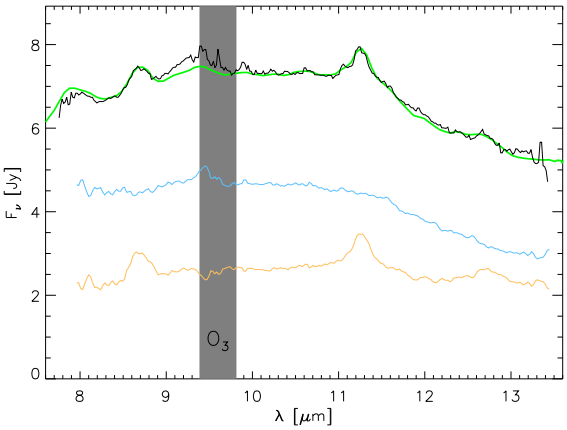

Fig. 7. The VISIR N-band spectrum of HD 95881 (black line). Overplotted using a blue line of intermediate thickness is the correlated flux as measured with MIDI. The thick green line is the Spitzer spectrum. The thin orange line is the difference between the Spitzer and MIDI spectra.

of an airmass interpolation of two calibrators. The observation of April 8 2006 appeared to be suffering strong atmospheric residuals. The spectrum of December 16 2005 was thus chosen as most representative. The missing observation of the 9.8 μm setting was replaced with the poor one from April 8 2006. We scaled the VISIR spectrum to the Spitzer spectrum at 10.6 μm using a factor of 1.36. The resulting spectrum in Fig. 7 has a SNR of ~300. The agreement with the Spitzer spectrum is encouraging. The slight deviation observable just left of the ozone band at 9.6 μm is typical for the quality of the data taken on April 8, 2006.

The Full Width at Half Maximum (FWHM) of the spatial emission profile of the target was determined by performing a Gauss-fit in 32 merged wavelength bins. Comparison of the science signals with the PSF shows that the target is unresolved in the continuum. After quadratic subtraction of the PSF and averaging over the median values of all measurements we find a three sigma upper-limit to the FWHM extent of the continuum emission region of $< 0.18''$, which corresponds to < 31 AU at the

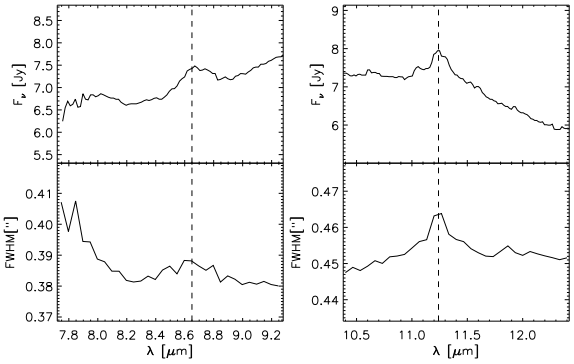

Fig. 8. VISIR measurement of the flux (top panels) and spatial extent (bottom panels) of HD 95881 as a function of wavelength. Both opacity features of PAHs at 8.6 and 11.2 μm are visible as a relative increase in the width of the signal. The relative upturn to the left of ~8 μm is related to the PAH complex at 7.7 μm.

adopted distance of 170 pc. Note however in Fig. 8 that the science signal displays a relative increase at 8.6 and 11.2 μm and an upturn to the left of ~8 μm, which are exactly the wavelengths at which the PAH molecules have emission features. We checked the significance of these FWHM features with respect to pixel-to-pixel variations and concluded that *the PAH emission is significantly more extended than the continuum.*

In order to estimate the spatial extent of the PAH emission we measured the spatial emission profile at the peak wavelengths of the PAH bands and we subtracted the spatial emission profile of the continuum contribution. This continuum profile was determined by interpolating the intensities and spatial profiles adjacent to the PAH bands. The resulting observed spatial profile of the PAH emission was Gaussian fitted to obtain the FWHM. Finally, the instrumental width (i.e. the PSF) was quadratically subtracted to obtain a measure for the intrinsic extent of the PAH emission. We found FWHM values of $0.34''^{+0.05}_{-0.08}$ and $0.40''^{+0.04}_{-0.06}$ for the 8.6 and 11.2 μm PAH bands respectively, which results in absolute sizes of 58 and 68 AU. In a Gaussian distribution of the PAH emission this would mean that 99% is confined in a radius of ~100 AU. Note that this is a conservative estimate of the PAH emission scale since the PAH surface brightness is expected to fall off with distance from the star together with the UV flux as $1/r^2$.

4.6. MIDI

In Fig. 7 we compare the spectrum *in correlated flux* as seen by MIDI to the spectra observed by VISIR and Spitzer. The correlated flux spectrum is dominated by the central few AU of the disk, the Spitzer and VISIR spectra probe the entire disk. Note the difference in the strength of the 8.6 and 11.2 μm PAH bands in the spectra. These bands are prominent in the total flux spectra, but essentially absent in the correlated flux spectra. The PAH emission region is apparently outside of the disk region probed by MIDI. This shows by direct measurement that *the PAH features arise at scales much larger than ~2 AU in the disk of HD 95881.* To stress this point we also plotted the difference between the Spitzer and the MIDI correlated flux spectrum in Fig. 7. This difference spectrum is dominated by the emission of the outer disk ($r \gtrsim 2$ AU) and shows very distinct PAH features.

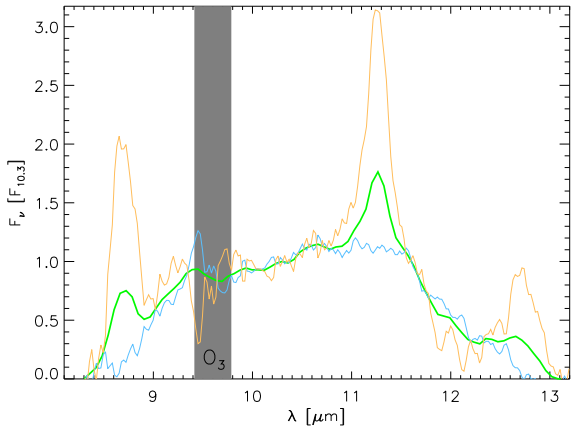

Fig. 9. The normalized continuum subtracted silicate feature. The Spitzer spectrum (thick green) represents the entire disk, the MIDI correlated flux spectrum (medium thickness blue) represents the inner disk ($r \lesssim 2$ AU), and the difference spectrum (thin orange) represents the outer disk ($r \gtrsim 2$ AU). The similar shape of the inner and outer disk silicate feature indicates a similar grain size distribution and crystallinity.

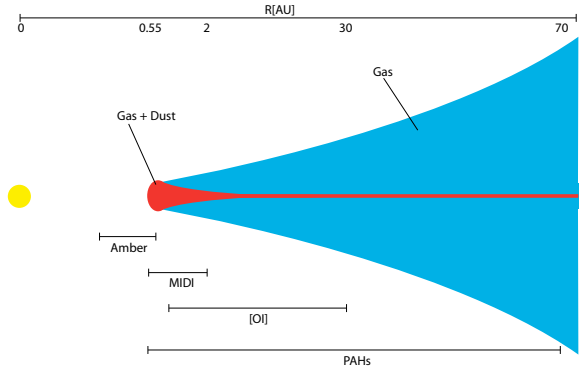

Fig. 10. Schematic depiction of the protoplanetary disk of HD 95881. Indicated are the different regions of the disk that are probed by diagnostics discussed in this paper.

To investigate spatial differences in the weak silicate emission we considered the shape of the feature in the Spitzer, MIDI, and difference spectrum in a consistent manner. We approximated a continuum with a straight line intersecting the spectra at 8.3 and 13.2 μm, subtracted this from the spectra and then normalized the spectra with the flux level at 10.3 μm. Figure 9 shows the result. The shape of the silicate feature of the inner and outer disk ($R \gtrsim 2$ AU) is very similar, which implies that the grain size distribution and crystallinity should also be very similar.

4.7. Observational picture

Before we describe a detailed modeling effort of the circumstellar material, we summarize the analyses of the various observations. This already gives an insight into the spatial distribution of the gas and the dust. In Fig. 10 we display a schematic representation of the disk, which aims to put the results of the data sets into perspective and combines them into a consistent picture.

The AMBER data probes the very inner parts of the disk. The analysis shows that the K-band emission could be explained with an emitting ring at ~0.4 AU. A more physical model, which will be presented in Sect. 5 has the inner rim of the disk at 0.55 AU. A part of the K-band emission was shown to originate from inside the dust-sublimation radius. This could be an indicator of ongoing accretion.

The [O I] 6300 Å emission line is formed by the photodissociation of OH molecules by UV photons. The detection of the [O I] 6300 Å at large distances (from one to tens of AU) from the central star is thus an indication that the outer disk has an illuminated gas surface.

The Spitzer data establish the presence of PAH emission and the VISIR spectrum pins it down to a circumstellar disk. The emission features of PAH molecules are caused by internal vibrational modes, which are mainly excited by UV photons. Since the PAH molecules are coupled to the gas, the PAH emission is another indicator of an illuminated gas surface. The resolved VISIR spectrum sets the radial scale of this gas surface at ~100 AU.

The VISIR Q-band image displays a faint extended emission component (~10% of the total flux) that stretches out to large radii (R ~150).

The MIDI correlated flux spectrum shows that the PAH features originate from radii much larger than ~2 AU and that the silicate composition is quite similar in the inner and outer disk.

5. Modeling

In this section we present a theoretical model for the disk around HD 95881 which quite accurately reproduces the observations described above. To obtain this model we use the Monte Carlo radiative transfer code MCMax by Min et al. (2009). This code can compute a self-consistent disk structure and a full range of observables. It has a build-in option that models the full PAH excitation, using the temperature distribution approximation (see e.g. Guhathakurta & Draine 1989; Siebenmorgen et al. 1992) including multi-photon events for the excitation. We use MCMax here to compute the temperature structure, the vertical density structure and the resulting SED, the Spitzer spectrum, the AMBER visibilities, the MIDI correlated flux, the VISIR images, and the FWHM as function of wavelength. The steps to come to the final model presented here were the following.

5.1. Initial constraints

First we fixed the composition and the size and shape distribution of the silicate component of the dust to be equal to that obtained from the 10 micron silicate feature by van Boekel et al. (2005) . For HD 95881 these are 80% large (1.5 μm) pyroxene grains, 11% large enstatite grains, 5% large forsterite grains, and 3% small (0.1 μm) silica grains. In order to get the required continuum opacity needed we added amorphous carbon grains. To model the irregular shape of the carbon grains we used a Distribution of Hollow Spheres (DHS; Min et al. 2005). For the refractive index of carbon we adopted the data by Preibisch et al. (1993). Note that this continuum component is most likely not all in the form of amorphous carbon. Small grains of metallic iron and/or iron sulfide have extinction properties similar to that of carbon. Also, large grains of various dust species could

produce the observed continuum component. The abundance of amorphous carbon is a fitting parameter. The other free parameters all have to do with the geometry of the disk. As a first step we focused on the thermal dust grains, ignoring the PAH bands. The density distribution of the dust disk was parameterized using a radial surface density (Hughes et al. 2008)

$$\Sigma(r) \propto r^{-p} \exp\left\{-\left(\frac{r}{R_0}\right)^{2-p}\right\}, \quad (1)$$

for $R_{\rm in} < r < R_{\rm out}$. Here R_0 is the turnover point from where an exponential decay of the surface density sets in and p sets the powerlaw in the inner region. We fix this powerlaw to $p = 1$, a commonly used value (see e.g. Dullemond et al. 2006). The vertical density structure was computed from hydrostatic equilibrium. However, since we found that this vertical structure cannot reproduce the SED, we included a scaling parameter Φ by which the scale-height of the disk is increased. For the density distribution we thus have the inner and outer radii $R_{\rm in}$ and $R_{\rm out}$, the turnover radius R_0, the total dust mass in small grains $M_{\rm dust}$, and the vertical density scaling parameter Φ, as free parameters.

5.2. Fitting the SED

We first constrained the parameters describing the density structure. We found that the vertical height of the disk needs to be significantly increased compared to hydrostatic equilibrium in order to obtain the large near IR excess. The height of the disk was scaled with a factor $\Phi = 2.75$. The exponential decay of the surface density sets in at $R_0 = 2.5$ AU. To put the density structure in some perspective, at ~7.5 AU our prescription produces the same density as does a $1/r^2$ density law, but beyond 10 AU the surface density becomes negligible. The inner radius of the disk is at 0.55 AU, while the outer radius has no influence on the observationally constrained part of the SED as long as it is beyond ~10 AU. We find a total mass in small dust grains of 10^{-8} $M_\odot$. Note that the total dust mass is probably much higher, because the mass in large dust grains is not constrained. To this dust distribution we added PAHs in an abundance needed to explain the features seen in the Spitzer spectrum. For the opacity of the PAHs we use those computed by Draine & Li (2001) for molecules consisting of 100 carbon atoms.

5.3. Spatial distribution of the gas

We consider two possibilities for the spatial distribution of the gas, as traced by the PAHs (see Fig. 11). The first is to assume that the gas and the dust have the same spatial distribution in the disk. The second is to assume that the gas does not have the exponential decay of the surface density for radii larger than 2.5 AU, but that this disappearance of the dust at these radii is caused by grain growth and settling, which do not affect the gas.

The first model, which has the gas and dust in the same spatial distribution, results in a fairly large abundance of PAH molecules needed to explain the strength of the features seen. The PAHs are in this case fairly well shielded from the stellar radiation by the dust grains, and thus a large amount is needed. Furthermore, in order to explain the absence of PAH emission in the MIDI correlated flux, we find that we have to remove the PAHs from the inner 2 AU. The total mass in PAHs in this case is $3{\cdot}10^{-8}$ $M_\odot$. This model does not reproduce the increase in FWHM at the wavelength of the PAH features that we found in the VISIR spectroscopic data (Fig.8).

Table 2. The parameters for our final model for the circumstellar disk of HD 95881. The small dust grains and the PAH molecules have a different spatial distribution.

Parameter	Dust	PAHs
Inner disk radius ($R_{\rm in}$)	0.55 AU	0.55 AU
Outer disk radius ($R_{\rm out}$)	200 AU	200 AU
Inclination angle (i)	55°	55°
Position angle (major axis E of N)	103°	103°
Vertical density scaling parameter (Φ)	2.75	2.75
Power law for the surface density (p)	1	1
Turnover point (R_0)	2.5 AU	∞
Mass (M)	10^{-8} $M_\odot$	$5{\cdot}10^{-9}$ $M_\odot$

The second model, which assumes the gas is distributed in a more extended flared disk (see Fig. 11) resulted in a very good overall fit of all the observables presented above. In this model we put the PAHs in a disk with a similar surface density as the dust grains but with $R_0 = \infty$, i.e. the surface density remains a powerlaw ($p = 1$) for all radii. In this way we create a flaring outer gas disk, which is able to catch much of the radiation from the star. We find that the PAH emission is dominated entirely by the outer regions. If the PAHs would be destroyed according to the mechanism proposed by Dullemond et al. (2007) we find that the inner 25 AU should be free of PAHs. However, even without destruction the PAH contribution from these inner regions is negligible. Thus, we cannot confirm whether or not PAH destruction takes place in this disk. Extrapolating the powerlaw surface density distribution of the PAHs to the inner edge (at 0.55 AU) we find that at $R_{\rm in}$ the PAH abundance is 0.25% of the dust mass. The total PAH mass we find is $5{\cdot}10^{-9}$ $M_\odot$, which is large compared to the mass in small dust grains, because the PAH disk is so much larger. Including PAH destruction in the inner disk would only lower the total PAH mass by 12%.

5.4. Final model

The second model, that assumes that the PAHs do not have an exponential decay with radius, reproduces the available spatial information much better. This second model was fine-tuned to best reproduce all available observables. The position angle and inclination of the disk were constrained using the interferometric data. We find that the AMBER interferometric observations put important constraints on the parameters for the inner regions of the disk, lifting some of the degeneracies present when these data are not considered. The parameters of the final model are summarized in table 2.

6. Discussion

6.1. Comparison of the model with the observations

Our disk model did a very good job in reproducing all the observables. The fits to the SED, the Spitzer spectrum, the MIDI correlated flux, the AMBER visibilities, the VISIR spectroscopic FWHM and the Q-band image are presented in Fig. 12.

Spitzer. The general slope and most features in the Spitzer spectrum are reproduced. However the observed 6.2, 7.9 and 8.6 μm PAH features are stronger than in our model and the predicted PAH features around 20 μm are not seen in the Spitzer spectrum. These differences are related to the PAH chemistry, which is a much debated subject (see Sect. 6.4).

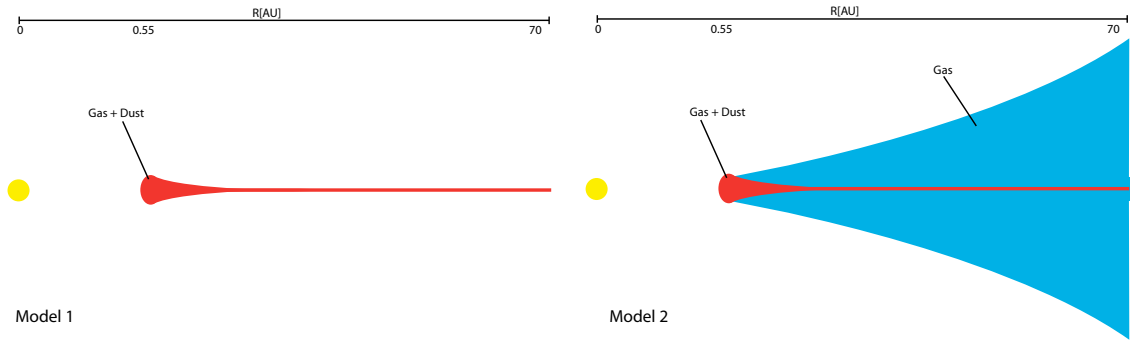

Fig. 11. Schematic depiction of the two considered disk models. First we consider a spatial distribution that is the same for both the dust and the gas. Second we consider a model that assumes that the surface density of the gas decays much slower with distance from the star.

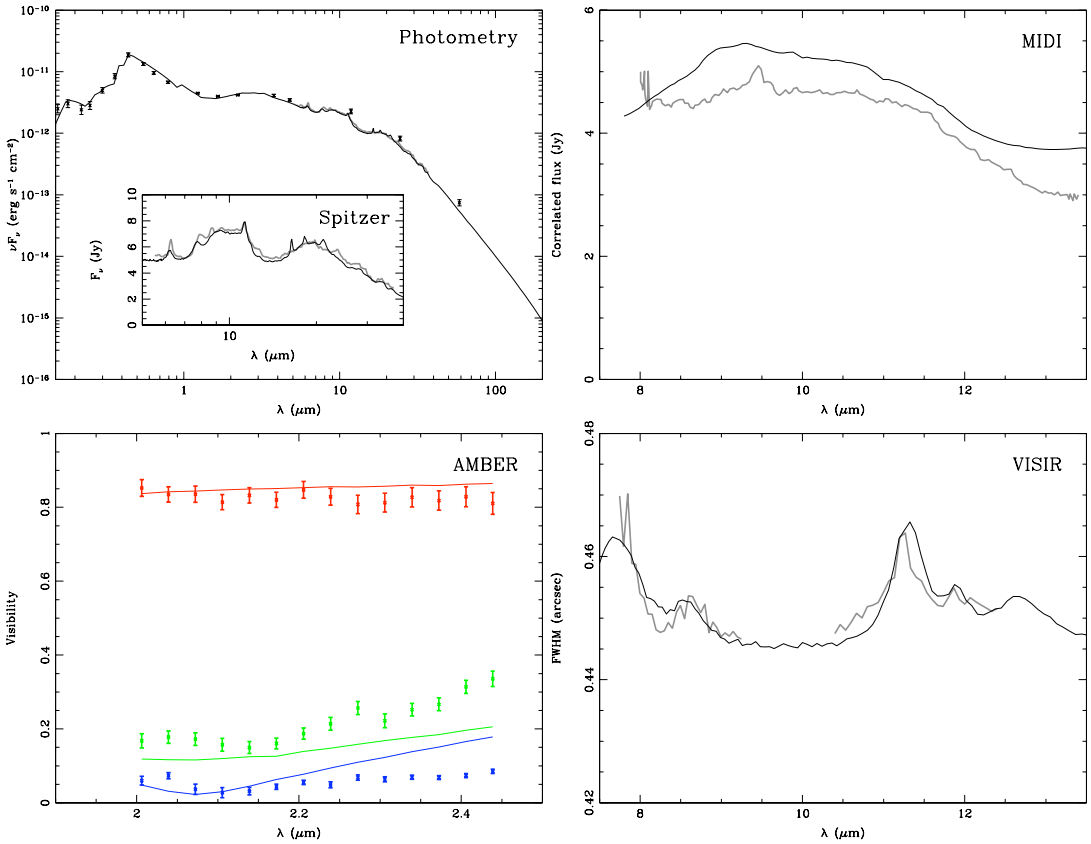

Fig. 12. The best model fit to the observables of HD 95881. The upper left panel shows the fit to the spectral energy distribution with an inset for the Spitzer spectrum. The gray line is the observed spectrum, the black line the model spectrum and the points with error bars are photometric measurements obtained from the literature. The upper right panel shows the correlated flux as obtained by MIDI. The gray line is the observed correlated flux and the black line the model. The bottom left panel shows the visibilities obtained by AMBER. The colored lines give the model results (color coding the same as Fig. 1). The bottom right panel shows the VISIR FWHM as a function of wavelength (black line is the model).

MIDI. The N-band correlated flux obtained by MIDI has an error on the absolute calibration of approximately 10%, similar to the difference with the model output. Thus our modeling of the spatial distribution of the small dust grains is consistent with the MIDI result.

AMBER. The simple flat ring+point-source model of Sect. 4.1 actually reproduced the inclination, position angle and

visibilities of the disk very well, although the inner rim radius (0.37 AU) is significantly below the 0.55 AU of our final model. Our more physical final model gives a slightly poorer fit to the visibilities. This indicates that the structure of the inner disk is more complicated than assumed. The exact structure is currently much debated (see Sect. 6.2).

VISIR spectrum. The model FWHM was obtained by making a Gaussian fit to the spatial profile after convolving the model with a Gaussian of the same width as the PSF of the VISIR 11.2 μm setting. The VISIR 8.5 μm setting was then scaled to the model assuming a variable seeing that can be quadratically added. The matching continuum levels are thus a result of our method, but the increase in the FWHM at the PAH wavelengths are a confirmation of the correct modeling of the spatial distribution of the PAHs.

VISIR image. A model of the Q2 image was obtained by taking the output of our model at 19.0 μm, just next to the artificial PAH feature. We convolved this model image with the VISIR PSF and we applied a PSF subtraction in analogy to the image analysis of Sect. 4.4. The resolved emission component of Fig. 5 is not reproduced by the model. A likely explanation for this is the photoluminescence of very small grains, which are not included in our model (see Flagey et al. 2006).

6.2. The distribution of gas and dust

Our modeling reveals that the spatial distribution of the gas and the dust in the disk around HD 95881 is different. The dust in the upper layers of the outer disk is heavily depleted, while the gas still has a large scale height. To reproduce the near IR flux we needed to assume a scale height, which is much larger than would be obtained from vertical hydrostatic equilibrium (Φ = 2.75). We do not have an explanation for this, but we note that the value of Φ is sensitive to the assumptions on the structure and composition of the material in the inner disk (see e.g. Isella et al., 2008; Tannirkulam et al., 2008a). Furthermore, our value is well within the range of scaling parameters (1.0-3.0) needed by Acke et al. (in prep.) to explain the near IR SED of about half of their sample of ~30 Herbig Ae/Be stars.

The spatial distribution of the small grain component was well constrained by the SED. The large grains could not be constrained directly, but are probably abundantly present in a settled outer disk. Observations of the millimeter flux will help to constrain the mass in this component as well as the size distribution. We can however make an estimate of the total dust mass, based on the modeled total PAH mass ($5{\cdot}10^{-9}$ $M_\odot$) and the modeled PAH abundance at the inner edge (0.25%). Assuming that the PAH to dust ratio is homogeneous throughout the disk we find that the total dust mass adds up to $2{\cdot}10^{-6}$ $M_\odot$. This means that most of the dust mass resides in large grains (200:1). Using the canonical gas to dust ratio of 100 the total disk mass becomes $2{\cdot}10^{-4}$ $M_\odot$. Note, that with a lower value of Φ in the outer disk a larger gas mass could be required to reproduce the observations.

The results presented above naturally lead to the picture of a disk in which the dust grains in the outer disk are coagulated and settled towards the midplane, while the gas is still available to keep the PAH molecules in the higher atmosphere of the disk. As already noted in the theoretical study by Dullemond et al. (2007), growth and settling of the dust grains leads to a natural increase of the relative strength of the PAH signature, as is observed in this disk and confirmed by our modeling effort.

6.3. Context

In general the study of Dullemond et al. (2007) showed that the natural outcome of a group I source after grain-growth and sedimentation of the dust is a group II source, that maintains the flaring structure for the gas. However, observational studies have shown that most group II sources lack a flaring gas distribution. Meeus et al. (2001) and Acke et al. (2004) showed that group I sources display significantly more PAH emission. Acke et al. (2005) showed that group I sources have in general stronger [O I] emission. Apparently the gas of most group II sources has either dramatically decreased its scale height because of the lack of heating or the gas has been dispersed from the disk. How disks can lose their gas is currently being debated (see Hillenbrand 2008), but photoevaporation seems to be the most likely mechanism.

On the other hand there is a fair number of group II sources that do show indications of a flaring gas distribution. Some group II sources display PAH emission in their 10 μm spectra, for example: HK Ori (van Boekel et al. 2005) and HD 142666 (Verhoeff et al. submitted to A&A). Some group II sources display the [O I] 6300 Å line in emission, for example: HD 98922 (Acke et al. 2005) and HD 101412 (Fedele et al. 2008). These sources all seem to be in a transitional phase from a gas rich flaring disk to a gas poor self-shadowed disk. Roughly half of the known group II sources are in this phase, which means we can infer that half of the life time of the disk of a group II source is spent on the dispersal of the gas. An estimation for this time scale is the photoevaporation time scale, which is on the order of $\sim 10^6$ yr (Gorti & Hollenbach 2009)

6.4. PAH emission

In Sect. 4.3 it was noted that the PAH spectrum of HD 95881 is typical for HAe stars, except for the 8.6 μm feature, which is relatively strong. This feature is created by the in-plane bending mode of the CH bonds. Why the emission from this mode should be preferred in HD 95881 is unclear. However we can think of a scenario in which the disks are eroded from the outside inward. Such a truncation process decreases the integrated PAH feature strength. An indication for this was found in the mild correlation between 11.2 μm PAH strength and its FWHM (Verhoeff et al. submitted to A&A). Putting this together with modeling results of Visser et al. (2007), who show that short wavelength features originate from regions closer to the star than long wavelength features, we are left to think that the amount of truncation is apparently favoring the 8.6 μm feature.

7. Conclusions

A comprehensive study was performed to map the distribution of the gas and dust in the protoplanetary disk around HD 95881. In Fig. 10 we displayed a schematic representation of the disk, which puts all results in perspective. The AMBER K-band interferometry showed that there is an extended hot inner region with emission coming from within the sublimation radius. The detection of the [O I] 6300 Å indicated that the disk has a flaring gas surface at large distances (from one to tens of AU) from the star. The finding of PAH features in the Spitzer and VISIR spectra confirmed the presence of an illuminated gas surface. The resolved VISIR spectrum traced this surface up to radii of ~70 AU. The MIDI correlated flux spectrum confirmed that the PAH emission comes from much larger radii than ~2 AU. The MIDI spectrum also showed that the silicate composition is quite

similar in the inner and outer disk. In the Q-band, VISIR imaging revealed faint dust emission at radii upto ∼150 AU, most likely due to very small grains.

We used the radiative transfer code MCMax (Min et al. 2009) to create a model of the disk's density and temperature structure. Our model satisfactorily reproduced all of our observations. The main conclusions that followed from our model are that the inner disk contains most of the small grains and has a puffed up inner rim, the dust grains in the outer disk have coagulated and settled towards the midplane, while the gas and PAH mixture maintain a flaring geometry. Theory predicted the existence of these type of disks (Dullemond et al. 2007), while observational trends showed that most of the sources with self-shadowed dust distributions have dispersed their gas. In this light HD 95881 is a special source: it is in the transition phase from a gas rich flaring dust disk to a gas poor self-shadowed disk.

Acknowledgements. This research was sponsored by NWO under grant number C.2320.0020. M. Min acknowledges financial support from the Netherlands Organization for Scientific Research (NWO) through a Veni grant. E. Pantin acknowledges financial support from the Agence Nationale de la Recherche (ANR) of France through contract ANR-07-BLAN-0221.

References

Acke, B. & van den Ancker, M. E. 2004, A&A, 426, 151
Acke, B., van den Ancker, M. E., & Dullemond, C. P. 2005, A&A, 436, 209
Acke, B., van den Ancker, M. E., Dullemond, C. P., van Boekel, R., & Waters, L. B. F. M. 2004, A&A, 422, 621
Acke, B., Verhoelst, T., van den Ancker, M. E., et al. 2008, A&A, 485, 209
de Zeeuw, P. T., Hoogerwerf, R., de Bruijne, J. H. J., Brown, A. G. A., & Blaauw, A. 1999, AJ, 117, 354
Draine, B. T. & Li, A. 2001, ApJ, 551, 807
Dullemond, C. P., Apai, D., & Walch, S. 2006, ApJ, 640, L67
Dullemond, C. P. & Dominik, C. 2004, A&A, 417, 159
Dullemond, C. P., Dominik, C., & Natta, A. 2001, ApJ, 560, 957
Dullemond, C. P., Henning, T., Visser, R., et al. 2007, A&A, 473, 457
Eisner, J. A., Chiang, E. I., Lane, B. F., & Akeson, R. L. 2007, ApJ, 657, 347
Eisner, J. A., Lane, B. F., Hillenbrand, L. A., Akeson, R. L., & Sargent, A. I. 2004, ApJ, 613, 1049
Fedele, D., van den Ancker, M. E., Acke, B., et al. 2008, A&A, 491, 809
Flagey, N., Boulanger, F., Verstraete, L., et al. 2006, A&A, 453, 969
Geers, V. C., van Dishoeck, E. F., Visser, R., et al. 2007, A&A, 476, 279
Gorti, U. & Hollenbach, D. 2009, ApJ, 690, 1539
Guhathakurta, P. & Draine, B. T. 1989, ApJ, 345, 230
Hillenbrand, L. A. 2008, ArXiv e-prints, 805
Houk, N. & Cowley, A. P. 1975, Michigan Catalogue of two-dimensional spectral types for the HD star (Ann Arbor: University of Michigan, Departement of Astronomy, 1975)
Hughes, A. M., Wilner, D. J., Qi, C., & Hogerheijde, M. R. 2008, ApJ, 678, 1119
Isella, A., Tatulli, E., Natta, A., & Testi, L. 2008, A&A, 483, L13
Kraus, S., Preibisch, T., & Ohnaka, K. 2008, ApJ, 676, 490
Lagage, P.-O., Doucet, C., Pantin, E., et al. 2006, Science, 314, 621
Lagage, P. O., Pel, J. W., Authier, M., et al. 2004, The Messenger, 117, 12
Leinert, C., Graser, U., Waters, L. B. F. M., et al. 2003, in Interferometry for Optical Astronomy II. Edited by Wesley A. Traub . Proceedings of the SPIE, Volume 4838, pp. 893-904 (2003)., ed. W. A. Traub, 893–904
Leinert, C., van Boekel, R., Waters, L. B. F. M., et al. 2004, A&A, 423, 537
Meeus, G., Waters, L. B. F. M., Bouwman, J., et al. 2001, A&A, 365, 476
Meynet, G., Maeder, A., Schaller, G., Schaerer, D., & Charbonnel, C. 1994, A&AS, 103, 97
Min, M., Dullemond, C. P., Dominik, C., de Koter, A., & Hovenier, J. W. 2009, ArXiv e-prints
Min, M., Hovenier, J. W., & de Koter, A. 2005, A&A, 432, 909
Pantin, E., Doucet, C., Käufl, H. U., et al. 2008, in Society of Photo-Optical Instrumentation Engineers (SPIE) Conference Series, Vol. 7014, Society of Photo-Optical Instrumentation Engineers (SPIE) Conference Series
Pantin, E., Siebenmorgen, R., Käufl, H. U., & Sterzik, M. 2009, in Science with the VLT in the ELT Era, ed. A. Moorwood, 261–+
Preibisch, T., Ossenkopf, V., Yorke, H. W., & Henning, T. 1993, A&A, 279, 577
Siebenmorgen, R., Kruegel, E., & Mathis, J. S. 1992, A&A, 266, 501
Tannirkulam, A., Monnier, J. D., Harries, T. J., et al. 2008a, ApJ, 689, 513
Tannirkulam, A., Monnier, J. D., Millan-Gabet, R., et al. 2008b, ApJ, 677, L51
Tatulli, E., Millour, F., Chelli, A., et al. 2007, A&A, 464, 29
van Boekel, R., Min, M., Waters, L. B. F. M., et al. 2005, A&A, 437, 189
van Boekel, R., Waters, L. B. F. M., Dominik, C., et al. 2004, A&A, 418, 177
Visser, R., Geers, V. C., Dullemond, C. P., et al. 2007, A&A, 466, 229

Chapter 5

Low-mass companions

Résumé

Les companions de faible masse, comme par exemple les planètes, se forment dans les disques circumstellaires. Il est donc important d'obtenir des contraintes observationnelles sur leur présence autour d'étoiles. Inversement, la présence de companions massifs (planètes géantes ou naines brunes) dans un disque peut avoir une très forte influence sur sa structure. Ce genre d'étude requiert donc d'arriver à détecter de tels companions. Les instruments modernes à haute résolution angulaire sont suffisamment puissants pour obtenir des images directes de tels companions. Ce chapitre décrit les campagnes et les résultats d'observations avec le systême d'optique adaptative ADONIS du télescope de 3.56 m de l'ESO (La Silla) ainsi qu'un résultat de l'instrument VLT/VISIR concernant un systême binaire de très faibles masses, ϵ Indi b.

Abstract

Low-mass companions such as planets form in circumstellar disks, hence the study in the chapter 4 to better the physical conditions in which these low-mass companions form. Inversely, it is also interesting to study the influence of low-mass companions with masses up to the brown dwarf regime onto the structure of the disks. This type of study requires first to be able to detect such companions and then assess their characteristics. Modern observing high angular resolution instruments are powerful enough to directly image such companions. This chapter reports the campaigns of observations and the results obtained with the ADONIS adaptive optics system on the ESO 3.6m telescope and the study of a binary brown dwarf system which forms a companion to the ϵ Indi star.

Contents

5.1 GL 86

5.1.1 Context

The first exoplanet has been discovered in 1995 by Mayor and Queloz by the method of radial velocities. In 2001 a large number (∼100) of sub-stellar companions had already be detected by the same method. A key question concerning the debris disks is whether their occurrence is linked or not to the presence/ absence of giant planets. In this context, we have selected a set of targets with known giant planetary companions to be observed using the ADONIS adaptive optics system in combination with the SHARP II+ instrument. The aim was to detect the eventual presence of dusty debris disks which could not have been detected by IRAS (infrared excess) if the disks are relatively depleted of matter in the inner regions.

5.1.2 Observations and results

The GL86 is a system located at 11 pc away from Earth. The observations were conducted in J, H, K broadband filters which are available in SHARPII+. Each band has its own advantages : the J band provides the best sensitivity (M_{lim}=20.6) and sharpness but at low Strehl ratio (≈10%), K band provides higher Strehl ratii (≈30%) and is better suited for red objects, but is intrinsically less sensitive (limiting magnitude ≈ 20). H band represents a compromise between J and K bands properties. A pre-focal coronagraph device has been used to suppress the starlight. The size of the occulting mask was 1 arcsec in diameter.

No debris disk was detected around GL86, down to limiting magnitudes varying between $m_H = 13$ and $m_H = 16$ at a distance of 1 arcsec (11 AU) and 2 arcsec (22 AU) respectively. However a sub-stellar companion has been serendipitously discovered at a projected distance of 1.72 arcsec from the star. Since GL96 is a high proper-motion star, this object has been confirmed as gravitationally bound to GL86 by using measurements obtained at different epochs. This object has measured magnitudes of $m_J = 14.7\pm0.2$, $m_H = 14.4\pm0.2$, and $m_K = 13.7\pm0.2$. This object is thus "red"; comparisons with models of brown dwarves ([Burrows et al., 1997, Chabrier et al., 2000]) lead us to conclude that this object is a brown dwarf in the L to T transition regime with an effective temperature of ∼1300 K and a mass in the range 40 to 70 Jupiter masses (5.4).

5.1.3 Perspectives

Further observations are needed to confirm the status of L-T dwarf of GL86B. Spectroscopic observations would be much more informative in that respect. An observing technique called "spectroscopic deconvolution" seems very attractive [Thatte et al., 2007] to detect faint companions around bright stars. In this mode, multi-spectral diffraction-limited observations are performed using an integral field unit spectrograph which provides simultaneously spatial (but restricted to narrow field) and spectral information. The primary star and the companion contributions can be disentangled thanks to a different behavior as a function of the wavelength. The spatial scale of the structures belonging to the primary star scale linearly with the wavelength (diffraction) while the companion "stays" at a fixed distance to the primary. A systematic geometric rescaling of the data allows to separate more easily the companion. This type of method has been already performed using the ESO VLT/SINFONI instrument fed by adaptive optics.

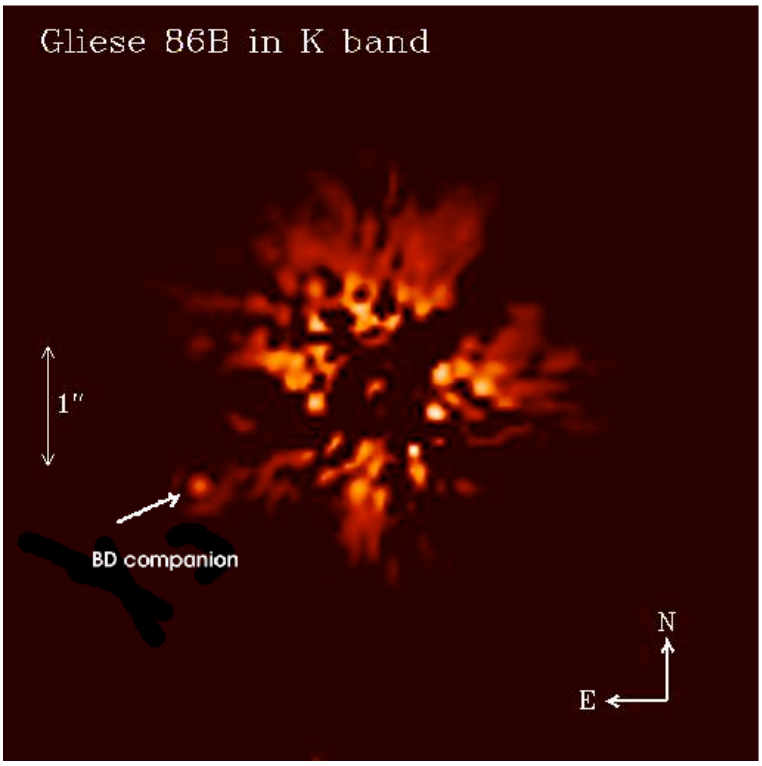

Figure 5.1: K band image of the GL96 system. A coronagraphic device is used to suppress the starlight; its diameter is 1 arcsec

5.2 Sirius

5.2.1 Context

Sirius is the brightest star of the sky (V=-1.45). It has thus played a major role among various people along the mankind history. It has been particularly observed over centuries by the Dogon tribu (Mali, west africa) or Chinese astronomers. A striking fact is that both report temporary reddenings along History. However, Sirius is a main-sequence A0-type star which has no physical reason to change of color so suddenly and recover its blue color afterwards. It is now established since 1844 (Bessel) that Sirius has a white dwarf companion which presence has been first detected by means of astrometric measurements. A third companion was suspected on the basis of periodic residuals (≈6 yr) noticed in the A-B binary orbit [Benest and Duvent, 1995]. The presence of a third interacting companion on an eccentric orbit was also put forward to explain the historical changes of color of Sirius [Gry and Bonnet-Bidaud, 1990].

5.2.2 Observations and results

Following large scale coronagraphic observations obtained by [Bonnet-Bidaud et al., 2000], which discarded the presence of a companion of mass larger than 0.08 $M_\odot$ at distances larger than 30 arcsec from the star, we persued the quest using the ADONIS adaptive optics system mounted on the 3.6m ESO telescope, in combination with the SHARPII+ near-infrared camera used in coronagraphic mode to reduce the intense blooming produced by Sirius A. The use of an adaptative optics system allowed us

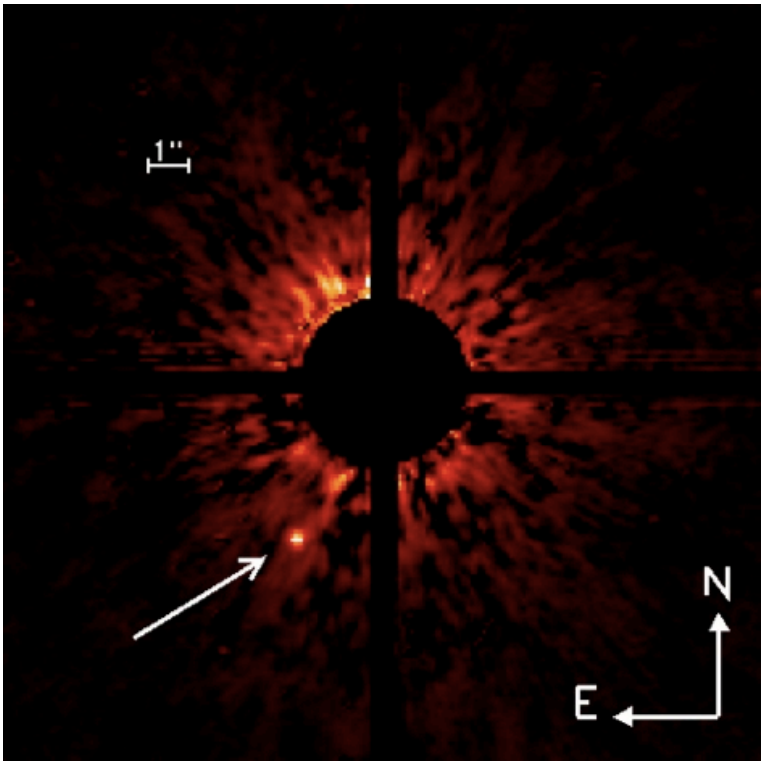

Figure 5.2: Image of the surroundings of Sirius in K_s band. The instrument Sharp II+ combined with a Lyot coronagraph with an occulting spot of 3 arcsec in diameter has been used. The inner 6 arcsec (diameter) have been numerically masked for clarity. The white arrow points to the white dwarf companion Sirius-B.

to significantly improve the lower limits on a possible companion. Two campains of observations were conducted in January 2000 and January 2001. We observed Sirius in J, H, and K_s filters, each one having its particular properties of sensitivity to a companion and sharpness. The result is that no only there is no low-mass stellar or sub-stellar companion in the regions outside of the coronographic mask, but we could also get some upper limits on putative planetary companions at distances larger than $\sim$ (e.g. 10 Jupiter masses at 10 arcsec (26.3 AU) from the star). On top of that, thanks to these very first precise near-infrared photometric measurements of the white dwarf Sirius-B, we found that an infrared excess is marginally detected in K_s band, which could indicate the presence of warm dust around the white dwarf. These results are reported in annex 5.4.

5.2.3 Perspectives

Sirius remains a very interesting target to search for planets around a close-by early type star. Radial velocities method does not reach the level of accuracy it achieves on later F-G-K stars because of the lack lines and mismatch between object and synthetic spectra ([Verschueren et al., 1999]). Therefore Sirius remains because of its short distance to Earth (thus a larger separation between primary and companions, at a constant contrast ratio) a privileged target for planet direct detection. Here again, observations based on spectroscopic deconvolution should be for instance well adapted to planet search around Sirius.

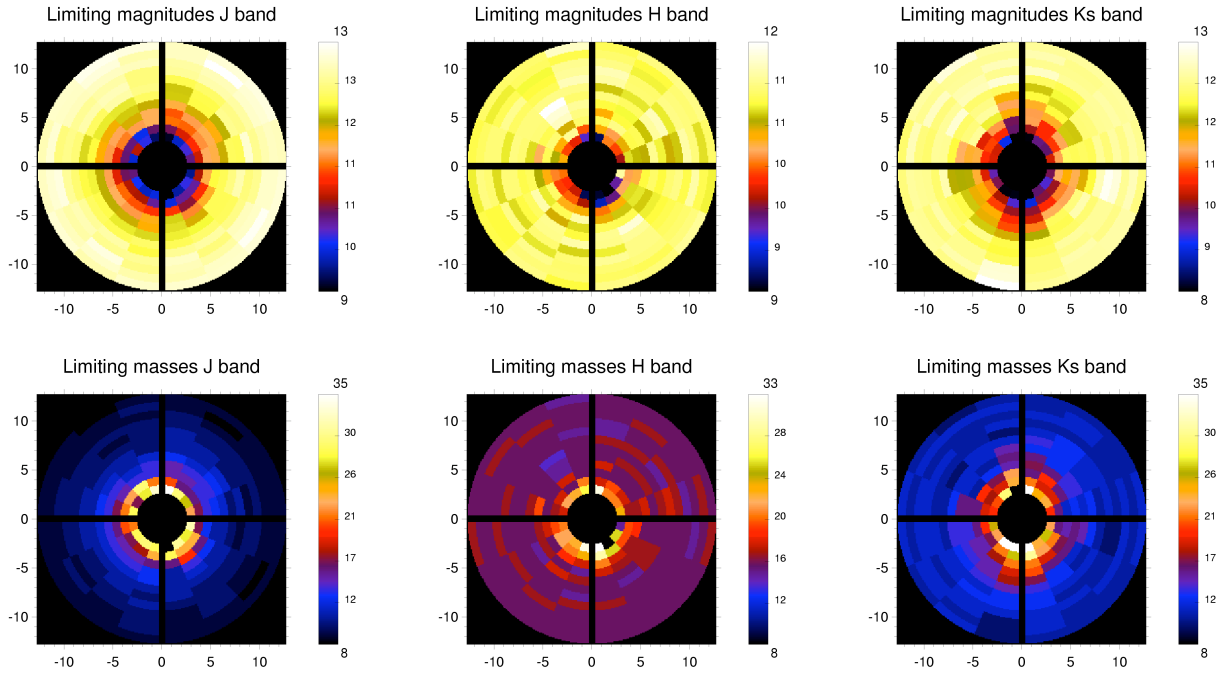

Figure 5.3: Upper panel: maps of the limiting magnitudes for companion detection in J, H, and K_s bands. Lower panel: the magnitudes have been converted into mass limits of brown dwarves of giant exoplanets using [Burrows et al., 1997] models. The best constraints concerning the giant exoplanets come from the J band map because they present an prominent emission feature around 1.25 µm (see Fig.5.4).

5.3 the Eps Indi B binary brown dwarf

5.3.1 Context

Up to 1995, the brown dwarfs were objects which existence was supposed when interpolating the mass distribution function between stars (0.07 $M_\odot$for pop.I) and massive giant planets (10 M_j). It was known from the theoretical works on stellar structure and evolution that these very-low mass objects would not have the required minimum mass to sustain hydrogen fusion. Their energy is produced by lithium burning down to 65 M_j (0.065 $M_\odot$) and deuterium fusion down to the brown dwarf limit range of 13 Jupiter masses. The presence of lithium is a key test to distinguish between a star and a brown dwarf since stars burn their (primordial) lithium in a little over 100 Myr while brown dwarfs will never acquire high enough core temperatures to do so. The brown dwarf sub-stellar type is divided into two categories : L dwarfs have effective temperatures in the range [1600-2200] K and show alkali metals and strong metal hydride features in the spectrum; T ones have an effective temperature in the range [500-1600] K and display methane absorption bands in their spectra. The L-T transition regime might be associated to dust settling in the atmosphere. Theoretical models of brown dwarfs ([Burrows et al., 2003]) predict also two situations : cloudy (similarly to giant planets) and cloud-free atmospheres. In the first case this means that full meteorological system exists in their atmosphere. This could explain the infrared photometric variations observed in some cases. We know now that brown dwarfs, alike the stars, have sometimes circumstellar disks (although probably less massive) which characteristics share numerous similarities with protoplanetary disks around stars : flattened or flaring geometries, amorphous or more crystalline

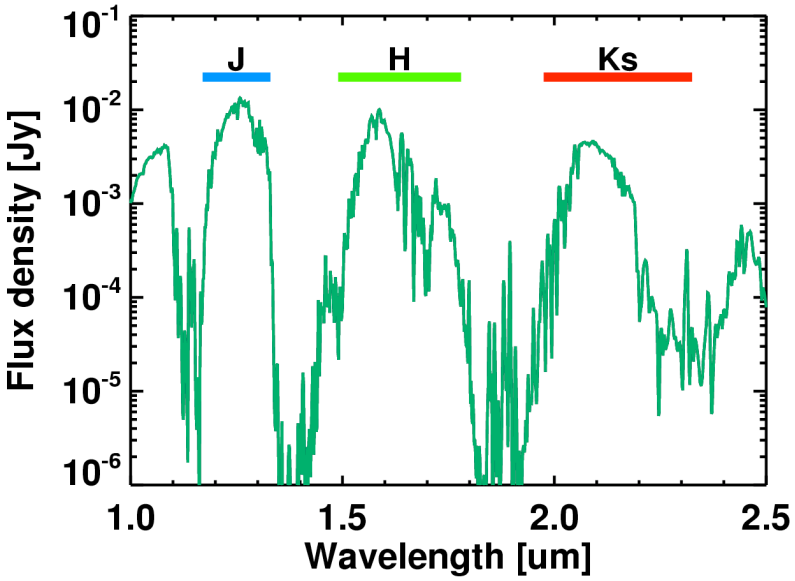

Figure 5.4: Near-infrared spectrum of a 10 M_j 300 Myr old giant exoplanet. The band-passes of the J, H, and K_S filters are indicated by the colored rectangles. A prominent feature covers the J filter which explains the better sensitivities limits in mass obtained in this filter.

silicates, etc...
In the 90's and the avent of sensitive near-infrared cameras, an efficient quest could be conducted and led to the discovery of the first T-type brown dwarf was discovered ([Nakajima et al., 1995]) around Gliese 229. Since then, hundreds of brown dwarfs have been identified. Among the closest to Earth is found the Eps Indi B system ([Scholz et al., 2003]). At a distance of only 3.63 pc, it features two T-type brown dwarfs separated by only 2.1 AU, at a distance of 1500 AU from the primary star.

5.3.2 Observations and results

The brown dwarfs emit most of their flux in the infrared range. Mid-infrared observations are particularly well suited to study this category of objects and characterize them. On top of that, mid-infrared observations are also an efficient tool to detect the presence of a circumstellar dust disk which presence would be betrayed by an excess in the mid and far infrared range. We have conducted a campaign of mid-infrared observations using VISIR in imaging mode. VISIR, unlike the more sensitive SPITZER observatory, is able to spatially separate the two brown dwarf components (separation of 0.8 arcsec) and study their characteristics individually. Photometric measurements were performed in the N band in the PAH1 (8.6 µm), SIV (10.4 µm), PAH2 (11.25 µm), NeII (12.8 µm) and NeII_2 (13.2 µm) filters. However, given their intrinsic weak luminosity, their fluxes ($\approx$ 6 and 12 mJy) are close to the limits in sensitivity of the VISIR instrument. Therefore, a particular care had to be taken to the data reduction and even though, some of the datasets had to be discarded because of too low quality. The results of a first campaign of observations are presented in the article in 5.4. In particular, the photometric measurements allowed us to probe the NH_3 feature for each component independently and better determine their characteristics. We compared our observations with theoretical modeling of atmospheric emission

([Burrows et al., 2003],[Baraffe et al., 2003]) and found that ϵ Indi Bb is in good agreement with cloud-free models and an effective temperature of 800 K while component Ba has a slightly higher effective temperature of 1100 K. The spectral type are in agreement with the T1 and T6 respectively previously estimated by [McCaughrean et al., 2004].
We have conducted a follow-up of observations using VISIR in order to test the variability of mid-infrared emission and particularly that of the NH_3 feature. This requires a much better precision since we aim at detecting typical 10 % variations of the emission. The simple method of optimal filtering that was developed for the first article is not accurate enough for this goal. VISIR data have relatively large errors at large spatials scales (see Sec.3.3) caused probably by a too slow chopper frequency. The photometric precision on a faint source depends critically how accurately the residual underlying background can be measured. This background in the case of VISIR is not flat but presents large amplitude variations which reduce dramatically the photometric accuracy achievable; this effect is even more pronounced in the case of extended sources. The method of background reconstruction presented in Sec.3.3.1 improves significantly the photometric accuracy (by a factor of $\sim$2 when the error is dominated by these background errors), but not enough given the goal of 10%. Since the excess of noise is mainly located a low spatial frequencies, I developed a new method based on wavelets filtering. The image is first decomposed in frequency bands using wavelets decomposition (A Trous algorithm). The wavelet planes corresponding to the lower spatial frequencies (3 and beyond) are suppressed and an image is reconstructed using the remaining higher frequencies. The two point sources are only moderately affected by the frequencies suppression while the spurious background is considerably reduced. This methods is only suited unfortunately to **point sources** for which the modification of the photometry can be controlled (calibrated) using the same method on a standard star. The photometric error after applying this method has been assessed using a bootstrap method on the data in which a known point source is artificially placed. The photometric error as a function of the source peak signal-to-noise ratio is evaluated from Fig.3.17 (see chapter 3).
Since the measured magnitudes in the N band are in agreement (within 20%) with the ones estimated from near-infrared observations, we can also conclude that any putative circumstellar dust disk would have to be more massive than 10^{10} of lunar masses to be detected in the N band.
The results described above were published in a article published in the review *A&A* (see annex 5.4).

5.3.3 Perspectives

We have now collected several VISIR observations at various epochs of the ϵ Indi b system. The photometric measurements show unexpected variations, especially in the SIV filter (10.4 μm, hence the NH_3 emission), that could reflect intrinsic variability of the brown dwarf eventually due to the presence of clouds in the photosphere. In collaboration with M.Sterzik (ESO, Chile) and K.Geibler we are investigating this possibility also on other brown dwarves.

5.4 Conclusions

I have presented in this chapter a set of observational results dealing with the search and the characterization of low-mass companions around main-sequence stars and the possible link with the presence of a dusty disk. In the case of the Gliese 86 system we did not find any evidence for a dusty disk but we discovered a low-mass companion that we identified as a brown dwarf. This observation is one the very few ones of a brown dwarf at the transition between the L and T type. In the case of Sirius, the detection limits that we achieved after a careful analysis allowed to go down to the giant planet regime. No evidence for the presence of a giant planet more massive than 10 Jupiter masses at projected distances larger than 25 AU was found. Finally, we have studied with VISIR N band observations the peculiar brown dwarf binary system which is itself a companion of the ϵ Indi main sequence star. These spatially

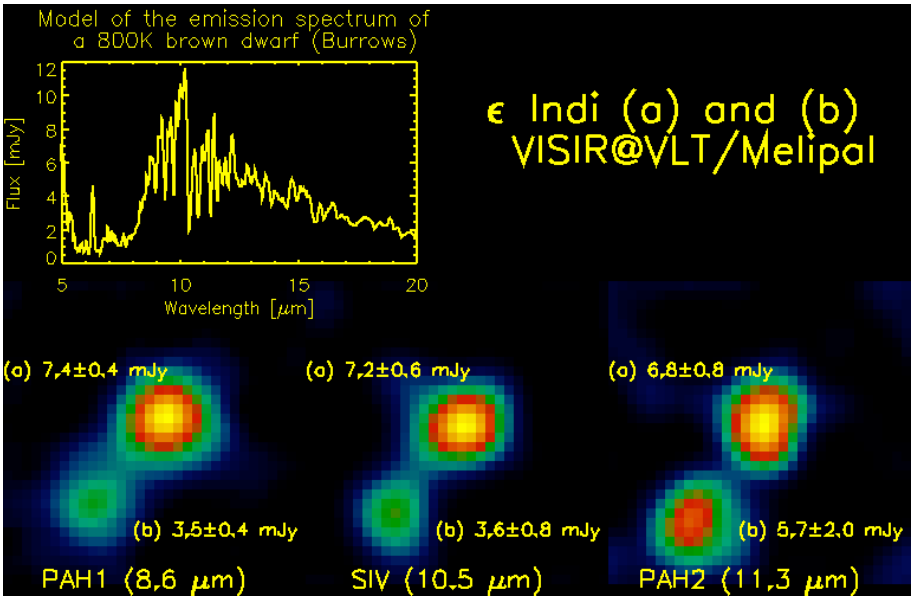

Figure 5.5: VISIR observations of the ϵ Indi B binary brown dwarf in several N-band filters. Upper panel shows a model ([Burrows et al., 2003] of emission of the b component.

resolved observations of the two components have allowed us to put some relatively tight constraints on the spectral type and the effective temperature of each component.
The search for sub-stellar companions is a expanding field which produces more and more results each year. The first generation of high angular resolution facilities based on adaptive optics will be soon replaced by very performant and optimized instruments (e.g. the VLT/SPHERE project, [Beuzit et al., 2008]) . These facilities specialized in in the detection of faint companions will produce in the beginning decade some full surveys of nearby stars that will undoubtly bring their quotas of new discoveries and surprises. In parallel, with the on-going projects of Extremely Large Telescopes, the ground-based mid-infrared observations will combine after 2018 both extreme point sources sensitivities (S$\leq$50 μJy) and angular resolutions better than 0.1 arcsec. Under such conditions it will be possible to characterize the companions found by the near-infrared/adaptative optics facilities. These perspectives are evaluated in the next chapter.

Related articles

Annex :

A second substellar companion in the Gliese 86 system. A brown dwarf in an extrasolar planetary system.

published in the journal *A&A*, April 2001

A&A 370, L1–L4 (2001)
DOI: 10.1051/0004-6361:20010298
© ESO 2001

Astronomy & Astrophysics

Letter to the Editor

A second substellar companion in the Gliese 86 system⋆

A brown dwarf in an extrasolar planetary system

S. G. Els[1,6], M. F. Sterzik[2], F. Marchis[3], E. Pantin[4], M. Endl[5], and M. Kürster[2]

[1] Thüringer Landessternwarte Tautenburg, Sternwarte 5, 07778 Tautenburg, Germany
[2] European Southern Observatory, Casilla 19001, Santiago 19, Chile
[3] University of California Berkeley/Center for Adaptive Optics, 601 Campbell Hall, Berkeley, CA 94720, USA
[4] DSM/DANIA/Service d'Astrophysique, CEA/Saclay, 91191 Gif-sur-Yvette, France
[5] Institut für Astronomie, Universität Wien, Türkenschanzstr. 17, 1180 Wien, Austria
[6] Universität Heidelberg, Institut für Theoretische Astrophysik, Tiergartenstr. 15, 69121 Heidelberg, Germany

Received 1 February 2001 / Accepted 22 February 2001

Abstract. We report observations using the ESO adaptive optics system ADONIS of the known extrasolar planetary system Gliese 86. This star has a known 4 $M_{\rm Jup} \sin i$ planet in a 15.8 day orbit and exhibits an additional, large, long-period, radial velocity drift (Queloz et al. 2000). The coronographic images reveal a faint ($J = 14.7, H = 14.4, K = 13.7$) object at a projected distance of $r = 1\farcs72 \pm 0\farcs02$ and PA $= 119 \pm 1°$. Gliese 86 and the discovered object share the same proper motion, as confirmed by independent measurements at three different epochs indicating that this system is gravitationally bound. From the infrared colors and magnitudes we infer an approximate spectral type for Gliese 86B at the transition from L to T dwarfs, also called "early T dwarf" assuming the classification by Leggett et al. (2000). Although present brown dwarf evolutionary models do not cover the mass and age range probed by this objects, an upper limit of the mass of about $M_{\rm GJ86B} \leq 70\ M_{\rm Jup}$ can be inferred from the models by Baraffe et al. (1998). Dusty model atmospheres appear not to be compatible with the IR colors.

Key words. stars: individual: Gliese 86 – stars: brown dwarfs – planetary systems

1. Introduction

Among the more than 50 extrasolar planetary systems inferred so far from high precision radial velocity surveys (e.g. Marcy et al. 2000) is the signature of a planetary companion with a minimum mass of 4 $M_{\rm Jup} \sin i$ in a 15.8 days period orbit around the K dwarf Gliese 86 (or Gl 86) (see Queloz et al. 2000).

The radial velocity data measured over the last 20 years do not only show the variation due to the planetary companion, but also exhibit a large, long term, drift of about 0.3 to 0.5 $\rm ms^{-1}\,day^{-1}$. The combination of these measurements with historical data led to the suspicion that Gl 86 has an additional companion in an orbit with a semi major axis larger than 20 AU. As the distance of Gl 86 is only 10.9 pc towards the sun, direct imaging of such a companion seems worthwhile. As reported in a poster by Sterzik, Marchis & Kürster (unpublished) the ESO adaptive optics system ADONIS was used to search for a companion close to Gl 86 but without success. Their sensitivity estimate in K band excluded any stellar companion earlier than M6 further then 1.″0 from Gl 86.

In this Letter we report on new, high angular resolution, adaptive optics observations of Gl 86 leading to the detection of another substellar companion in this extrasolar planetary system.

2. Observations and data reduction

We observed the Gl 86 system with ESO's adaptive optics system ADONIS (Rousset & Beuzit 1999), mounted on the 3.6 m telescope on La Silla, Chile. The SHARP II+ near infrared camera was attached to the instrument and a pixel scale of 50 mas/pixel was used throughout all observations. In order to increase the sensitivity to detect any faint, closeby companion, the light of Gl 86 was suppressed by a pre–focal coronographic mask (Beuzit et al. 1997). For all observations a mask with a size of 1″ in diameter was chosen. Usually, we took cubes containing 60 images of Gl 86 with 6 s of integration time each. Sky emission was corrected by observing a position 1.′5 north and south of Gl 86 immediately after the prime scientific target.

Send offprint requests to: S. G. Els,
e-mail: sels@kso.tls-tautenburg.de

⋆ Based on observations collected with the 3.6 m Telescope of the European Southern Observatory La Silla under proposal Nos. 66.C-0333, 266.C-5621 and 266.C-5634.

A brief observing log is given in Table 1.

For further data processing we got references of the Point–Spread–Function (PSF) by observing the star HD 13424 directly before or after each integration of Gl 86 (during the observations in September we observed an additional PSF reference star, namely HD 14112).

For the observing runs in November and December, the detector pixel scale and the absolute orientation of the camera were checked observing an astrometric reference field (θ Ori). The accuracy of the absolute field orientation is found better than 0.2°, fully consistent with systematic measurements taken over more than a year[1].

In general, the atmospheric conditions during our observations were good. Seeing conditions were always better than 1.″2 and in average around 0.″8. All observations were taken with an airmass of less than 1.5 except for the observations in December which were taken at an airmass of about 1.6. As photometric standard star we usually observed HR 0721. In the night of November 10, AS01 was observed as photometric standard star. The zero–points derived from the standard stars agree with the published values within 0.05 mag [2].

Table 1. Observing log for Gl 86. A coronographic mask with 1.″ in diameter was always used. For each filter setting, one data cube was acquired, except in the September night, when 5 independent measurements were performed

Date	filters used	remarks
08.09.2000	H	5 independent measurements
10.11.2000	J K	
11.11.2000	J K K_S	
13.11.2000	K_S	
12.12.2000	CVF	$\lambda = 1.51, 1.57$ and 1.61 μm

3. Results

After the standard reduction process (sky substraction, flatfielding and bad pixel removal), we applied an optimum PSF–substraction technique developed by Pantin et al. (2000). A faint object is located in the east direction of Gl 86 (see Fig. 1) and can already be seen in the non-PSF substracted images. But applying the PSF subtraction technique it is much easier to identify, because the residual light in the wings of the coronographic image of Gl 86 is efficiently reduced.

3.1. Astrometry

Gl 86 is a high proper motion star with $\mu_\alpha^* = 2092.7$ mas/yr and $\mu_\delta = 654.8$ mas/yr as measured by Hipparcos. We would therefore expect the object to move 9.08 mas/day in western and 1.79 mas/day in southern direction relative to Gl 86 if it is an unrelated background star. The high proper motion of this star enables therefore to check for the binding status within the relatively short time baseline of three months.

[1] see: http://www.bdl.fr/priam/adonis/

[2] see: http://www.ls.eso.org/lasilla/Telescopes/360cat/adonis/html/Table_Photometry_SHARP.html

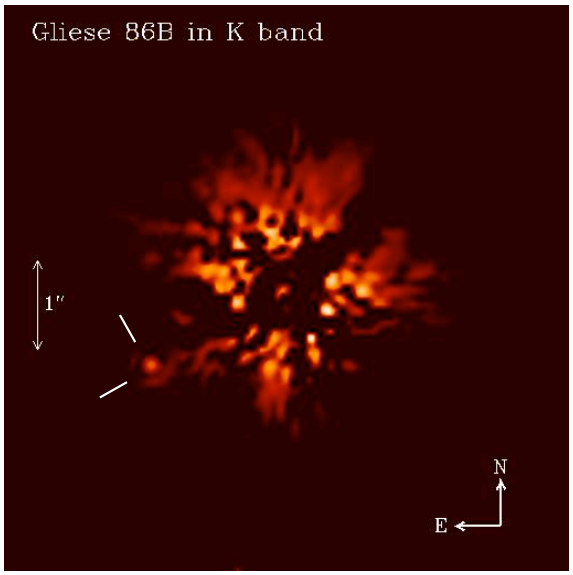

Fig. 1. Gl 86 in K band after applying the optimum PSF subtraction of Pantin et al. (2000). The PSF reference star HD 13424 was observed about 20 min after Gl 86. The total integration time on Gl 86 and on HD 13424 was 6 min each. The found companion is located between the two bars. Note also the *Airy ring* around the companion

We define the position of Gl 86 by fitting circular isophotes to the non PSF subtracted, coronographic, image. The center of the circle is determined at different isophot values, and agrees well within an error of less than about half a pixel size (i.e. $\leq$0.″025). The position of the faint object is then easily found relative to this central position by fitting a Gaussian to it in the PSF subtracted image.

Applying this procedure to our datasets we find that the distance between Gl 86 and the faint object does not change significantly during our time baseline (see Table 2). We conclude that this object is indeed a gravitationaly bound companion to Gl 86 at a projected distance of

Table 2. Astrometric data of the detected object relative to Gl 86. The first column shows the date of observation, the $\Delta\alpha$ and $\Delta\delta$ denote the *measured* offsets in right ascention and declination of the companion relative to Gl 86. $\Delta\alpha^*$ and $\Delta\delta^*$ denote the expected relative position of the object if unrelated to Gl 86 by using its proper motion

Date	$\Delta\alpha$ [mas]	$\Delta\delta$ [mas]	$\Delta\alpha^*$ [mas]	$\Delta\delta^*$ [mas]
08.09.2000	1510 ± 25	853 ± 6	1510	853
10.11.2000	1522 ± 3	789 ± 20	929.1	962.2
12.12.2000	1508 ± 10	851 ± 13	638.6	1019.5

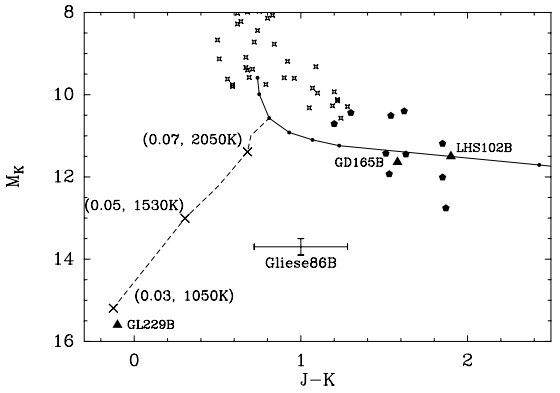

Fig. 2. Color–Magnitude diagram of Gl 86B. The DUSTY model track of a 1 Gyr old object is indicated by the solid line (dots mark from right to left the models with 0.06, 0.07, 0.072, 0.075, 0.08, 0.09 and 0.1 $M_\odot$) and the dashed line represents the COND model (from Chabrier et al. 2000) of the same age (the numbers and crosses at the COND track give the mass in $M_\odot$ and the temperature). Late M dwarfs are marked by small stars and are taken from Leggett et al. (1998). Some BD companions with known absolute photometry are marked by triangles and other BDs as polygons (data from Dahn et al. 2000; Goldman et al. 1999; Kirkpatrick et al. 1999). Gl 86B apparently falls in a region not covered by the two extreme model cases: dusty or dust free atmosphere

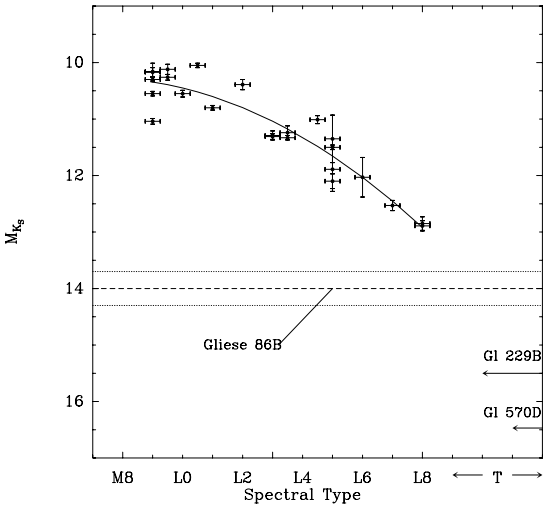

Fig. 3. Gl 86B placed into the Fig. 8 of Kirkpatrick et al. (2000). It shows that Gl 86B falls also in the K_S band between the known L and T dwarfs. The dashed line represents the measured K_S magnitude of Gl 86B with its error interval (dotted lines). The points with error bars represent known M and L dwarfs and are fitted by the solid line representing a second–order polynomial fit. The known T–dwarfs Gliese 229B and Gliese 570 D are also indicated and are more than 2.5 mag fainter than the latest L–dwarfs (after Kirkpatrick et al. 2000)

$r = 1\farcs72 \pm 0\farcs03$ and a position angle PA $= 119 \pm 1°$. From now on, we will call this object Gl 86B.

3.2. Photometry

Gl 86B is faint, and to derive its photometry is not without difficulties. In order to reduce the large gradient in the local background of the object, caused by the residual wing left from the occulting mask, we used the PSF–subtracted images for aperture photometry. This method turned out to be very robust and converges at a certain aperture size where the background is still flat enough and not affected by the increasing noise residuals towards the mask. Having at least *two* data cubes per filter during different nights, we find that the measured flux of Gl 86B does not vary by more than about 20% between these images. Conservatively, we estimate our photometric error to be within 0.2–0.3 mag. We find the following magnitudes for Gl 86B: $J = 14.7$ ($\pm$0.2), $H = 14.4$ ($\pm$0.2), $K = 13.7$ ($\pm$0.2) and $K_S = 14.2$ ($\pm$0.3). As the distance of Gl 86 is measured by Hipparcos a distance modulus of 0.19 can be adopted for this object. We also observed Gl 86B using the Circular Variable Filter (CVF) mode of SHARP II+ which is a narrow–band filter system allowing to select the central wavelength thus giving a resolving power of $R = 60$. We planned to test the presence of methane absorption bands (Brandner et al. 1997), but the low count–rates, and the unavailability of PSF reference star observations did not allow us to derive reliable flux ratios for the three CFV bands chosen. Thus these observations have been used for astrometric purpose only. The magnitude difference between Gl 86 and the companion is more than 9 mag in K band. This and their small separation explain why Sterzik, Marchis & Kürster could not detect this object in their images which were taken without a coronographic mask.

4. Discussion

In the color–magnitude diagram we find that Gl 86B appears in a region well below the hydrogen burning limit (Fig. 2). It is lying between the evolutionary model tracks of COND and DUSTY (see Chabrier et al. 2000). The COND model represents an atmosphere in which a rapid grain settlement below the photosphere takes place, thus ignoring the influence of condensates on the radiative transfer but taking dust into account in the equation of state. On the other hand, DUSTY models use all condensates in the equation of state as well as in the radiative transfer equations. As pointed out in Chabrier et al. (2000), these two models represent the two extreme possible cases of a brown dwarf atmospheres. As can be seen from Fig. 2 neither the DUSTY nor the COND models seem to fit Gl 86B. Assuming coevality, an age of Gl 86 of several billion years (Queloz et al. 2000), and using the NextGen track (Baraffe et al. 1998) for 1 and 10 Gyr objects we can at least infer an upper limit for the mass of Gl 86B of about $M_{\rm GJ86B} \leq 60{-}70\ M_{\rm Jup}$. As this object

seems to possess methane in its atmosphere we can follow the arguments by Leggett et al. (2000) and estimate a temperature to be about 1300 K which leads to a mass estimate of 40–70 $M_{\rm Jup}$ (Burrows et al. 1997).

Using the $K_{\rm S}$ band magnitude we infer an approximate spectral type of Gl 86B using the data of Kirkpatrick et al. (2000). Figure 3 is a reproduction of Fig. 8 from Kirkpatrick et al. (2000) including the Gl 86B data. As pointed out by these authors there is a gap of about 2.5 mag in the $K_{\rm S}$ band between the latest L dwarfs and the T dwarfs which is caused by the strong methane absorption features in this wavelength region. We find that Gl 86B is falling right into this gap; it seems to represent a transition object between the L and T dwarf regime. Due to the probable existance of methane it would be a so–called "early T–dwarf", a class proposed by Leggett et al. (2000) based on their finding of three objects with similar ($J-K \approx 1$) colours and spectroscopic confirmation of the presence of methane. We speculate that Gl 86B is a (several Gyr) old transition object between the L and T dwarf regime in whose atmosphere dust has already settled below the photosphere and does not dominate the appearance of this object. Detailed spectroscopy is necessary to prove this hypothesis.

Assuming a mass of 50 $M_{\rm Jup}$ for Gl 86B orbiting at a distance of 18.75 AU around Gl 86 introduces a Doppler-shift amplitude of the order of about 0.5 $\rm km\,s^{-1}$, with a period of ≈100 yrs, depending on the viewing geometry. The radial velocities available might contain this additional component. However, the companion found can not account for the long term trend in the radial velocities as observed by the CORAVEL survey: CORAVEL observed a long term drift of more than about 2 $\rm km\,s^{-1}$ over more than 10 years. This companion, if real, must be fairly massive, and we should have easily spotted it, unless it is hidden by the primary. New and higher precision radial velocities could clarify this point. The Gl 86 system might contain even more components.

The detection of Gl 86B was only possible by using the high angular resolution of an adaptive optics system combined with a coronographic mask to obtain a high sensitivity close to a bright star. In the near future several such systems at 8 m class telescopes will become available thus offering the opportunity to detect the orbital motion and to do spectroscopy of this very interesting object.

The Gl 86 system is one of the few systems where a brown dwarf is found as companion to a star. In addition Gl 86 is also orbited by an extrasolar planet. It is therefore the second such system as HD 168443 (Udry et al. 2000) was found by radial velocity data to also be orbited by a planet and a brown dwarf. In view of the very small number of brown dwarfs as companions to stars, the existance of already two systems hosting a brown dwarf and a planetary companion is even more puzzling and raises the question whether star–planet–BD systems are more frequent than previously thought.

Acknowledgements. It's a pleasure to acknowledge the support by the 3.6 m telescope team during the observations, especially by N. Ageorges, K. Brooks, A. Gonzalez, O. Marco, V. Meriño and E. Wenderoth. We thank A. Hatzes for his comments on an early version of this paper. Also J. Gizis, the referee, pointed out several improvements to this paper. We thank ESO's OPC and DDTC for the generous allocation of observing time. E.P. wishes to thank the CNRS–INSU Program for Planetogy for a supporting travel grant. This work has been supported in part by the National Science Foundation Science and Technology Center for Adaptive Optics, managed by the University of California at Santa Cruz under cooperative agreement No. AST-9876783.

References

Baraffe, I., Chabrier, G., Allard, F., & Hauschildt, P. H. 1998, A&A, 337, 403

Beuzit, J.-L., Mouillet, D., Lagrange, A.-M., & Paufique, J. 1997, A&AS, 125, 175

Brandner, W., Alcala, J. M., Frink, S., & Kunkel, M. 1997, ESO Messenger, 89, 37

Burrows, A., Marley, M., Hubbard, W. B., et al. 1997, ApJ, 491, 856

Chabrier, G., Baraffe, I., Allard, F., & Hauschildt 2000, ApJ, 542, 464

Dahn, C. C., Guetter, H. H., Harris, H. C., et al. 2000, in From Giant Planets to Cool Stars, ed. C. A. Griffith, & M. S. Marley, ASP Conf. Ser., 212, 74

Goldman, B., Delfosse, X., Forveille, T., et al. 1999, A&A, 351, L5

Kirkpatrick, J. D., Allard, F., Bida, T., et al. 1999, ApJ, 519, 834

Kirkpatrick, J. D., Reid, N., Liebert, J., et al. 2000, AJ, 120, 447

Leggett, S. K., Allard, F., & Hauschildt, P. H. 1998, ApJ, 509, 836

Leggett, S. K., Geballe, T. R., Xiaohui Fan, et al. 2000, ApJ, 536, L35

Marcy, G. W., Cochran, W. D., & Mayor, M. 2000, in Protostars and Planets IV, ed. V. Mannings, A. Boss, & S. Russell, 1285

Pantin, E., Waelkens, C., & Lagage, P. O. 2000, A&A, 361, L9

Queloz, D., Mayor, M., Weber, L., et al. 2000, A&A, 354, 99

Rousset, G., & Beuzit, J.–L. 1999, in Adaptive Optics in Astronomy, ed. Roddier (Cambridge University Press), 171

Udry, S., Mayor, M., & Queloz, D. 2000, IAU Symp. 202, in Planetary Systems in the Universe: Observation, Formation and Evolution, ed. A. Penny, P. Artymowicz, A.–M. Lagrange, & S. Russel, ASP Conf. Ser., in press

Annex :

ADONIS high contrast infrared imaging of Sirius-B

published in the journal *A&A*, October 2008

A&A 489, 651–655 (2008)
DOI: 10.1051/0004-6361:20078937
© ESO 2008

Astronomy & Astrophysics

ADONIS high contrast infrared imaging of Sirius-B

J. M. Bonnet-Bidaud[1,2] and E. Pantin[1,2]

[1] CEA, Irfu, Service d'Astrophysique, Centre de Saclay, 91191 Gif-sur-Yvette, France
e-mail: bonnetbidaud@cea.fr
[2] Laboratoire AIM, CEA-CNRS-Université Denis Diderot, Paris, France

Received 26 October 2007 / Accepted 29 May 2008

ABSTRACT

Context. Sirius is the brightest star in the sky and a strong source of diffuse light for modern telescopes so that the immediate surroundings of the star are still poorly known.
Aims. We study the close surroundings of the star (2 to 25″) by means of adaptive optics and coronographic device in the near-infrared, using the ESO/ADONIS system.
Methods. The resulting high contrast images in the JHKs bands have a resolution of ∼0.2″ and limiting apparent magnitude ranging from $m_K = 9.5$ at 3″ from Sirius-A to $m_K = 13.1$ at 10″. These are the first and deepest images of the Sirius system in this infrared range.
Results. From these observations, accurate infrared photometry of the Sirius-B white dwarf companion is obtained. The JH magnitudes of Sirius-B are found to agree with expectations for a DA white dwarf of temperature ($T = 25\,000$ K) and gravity (log g = 8.5), consistent with the characteristics determined from optical observations. However, a small, significant excess is measurable for the K band, similar to that detected for "dusty" isolated white dwarfs harbouring suspected planetary debris. The possible existence of such circumstellar material around Sirius-B has still to be confirmed by further observations.
Conclusions. These deep images allow us to search for small but yet undetected companions to Sirius. Apart from Sirius-B, no other source is detected within the total 25″ field. A comparison of the flux expected from the faintest known brown dwarfs at the distance of Sirius demonstrates that the above limiting magnitudes correspond to a star of spectral type later than T5 at 5″ and T7 at 10″. Using theoretical spectra of brown dwarfs and planet-size objects, we also show that the end of the brown dwarf sequence is reached in the outer part of the image. The minimum detectable mass is around 10 $M_{\rm Jup}$ inside the planetary limit, indicating that an extrasolar planet at a projected distance of ∼25 AU from Sirius would have been detected.

Key words. binaries: visual – stars: individual: Sirius – white dwarfs – stars: law-mass, brown dwarfs – planetary systems – infrared: stars

1. Introduction

Although Sirius is the brightest star in the sky, it is by no means an easy target for modern astronomy. Its extreme brightness ($m_v = -1.46$) in fact presents significant problems for both observations and precise photometric in the immediate surroundings of the star.

Sirius is known to be a binary system since the prediction of a companion by Bessel in 1844 and subsequent observation by Alvan Clark in 1862 of Sirius-B which worked out to be the closest white dwarf (see Wesemael & Fontaine 1982). The system was also proposed to be triple because a visual companion was reported consistently around 1930 (see Baize 1931) and persistent periodic (∼6 yr) residuals were also noticed in the A-B binary orbit (Volet 1932; Benest & Duvent 1995). The existence of an interacting third star in an eccentric orbit was also proposed to explain the apparent historical change in color of Sirius (Gry & Bonnet-Bidaud 1990; Bonnet-Bidaud & Gry 1991).

Over many years, Sirius-B was monitored extensively in the optical (Gatewood & Gatewood 1978), although the stellar field around Sirius was virtually unknown till recently. Due to the high diffuse background produced by the bright Sirius-A, long exposures such as those of the Palomar plates generate a large ∼1° overexposed spot at the star position. The first catalogue of stars in a (2.5 × 4)′ field around Sirius was provided in an effort to isolate possible companion candidates (Bonnet-Bidaud & Gry 1991; Bonnet-Bidaud et al. 2000). It enabled the identification of an unrelated $m_g \simeq 12$ background star that was in close (∼7″) conjunction with Sirius during the years around 1930, due to its high proper motion. This conjunction most likely explains the spurious companion reported at that time.

Modern techniques for data from space and ground-based observatories have allowed considerable progress to be achieved in the search and study of faint companions around bright stars. Schoeder et al. (2000) imaged Sirius-A at 1.02 μm, with the Hubble Space Telescope (HST) Planetary Camera and provided first constraints within 17″ of the star. Kuchner & Brown (2000) using the HST-NICMOS camera in coronographic mode covered the central 3.5″ at a similar 1.10 μm wavelength in a search of exozodiacal dust around Sirius-A. The HST-STIS spectrograph was also used to measure accurate UBVRI magnitudes of Sirius-B from its visual spectrum (Barstow et al. 2005).

Since these observations, ground-based coronographs using adaptive optics in the near infrared have emerged as a powerful new tool in searching for faint companions to nearby stars. We present the first JHK infrared images of a 25″ field around Sirius-A acquired using such a device. The high constrast images allow the precise determination of Sirius-B infrared colors and provide the strongest constraints in the region 3–10 arcsec from Sirius-A of the existence of a small companion in the Sirius system, down to a planetary size.

Article published by EDP Sciences

2. Observations

Sirius was observed during two epochs from 2000 January, 14 to 16 and 2001 January, 13, using the SHARP II+ camera coupled with the adaptive optics system ADONIS, and mounted onto the ESO 3.6m telescope at La Silla, Chile (Rousset & Beuzit 1999). A pre-focal optics coronograph (Beuzit et al. 1997) was used to reject the direct starlight of Sirius-A and increase the integration time in each elementary exposure. Because of the high brightness of Sirius-A, we had to use a large mask (diameter of 3.92″). The SHARP camera was used with a pixel scale of 100 mas to increase the sensitivity to point-like faint companion and provide a total $(25.6 \times 25.6)''$ field of view. J (1.25 μm), H (1.64 μm), and Ks (2.15 μm) large band exposures were obtained. The seeing was quite stable during these observations at ∼1″ on average (on a timescale of 1 night), but could reach a value of 1.7″ for H band data of January 2000. We spent a total observing time of 300 s in J band, 410 s in H band and 800 s in the Ks band. The Point Spread Function (PSF) was monitored frequently by interlaced observations of two reference stars, 2 Cma (B1 II/III, $m_V = 1.98$) and γ Cma (B8 II, $m_V = 4.097$). For selecting suitable reference stars and minimizing the PSF diffferences, three criteria were considered in order of importance : the distance on the sky to the target, the brightness match at the wavefront analysis wavelength (0.6 μm), and the spectral type match. The two reference stars are the most effective compromise and cover both the brightness and spectral type range. These reference stars were used later in the reduction process to subtract the wings of the stellar PSF, and increase the sensitivity to a faint companion. Typical FWHM of the PSF were 0.2″ in J band and 0.3″ in H and Ks bands. Observations of empty fields were also performed to estimate and remove the background flux, which can be significant in K band observations. The reference stars HR 3018 and HD 19904 were used for photometric calibration.

3. Reduction procedure

First, standard reduction techniques (including bias subtraction and flat-field correction) were applied to the data. For each filter, we obtained a set of Sirius observations and corresponding PSFs. In spite of the use of a coronograph mask, the image surface brightness was still dominated by the stellar emission at any distance from the star. To search for faint companions, we had to subtract numerically the starlight wings. The approximate subtraction of a scaled PSF to Sirius images provides inaccurate results because of slight shifts (up to 1 pixel) in position on the array between the reference star and the object, uncertainties in the fluxes (given by the literature), and a residual background (ADONIS bench emission, different airmasses). We developed a specific method to achieve an optimum subtraction.

3.1. Subtraction of the PSF

For a pair of Sirius image (Obj) and corresponding PSF (Psf), we attempt to estimate automatically three parameters: a shift $(\delta x, \delta y)$ between the two images, a scaling factor R, and a residual background Bg. These parameters are estimated by minimizing the following error functional:

$$J = J_{\chi^2} + \alpha_{\rm neg} J_{\rm neg} + \alpha_{\rm bal} J_{\rm bal} \quad (1)$$

where

$$J_{\chi^2} = \sum_{\rm subframe} |{\rm Obj} - S\,({\rm Psf}/R, \delta x, \delta y) - Bg| \quad (2)$$

$$J_{\rm neg} = \sum_{\rm negative\ pixels} |{\rm Obj} - S\,({\rm Psf}/R, \delta x, \delta y) - Bg| \quad (3)$$

and

$$J_{\rm bal} = \sqrt{\sum_i \sum_i ({\rm med}({\rm quad}_i) - {\rm med}({\rm quad}_j))^2} \quad (4)$$

where $[{\rm quad}_i]$ designates one of the 4 square quadrants around the star, the [S] function represents the image shift, and [med] function is the median estimator. The sum of the χ^2 term is performed over a subframe located in a region of the images close to the star (typically between circles of 25 and 50 pixels in radii), from which unreliable pixel values are excluded (bad pixels, pixels belonging to areas contaminated by diffracted light from the coronograph support/telescope spider). The J_{χ^2} expresses the fidelity of the shifted/rescaled PSF to the object image, the $J_{\rm neg}$ prevents overestimation of the ratio (R) parameter that would produce a large, centered zone of negative pixels in the PSF subtracted result, while, $J_{\rm bal}$ prevents non uniformities in the four quadrants, which are particularly high when the shift parameters are estimated incorrectly. We note that the central part of the images is not saturated and that bad pixels and the centermost region (where the coronographic mask is located) are excluded from the computation of the median value. $\alpha_{\rm neg}$ and $\alpha_{\rm bal}$ are two weight parameters with optimal values determined experimentally as 1.0 and 2.0 respectively, so that the χ^2 minimum value is of the order of the number of pixels.

The functional minimum is found using a zeroth-order minimization algorithm called "simplex" (Press 1993). The method was first verified using simulated data whose input parameters (shifts, scaling factor) were recovered with an accuracy of higher than 5%. To evaluate the errors in the subtraction process and test the stability of the PSF, the same subtraction process was applied using the two calibration stars.

Figure 1 shows the resulting subtracted image in the Ks filter. Residuals level can be seen from random structures around the coronographic mask. A point-like object can be seen easily in this subtracted high contrast image. This is the first direct image of the white dwarf companion of Sirius in this energy range. The image has a sharper contrast than a comparable one produced using the WFPC2 camera on the HST telescope (Barstow et al. 2005), although the A-B magnitude difference does not differ significantly between the optical and infrared.

4. Infrared photometry of Sirius-B

In spite of the high image quality, the photometric measurements for the companion observed in Fig. 1 is difficult. To obtain accurate photometric measurements, special care must be taken to remove systematic effects due to light contamination. The high level of surrounding residuals prevents the use of standard photometric estimation methods such as encircled energy summation. After assessing many methods using simulated data, the most accurate one proved to be a method based on PSF fitting of the source. It is unaffected by the surrounding residual structures produced by the PSF subtraction, and depends weakly on uncertainties when estimating the background in the image. The photometric measurements of the WD are given in Table 1 for the two epochs. The uncertainties given in this table were estimated by combining the actual surrounding residual uncertainties and the results of simulations based on Monte Carlo trial processes. Fluxes were converted into magnitudes using the filter responses

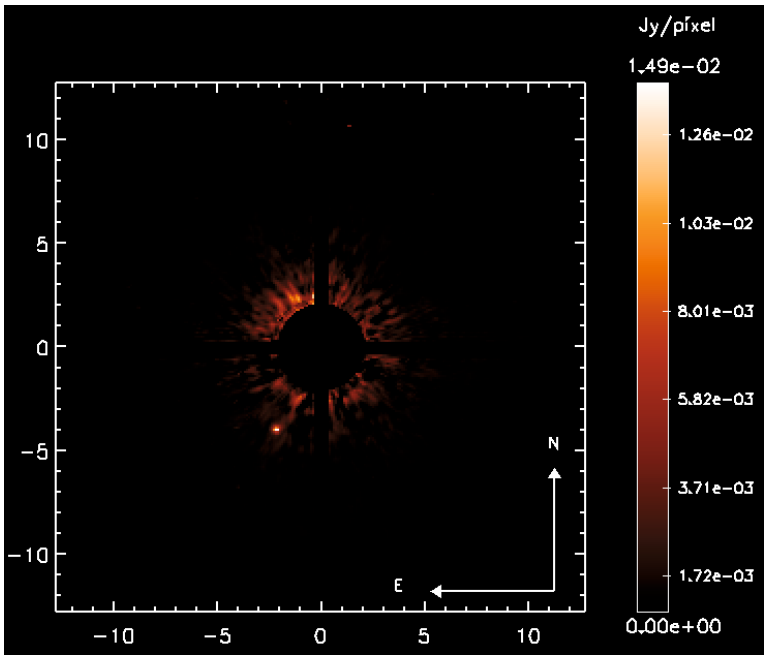

Fig. 1. ADONIS *Ks*-band image of the white dwarf companion of Sirius. The pixel scale is 0.1″/pixel, the total field is 25.6 × 25.6″ and the linear flux scale is given to the right. The Sirius star is centered under a 3.9″ diameter coronographic mask and an additive numerical mask has been added to provide a clearer display. The white dwarf companion, Sirius-B, is clearly seen in the lower-left quadrant at a separation of 5.0″.

Table 1. *JHK* hotometry of Sirius-B.

Band	Jan. 2000	Jan. 2001	Mean	Abs. Mag.(*)
J (1.215 μm)	$9.11^{+0.08}_{-0.06}$	$9.17^{+0.16}_{-0.13}$	$9.14^{+0.12}_{-0.09}$	$12.03^{+0.12}_{-0.09}$
H (1.654 μm)	$9.34^{+0.36}_{-0.24}$	$9.02^{+0.14}_{-0.09}$	$9.17^{+0.23}_{-0.16}$	$12.06^{+0.23}_{-0.16}$
K_s (2.157 μm)	$9.12^{+0.29}_{-0.23}$	$8.91^{+0.09}_{-0.07}$	$9.01^{+0.18}_{-0.14}$	$11.90^{+0.18}_{-0.14}$

(*) using the Hipparcos parallax $\pi = 0.3791''$.

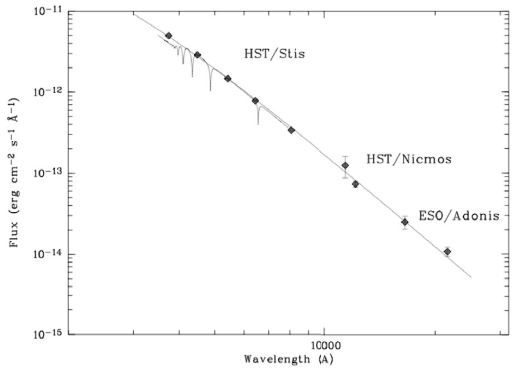

Fig. 2. Sirius-B energy distribution from optical to infrared. Monochromatic fluxes (black dots) are from UBVRI (HST-STIS), 1.104 μm (HST-NICMOS) and *JHKs* magnitudes (this work). Also shown in the optical is the best Koester theoretical model (see text). The full line corresponds to a pure blackbody at a $T = 25\,190$ K temperature. See text for a more detailed comparison to theoretical models in the infrared.

and zero-points defined by Tokunaga (2000) in the MKO system, which do not differ significantly from the calibration given by Cohen et al. (2003b). The last column of Table 1 provides the average absolute magnitudes computed using the parallax distance determined by the Hipparcos satellite (ESA 1997). These are the first accurate JHK magnitudes for Sirius-B, which can be compared to theoretical expectations.

The optical photometry as well as the temperature and gravity of the white dwarf ($\log T = 25\,190$ K, $\log g = 8.556$) were determined accurately using HST Balmer lines spectroscopy (Barstow et al. 2005). Figure 2 shows the measured energy distribution of Sirius-B from optical to infrared, compared to the flux distribution from a pure blackbody at $T = 25\,190$ K, scaled to the optical flux at 5500 Å. Also shown in the optical range is the synthetic WD spectrum interpolated in temperature and gravity from a grid of WD models with LTE atmospheres Finley et al. 1997; Koester 2000 private communication). UBVRI fluxes were converted to the magnitude system of Cohen et al. (2003a). The flux measured at 1.104 μm from HST-NICMOS observations (Kuchner & Brown 2000) is also shown. The *JHKs* infrared fluxes are already in remarkable agreement with this simple black body extrapolation.

In the infrared range, comparison to more detailed synthetic colors of DA white dwarfs was performed by interpolating the grid of synthetic photometry provided by Holberg & Bergeron (2006) on the basis of LTE model atmospheres. In these new models, *JHKs* magnitudes are computed in the filters and magnitude scale of Cohen et al. (2003b), which are equivalent to our measurements. Considering the remaining uncertainities in the WD mass and radius (Barstow et al. 2005), the model magnitudes for a pure H atmosphere white dwarf at the Sirius-B temperature and gravity were scaled to the V absolute magnitude ($M_v = 11.422$). The theoretical predictions for the Sirius white dwarf magnitudes are then $M_J = 12.033$, $M_H = 12.120$, and $M_{Ks} = 12.213$ which yield "observed-theoretical" magnitude differences of $0.001^{+0.12}_{-0.09}$, $-0.058^{+0.23}_{-0.16}$, and $-0.309^{+0.18}_{-0.14}$, respectively in the

*JHK*s bands. The error bars were computed here not from an "assumed" normal distribution but from the true distribution of residuals amplitudes, derived from the image statistics in the related region. They correspond to an exclusion of a false excess detection at a 99,64% confidence level. Whereas the J and H magnitudes reproduces accurately the predicted values, the K magnitude has a small but significant excess of ~0.3 mag. Interestingly, a similarly small K excess was also recently measured for selected cool ($T \leq 12\,000$ K), isolated white dwarfs for which an overall excess of flux at wavelength longer than 2 μm with characteristics consistent with circumstellar dust or debris is found (von Hippel et al. 2007). In a Spitzer mid-infrared survey of 124 white dwarfs, four "dusty" white dwarfs were found with dusty environment that may represent the remains of planetary systems (Reach et al. 2005) and a metal-rich gas disk was discovered around a hotter ($T = 22\,500$ K) WD, possibly associated with planetary debris material (Gaensicke et al. 2008). It is therefore possible that the small departure observed in the K band indicates a similar circumstellar material around Sirius-B.

5. Looking for a third star

The high contrast images obtained here in the near infrared are useful for constraining the existence of a possible small mass companion in the Sirius system. No point-source other than Sirius-B can be detected in the field, down to a certain limiting sensitivity that depends on the filter used. We estimate our limiting magnitudes in each filter (J, H, Ks) by simulating a point source hidden in the residuals of the PSF subtracted image. The minimum detectable magnitude in the different regions of the image was computed by evaluating the standard deviation and cumulative probability of the residuals in each sector. The detection limit was set from the true probability to correspond to a significance $P \geq 0.9$, which in our case corresponds to a 10σ limit for the peak intensity detection and a 500σ limit for a PSF integrated intensity.

Figure 3 shows the results for the K_s image. Significant azimuthal variations of up to ~1 mag. are present in the image with variations decreasing toward the outer part of the image as the level of PSF subtraction residuals decreases with the distance to Sirius. Typical limiting sensitivities as a function of distance to Sirius were derived by azimuthally averaging the residual levels of the PSF subtracted image and are shown in Fig. 4 for the different filters. The most robust constraints are obtained for the J and K_s filters. For the filter K_s, the upper limits range in absolute magnitude from $M_{Ks} \sim 12.4$ at 3″ of Sirius-A to $M_{Ks} \sim 16.0$ at 10″. At these levels, M dwarfs are already excluded. Using an extrapolation of the empirical mass-luminosity relations estimated by Delfosse et al. (2000), $M_{Ks} \geq 10$ as in Fig. 4 corresponds to a mass $M \leq 0.08\,M_{\odot}$. These magnitudes are only comparable with those observed for the faintest dwarfs known. In the last ten years, hundreds of L and T dwarfs have been discovered. We used the catalog of 71 L and T dwarfs of Knapp et al. (2004), in which 45 have known distances and therefore absolute K magnitudes (see their Table 8). Figure 5 shows this selected observed sample with our magnitude upper limits at the different distances from Sirius-A. Using the polynomial fit of Knapp et al. (2004, Table 12), the upper limits at 5″ and 10″ correspond to spectral types later than T4.8 and T7.0, respectively. There is no simple mass-luminosity relation for L and T dwarfs since many parameters (gravity, age, metallicity, ...) are involved (see Burrows et al. 2006) but a approximate estimation can be obtained from distributions computed from various

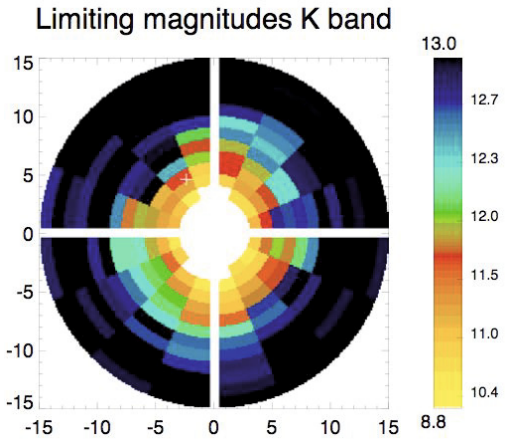

Fig. 3. Azimutal variation of the limiting magnitudes in the K_s band image for a point source in a 15″ field around Sirius (scale in arcsec). The vertical right color scale gives the range of limiting apparent magnitude for the different sectors.

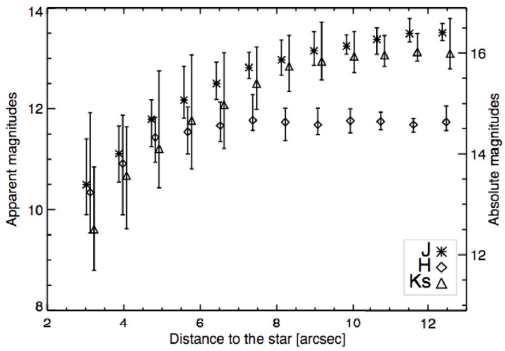

Fig. 4. Plot of the limiting sensitivities in magnitudes as a function of the angular separation to the star in the three near-infrared bands (crosses: J, open lozenges: H, open triangles: K_s). Points are slightly shifted horizontally for clarity. Note that the vertical lines are not statistical error bars but mark the minimum/maximum range of azimuthal variations at a given radius.The right scale gives the absolute magnitude at the Sirius distance.

models (Burgasser 2004). The upper limit at 10″ corresponds to a companion mass in the range $M = (0.042–0.052)\,M_{\odot}$ or $(44–54)\,M_{\rm Jup}$, down to the brown dwarf range and close to planetary limits.

Independent estimations can also be obtained using theoretical L-T dwarfs models. We used published spectral models for brown dwarf (see Burrows et al. 2006) and planetary (Burrows et al. 2003) masses to compute the expected infrared magnitudes. We selected the models with solar abundances and an age of 250 Myr appropriate for Sirius (Liebert et al. 2003) and derived the temperature and gravity corresponding to a given mass, using the Burrows Brown Dwarf and Extra-Solar Giant Planet Calculator. The corresponding theoretical spectra were then convolved with the filter response to compute the magnitudes. Table 2 gives the closest masses compatible with the observed upper limit at different projected distances from Sirius. From our K-image, a third star with a mass ~30 $M_{\rm Jup}$ could be detected close to Sirius (~8 AU), while a miminum mass of

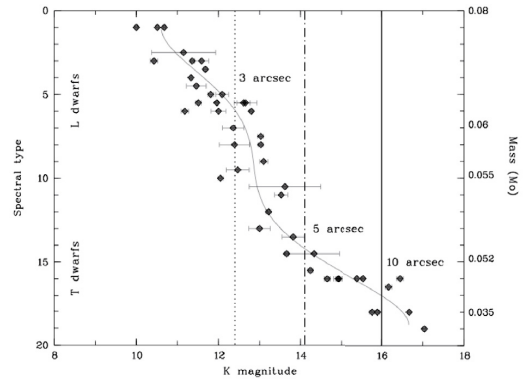

Fig. 5. Limiting K absolute magnitude at different angular separations from Sirius-A (10″: thick line – 5″: dash-dotted line – 3″: dotted line) compared to the faintest observed L and T dwarfs (black dots). Spectral types (left scale) are coded by 01 = L01, 10 = T0, 19 = T9 and representative masses are indicated on the right-hand side axis. The thin line is the best M_K-spectral type fit from Knapp et al. (2004).

Table 2. Limiting Ks magnitudes and masses around Sirius.

Separation	3″	5″	10″
Distance (AU)	7.9	13.2	26.4
m_{Ks}(obs)	9.5	11.2	13.1
M_{Ks}(obs)	12.4	14.1	16.0
*Models**			
M_{Ks}(models)	13.1	14.3	16.6
Mass (M_{Jup})	30	20	10

(*) Burrows et al. (2006) models.

~10 M_{Jup} is reached at a distance of ~26 AU. This final limit indicates that an extrasolar planet around Sirius at a distance comparable to the Sun-Neptune distance would have been detected. These are the best constraints in a (4–25″) region around Sirius-A. From the published HST-NICMOS upper limit at a shorter (1.1 μm) wavelength (Kuchner & Brown 2000), we used the same above method to derive a limit of ~ 45 M_{Jup} and ~ 15 M_{Jup}, closer to Sirius, at a separation of 2″ and 3″, respectively. With the negative optical search in the wider (2.5 × 4′) field (Bonnet-Bidaud et al. 2000), this weakens considerably the possibility of a third star in the Sirius system.

The high resolution achieved by adaptive optics also allows the search for a suspected faint star in a close orbit around Sirius-B. From an analysis of the orbit residuals, a ~6 yr periodicity is present and a general three-body model indicates that possible stable orbits exist with a restricted range of masses $M \leq 0.038\ M_{\odot}$ (40 M_{Jup}) and semi-major axis $a_0 = (1-2.5)$ AU (Benest & Duvent 1995). The reconstructed PSF of $FWHM = 0.31+/-0.05''$ in the Ks band is equivalent to a 0.8 AU separation from Sirius-B at the system distance therefore the companion could be resolved in our image. At the position of Sirius-B (5″), the upper limit in our K image is $M_{Ks} = 14.1$. This corresponds to a theoretical mass of ~20 M_{Jup} (Table 2), lower than the predicted mass. Our limit therefore also excludes a suspected faint component to Sirius-B unless the orientation is very unfavourable.

6. Conclusions

The infrared image of the Sirius field presented here is the first high constrast image in the JHK wavelength range. Despite the coronagraphic device associated with adaptive optics, the light contamination of the brightest Sirius dominates the field. A precise subtraction of the diffuse background and a careful calibration enable us however to derive very accurate constraints on the different objects in the field. The infrared absolute magnitudes of Sirius-B are determined to be $M_J = 12.03^{+0.12}_{-0.09}$, $M_H = 12.06^{+0.23}_{-0.16}$, and $M_{Ks} = 11.90^{+0.18}_{-0.14}$. The JH values are in excellent agreement with the white dwarf theoretical model of a DA white dwarf at a temperature and gravity determined accurately from the HST image. A small departure is visible in the K band, which may indicate a possible circumstellar material around Sirius-B, similar to that observed around some selected "dusty" white dwarfs. This has yet to be confirmed by observations at longer (2−15 μm) wavelengths, where most of the "dust" emission is expected. The high quality image also allows a deep search for possible low-mass objects in the field. Although the residual background after subtraction shows significant azimuthal variations, mean limiting magnitudes in the field reach the planetary limit for an object located at the Sirius distance. The deep field obtained here around Sirius provides a limit of (30–10) M_{Jup} in the (8–26) AU region and complementary HST-NICMOS observations yield a similar limit down to 5 AU. Since the most central part of the image (≤5 AU) has still not been covered, this does not fully eliminate the possibility of a third member in the sytem but the probability of a triple system is now low.

Acknowledgements. We thank the 3.6 m ESO team for their helpful support during the observations and F. Marchis and O. Marco for useful advices. We also thank an anonymous referee for very useful comments and insightful remarks to improve the manuscript.

References

Baize, P. 1931, L'Astronomie, 45, 383
Barstow, M. A., Bond, H. E., Holberg, J. B., et al., 2005, MNRAS, 362, 1134
Benest, D., & Duvent, J.-L. 1995, A&A, 299, 621
Beuzit, J.-L., Mouillet, D., Lagrange, A.-M., & Paufique, J. 1997, A&AS, 125, 175
Bonnet-Bidaud, J. M., & Gry, C. 1991, A&A, 252, 193
Bonnet-Bidaud, J.-M., Colas, A., & Lecacheux, J. 2000, A&A, 360, 991
Burrows, A., Sudarsky, D., & Ludine, J. 2003, ApJ, 596, 587
Burrows, A. Sudarsky, D., & Hubeny, I. 2006, ApJ, 640, 1063
Burgasser, A. 2004, ApJS, 155, 191
Cohen, M., Megeath, S. T., Hammersley P., Martin-Luis, F., & Stauffer, J. 2003, AJ, 125, 2645
Cohen, M., Wheaton, W. A., & Megeath, S. T. 2003, AJ, 126, 1096
Delfosse, X., Forweille, T., Segrensan, D., et al. 2000, A&A, 364, 217
ESA 1997, The Hipparchos and Tycho catalogues, ESA SP-1200 (Noordwijk)
Finley, D. S., Koester, D., & Basri, G. 1997, ApJ, 488, 375
Gatewood, G., & Gatewood, C., 1978, ApJ, 225, 191
Gaensicke, B. T., Marsh, T. R., Southworth J., & Rebassa-Mansergas, A. 2008, Science, 314, 1908
Gry, C., & Bonnet-Bidaud, J. M., 1990, Nat., 347, 625
Holdberg, J. B., & Bergeron, P. 2006, AJ, 132, 1121
Kuchner, M. J., & Brown, M. E 2000, PASP, 112, 827
Knapp, G. R., Leggett, S. K., Fan, X., et al. 2004, ApJ, 127, 3553
Liebert, J., Young P., Arnett, D., et al. 2003, ApJ, 630, 692
Press, W. H. 1993, in Numerical Recipes (Camb. Univ. Press)
Reach, W. T., Kuchner, M., von Hippel, T., et al. 2005, ApJ, 635, L161
Rousset, G., & Beuzit, J.-L. 1999 Adaptive optics in astronomy, ed. F. Roddier (Cambridge)
Schroeder, D. J., Golimowski, D. A., Brukardt, R. A., et al. 2000, AJ, 119, 906
Tokunaga, A. T. 2000, in Allen's Astrophysical Quantities, 4th edition, ed. A. N. Cox (NY, Springer-Verlag) 143
Volet, Ch. 1932, Bull. Astron. Paris, 8, 51
von Hippel, T., Kuchner, M., Kilic, M., Mullally, F., & Reach, W. T. 2007, ApJ, 662, 554
Wesemael, F., & Fontaine, G. 1982, J. R. Astron. Soc. Can., 76, 35

Annex :

The cool atmospheres of the binary brown dwarf ϵ Indi B

published in the journal *A&A*, June 2005

A&A 436, L39–L42 (2005)
DOI: 10.1051/0004-6361:200500121
© ESO 2005

Astronomy & Astrophysics

The cool atmospheres of the binary brown dwarf ε Indi B⋆

M. F. Sterzik[1], E. Pantin[1,2], M. Hartung[1], N. Huelamo[1], H. U. Käufl[3], A. Kaufer[1], C. Melo[1], D. Nürnberger[1], R. Siebenmorgen[3], and A. Smette[1]

[1] European Southern Observatory, Casilla 19001, Santiago 19, Chile
e-mail: msterzik@eso.org
[2] DSM/DAPNIA/Service d'Astrophysique, CEA/Saclay, 91191 Gif-sur-Yvette, France
[3] European Southern Observatory, 85748 Garching b. München, Germany

Received 15 March 2005 / Accepted 30 April 2005

Abstract. We have imaged ε Indi B, the closest brown dwarf binary known, with VISIR at the VLT in three narrow-band mid-infrared bandpasses located around 8.6 μm, 10.5 μm and 11.3 μm. We are able to spatially resolve both components, and determine accurate mid-infrared photometry for both components independently. In particular, our VISIR observations probe the NH_3 feature in the atmospheres of the cooler and warmer brown dwarfs. For the first time, we can disentangle the contributions of the two components, and find that ε IndiBb is in good agreement with recent "cloud-free" atmosphere models having an effective temperature of $T_{\rm eff}$ = 800 K. With an assumed age of 1 Gyr for the ε Indi system, component Ba agrees more with $T_{\rm eff} \approx 1100$ K rather than with $T_{\rm eff}$ = 1200 K, as suggested by SPITZER spectroscopic observations of the combined ε Indi B system (Roellig et al. 2004). Even higher effective temperatures appear inconsistent with our absolute photometry, as they would imply an unphysical small size of the brown dwarf ε IndiBa.

Key words. stars: low-mass, brown dwarfs – stars: binaries: general

1. Introduction

ε Indi B, the closest brown dwarf known (Scholz et al. 2003), has been recently discovered as a close binary, consisting of two brown dwarf components separated by 0.73″ (McCaughrean et al. 2004). The system has a well-established distance (3.626 pc, ESA 1997) and age (range 0.8–2 Gyr; Lachaume et al. 1999), and will allow the determination of fundamental physical parameters like its mass, luminosity, effective temperature, and surface gravity with unprecedented precision. Extending the analysis towards the mid-infrared (MIR) offers the opportunity to benchmark evolutionary and atmospheric models for very low temperatures.

Adaptive optics assisted near-infrared (H-band) low-resolution ($R \sim 1000$) spectroscopy (McCaughrean et al. 2004) of both components individually lead to a most likely spectral classification of T1 for ε Indi Ba and T6 for ε Indi Bb based on the Burgasser et al. (2002) H_2O and CH_4 spectral indices. Effective temperatures between 1238 K and 1312 K were derived for ε Indi Ba and between 835 K and 875 K for ε Indi Bb, bracketed by assuming the most likely ages between 0.8 and 2 Gyr. However, the comparison of high-resolution ($R \sim 50\,000$) near-infrared spectra of ε Indi Ba (Smith et al. 2003) with synthetic atmosphere spectra of Tsuji (2002) leads to a much higher $T_{\rm eff} = 1500 \pm 100$ K. The reasons for the large discrepancy are not known, but may be related to the radius of the brown dwarf or to uncertainties in the bolometric corrections assumed.

ε Indi B has recently been observed by the SPITZER Space Telescope in the mid-infrared (Roellig et al. 2004). Their low-resolution IRS spectrum is a composite spectrum of both components, as the limited angular resolution of SPITZER does not allow to resolve it spatially. Roellig et al. claim that their observation is the first evidence for NH_3 absorption in very cool brown dwarf atmospheres between 10 μm and 11 μm, although they cannot disentangle the contributions of both components individually. The SPITZER spectrum matches well a composite model described by Saumon et al. (2003, hereafter SML), assuming cloudless synthetic spectra.

Here, we report spatially resolved MIR photometry of ε Indi B obtained with VISIR, the new mid-infrared camera and spectrometer at the VLT (Lagage et al. 2004) during science verification. Our goal is to constrain the most pertinent brown dwarf model atmospheres with our data.

2. Observations

ε Indi B has been imaged with VISIR mounted on the UT3 (Melipal) of the VLT on Sep. 28, 2004 (in filters PAH1 and PAH2) and on Sep. 30, 2004 (in filter SIV) under clear and stable atmospheric conditions. A nominal pixel scale of 0.075″ was used in all bands, and standard chopping and nodding

⋆ Based on observations collected with the ESO VLT, Paranal, Chile, program 60.A-9245(A).

Article published by EDP Sciences and available at http://www.edpsciences.org/aa or http://dx.doi.org/10.1051/0004-6361:200500121

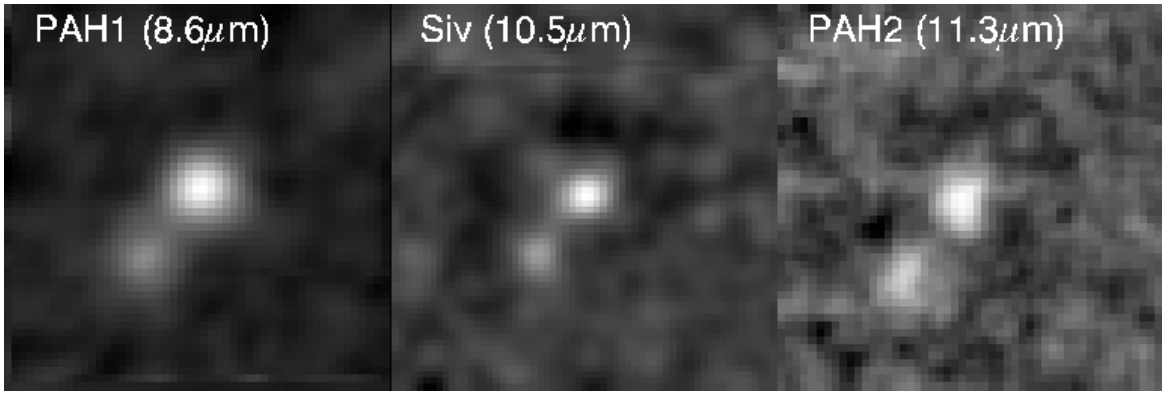

Fig. 1. VISIR images of ε Indi B in three filters PAH1, SIV and PAH2. Components a+b are clearly resolved in all three bandpasses. North is up, and east left: ε Indi Bb is the fainter source to the south-east.

Table 1. Log of the VISIR observations of ε Indi B.

RJD	Filter	λ_{cen}	$\Delta\lambda$	AM	Int[s]	Calibrator[a]
53 277.6	PAH1	8.59	0.42	1.18	3638	HD 224630
						HD 10550
53 277.7	PAH2	11.25	0.59	1.29	3587	HD 224630
53 279.6	SIV	10.49	0.16	1.18	3564	HD 178345

techniques (10″ amplitudes) were employed. Figure 1 show the final, co-added and median cleaned images that were used for sub-sequent photometry. The binary is clearly resolved, the measured image quality (*FWHM*) on the final frames is around 0.4–0.5″ for each point source, slightly above the diffraction limit. While the position angle from our three measurements ($137° \pm 6°$) is consistent with that determined by McCaughrean et al. (2004) using AO one year earlier ($136.81° \pm 0.14°$), our separation ($0.92'' \pm 0.06''$) is larger ($0.732'' \pm 0.002''$), and suggests orbital motion.

A summary of the observing log, filter central wavelengths, half band-width and total on-source integration times, is given in Table 1. Source count-rates were determined with standard aperture photometry. Curve-of-growth methods were applied to find the aperture radii that maximized the signal-to-noise ratio of the extracted source. Those radii were then also used for the calibration source to determine the count-rate to flux conversion factor. For faint sources, the optimal extraction aperture radius is not always well determined, and the presence of a second companion does not allow to grow the aperture to more then half of their distance. The variation of the count-rate to flux conversion factors with aperture radius was screened for aperture radii of 4, 5 and 6 pixel (corresponding to radii of 0.3″, 0.375″, 0.45″), and constitutes the main error in the *absolute flux calibration* of the targets. Different calibrator stars[1] observed at different airmasses give fully consistent results, and their contribution to the absolute photometric errors is negligible. *Flux ratios* between the components, and between different filter passbands can be obtained with a much higher accuracy, as the errors are only related the spread of the count rates in the four different beams, and rather independent on the actual choice of the aperture radius. Fluxes and ratios together with error estimates are summarized in Table 2.

[1] Taken from the list of Cohen et al. (1999).

Table 2. Mid-infrared flux densities and flux ratios of ε Indi B.

Object	PAH1 [mJy]	SIV [mJy]	PAH2 [mJy]	$\frac{\text{SIV}}{\text{PAH1}}$	$\frac{\text{SIV}}{\text{PAH2}}$
Ba	7.4 ± .4	7.2 ± .6	6.8 ± .8	.97 ± .02	1.06 ± .03
Bb	3.5 ± .4	3.5 ± .8	5.7 ± 1.	1.0 ± .04	0.61 ± .08

We note that the *combined* fluxes of components Ba and Bb agree with the spectrophotometric fluxes for the ε Indi B system deduced from the SPITZER spectrum shown in Fig. 2 of Roellig et al. (2004), albeit our fluxes are on the low side of their allowed 25% error range in absolute flux calibration. Component Ba dominates the mid-infrared emission, and component Bb contributes about 1/3 to the total flux density. Our SIV filter located at a central wavelength of 10.5 μm is particular well suited to probe the potential presence of NH_3 absorption features in brown dwarf atmospheres. In fact, a significant change of the relative spectral shape between both components becomes evident in the reddest passband around 11.3 μm (PAH2), where the flux of Bb comes close to that of Ba. The flux ratio SIV/PAH2 is small for component Bb, indicating the presence of a strong NH_3 absorption band. We find no indication for strong absorption in component Ba, though.

3. Comparison with atmosphere models

Atmosphere models are typically calculated on a grid of $T_{\rm eff}/g$ pairs, for specific metallicities. Taylor (2003) lists [Fe/H] = 0.056 ± 0.038 for ε Indi A; therefore we refer to solar metallicities also for ε Indi B.

The object radius R is the main parameter that determines the absolute spectral flux calibration of the model atmospheres, and is obtained from evolutionary calculations. Comparing the evolutionary models of Baraffe et al. (2003) with those

Article published by EDP Sciences and available at http://www.edpsciences.org/aa or http://dx.doi.org/10.1051/0004-6361:200500121

Table 3. Brown dwarf structural parameters according to evolutionary calculations of Burrows et al. (1997) for 1 Gyr.

Object	SpT[a]	$T_{\rm eff}$ [K]	log g [cm s^{-2}]	log $L_{\rm bol}$ [$L_\odot$]	M [$M_{\rm jup}$]	R [$R_\odot$]
Ba	T1	1200[b]	5.1	–4.78	46	0.093
		1500[c]	5.3	–4.42	59	0.090[d]
		1100	5.1	–4.92	41	0.095
Bb	T6	800[b]	4.8	–5.42	25	0.102

[a] Spectral types according to McCaughrean et al. (2003).
[b] $T_{\rm eff}$ assumed by Roellig et al. (2004).
[c] $T_{\rm eff}$ according to Smith et al. (2003).
[d] Smith et al. (2003) assume $R/R_\odot = 0.062$ and $L/L_\odot = -4.71$.

of Burrows et al. (1997) (in the given grid of ages and temperatures), we find that their radii agree within 2%. In the following we refer to the Burrows models, only, and note that different models do not contribute significantly to uncertainties in the absolute model fluxes. In Table 3 we summarize the (sub-)stellar parameters log g, $L_{\rm bol}$ and R assuming an age of 1 Gyr for the ε Indi B system. We note, however, that the age range allowed for ε Indi implies systematic variations of the model radius. While the younger age (0.8 Gyr) increases the radius by about 3%, the older age (2 Gyr) decreases the radius by 7% for all temperatures considered here. Systematic uncertainties up to 15% are therefore implicit in the absolute normalization of the model fluxes due to the age uncertainty of ε Indi.

Burrows et al. (2003) explore the age and mass dependance of H_2O, CH_4 and NH_3 molecular bands on MIR spectra of very cool brown dwarfs with $T_{\rm eff} \leq 800$ K. We have selected a suitable spectral model ($T_{\rm eff} = 800$ K, log $g = 5$) which represents a brown dwarf with a mass of $M = 25\ M_{\rm jup}$ and an age of 1 Gyr[2]. For the hotter component, the cloud-free model spectrum for an age of 1 Gyr corresponding to $M = 46\ M_{\rm jup}$ and $M = 41\ M_{\rm jup}$ for $T_{\rm eff} = 1200$ K and $T_{\rm eff} = 1100$ K, respectively, were supplied by A. Burrows (pers. comm.). Also Allard et al. (2001) provide model atmosphere spectra in the assumed parameter range. We concentrate our comparison to their "cloudless" models, which include the effects of condensation in chemical equilibrium, but ignore the effects of dust opacities altogether. Their model spectra are freely downloadable from the web[3]. Finally, also SML provide MIR spectra of brown dwarfs. In fact, their cloudless synthetic spectra for $T_{\rm eff} = 1200$ K and $T_{\rm eff} = 800$ K (log $g = 5$) were combined and compared to the SPITZER spectrum in Roellig et al. (2004). Both spectra were provided to us by D. Saumon directly.

For all model spectra we calculated the expected flux densities in the corresponding VISIR filter passbands by convolving the model spectrum with the respective filter transmission profiles[4]. In Table 4 we summarize and compare the predicted

[2] zenith.as.arizona.edu/~burrows/bsl/bsl.html
[3] ftp.ens-lyon.fr/pub/users/CRAL/fallard/AMES-Cond-2002
[4] http://www.eso.org/instruments/visir/inst/

Table 4. MIR flux densities for various model atmospheres. Values printed in **boldface** are consistent with our observations within 3σ. The 800 K models refer to ε Indi Bb, while the warmer models to Ba.

Reference	$T_{\rm eff}$ [K]	PAH1 [mJy]	SIV [mJy]	PAH2 [mJy]	$\frac{\rm SIV}{\rm PAH1}$	$\frac{\rm SIV}{\rm PAH2}$
Allard[a]	800	**4.32**	**3.64**	**6.98**	0.84	**0.52**
Burrows[b]	800	4.76	**4.10**	**6.04**	0.86	**0.68**
Saumon[c]	800	**3.68**	**2.18**	**4.86**	0.59	**0.45**
Allard[a]	1100	8.83	8.93	12.04	**1.01**	0.74
Burrows[d]	1100	**7.96**	**8.79**	**8.83**	1.10	**1.00**
Allard[a]	1200	10.67	11.36	13.21	1.06	0.86
Burrows[d]	1200	9.13	10.36	9.99	1.13	**1.04**
Saumon[c]	1200	9.21	9.87	11.68	1.07	0.85
Allard[a]	1500	17.09	16.97	16.60	**0.99**	**1.02**
Allard[e]	1500	**8.11**	**8.05**	**7.88**	**0.99**	**1.02**

[a] AMES-cond models from Allard et al. (2001).
[b] Cloud-free model from Burrows et al. (2003).
[c] Cloud-free models from Saumon et al. (2003, private communication).
[d] Cloud-free model from Burrows (private communication).
[e] Assuming $R/R_\odot = 0.062$.

model flux densities for the different model atmospheres. In **boldface** we mark those values that are consistent with our VISIR measurements (Table 2) allowing for a 3σ error range. From the comparison in Table 4 we infer that most of the available model spectra for the cooler component Bb are consistent with the *absolute* MIR photometry. They also essentially match the *flux ratios* (which are independent of absolute calibration issues like the radius assumed), but tend to underestimate the $\frac{\rm SIV}{\rm PAH1}$ color. All models predict a clear signature of a more or less pronounced NH_3 absorption feature, which is also present in our data. The predicted absolute fluxes appear somewhat (≈20%) higher than the measured ones, but are still within the allowed error range.

The warmer component Ba is more difficult to reconcile with current models and assumptions about the ε Indi B system. While cloud-free models, assuming an age of 1 Gyr and an effective temperature of 1200 K for Ba as used by Roellig et al. (2004) agree very well with their SST/IRS spectrum, they appear only *marginally consistent with our VISIR mid-infrared photometry*. The spectral shape measured for Ba (decreasing flux with increasing wavelength) is not reflected in these models. Also, their predicted MIR fluxes are ≈30%–100% higher then measured in the corresponding VISIR passbands. Assuming an age of 2 Gyr – at the high limit of the allowed age range – reduces the model radius to $R = 0.087\ R_\odot$, and the predicted MIR fluxes by 13%. This is not sufficient to explain the lower flux densities observed. An age of 5 Gyr with a radius of $R = 0.082\ R_\odot$ would be required in order to match the absolute fluxes. One straightforward way to reduce the absorption signatures of NH_3 is to increase the temperature of the atmosphere. In fact Allard's et al. AMES-cond model for $T_{\rm eff} = 1500$ K can be considered to be fully consistent with our *relative* photometry. However, when we apply the evolutionary models of Burrows et al. (1997) with a radius of $R = 0.09\ R_\odot$,

Article published by EDP Sciences and available at http://www.edpsciences.org/aa or http://dx.doi.org/10.1051/0004-6361:200500121

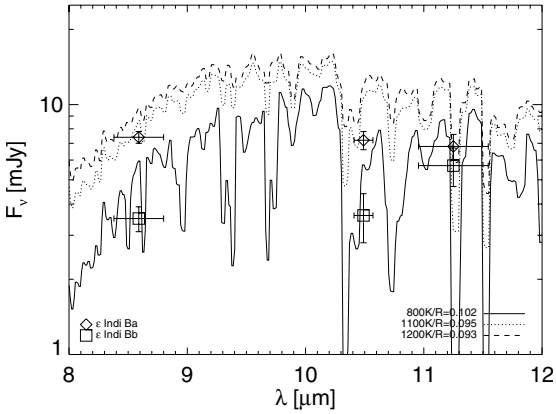

Fig. 2. Comparison of the VISIR photometry with various atmosphere spectra from BSL and Burrows (private communication). Radii assumed are consistent with evolutionary tracks of Burrows et al. (1997).

the *absolute* photometry is grossly off. $T_{\rm eff}$ = 1500 K for component Ba has also been favored by Smith et al. (2003) based on the analysis of high-resolution near-infrared spectroscopy. This temperature together with the published luminosity of component Ba (log $L_{\rm bol}$ = −4.71, McCaughrean et al. 2004), however, leads to a radius of only R = 0.062 $R_\odot$ (Smith et al. 2003). With this smaller radius, the *absolute* VISIR photometry can now be made consistent with the spectral model. But this radius is in contradiction to all known evolutionary models (see also McCaughrean et al. 2004). Moreover, it also seems empirically unlikely in view of recent measurements of the mass-radius relation for very-low mass stars and giant planets, which prove to be similar (Pont et al. 2005). But more, direct, determinations of radii in the brown dwarf mass regime are necessary to completely rule out this possibility. As can be inferred from Table 4, both available atmosphere models with $T_{\rm eff}$ = 1100 K tend to agree better with our measurements, assuming brown dwarf radii derived from evolutionary models at 1 Gyr. The Burrows et al. models (shown in Fig. 2 together with our photometry) for Ba seem to produce a slightly better match for the PAH2 measurement because of the presence of a strong absorption feature (that is less pronounced in the AMES-cond atmosphere).

4. Summary

We report the detection of both components of ε Indi B, the closest brown dwarf binary known, with VISIR at the VLT in three narrow-band mid-infrared bandpasses located around 8.6 μm, 10.5 μm and 11.3 μm. We are able to determine accurate mid-infrared absolute photometry for both components independently, with an error level of 5–10% for the brighter component Ba, and 10–20% for the fainter Bb. Relative photometry and flux ratios can be measured with even higher accuracy. Our data show that component Bb has a prominent absorption feature around 10.5 μm, most likely explained by NH_3. We then compare our MIR photometry with atmospheric model spectra, using the well-known distance, metallicity and age of the ε Indi B system as main input parameters. The MIR emission of the cool component Bb appears to be fully consistent with current atmosphere models assuming an effective temperature of $T_{\rm eff}$ = 800 K. The warmer component Ba appears only marginally consistent with $T_{\rm eff}$ = 1200 K, a temperature that has been inferred from SPITZER spectroscopic observations of the combined ε Indi B system (Roellig et al. 2004), and from near-infrared photometry (McCaughrean et al. 2004), if we assume a canonical age of 1 Gyr for the ε Indi B system. We instead favor a slightly lower effective temperature of $T_{\rm eff}$ = 1100 K to reconcile the absolute MIR fluxes and the spectral shape, which does not show any evidence for NH_3 absorption. A higher effective temperature of $T_{\rm eff}$ = 1500 K which would agree with the spectroscopic temperature derived for the ε Indi B system by Smith et al. (2003), implies a non-physical small radius of ε Indi Ba, and is therefore unlikely.

Acknowledgements. We like to thank the VISIR science verification team and the ESO director general for allocating observing time to this project. We appreciate to use the model spectra of F. Allard, A. Burrows and D. Saumon in electronic form. A. Burrows to supplied his 1100 K and 1200 K spectrum, and D. Saumon his 800 K and 1200 K model directly. The referee, A. Burgasser, helped to improve the paper.

References

Allard, F., Hauschildt, P. H., Alexander, D. R., Tamanai, A., & Schweitzer, A. 2001, ApJ, 556, 357
Baraffe, I., Chabrier, G., Barman, T. S., Allard, F., & Hauschildt, P. H. 2003, A&A, 402, 701
Burgasser, A. J., Kirkpatrick, D. J., Brown, M. E., et al. 2002, ApJ, 564, 421
Burrows, A., Marley, M., Hubbard, W. B., et al. 1997, ApJ, 491, 856
Burrows, A., Sudarsky, D., & Lunine, J. I. 2003, ApJ, 596, 587
Cohen, M., Walker, R. G., Carter, B., et al. 1999, AJ, 117, 1864
Creech-Eakman, M. J., Orton, G. S., Serabyn, E., & Hatward, T. L. 2004, ApJ, 602, L129
ESA 1997, Hipparcos and Tycho catalogues, ESA-SP 1200
Lagage, P. O., Pel, J. W., Claret, A., et al. 2003, SPIE, 4841, 923
Lauchaume, R., Dominik, C., Lanz, T., & Habing, H. J. 1999, A&A, 348, 897
McCaughrean, M. J., Close, L. M., Scholz, R.-D., et al. 2004, A&A, 413, 1029
Pont, F., Melo, C. H. F., Bouchy, F., et al. 2005, A&A, 433, L21
Roellig, T. L., van Cleve, J. E., Sloan, G. C., et al. 2004, ApJS, 154, 418
Scholz, R.-D., McCaughrean, M. J., Lodieu, N., & Kuhlbrodt, B. 2003, A&A, 389, L29
Saumon, D., Marley, M. S., & Lodders, K. 2003 [arXiv:astro-ph/0310805] (SML)
Smith, V., Tsuji, T., Hinkle, K. H., et al. 2003, ApJ, 599, L107
Taylor, B. J. 2003, A&A, 398, 73
Tsuji, T. 2002, ApJ, 575, 264

Article published by EDP Sciences and available at http://www.edpsciences.org/aa or http://dx.doi.org/10.1051/0004-6361:200500121

Chapter 6

Perspectives for mid-infrared imaging observations from the ground

Résumé

Dans un contexte construction de telescope géants de tailles 30 à 42 m à l'horizon 2018, il est est important d'examiner les perspectives scientifiques pour des instruments observant dans l'infrarouge moyen attachés à ces télescopes. Dans ce chapitre, de décris en détails le potentiel d'un imageur en infrarouge moyen monté sur un télescope de type ELT (Extremely Large Telescope). Je montre que pour qu'il soit possible d'observer et caractériser des exoplanètes dans leur régime d'émission thermique, nous allons devoir développer de nouvelles techniques d'observation héritées de celles utilisées en astronomie à haute résolution angulaire en infrarouge proche. J'identifie deux principales opportunités pour l'imagerie thermique sur ELT: - l'observation directe d'exoplanètes géantes chaudes placées sur des orbites relativement étroites (0.2-1 UA) et - potentiellement les toutes premières images de sillons formés par des exoplanètes en train de se former dans des disques protoplanétaires.

Abstract

In the context of the upcoming giant (30-42 m) ground-based telescopes at the horizon of 2018, it is important to assess the scientific perspectives for mid-infrared instruments. In this chapter I describe in details the potential of a mid-infrared imager mounted on an ELT (Extremely Large Telescope) telescope. It is shown that to be able achieve the challenging goal of the characterization of giant exoplanets in the thermal regime we need to develop some new observing modes inherited from the high angular resolution techniques used in the near-infrared range. I identify two major niches: - the direct observations of warm (irradiated) giant exoplanets placed on relatively close orbits (0.2-1 AU) and - potentially the first images of gaps generated by forming exoplanets in protoplanetary disks.

Contents

6.1 Introduction

In the next decade, the successor of the HST, the James Webb Space Telescope (JWST) which is optimized for thermal infrared observations will be launched. This space observatory features MIRI, an imaging and spectroscopic instrument in the mid-infrared range (5-27 μm). The size of the passively cooled telescope of 21.3 feet makes a breakthrough in the complementarity between space and ground in the field of mid-infrared observations (see Sec.1.4). Indeed when compared to the largest ground-based telescopes, space born mid-infrared observatories used to be an order of magnitude smaller in size; their relatively modest angular resolution was compensated by the awesome sensitivity they were featuring. The JWST will completely turn upside down this rather simplistic scheme since it will not only have a sensitivity about 100 times higher than SPITZER, but also have an angular resolution of 0.38 arcsec (FWHM) at 10 μm which is comparable to that of the current largest ground-based telescopes (0.30 arcsec for the VLT, 0.25 arcsec for the Keck). On top of that, its data will have a peerless stability when compared to ground-based observations, especially concerning the PSF stability recalling that on large ground-based telescopes the PSF cannot be as stable as in space (see Sec.3.6). The compared sensitivities are shown in Fig.1.9. On top of that, the MIRI instrument will be equipped with a phase mask coronagraph. This device is meant to cancel the stars light and image faint objects in their vicinity such as giant exoplanets or circumstellar disks.
In this context, one can wonder what is the niche for future ground-based mid-infrared astronomy. Next generation giant telescopes will have sizes in the range 30-40 meters. The TMT (Thirty Meters Telescope) is a project which includes participations from Californian universities and institutes and Canada. The European ELT (E-ELT) is a 42 m telescope that will be built by ESO. We will now focus on the E-ELT but the conclusions drawn in the following should also apply to any other ELT having a comparable size. One of the major topics that shall address the next generation of instruments and telescopes is the study of exoplanets. We know since the discovery of Mayor and Queloz in 1995 [Mayor and Queloz, 1995] that other star host also planets. 349 exoplanets have been found at the date of June, 5th 2009. Besides, exoplanets are (almost) ubiquitous around stars. The method of radial velocities is very effective to detect giant planets but is strongly biased towards the most massive planets in inclined systems w.r.t. the face on case. The method of the photometric transits is limited to edge-on systems but brings valuable constraints on the planet radius. Combined with radial velocities method, a density can be then estimated which is one of the key physical parameters to understand the nature of extrasolar giant planets. However, precise constraints on these giant extrasolar planets can be only obtained through direct multi-wavelength imaging. Imaging in the visible/near-infrared range (scattering regime) gives direct indications on the reflectivity properties of the planet (radius, composition to some extent) while the thermal emission regime is more linked to the composition, age, or mass. The observing constraints are also quite different between the scattering and the thermal emission regimes. Observations in the first case are facing a contrast ratio between the star and the exoplanet of 10^9 to overcome while in the mid-infrared range, this contrast is "only" about 10^6. We discuss in this chapter (Sec.6.2) some new modes of observation and their different options that are mandatory to reach the challenging goal of direct imaging of exoplanets in the mid-infrared range from the ground.
Circumstellar disks are also potentially very interesting targets for mid-infrared astronomy on Extremely Large Telescopes. The unprecedent accuracy provided by such telescopes will allow firstly to spatially resolve known proto-planetary and debris disks. Secondly, when traditional photometric detection methods (based on measuring infrared excesses) are limited by a photometric accuracy around 1 % to detect new faint debris/exo-zodiacal disks the ELT will be able to spatially disentangle the star and the disk emissions. We estimate that the ELT/METIS instrument will be able to detect disks that are only 10 times brighter than our zodiacal disk (see Sec.6.5).

6.2 Beyond the standard imaging mode

As already explained VISIR is one of the first mid-infrared instrument mounted on new-design active optics corrected large telescopes. Our experience with VISIR has shown that we must reassess how to adapt the existing, and even develop new, observing schemes that will allow to provide the best angular resolution on modern complex large telescopes. On the next generation of very large telescopes which will be mechanically and optically complex, the use adaptive optics systems will be mandatory at any wavelength. In this chapter we propose some new observing methods aiming at get the best scientific return from future mid-infrared instruments mounted on ELTs.

6.2.1 The need for a coronagraph for mid-infrared range observations from the ground

This section and the next one deal with potential science cases that can be addressed by a mid-infrared instrument mounted on a 42 m (E-ELT) telescope in the areas of disks and exoplanets. Based on the experience that we have obtained with VISIR we could show that as long as mid-infrared observations :

- have extremely stable PSF conditions (i.e. diffraction limited with a Strehl ratio larger than 0.8)
- target a source which maximum flux per pixel is not larger than ∼1.1 times the median value of a pixel in the background
- can be considered as limited in sensitivity by the background noise

a very faint object around can quite easily unveiled simply by subtracting a scaled observation of a "naked" reference star. However, mid-infrared observations on an ELT :

- will be seeing limited at any wavelength in absence of the use of an adaptive optics system (AO).
- will saturate the detector for sources brighter than ∼ 3 Jy (i.e. the flux a G2V star at 10 μm at 10 pc).
- will start to be Poisson-noise limited for sources brighter than ∼1 Jy.

Standard imaging mid-infrared observations of faint (secondary) objects around much brighter (primary) objects, e.g. an exoplanet or a barely resolved debris disk around a star would be thus extremely limited on an ELT in the same manner as current direct imaging near-infrared observations are. It is thus important to study the feasibility of adapting to the mid-IR range the techniques of high contrast and high angular imaging currently used in the near-infrared range. The coronagraph device ([Lyot, 1939]) is an elegant optical solution to attenuate the light of the main object and strongly damp the very high ratio between a primary (e.g. a star) and a secondary object (e.g. a faint companion). The basic principle consists in modifying the diffraction pattern so that the light of the primary can be either optically filtered out or interferes destructively. Mainly driven by the challenging goal of direct imaging of extrasolar planets in the visible and near-infrared range, significant progresses have been made in the field of high-contrast imaging the last decade and more particularly concerning coronagraphy. The historical Lyot mask which uses an opaque disk to block the primary's light is strongly limited in terms of minimum achievable distance to the primary (few λ/D i.e. ~ 0.15 to 0.3 arcsec on a ELT at 10 μm). The basic Lyot coronagraph has been nowadays completed by a collection of coronagraphs which present different advantages. Describing them all in details is out of the scope of the present document. An exhaustive description of the various types of coronagraph proposed in the last few years can be found

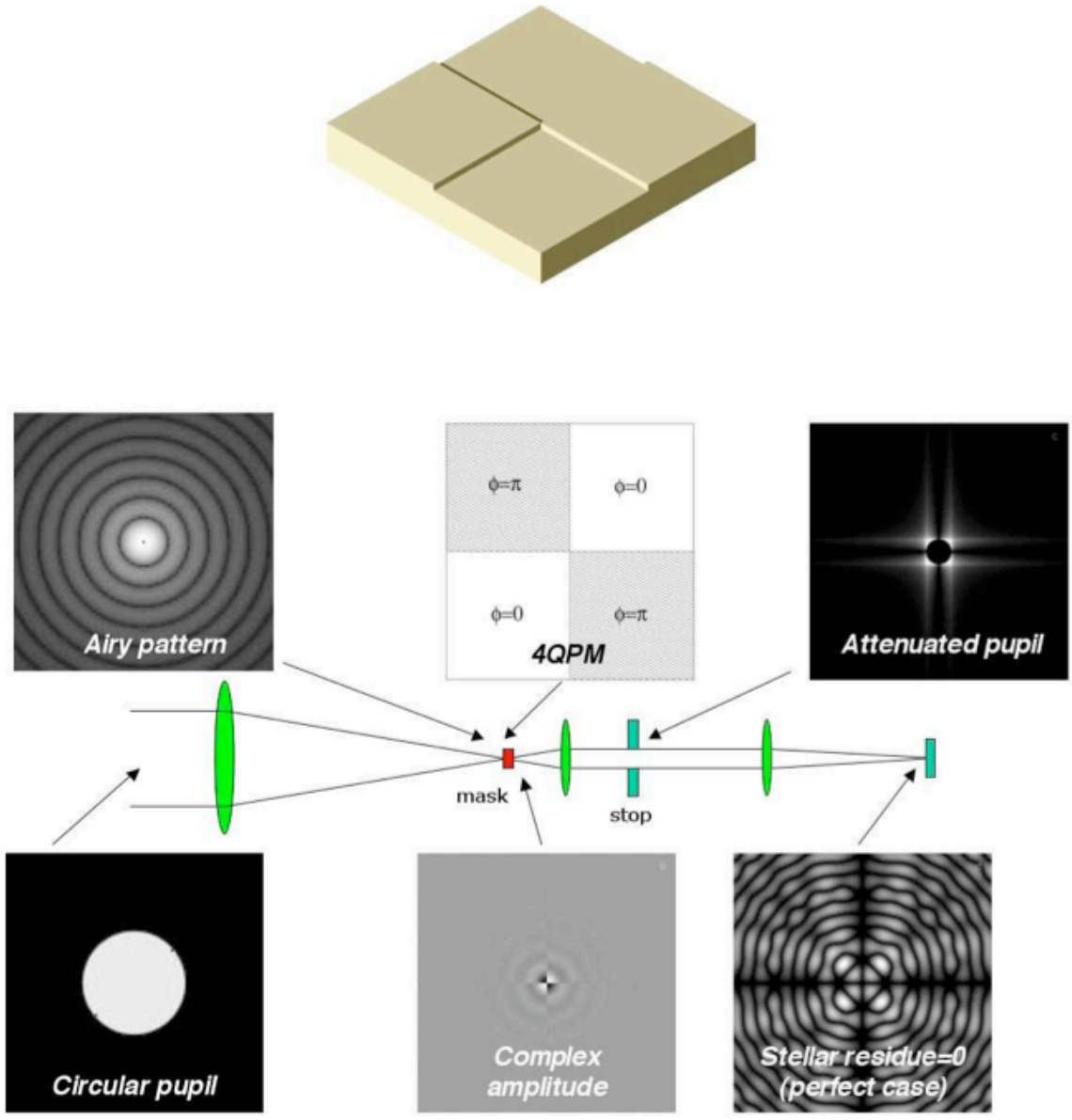

Figure 6.1: Cartoon of the 4QPM. The upper panel shows an artistic view of a four quadrants coronagraphic mask. The lower panel sketches the optical mounting of a 4QPM, the positions of the intermediate optical planes, and the appearance corresponding images in case of a perfect optical beam (perfect 4QPM device, no turbulence, no aberrations).

in [Guyon et al., 2006] and [Martinez et al., 2008] Among those, the four quadrant phase mask (4QPM, [Rouan et al., 2007]) is one of the very first that smartly produce destructive interferences at the level of the primary while partially (a gradual attenuation applies) preserving a faint source at any angular distance from the primary. This type of coronagraph has been successfully tested in AO assisted near-infrared imagers such as NACO on the VLT ([Boccaletti et al., 2004]). Its principle is based on the use of a focal plane mask which is divided into 4 quadrants (Fig.6.1)). Diagonally placed quadrants are designed to produce a phase shift of π while the two other ones produce a null phase shift. If the primary source is sufficiently precisely centered (this value is specific to each instrument/wavelength and will be discussed later in the specific context of ELT/METIS), half of the energy of primary's beam is dephased by π which produces then a self-destructive interference. In the pupil plane, a conjugate mask is placed to filter out the diffracted light of the primary. In the four-quadrant phase mask the phase shift $\Delta\Phi$ is obtained by different thicknesses of the materials in the quadrants ($\Delta\Phi = 2\pi n\Delta e/\lambda$, where n is the substrate refractive index, Δe the difference in thickness, and λ the wavelength). A strong limitation immediately arises: the four-quadrants phase mask is chromatic i.e. is designed to work optimally only at a given wavelength. Eventually, several phase masks can be implemented in the instrument to match all the imager filters but this solution is costly, forbids the use of broad-band filters, and cannot be combined with differential imaging (see below). Another solution is to combine the effects and the rejecting power of several 4QPM coronagraph plates placed one after another ([Baudoz et al., 2008]). However, this is a rather complex solution optically speaking since multiple focal and pupil planes musts be built. The various solutions to achromatize a 4QPM are described in [Rouan et al., 2007]. For instance, a solution based on the combination of 2 achromatic polarimetric half-wave plates has been proposed ([Mawet et al., 2006]) and will be the baseline of the VLT/SPHERE PlanetFinder instrument. This combination physically produces a phase shift which is approximatively constant over a spectral range with a resolution of the order of 2.

Another alternative lies in physically simulating a refractive index which is proportional to the wavelength (gradient of index). Such solutions have been already developed in the context of anti-reflective processing using sub-wavelength gratings (zero-order gratings). It can be shown that a such a etched at the surface of an optical device optically simulates a gradient of index. The zero-order grating 4QPM uses this optical solution to produce an achromatic solution over a fairly wide range of wavelength limited by theoretical differences between the gradient index of the two polar vectors. Any 4QPM-based coronagraph has the disadvantage of presenting discontinuities between two consecutive quadrants. The light falling onto these transitions is usually scattered and produces artifacts at the level of the focal plane. The instrument needs to be rotated to reconstruct information lost at the level of the transitions. The annular groove phase mask (AGPM) coronagraph (or vortex coronagraph) [Mawet et al., 2005] proposes an elegant way of azimuthally symmetrize a phase mask coronagraph an thus eliminate any transition edge while preserving the achromatic capability. The simulations shown in the following are based on the assumption of a chromatic 4QPM coronagraph; the expected performances of an achromatized coronagraph are evaluated using two or more chromatic 4QPMs centered on several different wavelengths.

6.2.2 The need for differential imaging

The PSF of a telescope has several reasons to vary in time. First, in case of seeing limited observations the PSF changes because the turbulence varies with time. Second, the alt-azimuthal mount of modern large telescopes produces a rotation of the pupil; the diffractive part of the PSF thus also rotates in time. Although it is possible to minimize the second effect by carefully choosing a standard star such that the parallactic angles corresponding to the science target and the standard observations are similar, the variations due to the seeing are difficult to eliminate even in the case of adaptive optics assisted observations. In the context of high-constrast imaging one powerful technique developed in the near-infrared range is the differential imaging. It consists in observing simultaneously an object at two or more close wavelengths. If an object contains an emission of absorption spectral feature in its spectrum at the wavelength of interest, the differential imaging technique allows to obtain a very accurate real-time estimate of the

PSF. Since all the (static aberrations and turbulence deformations) speckles are in essence achromatic, the subtraction of the "reference" image outside of the spectral feature to the image centered on the spectral feature will cancel efficiently most of the emission of the star (or the unresolved component) which is distributed over the residuals of seeing speckles and the common path static speckles. The only remaining residual speckles are those produced by the non-common path aberrations (different optical paths after the dichroic) in a dual channel differential imager. It must be noted that in the process the continuum emission of the companion/disk is also canceled; the higher the contrast of the feature, the more performant is the differential imaging method.
Following the METIS mid-term review in January 2009, the dual channel option has been discarded. The only remaining option to implement a differential imaging mode in METIS is based on a bi-spectral detector that performs the differential imaging on the chip (see Sec.6.5.1). In this option the non common path aberrations are negligible. Finally, given the very high contrasts one usually aims at in the context of exoplanets or disks the differential imaging mode has to be combined with coronography.
Preliminary results of simulations of differential imaging performances in the context of exoplanets detection are shown in Fig.6.7. When the seeing conditions degrade, only the 4QPM-differential imaging mode is able to maintain the rejection performances high enough for competitive exoplanets detection.

6.2.3 Performances of coronagraphy and differential imaging in the mid-IR on an ELT

As explained above, the coronagraphy combined with differential imaging is one of the most performant observing method to achieve high levels of stellar rejection. In order to quantify the expected performances as a function of the observing parameters (seeing, type of coronagraph, telescope jitter, etc) we have developed a numerical code that simulates coronagraphic observations with METIS. The simulation includes:

- the pupil of the ELT,
- an adaptative optics system which characteristics are those of the ELT system (84x84 sub-apertures),
- a 4QPM-based coronagraph subject to chromatism. This effect arises because the full rejection of a 4QPM coronagraph is reached in the case of a monochromatic light. When considering a broader range of wavelengths (e.g. over the full bandwidth of the filter), the performances in rejection are degraded. Indeed at a wavelength λ differing from the optimized wavelength λ_0 the degradation theoretically scales with $(\lambda/(\lambda - \lambda_0))^2$ ([Riaud et al., 2003]).

The relative rejection is defined as the flux ratio between the primary object and a secondary point source. The detectivity threshold has been set experimentally (by simulating a point source detection among coronagraph residuals) to 100 times the standard deviation of the residuals at a given distance from the star. Figure 6.3 shows the computed performances of star (or unresolved inner component in the case of protoplanetary disks) relative rejection as a function of the distance to the star. Two optional instrumental set-ups are studied. In the first one ('Dual channel coronagraph'), we assume that the differential imaging mode is based on an upstream optical beam splitting between the two wavelength followed by two distinct 4QPM devices each one beam centered on its "own" wavelength. In this case some pre-coronagraph and post-coronagraph differential aberrations have to be taken into account. The two beams fall at two different locations on the large-band detector.
In the second option studied ('Common coronagraph') the simulations assume a 4QPM-based coronographic device common to both wavelength and which is centered on the average wavelength. In this case the wavelength separation is carried out by a bi-spectral detector (e.g. a QWIP detector, see Sec.6.5.1). In this case, the post-coronagraph differential are reduced and correspond only to assumed aberrations potentially existing between the two layers of the detector. Ultimately, the goal would be to combine

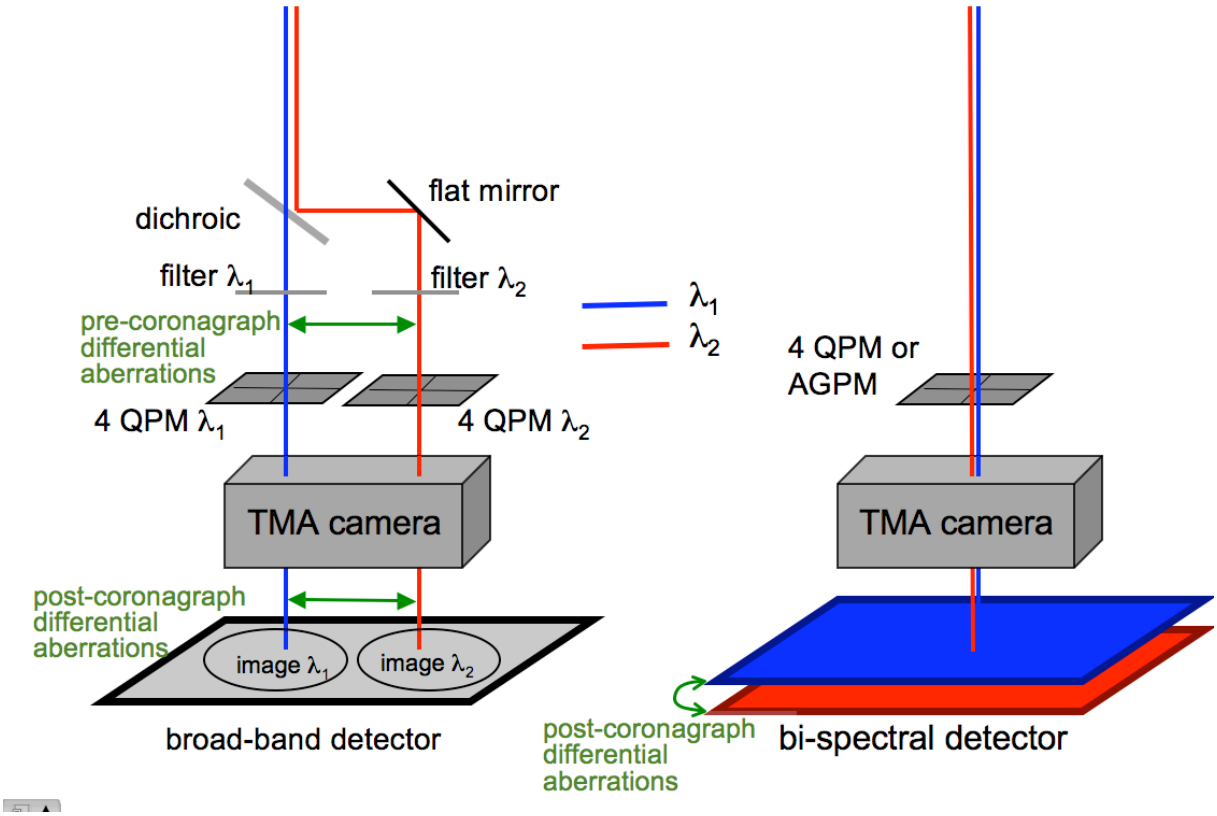

Figure 6.2: Sketch of the two differential imaging options for implementation. The TMA stands for a "Three Mirrors Anastigmat" system. The two wavelength λ_1 and λ_2 correspond to those selected for differential imaging.

a bi-spectral detector with an achromatized phase mask coronagraph (e.g. and AGPM, see Sec.6.2.1). The performances we can expect are shown in Fig.6.3 where a semi-perfect coronagraph is mimicked by assuming that each of the 2 wavelength beams is attenuated by an optimized (for each of the 2 wavelengths) 4QPM chromatic coronagraph. In this study, the influence of each parameters(chromaticity, jitter and atmopsheric turbulence) is studied *independantly*. The results obtained show that :

- the performances of the differential imaging mode depend strongly on the chromaticity of the coronagraph device
- the sequential PSF subtraction performances (direct and coronagraphy) are affected by the jitter essentially at the shortest angular distances (d<150 mas)
- the 4QPM coranagraphic mode is mandatory (in case of no differential imaging) to reach a rejection level of more than 10^{-4} at a distance of 0.1 arcsec from the star
- in case of degraded conditions because of strongly varying seeing or in presence of residual jitter the ultimate performances can be maintained when using the combined coronagraphy/DI mode

The study of the influence of the jitter is of particular importance since some efforts (design of the instrument, of the AO) can be made to minimize the jitter residuals. On the other hand, these values need also to be specificed for the E-ELT design. In Fig.6.4, the rejection levels obtained by simulation (assuming some typical values of atmospheric turbulence and an achromatized 4QPM coronagraph) have been converted into limiting masses of giant exoplanets. The star is assumed to be of solar-type (1 $L_{\odot}$, $T_{\rm eff}$=5770 K), 10 pc away. Apart from the extreme (and non physical) case of a null residual jitter which is shown for pedagogical purpose, one can notice that the gain obtained when decreasing the level of residual jitter "saturates" around 3.5 mas. This value should thus be considered as a goal for the E-ELT/METIS specifications.

6.3 Exoplanets

Giant gaseous planets are ubiquitous around stars. Radial velocity surveys have shown that at least 5-20% (depending on the metallicity of the host star, [Fischer and Valenti, 2005, Haywood, 2009]) of main-sequence stars with spectral types in the range F-M are surrounded by planetary systems. The chances to observe such giant planets are thus fairly high, even when being restricted because of sensitivity considerations to the close vicinity of Earth (d≤10-20 pc). Fig.6.5 shows the emission spectra of giant planets at 2 different ages we consider here as being illustrative of ages of the stars within 20 pc around Earth.

As seen in these plots, the mid-infrared relative emission from these objects is fairly high which makes it interesting to try to detect them around 10 μm. On top of that for mass smaller than 10 M_j, the NH_3 features is a potentially interesting feature to exploit the possibilities of differential imaging.

6.3.1 Thermal infrared observations of giant planets with ELTs

The typical (isolated) point source sensitivities on 30-42 m telescopes in the N band is about 10-30 μJy in one hour depending on the site and the observing conditions. In the vicinity of a star (angular distance smaller than 1 arcsec) having a flux of typically 3 Jy for a G2-type star at a distance of 10 pc, the task of detecting a faint point source is much harder; the point source sensitivity is typically degraded by a factor of ∼10 because of an imperfect PSF subtraction.

With fluxes ranging between ∼10 and 1000 μJy at 10 pc, giant exoplanets are not only bright enough in the mid-IR range to be detected but the most massive ones potentially overcome the PSF residual levels at moderate distances (5-10 AU) from the star. Stars located in a volume limited of 10-20 pc of radius

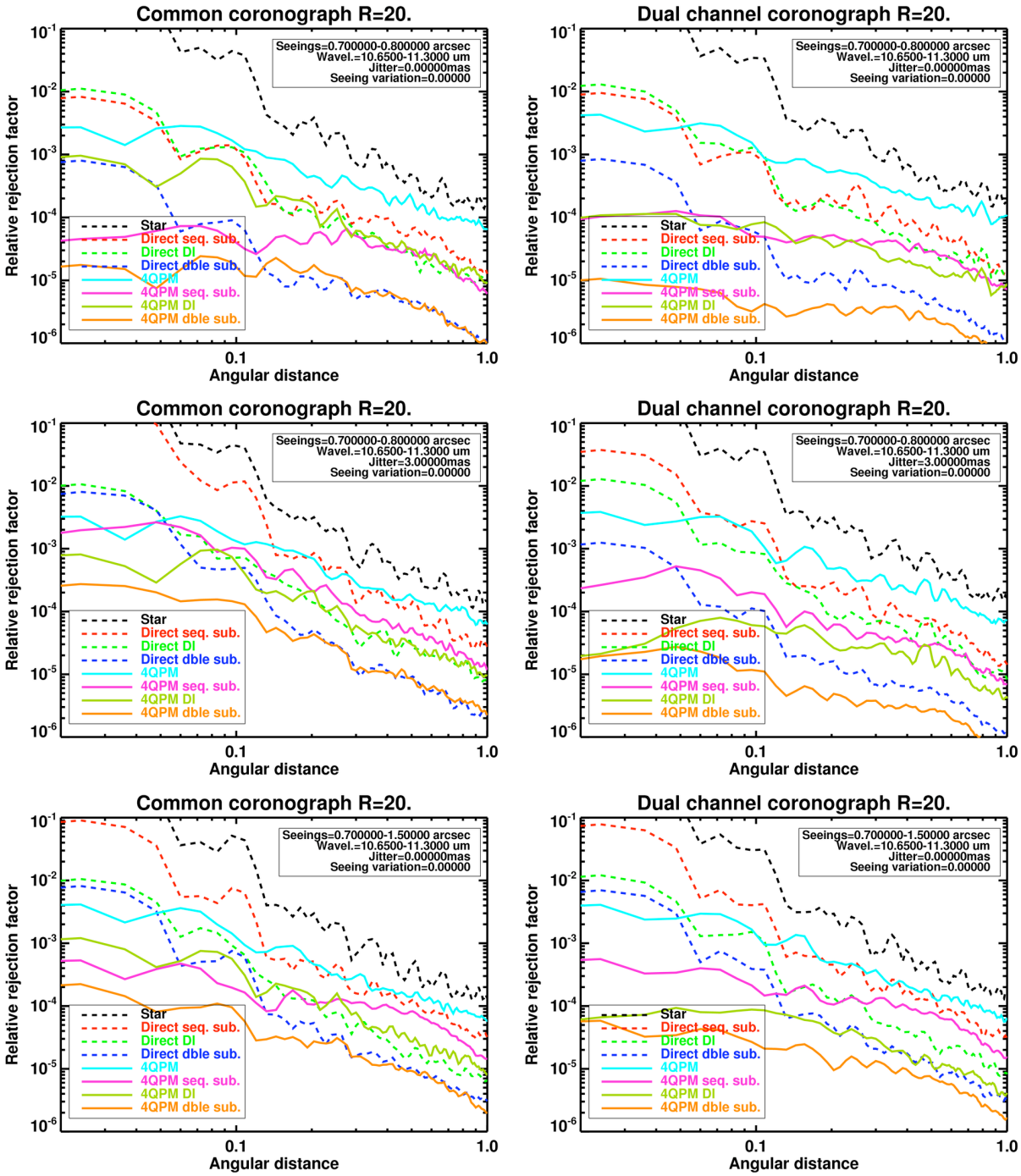

Figure 6.3: Star rejection levels as a function of the angular distance to the star. The two cases ("common" and "dual channel") are described in the text. The PSF and the 4QPM profiles are overplotted for comparison. The seq.sub. refers to the subsequent PSF method based on a standard star observation before or after the scientific target. DI stands for differential imaging at 10.65 and 11.3 μm (NH_3 feature). Dble sub. refers to a double subtraction methods which combines the two precedent ones. In all the cases a filter (or set of 2 filters in the case of DI) having a spectral resolution of R=20 is assumed.

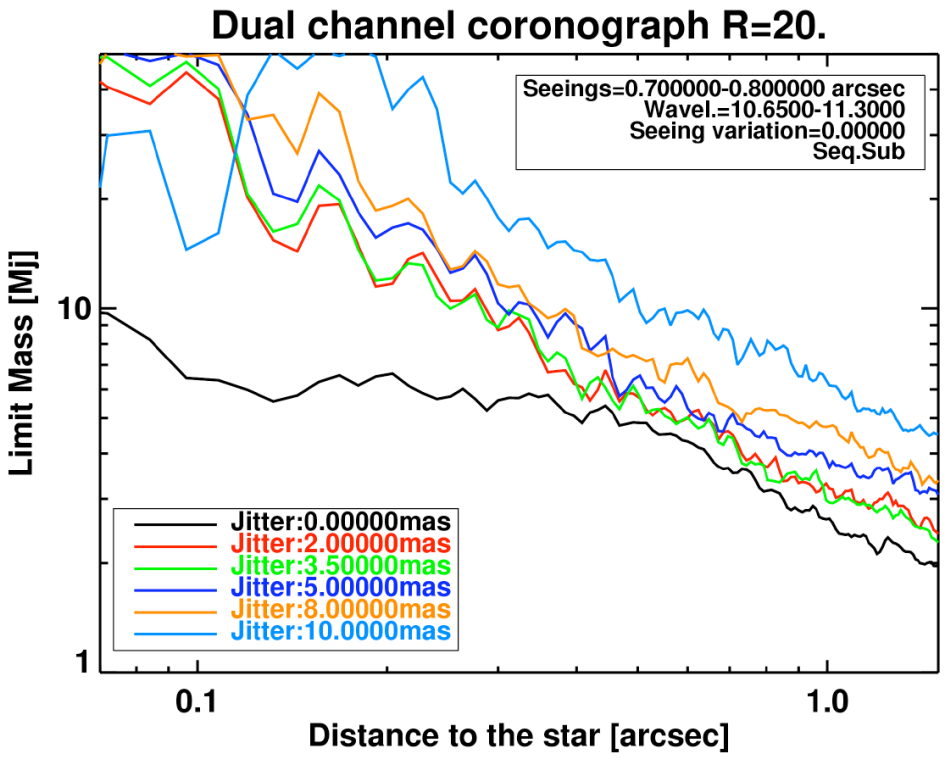

Figure 6.4: Limiting masses of detectable exoplanets as a function of the distance to the star for various residual jitter levels. The star is assumed to be of solar-type (1 $L_{\odot}$, T_{eff}=5770 K) and located 10 pc away. The observing mode is the subsequent standard star subtraction and the 4QPM coronagraph is achromatized on the 10-12 μm wavelength range. See the text for the discussion.

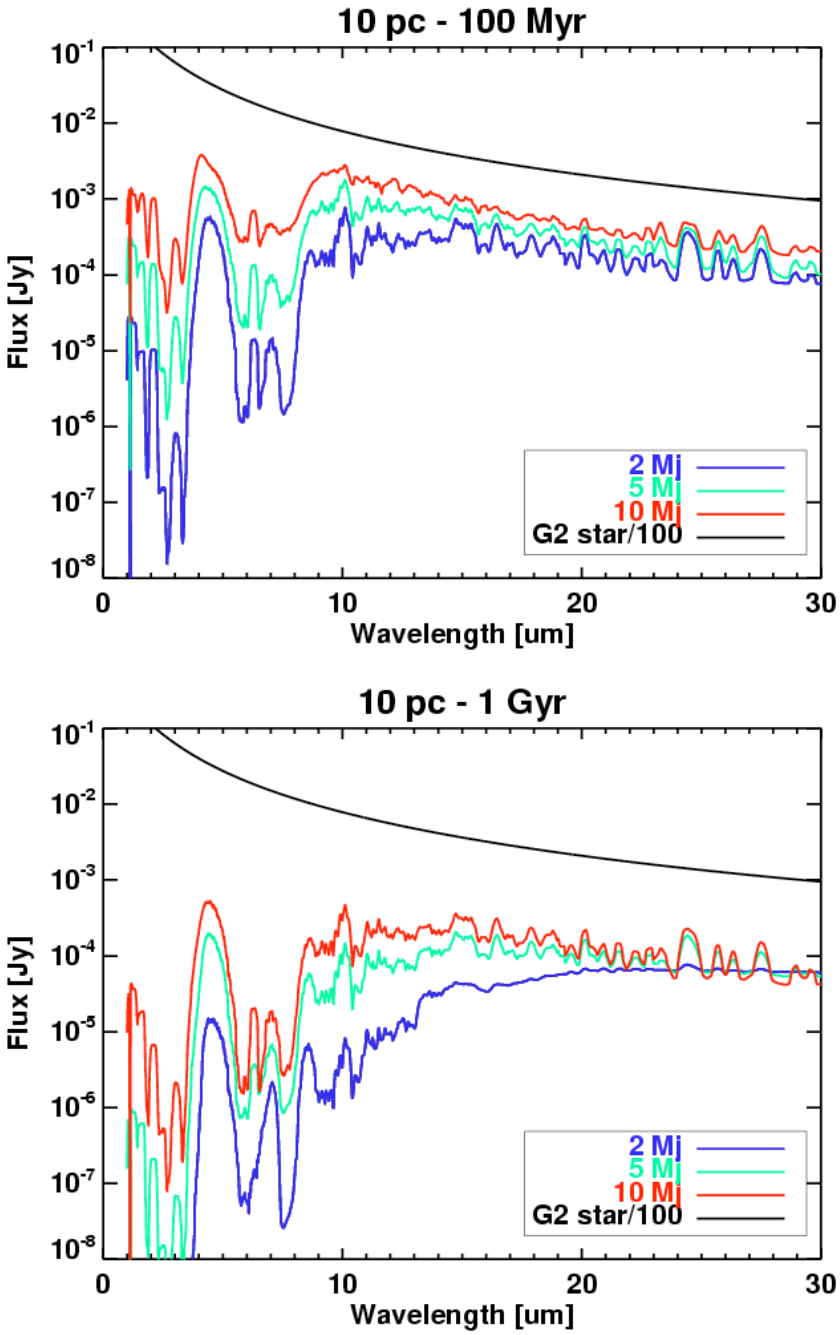

Figure 6.5: Low-resolution (R=100) infrared spectra of giant exoplanets. Upper panel: at an age of 100 Myr. Lower panel at an age of 1 Gyr. The emission from a G2 star (divided by 100) is also overplotted as a reference. The spectra are computed from [Burrows et al., 2003] models.

constitute thus a set of good targets for an ELT/mid-IR instrument and deserve further studies of the accessible physical parameters.
Figure 6.7 shows the performances of the E-ELT/METIS instrument terms of exoplanet detection as a function of the distance to the star for an object located 10 pc away from Earth. In Figure 6.8 are displayed some of the corresponding images. Concerning the coronagraph performances and configuration we assume that same cases as in Sec.6.2.3. In both options the influence of a residual telescope jitter and of degraded seeing conditions are also considered. In all cases, the filter considered has a spectral resolution of R=20. The detection levels have been experimentally set to 100 times the local residuals standard deviation which roughly corresponds to a 5 σ peak detection for a point source. The expected fluxes from putative giant exoplanets of various masses and placed at various distances from the star are also displayed to show the expectations in terms of possible detections. Their age is chosen to be 1 Gyr which is typical for systems located at 10 pc from Earth.

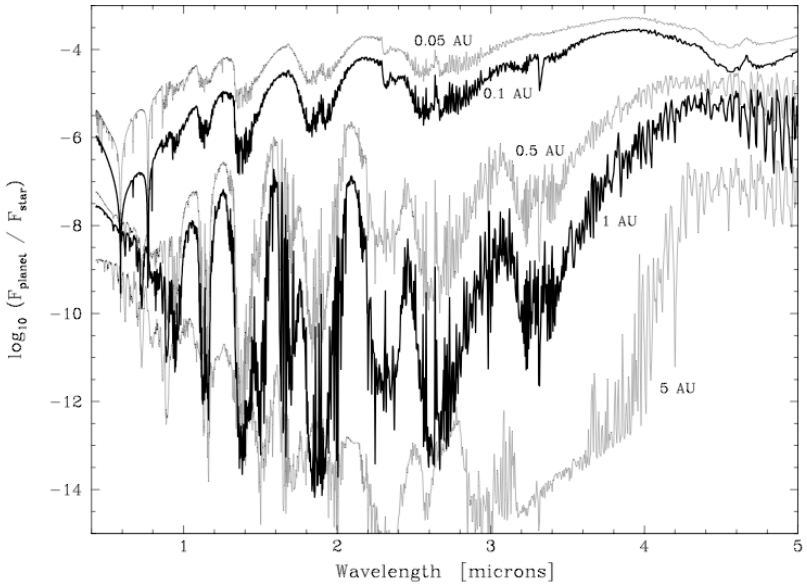

Figure 6.6: Compared spectra of irradiated (d≤1 AU) and self-luminous giant exoplanets (d=5 AU) around a G0V star. The spectra are relative w.r.t. the star (from [Sudarsky et al., 2003]).)

As already explained above, the E-ELT/METIS observations will be restricted to giant self-luminous exoplanets with masses in the range 2-13 Jupiter masses at angular distances of 2 and 0.13 arcsec respectively. There is however a clear niche for METIS which is the detection and the characterization of irradiated giant exoplanets. These exoplanets have orbital distances in the range [0.05-1] AU, such as 51 Peg b (0.05 AU), GJ 876 b (0.21 AU) or ν And c (0.83 AU). At such distances, the effective temperature of the giant exoplanet is significantly increased (e.g. from 125 K to 200 K at a distance of 1 UA from a GOV primary) by absorption of the stellar radiation [Burrows et al., 2003, Barman et al., 2001]. As a result, the planet becomes brighter in the IR range where most of the flux absorbed is re-emitted (see Fig.6.6).

Recently the SACY project ([Torres et al., 2006]) reported a census of close-by (d≤100 pc) young associations. Their sample comprises about 300 stars with ages ranging between 10 and 100 Myr and distances in the range 30-100 pc. These young systems are potentially a set of very interesting targets for an ELT instrument observing in the N band since the younger giant exoplanets are hotter and thus brighter at this wavelength. It becomes thus possible to detect a giant exoplanet around more distant stars

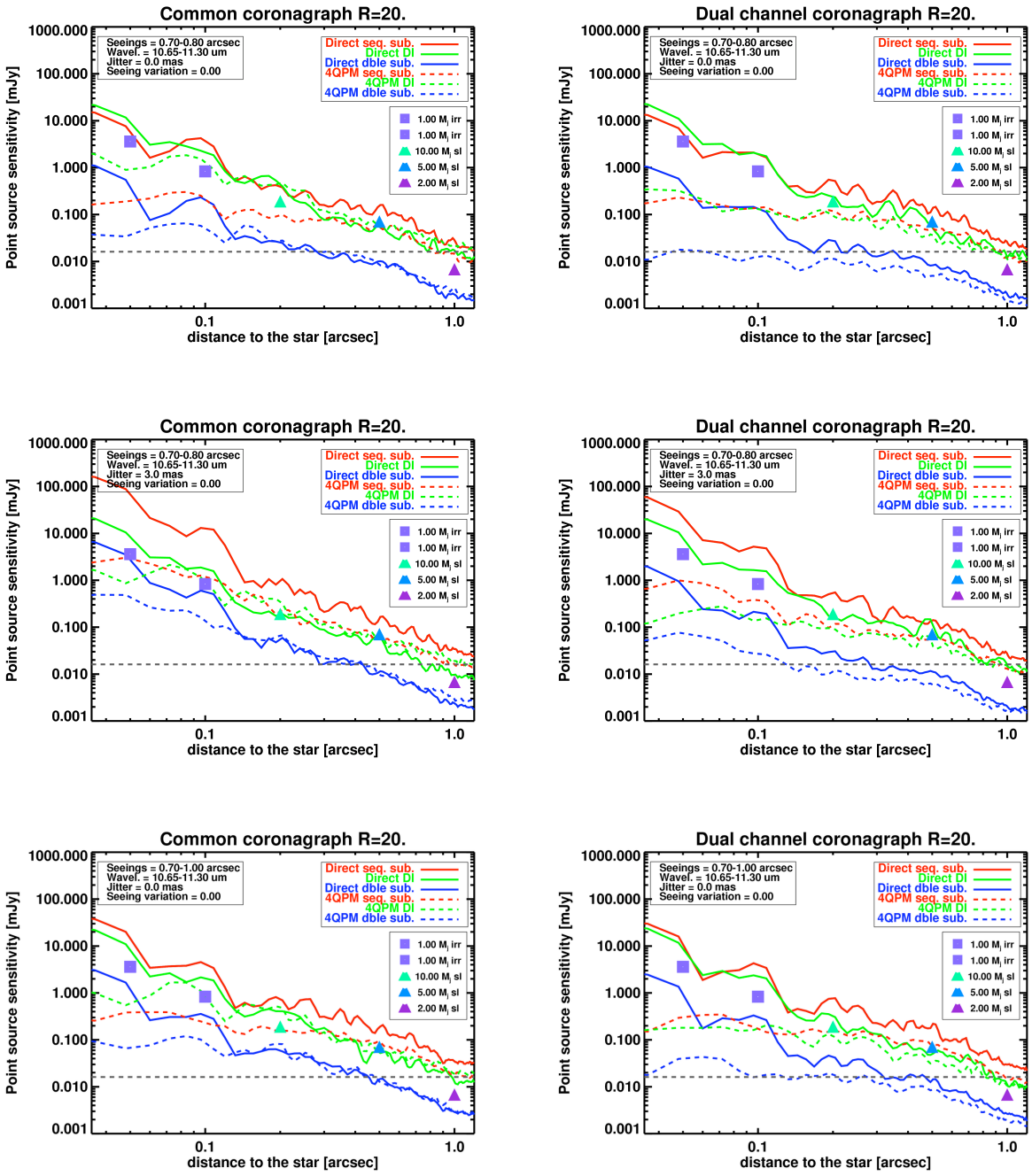

Figure 6.7: Performances of the E-ELT/METIS instrument in sensitivity to a point source as a function of the distance to the star. Several scenarios are considered to reject the starlight. The plain lines refer to direct imaging while the dashed ones refer to coronagraphic observations. In the sequential standard star subtraction scheme (seq.subs.), the starlight of the target is suppressed by subtracting an image of a reference star obtained before or after the main observation. In the differential imaging mode (DI), the starlight is suppressed by a simultaneous observation at 2 close wavelength corresponding to a spectral feature in exoplanet spectrum and the adjacent continuum (the NH_3 feature at 10.65 µm in the present case). In the double subtraction scheme (dble.sub.) the two precedent schemes are combined. The dashed grey line displays the background limited sensitivity reached in one hour of observation. The 0.7-0.8 arcsec seeing refer to the optical seeings during the observation of the target and that of the standard star used for residuals subtraction. The triangles correspond to self-luminous giant planets ([Burrows et al., 2003]) and the blue squares to the irradiated planets case ([Barman et al., 2001] models). The upper panel assumes some "perfect" observing conditions. Middle panel assumes some additional jitter residuals (3 mas RMS). The lower panel assumes varying seeing conditions between 0.7 and 1.0 arcsec in the visible range.

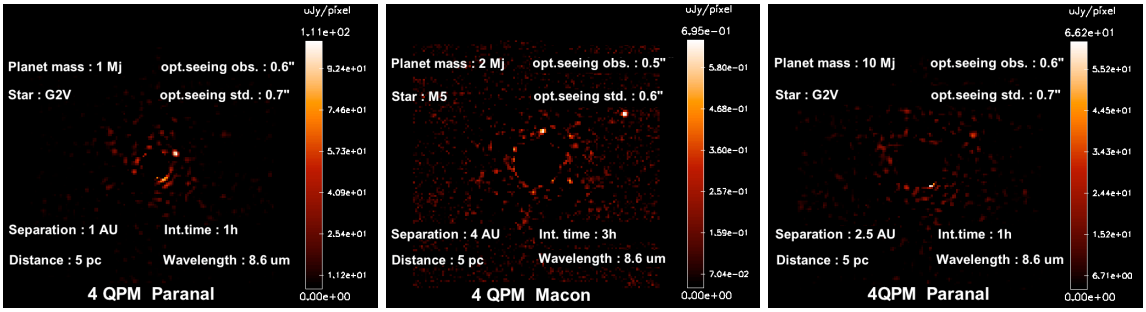

Figure 6.8: Simulated images of giant exoplanets observations with the E-ELT/METIS instrument. Several types of host stars and seeing conditions are assumed. All the parameters of the simulation are displayed in the figures.

(d≤100 pc). Fig.6.9 illustrates this and shows the performances when observing a 50 Myr system at 50 pc.

In conclusion METIS cannot be qualified as a highly competitive giant planet finder but its goal will be more focused on bringing valuable informations on the nature and the composition of already found exoplanets through the direct measurement of spectrophotometry at low spectral resolution. In the context of exoplanet detection it is interesting to compare the capabilities brought by mid-IR observations on an ELT to that of the other methods. Fig.6.10 compares the sensitivity in mass for the VLT/SPHERE ([Beuzit et al., 2008]) and the E-ELT/METIS instrument. It shows that once that the SPHERE survey of nearby stars is completed, the METIS instrument will be able to characterize the thermal emission of *all the giant exoplanets previously detected by SPHERE.*

6.3.2 A niche for Super-Earths ?

The recently discovered super-Earths (SE, [Beaulieu et al., 2006]) are the most massive versions of telluric planets i.e. planets mainly composed of solid and liquid materials [Valencia et al., 2007] e.g silicates, metals, ice, water, eventually liquid methane like on Titan. Their masses are limited to somewhat 10 Earth masses because of considerations on the available mass of solids contained in a protoplanetary disk at typical distances of 1-10 AU; a more massive protoplanetary disk would also have been gravitationally instable and would have formed therefore only gaseous giants. Considering a 10 Earth masses rocky planet having about the same density as Earth, its radius would be "only" slightly more than 2 Earth radii. Even less dense planets such as ocean planet [Leger et al., 2004] barely reach a maximum radius larger than 2 $R_{\oplus}$. The maximum surface of these planets are thus only 10 times that of Earth. Before going further in the discussion, it must be noted that:

- it will be virtually impossible to directly measure the thermal emission of the atmosphere of a planet having an atmospheric composition similar to that of Earth; only the surface (rocky or liquid) will be eventually detectable.
- water has a very weak emission in the N-band; the emission at 10 μm of an ocean planet will be probably below the sensitivity limits of an ELT in the mid-infrared range.

Taking these elements into account we focus then on a super-Earth planet that would have a transparent atmosphere in the N-band and a rocky surface. Let a being the planet albedo in the visible range, L the luminosity of the star in W, σ the Wien constant, r then distance of the planet to the star in

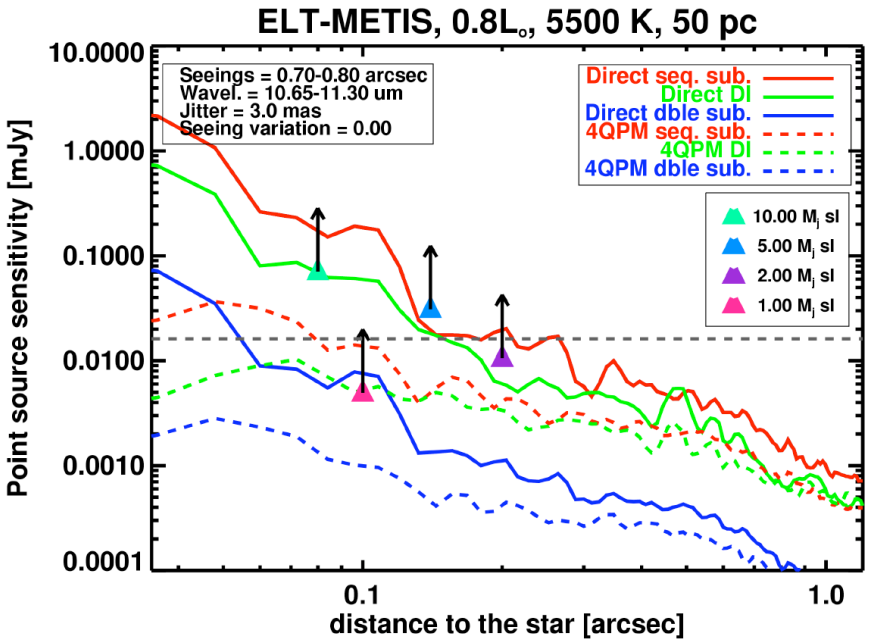

Figure 6.9: Young giant exoplanet detectability in the N band. The star is assumed to be a young 0.8 $M_\odot$ star with an effective temperature of 5500 K; this star represents the typical type of stars found in the sample of nearby young stars. The grey dashed line shows the point source detection limit for 1 hour of observing time imposed by the background thermal noise. The triangles overplotted correspond to the expected fluxes of exoplanets at an age of 100 Myr. Since the sample contains young stars having ages between 10 and 100 Myr, the arrows represent the expected increase of flux at younger ages (according to [Burrows et al., 1997], at an age of 50 Myr an increase of flux by a factor of 4 is expected). At 10 Myr, a factor of 10 of increase in flux is expected and is not displayed on the graph.

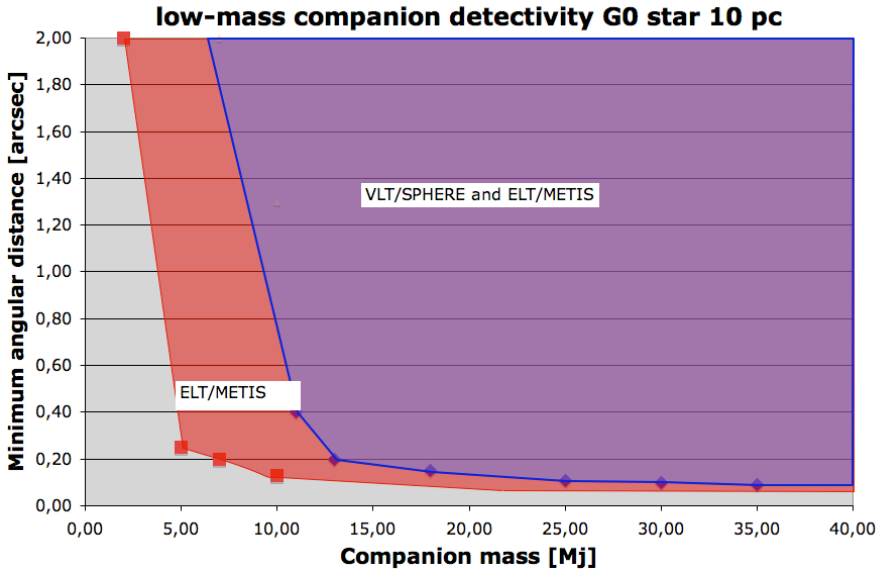

Figure 6.10: Compared performances of VLT/SPHERE and ELT/METIS for exoplanet detection as a function of the planets masses around a G0 star. Around a M0 star, the minimum mass detection achieved by E-ELT/METIS is constant ($\sim 2M_j$).

meters. Assuming thermal balance between the flux of the star absorbed by the planet and the planet emission, the temperature of the planet is given by:

$$T = (\frac{L(1-a)}{4\pi r^2 \sigma})^{1/4} \tag{6.1}$$

Molten super-Earths

In the past, the Earth has undergone numerous catastrophic events that have completely reshaped its surface and melted its surface to temperatures up to 1500 K. For instance, during the building of Earth, several tens of Mars-sized proto-planets collided to form the proto-Earth. The giant collision with a Mars-sized planet led to the formation of the Moon ([Canup, 2004]) when the solar system was at an age of only 30 to 50 Myr. During the late heavy bombardment (LHB) that produced the craters on the surface of the moon ([Koeberl, 2003]) some 3.8 Myr ago, ∼1000 tons of material coming from the proto-Kuiper belt ([Gomes et al., 2005]) impacted constantly each square meter of the proto-Earth during ∼100 Myr ([Graae Jorgensen et al., 2009]) and also eventually formed Saturn's rings ([Charnoz et al., 2009a]). There might be a direct link between the LHB and the Vega phenomenon The continuous flux of energy brought by these large-velocity impactors has maintained for about 100 Myr the surface of the proto-Earth to high temperatures, in a quasi-melted state. During this stage, the proto-Earth has been much more luminous in the infrared range than it is now. Although the systematic occurence of a late heavy bombardment is questionable for the exo-planetary systems we can however speculate that the telluric planets building phase in the young systems (10-50 Myr) must be rather common. Since the temperature of the planet's surface does not depend on the distance to the star the range in size of observable planets is rather simple to evaluate. Assuming a range of temperature of 500 to 1500 K and a typical limiting flux of 100 μJy in the N band for a point source at a distance of 0.2 arcsec from the star, Fig.6.11 displays

	dist. to star [AU]	dist. to star ["]	Planet temp. [K]	Flux [μJy]	Star flux [Jy]	Ratio planet /star
Sirius						
Teff=9910 K, 23 $L_\odot$, 2.6 pc						
	0.1	**0.04**	**1762**	**3282**	**130**	**2.52E-05**
	0.2	**0.08**	**1246**	**1952**	**130**	**1.50E-05**
	0.3	**0.12**	**1017**	**1390**	**130**	**1.07E-05**
	0.4	**0.15**	**880**	**1068**	**130**	**8.22E-06**
	0.5	**0.19**	**790**	**860**	**130**	**6.62E-06**
	0.75	**0.29**	**843**	**553**	**130**	**4.25E-06**
	1	**0.38**	**557**	**390**	**130**	**3.00E-06**
	1.5	**0.58**	**455**	**222**	**130**	**1.71E-06**
	2	**0.77**	**394**	**140**	**130**	**1.08E-06**
	4	**1.54**	**278**	**35**	**130**	**2.69E-07**
A5 star						
Teff=8200 K, 10 $L_\odot$, 2.5 pc						
	0.1	**0.04**	**1430**	**2422**	**100**	**2.42E-05**
	0.2	**0.08**	**1012**	**1380**	**100**	**1.38E-05**
	0.3	**0.12**	**826**	**943**	**100**	**9.43E-06**
	0.4	**0.16**	**715**	**701**	**100**	**7.01E-06**
	0.5	**0.20**	**640**	**546**	**100**	**5.46E-06**
	0.75	**0.30**	**522**	**330**	**100**	**3.30E-06**
	1	**0.40**	**452**	**220**	**100**	**2.20E-06**
	1.5	**0.60**	**370**	**112**	**100**	**1.12E-06**
	4	**1.60**	**226**	**12**	**100**	**1.20E-07**
F0 star						
Teff=7020 K, 6 $L_\odot$, 2.5 pc)						
	0.1	**0.04**	**1259**	**1986**	**91**	**2.18E-05**
	0.2	**0.08**	**890**	**1090**	**91**	**1.20E-05**
	0.3	**0.12**	**727**	**725**	**91**	**7.97E-06**
	0.4	**0.16**	**630**	**526**	**91**	**5.78E-06**
	0.5	**0.20**	**563**	**400**	**91**	**4.40E-06**
	0.75	**0.30**	**460**	**230**	**91**	**2.53E-06**
	1	**0.40**	**400**	**145**	**91**	**1.59E-06**
	1.5	**0.60**	**325**	**70**	**91**	**7.69E-07**
	2	**0.80**	**281**	**37**	**91**	**4.07E-07**
F5 star						
Teff=6530 K, 2.5 $L_\odot$, 2.5 pc)						
	0.1	**0.04**	**1012**	**1370**	**47**	**2.91E-05**
	0.2	**0.08**	**715**	**701**	**47**	**1.49E-05**
	0.3	**0.12**	**584**	**440**	**47**	**9.36E-06**
	0.4	**0.16**	**506**	**302**	**47**	**6.43E-06**
	0.5	**0.20**	**452**	**220**	**47**	**4.68E-06**
	0.75	**0.30**	**370**	**112**	**47**	**2.38E-06**
	1	**0.40**	**320**	**64**	**47**	**1.36E-06**
	1.5	**0.60**	**261**	**26**	**47**	**5.53E-07**
	2	**0.80**	**226**	**12**	**47**	**2.55E-07**

Table 6.1: Thermal characteristics of super-Earth exoplanets. The fluxes are given at a wavelength of 11.2 μm. The super-Earth exoplanet has a radius of 2.5 $R_\oplus$ and an average albedo of 0.3. Any planet producing a flux lower than ∼20 μJy below the background noise detection limit will be undetectable.

	dist. to star [AU]	dist. to star ["]	Planet temp. [K]	Flux [μJy]	Star flux [Jy]	Ratio planet /star
G2 star						
1 $L_\odot$, 2.5 pc						
	0.1	0.04	804	1000	30	3.33E-05
	0.2	0.08	570	444	30	1.48E-05
	0.3	0.12	464	256	30	8.53E-06
	0.4	0.16	402	163	30	5.43E-06
	0.5	0.20	360	110	30	3.67E-06
	0.75	0.30	293	50	30	1.67E-06
	1	0.40	254	24	30	8.00E-07
	1.5	0.60	207	8	30	2.67E-07
K5 star						
Teff= 4100 K, 0.2 $L_\odot$, 2.5 pc						
	0.1	0.04	538	385	15.5	2.48E-05
	0.2	0.08	380	135	15.5	8.71E-06
	0.3	0.12	310	62	15.5	4.00E-06
	0.4	0.16	270	32	15.5	2.06E-06
	0.5	0.20	240	18	15.5	1.16E-06
	1	0.40	170	2	15.5	1.29E-07
M0 star						
Teff= 3500 K, 0.1 $L_\odot$, 2.5 pc						
	0.1	0.04	452	236	12	1.97E-05
	0.2	0.08	320	70	12	5.83E-06
	0.3	0.12	261	28	12	2.33E-06
	0.4	0.16	226	13	12	1.08E-06
	0.5	0.20	202	6.7	12	5.58E-07
M5 star						
Teff= 2800 K, 0.01 $L_\odot$, 2.5 pc						
	0.05	0.02	360	110	2.25	4.89E-05
	0.1	0.04	254	24.6	2.25	1.09E-05
	0.2	0.08	180	3	2.25	1.33E-06
	0.3	0.12	146	0.6	2.25	2.67E-07
	0.4	0.16	127	0.15	2.25	6.67E-08

Table 6.2: Tab. 6.1 cont'd

the minimum planet radius required for the planet to be detected as a function of the distance to Earth. As seen in this Fig.6.11 the maximum achievable distance for the most massive SE is around 15 pc.

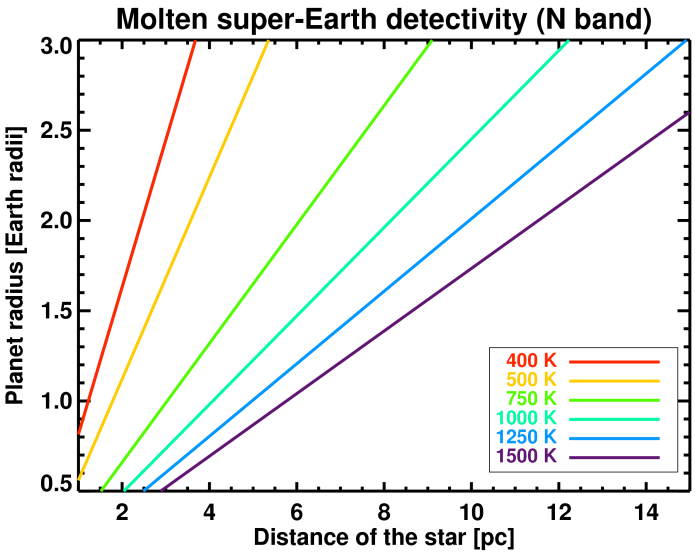

Figure 6.11: Molten telluric planets detectivity in the mid-IR (N band) from the ground. Different surface temperatures are considered (750, 1000, 1250 and 1500 K). The maximum realistic physical radius to consider is about 2.5 $R_\oplus$ (15 $M_\oplus$). See the text for more details.

Given the fairly high temperatures we deal with and an intrinsically better sensitivity expected for the E-ELT/METIS instrument in the L and M bands at distance of 0.2 arcsec from the star (3 and 40 μJy respectively obtained by simply rescaling the N band sensitivity), it is also interesting to assess the performances for molten telluric planet detection. Figure 6.12 shows these performances in terms of minimum planet radius as a function of the distance to the star. Figure 6.13 compares the performances of the various bands as a function of planet's temperature. First, the N band is able to provide valuable informations by direct imaging of the most massive super-Earths between distances of 3 (400 K) and 16 pc (1500 K). In the case of the highest temperatures awaited (1000-1500 K) the L band performs the best by almost an order of magnitude when compared to the N band. However, for the lowest temperatures (400-500 K), the apparent performances are similar. Given the fact that the performances of stellar light rejection are expected to be worse in the L band (strehl ratio about 65 % to be compared to a strehl ratio of about 93 % in the N band) the N band performances for the "coolest" objects should be equivalent and eventually better than in the L band. Therefore, a direct imaging characterization of the molten super-Earths using the N band

Although preliminary estimates of cooling timescales would be less than 0.1 Myr ([Stern, 1994]) implying that only one target out of ∼300 would be in a molten state, recent detailed calculations suggest that the cooling time might last up to a few Myr ([Elkins-Tanton, 2008]). In the later case and in a framework of a recent survey of close-by and young (d≤100 pc, ages between 10 and 100 Myr, [Torres et al., 2006]), the number of potential targets would increase to a more reasonable number (about several tens assuming that each protoplanetary system has 4 telluric planets).

As a conclusion, if the "standard" super-Earth exoplanets are at the edge of the detection limits of an ELT in the N band, the youngest ones in a transition state at a higher temperatures offer an interesting

niche for fruitful observations and characterization in the N band.

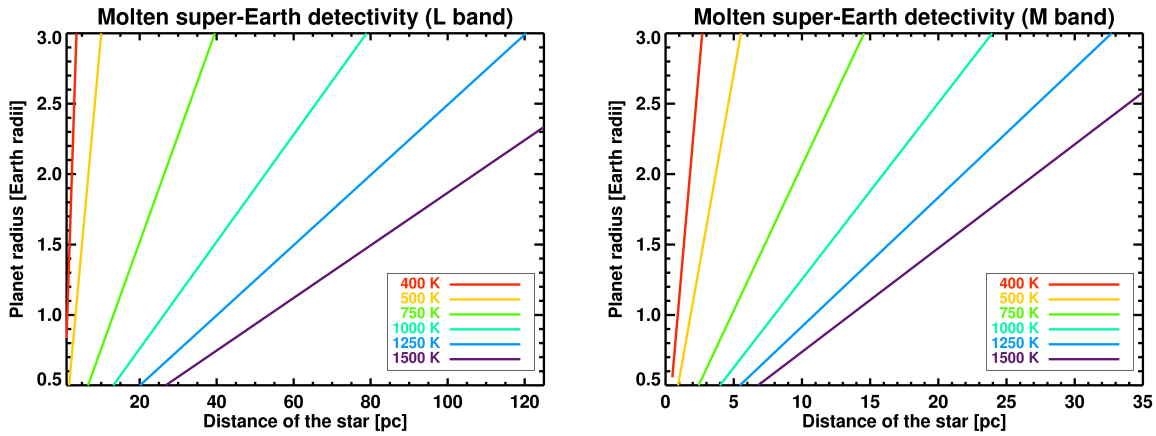

Figure 6.12: Same as Fig.6.11 but for the L and M bands.

6.4 Protoplanetary disks

In chapter 1 we have shown the already numerous and scientifically informative assets brought by high angular resolution mid-infrared imaging and spectroscopy from the ground. One can thus wonder what are the next steps to make in this field when using mid-infrared instruments on extremely large telescopes. The key parameter is the achieved angular resolution. On an ELT, it is around 50 mas at a wavelength of 10 µm. Consequently, the major improvement in this field will probably the *possibility to resolve the inner planetary regions of the closests T-tauri and Herbig Ae disks*. Indeed, such a resolution corresponds to distances to the star in the range 2.5-10 AU. These sizes are thus small enough to be able to probe the regions in the disks where the planets are formed and evolve. The expected sensitivities of an ELT are not good enough to have any hope to detect the direct thermal emission from exoplanets in these disks. At such large distances from Earth, the only possibility would be; but this is highly unlikely; to observe an giant exoplanet at the stage of runaway gas accretion ([Wuchterl et al., 2000, Bodenheimer and Pollack, 1986, Lissauer, 2007]). This phase (called "core-instability"), during which the exoplanet luminosity increases by 3 orders of magnitude, lasts unfortunately less than ∼100 000 years so only about 0.5% of the protoplanetary disk phase. However, we know thanks to numerical simulations that a giant planet placed in a protoplanetary disk interacts strongly with the later one. Let's assume that a giant gaseous planet has been formed in a massive enough ($M \geq 0.01\ M_{\odot}$) gaseous disk. In the rotating frame associated with the planet, the external parts of the disk are trailing? the planet's orbital motion while the inner parts are leading. The planet and the disk are constantly, simply because of the gravitational force and associated torque, exchanging angular momentum. The planet is extracting angular momentum from the inner disk and gives also large quantities to the external parts. However a tiny asymmetry in the balance between these two tidal effects ends in a net result which is negative in terms of quantity of angular momentum at the level of the planet. As a result the planet *migrates inwards*. When the planet is lighter than ∼10 Earth masses this linear physical mechanism is called *type I migration*, [Goldreich and Tremaine, 1979]. Planets more massive than ∼1 Jupiter mass also migrate inward after clearing up a gap on the planet's orbit. This non-linear mechanism is quoted *type I migration*, [Lin and Papaloizou, 1986]. The typical gap size is about 1/5 of the planet's orbital distance (see Fig.6.14, left panel). The gap is actually not completely void of material. Material continues to flow through the gap also as to accrete onto the planet by means of spiral arms and a circumplanetary disk (Fig.6.14,

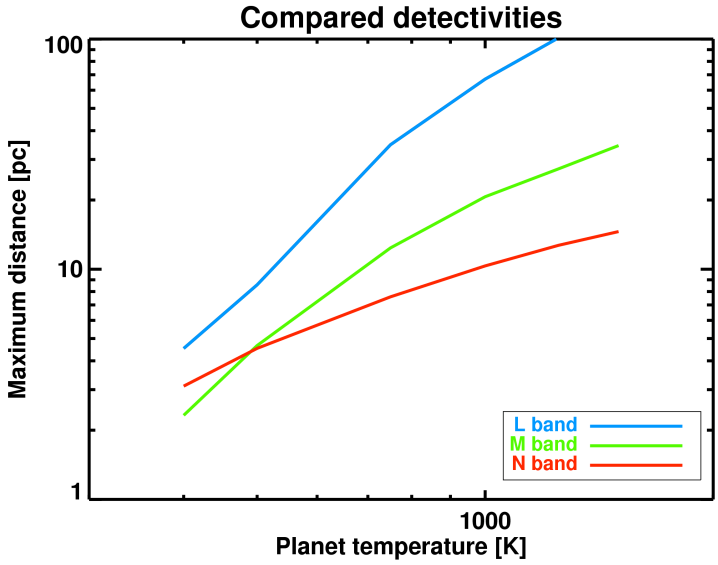

Figure 6.13: Compared sensitivities of the L, M, and N bands to a 2.5 $R_\oplus$ molten super-Earth. The assumed detection thresholds (at an angular distance of 0.25 arcsec) are 3, 40 and 100 μJy in the 3 bands respectively.

right panel), see [D'Angelo et al., 2003]. The *type III migration* concerns the planets with masses in the range 0.1-1 Jupiter mass embedded in massive disks. In this regime the planet is not massive enough to create a gap but the response of the disk remains non-linear. This runaway migration has been studied in details by [Masset and Papaloizou, 2003] and [Artymowicz, 2004].
In the case of type III migration the planet opens a gap in the disk. This gap has a typical size of 20% of the orbital distance and a contrast of at least 10 in the gas phase. Recent simulations by [Paardekooper and Mellema, 2004] predict a contrast ratio even higher concerning the dust phase. On top of that if the disk is flared, the opening of the gap uncovers a "wall" in the disk. This wall is in direct view of the starlight. As a consequence, the temperature locally increases. In turn, this increase of temperature produces a local puffing-up of the disk in an analog way than the inner rims are supposed to ([Dullemond et al., 2001]). A crude estimate shows that the full process will increase locally the surface brightness at 10 µm by at least a factor of 10 at a distance of 20 AU from the star. Mid-infrared high-angular imaging observations are thus a perfect tool to detect the signature of these gaps. Simulated observations of a protoplanetary disk featuring a 1 Jupiter mass planet are shown in Fig.6.14. The disk is face-on and shares the same physical characteristics as the HD97048 modeled disk described in Sec.4.1.5 (inner radius $r_{in} = 0.4$ AU, outer radius of 400 AU, mass of 0.01 $M_\odot$). The surface density follows a power-law $\Sigma = 444(r/r_{in})^{-3/2}$ except in the region where the planet is located (orbit radius of 20 AU). In this region the surface density is modulated by the gap density profile resulting from the FARGO ([Masset, 2000]) numerical model.

6.5 Debris disks and Exo-zodiacal disks

Debris disks are circumstellar disks of second generation found around stars having ages in the range 10 Myr to several Gyr [Meyer et al., 2007]. These disks are (almost, [Brandeker et al., 2004]) gas free and contain several lunar masses of grains having sizes typically larger than 1 µm. Since these disks are

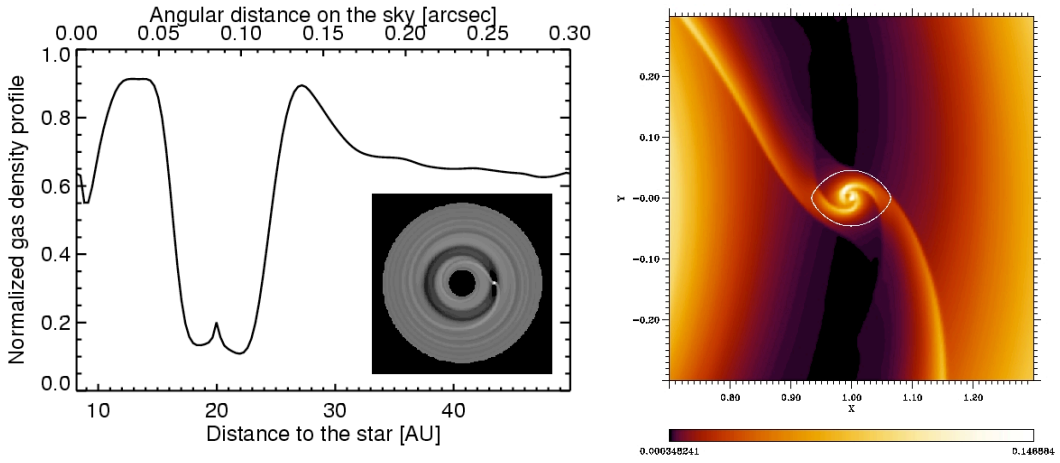

Figure 6.14: Left panel shows the density profile produced by a giant exoplanet in a protoplanetary disk. right panels shows a blow-up of the region around the exoplanet. Some material from the outer disk flows trough the gap and feeds an accretion disk around the planet (courtesy of P. Artymowicz).

expected to be eroded on timescales of 1000-10000 years by the combined effects of radiation pressure, Poynting-Robertson effect and grain-grain collisions, these disks are probably continuously replenished in dust particles by frequent collisions of large parent bodies. It is however observationally established that these disks fade with time and that their mass roughly follows a t^{-1} evolution [Carpenter et al., 2005, Meyer et al., 2007] as expected in the case of collisionally dominated disks [Dominik et al., 2003] The so-called "Vega phenomenon" is probably linked to major chaotic re-arrangements of the orbits of giant planets in these systems as the solar system has experienced at an age of 800 Myr (the Late Heavy Bombardment, [Levison et al., 2001]). The current statistical analysis on the occurrence of the phenomenon (thanks e.g. to sensitive photometric excess measurements by the SPITZER telescope) give a rate of 10-20 % for main-sequence stars (depending the spectral type) but the detections are probably biased towards early type stars around which the thermal emission produced by the warm dust is more easily detected. Most of the debris are *structured* i.e. their surface density does not follow a simple power-law but presents one to several maxima. A very common feature is the presence of an inner hole such as the ones found in the disks around β Pictoris [Lagage and Pantin, 1994, Pantin et al., 1997] or Fomalhaut [Kalas et al., 2005]. These holes are believed to be produced by giant exoplanets producing particles shepherding in mean-motion resonance regions [Liou and Zook, 1999, Wyatt, 1999] or simply by the absence parent bodies (gravitationally scattered) in the inner planetary regions ([Wisdom, 1980, Charnoz et al., 2009b]). In any case, the debris disks seem to be intimately linked to the planetary formation process; they are probably even the sign of an intense ongoing gravitational "planetary activity".

In this context it is therefore interesting to study the debris maybe not as an indirect method of exoplanet detection but maybe more as a key to understand the early phases the solar system went through. Figure 6.15 shows a density map of a debris disk in which lies a giant exoplanet. The gravitational mean-motion resonances create numerous structures in the disk. The most prominent one is an empty horseshoe region where the planet is located. The right panel of 6.15 shows that METIS has both the sensibility and the angular resolution to detect such a structure produced by a 1 Jupiter mass planet on a 1 AU orbit in a debris disk at 10 pc 100 times less massive than the β Pictoris dust disk.

In the context of direct detection and characterization of telluric planets the presence of faint debris disks (exo-zodiacal (EZ) disks) is of very high importance. Indeed, one of the most promising method to achieve this challenge is based on nulling interferometry in the mid-infrared range (e.g. the Darwin or TPF-I projects ([Fridlund et al., 2006, Beichman et al., 2006])). However, the presence of exo-zodiacal

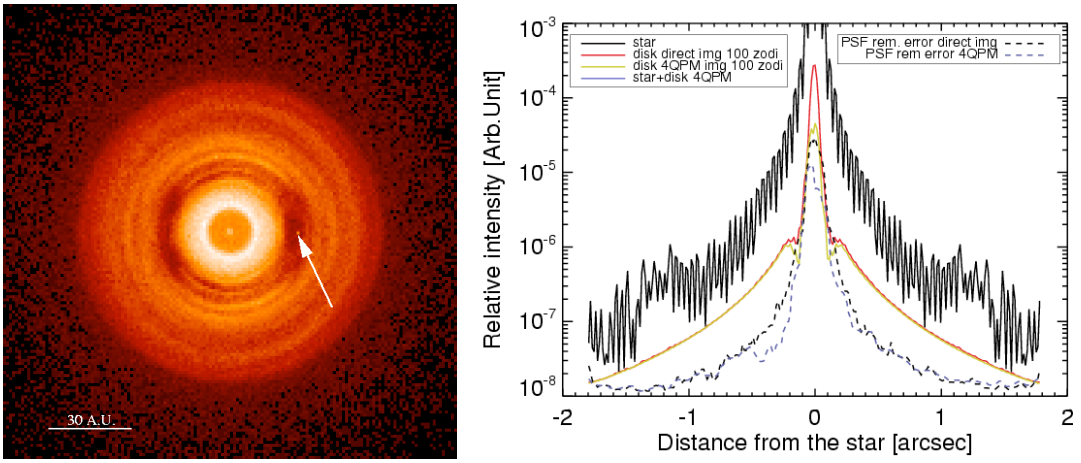

Figure 6.15: Left panel: simulated debris disk density structure produced by a giant exoplanet. The dust particles have a radiation pressure coefficient of β=0.1. The planet has a mass of 1 Jupiter mass. Right panel: image profiles and associated errors at 10 µm of an observation of a debris disk seen pole-on an containing a 1 Jupiter mass planet opening a gap in the dust density structure.

disks 10 to 100 times denser than our zodiacal disk will seriously hamper the detection of habitable terrestrial planets because the emission of such an extended object will completely mask out the signal due to the planets. Since the detection of a terrestrial planet will cost several hours of observing time it is therefore important in this context to carefully select stars with no or at least very faint EZ disks. Detection methods based on the photometric excess will be limited by photometric errors. It is still difficult to assess if the JWST/MIRI instrument will be able to detect these EZ disks down to the sought limit of an optical depth of 10^{-6}. On the other hand the ELT/METIS instrument combines both a fairly good sensitivity an angular resolution to detect this EZ by angularly separating them from their host star. Figure 6.16 presents simulations of EZ disks in different geometric and physical configurations. The simulations show that:

- the very extended disks are more difficult to detect than compact ones even when they are located close to the star.
- for the same physical parameters of the disk the inclined ones are more easily mistaken with PSF residuals.

6.5.1 Development of multi-spectral detectors in collaboration with THALES company

The THALES company has developed since 2002 a full process to realize matrices of detectors based on the principle of Quantum Well Infrared Photo-detectors (QWIP). The QWIP detectors operate by photo-excitation of electrons between ground and first excited state sub-bands of multi-quantum wells which are artificially fabricated by placing thin layers of two different, high-bandgap semiconductor materials alternately. The bandgap discontinuity of two materials creates quantized sub-bands in the potential wells associated with conduction bands or valence bands. The structure parameters are designed so that the photo-excited carriers escape from the potential wells and be collected as photo-current. The lattice matched GaAs/Al_xGaAs material system is commonly used to create a QWIP structure. Highly uniform and pure crystal layers of such semiconductors can be grown on large substrate wafers, with control of

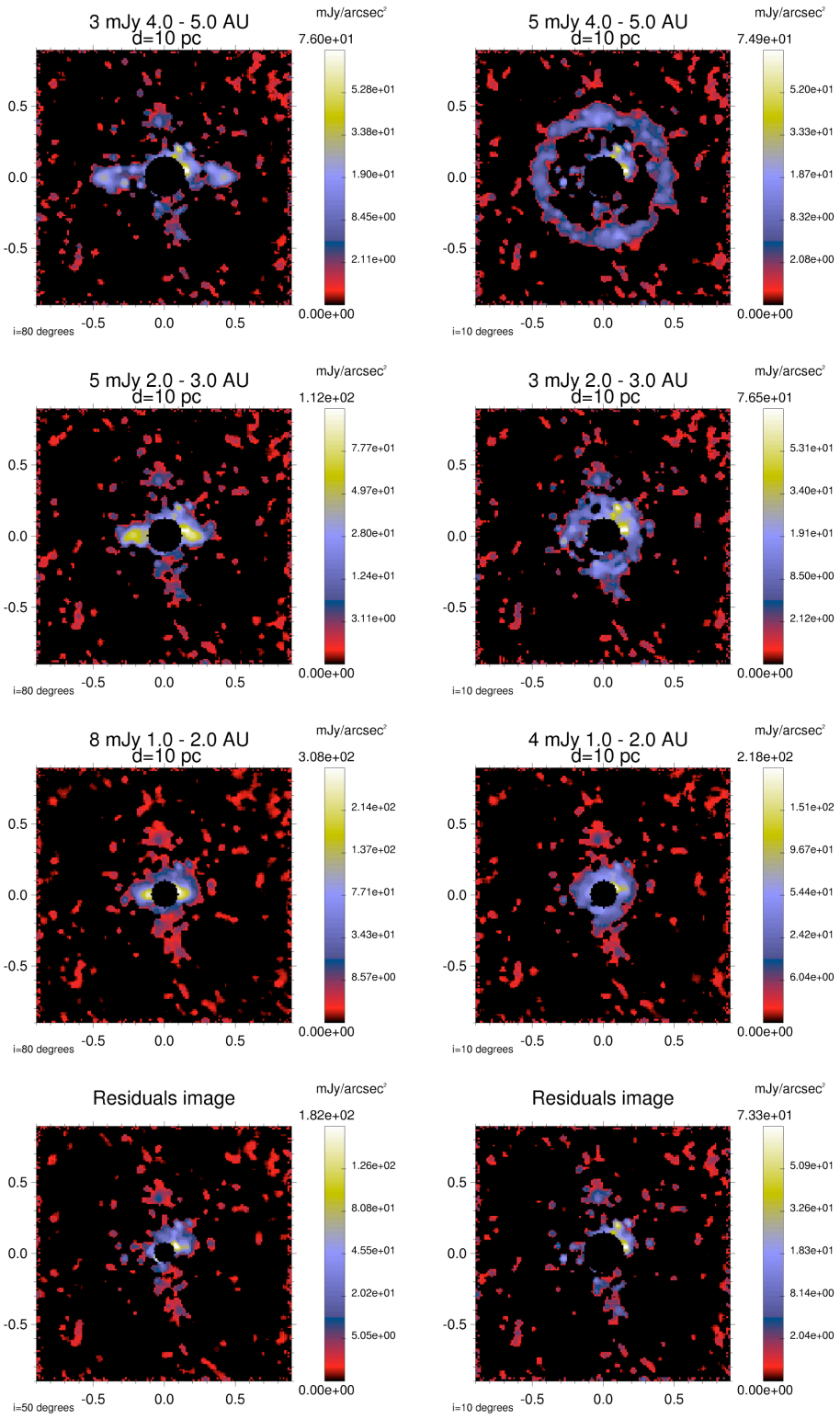

Figure 6.16: Simulated observations of exo-zodiacal disks in various configurations/fluxes at a distance of 10 pc. The integrated flux and the inner/outer boundaries of the disk are indicated in the titles of the frames. The external ticks give the spatial scale. In the two lower panels are displayed the star subtraction residuals that were used to build the simulations above. Two numerical masks corresponding to the two mask sizes used in the simulations are overlaid.

each layer thickness down to a fraction of a molecular layer, using modern crystal-growth methods like molecular beam epitaxy. By controlling the quantum well width and the barrier height (which depends on the Al content), the intersubband transition energy can be varied over a wide enough range to enable light detection at any wavelength between 3 and 20 µmwith a tunable peak detectivity wavelength.
The QWIP detectors are known for having a very low 1/f noise which is a key parameter concerning the background removal based on the chopping technique used in astronomical observations. The QWIPs are by essence relatively narrow band (R=10) photodetectors but the recent developments allow to extend their detectivity to Unlike the commonly used BIB extrinsic photoconductors for astronomical observations, the QWIPs are made with very *thin* (several tens of microns thick) active layers. The good wavelength selectivity of an active layer and its transparency to the other wavelengths allows to produce bi-spectral detectors by superimposing two active layers sensitive to two different wavelengths. The very recent progresses made by THALES in the manufacturing process of the QWIPs have brought a very good flexibility that allows to play on the absorption bandwidth, the accurate positioning of the peak absorption and the bi-spectral properties while producing high cosmetic quality large format detectors (640x512). These abilities makes the QWIPs to be a very good option for implementing an "on-the chip" differential imaging mode (see Sec.6.2.2) in a mid-infrared instrument.
We have initiated a collaboration with the THALES company to precisely assess the performances of the QWIPs for astronomy applications and develop a new generation of QWIP detectors optimized for this purpose. In a first time we will insert a bi-spectral detector into a mid-infrared test-bench developed at CEA/IRFU/Sap in the framework of the JWST/MIRI project. In a second time we plan to design and develop a new generation of QWIP detectors optimized for astronomical observation applications. This development will be funded by an ANR (Agence Nationale pour la Recherche) grant we have applied for and recently obtained.

6.6 Conclusions

I have tried to address in the most comprehensive way in this section the question of the future of mid-infrared imaging from the ground in the domain of exoplanetology.s Beyond the standard imaging mode that will mechanically benefit from a better angular resolution and sensitivity on larger telescope such as ELTs, I have shown that a mid-infrared imager is a competitive instrument to observe the very inner parts of the protoplanetary and debris disks to seek for the signatures of forming or already formed exoplanets. The very challenging (but very informative) characterization of giant exoplanets in the thermal regime can also be addressed but requires the development of new observing techniques derived from existing ones in the near-infrared range such as phase mask coronagraphy and differential imaging. We have proposed to implement these modes in the ELT/METIS instrument which are now fully part of the instrument baseline. However, although we are able now to develop fairly accurate numerical simulation tools that predict the performances of these new modes depending on the type of device and the design chosen, some real measurements and prototyping is always a mandatory intermediate step. In the present document we have not considered two attractive alternative exoplanets detection methods which are the ADI (angular differential imaging, [Marois et al., 2006]) and the spectral deconvolution ([Thatte et al., 2007]). Concerning the first one the lack of precise informations on the telescope prevent us for the moment to make realistic estimates of its performances. In the case of the spectral deconvolution the main limitation will probably be a lack of sensitivity when dispersing the signal; however some medium resolution spectral niches where the background noise is low enough can probably be found.

Related articles

Annex :

Direct thermal imaging of circumstallar discs and exo-planets.

published in "Ground-based and Airborne Instrumentation for Astronomy II". Edited by McLean, Ian S.; Casali, Mark M. Proceedings of the SPIE, Volume 7014, pp. 70142D-70142D-12 (2008), 2008

Direct thermal imaging of circumstellar discs and exo-planets

Eric Pantin[a], Ralf Siebenmorgen[b], Celine Cavarroc[a], Michael F. Sterzik[c]

[a]Laboratoire AIM, CEA/DSM - CNRS - Université Paris Diderot, IRFU/SAp, France;
[b]European Southern Observatory, Karl-Schwarzschildstr. 2, 85748 Garching, Germany;
[c]European Southern Observatory, Chile;

ABSTRACT

The phase A study of a mid infrared imager and spectrograph for the European Extremely Large Telescope (E-ELT), called METIS, was endorsed in May 2008.[1] Two key science drivers of METIS are: a) direct thermal imaging of exo–planets and b) characterization of circumstellar discs from the early proto-planetary to the late debris phase. Observations in the 10μm atmospheric window (N band) require a contrast ratio between stellar light and emitted photons from the exo-planet or the disc of $\sim 10^5$. At shorter wavelengths the contrast between star and reflected light from the planet-disc system exceeds $\gtrsim 10^7$ posing technical challenges. By means of end-to-end detailed simulations we demonstrate that the superb spatial resolution of a 42m telescope in combination with stellar light rejection methods such as coronagraphic or differential imaging will allow detections at 10μm for a solar type system down to a star-planet separation of $0.1''$ and a mass limit for irradiated planets of 1 Jupiter (M_J) mass. In case of self-luminous planets observations are possible further out e.g. at the separation limit of JWST of $\sim 0.7''$, METIS will detect planets $\gtrsim 5 M_J$. This allows to derive a census of all such exo-planets by means of thermal imaging in a volume limited sample of up to 6pc. In addition, METIS will provide the possibility to study the chemical composition of atmospheres of exo-planets using spectroscopy at moderate spectral resolution ($\lambda/\Delta\lambda \sim 100$) for the brightest targets. Based on detailed performance and sensitivity estimates, we demonstrate that a mid-infrared instrument on an ELT is perfectly suited to observe gravitationally created structures such as gaps in proto– and post– planetary discs, in a complementary way to space missions (e.g. JWST, SOFIA) and ALMA which can only probe the cold dust emission further out.

Keywords: thermal infrared, mid infrared, exo-planet, proto-planetary discs, debris discs, coronagraphy

1. INTRODUCTION

Since the first identification of a planet outside the solar system[2] more than 200 exo-planets have been discovered, the vast majority by means of precise radial velocity measurements (The Extrasolar Planet Encyclopaedia presents a comprehensive list of all known exoplanets. It is available at the following URL:
http://www.obspm.fr/planets). The direct detection of exo-planets is of wide public interest because philosophical questions concerning possible existence of extra-terrestrial life are linked. In modern astronomy theories related to the formation and origin of planetary systems require input which can only be obtained from direct imaging of such systems. Therefore direct imaging of exo-planets is taken as one key science driver for the instrumentation suite of many next generation large telescopes, including the E-ELT.
Protoplanetary discs are nurseries in which the planet embryos form. Once a sufficiently massive proto–planet exists in the disc and before eventual migration a gap in the disc structure opens.[3] Although based on slightly different physics, the gravitational interaction of the planet with dust particles produces a footprint in the density structure of the debris disc. While direct imaging of exo-planets is limited by the relatively modest sensitivity of ground-based observations a study of the disc structure offers another although indirect detection method of exo-planets. It has the advantage to be applicable to lower mass planets located further out in the disc or to planetary systems at larger distances from Earth.
For direct and indirect exo-planet detection strategies a mid-infrared instrument mounted at an ELT like METIS offers a unique combination of a relatively low contrast between star and the emission from the planetary disc system at ultimate sharp angular resolution.
In the following sections a description of our modeling efforts is first given. Concerning exo-planets direct observations, simulated data and performances are shown; sensitivity limits in terms of minimum mass as a function of the distance to the star are assessed, either using direct imaging, or using four quadrants phase mask (4 QPM)

coronagraphs. In the case of proto-planetary discs and debris discs, relevant simulations are shown to prove that planet-induced footprints are easily detectable when using 4 QPMs coronagraphs as well.

2. PSF MODEL

Imaging the dust density structure of circumstellar discs or the direct detection of exo-planets requires precise understanding of the point spread function (PSF) of the observing system. In the modeling efforts we consider PSF computed using present knowledge of the E-ELT pupil design. Assumed properties are a segmented M1 with 42m and an adaptive optics system with cut-off frequency at 500Hz and 84×84 actuators of the deformable mirror. In the simulations a Monte Carlo scheme is applied in which an ad–hoc degradation of the AO corrected power-spectrum of the wavefront error is included to simulate e.g. the static aberrations also as any other source of AO performances degradation. This provides a set of short exposure phase maps which after averaging gives a reasonable representation of the long-exposure PSF ($\sim$1h) which have Strehl ratii in the range 0.93–0.95 at 10μm.

In Fig.2 and Fig.3 we show the residual noise, $\sigma_{\rm R}$, derived for different observing techniques as function of distance from the star. The residual noise is estimated from azimuthal averages of the image. One notice that $\sigma_{\rm R}$ always exceeds the background noise, $\sigma_{\rm B}$, up to large angular separations ($\gtrsim 2''$) from the star. For the instrument we assume background noise limited performances. In case of a direct image without further contrast enhancement the noise from the stellar profile exceeds the background noise by $\sim$5 orders of magnitude at 0.1".

Computing PSF under different seeing conditions allows to estimate residuals after star subtraction. We assumed seeing variations of $0.6''$ and $0.7''$ between two 1h long observations, respectively. Standard subtraction techniques using a reference star image provide only some advantages compared to direct imaging at separations $\lesssim 0.1''$ but not further out. This is because seeing induced PSF variations are mainly located in the wings of the PSF. Again, the residuals noise exceeds the background noise by a very large factor (see e.g. Fig.2).

Significant contrast enhancement can be achieved by using a coronagraph. In the simulations we applied a four quadrants phase mask (4QPM) as baseline for which the 4QPM model ([4]) is in good agreement with existing performance tests of the real system. As above for standard PSF subtraction techniques we utilize reference star observations with such a coronagraph at seeing variation of $0.6''$ and $0.7''$ and subtract both coronagraphic images from each other. The use of a coronagraph reduces the residual noise by 1 or even 2 orders of magnitude as compared to standard techniques (Fig. 4 and Fig.5). In addition the use of a coronagraph prevents the appearance of other spurious artifacts caused by detector saturation. Note that the 4QPM simulations have been carried out at a single wavelength, assuming a R=10 imaging filter. Other types of achromatic coronagraphs have to be studied in combination with e.g. differential imaging, to push further the sensitivity limits.

3. DIRECT THERMAL IMAGING OF EXO–PLANETS

The direct imaging of a exo–planet remains challenging with present day technology. This can be understood by inspecting the solar system. In Fig.1, the contrast in peak brightness between the Sun and Jupiter is 5×10^{10} in the optical (V band), some 10^9 in the NIR (J band) and diminishes to a few 10^6 in the thermal infrared (N band). Another important advantage of the thermal infrared in particular around 10μm is that such long waveband observations are accompanied by much better behaved PSF with high Strehl ratios and reduced requirements on the performance of the AO system. The expected Strehl ratios provided by an E-ELT AO system are of the order of $\sim 65\%$ in H band but exceeding $>90\%$ in the N band. Furthermore, the thermal infrared is quite complementary to shorter wavelength observations. While in the latter exo-planets are detected from reflected star light one observes in the mid infrared the direct thermal emission of the stellar heated or self-luminous planet. The distinct detection mechanisms in the near and mid infrared are of utmost importance for characterizing the physical and chemical properties of the exo–planets and their atmospheres.

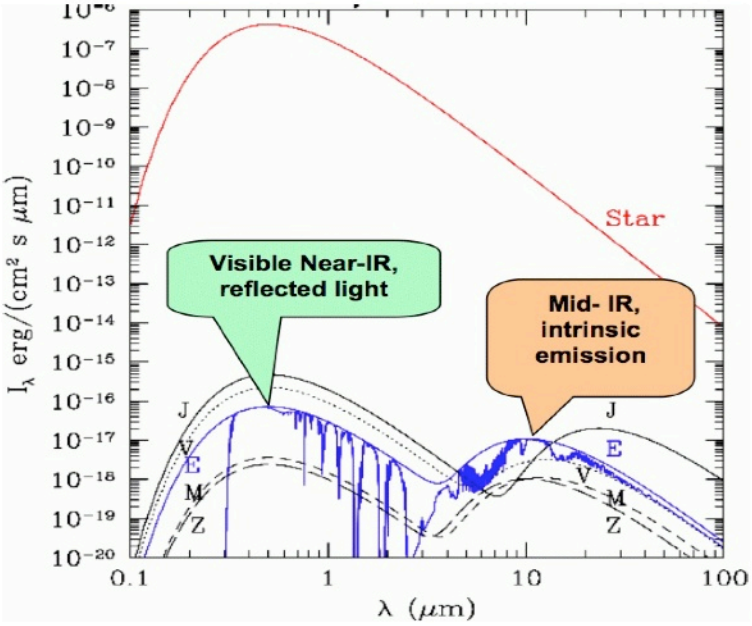

Figure 1. Comparison between the flux emitted by the Sun (a G2V star shown in red) and those (black lines) coming from the planets of the solar system assumed to be black-body emitters(J=Jupiter, V=Venus, E=Earth, M=Mars). Z represents the spectral distribution of the zodiacal light. The blue line is a more realistic emission model of Earth.

3.1 Detection likelihood for super–Earths

The so-called super-Earths are probably the most massive telluric planets that nature can form,[5] some of them being discovered within the habitable zone.[6] Except for some exceptional physical circumstances a rocky planetary core of mass 10 times the Earth will attract the surrounding material of the disc and finally form a giant gaseous planet.[7] Super-Earth like planets are therefore limited to a maximum of 10 Earth masses which translates to a upper limit of the radius for super–Earths of less than twice the Earth radius.

For estimating the emission of a super-Earth we consider an irradiated planet*. To first order the planet flux can be derived from a black-body heated by a star of luminosity L and located at an orbital separation r to a temperature: $T^4 \propto L/r^2$ ([8]). Therefore irradiated exo-planets such as super-Earths become brighter with increasing stellar luminosity and smaller separation from the star. However, increasing star brightness results in an increase of the residual noise level from stellar light rejection (Sect. 2) so that the planet detection becomes unfortunately also more challenging. For main–sequence stars and including a 4QPM coronagraph in the simulations we find that in any configuration of stellar type and orbital separation a super-Earth like exo–planet is most likely below the detection threshold at an E-ELT. This prediction is either caused by the expected sensitivity of a background noise limited instrument which is for the E–ELT of order $\sim 20\mu$Jy/10σ/1h in the N band for a site similar to Paranal or by the achievable contrast at small separation form the star which is given by the residual noise floor of the stellar light rejection.

3.2 Giant gaseous planets

Two types of models are considered to estimate detection thresholds of giant gaseous planets. In the first an irradiated giant planet is supposed to be in close orbit of $0.2-1$AU from the star and in the second we take self-

*Irradiated planets are exclusively heated by the star and have no self–luminosity.

luminous giant planets at distances further out: $3-10$AU. Planetary model atmospheres are taken for irradiated planets from Barman et al.[9] and self–luminous planets from Burrows et al.[10]

The star is $\sim 10^5$ times brighter than giant exo-planets and stellar light rejection as discussed in Sect.2 is an essential issue. Fig.2 and Fig.3 show : i) the azimuthally averaged profile the star, ii) the detection limits (100 times the standard deviation of the residuals) after subtraction by a reference star and iii) detection limits after subtraction of two coronagraphic stellar images. PSFs have been computed for observing time of 1h and seeing of $0.6''$ and $0.7''$. The detection threshold (10σ) set by the background noise limit for a 1h integration at Paranal is also indicated.

Around solar-type stars (G – K) with luminosity $L = 1$ L$_\odot$, temperature $T = 5780$ K irradiated giant planets of 1 Jupiter mass are detected in coronagraphic images as close as $\sim 0.1''$ from the star. We considered in the models a 5pc distance from Earth. The expected flux of ~ 25 mJy of an irradiated giant planet at a distance of 0.5 AU from a G-type star is remarkably strong. Therefore, detection of such planets is in principle possible up to fairly large distances of ~ 50 pc from Earth when extrapolating the quantities of Fig.2. Further away the flux of the planet starves in the background noise. The reasons to explain these remarkable detection performances are twofold. First, the radius of an irradiated giant planet is weakly dependent on the mass or the age.[11] Second, the temperature of an irradiated exo–planet, mainly determined by the stellar flux and the orbital distance, is considerably higher than the temperature of self-luminous planets.

For self-luminous exo-planets, depending in the site and the observing time, the minimum masses are, assuming a distance of 5 pc from Earth :

- For a G2 star ($T_{eff} = 5780$ K, L = 1 L$_\odot$):
  - 7 M$_j$ for a$\geq$1 arcsec
  - 2 M$_j$ marginally detectable at 2 arcsec and more

  where a is the orbital distance of the planet.
- For a M5 star ($T_{eff} = 2800$ K, L = 0.01 L$_\odot$, see Fig.3):
  - 2 M$_j$ at 1.0 arcsec
  - 5 M$_j$ at 0.1 arcsec

Fig.4,5,6 display examples of simulated imaging observations of 1 Gyr old, 1-10 Jupiter mass giant exo-planets with orbital distances in the range 1-4 AU around a solar-type G2V and a M5 later type stars. The observations are carried out in N-band at 8.6 μm where one gets an optimum combination of planet flux/sensitivity/spatial resolution. The simulations include the effects of sky shot noise and PSF variations with the seeing.

More advanced PSF suppression, using i.e. differential techniques like spectral differential imaging (SDI) which allow to reduce considerably PSF variations are foreseen strategies to even improve the detection thresholds.

3.3 Low-resolution spectroscopy

In Fig.7 we summarize up to which limiting distance one can expect to perform MIR low-resolution spectroscopy depending on the companion mass, assuming a sensitivity limit of 1mJy/10σ/1h. In this case we assume a solar analogue as illuminating source. Clearly, rather young host stars are preferred. Intense efforts to find and characterize young stars near the sun have already been pursued (see Ref.12), and suggest promising targets, e.g. about 50 stars located in the β Pictoris association, estimated to be only 10-15 Myrs old at a mean distance of 31 pc.

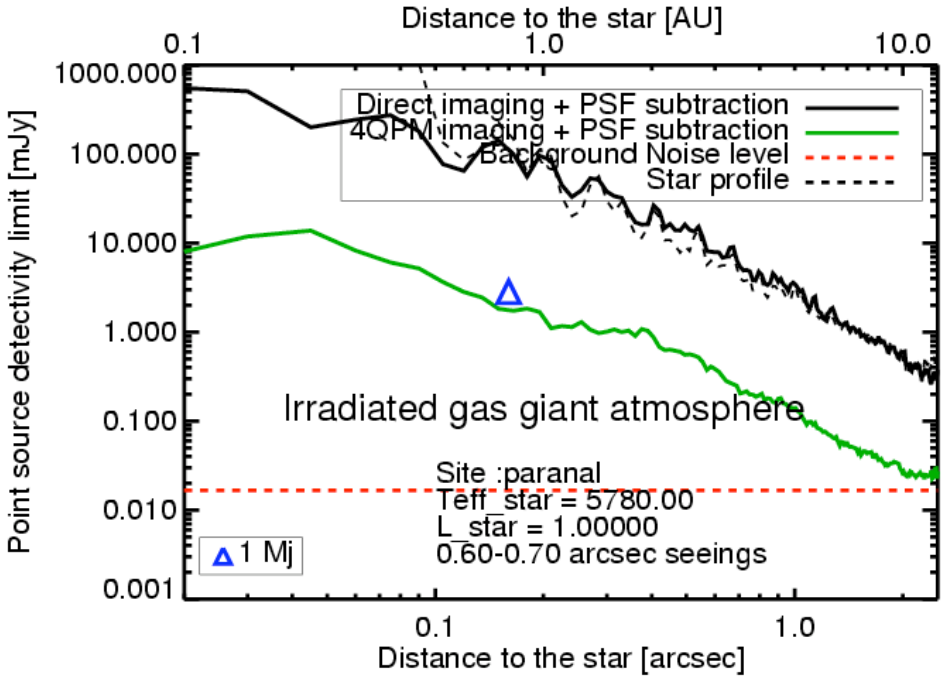

Figure 2. Detection limit (set experimentally to 100 times the residuals standard deviation) as a function of angular distance from G2V star ($L = 1$ L$_\odot$, $T = 5780$ K) is shown for: i) the direct stellar profile (black dashed), ii) as derived by standard star subtraction (black) and iii) after subtraction of coronagraphic stellar images utilizing a 4QPM (green). PSFs have been computed for observing time of 1h and seeing of $0.6''$ and $0.7''$, respectively. The detection threshold (10σ) set by the background noise limit for a 1h integration at Paranal is indicated (red dashes). The expected flux of a 1 Jupiter mass irradiated exo-planet is marked by the blue triangle.

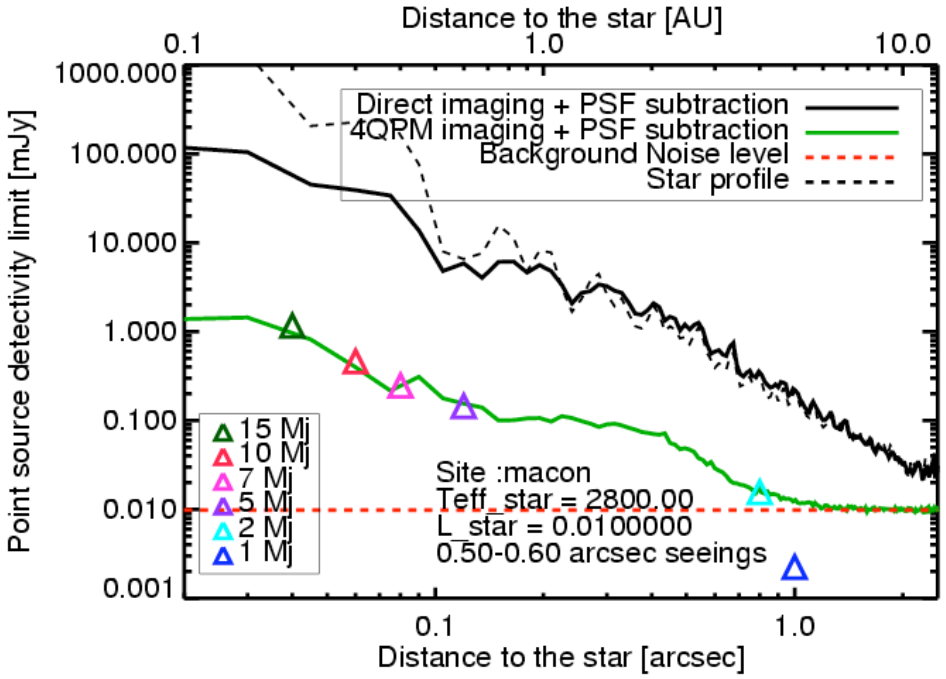

Figure 3. Detection limit (set experimentally to 100 times the residuals standard deviation) as a function of angular distance from M5 star ($L = 0.01$ L$_\odot$, $T = 2800$ K) is shown for: i) the direct stellar profile (black dashed), ii) as derived by standard star subtraction (black) and iii) after subtraction of coronagraphic stellar images utilizing a 4QPM (green). PSF have been computed for observing time of 3h and seeing of $0.5''$ and $0.6''$, respectively. The detection threshold (10σ) set by the background noise limit for a 3h integration at Macon is indicated (red dashes). The expected flux of self-luminous giant exo-planets are marked for masses between 1 and 15 times of Jupiter (triangular).

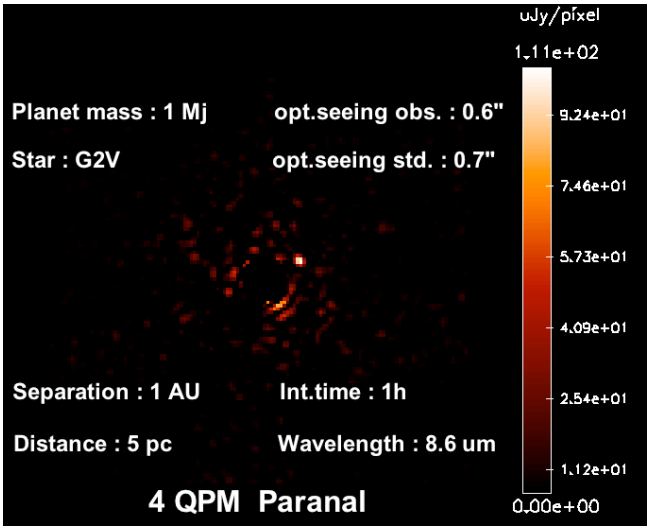

Figure 4. Simulated image observations of a 1 Gyr old, 1.234 R_j and 1 M_j irradiated planet at 1 AU/5 pc around a G2V star. The parameters assumed for the simulated are displayed on the images. Inner (r≤0.1") regions have been masked.

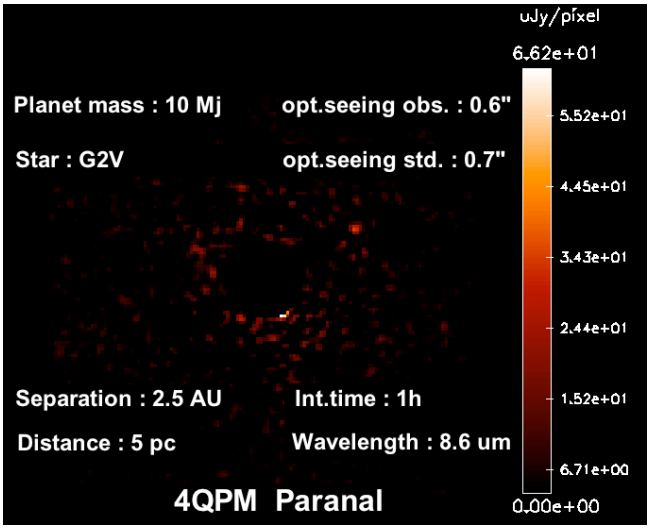

Figure 5. Simulated image observations of a 1 Gyr old, 10 M_j planet at 2.5 AU/5 pc around a G2V star. Inner (r≤0.2") regions have been masked.

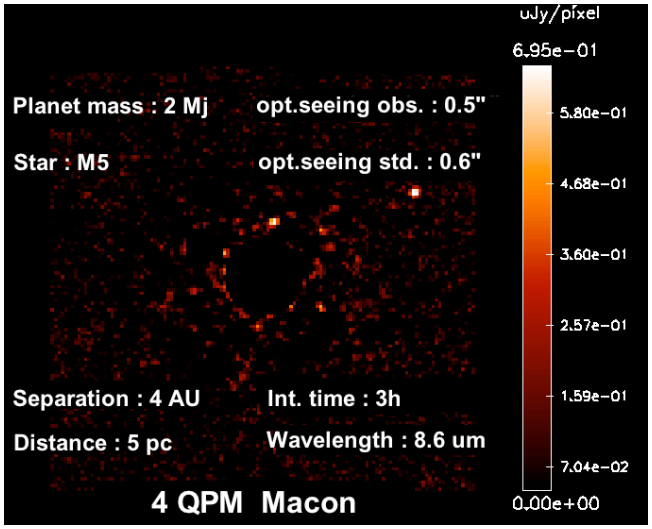

Figure 6. Simulated image observations of a 1 Gyr old, 2 M_j planet at 4.0 AU/5 pc around a M5 star. Inner (r≤0.2") have been masked.

4. DUSTY DISCS AND EXO-PLANETS

Based on the large number of known planetary systems and on the wealth of observations of dusty discs around solar-mass young stellar objects,[13] it is now well established that planets around main-sequence solar-type stars form in massive, gaseous and dusty proto-planetary discs that survive for several million years around the nascent stars.[14] Dusty discs are thus also targets of highest interest to understand in which physical conditions, with which timescales, exoplanetary systems form from the T-Tauri disc material. However, very few young stars exist in the close vicinity of the Sun. Closest star forming regions younger than 10 Myr are 150 pc away; the closest T-Tauri star; TW Hya; is 51 pc away from Earth.

The situation is less clear for stars of more than ∼2 solar masses. Such stars have a much higher luminosity than solar-type stars and, according to models, processus like photoevaporation may be at work clearing the inner disc in a few million years.[15] Whereas radial velocity surveys have just started to reveal planets around stars about twice as massive as the sun,[16] current imaging observations of proto-planetary discs around stars with such a mass remain very sparse. The lack of well-resolved images of proto-planetary discs around much younger A-type stars, still on the pre-main-sequence, is due to the fact that massive stars are less numerous than solar-type stars, and in general located farther away than solar-type ones (the closest, is more than 100 pc away; the typical distance of closest ones is 150 pc). It will be therefore extremely challenging to perform direct exoplanets detections in young systems at ages of 1-10 millions years at stages at which the giant planets are forming.

However, indirect detections, based on the gravitational interactions between an exoplanet and its surroundings disc material will be achievable given the awaited performances of future instruments. Disc gravitational structuring has been already found in older, main-sequence star, gas-depleted dusty discs[17]/[18]/[19] . This structuring has been interpreted in terms of massive planets-induced footprints. Similar gravitational processes are expected to produce gaps and spiral structures in the optically thick, gas supported, proto-planetary discs,[3] see Fig.8.

4.1 Simulations of discs observations using METIS on the E-ELT

Adopting the same telescope and instrumental models described in Sec.2, we have simulated METIS observations of two types of discs. One is a protoplanetary disc having the same physical parameters as the HD97048 disc;[20] the second one is debris disc having the same structure as the Beta Pictoris one,[21] but 100 times less massive

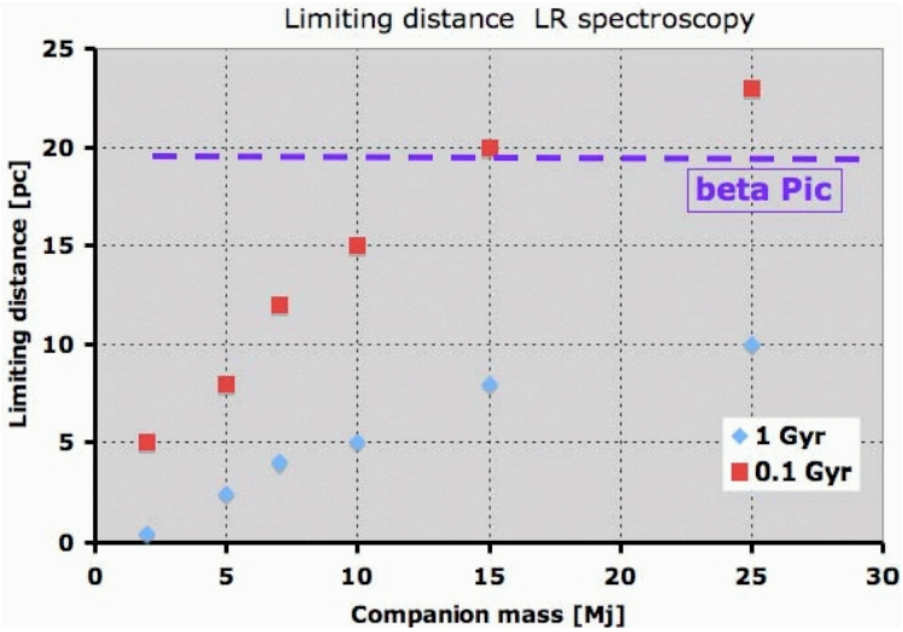

Figure 7. Distance limit, measured from Earth in pc, up to which a exo-planet of given mass, in units of Jupiter mass M_J, can be detected in MIR low resolution ($R = \lambda/\Delta\lambda \sim 200$) mode of METIS. The assumed limiting flux is 1 mJy at Paranal site, for 1h exposition and a signal-to-noise ratio of 10. The emissions of the exo-planet is computed by assuming two ages: 0.1 Gyr (squares) and 1 Gyr (diamonds).

and placed at 10 pc.

In this simulation we have taken a disc model of emission. in the mid-infrared range. Following Chianf&Goldreich model,[22] the surface of the disc is flared. Once the star,the disc geometry and composition of the dust are set, the model uses a full 1D+1D radiative transfer model to compute the output profile of disc emission at a given wavelength (here, 8.6 μm). The model parameters are those of the HD97048 flaring disc given in Ref.20 i.e. : D(distance to Earth)=175 pc, H(scale height at 135 AU) = 43 AU, Star : 40 $L_\odot$and 2.5 $M_\odot$. Inner and outer boundary radii of 0.3 au 500 AU respectively. The disc mass is set to 0.01 $M_\odot$. The flaring index (of the disc height) is 1.26. For simplicity, the disc is assumed to be observed pole-on.
A simulated gap of matter procued by a giant planet in the disc is added. Its characteristics (depth, width) are computed by the hydro-dynamics code "FARGO" written by F.Masset.[23] The planet is actually migrating in the disc, but we will assume in the following that the planet has a fixed orbit radius which is true on an 1h timescale of observation. Depth and width are then transformed into a local modification of the emission profile using simple physical rules of gas physics local energy balance. Fig.8, right panels, shows the observed profiles of a proto-planetary disc emission derived from the model described above. A 1 Jupiter mass exoplanet has been put in the disc at a orbital distance of 20 AU (0.12 arcsec) from the star. The "wiggles" observed on the profiles are due to the Airy pattern in the telescope and instrument PSF. In the first case (black line), direct imaging of object reduces the true gap contrast (initially of a factor ≈ 100) by a factor of ≈ 50 because of a combination of gap "contamination" by the wings of the central object (either the star or the inner rim emission) and structure smearing by the convolution with the PSF. Note also that the apparition of a gap should in principle also, in a flared disc, lead to the apparition of a "wall"-like heated structure just beyond the gap. A local flux enhancement at 10 μm would be thus expected just after the gap. The expected constrast of this structure is of the order of $1/cos(\alpha)$ where α is the grazing angle of the star radiation onto the disc flared surface

(in addition the local higher warming should in principle in turn, produce locally an increase of the disc height i.e. a local "puffing-up"). This flux amplification is not yet implemented in the models shown here. When using a 4 quadrants coronagraph mask (blue line), the contrast is regained by a typical factor of ≈ 2.
Simulated observations of a faint debris disc lead to similar conclusions : the use of a 4QPM coronagraphic mask is a valuable help to enhance the contrast of the gravitational structures (in particular, the strongest structure which is the "horseshoe" gap along the planet orbit), see Fig.8.

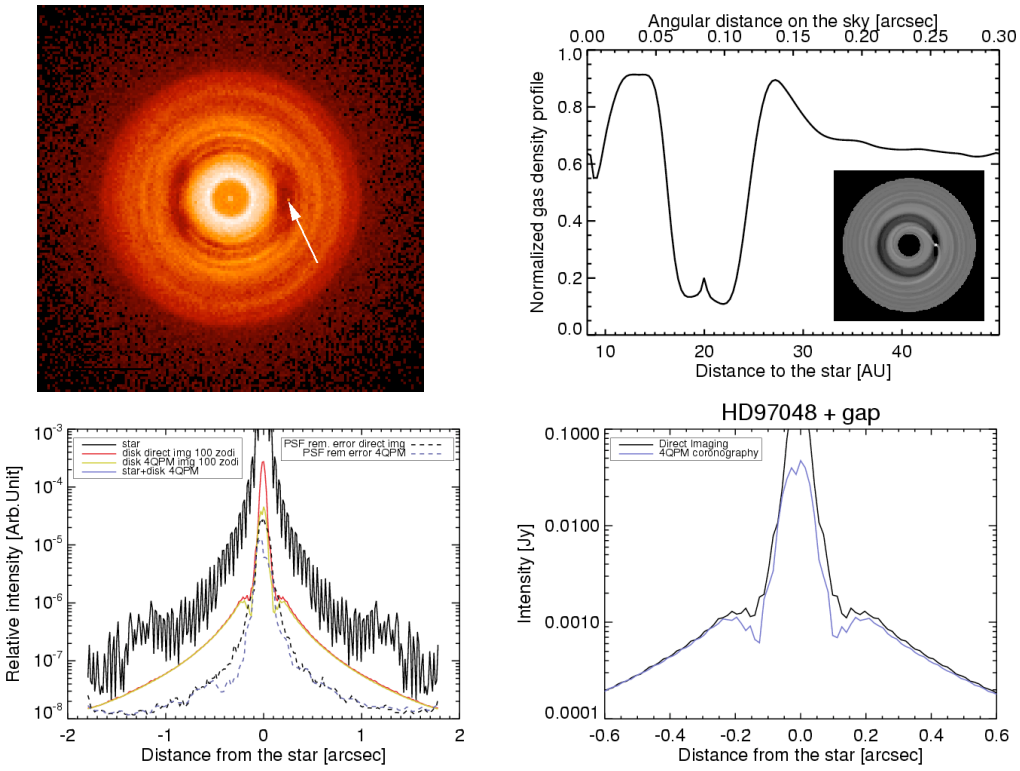

Figure 8. Upper left panel represents the results an example of dynamical simulation of a disc of particles (dust) experiencing radiation pressure from the star (parameter β=0.2); a 1 Jupiter mass planet is embedded (arrow). The planet structures the disc, creating minima and maxima of density. The lower panel shows an observed (using ELT/METIS) debris disc profile. The disc has the same density structure as the β Pictoris dust disc, but contains 100 times less mass and is 10 pc away from Earth. A 1 M_j planet has been placed on a 2 AU orbit. The use of a four quadrants phase mask coronagraph allows to strengthen contrast of the main "horseshoe" structure observed. The right panels show the same type of simulations, but with a proto-planetary disc similar to HD97048. Upper panel shows the modulation (gap) of the disc density due to a 1 Jupiter mass embedded planet; inset is the disc structure seen pole-on. Lower panel shows the observed disc profiles using the ELT-METIS instrument. The observed gap constrast is also enhanced by 30% when using a 4QPM coronagraph.

5. CONCLUSIONS

We have addressed in this paper the potential of METIS mounted on the E-ELT to make direct imaging of extra-solar giant planets around nearby stars. We show that, depending on the planet type i.e. close-in irradiated or self-luminous one, METIS will be able to directly image a 1 Jupiter mass (respectively a 2 Jupiter masses) on a 1 AU (respectively a 10 AU orbit) for nearby solar-type stars. Around fainter, later-type M5 stars, the minimum

separation drops to 5 AU for a self-luminous 2 M_j planet. METIS is thus a powerful instrument to discover and characterize giant exoplanets are short angular separations ($\alpha \leq 0.5$") complementary to MIRI on-board the JWST which is typically limited to ~ 7 M_j at 5 AU (1") for a system 5 pc away.
The E-ELT/METIS instrument is also the perfect tool to study proto– and post– planetary discs. If massive planets are present in a proto-planetary disc, they produce gravitational structures easily detected which will provide us with valuable constraints on planetary formation in the closest star forming regions. In the same order of idea, high angular resolution imaging of closer (d≤40 pc) debris discs is an interesting indirect method of planet detection complementary to the radial velocities one.
The simulations shown in the present paper assume a monochromatic 4QPM coronagraph. The use of future achromatized coronagraphs such as Annular Groove Phase Masks[24] will allow to combine coronagraphy with differential imaging. In this case, the temporal variations we assumed here are not relevant any longer and the expected performances will be largely improved.

REFERENCES

[1] Brandl, B., Lenzen, R., Glasse, A., Blommaert, J., Lagage, P., Siebenmorgen, R., and al.., "MIDIR : a mid-infrared instrument for the E-ELT," in [*SPIE , Proc. SPIE 7014, id. #7014M (2008)*], *Presented at the Society of Photo-Optical Instrumentation Engineers (SPIE) Conference* **7014** (June 2008).

[2] Mayor, M. and Queloz, D., "A Jupiter-Mass Companion to a Solar-Type Star," Nature **378**, 355–+ (Nov. 1995).

[3] Artymowicz, P., "Growth and interactions of planets (Invited Review)," in [*Planetary Systems in the Universe*], Penny, A., ed., *IAU Symposium* **202**, 149–+ (2004).

[4] Rouan, D., Riaud, P., Boccaletti, A., Clénet, Y., and Labeyrie, A., "The Four-Quadrant Phase-Mask Coronagraph. I. Principle," PASP **112**, 1479–1486 (Nov. 2000).

[5] Rivera, E. J., Lissauer, J. J., Butler, R. P., Marcy, G. W., Vogt, S. S., Fischer, D. A., Brown, T. M., Laughlin, G., and Henry, G. W., "A ˜7.5 Earth masses Planet Orbiting the Nearby Star, GJ 876," ApJ **634**, 625–640 (Nov. 2005).

[6] Udry, S., Bonfils, X., Delfosse, X., Forveille, T., Mayor, M., Perrier, C., Bouchy, F., Lovis, C., Pepe, F., Queloz, D., and Bertaux, J.-L., "The HARPS search for southern extra-solar planets. XI. Super-Earths (5 and 8 earth masses) in a 3-planet system," A&A **469**, L43–L47 (July 2007).

[7] Lissauer, J. J., "Planet formation," ARA&A **31**, 129–174 (1993).

[8] Kruegel, E., [*The physics of interstellar dust*], The physics of interstellar dust, by Endrik Kruegel. IoP Series in astronomy and astrophysics, ISBN 0750308613. Bristol, UK: The Institute of Physics, 2003. (2003).

[9] Barman, T. S., Hauschildt, P. H., and Allard, F., "Irradiated Planets," ApJ **556**, 885–895 (Aug. 2001).

[10] Burrows, A., Sudarsky, D., and Lunine, J. I., "Beyond the T Dwarfs: Theoretical Spectra, Colors, and Detectability of the Coolest Brown Dwarfs," ApJ **596**, 587–596 (Oct. 2003).

[11] Fortney, J. J., Marley, M. S., and Barnes, J. W., "Planetary Radii across Five Orders of Magnitude in Mass and Stellar Insolation: Application to Transits," ApJ **659**, 1661–1672 (Apr. 2007).

[12] Torres, C. A. O., Quast, G. R., da Silva, L., de La Reza, R., Melo, C. H. F., and Sterzik, M., "Search for associations containing young stars (SACY). I. Sample and searching method," A&A **460**, 695–708 (Dec. 2006).

[13] O'Dell, C. R. and Beckwith, S. V. W., "Young stars and their surroundings.," *Science* **276**, 1355–1359 (1997).

[14] Greaves, J. S., "Disks Around Stars and the Growth of Planetary Systems," *Science* **307**, 68–71 (Jan. 2005).

[15] Takeuchi, T., Clarke, C. J., and Lin, D. N. C., "The Differential Lifetimes of Protostellar Gas and Dust Disks," ApJ **627**, 286–292 (July 2005).

[16] Setiawan, J., Rodmann, J., da Silva, L., Hatzes, A. P., Pasquini, L., von der Lühe, O., de Medeiros, J. R., Döllinger, M. P., and Girardi, L., "A substellar companion around the intermediate-mass giant star HD 11977," A&A **437**, L31–L34 (July 2005).

[17] Lagage, P. O. and Pantin, E., "Dust Depletion in the Inner Disk of Beta-Pictoris as a Possible Indicator of Planets," Nature **369**, 628–+ (June 1994).

[18] Mouillet, D., Larwood, J. D., Papaloizou, J. C. B., and Lagrange, A. M., "A planet on an inclined orbit as an explanation of the warp in the Beta Pictoris disc," MNRAS **292**, 896–+ (Dec. 1997).

[19] Holland, W. S., Greaves, J. S., Zuckerman, B., Webb, R. A., McCarthy, C., Coulson, I. M., Walther, D. M., Dent, W. R. F., Gear, W. K., and Robson, I., "Submillimetre images of dusty debris around nearby stars," Nature **392**, 788–791 (Apr. 1998).

[20] Lagage, P.-O., Doucet, C., Pantin, E., Habart, E., Duchêne, G., Ménard, F., Pinte, C., Charnoz, S., and Pel, J.-W., "Anatomy of a Flaring Proto-Planetary Disk Around a Young Intermediate-Mass Star," *Science* **314**, 621–623 (Oct. 2006).

[21] Augereau, J. C., Nelson, R. P., Lagrange, A. M., Papaloizou, J. C. B., and Mouillet, D., "Dynamical modeling of large scale asymmetries in the beta Pictoris dust disk," A&A **370**, 447–455 (May 2001).

[22] Chiang, E. I. and Goldreich, P., "Spectral Energy Distributions of T Tauri Stars with Passive Circumstellar Disks," ApJ **490**, 368–+ (Nov. 1997).

[23] Masset, F., "FARGO: A fast eulerian transport algorithm for differentially rotating disks," A&AS **141**, 165–173 (Jan. 2000).

[24] Mawet, D., Riaud, P., Hanot, C., Vandormael, D., Loicq, J., Baudrand, J., Surdej, J., and Habraken, S., "The annular groove phase mask coronagraph: an achromatic optical vortex," in [*SPIE , Proc. SPIE 6693, id. #66931M (2007)*], *Presented at the Society of Photo-Optical Instrumentation Engineers (SPIE) Conference* **6693**, 52–+ (Sept. 2007).

General conclusions

J'ai décrit dans ce manuscrit ce qui a constitué le coeur de mes dix derniéres années de recherche. Celles-ci s'articulent autour de l'instrumentation infrarouge moyen pour des observations sur trés grands télescopes depuis le sol ainsi que la science associée concernant la formation des systémes planétaires. J'espère avoir convaincu le lecteur des potentialités apportés par l'infrarouge moyen á haute résolution angulaire pour apporter informations scientifiques uniques. Cependant, cette information n'est pas toujours facile á extraire des données. Ceci est illustré notamment avec l'exemple de l'instrument VLT/VISIR construit par le CEA et qui nécessite aujourd'hui encore un certain nombre d'améliorations et de réglages pour délivrer ses pleines performances. J'ai montré qu'il est cependant possible dans l'immédiat de pallier á certains manques grce á des méthodes avancées de traitement des données. Ces méthodes ont permis plusieurs avancées scientifiques dans le domaine des disques protoplanétaires et plus particuliérement concernant la connaissance de leur structure géométrique á grande échelle.
La prochaine génération de trés grands télescopes qui seront achevés de construire dans la prochaine décade offriront aux astronomes un potentiel scientifique sans précédent dans le domaine de l'observation en infrarouge moyen du phénomène de formation planétaire. En extrapolant á partir des performances obtenues aujourd'hui sur des télescopes de 8m et á l'aide d'outils de simulation numérique, je montre que l'on sera capable d'observer des planétes entrain de se former dans les disques protoplanétaires ainsi que des planétes déjá formées au sein de systémes plus matures. Pour cela, il faudra faire évoluer les techniques d'observation en infrarouge moyen et emprunter certaines méthodes développées dans le cadre la haute résolution angulaire á plus courtes longueurs d'onde. Parmi celles-ci on trouve la coronographie á masque de phase et l'imagerie différentielle. La mise en pratique de ces techniques d'observation ne pourra s'effectuer sans un bond technologique. Ce saut technologique reste encore á faire et demandera de nombreux efforts en recherche et développement dans les prochaines années.

I have described in this manuscript the core of my work during the last ten years. This work has mainly dealt with the instrumentation in the mid-infrared range from the ground on large telescopes and the associated science about planetary formation. I hope to have convinced the reader of the large panel of unique potentialities brought by the mid-infrared observations at high angular resolution. However, this type of information is not always straightforward to extract and requires sometimes considerable efforts. This point is illustrated by the example of the VLT/VISIR instrument built by the CEA. This instrument does not perform yet at its maximum capability and some analysis and fine tuning tasks have still to be made. I have shown however that it is possible to approach the optimum performances by developing and using high level post-processing and data analysis techniques. These techniques have

allowed to make singificant steps for the understanding of the protoplanetary disks and more precisely concerning their large-scale geometry.
The next generation of extremely large telescopes which building should be finished by the second half of the next decade. They will offer to the astronomers a unprecedented potential in the domain of the observations in the mid-infrared range of the planetary formation process. By extrapolating from current performances on 8m-class telescopes and using numerical simulations I show that we will be able to observe forming planetary systems in protoplanetary disks also as more mature already formed ones. To reach this challenging goal the mid-infrared range observing techniques will need to make siginficant progresses. For instance several obsering techniques currently used in the domain of high angular resolution at shorter wavelengths will have to be adapted to the mid-infrared range. Among those, I have identified that the phase-mask coronagraphy and the diffential imaging techniques. However their implementation will require to make some preliminary technological steps. These steps still need to be made and will require some important efforts in research and develoment in the coming years.

Bibliography

[Acke and van den Ancker, 2004] Acke, B. and van den Ancker, M. E. (2004). ISO spectroscopy of disks around Herbig Ae/Be stars. A&A, 426:151–170.

[Acke et al., 2005] Acke, B., van den Ancker, M. E., and Dullemond, C. P. (2005). [O I] 6300 Å emission in Herbig Ae/Be systems: Signature of Keplerian rotation. A&A, 436:209–230.

[Artymowicz, 2004] Artymowicz, P. (2004). Growth and interactions of planets (Invited Review). In Penny, A., editor, *Planetary Systems in the Universe*, volume 202 of *IAU Symposium*, pages 149–+.

[Baraffe et al., 2003] Baraffe, I., Chabrier, G., Barman, T. S., Allard, F., and Hauschildt, P. H. (2003). Evolutionary models for cool brown dwarfs and extrasolar giant planets. The case of HD 209458. A&A, 402:701–712.

[Barman et al., 2001] Barman, T. S., Hauschildt, P. H., and Allard, F. (2001). Irradiated Planets. ApJ, 556:885–895.

[Baudoz et al., 2008] Baudoz, P., Galicher, R., Baudrand, J., and Boccaletti, A. (2008). Theory and laboratory tests of the multi-stage phase mask coronagraph. In *Society of Photo-Optical Instrumentation Engineers (SPIE) Conference Series*, volume 7015 of *Presented at the Society of Photo-Optical Instrumentation Engineers (SPIE) Conference*.

[Beaulieu et al., 2006] Beaulieu, J.-P., Bennett, D. P., Fouqué, P., Williams, A., Dominik, M., Jørgensen, U. G., Kubas, D., Cassan, A., Coutures, C., Greenhill, J., Hill, K., Menzies, J., Sackett, P. D., Albrow, M., Brillant, S., Caldwell, J. A. R., Calitz, J. J., Cook, K. H., Corrales, E., Desort, M., Dieters, S., Dominis, D., Donatowicz, J., Hoffman, M., Kane, S., Marquette, J.-B., Martin, R., Meintjes, P., Pollard, K., Sahu, K., Vinter, C., Wambsganss, J., Woller, K., Horne, K., Steele, I., Bramich, D. M., Burgdorf, M., Snodgrass, C., Bode, M., Udalski, A., Szymański, M. K., Kubiak, M., Więckowski, T., Pietrzyński, G., Soszyński, I., Szewczyk, O., Wyrzykowski, Ł., Paczyński, B., Abe, F., Bond, I. A., Britton, T. R., Gilmore, A. C., Hearnshaw, J. B., Itow, Y., Kamiya, K., Kilmartin, P. M., Korpela, A. V., Masuda, K., Matsubara, Y., Motomura, M., Muraki, Y., Nakamura, S., Okada, C., Ohnishi, K., Rattenbury, N. J., Sako, T., Sato, S., Sasaki, M., Sekiguchi, T., Sullivan, D. J., Tristram, P. J., Yock, P. C. M., and Yoshioka, T. (2006). Discovery of a cool planet of 5.5 Earth masses through gravitational microlensing. Nature, 439:437–440.

[Beichman et al., 2006] Beichman, C., Lawson, P., Lay, O., Ahmed, A., Unwin, S., and Johnston, K. (2006). Status of the terrestrial planet finder interferometer (TPF-I). In *Society of Photo-Optical Instrumentation Engineers (SPIE) Conference Series*, volume 6268 of *Presented at the Society of Photo-Optical Instrumentation Engineers (SPIE) Conference*.

[Benest and Duvent, 1995] Benest, D. and Duvent, J. L. (1995). Is Sirius a triple star? A&A, 299:621–+.

[Bertero et al., 2003] Bertero, M., Boccacci, P., Custo, A., De Mol, C., and Robberto, M. (2003). A Fourier-based method for the restoration of chopped and nodded images. A&A, 406:765–772.

[Beuzit et al., 2008] Beuzit, J.-L., Feldt, M., Dohlen, K., Mouillet, D., Puget, P., Wildi, F., Abe, L., Antichi, J., Baruffolo, A., Baudoz, P., Boccaletti, A., Carbillet, M., Charton, J., Claudi, R., Downing, M., Fabron, C., Feautrier, P., Fedrigo, E., Fusco, T., Gach, J.-L., Gratton, R., Henning, T., Hubin, N., Joos, F., Kasper, M., Langlois, M., Lenzen, R., Moutou, C., Pavlov, A., Petit, C., Pragt, J., Rabou, P., Rigal, F., Roelfsema, R., Rousset, G., Saisse, M., Schmid, H.-M., Stadler, E., Thalmann, C., Turatto, M., Udry, S., Vakili, F., and Waters, R. (2008). SPHERE: a planet finder instrument for the VLT. In *Society of Photo-Optical Instrumentation Engineers (SPIE) Conference Series*, volume 7014 of *Society of Photo-Optical Instrumentation Engineers (SPIE) Conference Series*.

[Bitner et al., 2007] Bitner, M. A., Richter, M. J., Lacy, J. H., Greathouse, T. K., Jaffe, D. T., and Blake, G. A. (2007). TEXES Observations of Pure Rotational H_2 Emission from AB Aurigae. ApJ, 661:L69–L72.

[Blondel et al., 1993] Blondel, P. F. C., Talavera, A., and Djie, H. R. E. T. A. (1993). Lyman alpha emission in spectra of Herbig AE stars - an indication of accretion? A&A, 268:624–640.

[Boccaletti et al., 2004] Boccaletti, A., Riaud, P., Baudoz, P., Baudrand, J., Rouan, D., Gratadour, D., Lacombe, F., and Lagrange, A.-M. (2004). The Four-Quadrant Phase Mask Coronagraph. IV. First Light at the Very Large Telescope. PASP, 116:1061–1071.

[Bodenheimer and Pollack, 1986] Bodenheimer, P. and Pollack, J. B. (1986). Calculations of the accretion and evolution of giant planets The effects of solid cores. *Icarus*, 67:391–408.

[Bonnet-Bidaud et al., 2000] Bonnet-Bidaud, J. M., Colas, F., and Lecacheux, J. (2000). Search for companions around Sirius. A&A, 360:991–996.

[Boss, 2001] Boss, A. P. (2001). Formation of Planetary-Mass Objects by Protostellar Collapse and Fragmentation. ApJ, 551:L167–L170.

[Bouwman et al., 2000] Bouwman, J., de Koter, A., van den Ancker, M. E., and Waters, L. B. F. M. (2000). The composition of the circumstellar dust around the Herbig Ae stars AB Aur and HD 163296. A&A, 360:213–226.

[Bouwman et al., 2008] Bouwman, J., Henning, T., Hillenbrand, L. A., Meyer, M. R., Pascucci, I., Carpenter, J., Hines, D., Kim, J. S., Silverstone, M. D., Hollenbach, D., and Wolf, S. (2008). The Formation and Evolution of Planetary Systems: Grain Growth and Chemical Processing of Dust in T Tauri Systems. ApJ, 683:479–498.

[Brandeker et al., 2004] Brandeker, A., Liseau, R., Olofsson, G., and Fridlund, M. (2004). The spatial structure of the β Pictoris gas disk. A&A, 413:681–691.

[Brittain et al., 2005] Brittain, S. D., Rettig, T. W., Simon, T., and Kulesa, C. (2005). CO Line Emission and Absorption from the HL Tauri Disk-Where Is All the Dust? ApJ, 626:283–291.

[Burrows et al., 1997] Burrows, A., Marley, M., Hubbard, W. B., Lunine, J. I., Guillot, T., Saumon, D., Freedman, R., Sudarsky, D., and Sharp, C. (1997). A Nongray Theory of Extrasolar Giant Planets and Brown Dwarfs. ApJ, 491:856–+.

[Burrows et al., 2003] Burrows, A., Sudarsky, D., and Lunine, J. I. (2003). Beyond the T Dwarfs: Theoretical Spectra, Colors, and Detectability of the Coolest Brown Dwarfs. ApJ, 596:587–596.

[Canup, 2004] Canup, R. M. (2004). Simulations of a late lunar-forming impact. *Icarus*, 168:433–456.

[Carmona et al., 2008] Carmona, A., van den Ancker, M. E., Henning, T., Pavlyuchenkov, Y., Dullemond, C. P., Goto, M., Thi, W. F., Bouwman, J., and Waters, L. B. F. M. (2008). A search for mid-infrared molecular hydrogen emission from protoplanetary disks. A&A, 477:839–852.

[Carpenter et al., 2005] Carpenter, J. M., Wolf, S., Schreyer, K., Launhardt, R., and Henning, T. (2005). Evolution of Cold Circumstellar Dust around Solar-type Stars. AJ, 129:1049–1062.

[Ceccarelli et al., 2002] Ceccarelli, C., Boogert, A. C. A., Tielens, A. G. G. M., Caux, E., Hogerheijde, M. R., and Parise, B. (2002). Submm/FIR CO line emission from the disk of the Class I protostar EL 29. A&A, 395:863–871.

[Chabrier et al., 2000] Chabrier, G., Baraffe, I., Allard, F., and Hauschildt, P. (2000). Evolutionary Models for Very Low-Mass Stars and Brown Dwarfs with Dusty Atmospheres. ApJ, 542:464–472.

[Charnoz et al., 2009a] Charnoz, S., Morbidelli, A., Dones, L., and Salmon, J. (2009a). Did Saturn's rings form during the Late Heavy Bombardment? *Icarus*, 199:413–428.

[Charnoz et al., 2009b] Charnoz, S., Morbidelli, A., Dones, L., and Salmon, J. (2009b). Did Saturn's rings form during the Late Heavy Bombardment? *Icarus*, 199:413–428.

[Chiang and Goldreich, 1997] Chiang, E. I. and Goldreich, P. (1997). Spectral Energy Distributions of T Tauri Stars with Passive Circumstellar Disks. ApJ, 490:368–+.

[Cohen et al., 1992a] Cohen, M., Walker, R. G., Barlow, M. J., and Deacon, J. R. (1992a). Spectral irradiance calibration in the infrared. I - Ground-based and IRAS broadband calibrations. AJ, 104:1650–1657.

[Cohen et al., 1999] Cohen, M., Walker, R. G., Carter, B., Hammersley, P., Kidger, M., and Noguchi, K. (1999). Spectral Irradiance Calibration in the Infrared. X. A Self-Consistent Radiometric All-Sky Network of Absolutely Calibrated Stellar Spectra. AJ, 117:1864–1889.

[Cohen et al., 1992b] Cohen, M., Walker, R. G., and Witteborn, F. C. (1992b). Spectral irradiance calibration in the infrared. II - Alpha Tau and the recalibration of the IRAS low resolution spectrometer. AJ, 104:2030–2044.

[Cohen et al., 1996a] Cohen, M., Witteborn, F. C., Bregman, J. D., Wooden, D. H., Salama, A., and Metcalfe, L. (1996a). Spectral Irradiance Calibration in the Infrared. VI. 3-35 micron Spectra of Three Southern Standard Stars. AJ, 112:241–+.

[Cohen et al., 1996b] Cohen, M., Witteborn, F. C., Carbon, D. F., Davies, J. K., Wooden, D. H., and Bregman, J. D. (1996b). Spectral Irradiance Calibration in the Infrared.VII.New Composite Spectra, Comparison with Model Atmospheres, and Far-Infrared Extrapolations. AJ, 112:2274–+.

[Cohen et al., 1995] Cohen, M., Witteborn, F. C., Walker, R. G., Bregman, J. D., and Wooden, D. H. (1995). Spectral Irradiance Calibration in the Infrared.IV. 1.2-35 micron spectra of six standard stars. AJ, 110:275–+.

[D'Alessio, 2001] D'Alessio, P. (2001). Accretion Disks around Young Low Mass Stars. In *Revista Mexicana de Astronomia y Astrofisica Conference Series*, volume 11 of *Revista Mexicana de Astronomia y Astrofisica, vol. 27*, pages 177–+.

[D'Angelo et al., 2003] D'Angelo, G., Kley, W., and Henning, T. (2003). Orbital Migration and Mass Accretion of Protoplanets in Three-dimensional Global Computations with Nested Grids. ApJ, 586:540–561.

[Decin et al., 2000] Decin, L., Waelkens, C., Eriksson, K., Gustafsson, B., Plez, B., Sauval, A. J., Van Assche, W., and Vandenbussche, B. (2000). ISO-SWS calibration and the accurate modelling of cool-star atmospheres. I. Method. A&A, 364:137–156.

[Doering et al., 2007] Doering, R. L., Meixner, M., Holfeltz, S. T., Krist, J. E., Ardila, D. R., Kamp, I., Clampin, M. C., and Lubow, S. H. (2007). HD 97048's Circumstellar Environment as Revealed by a Hubble Space Telescope ACS Coronagraphic Study of Disk Candidate Stars. AJ, 133:2122–2131.

[Dominik et al., 2007] Dominik, C., Blum, J., Cuzzi, J. N., and Wurm, G. (2007). Growth of Dust as the Initial Step Toward Planet Formation. In Reipurth, B., Jewitt, D., and Keil, K., editors, *Protostars and Planets V*, pages 783–800.

[Dominik et al., 2003] Dominik, C., Dullemond, C. P., Waters, L. B. F. M., and Natta, A. (2003). Models of Passive Disks with Inner Holes: Evidence for Disks around Intermediate Mass Pre-Main-Sequence Stars. In De Buizer, J. M. and van der Bliek, N. S., editors, *Galactic Star Formation Across the Stellar Mass Spectrum*, volume 287 of *Astronomical Society of the Pacific Conference Series*, pages 313–318.

[Doucet et al., 2007] Doucet, C., Habart, E., Pantin, E., Dullemond, C., Lagage, P. O., Pinte, C., Duchêne, G., and Ménard, F. (2007). HD 97048: a closer look at the disk. A&A, 470:625–631.

[Doucet et al., 2006a] Doucet, C., Lagage, P., and Pantin, E. (2006a). High resolution Mid-Infrared Imaging of Dust Disks Structures around Herbig Ae Stars with VISIR. In Coudé Du Foresto, V., Rouan, D., and Rousset, G., editors, *Visions for Infrared Astronomy, Instrumentation, Mesure, Métrologie*, pages 25–30.

[Doucet et al., 2004] Doucet, C., Pantin, E., and Lagage, P.-O. (2004). 20 microns views on intermediate Haebe dust disk. In Combes, F., Barret, D., Contini, T., Meynadier, F., and Pagani, L., editors, *SF2A-2004: Semaine de l'Astrophysique Francaise*, pages 73–+.

[Doucet et al., 2006b] Doucet, C., Pantin, E., Lagage, P. O., and Dullemond, C. P. (2006b). Mid-infrared imaging of the circumstellar dust around three Herbig Ae stars: HD 135344, CQ Tau, and HD 163296. A&A, 460:117–124.

[Duchêne et al., 2004] Duchêne, G., McCabe, C., Ghez, A. M., and Macintosh, B. A. (2004). A Multiwavelength Scattered Light Analysis of the Dust Grain Population in the GG Tauri Circumbinary Ring. ApJ, 606:969–982.

[Dudhia, A., 2005] Dudhia, A. (2005). Reference forward model (rfm). http://www.atm.ox.ac.uk/RFM/.

[Dullemond and Dominik, 2004a] Dullemond, C. P. and Dominik, C. (2004a). The effect of dust settling on the appearance of protoplanetary disks. A&A, 421:1075–1086.

[Dullemond and Dominik, 2004b] Dullemond, C. P. and Dominik, C. (2004b). The Global Structure of Protoplanetary Disks. In Beaulieu, J., Lecavelier Des Etangs, A., and Terquem, C., editors, *Extrasolar Planets: Today and Tomorrow*, volume 321 of *Astronomical Society of the Pacific Conference Series*, pages 361–+.

[Dullemond et al., 2001] Dullemond, C. P., Dominik, C., and Natta, A. (2001). Passive Irradiated Circumstellar Disks with an Inner Hole. ApJ, 560:957–969.

[Dutrey et al., 1998] Dutrey, A., Guilloteau, S., Prato, L., Simon, M., Duvert, G., Schuster, K., and Menard, F. (1998). CO study of the GM Aurigae Keplerian disk. A&A, 338:L63–L66.

[Elad et al., 2005] Elad, M., Starck, J. L., Donoho, D., and Querre, P. (2005). Simultaneous Cartoon and Texture Image Inpainting Using Morphological Component Analysis (MCA). *Journal on Applied and Computational Harmonic Analysis*, 19:340–358.

[Elkins-Tanton, 2008] Elkins-Tanton, L. T. (2008). Linked magma ocean solidification and atmospheric growth for Earth and Mars. *Earth and Planetary Science Letters*, 271:181–191.

[Fischer and Valenti, 2005] Fischer, D. A. and Valenti, J. (2005). The Planet-Metallicity Correlation. ApJ, 622:1102–1117.

[Fridlund et al., 2006] Fridlund, C. V. M., d'Arcio, L., den Hartog, R., and Karlsson, A. (2006). Status and recent progress of the Darwin mission in the Cosmic Vision program. In *Society of Photo-Optical Instrumentation Engineers (SPIE) Conference Series*, volume 6268 of *Presented at the Society of Photo-Optical Instrumentation Engineers (SPIE) Conference*.

[Fukagawa et al., 2004] Fukagawa, M., Hayashi, M., Tamura, M., Itoh, Y., Hayashi, S. S., Oasa, Y., Takeuchi, T., Morino, J.-i., Murakawa, K., Oya, S., Yamashita, T., Suto, H., Mayama, S., Naoi, T., Ishii, M., Pyo, T.-S., Nishikawa, T., Takato, N., Usuda, T., Ando, H., Iye, M., Miyama, S. M., and Kaifu, N. (2004). Spiral Structure in the Circumstellar Disk around AB Aurigae. ApJ, 605:L53–L56.

[Gail, 2001] Gail, H.-P. (2001). Radial mixing in protoplanetary accretion disks. I. Stationary disc models with annealing and carbon combustion. A&A, 378:192–213.

[Gail, 2004] Gail, H.-P. (2004). Radial mixing in protoplanetary accretion disks. IV. Metamorphosis of the silicate dust complex. A&A, 413:571–591.

[Galdemard et al., 2003] Galdemard, P., Garnier, F., Mulet, P., and Reynolds, D. (2003). Characterization of DRS Technologies' 256x256 mid-IR arrays for VISIR. In Iye, M. and Moorwood, A. F. M., editors, *Instrument Design and Performance for Optical/Infrared Ground-based Telescopes. Edited by Iye, Masanori; Moorwood, Alan F. M. Proceedings of the SPIE, Volume 4841, pp. 129-140 (2003).*, volume 4841 of *Presented at the Society of Photo-Optical Instrumentation Engineers (SPIE) Conference*, pages 129–140.

[Galdemard et al., 1998] Galdemard, P., Lagage, P. O., Jouan, R., Masse, P., and Dubreuil, D. (1998). CAMIRAS 192x128: instrumental upgrades and latest results. In Fowler, A. M., editor, *Society of Photo-Optical Instrumentation Engineers (SPIE) Conference Series*, volume 3354 of *Society of Photo-Optical Instrumentation Engineers (SPIE) Conference Series*, pages 704–710.

[Glassgold et al., 2007] Glassgold, A. E., Najita, J. R., and Igea, J. (2007). Neon Fine-Structure Line Emission by X-Ray Irradiated Protoplanetary Disks. ApJ, 656:515–523.

[Goldreich and Tremaine, 1979] Goldreich, P. and Tremaine, S. (1979). The excitation of density waves at the Lindblad and corotation resonances by an external potential. ApJ, 233:857–871.

[Gomes et al., 2005] Gomes, R., Levison, H. F., Tsiganis, K., and Morbidelli, A. (2005). Origin of the cataclysmic Late Heavy Bombardment period of the terrestrial planets. Nature, 435:466–469.

[Gorti and Hollenbach, 2008] Gorti, U. and Hollenbach, D. (2008). Photoevaporation of Circumstellar Disks by FUV, EUV and X-ray Radiation from the Central Star. *ArXiv e-prints*.

[Graae Jorgensen et al., 2009] Graae Jorgensen, U., Appel, P. W. U., Hatsukawa, Y., Frei, R., Oshima, M., Toh, Y., and Kimura, A. (2009). The Earth-Moon system during the Late Heavy Bombardment period. *ArXiv e-prints*.

[Grady et al., 1999] Grady, C. A., Woodgate, B., Bruhweiler, F. C., Boggess, A., Plait, P., Lindler, D. J., Clampin, M., and Kalas, P. (1999). Hubble Space Telescope Space Telescope Imaging Spectrograph Coronagraphic Imaging of the Herbig AE Star AB Aurigae. ApJ, 523:L151–L154.

[Grady et al., 2005] Grady, C. A., Woodgate, B. E., Bowers, C. W., Gull, T. R., Sitko, M. L., Carpenter, W. J., Lynch, D. K., Russell, R. W., Perry, R. B., Williger, G. M., Roberge, A., Bouret, J.-C., and Sahu, M. (2005). Coronagraphic Imaging of Pre-Main-Sequence Stars with the Hubble Space Telescope Space Telescope Imaging Spectrograph. I. The Herbig Ae Stars. ApJ, 630:958–975.

[Gry and Bonnet-Bidaud, 1990] Gry, C. and Bonnet-Bidaud, J. M. (1990). Sirius and the Colour Enigma. Nature, 347:625–+.

[Guyon et al., 2006] Guyon, O., Pluzhnik, E. A., Kuchner, M. J., Collins, B., and Ridgway, S. T. (2006). Theoretical Limits on Extrasolar Terrestrial Planet Detection with Coronagraphs. ApJS, 167:81–99.

[Habart et al., 2004] Habart, E., Testi, L., Natta, A., and Carbillet, M. (2004). Diamonds in HD 97048: A Closer Look. ApJ, 614:L129–L132.

[Haisch et al., 2001] Haisch, Jr., K. E., Lada, E. A., and Lada, C. J. (2001). Disk Frequencies and Lifetimes in Young Clusters. ApJ, 553:L153–L156.

[Hauschildt et al., 1999] Hauschildt, P. H., Allard, F., and Baron, E. (1999). The NextGen Model Atmosphere Grid for 3000-10,000 K. ApJ, 512:377–385.

[Haywood, 2009] Haywood, M. (2009). On the Correlation Between Metallicity and the Presence of Giant Planets. ApJ, 698:L1–L5.

[Henning et al., 1998] Henning, T., Burkert, A., Launhardt, R., Leinert, C., and Stecklum, B. (1998). Infrared imaging and millimetre continuum mapping of Herbig Ae/Be and FU Orionis stars. A&A, 336:565–586.

[Hernández et al., 2004] Hernández, J., Calvet, N., Briceño, C., Hartmann, L., and Berlind, P. (2004). Spectral Analysis and Classification of Herbig Ae/Be Stars. AJ, 127:1682–1701.

[Hollenbach et al., 2005] Hollenbach, D., Gorti, U., Meyer, M., Kim, J. S., Morris, P., Najita, J., Pascucci, I., Carpenter, J., Rodmann, J., Brooke, T., Hillenbrand, L., Mamajek, E., Padgett, D., Soderblom, D., Wolf, S., and Lunine, J. (2005). Formation and Evolution of Planetary Systems: Upper Limits to the Gas Mass in HD 105. ApJ, 631:1180–1190.

[Horne, 1986] Horne, K. (1986). An optimal extraction algorithm for CCD spectroscopy. PASP, 98:609–617.

[Johansen et al., 2007] Johansen, A., Oishi, J. S., Low, M.-M. M., Klahr, H., Henning, T., and Youdin, A. (2007). Rapid planetesimal formation in turbulent circumstellar disks. Nature, 448:1022–1025.

[Kaeufl et al., 1991] Kaeufl, H. U., Bouchet, P., van Dijsseldonk, A., and Weilenmann, U. (1991). A sky-noise measurement and its implication for ground-based infrared astronomy in the 10-micron atmospheric window. *Experimental Astronomy*, 2:115–122.

[Kalas et al., 2005] Kalas, P., Graham, J. R., and Clampin, M. (2005). A planetary system as the origin of structure in Fomalhaut's dust belt. Nature, 435:1067–1070.

[Kemper et al., 2004] Kemper, F., Vriend, W. J., and Tielens, A. G. G. M. (2004). The Absence of Crystalline Silicates in the Diffuse Interstellar Medium. ApJ, 609:826–837.

[Koeberl, 2003] Koeberl, C. (2003). The Late Heavy Bombardment in the Inner Solar System: Is there any Connection to Kuiper Belt Objects? *Earth Moon and Planets*, 92:79–87.

[Lacy et al., 2006] Lacy, J. H., Jaffe, D. T., Richter, M. J., Greathouse, T. K., Bitner, M., Segura, P., Moller, W., Geballe, T. R., and Volk, K. (2006). TEXES on Gemini. In *Society of Photo-Optical Instrumentation Engineers (SPIE) Conference Series*, volume 6269 of *Presented at the Society of Photo-Optical Instrumentation Engineers (SPIE) Conference*.

[Lagage et al., 2006] Lagage, P.-O., Doucet, C., Pantin, E., Habart, E., Duchêne, G., Ménard, F., Pinte, C., Charnoz, S., and Pel, J.-W. (2006). Anatomy of a Flaring Proto-Planetary Disk Around a Young Intermediate-Mass Star. *Science*, 314:621–623.

[Lagage and Pantin, 1994] Lagage, P. O. and Pantin, E. (1994). Dust Depletion in the Inner Disk of Beta-Pictoris as a Possible Indicator of Planets. Nature, 369:628–+.

[Leger et al., 2004] Leger, A., Selsis, F., Sotin, C., Guillot, T., Despois, D., Mawet, D., Ollivier, M., Labèque, A., Valette, C., Brachet, F., Chazelas, B., and Lammer, H. (2004). A new family of planets? "Ocean-Planets". *Icarus*, 169:499–504.

[Levison et al., 2001] Levison, H. F., Dones, L., Chapman, C. R., Stern, S. A., Duncan, M. J., and Zahnle, K. (2001). Could the Lunar "Late Heavy Bombardment" Have Been Triggered by the Formation of Uranus and Neptune? *Icarus*, 151:286–306.

[Lin and Papaloizou, 1986] Lin, D. N. C. and Papaloizou, J. (1986). On the tidal interaction between protoplanets and the protoplanetary disk. III - Orbital migration of protoplanets. ApJ, 309:846–857.

[Liou and Zook, 1999] Liou, J.-C. and Zook, H. A. (1999). Signatures of the Giant Planets Imprinted on the Edgeworth-Kuiper Belt Dust Disk. AJ, 118:580–590.

[Lissauer, 2007] Lissauer, J. J. (2007). Planets Formed in Habitable Zones of M Dwarf Stars Probably Are Deficient in Volatiles. ApJ, 660:L149–L152.

[Lord, 1992] Lord, S. D. (1992). NASA technical memorandum. Technical Report 103957, NASA.

[Lyot, 1939] Lyot, B. (1939). The study of the solar corona and prominences without eclipses (George Darwin Lecture, 1939). MNRAS, 99:580–+.

[Mannings and Sargent, 1997] Mannings, V. and Sargent, A. I. (1997). A High-Resolution Study of Gas and Dust around Young Intermediate-Mass Stars: Evidence for Circumstellar Disks in Herbig AE Systems. ApJ, 490:792–+.

[Marois et al., 2006] Marois, C., Lafrenière, D., Doyon, R., Macintosh, B., and Nadeau, D. (2006). Angular Differential Imaging: A Powerful High-Contrast Imaging Technique. ApJ, 641:556–564.

[Martin-Zaidi et al., 2009] Martin-Zaidi, C., Pantin, E., Lagage, P., Habart, E., Ménard, F., Augerau, J., and Pinte, C. (2009). MOLECULAR HYDROGEN IN THE DISK OF THE HERBIG STAR HD 97048 . A&A. In preparation.

[Martinez et al., 2008] Martinez, P., Boccaletti, A., Kasper, M., Cavarroc, C., Yaitskova, N., Fusco, T., and Vérinaud, C. (2008). Comparison of coronagraphs for high-contrast imaging in the context of extremely large telescopes. A&A, 492:289–300.

[Masset, 2000] Masset, F. (2000). FARGO: A fast eulerian transport algorithm for differentially rotating disks. A&AS, 141:165–173.

[Masset and Papaloizou, 2003] Masset, F. S. and Papaloizou, J. C. B. (2003). Runaway Migration and the Formation of Hot Jupiters. ApJ, 588:494–508.

[Mawet et al., 2006] Mawet, D., Riaud, P., Baudrand, J., Baudoz, P., Boccaletti, A., Dupuis, O., and Rouan, D. (2006). The four-quadrant phase-mask coronagraph: white light laboratory results with an achromatic device. A&A, 448:801–808.

[Mawet et al., 2005] Mawet, D., Riaud, P., Surdej, J., and Baudrand, J. (2005). Subwavelength surface-relief gratings for stellar coronagraphy. Appl. Opt., 44:7313–7321.

[Mayor and Queloz, 1995] Mayor, M. and Queloz, D. (1995). A Jupiter-Mass Companion to a Solar-Type Star. Nature, 378:355–+.

[McCaughrean et al., 2004] McCaughrean, M. J., Close, L. M., Scholz, R.-D., Lenzen, R., Biller, B., Brandner, W., Hartung, M., and Lodieu, N. (2004). ϵ Indi Ba,Bb: The nearest binary brown dwarf. A&A, 413:1029–1036.

[Meeus et al., 2001] Meeus, G., Waters, L. B. F. M., Bouwman, J., van den Ancker, M. E., Waelkens, C., and Malfait, K. (2001). ISO spectroscopy of circumstellar dust in 14 Herbig Ae/Be systems: Towards an understanding of dust processing. A&A, 365:476–490.

[Megeath et al., 2005] Megeath, S. T., Hartmann, L., Luhman, K. L., and Fazio, G. G. (2005). Spitzer/IRAC Photometry of the η Chameleontis Association. ApJ, 634:L113–L116.

[Meyer et al., 2007] Meyer, M. R., Backman, D. E., Weinberger, A. J., and Wyatt, M. C. (2007). Evolution of Circumstellar Disks Around Normal Stars: Placing Our Solar System in Context. In Reipurth, B., Jewitt, D., and Keil, K., editors, *Protostars and Planets V*, pages 573–588.

[Meyer et al., 2006] Meyer, M. R., Hillenbrand, L. A., Backman, D., Beckwith, S., Bouwman, J., Brooke, T., Carpenter, J., Cohen, M., Cortes, S., Crockett, N., Gorti, U., Henning, T., Hines, D., Hollenbach, D., Kim, J. S., Lunine, J., Malhotra, R., Mamajek, E., Metchev, S., Moro-Martin, A., Morris, P., Najita, J., Padgett, D., Pascucci, I., Rodmann, J., Schlingman, W., Silverstone, M., Soderblom, D., Stauffer, J., Stobie, E., Strom, S., Watson, D., Weidenschilling, S., Wolf, S., and Young, E. (2006). The Formation and Evolution of Planetary Systems: Placing Our Solar System in Context with Spitzer. PASP, 118:1690–1710.

[Monnier et al., 2005] Monnier, J. D., Millan-Gabet, R., Billmeier, R., Akeson, R. L., Wallace, D., Berger, J.-P., Calvet, N., D'Alessio, P., Danchi, W. C., Hartmann, L., Hillenbrand, L. A., Kuchner, M., Rajagopal, J., Traub, W. A., Tuthill, P. G., Boden, A., Booth, A., Colavita, M., Gathright, J., Hrynevych, M., Le Mignant, D., Ligon, R., Neyman, C., Swain, M., Thompson, R., Vasisht, G., Wizinowich, P., Beichman, C., Beletic, J., Creech-Eakman, M., Koresko, C., Sargent, A., Shao, M., and van Belle, G. (2005). The Near-Infrared Size-Luminosity Relations for Herbig Ae/Be Disks. ApJ, 624:832–840.

[Mueller and Lagerros, 1998] Mueller, T. G. and Lagerros, J. S. V. (1998). Asteroids as far-infrared photometric standards for ISOPHOT. A&A, 338:340–352.

[Nakajima et al., 1995] Nakajima, T., Oppenheimer, B. R., Kulkarni, S. R., Golimowski, D. A., Matthews, K., and Durrance, S. T. (1995). Discovery of a Cool Brown Dwarf. Nature, 378:463–+.

[Nomura et al., 2007] Nomura, H., Aikawa, Y., Tsujimoto, M., Nakagawa, Y., and Millar, T. J. (2007). Molecular Hydrogen Emission from Protoplanetary Disks. II. Effects of X-Ray Irradiation and Dust Evolution. ApJ, 661:334–353.

[Nomura and Nakagawa, 2006] Nomura, H. and Nakagawa, Y. (2006). Dust Size Growth and Settling in a Protoplanetary Disk. ApJ, 640:1099–1109.

[Ozernoy et al., 2000] Ozernoy, L. M., Gorkavyi, N. N., Mather, J. C., and Taidakova, T. A. (2000). Signatures of Exosolar Planets in Dust Debris Disks. ApJ, 537:L147–L151.

[Paardekooper and Mellema, 2004] Paardekooper, S.-J. and Mellema, G. (2004). Planets opening dust gaps in gas disks. A&A, 425:L9–L12.

[Pantin et al., 2005] Pantin, E., Bouwman, J., and Lagage, P. O. (2005). An emission ring at 20.5 μm around the HAEBE star AB Aurigæ: Unveiling the disk structure. A&A, 437:525–530.

[Pantin et al., 1997] Pantin, E., Lagage, P. O., and Artymowicz, P. (1997). Mid-infrared images and models of the beta Pictoris dust disk. A&A, 327:1123–1136.

[Pantin and Starck, 1996] Pantin, E. and Starck, J.-L. (1996). Deconvolution of astronomical images using the multiscale maximum entropy method. A&AS, 118:575–585.

[Pantin et al., 2000] Pantin, E., Waelkens, C., and Lagage, P. O. (2000). ADONIS observations of the HD 100546 circumstellar dust disk. A&A, 361:L9–L12.

[Papoular, 1983] Papoular, R. (1983). The processing of infrared sky noise by chopping, nodding and filtering. A&A, 117:46–52.

[Piétu et al., 2005] Piétu, V., Guilloteau, S., and Dutrey, A. (2005). Sub-arcsec imaging of the AB Aur molecular disk and envelope at millimeter wavelengths: a non Keplerian disk. A&A, 443:945–954.

[Pinte et al., 2006] Pinte, C., Ménard, F., Duchêne, G., and Bastien, P. (2006). Monte Carlo radiative transfer in protoplanetary disks. A&A, 459:797–804.

[Pollack et al., 1996] Pollack, J. B., Hubickyj, O., Bodenheimer, P., Lissauer, J. J., Podolak, M., and Greenzweig, Y. (1996). Formation of the Giant Planets by Concurrent Accretion of Solids and Gas. *Icarus*, 124:62–85.

[Poncelet et al., 2007] Poncelet, A., Doucet, C., Perrin, G., Sol, H., and Lagage, P. O. (2007). An original interferometric study of NGC 1068 with VISIR BURST mode images. A&A, 472:823–831.

[Pontoppidan et al., 2008] Pontoppidan, K. M., Blake, G. A., van Dishoeck, E. F., Smette, A., Ireland, M. J., and Brown, J. (2008). Spectroastrometric Imaging of Molecular Gas within Protoplanetary Disk Gaps. ApJ, 684:1323–1329.

[Puget et al., 1985] Puget, J. L., Leger, A., and Boulanger, F. (1985). Contribution of large polycyclic aromatic molecules to the infrared emission of the interstellar medium. A&A, 142:L19–L22.

[Qi et al., 2004] Qi, C., Ho, P. T. P., Wilner, D. J., Takakuwa, S., Hirano, N., Ohashi, N., Bourke, T. L., Zhang, Q., Blake, G. A., Hogerheijde, M., Saito, M., Choi, M., and Yang, J. (2004). Imaging the Disk around TW Hydrae with the Submillimeter Array. ApJ, 616:L11–L14.

[Regan and Haehnelt, 2008] Regan, J. A. and Haehnelt, M. G. (2008). The formation of compact massive self-gravitating discs in metal-free haloes with virial temperatures of ˜ 13000-30000 K. *ArXiv e-prints*.

[Riaud et al., 2003] Riaud, P., Boccaletti, A., Baudrand, J., and Rouan, D. (2003). The Four-Quadrant Phase Mask Coronagraph. III. Laboratory Performance. PASP, 115:712–719.

[Richter et al., 2005] Richter, M. J., Lacy, J. H., Jaffe, D. T., Bitner, M. A., Greathouse, T. K., and Blake, G. A. (2005). The TEXES/IRTF H_2 Survey of Disk Sources. In *Bulletin of the American Astronomical Society*, volume 37 of *Bulletin of the American Astronomical Society*, pages 1163–+.

[Robertson, 1986] Robertson, J. G. (1986). Optimal extraction of single-object spectra from observations with two-dimensional detectors. PASP, 98:1220–1231.

[Rodríguez et al., 2005] Rodríguez, L. F., Loinard, L., D'Alessio, P., Wilner, D. J., and Ho, P. T. P. (2005). IRAS 16293-2422B: A Compact, Possibly Isolated Protoplanetary Disk in a Class 0 Object. ApJ, 621:L133–L136.

[Rothman et al., 1992] Rothman, L. S., Gamache, R. R., Tipping, R. H., Rinsland, C. P., Smith, M. A. H., Benner, D. C., Devi, V. M., Flaud, J.-M., Camy-Peyret, C., and Perrin, A. (1992). The HITRAN molecular data base - Editions of 1991 and 1992. *Journal of Quantitative Spectroscopy and Radiative Transfer*, 48:469–507.

[Rouan et al., 2007] Rouan, D., Baudrand, J., Boccaletti, A., Baudoz, P., Mawet, D., and Riaud, P. (2007). The Four Quadrant Phase Mask Coronagraph and its avatars. *Comptes Rendus Physique*, 8:298–311.

[Sako et al., 2003] Sako, S., Okamoto, Y. K., Kataza, H., Miyata, T., Takubo, S., Honda, M., Fujiyoshi, T., Onaka, T., and Yamashita, T. (2003). Improvements in Operating the Raytheon 320 x 240 Pixel Si:As Impurity Band Conduction Mid-Infrared Array. PASP, 115:1407–1418.

[Salyk et al., 2008] Salyk, C., Pontoppidan, K. M., Blake, G. A., Lahuis, F., van Dishoeck, E. F., and Evans, II, N. J. (2008). H_2O and OH Gas in the Terrestrial Planet-forming Zones of Protoplanetary Disks. ApJ, 676:L49–L52.

[Scholz et al., 2003] Scholz, R.-D., McCaughrean, M. J., Lodieu, N., and Kuhlbrodt, B. (2003). varepsilon Indi B: A new benchmark T dwarf. A&A, 398:L29–L33.

[Siebenmorgen et al., 2000] Siebenmorgen, R., Prusti, T., Natta, A., and Müller, T. G. (2000). Mid infrared emission of nearby Herbig Ae/Be stars. A&A, 361:258–264.

[Starck et al., 2002] Starck, J. L., Pantin, E., and Murtagh, F. (2002). Deconvolution in Astronomy: A Review. PASP, 114:1051–1069.

[Stecklum et al., 1999] Stecklum, B., Käufl, H.-U., and Richichi, A. (1999). The lunar occultation of CW Leo - a great finale for TIMMI. *The Messenger*, 95:25–27.

[Stern, 1994] Stern, S. A. (1994). The detectability of extrasolar terrestrial and giant planets during their luminous final accretion. AJ, 108:2312–2317.

[Sudarsky et al., 2003] Sudarsky, D., Burrows, A., and Hubeny, I. (2003). Theoretical Spectra and Atmospheres of Extrasolar Giant Planets. ApJ, 588:1121–1148.

[Takeuchi et al., 2005] Takeuchi, T., Clarke, C. J., and Lin, D. N. C. (2005). The Differential Lifetimes of Protostellar Gas and Dust Disks. ApJ, 627:286–292.

[Testi et al., 2001] Testi, L., Natta, A., Shepherd, D. S., and Wilner, D. J. (2001). Constraints on Properties of the Protoplanetary Disks around UX Orionis and CQ Tauri. ApJ, 554:1087–1094.

[Thatte et al., 2007] Thatte, N., Abuter, R., Tecza, M., Nielsen, E. L., Clarke, F. J., and Close, L. M. (2007). Very high contrast integral field spectroscopy of AB Doradus C: 9-mag contrast at 0.2arcsec without a coronagraph using spectral deconvolution. MNRAS, 378:1229–1236.

[The et al., 1986] The, P. S., Tjin, H. R. E., Steenman, H., and Wesselius, P. R. (1986). Studies of the Chamaeleon star-forming region. II - The pre-main-sequence stars HD 97048 and HD 97300. A&A, 155:347–355.

[Thi et al., 2001] Thi, W. F., van Dishoeck, E. F., Blake, G. A., van Zadelhoff, G. J., Horn, J., Becklin, E. E., Mannings, V., Sargent, A. I., van den Ancker, M. E., Natta, A., and Kessler, J. (2001). H_2 and CO Emission from Disks around T Tauri and Herbig Ae Pre-Main-Sequence Stars and from Debris Disks around Young Stars: Warm and Cold Circumstellar Gas. ApJ, 561:1074–1094.

[Thi et al., 2004] Thi, W.-F., van Zadelhoff, G.-J., and van Dishoeck, E. F. (2004). Organic molecules in protoplanetary disks around T Tauri and Herbig Ae stars. A&A, 425:955–972.

[Torres et al., 2006] Torres, C. A. O., Quast, G. R., da Silva, L., de La Reza, R., Melo, C. H. F., and Sterzik, M. (2006). Search for associations containing young stars (SACY). I. Sample and searching method. A&A, 460:695–708.

[Valencia et al., 2007] Valencia, D., Sasselov, D. D., and O'Connell, R. J. (2007). Radius and Structure Models of the First Super-Earth Planet. ApJ, 656:545–551.

[van Boekel et al., 2004] van Boekel, R., Waters, L. B. F. M., Dominik, C., Dullemond, C. P., Tielens, A. G. G. M., and de Koter, A. (2004). Spatially and spectrally resolved 10 μm emission in Herbig Ae/Be stars. A&A, 418:177–184.

[van den Ancker et al., 2004] van den Ancker, M. E., Acke, B., and Dullemond, C. P. (2004). [O I] 6300 A Emission from Disks Around Herbig Ae/Be Stars. *ArXiv Astrophysics e-prints*.

[van den Ancker et al., 1998] van den Ancker, M. E., de Winter, D., and Tjin A Djie, H. R. E. (1998). HIPPARCOS photometry of Herbig Ae/Be stars. A&A, 330:145–154.

[van der Plas et al., 2008] van der Plas, G., van den Ancker, M. E., Acke, B., Carmona, A., Dominik, C., Fedele, D., and Waters, L. B. F. M. (2008). Spatially resolved 4.7 μm CO fundamental emission in two protoplanetary disks. *ArXiv e-prints*.

[Verhoeff et al., 2009] Verhoeff, A. P., Min, M., Acke, B., van Boekel, R., Pantin, E., Waters, L. B. F. M., Tielens, A. G. G. M., van den Ancker, M., Mulders, G. D., de Koter, A., and Bouwman, J. (2009). HD95881: A gas rich to gas poor transition disk ? A&A.

[Verschueren et al., 1999] Verschueren, W., David, M., and Griffin, R. E. M. (1999). Accuracy of radial-velocity measurements for early-type stars. I. Spectral-type mismatch in A-type synthetic spectra. A&AS, 140:107–123.

[Wang et al., 2006] Wang, Z., Chakrabarty, D., and Kaplan, D. L. (2006). A debris disk around an isolated young neutron star. Nature, 440:772–775.

[Weidenschilling, 1977] Weidenschilling, S. J. (1977). Aerodynamics of solid bodies in the solar nebula. MNRAS, 180:57–70.

[Weidenschilling and Cuzzi, 1993] Weidenschilling, S. J. and Cuzzi, J. N. (1993). Formation of planetesimals in the solar nebula. In Levy, E. H. and Lunine, J. I., editors, *Protostars and Planets III*, pages 1031–1060.

[Weintraub et al., 2000] Weintraub, D. A., Kastner, J. H., and Bary, J. S. (2000). Detection of Quiescent Molecular Hydrogen Gas in the Circumstellar Disk of a Classical T Tauri Star. ApJ, 541:767–771.

[Wetherill, 1990] Wetherill, G. W. (1990). Formation of the earth. *Annual Review of Earth and Planetary Sciences*, 18:205–256.

[Wisdom, 1980] Wisdom, J. (1980). The resonance overlap criterion and the onset of stochastic behavior in the restricted three-body problem. AJ, 85:1122–1133.

[Wolf et al., 2007] Wolf, S., Moro-Martin, A., and D'Angelo, G. (2007). Signatures of planets in protoplanetary and debris disks. Planet. Space Sci., 55:569–581.

[Wuchterl et al., 2000] Wuchterl, G., Guillot, T., and Lissauer, J. J. (2000). Giant Planet Formation. *Protostars and Planets IV*, pages 1081–+.

[Wyatt, 1999] Wyatt, M. C. (1999). *Signatures of planets in the observable structure of circumstellar debris disks*. PhD thesis, AA(Royal Observatory, Blackford Hill, Edinburgh EH9 3HJ, UK; ¡EMAIL¿wyatt@roe.ac.uk¡/EMAIL¿).

100 ADS entries over 16 years

This section presents very roughly the 100 ADS entries concerning my work over 16 years of research. I have deliberately not sorted out these references between refereed papers, conference proceedings or even observation proposals because all of them are fully part of my work. All these articles are available upon request to eric.pantin@cea.fr.

References

[1] E. Galliano, D. Alloin, E. Pantin, G. L. Granato, P. Delva, L. Silva, P. O. Lagage, and P. Panuzzo. Extremely massive young clusters in NGC 1365. A&A, 492:3–22, December 2008.

[2] C. Martin-Zädi, P.-O. Lagage, E. Pantin, E. Habart, F. Ménard, J.-C. Augereau, and C. Pinte. Molecular hydrogen in the disk of the Herbig star HD 97048. In C. Charbonnel, F. Combes, and R. Samadi, editors, *SF2A-2008: Proceedings of the Annual meeting of the French Society of Astronomy and Astrophysics Eds.: C. Charbonnel, F. Combes and R. Samadi. Available online at http://proc.sf2a.asso.fr, p.503*, pages 503–+, November 2008.

[3] J.-C. Augereau, O. Absil, J. Bouvier, G. Duchêne, J.-F. Lestrade, S. Maret, C. Martin-Zaïdi, F. Ménard, A. Morbidelli, J. Olofsson, E. Pantin, C. Pinte, and P. Thébault. DIGIT, GASPS, DEBRIS and DUNES: four HERSCHEL Open Time Key Programs to survey the dust cycle in circumstellar disks. In C. Charbonnel, F. Combes, and R. Samadi, editors, *SF2A-2008: Proceedings of the Annual meeting of the French Society of Astronomy and Astrophysics Eds.: C. Charbonnel, F. Combes and R. Samadi. Available online at http://proc.sf2a.asso.fr, p.443*, pages 443–+, November 2008.

[4] P. André, V. Minier, P. Gallais, V. Revéret, J. Le Pennec, L. Rodriguez, O. Boulade, E. Doumayrou, D. Dubreuil, M. Lortholary, J. Martignac, M. Talvard, C. De Breuck, G. Hamon, N. Schneider, S. Bontemps, P. O. Lagage, E. Pantin, H. Roussel, M. Miller, C. R. Purcell, T. Hill, and J. Stutzki. First 450 μm dust continuum mapping of the massive star-forming region NGC 3576 with the P-ArTéMiS bolometer camera. A&A, 490:L27–L30, November 2008.

[5] J. M. Bonnet-Bidaud and E. Pantin. ADONIS high contrast infrared imaging of Sirius-B. A&A, 489:651–655, October 2008.

[6] C. Martin-Zaïdi, E. F. van Dishoeck, J.-C. Augereau, P.-O. Lagage, and E. Pantin. Searching for molecular hydrogen mid-infrared emission in the circumstellar environments of Herbig Be stars. A&A, 489:601–605, October 2008.

[7] R. Siebenmorgen, M. Haas, E. Pantin, E. Krügel, C. Leipski, H. U. Käufl, P. O. Lagage, A. Moorwood, A. Smette, and M. Sterzik. Nuclear activity in nearby galaxies. Mid-infrared imaging with the VLT. A&A, 488:83–90, September 2008.

[8] M. Talvard, P. André, L. Rodriguez, Y. Le-Pennec, C. De Breuck, V. Revéret, P. Agnèse, O. Boulade, E. Doumayrou, D. Dubreuil, E. Ercolani, P. Gallais, B. Horeau, P. Lagage, B. Leriche, M. Lortholary, J. Martignac, V. Minier, E. Pantin, D. Rabanus, J. Relland, and G. Willmann.

Recent results obtained on the APEX 12 m antenna with the ArTeMiS prototype camera. In *Society of Photo-Optical Instrumentation Engineers (SPIE) Conference Series*, volume 7020 of *Society of Photo-Optical Instrumentation Engineers (SPIE) Conference Series*, August 2008.

[9] E. Pantin, R. Siebenmorgen, C. Cavarroc, and M. F. Sterzik. Direct thermal imaging of circumstellar discs and exo-planets. In *Society of Photo-Optical Instrumentation Engineers (SPIE) Conference Series*, volume 7014 of *Society of Photo-Optical Instrumentation Engineers (SPIE) Conference Series*, August 2008.

[10] E. Pantin, C. Doucet, H. U. Käufl, P. O. Lagage, R. Siebenmorgen, and M. Sterzik. Lessons learned from VISIR. In *Society of Photo-Optical Instrumentation Engineers (SPIE) Conference Series*, volume 7014 of *Society of Photo-Optical Instrumentation Engineers (SPIE) Conference Series*, August 2008.

[11] B. R. Brandl, R. Lenzen, E. Pantin, A. Glasse, J. Blommaert, L. Venema, F. Molster, R. Siebenmorgen, H. Boehnhardt, E. van Dishoeck, P. van der Werf, T. Henning, W. Brandner, P.-O. Lagage, T. J. T. Moore, M. Baes, C. Waelkens, C. Wright, H. U. Käufl, S. Kendrew, R. Stuik, and L. Jolissaint. METIS: the mid-infrared E-ELT imager and spectrograph. In *Society of Photo-Optical Instrumentation Engineers (SPIE) Conference Series*, volume 7014 of *Society of Photo-Optical Instrumentation Engineers (SPIE) Conference Series*, August 2008.

[12] H. Bouy, N. Huélamo, C. Pinte, J. Olofsson, D. Barrado Y Navascués, E. L. Martín, E. Pantin, J.-L. Monin, G. Basri, J.-C. Augereau, F. Ménard, G. Duvert, G. Duchêne, F. Marchis, A. Bayo, S. Bottinelli, B. Lefort, and S. Guieu. Structural and compositional properties of brown dwarf disks: the case of 2MASS J04442713+2512164. A&A, 486:877–890, August 2008.

[13] A. F. Cheng, A. A. Simon-Miller, H. A. Weaver, K. H. Baines, G. S. Orton, P. A. Yanamandra-Fisher, O. Mousis, E. Pantin, L. Vanzi, L. N. Fletcher, J. R. Spencer, S. A. Stern, J. T. Clarke, M. J. Mutchler, and K. S. Noll. Changing Characteristics of Jupiter's Little Red SPOT. AJ, 135:2446–2452, June 2008.

[14] F. Rahoui, S. Chaty, P.-O. Lagage, and E. Pantin. Multi-wavelength observations of Galactic hard X-ray sources discovered by INTEGRAL. II. The environment of the companion star. A&A, 484:801–813, June 2008.

[15] F. Rahoui, S. Chaty, P.-O. Lagage, and E. Pantin. Mid-infrared Observations of Twelve Supergiant X-ray Binaries Discovered by INTEGRAL. In R. M. Bandyopadhyay, S. Wachter, D. Gelino, and C. R. Gelino, editors, *A Population Explosion: The Nature & Evolution of X-ray Binaries in Diverse Environments*, volume 1010 of *American Institute of Physics Conference Series*, pages 242–246, May 2008.

[16] M. van den Ancker, B. Acke, A. Bik, J. Bouwman, C. Dominik, K. Dullemond, T. Henning, M. Min, E. Pantin, X. Tielens, A. Verhoeff, C. Waelkens, L. Waters, and R. van Boekel. Structure and composition of disks surrounding Herbig Be stars. In *Spitzer Proposal ID #50180*, pages 50180–+, March 2008.

[17] V. Minier, L. Olmi, P.-O. Lagage, L. Spinoglio, G. A. Durand, E. Daddi, D. Galilei, H. Gallée, C. Kramer, D. Marrone, E. Pantin, L. Sabbatini, N. Schneider, N. F. H. Tothill, L. Valenziano, and C. Veyssière. Submm/FIR Astronomy in Antarctica: Potential for a large telescope facility. In H. Zinnecker, N. Epchtein, and H. Rauer, editors, *EAS Publications Series*, volume 33 of *EAS Publications Series*, pages 21–40, 2008.

[18] T. Encrenaz, G. S. Orton, C. Leyrat, R. C. Puetter, A. J. Friedson, and E. Pantin. First Thermal IR Images of Neptune: Evidence forSouthern Polar Heating and Methane Escape. *The Messenger*, 130:23–+, December 2007.

[19] H. U. Käufl, D. Nürnberger, L. Vanzi, P. Baksai, D. Dobrzycka, J. Jimenez, A. Leiva, L. Lundin, M. Marchesi, P. Mardones, L. Mehrgan, J.-F. Pirard, C. Rojas, D. Salazar, R. Siebenmorgen, A. Silber, M. van den Ancker, U. Weilenmann, G. Durand, E. Pantin, and M. Moerchen. Peering into the Dust: News from VISIR. *The Messenger*, 130:8–+, December 2007.

[20] C. Martin-Zaïdi, P.-O. Lagage, E. Pantin, and E. Habart. VISIR observation of H2 emission from the cs disk around the Herbig Ae star HD97048. In *Molecules in Space and Laboratory*, December 2007.

[21] G. P. Tozzi, H. Boehnhardt, L. Kolokolova, T. Bonev, E. Pompei, S. Bagnulo, N. Ageorges, L. Barrera, O. Hainaut, H. U. Käufl, F. Kerber, G. Locurto, O. Marco, E. Pantin, H. Rauer, I. Saviane, C. Sterken, and M. Weiler. Dust observations of Comet 9P/Tempel 1 at the time of the Deep Impact. A&A, 476:979–988, December 2007.

[22] A. F. Cheng, A. Simon-Miller, H. A. Weaver, K. H. Baines, G. S. Orton, P. A. Yanamandra-Fisher, O. Mousis, E. Pantin, L. Vanzi, L. N. Fletcher, J. Spencer, A. Stern, and New Horizons Team. Structure and Dynamics of the Little Red Spot on Jupiter. In *Bulletin of the American Astronomical Society*, volume 38 of *Bulletin of the American Astronomical Society*, pages 444–+, October 2007.

[23] M. Haas, R. Siebenmorgen, E. Pantin, H. Horst, A. Smette, H.-U. Käufl, P.-O. Lagage, and R. Chini. VISIR/VLT mid-infrared imaging of Seyfert nuclei: nuclear dust emission and the Seyfert-2 dichotomy. A&A, 473:369–376, October 2007.

[24] M. Haas, R. Siebenmorgen, E. Pantin, H. Horst, A. Smette, H.-U. Kaufl, P.-O. Lagage, and R. Chini. VISIR/VLT mid-infrared imaging of Seyfert

nuclei (Haas+, 2007). *VizieR Online Data Catalog*, 347:30369–+, September 2007.

[25] C. Martin-Zaïdi, P.-O. Lagage, E. Pantin, and E. Habart. Detection of Warm Molecular Hydrogen in the Circumstellar Disk around the Herbig Ae Star HD 97048. ApJ, 666:L117–L120, September 2007.

[26] H. Boehnhardt, E. Pompei, G. P. Tozzi, O. Hainaut, N. Ageorges, S. Bagnulo, L. Barrera, T. Bonev, H. U. Käufl, F. Kerber, G. Locurto, O. Marco, E. Pantin, H. Rauer, I. Saviane, F. Selman, C. Sterken, and M. Weiler. Broad- and narrowband visible imaging of comet 9P/Tempel 1 at ESO around the time of the Deep Impact event. A&A, 470:1175–1183, August 2007.

[27] C. Doucet, E. Habart, E. Pantin, C. Dullemond, P. O. Lagage, C. Pinte, G. Duchêne, and F. Ménard. HD 97048: a closer look at the disk. A&A, 470:625–631, August 2007.

[28] C. Martin-Zaïdi, P.-O. Lagage, E. Pantin, and E. Habart.

[29] C. Martin-Zaïdi, M. Deleuil, J.-C. Bouret, C. Doucet, P.-O. Lagage, and E. Pantin. Gaseous component in the circumstellar environment of Herbig Ae/Be stars. In D. Barret, F. Casoli, G. Lagache, A. Lecavelier, and L. Pagani, editors, *SF2A-2006: Semaine de l'Astrophysique Francaise*, pages 585–+, June 2006.

[30] C. Doucet, P. Lagage, and E. Pantin. High resolution Mid-Infrared Imaging of Dust Disks Structures around Herbig Ae Stars with VISIR. In V. Coudé Du Foresto, D. Rouan, and G. Rousset, editors, *Visions for Infrared Astronomy, Instrumentation, Mesure, Métrologie*, pages 25–30, 2006.

[31] G. Orton, P. Parrish, P. Yanamandra-Fisher, K. Baines, O. Mousis, E. Pantin, T. Fujiyoshi, T. Fuse, and A. Simon-Miller. Multi-spectral remote sensing of the vortex formerly known as White Oval BA: Temperature structure and cloud properties. In *European Planetary Science Congress 2006*, pages 195–+, 2006.

[32] N. Huélamo, H. Bouy, M. Sterzik, E. Pantin, and E. L. Martín. VISIR/VLT observations of brown dwarfs in Upper Scorpius. *Astronomische Nachrichten*, 326:1022–1023, December 2005.

[33] K. J. Meech, N. Ageorges, M. F. A'Hearn, C. Arpigny, A. Ates, J. Aycock, S. Bagnulo, J. Bailey, R. Barber, L. Barrera, R. Barrena, J. M. Bauer, M. J. S. Belton, F. Bensch, B. Bhattacharya, N. Biver, G. Blake, D. Bockelée-Morvan, H. Boehnhardt, B. P. Bonev, T. Bonev, M. W. Buie, M. G. Burton, H. M. Butner, R. Cabanac, R. Campbell, H. Campins, M. T. Capria, T. Carroll, F. Chaffee, S. B. Charnley, R. Cleis, A. Coates, A. Cochran, P. Colom, A. Conrad, I. M. Coulson, J. Crovisier, J. deBuizer, R. Dekany, J. de Léon, N. Dello Russo, A. Delsanti, M. DiSanti,

J. Drummond, L. Dundon, P. B. Etzel, T. L. Farnham, P. Feldman, Y. R. Fernández, M. D. Filipovic, S. Fisher, A. Fitzsimmons, D. Fong, R. Fugate, H. Fujiwara, T. Fujiyoshi, R. Furusho, T. Fuse, E. Gibb, O. Groussin, S. Gulkis, M. Gurwell, E. Hadamcik, O. Hainaut, D. Harker, D. Harrington, M. Harwit, S. Hasegawa, C. W. Hergenrother, P. Hirst, K. Hodapp, M. Honda, E. S. Howell, D. Hutsemékers, D. Iono, W.-H. Ip, W. Jackson, E. Jehin, Z. J. Jiang, G. H. Jones, P. A. Jones, T. Kadono, U. W. Kamath, H. U. Käufl, T. Kasuga, H. Kawakita, M. S. Kelley, F. Kerber, M. Kidger, D. Kinoshita, M. Knight, L. Lara, S. M. Larson, S. Lederer, C.-F. Lee, A. C. Levasseur-Regourd, J. Y. Li, Q.-S. Li, J. Licandro, Z.-Y. Lin, C. M. Lisse, G. LoCurto, A. J. Lovell, S. C. Lowry, J. Lyke, D. Lynch, J. Ma, K. Magee-Sauer, G. Maheswar, J. Manfroid, O. Marco, P. Martin, G. Melnick, S. Miller, T. Miyata, G. H. Moriarty-Schieven, N. Moskovitz, B. E. A. Mueller, M. J. Mumma, S. Muneer, D. A. Neufeld, T. Ootsubo, D. Osip, S. K. Pandea, E. Pantin, R. Paterno-Mahler, B. Patten, B. E. Penprase, A. Peck, G. Petitpas, N. Pinilla-Alonso, J. Pittichova, E. Pompei, T. P. Prabhu, C. Qi, R. Rao, H. Rauer, H. Reitsema, S. D. Rodgers, P. Rodriguez, R. Ruane, G. Ruch, W. Rujopakarn, D. K. Sahu, S. Sako, I. Sakon, N. Samarasinha, J. M. Sarkissian, I. Saviane, M. Schirmer, P. Schultz, R. Schulz, P. Seitzer, T. Sekiguchi, F. Selman, M. Serra-Ricart, R. Sharp, R. L. Snell, C. Snodgrass, T. Stallard, G. Stecklein, C. Sterken, J. A. Stüwe, S. Sugita, M. Sumner, N. Suntzeff, R. Swaters, S. Takakuwa, N. Takato, J. Thomas-Osip, E. Thompson, A. T. Tokunaga, G. P. Tozzi, H. Tran, M. Troy, C. Trujillo, J. Van Cleve, R. Vasundhara, R. Vazquez, F. Vilas, G. Villanueva, K. von Braun, P. Vora, R. J. Wainscoat, K. Walsh, J. Watanabe, H. A. Weaver, W. Weaver, M. Weiler, P. R. Weissman, W. F. Welsh, D. Wilner, S. Wolk, M. Womack, D. Wooden, L. M. Woodney, C. Woodward, Z.-Y. Wu, J.-H. Wu, T. Yamashita, B. Yang, Y.-B. Yang, S. Yokogawa, A. C. Zook, A. Zauderer, X. Zhao, X. Zhou, and J.-M. Zucconi. Deep Impact: Observations from a Worldwide Earth-Based Campaign. *Science*, 310:265–269, October 2005.

[34] E. Galliano, E. Pantin, D. Alloin, and P. O. Lagage. Mid-infrared imaging of NGC 1068 with VISIR at the Very Large Telescope. MNRAS, 363:L1–L5, October 2005.

[35] C. Ferrari, P. Galdemard, P. O. Lagage, E. Pantin, and C. Quoirin. Imaging Saturn's rings with CAMIRAS: thermal inertia of B and C rings. A&A, 441:379–389, October 2005.

[36] H.-U. Kaufl, N. Ageorges, S. Bagnulo, L. Barrera, H. Böhnhardt, T. Bonev, O. Hainaut, E. Jehin, F. Kerber, G. Locurto, J. Manfroid, O. Marco, E. Pantin, E. Pompei, I. Saviene, F. Selman, C. Sterken, H. Rauer, and G. P. M. Tozzi. Deep Impact at ESO Telescopes. *The Messenger*, 121:11–16, September 2005.

[37] C. Leyrat, C. Ferrari, P. O. Lagage, and E. Pantin. VISIR/VLT observations of Saturn's rings. In *Bulletin of the American Astronomical Society*,

volume 37 of *Bulletin of the American Astronomical Society*, pages 764–+, August 2005.

[38] E. Galliano, D. Alloin, E. Pantin, P. O. Lagage, and O. Marco. Mid-infrared imaging of active galaxies. Active nuclei and embedded star clusters. A&A, 438:803–820, August 2005.

[39] E. Pantin, J. Bouwman, and P. O. Lagage. An emission ring at 20.5 μm around the HAEBE star AB Aurigæ: Unveiling the disk structure. A&A, 437:525–530, July 2005.

[40] M. F. Sterzik, E. Pantin, M. Hartung, N. Huelamo, H. U. Käufl, A. Kaufer, C. Melo, D. Nürnberger, R. Siebenmorgen, and A. Smette. The cool atmospheres of the binary brown dwarf ϵ Indi B. A&A, 436:L39–L42, June 2005.

[41] E. Pantin, O.-P. Lagage, A. Claret, C. Doucet, A. Kaufer, H.-U. Käufl, J.-W. Pel, R. F. Peletier, R. Siebenmorgen, A. Smette, and M. Sterzik. VISIR, a Taste of Scientific Potential. *The Messenger*, 119:25–29, March 2005.

[42] E. Pantin, P. O. Lagage, C. Doucet, J. W. Pel, R. F. Peletier, and A. Claret. View of Beta Pictoris by the VLT. In *Protostars and Planets V*, pages 8162–+, 2005.

[43] C. Doucet, E. Pantin, P. O. Lagage, E. Habart, C. Pinte, and G. Duchene. Imaging Dust Disks Structures Around Herbig Ae Stars with VISIR. In *Protostars and Planets V*, pages 8127–+, 2005.

[44] C. Doucet, E. Pantin, and P.-O. Lagage. 20 microns views on intermediate Haebe dust disk. In F. Combes, D. Barret, T. Contini, F. Meynadier, and L. Pagani, editors, *SF2A-2004: Semaine de l'Astrophysique Francaise*, pages 73–+, December 2004.

[45] P. O. Lagage, J. W. Pel, M. Authier, J. Belorgey, A. Claret, C. Doucet, D. Dubreuil, G. Durand, E. Elswijk, P. Girardot, H. U. Käufl, G. Kroes, M. Lortholary, Y. Lussignol, M. Marchesi, E. Pantin, R. Peletier, J.-F. Pirard, J. Pragt, Y. Rio, T. Schoenmaker, R. Siebenmorgen, A. Silber, A. Smette, M. Sterzik, and C. Veyssiere. Successful Commissioning of VISIR: The Mid-Infrared VLT Instrument. *The Messenger*, 117:12–16, September 2004.

[46] O. Schütz, H. Böhnhardt, E. Pantin, M. Sterzik, S. Els, J. Hahn, and T. Henning. A search for circumstellar dust disks with ADONIS. A&A, 424:613–618, September 2004.

[47] O. Schütz, H. Böhnhardt, E. Pantin, S. Els, J. Hahn, and M. Sterzik. A Search for Circum-stellar Dust Disks with ADONIS. *Astronomische Nachrichten Supplement*, 324:58–+, July 2003.

[48] H. Campins, J. Licandro, J. Guerra, M. Chamberlain, and E. Pantin. Variations in the Nuclear Spectra of Comet 28P/Neujmin 1. In *Bulletin of the American Astronomical Society*, volume 35 of *Bulletin of the American Astronomical Society*, pages 1011–+, May 2003.

[49] P.-O. Lagage, J.-W. Pel, A. Claret, S. Damstra, D. Dubreuil, G. A. Durand, E. Elswijk, P. Galdemard, A. N. de Jong, G. Kroes, C. Lyraud, E. Pantin, J. Pragt, Y. Rio, A. Schoenmaker, M. Authier, J. Belorgey, J.-F. Gournay, M. Lortholary, Y. Lussignol, and C. Veyssiere. Characterization in the laboratory of VISIR, the mid-infrared imager and spectrometer for the VLT. In M. Iye and A. F. M. Moorwood, editors, *Society of Photo-Optical Instrumentation Engineers (SPIE) Conference Series*, volume 4841 of *Society of Photo-Optical Instrumentation Engineers (SPIE) Conference Series*, pages 923–931, March 2003.

[50] A. J. Claret, P.-O. Lagage, E. Pantin, D. Dubreuil, P. Galdemard, A. Schoenmaker, and J.-W. Pel. Calibration of VISIR, the VLT mid-infrared imager/spectrometer. In M. Iye and A. F. M. Moorwood, editors, *Society of Photo-Optical Instrumentation Engineers (SPIE) Conference Series*, volume 4841 of *Society of Photo-Optical Instrumentation Engineers (SPIE) Conference Series*, pages 252–262, March 2003.

[51] J. Bouwman and E. Pantin. Mid-infrared imaging and modeling of the dust disk around the PMS star AB Aurigae. In *Astrophysics of Dust*, 2003.

[52] E. Pantin. Deconvolution of astronomical data: what for and where do we go? In J.-L. Starck and F. D. Murtagh, editors, *Society of Photo-Optical Instrumentation Engineers (SPIE) Conference Series*, volume 4847 of *Society of Photo-Optical Instrumentation Engineers (SPIE) Conference Series*, pages 144–155, December 2002.

[53] J. L. Starck, E. Pantin, and F. Murtagh. Deconvolution in Astronomy: A Review. PASP, 114:1051–1069, October 2002.

[54] J.-C. Augereau, P. O. Lagage, and E. Pantin. Observability of extra-solar planetary disks in the mid-infrared with VLT/VISIR and NGST/MIRI. In F. Combes and D. Barret, editors, *SF2A-2002: Semaine de l'Astrophysique Francaise*, pages 603–+, June 2002.

[55] L. Koch-Miramond, M. Haas, E. Pantin, P. Podsiadlowski, T. Naylor, and M. Sauvage. Determination of limits on disc masses around six pulsars at 15 and 90 μm. A&A, 387:233–239, May 2002.

[56] E. Pantin and S. Charnoz. From the observation of circumstellar dust disks to orbital structure. In *Bulletin of the American Astronomical Society*, volume 33 of *Bulletin of the American Astronomical Society*, pages 1151–+, November 2001.

[57] S. G. Els, M. F. Sterzik, F. Marchis, E. Pantin, M. Endl, and M. Kürster. A second substellar companion in the Gliese 86 system. A brown dwarf in an extrasolar planetary system. A&A, 370:L1–L4, April 2001.

[58] T. Douvion, P. O. Lagage, and E. Pantin. Cassiopeia A dust composition and heating. A&A, 369:589–593, April 2001.

[59] E. Pantin, S. Els, F. Marchis, M. Endl, M. Kürster, and M. Sterzik. First Detection of a Dust Disk around Iota Horologii, a Southern Star Orbitted by an Extrasolar Giant Planet. In *Bulletin of the American Astronomical Society*, volume 32 of *Bulletin of the American Astronomical Society*, pages 1646–+, December 2000.

[60] D. Alloin, E. Pantin, P. O. Lagage, and G. L. Granato. 0.6 resolution images at 11 and 20 mu m of the active galactic nucleus in NGC 1068. A&A, 363:926–932, November 2000.

[61] E. Pantin, C. Waelkens, and P. O. Lagage. ADONIS observations of the HD 100546 circumstellar dust disk. A&A, 361:L9–L12, September 2000.

[62] D. M. Neumann and E. Pantin. X-ray Profiles of Clusters - Beyond the b-Model. In M. Plionis and I. Georgantopoulos, editors, *Large Scale Structure in the X-ray Universe, Proceedings of the 20-22 September 1999 Workshop, Santorini, Greece, eds. Plionis, M. Georgantopoulos, I., Atlantisciences, Paris, France, p.391*, pages 391–+, March 2000.

[63] E. Pantin and D. Le Mignant. 17 μm imaging of eta Carinaea: an onion-like structure for the lobes? A&A, 355:155–164, March 2000.

[64] P.-O. Lagage and E. Pantin. The β Pictoris Dust Disk at 20 Microns. In G. Garzón, C. Eiroa, D. de Winter, and T. J. Mahoney, editors, *Disks, Planetesimals, and Planets*, volume 219 of *Astronomical Society of the Pacific Conference Series*, pages 393–+, 2000.

[65] E. Pantin, C. Waelkens, K. Malfait, and P. O. Lagage. ADONIS Detection and Models of the Pre-Main-Sequence Disk of HD 100546 (Contributed Talk). In G. Garzón, C. Eiroa, D. de Winter, and T. J. Mahoney, editors, *Disks, Planetesimals, and Planets*, volume 219 of *Astronomical Society of the Pacific Conference Series*, pages 281–+, 2000.

[66] C. Ferrari, P. Galdemard, P. O. Lagage, and E. Pantin. Thermal inertia of Saturn's ring particles. In *Bulletin of the American Astronomical Society*, volume 31 of *Bulletin of the American Astronomical Society*, pages 1588–+, December 1999.

[67] E. Pantin, C. Waelkens, and K. Malfait. SWS observations of the β Pictoris dust disk. In P. Cox and M. Kessler, editors, *The Universe as Seen by ISO*, volume 427 of *ESA Special Publication*, pages 385–+, March 1999.

[68] P. O. Lagage, de Boula O., C. J. Cesarsky, T. Douvion, V. Mannings, E. Pantin, and A. I. Sargent. ISOCAM spectro-imaging observations of the β-Pictoris dust disk. In P. Cox and M. Kessler, editors, *The Universe as Seen by ISO*, volume 427 of *ESA Special Publication*, pages 207–+, March 1999.

[69] J. L. Starck, A. Abergel, H. Aussel, M. Sauvage, R. Gastaud, A. Claret, X. Desert, C. Delattre, and E. Pantin. ISOCAM data processing. A&AS, 134:135–148, January 1999.

[70] E. Pantin, P. O. Lagage, and P. Artymowicz. Mid-infrared images and models of the beta Pictoris dust disk. A&A, 327:1123–1136, November 1997.

[71] P. Galdemard, B. Mosser, P. O. Lagage, R. Jouan, P. Masse, and E. Pantin. 3-D analysis of the seismic response of Jupiter to the SL9 impacts: application to the CAMIRAS infrared images. Planet. Space Sci., 45:1223–1229, October 1997.

[72] P. Galdemard, P. O. Lagage, D. Dubreuil, R. Jouan, P. Masse, E. Pantin, and D. Bockelée-Morvan. Mid-Infrared Spectro-Imaging Observations Of Comet Hale-Bopp. *Earth Moon and Planets*, 78:271–277, July 1997.

[73] J.-L. Starck and E. Pantin. Astronomical Images Restoration by the Multiscale Maximum Entropy Method. In G. J. Babu and E. D. Feigelson, editors, *Statistical Challenges in Modern Astronomy II*, pages 405–+, 1997.

[74] E. Pantin and J.-L. Starck. Deconvolution of astronomical images using the multiscale maximum entropy method. A&AS, 118:575–585, September 1996.

[75] B. Mosser, P. Galdemard, P. Lagage, E. Pantin, M. Sauvage, P. Lognonne, D. Gautier, F. Billebaud, T. Livengood, and H. U. Kaufl. Impact Seismology: A Search for Primary Pressure Waves Following Impacts A and H. *Icarus*, 121:331–340, June 1996.

[76] J.-L. Starck and E. Pantin. Multiscale maximum entropy images restoration. *Vistas in Astronomy*, 40:563–569, 1996.

[77] E. Pantin and P.-O. Lagage. Composition and Distribution of Dust in the β-Pictoris Disk. In H. U. Käufl and R. Siebenmorgen, editors, *The Role of Dust in the Formation of Stars*, pages 207–+, 1996.

[78] J.-L. Starck and E. Pantin. Deconvolution by the Multiscale Maximum Entropy Method. In G. H. Jacoby and J. Barnes, editors, *Astronomical Data Analysis Software and Systems V*, volume 101 of *Astronomical Society of the Pacific Conference Series*, pages 191–+, 1996.

[79] E. Pantin and P. O. Lagage. Observations à 10 microns et étude des poussières du disque de beta Pictoris. *Journal des Astronomes Francais*, 49:48–+, November 1995.

[80] E. Pantin and J.-L. Starck. Wavelet transform and maximum entropy method. In R. L. Barbour, M. J. Carvlin, and M. A. Fiddy, editors, *Society of Photo-Optical Instrumentation Engineers (SPIE) Conference Series*, volume 2570 of *Society of Photo-Optical Instrumentation Engineers (SPIE) Conference Series*, pages 282–290, October 1995.

[81] P. O. Lagage, P. Galdemard, E. Pantin, R. Jouan, P. Masse, M. Sauvage, G. Olofsson, M. Huldtgren, J. A. Belmonte, C. Regulo, J. M. Rodriguez Espinosa, L. Vidal, B. Mosser, and D. Gautier. SL-9 fragments A, E, H, L, Q1 collision onto Jupiter: Mid-infrared light curves. *Highlights of Astronomy*, 10:633–+, 1995.

[82] P. O. Lagage, P. Galdemard, E. Pantin, R. Jouan, P. Masse, M. Sauvage, G. Olofsson, M. Huldtgren, L. Nordh, J. A. Belmonte, C. Regulo, J. M. Rodriguez Espinosa, L. Vidal, B. Mosser, A. Ulla, and D. Gautier. Collision of Schoemaker-Levy 9 fragments A, E, H, L , Q1 with Jupiter: Mid-infrared light curves. Geophys. Res. Lett., 22:1773–1776, 1995.

[83] B. Mosser, P. Galdemard, R. Jouan, P. Lagage, P. Masse, E. Pantin, M. Sauvage, P. Lognonné, D. Gautier, P. Drossart, P. Merlin, F. Sibille, I. Vauglin, F. Billebaud, T. Livengood, H. U. Käufl, M. Marley, M. Hultdgren, L. Nordh, G. Olofsson, A. Ulla, J. A. Belmonte, C. Regulo, T. Roca-Cortes, M. Selby, J. M. Rodriguez Espinosa, and I. Vidal. Seismic studies of Jupiter at the time of SL-9 impacts. In R. M. West and H. Böhnhardt, editors, *European Southern Observatory Astrophysics Symposia*, volume 52 of *European Southern Observatory Astrophysics Symposia*, pages 397–402, 1995.

[84] P. O. Lagage, P. Galdemard, R. Jouan, P. Masse, E. Pantin, M. Sauvage, B. Mosser, G. Olofsson, M. Huldtgren, L. Nordh, J. A. Belmonte, C. Regulo, T. Roca Cortes, J. M. Rodriguez Espinosa, I. Vidal, D. Gautier, and A. Ulla. 10 μm observations of SL-9 crash onto Jupiter with CAMIRAS at NOT. In R. M. West and H. Böhnhardt, editors, *European Southern Observatory Astrophysics Symposia*, volume 52 of *European Southern Observatory Astrophysics Symposia*, pages 147–152, 1995.

[85] P. O. Lagage and E. Pantin. Dust Depletion in the Inner Disk of Beta-Pictoris as a Possible Indicator of Planets. Nature, 369:628–+, June 1994.

[86] P. O. Lagage, P. Galdernard, R. Jouan, P. Masse, E. Pantin, M. Sauvage, G. Olofsson, M. Huldtgren, J. A. Belmonte, C. Regulo, T. Roca Cortes, J.-M. Rodriguez Espinosa, M. Selby, L. Vidal, B. Mosser, and D. Gautier. 10 μm Observations of SL9 Impacts with CAMIRAS at NOT. In *Bulletin of the American Astronomical Society*, volume 26 of *Bulletin of the American Astronomical Society*, pages 1586–+, June 1994.

[87] P. O. Lagage and E. Pantin. Probing dust around main-sequence stars with TIMMI. *The Messenger*, 75:24–26, March 1994.

[88] S. Cabrit, P. O. Lagage, and E. Pantin. Subarcsec 10 micrometer imaging of bipolar flow sources. *Experimental Astronomy*, 3:151–152, March 1994.

[89] P. O. Lagage and E. Pantin. Sub-arcsec 10 micrometer imaging of beta pictoris and other star disk candidates. *Experimental Astronomy*, 3:57–60, March 1994.

[90] E. Pantin, A. Lecavelier Des Etangs, P. O. Lagage, R. Ferlet, and A. Vidal-Madjar. The β Pictoris Disk Assymetries Revisited. In R. Ferlet and A. Vidal-Madjar, editors, *Circumstellar Dust Disks and Planet Formation*, pages 385–+, 1994.

[91] E. Pantin and P. O. Lagage. Probing the Inner β Pictoris Dust Disk at 10 μm. In R. Ferlet and A. Vidal-Madjar, editors, *Circumstellar Dust Disks and Planet Formation*, pages 75–+, 1994.

[92] S. Cabrit, P. O. Lagage, and E. Pantin. Subarcsec 10 micron Imaging of Bipolar Flow Sources. In I. S. McLean, editor, *Astronomy with Arrays, The Next Generation*, volume 190 of *Astrophysics and Space Science Library*, pages 311–+, 1994.

[93] P. O. Lagage and E. Pantin. Sub-Arcsec 10 micron Imaging of Beta Pictoris and Other Star Disk Candidates. In I. S. McLean, editor, *Astronomy with Arrays, The Next Generation*, volume 190 of *Astrophysics and Space Science Library*, pages 211–+, 1994.

Résumé

Les premiers détecteurs aptes à faire de l'imagerie dans le domaine de l'infrarouge thermique (5-25 μm) depuis le sol sont apparus dans les années 90. Comme nous connaissons relativement mal les objets astrophysiques à ces longueurs d'onde, il y a avait là un très fort potentiel de nouvelles découvertes sur les objets "tièdes" (100-500 K) ou faiblement enfouis.

Ce manuscrit décrit mes travaux de recherche durant les dix dernières années dans les domaines de l'instrumentation infrarouge thermique sur grand télescopes au sol et les applications astrophysiques centrées essentiellement sur de domaine de l'observation de disques circumstellaires autour d'étoiles de pré-séquence principale de type Herbig Ae. En particulier, l'imagerie infrarouge à haute résolution angulaire de ces disques (0.25-1.0 arcsec) m'a permis d'en étudier la géométrie à relativement grande échelle (30-500 UA). La diversité de géometries rencontrée montre que ces disques ont chacun leurs particularités et que l'on commence aujourd'hui à être capables de mettre en évidence leurs processus évolutifs. En outre, certaines structures observées, comme des anneaux brillants d'émission, pourraient être en lien étroit avec le processus de formation planétaire.

Le dernier chapitre est consacré à l'étude des perspectives scientifiques concernant l'observation en infrarouge moyen depuis le sol en lien avec le domaine de la planétologie. Je montre qu'un instrument infrarouge moyen installé sur un Extremely Large Telescope aura la capacité de détecter et de caractériser les planètes géantes extra-solaires les plus proches ($d \lesssim 20$ pc). En outre, un tel instrument présentera des capacités uniques pour étudier la formation planétaire dans les disques protoplanétaires.

Summary

The first mid-infrared (5-25 μm) imaging detectors have appeared in the 90's. Since the properties of the astrophysical objects are relatively poorly known at these wavelength, this domain had a quite large potential to make new scientific discoveries on warm (100-500 K) or relatively embedded objects.

This manuscript describes my work in research during the last ten years in the areas of mid-infrared instrumentation on large ground-based telescopes and the associated astrophysical applications such as the observation of of protoplanetarey circumstellar disks around Herbig Ae pre-main-sequence stars. In particular the thermal imaging of these disks at high angular resolution (0.25-1.0 arcsec) has permitted a careful study of their large-scale geometry (30-500 AU). The variety of the observed geometries shows that each one of these disks has its own particularities; we are just starting to being able to distinguish them in terms of evolutionary status. Furthermore, several peculiar structures observed such as bright rings in the mid-IR could be in direct link with the process of planetary formation in these disks.

The last chapter deals with the scientific perspectives regarding the observations in the mid-IR range from the ground, in link with the exo-planetology sciences. I show that a mid-IR instrument mounted on a Extremely Large Telescope will have the ability to detect and characterize the closest ($d \lesssim 20$ pc) extra-solar planets. In addition such an instrument will feature unique capacities to study the planetary formation process in protoplanetary disks.